HUNGARIAN

Journal of

INDUSTRIAL CHEMISTRY

Edited by

the Hungarian Oil & Gas Research Institute (MÁFKI),
the Research Institute for Heavy Chemical Industries (NEVIKI),
the Research Institute for Technical Chemistry of the
Hungarian Academy of Sciences (MÜKKI),
the Veszprém University of Chemical Engineering (VVE).
Veszprém (Hungary)

Volume 11. **1983.** **Number 1.**

HU ISSN: 0133—0276
CODEN: HJICAI

Editorial Board:

R. Csikós and Gy. Mózes
Hungarian Oil & Gas Research Institute
(MÁFKI) Veszprém

A. Szántó and M. Nádasy
Research Institute for Heavy Chemical Industries
(NEVIKI) Veszprém

T. Blickle and O. Borlai
Research Institute for Technical Chemistry
of the Hungarian Academy of Sciences
(MÜKKI) Veszprém

P. Árva and Gy. Deák
Veszprém University of Chemical Engineering
(VVE) Veszprém

Editor-in Chief:
E. Bodor

Assistant Editor:
J. De Jonge

Veszprém University of Chemical Engineering
(VVE) Veszprém

The "Hungarian Journal of Industrial Chemistry" is a joint publication of the Veszprém scientific institutions of the chemical industry that deals with the results of applied and fundamental research in the field of chemical processes, unit operations and chemical engineering. The papers are published in four numbers at irregular intervals in one annual volume, in the English, Russian, French and German languages

Editorial Office:
Veszprémi Vegyipari Egyetem
"Hungarian Journal of Industrial Chemistry"
H—8201 Veszprém, P.O. Box: 158
Hungary

Orders may be placed with
KULTURA
Foreign Trading Co. for Books and Newspapers
Budapest 62. POB 149
or with its representatives abroad, listed on the verso of the cover

FELELŐS SZERKESZTŐ: DR. BODOR ENDRE

KIADJA A LAPKIADÓ VÁLLALAT, 1073 BP. VII., LENIN KRT. 9—11.
TELEFON: 221-285. LEVÉLCÍM: 1906 BP. PF. 223
FELELŐS KIADÓ: SIKLÓSI NORBERT IGAZGATÓ

HUNGARIAN

Journal of

INDUSTRIAL CHEMISTRY

Edited by

the Hungarian Oil & Gas Research Institute (MÁFKI),
the Research Institute for Heavy Chemical Industries (NEVIKI),
the Research Institute for Technical Chemistry of the
Hungarian Academy of Sciences (MÜKKI),
the Veszprém University of Chemical Engineering (VVE).
Veszprém (Hungary)

Volume 11. **1983** **Number 1—4.**

HU ISSN: 0133—0276
CODEN: HJICAI

Editorial Board:

R. Csikós and Gy. Mózes
Hungarian Oil & Gas Research Institute
(MÁFKI Veszprém)

A. Szántó and M. Nádasy
Research Institute for Heavy Chemical Industries
(NEVIKI Veszprém)

T. Blickle and O. Borlai
Research Institute for Technical Chemistry
of the Hungarian Academy of Sciences
(MÜKKI Veszprém)

P. Árva and G. Deák
Veszprém University of Chemical Engineering
(VVE Veszprém)

Editor-in Chief:
E. Bodor

Assistant Editor:
J. De Jonge

Veszprém University of Chemical Engineering
(VVE Veszprém)

The "Hungarian Journal of Industrial Chemistry" is a joint publication of the Veszprém scientific institutions of the chemical industry that deals with the results of applied and fundamental research in the field of chemical processes, unit operations and chemical engineering. The papers are published in four numbers at irregular intervals in one annual volume, in the English, Russian, French and German languages

Editorial Office:
Veszprémi Vegyipari Egyetem
"Hungarian Journal of Industrial Chemistry"
H – 8201 Veszprém, P.O. Box: 158.
Hungary

Orders may be placed with
KULTURA
Foreign Trading Co. for Books and Newspapers
Budapest 62. POB 149.
or with its representatives abroad, listed on the verso of the cover

FELELŐS SZERKESZTŐ: DR. BODOR ENDRE

KIADJA A LAPKIADÓ VÁLLALAT, 1073 Bp. VII., LENIN KRT. 9–11.
TELEFON: 221-285. LEVÉLCÍM: 1906 BP. PF. 223.
FELELŐS KIADÓ: SIKLÓSI NORBERT VEZÉRIGAZGATÓ

INDEX

ARGYELÁN, J.: see KOTSIS, L.
BAKOS, M.: ANTAL LÁSZLÓ 1
BATICZ, S.: see NÉMETH, J.
BATMEND RENCENGIN and ERDÉSZ, K.: Modelling and Experimental Investigation of Vibro-Pneumatic Separation 371
BENE, L., BITTNER, P. and ISASZEGI, J.: Labour Requirement Estimation of Continuously Operated Chemical Technologies 329
BITTNER, P.: see BENE, L.
BLICKLE, T. and SZENTMARJAY, T.: Use of Dispersion Characteristics in Modelling of Grinding 13
BLICKLE, T.: see KIRÁLY, L.
BLICKLE, T.: see NAGY, E.
BORODULYA, V. A, TEPLITSKY, YU. S., EPANOV, YU. G. and YANOVICH, I. I.: Lateral Thermal Diffusivity of a Fluidized Bed Packed with Tube Bundles 193
BUCSKY, GY.: see MRS. SIMON, Á.
COCA, J.: see DIAZ, J. M.
CSORBA, L.: see ÓVÁRI, F.
DEÁK, GY.: see Mrs. FRANK, E.
DEÁK, GY.: see KÁSA, Z.
DENCS, B. and ORMÓS, Z.: Particle Formation from Solutions in Gas Fluidized Beds. VI. Establishment of Steady State Operation Conditions by Grinding 339
DENCS, B. and ORMÓS, Z.: Particle Formation from Solutions in Gas Fluidized Beds. VII. Operation Parameters and Product Particle Size Distribution Obtained with the Use of a Particle Grinder 349
DÉNES, F.: see GÁRDOS, GY.
DIAZ, J. M., FONSECA, L. and COCA, J.: Chemical and Geometrical Factors in Limestone Slurries Dissolution in Stirred Tanks 81
EGYHÁZY, T.: see KÁLDI, P.
EISSA, A. I.: see KASSEM, T. M.
EL-ASHRY, S. M.: see KASSEM, T. M.
EPANOV, YU. G.: see BORODULYA, V. A.
ERDÉSZ, K. and ORMÓS, Z.: Hydrodynamical Studies on Fluidized Beds. VI. Bed Expansion and Pressure Drop in Vibrofluidized Layers 21
ERDÉSZ, K.: see BATMEND RENCENGIN
ERMAKOVA, A., KUZMIN, V. A. and UMBETOV, A. S.: Local Mass Transfer from Particle to Liquid. IV. Three Phase Systems: Fixed and Fluidized Bed, Mass Transfer, General Equation (in the Russian) 247

FÁY, GY., FÜLÖP, J. and TŐRÖS, R.: On the Determination of the Thermostatic State Equations. I. 3

MRS. FEHÉR-SZÜCS, M. and JÓZSEF, G.: On the Possibilities of Decreasing the Sulphur Emission of a Claus-Plant 139

FERENCZ, B.: see MOHILLA, R.

FONSECA, L.: see DIAZ, J. M.

MISS FRANK, E. and DEÁK, GY.: Comparison of Estimation Methods of Vaporisation Heat 241

FÜLÖP, J.: see FÁY, GY.

GÁRDOS, GY., RÉDEY, Á. and SOKORAI, I.: Utilization of the C_4-Fraction as Motor Fuel 125

GÁRDOS, GY., KOVÁCS, M., KUN-SZABÓ, T., MIKÓ, F. and DÉNES, F.: Investigation of Energy Conserving Lubricating Oil Producing Process. I. 301

GÁRDOS, GY., RÉDEY, Á., KOVÁCS, M. and KRISTÓF, J.: The Activity Change of the $H(NH_4)$, La-FAU, Y Zeolite with the Time in the Alkylating Reactions of Isobutane 403

GÁRDOS, GY., RÉDEY, Á., KOVÁCS, M. and KRISTÓF, J.: Study on Alkylate Composition 409

GÁRDOS, GY., KOVÁCS, M., KUN-SZABÓ, T., DÉNES, F. and MIKÓ, F.: Investigations on Energy Conserving Lubricating Oil Producing Processes. III. Recovery of the Solvent N-Methyl-2-Pyrrolidone ... 435

GRUHN, G., NEUMANN, W. and SEIDEL, R.: Reliability Analysis of Complex Chemical Engineering Systems 275

HABIB, O. M. O.: see KASSEM, T. M.

HUSSEIN, M. H.: see KASSEM, T. M.

IBRAGIMOV, CH. SH., NEMET, E., MAMEDOV, A. A. and SHAKHTAKHTINSKII, T. N.: Benzene Vapour Adsorption on NUXIT-BO Active Carbon Bed (in the Russian) 231

ISASZEGI, J.: see BENE, L.

JÄNICKE, W.: Two Measures for the Variability of Multi-Purpose Batch Chemical Plants 59

JÓZSEF, G.: see Mrs. FEHÉR-SZÜCS, M.

KÁLDI, P., SCHOLTZ, J. and EGYHÁZY, T.: Examination of SA-1-Type Ammonia Synthesis Catalyst 131

KÁLDI, P., SCHOLTZ, J., SZIKLAY, G. and EGYHÁZY, T.: Investigations on the Activity and Morphology of Spent Ammonia Synthesis Catalysts 147

KÁLDI, P.: see KÖVECSES, J.

KÁLDI, P.: see SZABÓ, J.

KÁSA, Z. and DEÁK, GY.: Investigation of the Hydration of Maleic to Malic Acid 313

KASSEM, T. M., HABIB, O. M. O., HUSSEIN, M. H. and EISSA, A. I.: New Biocides from Petroleum Hydrocarbons. I. Biocidal Active Products from 4-Substituted Phenols and 4-Substituted 1-Naphtols 157

KASSEM, T. M., HABIB, O. M. O., EL-ASHRY, S. M. and EISSA, A. I.: Synthesis of Some Biologically Active Products from Egyptian Petroleum Distillates 307

KHANAEV, V. M.: see KIRILLOV, V. A.
KIRÁLY, L., LAKATOS, B. and BLICKLE, T.: Use of the Weighted-Moment Method for Parameter Identification and Approximation of Distribution Functions 165
KIRILLOV, V. A., KUZMIN, V. A., PJYANOV, V. I. and KHANAEV, V. M.: Analysis of Transfer Processes in a Fixed Granular Bed at a Co-Current Upflow of Gas and Liquid (in the Russian) 263
KOTSIS, L. and ARGYELÁN, J.: Transfer Processes upon Pressure Swing Adsorption. IV. The Problems of Scale-Up 417
KOVÁCS, B., MAJOR, R. and MAJTÉNYI, M.: Electrostatic Precipitation of Various Dusts 63
KOVÁCS, M.: see GÁRDOS, Gy.
KÖVECSES, J., ÓVÁRI, F. and KÁLDI, P.: Production of Manganese Dioxide by Anodic Oxidation 321
KREIDL, J.: see MRS. SIMON, Á.
KRISTÓF, J.: see GÁRDOS, Gy.
KUN-SZABÓ, T.: see GÁRDOS, Gy.
KUZMIN, V. A.: see ERMAKOVA, A.
KUZMIN, V. A.: see KIRILLOV, V. A.
LAKATOS, B.: see KIRÁLY, L.
LAKATOS, B.: see MRS. VARGA, E.
MAJOR, R.: see KOVÁCS, B.
MAJTÉNYI, M.: see KOVÁCS, B.
MAMEDOV, A. A.: see IBRAGIMOV, Ch. Sh.
MIKÓ, F.: see GÁRDOS, Gy.
MOHILLA, R. and FERENCZ, B.: Computerized Simulation of an Industrial pH Control System 425
NAGY, E. and BLICKLE, T.: The Influence of Dispersion Conditions on Mass Transfer Accompanied by First Order Moderate Reaction 71
NEMET, E.: see IBRAGIMOV, Ch. Sh.
NÉMETH, J., BATICZ, S. and PÉTER-HORÁNYI, M.: Adsorption of Vapour Mixtures on Activated Carcoal. I. Equilibrium and Kinetic Investigations 357
NÉMETH, J : see MRS. SIMON, Á.
NEUMANN, W.: see GRUHN, G.
ORMÓS, Z.: see DENCS, B.
ORMÓS, Z.: see ERDÉSZ, K.
ÓVÁRI, F., CSORBA, L. and URBANKOVICS, I.: New Developments in the Production of Positive Electrodes for Stationary Large Lead Batteries 119
ÓVÁRI, F.: see KÖVECSES, J.
PAPP, S.: see SCHÖNWEITZ, T.
PÉTER-HORÁNYI, M.: see NÉMETH, J.
PJYANOV, V. I.: see KIRILLOV, V. A.
RÉDEY, Á.: see GÁRDOS, Gy.
SCHOLTZ, J.: see KÁLDI, P.
SCHÖNWEITZ, T., VINCZE, L. and PAPP, S.: Oxidation of Copper (I) Ions in the Presence of Ammonia and Various Amines 387

SHAKHTAKHTINSKII, T. N.: see IBRAGIMOV, Ch. Sh.
SEIDEL, R.: see GRUHN, G.
MRS. SIMON, Á., NÉMETH, J., BUCSKY, GY. and KREIDL, J.: Investigations of a Baffle Plate Tube Reactor 33
MRS. SIMON, K.: Calculation of Glass Density from its Composition 283
MRS. SIMON, K.: Analytical Investigation of the Process for Manufacturing 1, 2, 4-1H-Triazole 291
SOKORAI, I.: see GÁRDOS, GY.
STUDNICKI, M.: Thermodynamical Properties of Nonaqueous Solutions of Hydrogen Chloride 209
STUDNICKI, M.: Thermodynamical Properties of Nonaqueous Solutions of Aromatic Amines 223
SZABÓ, J. and KÁLDI, P.: Adsorption Rate on Natural Mordenites 185
Frau SZABÓ-SIPOS, L., UJHIDY, A. and VASSÁNYI I.: Beitrag zur Chlorierung von Eisenoxyd 91
SZENTMARJAY, T.: see BLICKLE, T.
SZIKLAI, G.: see KÁLDI, P.
SZIKLAI, G.: see SZÜCS, I.
SZÜCS, I. and SZIKLAI, G.: On the Relationship of Colour Characteristics and Particle Size Distribution and Specific Surface Area of Certain Pigments. I. 113
TEPLITSKY, YU. S.: see BORODULYA, V. A.
TIMÁR, L.: A Two-Algorithm Approach to Calculate Reboiled Absorbers 47
TŐRÖS, R.: see FÁY, GY.
URBANKOVICS, I.: see ÓVÁRI, F.
UJHIDY, A.: see Frau SZABÓ-SIPOS, L.
UMBETOV, A. S.: see ERMAKOVA, A.
MRS. VARGA, E. and LAKATOS, B.: Calculation of the Dynamic Processes of a Perfectly Mixed Tank by Orthogonal Collocation 173
VASSÁNYI, I.: see FRAU SZABÓ-SIPOS, L.
VINCZE, L.: see SCHÖNWEITZ, T.
WOLFF, A.: An Analysis of a Refinery Naphtha Reforming Plant 97
YANOVICH, I. I.: see BORODULYA, V. A.

THE FOLLOWING ARE PLEASED TO ACCEPT SUBSCRIPTIONS TO THIS JOURNAL:

AUSTRALIA

C.B.D. Library and Subscription Service
Box 4886 G.P.O.
Sydney 2000

Cosmos Book and Record Shop
145 Acland Street
St. Kilda 3182

Globe and Co.
694—696 George Street
Sydney 2000

AUSTRIA

Globus (VAZ)
Höchstädtplatz 3
A—1200 Wien XX

BELGIUM

"Du Monde Entier" S. A.
Rue du Midi 162
B—1000 Bruxelles

Office International de Librairie
Avenue Marnix 30
B—1050 Bruxelles

CANADA

Pannonia Books
P.O. Box 1017
Postal Station "B"
Toronto, Ontario M5T 2T8

DENMARK

Munksgaard's Boghandel
Norregade 6
DK—1165 Copenhagen K

FINLAND

Akateeminen Kirjakauppa
Keskuskatu 2, P.O.B. 128
SF—00 100 Helsinki 10

FRANCE

Office International de Documentation et Librairie
48 Rue Gay Lussac
75 Paris 5

GERMAN FEDERAL REPUBLIC

Kubon und Sagner
Pf 68
D—8 München 34
BRD

GREAT BRITAIN

Bailey Bros and Swinfen Ltd.
Warner House, Folkestone
Kent CT 19 6PH England

HOLLAND

Martinus Nijhoff
Periodicals Department
P.O. Box 269
The Hague

Swets and Zeitlinger
Keizersgracht 487
Amsterdam C

ITALY

Licosa
P.O.B. 552, Via Lamarmora 45
50121 Firenze

JAPAN

Igaku Shoin Ltd.
Foreign Department
Tokyo International P.O. Box 5063
Tokyo

Maruzen Co. Ltd.
P.O. Box 5050
Tokyo International 100—31

Nauka Ltd.
Yasutomi Bldg. 5F 2—12 Kanda
Jinbocho, Chiyoda-ku
Tokyo 101

NORWAY

Tanum—Cammermayer
Karl Johangt. 41—43
Oslo 1

SWEDEN

Almqvist and Wiksell Förlag A. B.
Box 2120
S—103 13 Stockholm 2

Wennegren—Williams AB
Subscription Department Fack
S—104 Stockholm 30

SWITZERLAND

Karger Libri A. G.
Petersgraben 31
CH—4011 Basel

USA

Ebsco Subs. Services
1 st Ave North at 13th street
Birmingham, Ala. 35201

ANTAL LÁSZLÓ

June 7, 1922—December 8, 1982

After a long illness, DR. A. LÁSZLÓ, D.Sc., Kossuth Prize winner and former Rector of the Veszprém University for Chemical Engineering, the member of the Editorial Board of the Hungarian Journal of Industrial Chemistry, died on December 8, 1982.

A. LÁSZLÓ came from Transylvania. He was born in Gyergyóújfalu, at June 7, 1922. After attending high school at Csíkszereda, he enrolled at the József Nádor Technical University, Budapest, where he graduated as a chemical engineer in 1945. He became an assistant, and later, a first assistant at the University's Electrochemistry Department. He studied high temperature gas phase reactions and became involved with chemical engineering. For a short period (1948–1950), he was a research fellow at the Research Institute for Aluminium, where he developed a method for producing anode carbon. However, he never abandoned his original research field, and from 1950, he became a research fellow at the Hungarian Oil and Gas Research Institute. In 1953, he became the head of the physico-chemical department. His research interest focused on the conversion of natural gas, primarily on the atmospheric partial oxidation of methane.

That was perhaps the most vividly active period of his life. Between 1952 and 1956, he was the chief engineer of the Joint Romanian–Hungarian Petrochemical Plant built in Buciumeni, Romania, and he directly supervised the completion and start-up of the partial oxidation plant. In 1953, he married ZSUZSANNA KÖRÖSI M.D., his faithful companion during his life. It was that period that he completed his thesis on the partial oxidation of methane for which he gained the degrees: Candidate of Science and Ph.D. at Veszprém University.

In September 1957, he became the professor of physical chemistry at the Veszprém University of Chemical Engineering. At first, he organized Chemical Process Engineering Department (1963). He remained the Head of this Department until 1976. Between 1964 to 1966, he was elected Rector of Veszprém University. He completed his thesis on the fundamentals of control and scale-up of chemical operation units, and in 1963 he gained the distinction: D.Sc.

A. LÁSZLÓ became scientist of world-fame. He was awarded many distinctions and decorations for his work, including the highest Hungarian scientific award, the Kossuth Prize (1952), the Golden Medal for Work (1974), and the Wartha Vince Memorial Medal (1961), etc.

He made many journeys abroad from the USA to the USSR, and for a year, he worked as visiting professor at the University of Nancy, France (1967).

His work and personality were acknowledged everywhere. He was a member of the Hungarian National Section of the Combustion Institute, the president of the Chemical Engineering Science Committee of the Hungarian Academy of Sciences and the Chemical Committee of the Veszprém County Branch of the Hungarian Academy of Sciences.

He established the new field of chemical engineering science in Hungary, and remained its leader throughout his life. His book, "The Principles of Chemical Engineering Science" (1964), jointly written with Professor PÁL BENEDEK, became an immediate success and was translated to German (1967, 1970), Russian (1970) and French (1972).

In additon to his industrial research activity, Professor A. LÁSZLÓ established a scientific school and trained generations of outstanding engineers and scientists. Several of his students took up responsible positions both in Hungary and abroad.

His standards were high and demanding, both towards himself and others. When prolonged illness prevented him from meeting these standards, he resigned as head of the Chemical Process Engineering Department, but he continued to work until his illness prevented him from doing so.

His example and true humanity gained him the affection and respect of his colleagues and students, and also brought him respect and honour, wherever he was known. The spirit and example he displayed will long be remembered and his work will be continued by his followers.

Corpus humo tegitur
Fama per ora volat
Spiritus astra tenet

M. BAKOS

HUNGARIAN JOURNAL
OF INDUSTRIAL CHEMISTRY
VESZPRÉM
Vol. 11. pp. 3—12 (1983)

ON THE DETERMINATION OF THE THERMOSTATIC STATE EQUATIONS PART 1.

GY. FÁY, J. FÜLÖP and R. TŐRÖS

(Research Intitute for Technical Chemistry of the Hungarian Academy of Sciences, Veszprém, Hungary)

Received: June 4, 1982

The state-equation-set of homogeneous thermodynamic systems with two degrees of freedom is presented here, using the characteristic thermodynamic quantities. Depending on the complexity of the solution methods, three cases can be distinguished. This paper deals with six easy-to-solve cases. More complicated cases will be dealt with in forthcoming papers. The cases are identified when the characteristic quantities allow for the construction of one state equation, but not the state equation set. A theorem will be proved, which can be used for the identification of such cases.

Introduction

In a previous paper [1] the solution of the following problem was dealt with.

Let us consider the following eight thermodynamic characteristic quantities:

$$C_p = T\left(\frac{\partial S}{\partial T}\right)_p \quad \text{isobar} \quad \text{specific heat} \tag{1}$$

$$C_V = T\left(\frac{\partial S}{\partial T}\right)_V \quad \text{isochore} \quad \text{specific heat} \tag{2}$$

$$\chi_T = -\frac{1}{V}\left(\frac{\partial V}{\partial p}\right)_T \quad \text{isotherm} \quad \text{compressibility factor} \tag{3}$$

$$\chi_S = -\frac{1}{V}\left(\frac{\partial V}{\partial p}\right)_S \quad \text{adiabatic} \quad \text{compressibility factor} \tag{4}$$

$$\beta_V = \frac{1}{p}\left(\frac{\partial p}{\partial T}\right)_V \quad \text{isochore} \quad \text{stress coefficient} \tag{5}$$

$$\beta_S = \frac{1}{p}\left(\frac{\partial p}{\partial T}\right)_S \quad \text{adiabatic} \quad \text{stress coefficient} \tag{6}$$

$$\left.\begin{aligned} \alpha_p &= \frac{1}{V}\left(\frac{\partial V}{\partial T}\right)_p && \text{isobar} && (7) \\ \alpha_S &= -\frac{1}{V}\left(\frac{\partial V}{\partial T}\right)_S && \text{adiabatic} && (8) \end{aligned}\right\} \text{dilatation coefficient}$$

Let us now seek those cases, when 3 quantities out of the 8 $[\binom{8}{3}=56$ variations]:

1. determine the other 5 characteristics, and
2. let us determine the actual functional relationship.

These questions were answered in [1]. Now our latest results are shown. It is shown that the three quantities selected from Eq. 1–8 are sufficient for the generation of the state equation set of a homogeneous thermodynamic system with two degrees of freedom. More precisely:

1. those cases are determined when the three quantities are sufficient for the solution of the problem;
2. if they are sufficient, then in which cases and to what extent can the state equations be generated (and give a routine calculation method, if any)?

Only the fundamental MAXWELL relations can be used for Eq. (1–8), i.e.:

$$\left(\frac{\partial T}{\partial V}\right)_S = -\left(\frac{\partial p}{\partial S}\right)_V \tag{I}$$

$$\left(\frac{\partial T}{\partial p}\right)_S = \left(\frac{\partial V}{\partial S}\right)_p \tag{II}$$

$$\left(\frac{\partial S}{\partial V}\right)_T = \left(\frac{\partial p}{\partial T}\right)_V \tag{III}$$

$$-\left(\frac{\partial S}{\partial p}\right)_T = \left(\frac{\partial V}{\partial T}\right)_p \tag{IV}$$

Generation of the State Equations

In the case of a homogeneous thermodynamic system with two degrees of freedom four characteristic quantities (p, V, S, T) and two functional relationships have to be given. If Eq. (1–8) are analyzed, then it becomes obvious that the independent variables are not always the same as shown in *Table 1.*

The system of expressions[1] given in [1] can be used as a "mechanical tool" in studying material characteristics when:

1. the expressions are accompanied by the full knowledge of the state (i.e. p, V, S, T are numerically known);
2. two out of the four variables: p, V, S, T and two state equations are given;

[1] Unfortunately, the minus sign is missing in [1] and [2]. However, in the calculations $\alpha_S > 0$ is used according to the present definition, and it should be understood as such in the expressions as well.

Table 1

Independent variables	Equations
p, T	(1), (3), (7)
T, V	(2), (5)
T, S	(6), (8)
p, S	(4)

3. the expressions are such that no state variable is used explicitly in the relationships between the characteristics, e.g.:

$$\frac{\alpha_S}{\alpha_p}=\frac{C_V}{C_p-C_V}, \quad \text{or} \quad \frac{\chi_S}{\chi_T}=\frac{C_V}{C_p}.$$

In system-engineering applications [3] the most frequent case is the second shown above. When none of the above first-third cases occurs, then both the state of the system and its two state equations have to be known. These are discussed here. In this paper the term "determination" means that the state equation is a generated form of a reference point, such as p_0 or V_0, and one or two constants. Thus, we do not consider the equation:

$$C_V=T\left(\frac{\partial S}{\partial T}\right)_V \rightarrow S(T,V)=\int_{T_0}^{T}\frac{C_V}{T}\mathrm{d}T+S_0(V)$$

determined because here $S_0(V)$ is undetermined.

This results in the following alternatives:

1. Three equations selected from Eq. (1–8) are such that even two determine a state equation. Then, this state equation is used in its transcendent (or algebraic) form and the second state equation is given by the third equation calculated from Eq. (1–8). For example, once the pair:

$$\alpha_p=\frac{1}{V}\left(\frac{\partial V}{\partial T}\right)_p; \quad \chi_T=-\frac{1}{V}\left(\frac{\partial V}{\partial p}\right)_T$$

is given, then the generation of $V(p, T)$ is a so-called multivariable quadrature-problem:

$$\mathrm{d}\ln V=\frac{1}{V}\left(\frac{\partial V}{\partial T}\right)_p \mathrm{d}T+\frac{1}{V}\left(\frac{\partial V}{\partial p}\right)_T \mathrm{d}p$$

and:

$$\ln\left(\frac{V(p,T)}{V(p_0T_0)}\right)=\int_{p_0T_0}^{p,T}(\alpha_p\,\mathrm{d}T-\chi_T\,\mathrm{d}p),$$

where the line integral can be obtained along any arbitrary path between p_0, T_0 and p, T. This paper deals with the simple case, and as for the third characteristic, each of the six logicaly possible cases will be tested.

2. The structure of the three equations selected from Eq. 1–8 is such that two of the equations define the derivative with respect to two variables of a single state function. For example, from Eq. (2) and (8):

$$\left(\frac{\partial T}{\partial S}\right)_V = \frac{T}{C_V}; \qquad \left(\frac{\partial T}{\partial V}\right)_S = \frac{1}{V\alpha_S},$$

Here, the problem is not a quadrature problem, because the right-hand-sides contain not only the variables V, S but also the unknown function, $T(S, V)$. However, even this problem has its solution taken from the theory of the-so-called overdetermined differential equations (4, 5)[2].

3. The third, and most difficult case is, when the structure of the three equations selected from Eq. (1–8) is such that any two of the equations contain all four variables. For example:

Eq·(6)	S, p, T
Eq·(7)	p, V, T
Eq·(8)	S, V, T

More separated forms can be obtained by the transformation of the particular structure of the equations (which, nevertheless, is still independent of the peculiarities of the thermodynamical system examined). This third, and most complicated case will be discussed in Part 3 of this series.

Here an auxiliary theorem will be proved and cases 1, 2, 4, 5, 6 and 8 which belong to the equation diad 3, 7, will be discussed.

Lemma: Definition of triads:

$$C_p,\ \beta_S,\ \alpha_p$$
$$C_V,\ \beta_V,\ \alpha_S$$
$$\chi_T,\ \beta_V,\ \alpha_p$$
$$\chi_S,\ \beta_S,\ \alpha_S$$

is insufficient for the generation of the two state equations (i.e. the definition of the system). However, it is sufficient for the generation of a one state equation.

Derivation:

To prove the Lemma let us recall from the theory of first-order differential equations (4, 5) the relationship of the partial derivatives of function $z(x, y)$:

$$dz = \frac{\partial z}{\partial x}\,dx + \frac{\partial z}{\partial y}\,dy. \tag{9}$$

If: $z(x, y) = z_0 = \text{constant}$

then: $dz = 0$

and:

$$\left(\frac{\partial z}{\partial x}\right) + \left(\frac{\partial z}{\partial y}\right)_x \left(\frac{\partial y}{\partial x}\right)_z = 0. \tag{10}$$

[2] The expression used in German is „Überbestimmte System".

Now let z be:

$$S(p, T) \tag{11}$$

$$S(V, T) \tag{12}$$

$$V(p, T) \tag{13}$$

$$V(S\ p) \tag{14}$$

It follows from Eq. (11) that:

$$\left(\frac{\partial S}{\partial p}\right)_{\mathrm{T}}+\left(\frac{\partial S}{\partial T}\right)_{\mathrm{p}}\left(\frac{\partial T}{\partial p}\right)_{\mathrm{s}}=0. \tag{14'}$$

Substituting Eq. 1, (IV), (6) and (7) into Eq. (14) we obtain:

$$C_{\mathrm{p}}=V_{\mathrm{p}}T\alpha_{\mathrm{p}}\beta_{\mathrm{s}} \tag{15}$$

i.e. by definition, α_{p}, β_{s} and C_{s} are not independent.

Let us take Eq. 12 and 9, then:

$$\left(\frac{\partial S}{\partial V}\right)_{\mathrm{T}}+\left(\frac{\partial S}{\partial T}\right)_{\mathrm{V}}\left(\frac{\partial T}{\partial V}\right)_{\mathrm{s}}=0.$$

Using Eq. (2), (5), III and (8) we obtain:

$$\begin{gathered} p\beta_{\mathrm{V}}-\frac{C_{\mathrm{v}}}{T}\,\frac{1}{\alpha_{\mathrm{s}}V}=0 \\ C_{\mathrm{V}}=pVT\beta_{\mathrm{V}}\alpha_{\mathrm{s}} \end{gathered} \tag{16}$$

just as in Eq. (15)
Then, from Eq. (13):

$$\begin{gathered} \left(\frac{\partial V}{\partial p}\right)_{\mathrm{T}}+\left(\frac{\partial V}{\partial T}\right)_{\mathrm{p}}\left(\frac{\partial T}{\partial p}\right)_{\mathrm{V}}=0 \\ \alpha_{\mathrm{p}}=\chi_{\mathrm{T}}\beta_{\mathrm{V}}p \end{gathered} \tag{17}$$

From Eq. (14):

$$\left(\frac{\partial V}{\partial S}\right)_{\mathrm{p}}+\left(\frac{\partial V}{\partial p}\right)_{\mathrm{s}}\left(\frac{\partial p}{\partial S}\right)_{\mathrm{V}}=0.$$

Using Eq. (II), (4), T, and (8) we obtain:

$$\begin{gathered} \left(\frac{\partial T}{\partial p}\right)_{\mathrm{s}}-V\chi_{\mathrm{s}}\left[-\left(\frac{\partial T}{\partial V}\right)_{\mathrm{s}}\right]=0 \\ \alpha_{\mathrm{s}}=p\beta_{\mathrm{s}}\chi_{\mathrm{s}} \end{gathered} \tag{18}$$

quod erat demonstrandum.
This is why the four function triads in Eq. (15)–(18) were called in [1] a *non-complete base.*

Let us now consider only those equation triads selected from Eq. 1–8, which contain Eq. (3) and (7). These are as follows:

3, 7 and 1
3, 7 and 2
3, 7 and 4
3, 7 and 5 (insufficient according to the Lemma) (19)
3, 7 and 6
3, 7 and 8

Now the two state equations, which sufficiently define the system, will be generated according to Eq. (19).

It has to be noted that Eq. (1)–(8) can be handled as differential equations and so the general solution can be given immediately. One of the important points of our method is that it is *not the general solution* which we generate (because due to the appearance of arbitrary functions, it is still an undetermined problem), rather it is the so-called full solution, which contains three constants in agreement with the number or variables: two independent ones and one dependent variable. The full solution can be generated, because the three equations selected from the over-determined differential equation set are the two state equations sought (4).

Let us now turn to Eq. (19). It follows from Eq. (3) and (7) that:

$$\left(\frac{\partial \ln V}{\partial T}\right)_{\mathrm{p}} = \alpha_{\mathrm{p}} \quad \left(\frac{\partial \ln V}{\partial p}\right)_{\mathrm{T}} = -\chi_{\mathrm{T}} \tag{20}$$

that is:

$$V(p, T) = V(p_0, T_0) \exp\left[\int_{T_0}^{T} \alpha_{\mathrm{p}}\, \mathrm{d}T - \int_{p_0}^{p} \chi_{\mathrm{T}}\, \mathrm{d}p\right] \tag{21}$$

Eq. (21) is a line integral which, because of Eq. (20), is necessarily independent from the path of integration between p_0, T_0 and p, T. This means that one of the state equations is given (with constants p_0, T_0). Eq. (21) can be considered to be known, and the method used to generate the second state equation in the case of Eq. (1), (2), (4), (6) and (8), will be shown.

For Eq. (3) (7) and (1)

If Eq. (1) is given, then with Eq. (IV):

$$\mathrm{d}S = \frac{C_{\mathrm{p}}}{T}\,\mathrm{d}T + \left(\frac{\partial S}{\partial p}\right)_{\mathrm{T}} \mathrm{d}p = \frac{C_{\mathrm{p}}}{T}\,\mathrm{d}T - \left(\frac{\partial V}{\partial T}\right)_{\mathrm{p}} \mathrm{d}p$$

$$S = S(p_0, T_0) + \int_{T_0}^{T} \frac{C_{\mathrm{p}}(p, T)}{T}\,\mathrm{d}T - \int_{p_0}^{p} V(\xi, T)\alpha_{\mathrm{p}}(\xi, T)\,\mathrm{d}\xi \tag{22}$$

which means that the second state equation, $S(p, T)$ has been generated.

For Eq. 3, 7 and 2

$$\mathrm{d}S = \left(\frac{\partial S}{\partial V}\right)_{\mathrm{T}} \mathrm{d}V + \left(\frac{\partial S}{\partial T}\right)_{\mathrm{V}} \mathrm{d}T = \left(\frac{\partial p}{\partial T}\right)_{\mathrm{V}} \mathrm{d}V + \frac{C_{\mathrm{V}}}{T}\,\mathrm{d}T$$

However, $\left(\frac{\partial p}{\partial T}\right)_{\mathrm{V}}$ can be calculated according to Eq. (21):

$$S = S(T_0, V_0) + \int_{T_0}^{T} \frac{C_V}{T} \mathrm{d}T + \int_{V_0}^{V} \left(\frac{\partial p}{\partial T}\right)_V \mathrm{d}V \tag{23}$$

which means that the second state equation, $S(T, V)$ has been generated.

For Eq. (3), (7) and (4)

If Eq. (4) is given, then by rearrangement it follows from function $V = V[p, T(S, p)]$ that:

$$\left(\frac{\partial V}{\partial p}\right)_S = \left(\frac{\partial V}{\partial p}\right)_T + \left(\frac{\partial V}{\partial T}\right)_p \left(\frac{\partial T}{\partial V}\right)_S. \tag{24}$$

The left hand side of Eq. (24) is $-\chi_S V$, while the first term and the first fraction of the second term of the right-hand-side is known from Eq. (21). The second fraction is known from Eq. (11) as $\left(\frac{\partial V}{\partial S}\right)_p$, thus:

$$\left(\frac{\partial V}{\partial p}\right)_p = -\frac{\left(\frac{\partial V}{\partial p}\right)_T + \chi_S V}{\left(\frac{\partial V}{\partial T}\right)_p} \tag{25}$$

leading directly to:

$$\left(\frac{\partial V}{\partial p}\right)_S = -\chi_S V \tag{26}$$

With $S = S_0$, Eq. (26) becomes an ordinary differential equation and its solution is:

$$V = V(S_0, p_0) e^{\int_{p_0}^{p} \chi_S(S_0, p)\, \mathrm{d}p} = V\left[S_0, p_0 \exp \int_{p_0}^{p} \chi_S(S_0, p)\, \mathrm{d}p\right] \tag{27}$$

If $p = \text{constant}$, then Eq. (25) is an ordinary, though inseparable differential equation, thus in general, its solution cannot be generated by quadrature. However, let its solution be Φ:

$$V = \Phi(S, p, S_0, \xi) \tag{28}$$

where for Φ:

$$\Phi(S_0, p, S_0, \xi) = \xi \tag{29}$$

and substitution of Eq. (27) for ξ in Eq. (28) results in the solution:

$$V = \Phi\left[S, p, S_0, V_0 \exp \int_{p_0}^{p} \chi_S(S_0, p)\, \mathrm{d}p\right] \tag{30}$$

where:

$$V_0 = V(S_0, p_0)$$

No simpler form could be found. This at least designates the second state equation, $V(S, p)$.

For Eq. (3), (7) and (5)

This case was discussed in connection with the Lemma.

For Eq. (3), (7) and (6)

Based Eq. (21), Eq. (6) is combined with $V(p, T)$. According to Eq. (II):

$$\left(\frac{\partial S}{\partial p}\right)_T = -\left(\frac{\partial V}{\partial T}\right)_p, \tag{31}$$

The right-hand-side of Eq. (31) is given by Eq. (21) as a function of T, p. Taking:

$$dS = \left(\frac{\partial S}{\partial p}\right)_T dp + \left(\frac{\partial S}{\partial T}\right)_p dT = 0$$

translates to:

$$\left(\frac{\partial S}{\partial T}\right)_p = -\left(\frac{\partial S}{\partial p}\right)_T \left(\frac{\partial p}{\partial T}\right)_S \tag{32}$$

If Eq. (31) and (6) are substituted into Eq. (32) then:

$$\left(\frac{\partial S}{\partial T}\right)_p = \left(\frac{\partial V}{\partial T}\right)_p p\beta_S(S, T) \tag{33}$$

$\left(\frac{\partial V}{\partial T}\right)_p = f(p, T)$ is given, but the right-hand-side of Eq. (33) also depends on S, so the method followed with Eq. (3), (7) and (4) is applied to $S(p, T)$ yielding:

$$\left(\frac{\partial S}{\partial T}\right)_p = f(p, T) p\beta_S(S, T) \tag{33'}$$

For the calculations let us use T in Eq. (31). Then:

$$\left(\frac{\partial S}{\partial p}\right)_T = -f(p, T) \tag{34}$$

$$S = -\int_{T_0 p_0}^{T_0 p} f(p, T_0)\, dp + S(T_0, p_0) \tag{35}$$

For $p =$ constant Eq. (33) becomes an ordinary, but non-separable differential equation, just like Eq. (25). Let the solution be Φ_1:

$$S = \Phi_1(p, T, p_0, \xi) \tag{36}$$

where:

$$\xi = \Phi_1(p_0, T, p_0, \xi) \tag{37}$$

Let us substitute Eq. (35) for ξ in Eq. (36), and then the solution is obtained as:

$$S = \Phi_1\left[p, T, p_0 - \int_{T_0, p_0}^{T_0, p} f(p, T_0)\, dp + S(T_0, p_0)\right] \tag{38}$$

For Eq. (3), (7) and (8)

Eq. (21) in used again, but here, from Eq. (III):

$$\left(\frac{\partial V}{\partial S}\right)_T = \frac{1}{\left(\frac{\partial p}{\partial T}\right)_V}, \tag{39}$$

where the right-hand-side can be expressed according to Eq. (21) as a function of V and T. Then, for constant T_0 its integral becomes:

$$S(T_0, V) = \int_{T_0 V_0}^{T_0 V} \left(\frac{\partial p}{\partial T}\right)_V \mathrm{d}V + S(T_0, V_0). \tag{40}$$

If Eq. (8) is integrated for S = constant then:

$$V(S, T_0) \exp\left(-\int_{S, T_0}^{S, T} \alpha_S \, \mathrm{d}T\right) \tag{41}$$

Eq. (40) can be solved for $V(S, T_0)$ which, upon substitution into Eq. (41) yields the second state equation:

$$V = V(S, T) \tag{42}$$

In conclusion, it can be stated that the following state equations could be determined by the characteristics listed (cf. *Table 2*).

Table 2

Characteristic quantities symbol/Eq.			State equations type/Eq.			
T (3)	p (7)	C_p (1)	$V(p, T)$	(21)	$S(p, T)$	(22)
T (3)	p (7)	C_V (2)	$V(p, T)$	(21)	$S(T, V)$	(23)
T (3)	p (7)	S (4)	$V(p, T)$	(21)	$V(S, p)$	(30)
T (3)	p (7)	v (5)	$V(p, T)$	(21)	—	
T (3)	p (7)	S (8)	$V(p, T)$	(21)	$V(S, T)$	(41)

REFERENCES

1. Fáy Gy. and Tőrös R.: Hung. J. Ind. Chem. *1981*, 9, 209–231.
2. Miniature Encyclopedia of Modern Physics.
3. T. Blickle: Algebraic Description of the Systems of Technical Chemistry (Recent Development in Chemistry Series, Vol. 16, 1973, p. 79–81) (in Hungarian).

4. BIEBERBACH, L.: Einführung in die Theorie der Differentialgleichungen. Springer Verlag, Berlin–Göttingen–Heidelberg, 1956, pp. 272–274.
5. I. FÉNYES: Thermostatics and Thermodynamics, Műszaki Könyvkiadó, Budapest, 1968, p. 93–94.
6. BIEBERBACH, L.: Theorie der Differentialgleichungen, Springer Verlag, Berlin, 1926. pp. 240–242.
7. Calculation of the Thermodynamic Characteristics of Gases and Vapours, Műszaki Könyvkiadó, Budapest, 1972.

РЕЗЮМЕ

Авторами разработана система уравнений состояния однородных термодинамических тел с помощью термодинамических характеристических величин. При составлении системы различают три случая в зависимости от сложности методики. В данном первом сообщении излагаются шесть наиболее легко решаемых задач. Более сложные задачи будут излагаться в последующих сообщениях. Также отделяем те типы задач в которых задание характеристических величин достаточно для составления уравнения состояния но не достаточно для составления системы уравнений. Такие типы выделены на основе доказательства некоторой теоремы.

HUNGARIAN JOURNAL
OF INDUSTRIAL CHEMISTRY
VESZPRÉM
Vol. 11. pp. 13—19 (1983)

USE OF DISPERSION CHARACTERISTICS IN MODELLING OF GRINDING

T. BLICKLE and T. SZENTMARJAY

(Research Institute for Technical Chemistry of the Hungarian Academy of Sciences, Veszprém, Hungary)

Received: August 1, 1982.

Extensive quantities characterizing dispersions (such as numerousness, size, and surface area) were used in the mathematical model of grinding. The method of model development shown here is followed by a comparison of measured and calculated characteristics (numerousness, and surface area, etc.). It was concluded that size and surface area changes during grinding are proportional to the number of impacts and the size and surface area of the particle. For a given geometric shape, the proportinonality factor can be determined and shown to be constant.

Introduction

Dispersion characteristics, such as numerousness, size and surface area can be used to describe operations accompanied by size changes, such as granulation, crystallization, and grinding, etc.

Numerousness (N) is the number of particles in a dispersion of unit mass and particle fractions:

$$N = \frac{\sum_{i=1}^{k} n_i}{m} \quad (\mathrm{kg}^{-1}) \tag{1}$$

Size (D) is the sum of the size of the particles present in a unit mass dispersion:

$$D = \frac{\sum_{i=1}^{k} n_i d_i}{m} \quad (\mathrm{m\ kg}^{-1}) \tag{2}$$

The average particle size of a given particle fraction is defined as the algebraic average of the sieve openings limiting the given particle fraction.

For the sake of simplicity it is assumed that the particles are spherical.

Surface (F) is the sum of the surface area of all the particles present in a dispersion of unit mass with k particle fractions:

$$F=\frac{\sum_{i=1}^{k} f_i}{m}=\frac{\sum_{i=1}^{k} n_i d_i^2 \pi}{m} \quad (\mathrm{m^2\,kg^{-1}}). \tag{3}$$

Mathematical Model

The probability that a given particle of size d cleaves under the effect of the grinding force is:

$$p=\frac{d-d_\infty}{d} \tag{4}$$

where d_∞ is the size of the elementary cell.

During grinding, particle size and the number of particles are related as:

$$N\times d=N_0\times d_0=N_\infty d_\infty \tag{5}$$

It is assumed that the time-dependent change of numerousness is proportional to the number of particles, the probability of disintegration, and the number of collisions and disintegrations, i.e.:

$$\frac{dN}{dt}=\varphi_N\cdot\beta_N\frac{N_\infty-N}{N_\infty} \tag{6}$$

where: β_N is the number of collisions in unit time per a single particle (s^{-1}).
φ_N is the number of disintegrations per a single collision (—).

The above mentioned relationship holds for both the size and the surface area:

$$\frac{dD}{dt}=\varphi_D\times\beta_D\frac{N_\infty-N}{N_\infty} \tag{7}$$

and

$$\frac{dF}{dt}=\varphi_F\times\beta_F\frac{N_\infty-N}{N_\infty} \tag{8}$$

During grinding the size of the particles and the increase of the surface area proportional to the number of collisions, the size of a particle (D/N) and the surface area of a particle (F/N).

Dividing Eq. (7) and (8) by Eq. (6) the increase of particle size and surface area are obtained:

$$\frac{dD}{dN}=\xi_D\frac{D}{N} \qquad \xi_D=\frac{\varphi_D}{\varphi_N} \tag{9}$$

and:

$$\frac{dF}{dN}=\xi_F\frac{F}{N} \qquad \xi_F=\frac{\varphi_F}{\varphi_N} \tag{10}$$

For a geometric shape proportionality factor ξ can be determined and it can be shown to be constant.

The differential equation given in Eq. (6) can be solved under the following initial and boundary conditions:

$$t_0=0 \quad \text{and}$$

$$N(0)=N_0$$

yielding:

$$\frac{1}{N}=\left(\frac{N_\infty-N_0}{N_0}\,e^{-\varphi_N\beta t}+1\right)\frac{1}{N_\infty}. \tag{11}$$

Application of the Model

In the numerator of the ratio $\frac{N_\infty-N_0}{N_0}$ in Eq. 11 $N_0 \ll N_\infty$, consequently the omission of N_0 does not introduce a major error. Thus, the time-dependent change of numerousness is described as:

$$N=\frac{N_\infty}{\frac{N_\infty}{N_0}\,e^{-\varphi_N\beta t}+1}. \tag{12}$$

The error introduced by neglecting N_0 and 1 in the denominator in Eq. (12) is small, because $N_\infty \gg N_0$.

Thus, Eq. (12) is simplified to:

$$N=N_0 e^{\varphi_N\beta t}. \tag{13}$$

If ln N is plotted against t then $\varphi_N\beta t$ and N_0 can be determined. If N^{-1} is plotted against $\exp(-\varphi_N\beta t)$ then N_∞ can be calculated.

Once the coefficients in Eq. (12) are obtained by these plots, the equation can be used to calculate the value of numerousness of various materials at any given moment.

Grinding experiments were carried out with various materials in a ball-mill under identical conditions. The particle size distribution of the fractions at various time intervals were determined by sieve analysis. The coefficients of Eq. (12) were determined from these particle size distributions as described above (cf. *Table 1*).

Numerousness values obtained from the measured data and calculated by the model were compared (cf. *Fig. 1*). It can be seen that measured and calculated values agree well. The ln D vs. ln N and ln F vs ln N diagrams were used to determine the coefficients ξ_D and ξ_F in Eq. (9) and (10). The grinding-

Table 1

Coefficients of Eq. 12 for various materials

No.	Material	$\varphi_N\beta$ (s^{-1})	N_0 (kg^{-1})	N_∞ (kg^{-1})
1	bauxite (1.25–1.6 mm)	7.77×10^{-4}	8.48×10^{7}	2.11×10^{10}
2	limestone (1.25–1.6 mm)	4.92×10^{-4}	2.68×10^{8}	5.51×10^{8}
3	limestone (1.6–2.0 mm)	5.26×10^{-4}	6.57×10^{7}	4.14×10^{9}
4	zeolite (1.4–2.0 mm)	1.32×10^{-4}	8.69×10^{7}	2.14×10^{10}

Table 2

Constants of Eq. 9 and 10

No.	Material	D_0 (m kg^{-1})	F_0 (m^2 kg^{-1})	ξ_D	ξ_F
1	bauxite (1.25–1.6 mm)	3.96×10^3	2.65	0.90	0.44
2	limestone (1.25–1.6 mm)	9.62×10^3	2.42	0.96	0.67
3	limestone (1.6–2.0 mm)	2.92×10^3	1.75	0.93	0.43
4	zeolite (1.4–2.0 mm)	4.74×10^3	3.82	0.87	0.50

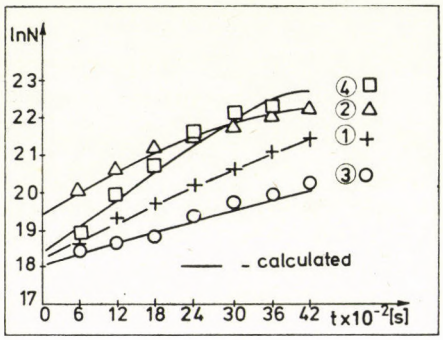

Fig. 1
Numerousness calculated from experimental data and the model

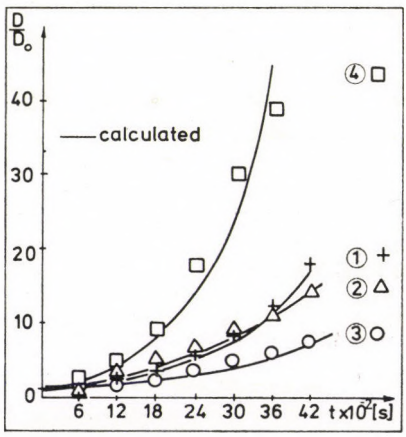

Fig. 2
Size increase as a function of time

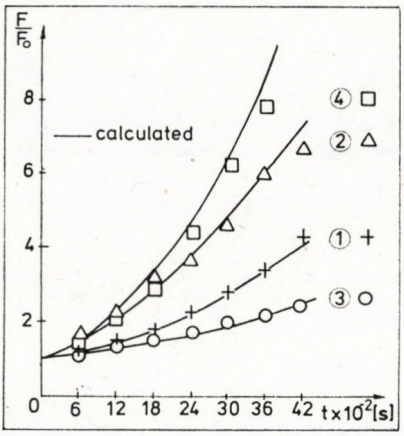

Fig. 3
Surface area increase as a function of time

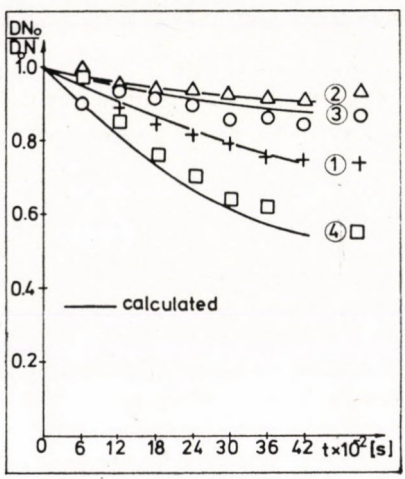

Fig. 4
Changes of particle size with reference to numerousness

induced size and surface area changes were then calculated with the known coefficients. Calculated constants of various materials are listed in *Table 2*.

The grinding-induced size changes D/D_0 and surface area changes (F/F_0) are plotted in *Fig. 2* and *3*. It can be seen that the discrepancy between the data calculated from the sieve analysis figures the and model is small.

The same behaviour is seen when changes of particle size and surface area, with reference to the changes of the number of particles, are compared (cf. *Fig. 4* and *5*).

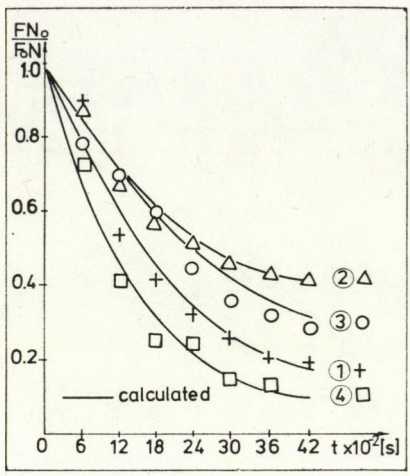

Fig. 5
Changes of surface area with reference to numerousness

Summary

Results calculated from the dispersion model based on the various dispersion characteristics were compared to those calculated from the experimental data.

It was proved that the model developed correctly describes the griding process.

It was proved that changes of the particle size and surface area are proportional to the number of particles, and the size and surface area of a particle. Grinding experiments were carried out with various materials, the ξ coefficients were calculated. The ξ coefficients proved to be constant.

SYMBOLS

d average particle size, m
D size with reference to the unit mass, m kg^{-1}
F surface area with reference to the unit mass, m^2 kg^{-1}
m mass, kg
N numerousness with reference to the unit mass, kg^{-1}
n number of particles in a fraction, —
t time, s
β number of collisions in unit time per particle, s^{-1}
φ number of disintegrations per collision, —
ξ proportionality coefficient, —

SUBSCRIPTS

0 at time $t=0$
∞ at time $t=\infty$
k number of particle fractions
D size
F surface area
N numerousness

РЕЗЮМЕ

Математическая модель операции дробления описана с помощью экстенсивных величин (численность, поверхность частиц, их размер) характеризующих дисперсные системы. Приведена методика разработки модели, и сравнение расчётных и экспериментальных данных (численность, поверхность и т. д.). Установлено, что в операции дробления рост размера и поверхности частиц пропорционален числу соударений, размеру и поверхностю единичной частицы. При определенной геометрической форме частиц можно определить численное значение коэффициента пропорциональности и можно доказать, что эта величина является постоянной.

HUNGARIAN JOURNAL
OF INDUSTRIAL CHEMISTRY
VESZPRÉM
Vol. 11. pp. 21—32 (1983)

HYDRODYNAMICAL STUDIES ON FLUIDIZED BEDS VI.

BED EXPANSION AND PRESSURE DROP IN VIBROFLUIDIZED LAYERS

K. Erdész and Z. Ormós

(Research Institute for Technical Chemistry of the Hungarian Academy of Sciences, Veszprém, Hungary)

Received: August 17, 1982.

This paper summarizes the results of tests carried out to lay the groundwork of vibrofluidization operations. Experiments were carried out in a specially designed, batch-operated vibrofluidization system equipped with a swinging plate. The energy requirement of vibrofluidization was also determined. It was concluded that compared with simple gas fluidization, vibrofluidization improved the flow pattern of the particulate material, and that the optimum range of vibrational acceleration—with respect to energy consumption—was between 1 g and 5 g.

Introduction

Use of vibrofluidization increases in technologies dealing with particulate materials. Essentially, in suitably designed fluidization systems extra energy is introduced into the fluidized layer via mechanical vibration. Vibrofluidization is often advantageous because the intensive motion of the layer creates uniform, controlled and directed mixing [1], the pressure drop across the layer and the minimum fluidization velocity are decreased [2, 3], heat and mass transfer are considerably improved [4, 5] and vibration promotes the fluidization of so-called hard-to-fluidize materials, etc.

These advantages can be utilized in a number of drying, granulation, separation and other operations common in food processing and chemical tehcnologies. At present several major companies (e.g. Aeromatic, Anhydro, and Wedag, etc.) produce in series continuous vibrofluidization systems for the food processing industry. The special equipment used in chemical industries, which takes advantage of vibration, also increases (rectification columns, absorbers, and catalytic reactors, etc.).

Theoretical study of vibrofluidization began about twenty years ago, and a number of publications followed which were recently reviewed in [6] and [7]. A monograph [8] and several texts [9, 10] were also published.

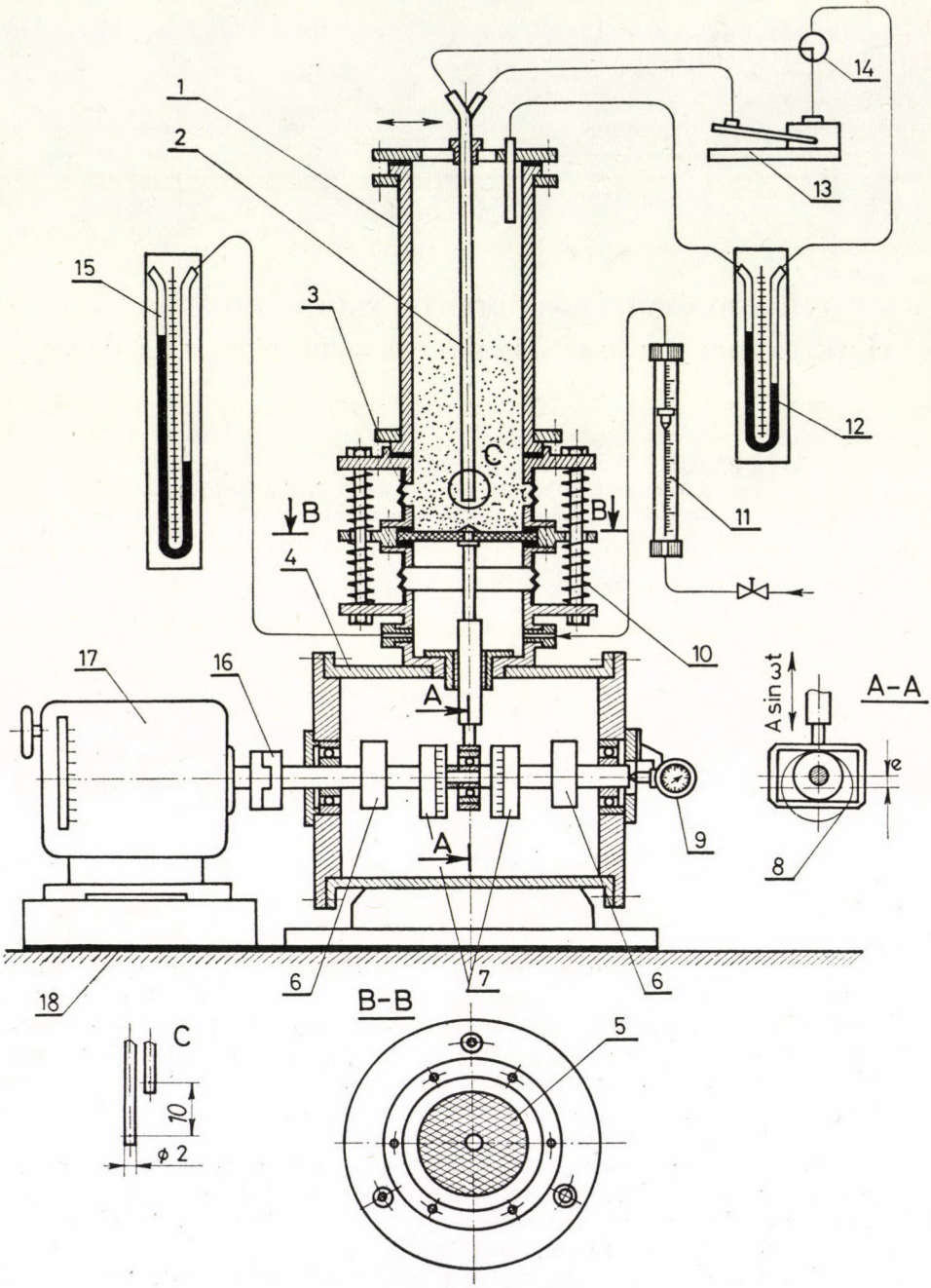

Fig. 1 Experimental apparatus

1 — cylindrical glass column, $D = 0.108$ m; *2* — probe, *3* — flexible gasket; *4* — drive mechanism; *5* — gas distributor plate; *6* — balancing mass; *7* — excenter; *8* — crank mechanism; *9* — tachometer; *10* — spring, *11* — rotameter; *12*, *15* — *U*-tube manometer; *13* — micromanometer; *14* — valve; *16* — flexible clutch; *17* — variable speed electromotor; *18* — rubber plate

Primarily these investigation dealt with flow patterns and heat transfer characteristics of vibrofluidized layers. Practical application of vibrofluidizers proved that considerable energy savings were possible. Therefore, based on hydrodynamic measurements, the system was energetically analysed using the swinging mass model.

Results

Most hydrodynamic measurements were carried out in systems which were filled with particulate material and the entire apparatus was vibrated [1, 2, 3]. On the other hand, from a technological point of view it is more advantageous if the system is stationary and only the layer supporting plate is vibrated. This reduction in the moving masses decreases the energy consumption. Such a system is shown schematically in *Fig. 1.*

The supporting plate is vibrated by a sinusoidal drive machanism, which ensures the harmonic vibration of the plate. The cylindrical springs located between the supporting plate and the drive mechanism establish the eigenfrequency of the system selected in such a manner that the system proper will not resonate. To decrease the amount of vibration transfered to the base, the system is mounted on a heavy welded supporting frame.

Primarily, the hydrodynamic measurements were designed to reveal the relationship of vibration energy input and fluidization characteristics, such as minimum fluidization pressure and bed expansion.

Experiments were carried out with sand of varying particle size, bed height and supporting plates of varying flow resistance.

Vibration parameters were changed as follows:

— Amplitude: A = from 0.6 to 0.9 and 1.85 mm
— ω = from 0 to 267 s^{-1}

Accordingly, the vibration characteristic, $\Gamma = \frac{A\omega^2}{g}$ was changed in the

$\Gamma =$ from 0 to 13.4 range.

Pressure drop across the layer, Δp as a function of fluidization gas velocity u'' was measured along with bed expansion Y/Y_0. The characteristic fluidization curves are shown in *Fig. 2* and *3*. It can be seen that in the presence of vibration, the characteristic pressure peak of gas fluidization *(Fig. 2)* is missing and realtive bed expansion is linear *(Fig. 3)*. When the intensity of vibration is lower, then the layer is at first compacted, followed by bed expansion at higher gas velocities.

The effect of increasing vibration amplitude is shown in *Fig. 4*. Increasing vibration amplitude results in decreased pressure drop across the layer.

The minimum fluidization pressure drop (Δ_{mf}) was determined by visually observing the onset of fluidization. Changes of Δ_{mf} as a function of vibrational characteristic, Γ, is shown in *Fig. 5*. Initially, its value increases (up to $\Gamma = 1/1.5$), then it decreases. The effects of bed height, H is also apparent in the Figure. It also increases the pressure drop, but the decrease of minimum fluidization pressure drop is faster at higher bed heights. At gas velocities above the minimum fluidization velocity, U''_{mf}, the pressure drop, Δ_p, decreases

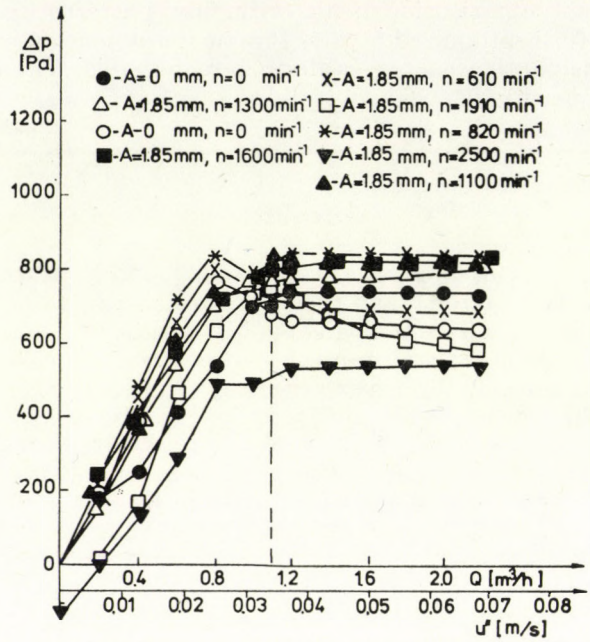

Fig. 2

Pressure drop across the layer as a function of fluidization gas velocity at varying bed heights and vibration parameters (● – $Y_0 = 100$ mm, ○ – $Y_0 = 90$ mm).

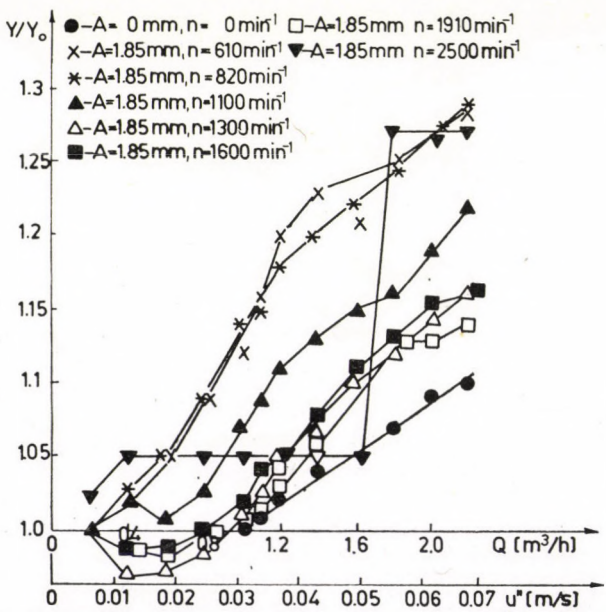

Fig. 3

Relative bed expansion, Y/Y_0 as a function of fluidization gas velocity, u''

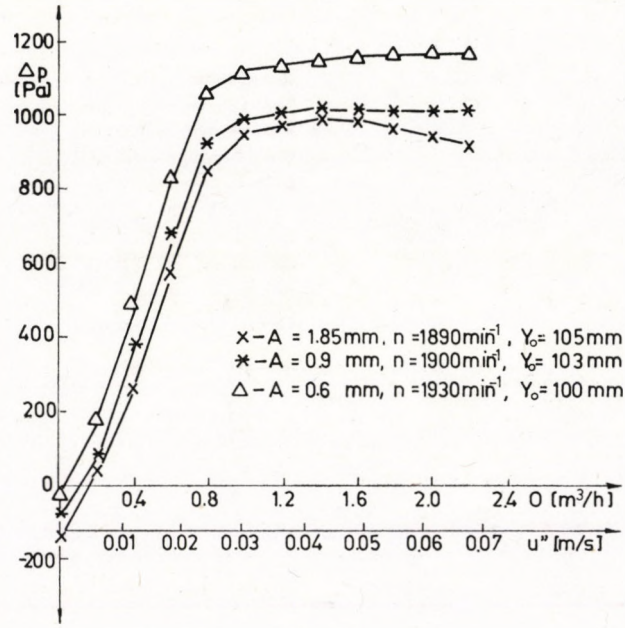

Fig. 4

Pressure drop a cross the layer as a function of the amplitude

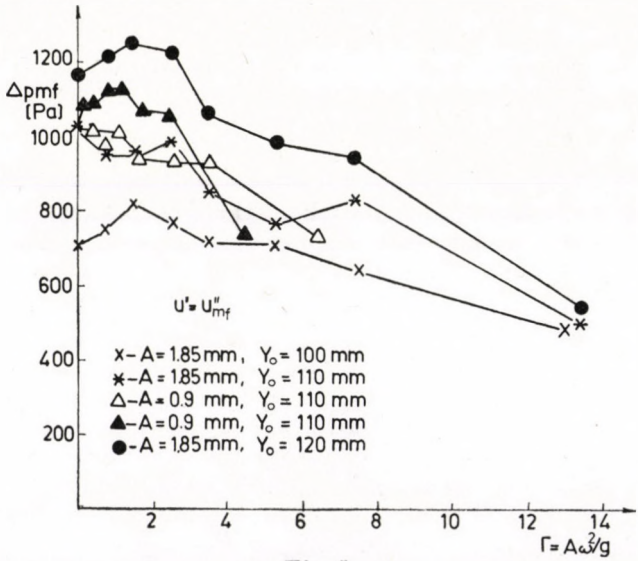

Fig. 5

$\Delta_{p_{mf}}$ as a function of vibration parameter

(up to $\Gamma=1$), then it increases, becomes constant in the $\Gamma=2/5.5$ range, then slowly decreases again *(Fig. 6)*. This means that from a hydrodynamic point of view, once the gas-fludized layer is established, the role of vibration becomes

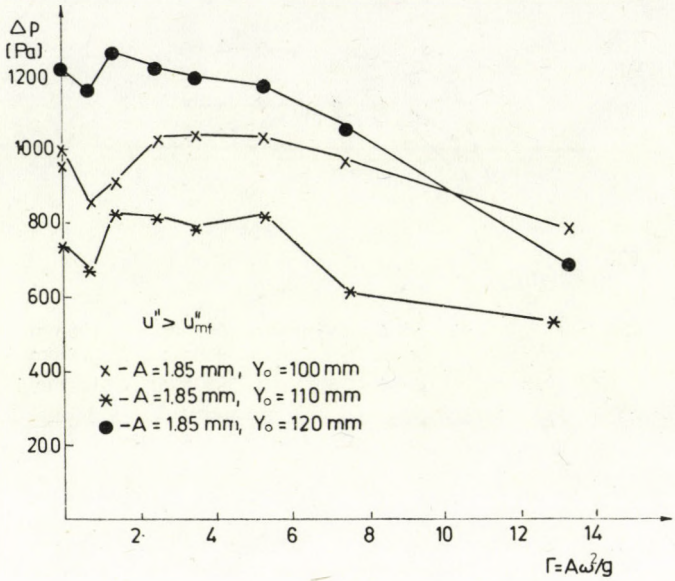

Fig. 6

Pressure drop across the layer at a $u'' > u''_{mf}$ gas velocity

negligible, more correctly, its effects become manifest only at higher intensities, resulting in an operation which demands excessive amounts of energy.

The following polynomial regression equation was obtained from the statistical analysis of measured values for the vibration efficiency, K_v:

$$K_v = 1.06 - 0.034{,}52\ \Gamma + 0.005{,}6\ \Gamma^2 - 0.000{,}07\ \Gamma^3 \tag{1}$$

where:

K_v is the vibration efficiency, the ratio of minimum fluidization pressure in the presence and absence of vibration:

$$K_v = \frac{(\Delta p_{mf})_v}{(\Delta p_{mf})_s}.$$

K_v values derived from measured data are shown in *Fig. 7* against Γ. The full curve is the regression function corresponding to Eq. 1. It can be seen that due to layer compaction, vibration initially hampers fluidization (in the $\Gamma = 0$–1 range), but above this limit significant improvement occurs, i.e. vibration almost halves the minimum fluidization pressure. A deficiency of the regression equation is that it does not account for the initial layer compaction, correspondingly it is valid only for $\Gamma > 1$.

Changes of relative bed expansion are shown in *Fig. 8* in the case of vibration only, and in *Fig. 9* for simultaneous vibration and fluidization. It is apparent in *Fig. 8* that vibration initially causes a compaction of the bed (up to $\Gamma = 1$), followed by bed expansion (up to $\Gamma = 5$), and then bed expansion remains practically constant. At a gas flow rate, which corresponds to the minimum fluidization gas velocity, the layer contracts somewhat up to $\Gamma = 5$,

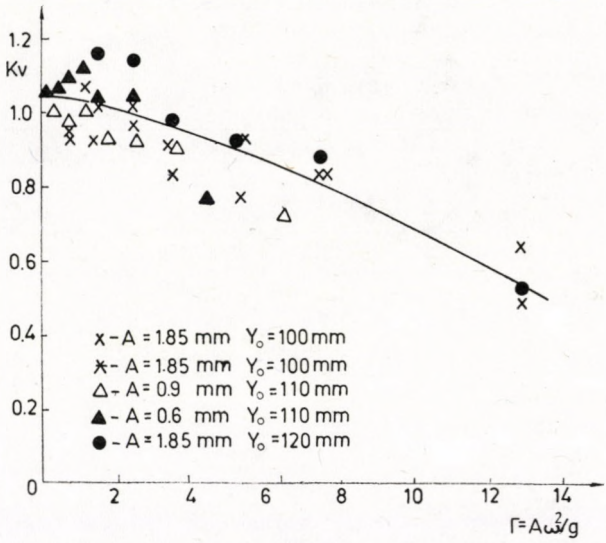

Fig. 7

Vibration efficiency, K_v as a function of the vibration parameter

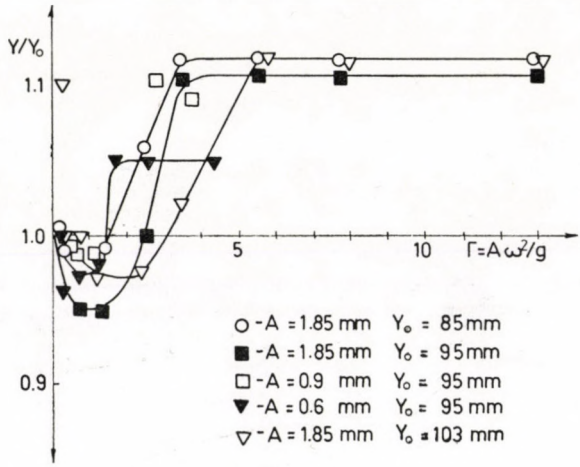

Fig. 8

Relative bed expansion as a function of the vibration parameter

then at more intense vibration it expands, but does not exceed the value obtained in the absence of vibration (i.e. gas fluidization only).

The effect of support plate resistance is shown in *Fig. 10*. It can be seen that with less permeable support plates (higher support resistance), the minimum fluidization pressure is lower over the entire range tested. Data obtained with various particle size fractions are shown in *Fig. 11*. It can be seen that with increasing particle size the pressure decreasing effects of vibration are hindered.

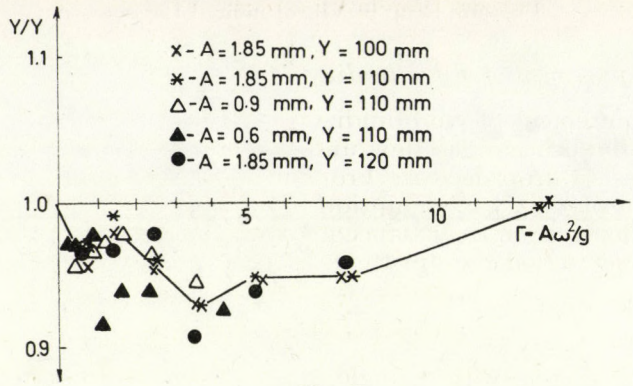

Fig. 9
Relative bed expansion at $u'' = u''_{mf}$ gas velocity

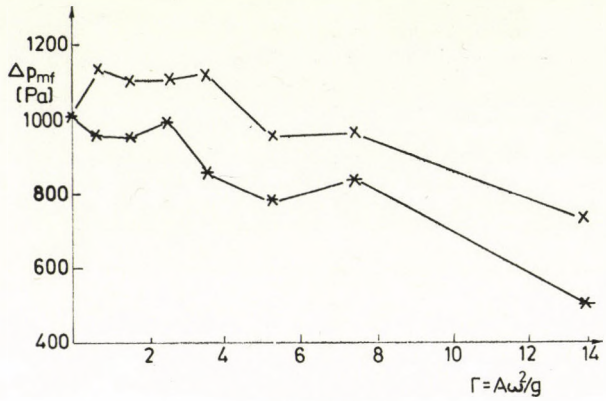

Fig. 10
Effect of support plate resistance upon pressure drop across the layer
× — sieve mesh ✳ — porous bronze

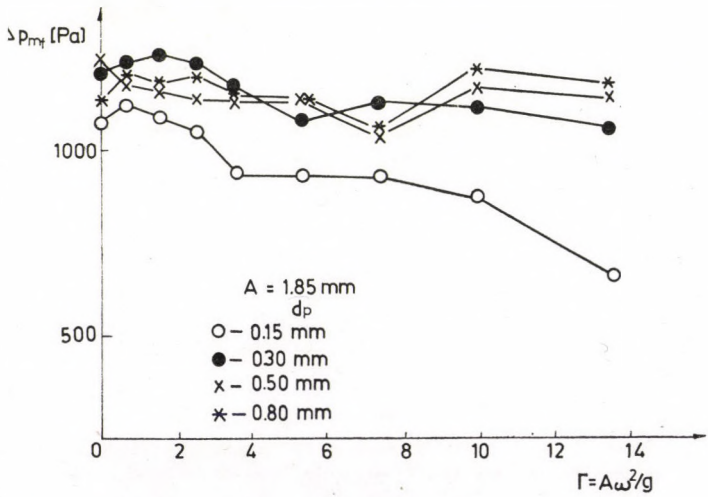

Fig. 11
Pressure drop across the layer as a function of particle size d_p.

The Energy Requirement of Vibrofluidization

The energy requirement of vibrofluidization consists of two parts: the kinetic energy of the fluidization gas flow and the vibration energy transmitted to the layer. Pressure drop decrease brought about by vibration decreases the first component of energy consumption, but vibration itself consumes energy. The economy depends on the balance of these processes.

For a swinging period the kinetic energy of gas flow can be calculated by Eq. 2:

$$E_p = \Delta_{p_{mf}} \times U''_{mf} \times F/n \tag{2}$$

In a swinging system with a single mass, the energy required to maintain vibration can be calculated by Eq. 3 [11]:

$$E_v = m\pi A^2\omega^2 \left[\frac{\omega^2}{\sqrt{(\omega_0^2 - \omega^2)^2 + 4h^2\omega^2}} \right] \sin\varphi \tag{3}$$

where:

$$\omega_0 = \sqrt{\frac{1}{mc}} \tag{4}$$

$$h = \frac{K}{2m} \tag{5}$$

$$\varphi = \operatorname{arctg}\left(\frac{2h\omega}{\omega_0^2 - \omega^2} \right) \tag{6}$$

$$K = D_1 2 \sqrt{\frac{m}{c}} \tag{7}$$

$$c = \frac{8 \cdot D^3 \cdot i}{d^4 \cdot G} \tag{8}$$

Calculations were carried out with the following constants:

— swinging mass: $m = 3.68$ kg;
— slip modulus of spring steel: $G = 8.3 \times 10^{10}$ N/m^2;
— outer diameter of screw-spring: $D = 2.2 \times 10^{-2}$ m;
— diameter of spring-wiwe: $d = 0.2 \times 10^{-2}$ m;
— number of turnus: $i = 6$.

From these data the spring constant becomes:

$$c = 3.92 \times 10^{-2} \text{ m/N}, \quad \text{and}$$

the eigen-frequency of the swinging system is:

$$\omega_0 = 26.38 \text{ s}^{-1}.$$

The damping coefficient of the swinging system, D_1 which is influenced by the characteristics of the particulate material was not determined, rather two extreme values were tested as $D_{1,\max} = 0.1$ and $D_{1,\min} = 0{,}01$. These data are based on values measured with various test materials.

The results of the calculations are shown in *Fig. 12*. The full line depicts the vibration energy, the dotted line the kinetic energy of gas flow determined

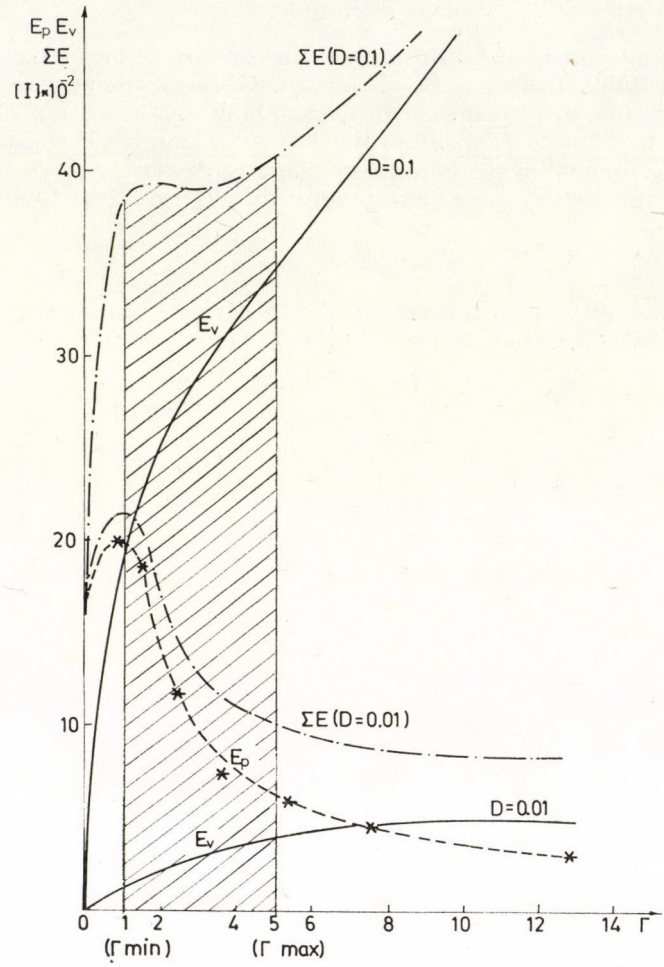

Fig. 12

Energy consumption as a function of the vibration parameter,
– – – kinetic energy of fluidizing gas
—— vibration energy
–·–· overall energy requirement.

from measured data The dot/dash line represents the resultant energy consumption as a function of Γ.

It can be seen that when the damping of the swinging system is small (readily flowing powders) increasing vibration intensity enhances the overall energy consumption up to $\Gamma=1$, then it decreases. Above $\Gamma=5$ the decrease is longer significant. If the damping is large (e.g. with sticking powders) then the overall energy consumption increases rapidly up to $\Gamma=1$, then it is practi-

cally constant between $\Gamma = 1$ and 5, and then it increases again. Therefore' it is not advantageous to increase Γ beyond 5, because no significant energy saving can be realized, while equipment wear increases rapidly.

Conclusions

The following conclusions can be drawn from the hydrodynamic studies of vibrofluidization of particulate materials:

- the minimum fluidization pressure in the vibrofluidization layer decreases with increasing vibration intensity. The minimum fluidization velocity also decreases and can be described by a regression equation;
- bed expansion cannot be increased by increasing the vibration parameter beyond a limit, which is determined by material characteristics;
- the characteristics of the bed supporting plate influence the pressure drop across the layer, the higher the plate resistance the smaller the pressure drop;
- in batch-operated systems the optimum vibration parameters are in the range Γ fro = m 1 to 5. At first the maximum vibration amplitude has to be selected with respect to the strength of the mechanical units, then the vibration frequency has to be optimalized to avoid resonance of the apparatus (or its components). With known swinging masses, resonance can be avoided by adjusting the spring coefficient.

SYMBOLS

A — amplitude, m
c — spring constant, m/N
d — diameter of spring wire, m
d_p — particle diameter
D — outer diameter of spiral-spring, m
D_1 — damping coefficient
E_p — kinetic energy of gas flow, J
E_v — vibration energy of the swinging system, J
F — bed cross section area, m^2
g — gravity constant, $g = 9.81\ ms^{-2}$
G — slip modulus, N/m^2
h — damping frequency, s^{-1}
i — number of turns of the spring
K — damping coefficient, kg/s
K_v — vibrational efficiency
m — mass, kg
n — frequency, s^{-1}
Q — volumetric flow rate of fluidizing gas, m^3/h
u'' — linear velocity of fluidizing gas, $u'' = Q/F$, m/s
u''_{mf} — minimum fluidization gas velocity, m/s
Y — bed height, mm
Y_0 — initial bed height, mm
Δp_{mf} — pressure drop at minimum fluidization velocity, Pa
Γ — vibration parameter
φ — phase angle, rad
ω — frequency, s^{-1}
ω_0 — eigen-frequency, s^{-1}

REFERENCES

1. KROLL, W. Chem. Ing. Techn. *1955*, 1, 27.
2. BRATU, E., JINESCU, J.: B. Chem. Eng. *1971*, 8, 16.
3. MUSTAEV, V. I. i KOROTKOV, B. M.: Khimicheskoe i neftanoe mashinostroenie *1973*, 12.
4. YAMAZAKI, R., KANAGAWA, Y. and, JIMBO, G.: Journ. Chem. Eng. Japan, *1974*, 5, 7.
5. GUTMAN, R. G.: Trans. Inst. Chem. Engr. *1976*, 54.
6. RAHUL GUPTA and MUJUMDAR, A. S.: The Canad. Journ. of Chem. Engg. *1980*, 6, 58.
7. STRUMILLO, C., PAKOWSKI, Z.: DRYING '80 ed. Mujumdar, A. S. Hemisphere Publishing Co. New York, 1980. pp. 211–226.
8. CHLENOV, V. A., MIHAILOV, N. V.: Vibrokipyashchii Sloi, Nauka, Moscow, 1972.
9. KARMAZIN, V. D.: Tekhnika i primenenie vibrokipyashchevo sloya. Naukova Dumka, Kiew, 1977.
10. J. DÖRNYEI: Production of Instant Food Products, Agricultural Publ. House, Budapest 1981 (in Hungarian).
11. BIKOVSKI, I.: Fundamentals of Vibration Engineering, Mir Publishers, Moscow, 1972.

РЕЗЮМЕ

В стати приведены результаты гидродинамических измерений неодходимых для подготовки технологических операций в виброкипящем слое. Измерения осуществлены разработанной для этой цели экспериментальной установке периодического действия с вибрированием газораспределительной решетки. Изучена энергопотребность викрокипения и установлено, что гидродинамические характеристики улучшаются по отношению псевдоожиженного слоя, оптимальные значения вибрационного ускорения найдены в пределах 1g – 5g.

HUNGARIAN JOURNAL
OF INDUSTRIAL CHEMISTRY
VESZPRÉM
Vol. 11. pp. 33—46 (1983)

INVESTIGATIONS OF A BAFFLE-PLATE TUBE-REACTOR

MRS. Á. SIMON, J. NÉMETH, GY. BUCSKY and J. KREIDL*

(Research Institute for Technical Chemistry of the Hungarian Academy of Sciences, Veszprém, Hungary
* Gedeon Richter Pharmaceutical Works Ltd. Budapest, Hungary)

Received: October 11, 1982.

The effects of the free-surface-area fraction of baffle-plates, φ and of their positioning upon the flow-pattern were investigated in 0.1 and 0.3 m diameter tube-reactors, in the $50 < Re_0 < 5800$ flow rate range. Laboratory-scale and pilot-plant scale units of identical geometries were compared with respect to their flow patterns by visual observation and average residence time measurements.

Introduction

The flow-pattern established in tube-reactors significantly influences the rate of chemical reactions taking place in such reactors [1]. In the case of liquid-phase, and homogeneous chemical reactions, optimum reaction conditions can be ensured by establishing homogeneous reactant-distribution and identical residence times. Under ideal conditions each portion of the reactant fed-in spends the same amount of time in the reactor and the components travel in a plug over the entire cross section of the apparatus. However, this ideal case cannot be achieved in plant-scale reactors, it can at best only be approximated, for mixing phenomena occur, and there is an inner drag force acting between the fluid elements. In tube reactors without baffle-plates, the approximation of the ideal conditions is best in the turbulent flow range, where the velocity-distribution over the cross section approaches the step-like distribution of the plug-flow. However, a longer residence time demands longer tube sections.

If the flow velocity is kept constant, and the length-to-diameter ratio of tube-reactors is decreased, then the motion of the fluid elements deviates more and more strongly from the flow-pattern assumed in ideal tube reactors. The standard deviation of the residence time distribution also becomes larger. The most unfavourable flow pattern occurs in the continuously operated, tank-like tube-reactors, in which mixing is almost complete.

In tube-reactors operated in the laminar flow rate range, the flow patterns obtained resemble transitions between the two limiting cases mentioned above. In these cases, the plug-flow pattern can be approached by appropriate modification of the flow-structure (e.g. by baffle elements).

Work on the elimination of the unfavourable characteristics of tube-reactors, operated in the laminar flow range, started in the early fifties. These characteristics include the occurrence of axial mixing and the lack of a defined feed section [2–4]. Baffle-elements, packing and agitators were placed into the tube-reactor to form a series of perfectly mixed chambers. The efficiency of the cascade system thus obtained approaches that of the plug-flow reactor (if $n > 10$). BENKŐ et al [5, 6] showed that tube-reactors equipped with baffle-plates can be treated as a cascade of tank-reactors. The baffle-plates used in these investigations were circular sections of varying free-surface-area. They were located at various places along the tube axis. The baffle series changed the direction of flow, it created significant turbulence, and decreased the extent of back-mixing in the apparatus [7]. HOVORKA and KENDALL [8, 9] examined a homogeneous chemical reaction in a 0.05 m laboratory-scale-tube-reactor. The free surface area fraction of the baffle-plates was 0.2. The distance between the baffle-plates, L was changed between $3D$ and $6D$. The conversion values indicated that closely spaced baffle-plates were advantageous for the reaction. BENKŐ et al [5, 6] used a similar system, and then determined the optimum values of the free-surface-area fraction and of the spacing of the baffle-plates. The free-surface-area fraction, φ was found to be a less significant parameter than the baffle-plate spacing as characterized by the L/D ratio. At close spacing ($L/D = 0.5$) the flow pattern approached that of the plug-flow. Of course, the hydrodynamic resistance of the apparatus depended on the parameters of the baffle system [10].

The use of baffle-plates in industrial tube-reactors is amply justified by the above considerations. However, further studies are required to learn more about the problems of system-scale-up. Apart from geometric similarity, the similarity of flow-patterns requires the invariance of the Re and Fr numbers. However, complete invariance is impossible, even theoretically, so only a partial similarity can be obtained [1]. Valuable data could be obtained by the comparison of laboratory-scale and pilot-plant-scale tube-reactors, facilitating a sensible compromise.

This paper reviews the work carried out to study the flow-modifying effects of the free-surface-area fraction and spacing of baffle-plates in 0.1 and 0.3 m diameter tube-reactors. The free-surface-area fraction of the baffles was changed in the 0.035 to 0.35 range, while their spacing was varied in the $0.3D$–$1.0D$ range. The flow characteristics were examined over the $50 < Re_0 < 5800$ range, where Re_0 denotes the Reynolds number relating to the overall cross section area of the tube-reactor. The flow pattern was monitored by visual observation and photography. Mixing in the tube-reactor was characterized by the average residence time and pressure drop values. Measurements were carried out in the 0.3 m diameter pilot-plant-scale tube-reactor to find out the effects of a three-fold increase in tube diameter upon the flow pattern, while the geometry of the baffle-plates and the Re-criterion were kept constant.

Experimental Apparatus

The schematics of the experimental set-up is shown in *Fig. 1.*

The liquid phase is fed in tangentially at the bottom of the vertically oriented tube-reactor (4) by centrifuge-pump (10), which is connected to reservoir (9). The feed rate is controlled by valves. The step-function concentration-signal is produced by signal generator (6), which switches the flow to the 0.6 kg/m^3 sodium chloride solution. Electrodes (1–3), located in measurement space (11) and connected to conductometer (12) and recorder (13) were used to measure the concentration distribution. The pressure-drop across the baffle-plates was measured by differential manometer (15). The temperature of the feed-water was below 20 °C.

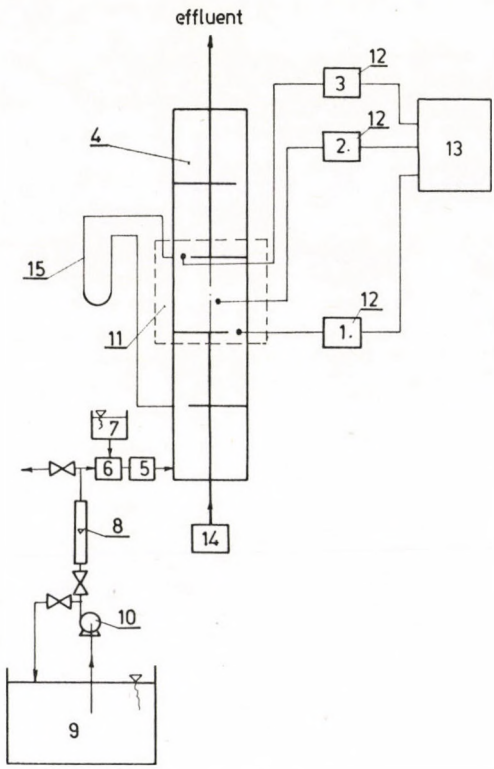

Fig. 1

Schematics of the apparatus used for the residence time distribution measurements *1, 2, 3* — electrodes; *4* — reactor; *5* — flow mixer; *6* — front generator; *7* — tracer reservoir; *8* — rotameter; *9* — reservoir; *10* — pump; *11* — tested reactor section; *12* — conductometer; *13* — recorder; *14* — coloured tracer liquid; *15* — manometer

Measurements were carried out in 0.1 and 0.3 m diameter tube-reactors. The 0.1 m diameter apparatus consisted of three metal sections each 0.4 m long, with a replacable middle section made of glass, which facilitated the visual observation of the flow pattern. The tube-reactor contained five baffle-

plates on an upper support, and five baffle-plates on a lower support. Thus, test compartment (11) was a disturbance-free section. The geometry of the baffle-plates and electrode location are shown in *Fig. 2* for $\varphi = 0.2$ free-surface-area fraction baffle-plates.

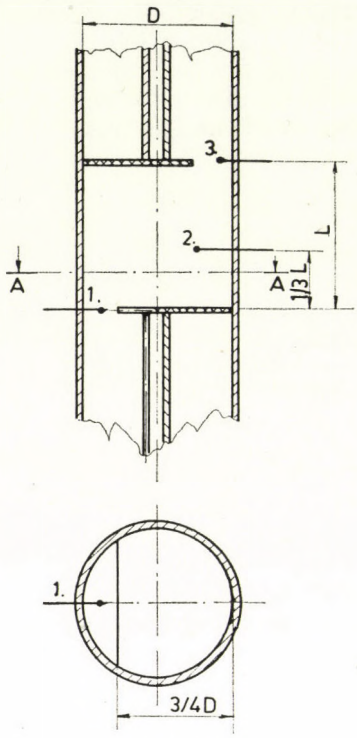

Fig. 2
Schematics of the tested tube section

The pilot-plant-scale tube-reactor had a diameter of 0.3 m and a height of 0.6 m. A baffle-plate resembling a valve-cap ensured the uniform distribution of the incoming flow. The concentration distribution was measured in the vicinity of the two upper baffle-plates.

Measurement Methods

Visual Observation Methods

5–10 μm precipitate-floccules introduced into the system readily indicate the flow-pattern inside the tube-reactor, over its entire cross section. Precipitate deposition indicates the presence of low-flow-rate sections. However, the flow pattern could not be photographed.

The motion of the elements of flowing water could be photographed when a coloured liquid was introduced through the lower baffle-plate of the test section. Feed took place through the holes at the edge of the baffle-plate, into the fastest stream-lines. Thus, the coloured liquid "strings" showed the motion of the fastest-flowing liquid elements. The advantage of this method is that the flow-pattern can be photographed, and the flow-patterns obtained at various flow rates can be compared.

The displacement method, in which water and a coloured liquid were fed in alternatingly, allowed for the observation of the advancing coloured front, and the detection of the low and high flow-velocity sections.

Measurement of the Average Residence Time

Mixing phenomena are most often studied via the measurement of the residence-time distribution curves and the determination of its respective moments. The general test method [1] calls for a pulse, step or periodic disturbance input-signal and for the recording of the response function at the outlet. However, the response function might be distorted by disturbances unrelated to the mixing phenomena studied, such as the poor definition of the input and output sections. In order to eliminate the unwanted disturbances over the wide flow-rate range envisioned for this study, the following measurement strategy was adopted [11]:

A step-function concentration signal was generated at the input. Then, a test section determined by two baffle-plates, was selected in that portion of the tube-reactor where the flow pattern was stabilized (cf. *Fig. 2*). Here, the concentration distribution was recorded via electrodes (1–3) and conductometer (11). The absolute moments were calculated from the concentration distributions thus recorded. Disturbances unrelated to the mixing phenomena inside the test section caused identical upsets in the recorded signals, so the difference of the two signals truly characterized the test section. Electrode (2) located in-between the baffle-plates was used to detect the formation of any occasional "dead-space".

Results and Discussion

Visual Observations

Using the displacement method, the classical laminar flow-pattern could be observed in the 0.1 m diameter tube-reactor, when the baffle-plates were absent. The motion of the fastest liquid elements in the presence of baffle-plates is shown in *Fig. 3* for increasing flow rate and Re_0. It can be seen that the flow-pattern is characteristically different over the entire cross section from that of the baffle-plate-free tube. At low Re_0 numbers the direction of the flow through the slots of the baffle-plates is vertical, followed by a horizontal motion along the upper plate. A "dead space" occurs between the two baffle-plates, under the flow through cross section. Its size decreases with increasing slot-size and decreasing baffle-plate distance. If Re_0 increases beyond 200, the thread-like streamlines become disturbed by inner vortexes and turn-backs. Above $Re_0 = 700$ the whirling eddies, which spin off the pri-

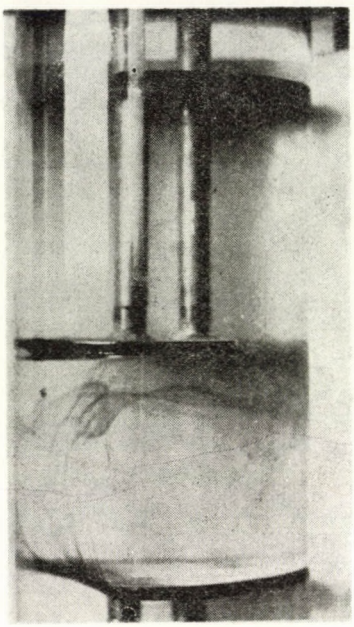

$Re_0 = 50$

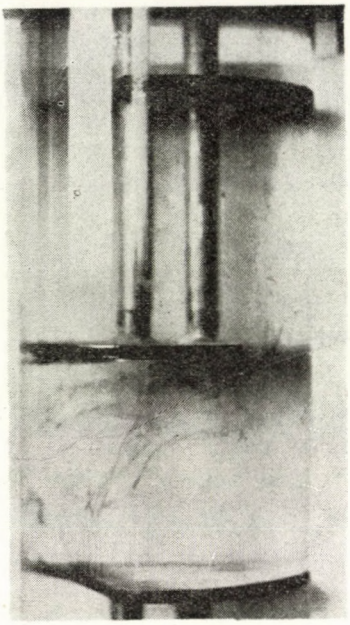

$Re_0 = 250$

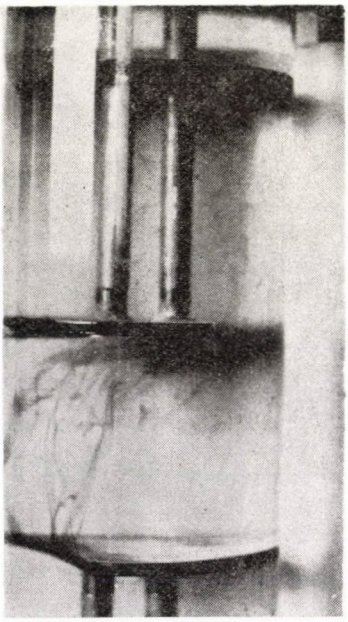

$Re_0 = 500$

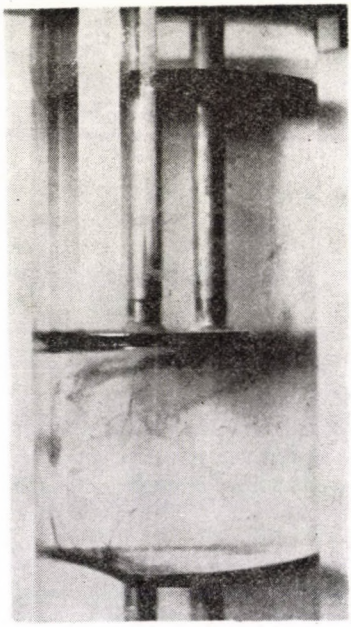

$Re_0 = 700$

Fig. 3

The flow-path of the fastest streamlines in the apparatus ∅0.1 m

mary streamlines, fill the entire space between the baffle-plates. Sedimentation of the precipitate floccules carried by the liquid flow substantiated the existence of "dead space". Therefore, electrode (2) was mounted into this space to facilitate its further study.

The Effects of Flow-Rate and Geometry in the Case of the Laboratory-Scale Apparatus

The effects of the geometry and spacing of the baffle-plates upon the mixing phenomena were studied over a wide flow-rate interval. In the 0.1 m diameter apparatus the main parameters were as follows:

the volumetric flow rate, $Q = 0.05$–1.7 m^3/h,
the empty-tube $Re_0 = 50$–5800,
the free-surface-area fraction of the baffle-plates, $\varphi = 0.035 - 0.35$,
the spacing of the baffle-plates, $L/D = 0.3 - 1.0$.

The results obtained were compared according to Re_0. However, one has to remember that depending on the free-surface-area fraction of the baffle-plates, the actual Re number in the plane of the baffle-plate can be much higher than Re_0, while in the "dead space" the Re number can be much lower than Re_0.

The conductometric measurement-technique yielded a series of curves for various baffle-plate parameters and Re_0. As an example, the curve series obtained with $L/D = 0.5$ and $\varphi = 0.35$ is shown in *Fig. 4*.

The first absolute moments of each curve, and their differences were determined. The signal measured by electrode (1) was taken as reference signal

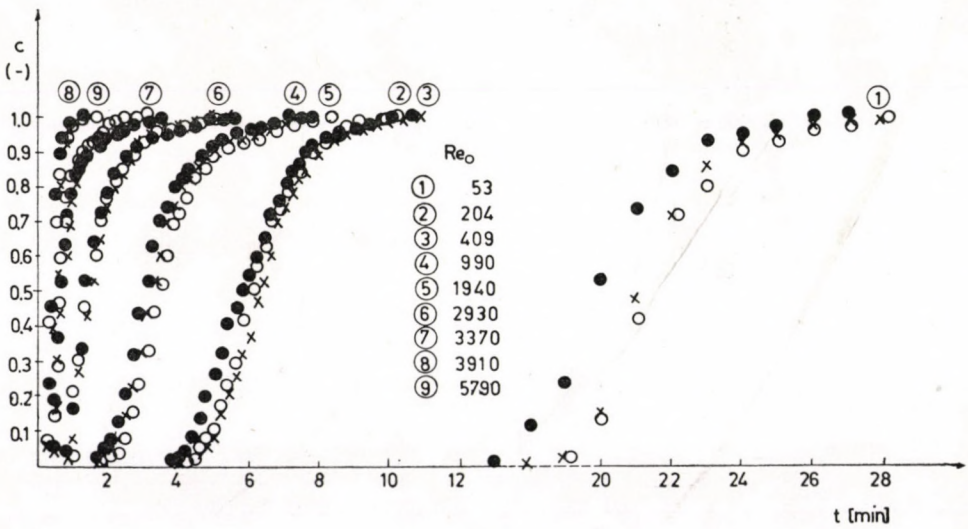

Fig. 4
Concentration distribution of the tracer as a function of time.
$L/D = 0.5$; $\varphi = 0.35$; $\varnothing = 0.1$ m
Sampling points: ● – 1; ○ – 2; × – 3.

(input signal). Thus, the average residence time, t corresponding to a given flow-rate was obtained as the difference between the absolute first moments, μ_1 at the output and input of the test section:

$$t_1 = \mu_{13} - \mu_{11} \quad \text{(s)}$$

Measured average residence time values were compared with the apparent residence time values, t_B belonging to a section of identical volume. Apparent residence time t_B was calculated as the ratio of the test volume and the flow-rate:

$$t_{B1} = \frac{V_1}{Q} \quad \text{(s)}$$

For the comparison of measurements carried out at different flow-rates and baffle-plate geometries, a Θ_1 dimensionless average residence time was defined as:

$$\Theta_1 = \frac{t_1}{t_{B1}} \quad (-)$$

Visual observations suggesting the presence of a "dead-space" indicated the need for accompanying instrumental measurements. Apparent and measured average residence times as a function of Re_0 for the entire test section, V_1 and the intermediate test section defined by electrode (2), V_2 are shown in *Fig. 5* for $\varphi = 0.035$ and $L/D = 1$ baffle-plates. It can be seen that in the laminar flow-rate range and for low free-surface-area-fraction baffle-plates it holds that $t \ll t_B$ for both test sections, which indicates the presence of a "dead space". For $Re_0 > 400$, the measured average residence time values of the entire test section are close to the apparent residence time values. Nevertheless, residence time values (Θ_2) measured by electrode (2) are 2–2.5 times higher than the calculated values. This indicates that the test section cannot be considered a perfectly mixed unit.

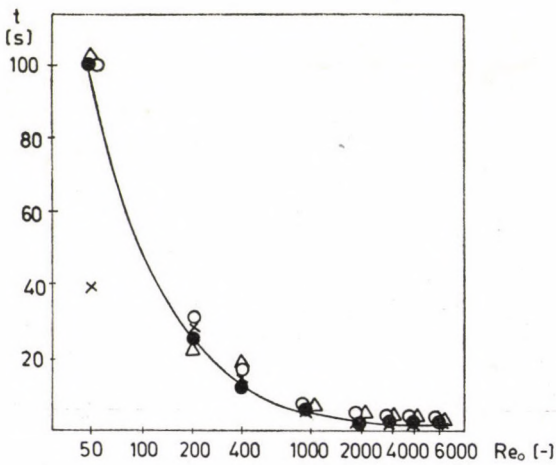

Fig. 5

The dependence of measured and apparent residence time values on the Re_0 number. $L/D = 1$; $\varphi = 0.035$; $\varnothing = 0.1$ m

Calculated = ● — t_{B1}; × — t_{B2}; Measured = ○ — t_1; △ — t_2

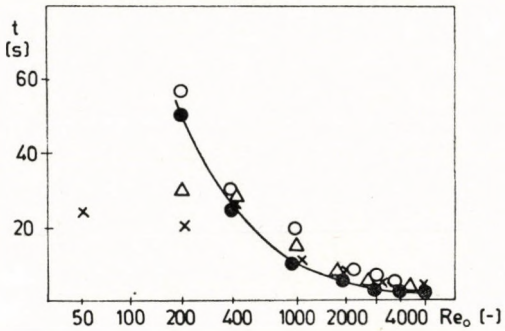

Fig. 6

The dependence of measured and apparent residence time values on the Re_0 number. $L/D=1$; $\varnothing=0.1$ m

Calculated = ● — t_{B1}; Measured = $\underbrace{\times\ -\varphi=0.035;\ \bigcirc\ -\ \varphi=0.20;\ \triangle\ -\ \varphi=0.35}_{t_1}$

It can be seen in *Fig. 6* that for $L/D=1$ a similar tendency holds for any free-surface-area-fraction baffle-plate. No characteristic trend could be observed for Θ_1 when it was plotted against the free-surface-area-fraction. The Θ_1 values were between 1.0 and 1.7.

For $L/D=0.5$ baffle-plate spacing (cf. *Fig. 7*) the average residence time becomes equal to or higher than the apparent residence time—even at low flow rates—for each free-surface-area-fraction. At $Re_0>1000$ even Θ_1 and Θ_2 became similar to each other, indicating that "dead space" formation was negligible for this baffle-plate spacing.

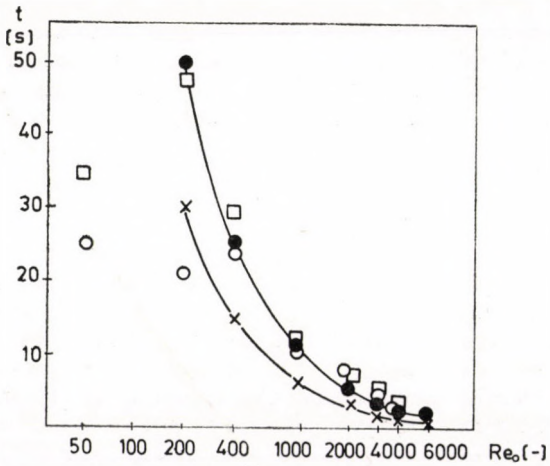

Fig. 7

The dependence of measured and apparent residence time values on the Re_0 number. $L/D=0.5$; $\varnothing=0.1$ m

(Data points are the same as given in *Fig. 6*)

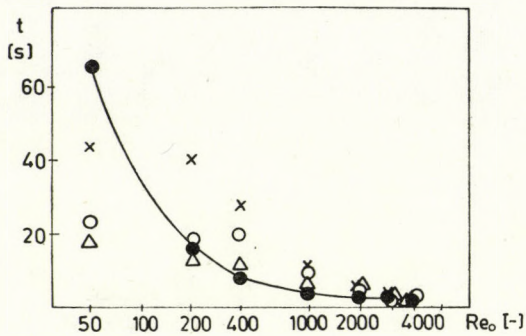

Fig. 8

The dependence of measured and apparent residence time values on the Re_0 number. $L/D=0.3$; $\varnothing=0.1$ m
(Data points are the same as given in *Fig. 6*)

The residence time values measured at $L/D=0.3$ are shown in *Fig. 8*. The measured average residence time values were smaller than the apparent ones at $Re_0=50$, indicating that "dead space" was present though the baffle-plates were closely spaced. Contrary to the previously discussed results, the residence time changed with the free-surface-area-fraction over the entire flow-rate range. Residence time was the longest for the smallest free-surface-area-fraction baffle-plates: $\Theta_1=3.8$. Θ_1 decreased with increasing φ. Apart from the initial section, values measured with electrode (2) did not differ from the calculated ones, i.e. "dead space" was absent.

Measurements indicated that at $L/D=0.3$; $\varphi=0.035$ and $1000<Re_0<4000$ eddy formation became very pronounced, and the entire test section could be considered a perfectly mixed unit. Compared with the apparent residence time, the measured relative residence time also increased. Therefore, tube-reactors equipped with such a baffle-plate system are hydrodynamically favourable for homogeneous chemical reactors.

Pressure Drop

Pressure drop values of tube-reactors increase when baffle-plates are introduced. Pressure drop is higher for narrow-slot, closely spaced baffles. Measured pressure drop as a function of the flow-rate is shown is *Fig. 9* for $\varphi=0.035$ and $L/D=0.3$. For comparison purposes, the calculated pressure drop values Δp_0 for a tube-reactor without baffle-plates are also shown in the Figure.

Under the present test conditions the pressure drop can be described in the $2\cdot10^{-3}$ to $5\cdot10^{-2}$ m/s flow-velocity range as:

$$\Delta p=2.46\times10^6 v^2$$

where Δp = the pressure drop, (Pa)

v = the flow velocity, ms^{-1}

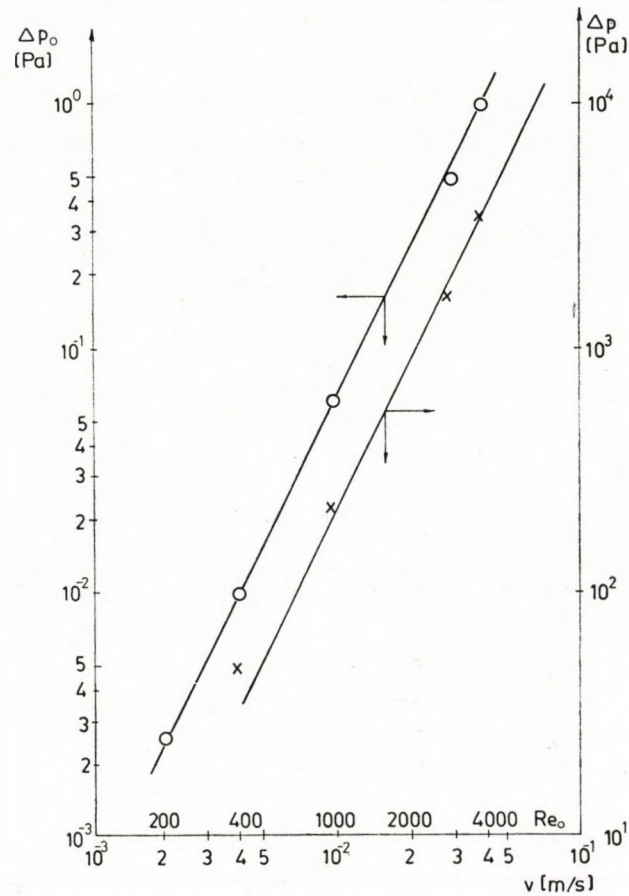

Fig. 9
Pressure drop as a function of the flow rate

Experiences with the Pilot-Plant-Scale Tube-Reactor

Experiences obtained with the 0.3 m tube-reactor operated in the $1000 < Re_0 < 4000$ flow range and with identical geometrical simplexes, include the following.

Visual observation indicated that flow patterns were similar to those observed in the laboratory-scale unit. Baffle-plates with $\varphi = 0.035$ and 0.2 were tested at $L/D = 1$ plate-spacing. Measured and calculated average residence time values as a function of the flow rate are shown in *Fig. 10*. Contrary to observations with the laboratory-scale unit, the measured average residence time values were smaller than the calculated values. The effects of the free-surface-area of the baffle-plate are quite noticeable. Measured and calculated average residence time values agreed better, for smaller φ values. The relative

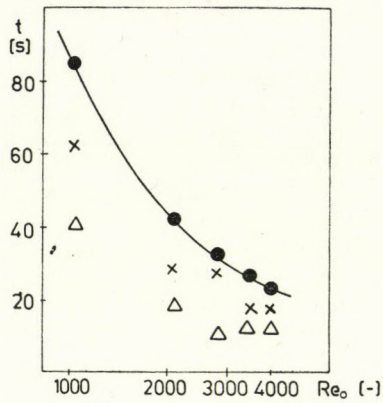

Fig. 10

The depedence of measured and apparent residence time values on the Re_0 number. $L/D=1$; $\varnothing=0.3$ m

Calculated = ● — t_{B1}; Measured = $\underbrace{\times - \varphi=0.035;\ \triangle - \varphi=0.20}_{t_1}$

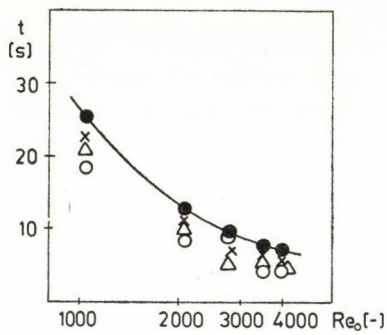

Fig. 11

The dependence of measured and apparent residence time values on the Re_0 number. $L/D=0.3$; $\varnothing=0.3$ m

(Data points are the same as given in *Fig. 6*)

residence times in test section V_1 and V_2 were different, indicating the presence of "dead space".

Residence time values measured with $L/D=0.3$ showed similar tendencies to those obtained at $L/D=1$ (cf. *Fig. 11*). Measured and calculated residence time values agreed best for the smallest φ.

It can be theoretized that closer baffle-plate spacing and lower φ values could result in high relative residence time values as observed in the laboratory-scale unit.

Conclusions

The effects of baffle-plate spacing and of their free-surface-area-fraction upon the flow-pattern were investigated by direct (visual) and indirect methods (residence time distribution) in a 0.1 m diameter baffle-plate tube-reactor.

The introduction of coloured liquid into the apparatus aided the selection of the instrumental measurement technique, and the placing of the electrodes. The method selected for the determination of the average residence time, i.e. measurements between two neighbouring baffle-plates allowed for direct comparisons of the effects of baffle-plate spacing and of their free-surface-area-fraction. From the comparison of the signals of the electrodes located at the two baffle-plates and inside the test-space, the homogeneity of the flow in the test-section could be determined. The smaller the difference of the signals, the more homogeneous is the test-space from a hydrodynamical point of view.

The following conclusions can be drawn from the results:

In the case of baffle-plate free tube-reactors the flow rate range studied ($50 < Re_0 < 5{,}800$) encompasses the laminar and the transitional flow regimes. With baffle-plates installed the upper limit of the laminar region decreased from $Re_0 = 2{,}300$ to $Re_0 = 200$, because the pure laminar flow-pattern could not be observed above this value. Up to $Re_0 = 1{,}000$ "dead space" is formed in the test-section between the baffle-plates. Therefore, this range is not suited to carry out homogeneous-plase chemical reactions.

Upon increasing the flow-rate, a strongly turbulent flow-pattern ($Re_0 = 15{,}600$) occurred in the slot of the baffle-plates, so the homogeneity of the test space between the baffle-plates increased significantly.

The average residence time values obtained for the smallest free-surface-area-fraction and most closely spaced baffle-plates ($L/D = 0.3$; $\varphi = 0.035$) indicated that the test compartments were perfectly mixed above $Re_0 > 1{,}000$.

As expected, the hydrodynamic resistance of the system increased when the baffle-plates were spaced more closely and their free-surface-area-fraction was decreased. However, this increased pressure drop value was well within the operational range of the system.

Experiments caried out in the laboratory-scale apparatus indicated that the use of closely-spaced, low free-surface area-fraction baffle-plates created a turbulent flow pattern in the $1{,}000 < Re_0 < 4{,}000$ range, which proved advantageous for the chemical reactions.

Residence time values measured in the $1{,}000 < Re_0 < 4{,}000$ flow rate range were not as high as the apparent residence time values, when the diameter of the tube-reactor was increased threefold, even though the baffle-plate system had an identical geometrical arangement. This means that complete geometric similarity was accompanied by a partical flow similarity. The advantageously high relative residence time observed in the laboratory-scale tube-reactor can only be achieved by more closely spaced baffle-plates, which have a lower free-surface-area-fraction value.

SYMBOLS

D — tube diameter, m
L — baffle spacing, m
Re — Reynolds number

Re_0 — Reynolds number defined for the entire cross section
Q — volumetric flow rate, m^3/h
V — test space, m^3
Θ — dimensionless residence time, —
n — cascade number
t — average residence time, s
t_B — average residence time calculated as the ratio of test space and flow-rate, s
v — linear flow velocity, m/s
φ — free-surface-area-fraction of the baffle-plates, m^2/m^2
μ_1 — first absolute moment of the concentration distribution, s

REFERENCES

1. BENEDEK, P., LÁSZLÓ, A.: „A vegyészmérnöki tudományok alapjai" (The Principles of Chemical Engineering Science) Műszaki Könyvkiadó, Budapest, 1964.
2. ULRICHSON, D. L. and SMITHZ, R. A.: Ind. Chem. Eng. Fund. *1965*, 4. 2.
3. DENBIGH, K. G.: J. Appl. Chem. *1951* 1, 227.
4. CLELAND, F. A. and WILHELM, R. H.: A. I. Ch. E. Journal *1956*, 2, (4) 489.
5. LÁSZLÓ, A, BENKŐ, B., STEFKO, B. and KREIDL, J.: Hung. J. Ind. Chem. *1975*, 3, (1) 141.
6. BENKŐ, B. and MARTON, GY.: Ibid *1975*, 3, (1) 157.
7. HENZLER, H. J.: Verfahrenstechnische Fortschritte beim Misch. Dispr. Wärmeübertr. in Flüssigkeiten, Düsseldorf, 1978.
8. HOVORKA, R. B., KENDALL, H. B.: Chem. Eng. Progr. *1960*, 56, (8) 58.
9. KENDALL, H. B.: Chem. Eng. Progr. Symp. Ser. 63, 70.
10. HARTUNG, K. H. and HIBY, J. W.: Chem. Ing. Techn. *1972*, 44, (18) 1052.
11. BLICKLE, T., LAKATOS, B., BUCSKY, GY.: Proc. of 2nd European Conference on Mixing, Cambridge 1977.

РЕЗЮМЕ

Изучали влияние коэффициента свободной поверхности и размещения ламелл на гидродинамику потока в трубах с диаметром 0,1 и 0,3 м в интервале числа Рэйнолдса $50<Re<580$. Визуальным наблюдением и измерением среднего времени пребывания сопоставлены лабораторные и полупромышленные установки.

HUNGARIAN JOURNAL
OF INDUSTRIAL CHEMISTRY
VESZPRÉM
Vol. 11. pp. 47—57 (1983)

A TWO-ALGORITHM APPROACH TO CALCULATE REBOILED ABSORBERS

L. TIMÁR

(Hungarian Oil and Gas Research Institute, Veszprém)

Received: November 5, 1982.

A two-algorithm approach is proposed to calculate reboiled absorbers. It is based on the segmentation of the column into absorption and stripping sections in order to compute each with most suitable algorithm. The interconnection of the sectional calculations occurs on a system level, by a special combination of the sequential and simultaneous modular simulation strategies. The advantages of this new approach over the conventional, single-algorithm concept is discussed with some examples.

Introduction

The simulation of reboiled absorbers used in natural gas plants for deethanization or demethanization is considered to be a difficult convergence problem, due to the different character of the absorption and stripping process taking place within the same column *(Fig. 1)*. In accordance with the analysis of FRIDAY and SMITH [1], the absorption (upper) section needs an algorithm that uses the heat balances to correct the temperatures and the stripping (lower) section, on the other hand, an algorithm that uses the heat balances to correct the vapour (or liquid) flow rates. In other words, the upper section ought to be simulated with the sum-rate (SR) method [2] and the lower one with the bubble-point (BP) [3] or some other method proposed for nonabsorption cases. In general, neither the SR, nor the BP-algorithm, in itself, is suitable for solving such intermediate problems. To overcome the difficulties associated with the interconnection of two different algorithms, usually global methods carrying out simultaneous temperature and flow rate correction (e.g. [4], [5]), were proposed for reboiled absorbers. The simultaneous solution of the heat balances (E) and the so-called mole fraction summations (S) based on the NEWTON–RAPHSON technique, may, however, become very storage and time-consuming especially in the case of a large number of plates. This, seemingly practical drawback can prevent the use of relatively small or moderate size computers (e.g. HEWLETT–PACKARD Model 45 desktop computer with flexible disc).

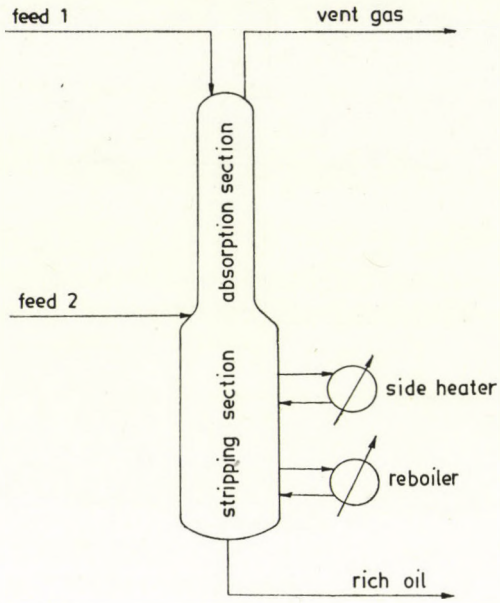

Fig. 1
Scheme of the reboiled absorber

The other method of treating intermediate cases is the segmentation of the column into sections, each to be solved with the most appropriate, possibly less complicated algorithm. Sectional calculations have to be interconnected by suitable system simulation strategy capable of handling recycle-type non-linear equations.

A similar segmentation technique working with a vapour-liquid equilibrium cascade as the building element was suggested by JVANECKI et al [6] to simulate complex columns with side strippers. FONYÓ et al [7] used the theoretical plate as a building element. Some advantageous applications of the segmentation approach over the conventional one-algorithm-one-column concept were already discussed in our previous article [8]. A succesful application of this segmentation approach (called the two-algorithm-approach) to reboiled absorbers is outlined here.

Two-Algorithm Approach

Segments and Algorithms

The rectisorber, in accordance with the essence of the approach, is segmented into an absorption and a stripping section. The reboiler and side heaters, if there are any, are considered to be attached to the stripping section. The vapour and liquid phase of the feed to be deethanized or demethanized are mixed with the vapour leaving the stripping part and with the liquid leaving the absorption segment, respectively. In the case of more than one feed,

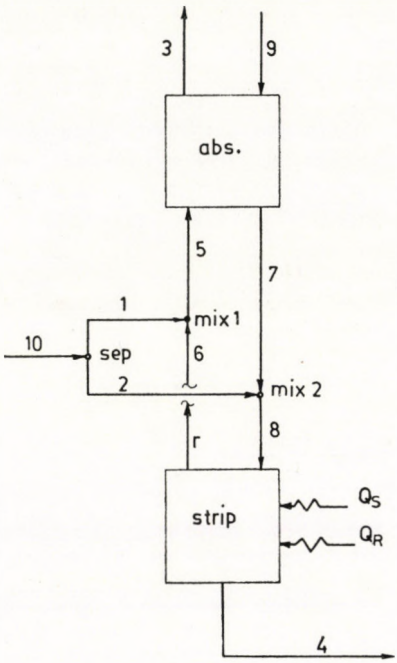

Fig. 2
Segmentation of the reboiled absorber

usually methane-rich vapours, the absorption section ends above the last vapour feed. The result of this segmentation is shown in *Fig. 2.*

For the calculation of the absorption section the SR-method developed for typical absorption problems [2, 9] has proved to be most efficient. As for the stripping section, the so-called XT-method [10] which we developed was found to be appropriate. The XT-algorithm is based on the simultaneous correction of the liquid mole fractions (X) and plate temperatures (T) using the linearized component mass balance (C) and summation equations (S), while the mass flows (V) are corrected by solving the enthalpy balances (E). The main steps of the algorithm are summarized in the Appendix. More details can be taken from reference [10]. In order to facilitate some specifications on product quality (e.g. mole fraction of the key, instead of the distillate rate, D), the method was combined with the so-called Θ-convergence formula [10].

Since the calculation procedures applied to mixing and vapour-liquid equilibrium separation processes are simple and well-known algorithms, their description is omitted here.

Interconnection of the Algorithms

Starting the calculation from whatever section, a recycle stram arises. If beginning with the absorber section, the flow-rates of the stream leaving the stripping section must be assumed (m_{6j}, $j=1, 2, \ldots, k$).

Based on the results of the unit-to-unit calculations, a new recycle stream (r) is obtained. The solution of the

$$r_j(m_{6j}) - m_{6j} = 0 \qquad j = 1, 2, \ldots, k \tag{1}$$

nonlinear equation set brings an additional requirement over the single-algorithm approaches. Accordingly, the question is justified whether such a decomposition can be advantageous. Thus, the efficient applicability of the new approach greatly depends on the convergence method used to solve the equation (1).

The experiences gained with the various convergence methods (direct substitution, dominant eigenvalue, WEGSTEIN, and NEWTON–RAPHSON, etc.) showed that the direct substitution is generally sufficient to converge the recycle flow rates. It is due to the relatively good estimates based on KREMSER's separation (absorption and stripping) fractions [11]:

$$m_{6j} = \frac{-[(m_{1j} + m_{5j})S_j^A + m_{2j}]S_j^s}{S_j^A S_j^s - 1} \tag{2}$$

where:

$$S_j^A = \frac{\left[\frac{L}{K_j V}\right]^{n+1} - \left[\frac{L}{K_j V}\right]}{\left[\frac{L}{K_j V}\right]^{n+1} - 1} = \frac{m_{7j}}{m_{5j} + m_{9j}} \tag{3}$$

$$S_j^s = \frac{\left[\frac{K_j V}{L}\right]^{n+1} - \left[\frac{K_j V}{L}\right]}{\left[\frac{K_j V}{L}\right]^{n+1} - 1} = \frac{m_{4j}}{m_{8j}} \qquad j = 1, 2, \ldots, k \tag{4}$$

It should be noted that the same result would be obtained for m_{6j} when solving all the mass balance and separation fraction defining equations simultaneously, as in the case of the so-called quasilinear (simultaneous modular) simulation approach [12]. In our procedure, however, this quasilinear step is simplified and restricted only to the recalculation of the recycle flow rates. Hence, the simultaneous solution of the linearized equation set, which constitutes a particular step in the simultaneous modular simulation strategy is applied here as a convergence method to recycle-generated nonlinear equations existing in the sequential modular strategy. Earlier and new experiences [13, 14] with flow sheeting indicated that this "simultaneous" convergence method can be used as a convergence promoter in the direct substitution. Similarly, as for other accellerators (e.g. [15]), it must be activated only at the slowing point, i.e. in every third of fourth iteration. Accordingly, the calculation procedure looks similar to *Fig. 3*.

Programme and Examples

The calculation procedure proposed in *Fig. 3* could be realized in our flow sheeting programme system [16] which enables the user to select either the sequential or the simultaneous modular strategy or to change over from the one to the other during the simulation.

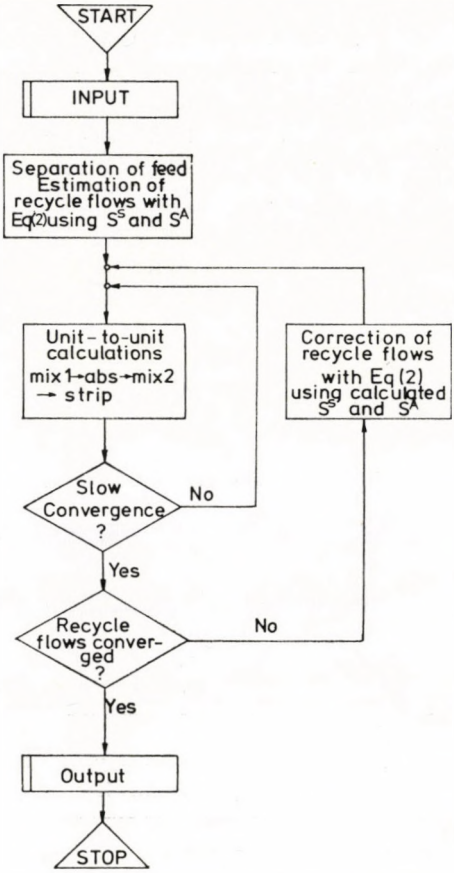

Fig. 3
Scheme of the calculation procedure

The examples picked out for the demonstration were encountered in the field of natural gas processing. Example 1 represents a classical deethanizator with sponge oil and example 2a and 2b are demethanization problems. The specifications are given in *Tables 1–2*. The segmentation of the column is shown in *Fig. 4*. For comparison of the two-algorithm approach (TA) with the single-algorithm one, three representative algorithms were selected each bei ngsuitable for handling some or all reboiled absorber cases, namely:

BP [3]: bubble point method
XT [10]: simultaneous X-T-correction
XTV [5]: simultaneous X-T-V-correction (global).

The estimates for the recycle flow rates were set equal to the values resulted after the solution of the component balances of the whole (unsegmented) system. The convergence criterion was given by the following inequalities:

Table 1

Specification of example 1

1. Feed conditions	feed 1	feed 2
Mass flow, kmol/h	100.58	900.93
Temperature, K	259	283
Composition, mole farction		
methane	0.0943	0.2945
ethane	0.2970	0.1250
propane	0.0878	0.0918
i-butane	0.0018	0.0293
butane	0.0003	0.0248
i-pentane	0.0011	0.0084
pentane	0.0034	0.0069
hexane	0.2152	0.1730
heptane	0.1704	0.1396
octane	0.0683	0.0566
nonane	0.0316	0.0262
decane	0.0288	0.0239
2. Operating parameters		
Pressure, MPa	1.85	
Number of theoretical plates	16	
Location of feed 1	1	
Location of feed 2	6	
Temperature of bottom product, K	442	
Reboiler	partial	
3. Property calculation		
Vapour-liquid equilibrium:	Grayson-Streed/Hildebrand	
Enthalpy	Redlich-Kwong	
4. Initial profiles		
Temperature, K		
top plate	270	
bottom plate	375	
reboiler	445	
Vapour mass flows, kmol/h		
$V_i = D_i = 430, \quad i = 1, 2, \ldots, 17$		

$$\text{Max}\ (|\Delta T_i|,\ i=1,\ 2,\ \ldots,\ n) < 0.1$$

$$\text{Max}\left(\left|\sum_{j=1}^{k} y_{ij} - 1\right|,\ i=1,\ 2,\ \ldots,\ n\right) < 0.000{,}1$$

that proved to be a sufficient and necessary condition in the practical applicability of the results.

The computation times attained for the various algorithms were related to the XTV-method that is considered to be the best algorithm for reboiled absorbers. The figures referring to the ratios of computation times are summarized in *Table 3*. These values demonstrate that the application of the two-algorithm approach can be advantageous. In the case of deethanization, it proved to be competitive with the other single-algorithm methods, even

Table 2

Specification of example 2

1. Feed conditions	feed 1	feed 2
Mass flow, kmol/h	652.83	444.24
Temperature, K	256	265
Composition, mole fraction		
methane	0.1440	0.7940
ethane	0.0970	0.1554
propane	0.1277	0.0348
i-butane	0.0517	0.0060
butane	0.0579	0.0059
i-pentane	0.0195	0.0020
pentane	0.0164	0.0014
hexane	0.0114	0.0004
heptane	0.2191	0.0001
octane	0.1750	0.0000
nonane	0.0589	0.0000
decane	0.0214	0.0000
2. Operating parameters		
Pressure, MPa	2.5	
Number of theoretical plates	11	
Location of feed 1	1	
Location of feed 2	8	
Mole fraction of methane in bottom kmol/kmol	0.0100	
Location of side heater	10	
Reboiler	partial	
Side heat flow J/h	5×10^5 (for example 2b, only)	
3. Property calculation		
Vapour-liquid equilibrium:	GPSA-chart-based-polynomial	
Convergence pressure, MPa:	15	
Enthalpy:	Redlich-Kwong	
4. Initial profiles		
Temperature, K		
top plate	290	
bottom plate	305	
reboiler	360	
Vapour mass flows, kmol/h		
$V_i = 447$, $i = 1, 2, \ldots, 8$		
$V_i = 44.7$, $i = 9 \ldots 12$		

Table 3

Comparison of the Two-Algorithm Approach (TA) with other methods

Example	Problem	Computation time			
		XTV	XT	BP	TA
1	deethanization	1	0.81	2.1	1.45
2a	demethanization	1	divergence	divergence	0.92
2b	the same as 2a, but with working side heater	1	divergence	divergence	0.89

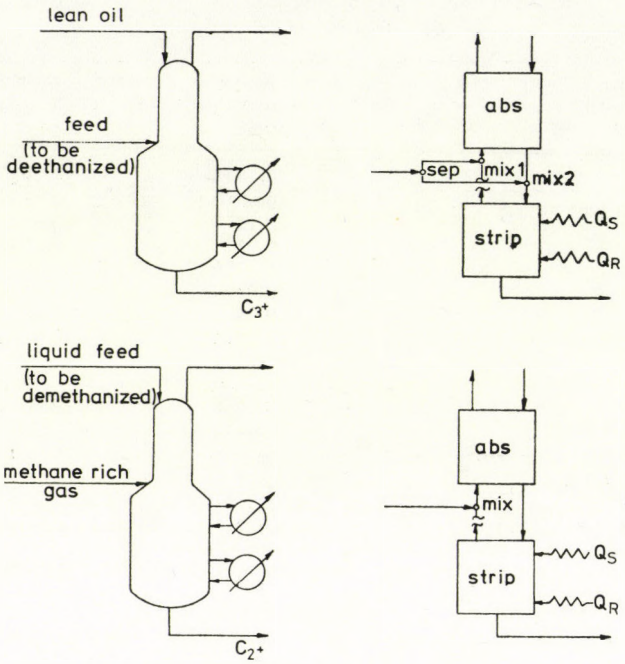

Fig. 4
Segmentation for example 1 and 2

with the most efficient XT-algorithm. On the other hand, in the case of the demethanization, it was the new approach that turned out to be superior to the others. The XT-method and BP-method failed to converge. A similar conclusion, but with somewhat different ratios, could be drawn when discussing the results of the other examples arising in our practice. Using recycle estimates calculated with e.g. (2), the figures referring to the computation time ratio look more favourable for the two-algorithm approach. Moreover, the new approach led to a convergence even in the case of very poor guesses (100–200% for from the solution) which indicates the robustness of the procedure.

Significance

The two-algorithm approach, with a special recycle solving technique, was successfully applied in the calculation of several industrial reboiled absorption problems encountered in natural gas processing. For the demethanization case, the new approach generally proved more efficient than any global, NEWTON–RAPHSON algorithm developed for this purpose. For deethanization, however, the conventional, single-algorithm approach (e.g. XT-method, and BP-method) seems to be somewhat better concerning computation time. Nevertheless, if one has no global method as a computer programme or the available computer is small for its implementation, the segmentation and the alternate application of two relatively single algorithms (e.g. SR-method and

BP-method) may overcome the difficulties. As for the interconnection of the algorithms, it can be realized either within any modularly structured simulation programme containing these algorithms as modules, or within a separate reboiled absorber programme (or module) containing the two algorithms and an organizing part for the interconnection.

SYMBOLS

k number of components
K vapour-liquid equilibrium ratio
L (effective) liquid mass flow, kmol/h
m component flow of stream, kmol/h
n number of theoretical plates
r recycle flow rate, kmol/h
S^A fraction absorbed according to Eq. (3)
S^s fraction stripped according to Eq. (4)
T (effective) temperature, K
V (effective) vapour mass flow, kmol/h
y mole fraction in vapour phase
indices
i plate
j component

Appendix

XT-method

I. Model
component balances (C-equations):

$$\mathbf{c}_j(\mathbf{x}_j, \mathbf{t}, \mathbf{v}) = 0 \qquad j = 1, 2, \ldots, k \tag{1}$$

summation equations (S-equations):

$$\sum_{j=1}^{k} x_{ij} - 1 = 0 \qquad i = 1, 2, \ldots, n \tag{2}$$

enthalpy balances (E-equations):

$$\mathbf{e}(\mathbf{x}, \mathbf{t}, \mathbf{v}) = 0 \tag{3}$$

II. Linearization of C- and S-equations:

$$\mathbf{A}_j \, \Delta\mathbf{x}_j + \mathbf{B}_j \, \Delta\mathbf{t} = -\mathbf{c}_j \qquad j = 1, 2, \ldots, k \tag{4}$$

$$\sum_{j=1}^{k} \Delta x_{ij} = 1 - \sum_{j=1}^{k} x_{ij} \qquad i = 1, 2, \ldots, n \tag{5}$$

where:

$$\mathbf{A}_j = \frac{\partial \mathbf{c}_j}{\partial \mathbf{x}_j} \quad \mathbf{B}_j = \frac{\partial \mathbf{c}_j}{\partial \mathbf{t}}$$

III. Algorithm

0. Estimate t, v; using Eq. (1) calculate x_j.
1. Multiply Eq. (4) with $\mathbf{A}_j^{-1}$:

$$\mathbf{I} \, \Delta\mathbf{x}_j + \mathbf{A}_j^{-1}\mathbf{B}_j \, \Delta\mathbf{t} = -\mathbf{A}_j^{-1}\mathbf{c}_j \tag{6}$$

2. Summarize Eq. (6) with respect to j:

$$\mathbf{I} \sum_{j=1}^{k} \Delta \mathbf{x}_j + \sum_{j=1}^{k} \mathbf{F}_j \, \Delta \mathbf{t} = \sum_{j=1}^{k} \mathbf{g}_j \tag{7}$$

where:

$$\mathbf{F}_j = \mathbf{A}_j^{-1} \mathbf{B}_j$$

$$\mathbf{g}_j = -\mathbf{A}_j^{-1} \mathbf{c}_j .$$

3. Let:

$$\sum_{j=1}^{k} x_j = 1$$

and introducing:

$$\sum_{j=1}^{k} \mathbf{F}_j = \mathbf{F}_s$$

$$\sum_{j=1}^{k} \mathbf{g}_j = \mathbf{g}_s$$

Eq. (7) can be rewritten as:

$$\mathbf{F}_s \, \Delta \mathbf{t} = \mathbf{g}_s \tag{8}$$

4. Solve Eq. (8) for Δt:

$$\Delta \mathbf{t} = \mathbf{F}_s^{-1} \mathbf{g}_s \tag{9}$$

5. Using Δt, calculate Δx_j from Eq. (6):

$$\Delta \mathbf{x}_j = -\mathbf{A}_j^{-1} \mathbf{c}_j - \mathbf{A}_j^{-1} \mathbf{B}_j \, \Delta \mathbf{t} \qquad j = 1, 2, \ldots, k \tag{10}$$

6. Calculate corrected $\mathbf{x}$ and t:

$$\mathbf{X}^{\text{new}} = \mathbf{X}^{\text{old}} + \Delta \mathbf{X} \tag{11}$$

$$\mathbf{t}^{\text{new}} = \mathbf{t}^{\text{old}} + \Delta \mathbf{t} \tag{12}$$

7. Calculate V from Eq. (3):

$$\mathbf{v} = \mathbf{v}(\mathbf{X}, \mathbf{t}) \tag{13}$$

8. Check if convergence is reached. If not, go to 1, otherwise STOP.

REFERENCES

1. FRIDAY, J. R. and SMITH, B. D.: A.I.Ch.E.J. *1964*, 10 (5) 698.
2. SUJATA, A. D.: Hydrocarbon Process. *1967*, 40 (12) 137.
3. WANG, J. C. and HENKE, G. E.: Hydrocarbon Process, *1966*, 45 (8) 155.
4. TOMICH, J. F.: A.I.Ch.E.J. *1970*, 16 (2) 229.
5. ISHII, Y. and OTTO, F. D.: Can. J. Chem. Eng. *1973*, 51, 601.
6. JVANECKI, I. B., MAKLASHINA, N. S., PLATONOV, V. M., WOLIN, YU. M., PEVZNER, S. P., OSTROVSKI, G. M.: Teor. Osnov. Khim. Tekhn. *1979*, 13 (2) 249.
7. FONYÓ, ZS. and RÉV, E.: Hierarchical Approach for Process Flowsheeting by Simultaneous Modular Strategy. Process Systems Engng. Symposium, Kyoto, Japan, 1982.
8. TIMÁR, L., CSERMELY, Z. and BÁCSKAI, S.: Hung. J. Ind. Chem., *1979*, 7, 377.
9. BURMINGHAM, D. W. and OTTO, F. D.: Hydrocarbon Process, *1967*, 46 (10) 163.
10. TIMÁR, L. and ÉDES, J.: Hung. J. Ind. Chem., *1982*, 10, 107.

11. KREMSER, A.: National Petroleum News, *1930*, 22 (21) 48.
12. WESTENBERG, A. W., HUTCHISON, H. P., MOTARD, R. L. and WINTER, P.: Process Flowsheeting, Cambridge, 1979.
13. TIMÁR, L. and PILHOFER, Th.: Verfahrenstechnik, *1973*, 7 (2) 53.
14. WEISENFELDER, A. J., OLSON, R. E. and BRAUN, C. F.: CEP, *1980*, 1, 41.
15. ORBACH, O. and CROWE, C. M.: Can. J. Chem. Eng. *1971*, 49, 509.
16. TIMÁR, L., SIMON, F., CSERMELY, Z., SIKLÓS, J. and BÁCSKAI, S.: MASTEP — Sequential and Simultaneous Modular Algorithm in a Flowsheeting Programme. Proc. of CHEMPLANT '80 EFCE Symposium (EFCE Publ. Ser. No. 10) 1980, Hévíz, Hungary, p. 115.

РЕЗЮМЕ

В стати для расчета абсорбуонно-отпорных колонн изложен секционный подход составленя алгоритмов. Данная методика основывается на сегментации колонн на абсорбционную и отпарную секции для выбора подходящих алгоритмов. Расчёты секций организуются специальной комбинацией последовательной и параллельной стратегий употребляемых при моделировании сложных схем. Решение промышленных задач демонстрирует преимущества нового подхода.

HUNGARIAN JOURNAL
OF INDUSTRIAL CHEMISTRY
VESZPRÉM
Vol. 11 pp. 59—62 (1983)

TWO MEASURES FOR THE VARIABILITY OF MULTI-PURPOSE BATCH CHEMICAL PLANTS

W. JÄNICKE

(Technische Hochschule „Carl Schorlemmer" Leuna-Merseburg, Merseburg, German Democratic Republic)

Received: November 9, 1982.

Several batches of similar or different products can be manufactured simultaneously and (or) successively on multipurpose plants. To evaluate the capacity, variability and reliability of such plants, the following questions are of interest:

- Given the starting time, how many possibilities are there for manufacturing a batch in the plant?
- How many batches of equal kind can be produced simultaneously?

The note informs about a backtrack algorithm for solving the first question and proposes a graph theoretical solution to the second problem by determining a maximum stable set of undirected graph.

Multi-purpose batch chemical plants are used in the production of medicines, paints, and cosmetics, etc. Similar or different products are manufactured batch-wise—simultaneously and (or) successively—in such plants.

Batch (discontinuous) production results from requirements such as:

— small scale production with large assortment;

— easy adaptability to changes in raw material and marketing conditions.

These demands require the use of plants of variable applications. In order to evaluate these plants, it appears to be useful to define measures describing the variability of the plant. Such measures are of interest for obtaining information on reliability and evaluating the maximum yield of the preferred products.

Problem Description

In the following, a multi-purpose batch chemical plant, such as in EGLI/RIPPIN [1] or BIECHELE et al [2], is described. This plant is represented by a directed graph $G=(X, U)$, where $X=x_1, \ldots, x_n$ are vertices, and $U=u_1, \ldots, u_m$ are arcs. Each arc $u=(x_i, x_j)$ is characterized by its starting vertex x_i and end vertex x_j.

The existence of an arc u means that the process unit x_j can be supplied with a product which previously was in process unit x_i. Data concerning type, size, change-over time, and allocated process unit are assigned to each vertex x.

The plant is to manufacture several products $P_1, \ldots, P_p$. For these products, production specifications $H_1, \ldots, H_p$ exist which describe the required type of process units, their sequence, utilization time, and further data. It is to be noted that the time of transition one process unit to the other is specified, consequently, no intermediate storage is allowed.

In contrast to the works mentioned, it is desired that it should be possible to manufacture similar products in different parts of the plant, despite the fact that there are unequivocal production specifications. However, these production specifications specify the type of process units required, rather than the number of the part of the plant which represents the type. Hence, if the plant includes several parts of the same type, a product can be scheduled in different ways in the plant.

The number of different possiblities of scheduling can be used as a measure.

Measure 1: Number of possibilities of scheduling a batch characterized by product specification H in the plant with the starting time A.

Another point of interest is the number of batches of equal type, which in the best case can be produced simultaneously.

Measure 2: Number of batches of a product with the same starting time which can be produced simultaneously in the plant.

Determination of the Measures

The two measures are determined on the basis of the solution of a partial problem, such as occurs in the scheduling of multi-purpose batch chemical plants:

Given a partially scheduled machine allocation plan, a batch H, and a starting time A. Determine all possibilities of manufacturing this batch H on the plant.

This partial problem can be solved by means of a backtrack proceduer which was described in detail by JÄNICKE [3]. Starting from a non-occupied machine allocation matrix, the first measure is determined when the backtrack procedure has been carried out. For the second measure to be approximately determined, it is sufficient to schedule the first batch and to use the machine allocation matrix obtained in this way as a starting value for another experiment, etc.

The exact determination of the second measure is more expensive. All possible schedulings are determined. If the scheduling is considered as a vertex of an undirected graph $G' = [V, E]$, two vertices of this graph can be connected by an edge if and only if process units are jointly occupied by the appropriate scheduling.

BERGE [4] gives the following definition:

A set S of vertices is called a stable set if no arc joins two distinct vertices in S.

Thus, determination of the maximum stable set gives the maximum number of schedulings which do not occupy any process unit jointly, i.e. the second measure.

In this case, the graph theoretical formulation offers itself for use, as algorithms can be easily developed using a graph. It may be formulated as an integer linear optimization problem. It is to be noted, however, that this is an NP problem, i.e. that in all cases branch and bound algorithms will have to be developed (for an explanation of the term "NP" cf. GAREY [5]).

Some Information Concerning the Expense

Measures 1 and 2 were determined by means of an existing plant for manufacturing highly refined products of organic synthesis (cf. GRUHN et al [6]). It consists of 68 process units, 132 connections in which 20 products can be manufactured. Measure 1 ranges between 2 and 20, measure 2 ranges between 1 and 4. The computing time on an EC 1040 computer ranges between 0.01 and 0.11 seconds.

Further Measurements

It might be possible to obtain further measurements using the time and the failure probability of the process units of the plant. However, a test should be carried out to establish whether or not the expense in determining complicated measurements will be justified by an improved description of the plant.

SYMBOLS

$G=(X, U)$	graph representing a plant
$X=x_1, \ldots, x_n$	vertices (process units)
$U=u_1, \ldots, u_m$	arcs (connections between process units)
$P_1, \ldots, P_p$	products
$H_1, \ldots, H_p$	production specifications
$G'=[V, E]$	constructed graph
S	stable set

LITERATURE

1. EGLI, U. M. and RIPPIN, D. T. W.: "Short term scheduling for multi-product batch chemical plants" AIChE Meeting, New Orleans, November 1981.
2. BIECHELE, E., BIESS, G., SCHMIDT, F. and JÄNICKE, W.: Hung. J. Ind. Chem. *1981*, 9, 233–240.
3. JÄNICKE, W.: "A scheduling problem for multi-purpose batch chemical plants" (Submitted for Computers and Chem. Eng.).
4. BERGE, C.: "Graphs and Hypergraphs" North Holland Publishing Company, Amsterdam–London, 1973.
5. GAREY, M. R. and JOHNSON, D. S.: "Computers and Intractibility — A Guide to the Theory of NP–Completeness" Freeman, San Francisco, 1979.
6. GRUHN, G., FICHTNER, G., and JÄNICKE, W.: "Scheduling of a multi-purpose batch chemical plant" 3rd International Congress "Computers and Chemical Engineering", Paris 1983.

РЕЗЮМЕ

На заводе производящем различные продукты можно осуществить технологии либо одновидных продуктов в большом количестве, либо продуктов широкого ассортимента. При определении производительности, варируемости и степени надёжности работы возникают следующие вопросы:

— задано время пуска, какие есть возможности работы периодического режима,
— сколько потоков периодического режима производящего одинаковые продукты можно составить?

В стати приведен алгоритм для решения первого вопроса, а для решения второго приведено решение основанное на теории графов.

HUNGARIAN JOURNAL
OF INDUSTRIAL CHEMISTRY
VESZPRÉM
Vol. 11. pp. 63—69 (1983)

ELECTROSTATIC PRECIPITATION OF VARIOUS DUSTS

B. Kovács, R Major, M. Majtényi

(Department of Chemical Technology, University of Chemical Engineering, Veszprém, Hungary)

Received: November 12, 1982.

Precipitation experiments were carried out in a pilot-plant-scale electrostatic dust-precipitator with quartz, alumina, bentonite and kaoline dusts (particle size below 32 μm). Dust concentration, space-velocity, current intensity and carrier gas humidity were changed during the experiments. Increased space-velocity decreased the precipitation efficiency. Increased current intensity and carrier gas humidity decreased the residual dust concentration. Kaoline dust could not be precipitated efficiently. Precipitation efficiency was at least 90% for the 0–10 μm fraction of all the other dusts studied.

Environmental protection measures have intensified throughout the world. Power plants, smelters, and chemical and cement factories emit large amounts of pollutants — dust. This pollution is not only harmful for the ecosystem, but also represents an economic loss, for the emitted pollutants could be often utilized as raw materials or auxiliary materials [1].

Experiments were carried out in this Institute with both dry and wet gas-scrubbing methods, allowing their efficiences and economics to be compared in various cases. Apart from the overall precipitation efficiency, the so-called fraction — precipitation efficiency is also of importance, because particles in the 0.1–5 μm range represent an increased health-hazard. Wet scrubbing was carried out in a high-capacity, countercurrent plate system equipped with combined plates, while dry dust removal was effected by an electrostatic precipitator. Literature references indicate that electrostatic precipitators can remove even the 1 μm particles, at efficiencies better than 90% [2, 3].

Electrostatic precipitation is based on the crown-discharge phenomenon. Dust-containing carrier gas is passed through an ionizing electrostatic field, whereby the particles acquire an electric charge and rapidly begin to move towards the oppositely charged electrodes.

Deutsch [4] established the relationship of overall precipitation efficiency (ε_0) and particle velocity:

$$\varepsilon_0 = l - e^{-\frac{w \times l}{a \times v}} = l - e^{-k \times w}$$

where, for flat-plate precipitators:

l is the length of the precipitating electrode, m
a is the distance between the charging and the precipitating electrode, m
v is the gas flow rate in the precipitator, m^3/s
w is the particle velocity, m/s.

Here, k reflects the operation conditions and equipment characteritics, while w represents the electric field, particle size and its properties. For a given precipitator the overall efficiency depends on w. Field strength is limited by the arching potential. Therefore, precipitation efficiency can only be increased by influencing the electric properties of the particles. Dusts with specific resistance in the 10^4–10^{11} ohm·cm range can be efficiently removed in electrostatic precipitators. Specific resistance can be optimized by the use of so-called conditioning agents. The most popular conditioning agents are sulphur trioxide, ammonia and water vapour. These agents decrease the specific resistance of dust [5, 6].

Measurements were carried out with a pilot-plant-scale electrostatic precipitator installed in this Institute. Its schematics is shown in *Fig. 1.* Air is supplied by a high capacity fan (1). Air is delivered through a 124 mm nominal diameter duct (2), to precipitator (9), from where it is exhausted through stack (10). Gate valve (4) is used to control the flow rate of air as measured by orifice gauge (3) and a protected thermometer (5). Dust is fed into the system by screw-feeder (6), while the dust concentration in the input and output flows is determined by an isokinetic dust sampler according to (7). Partial flow rate was measured by rotameter (11). Suction was accomplished

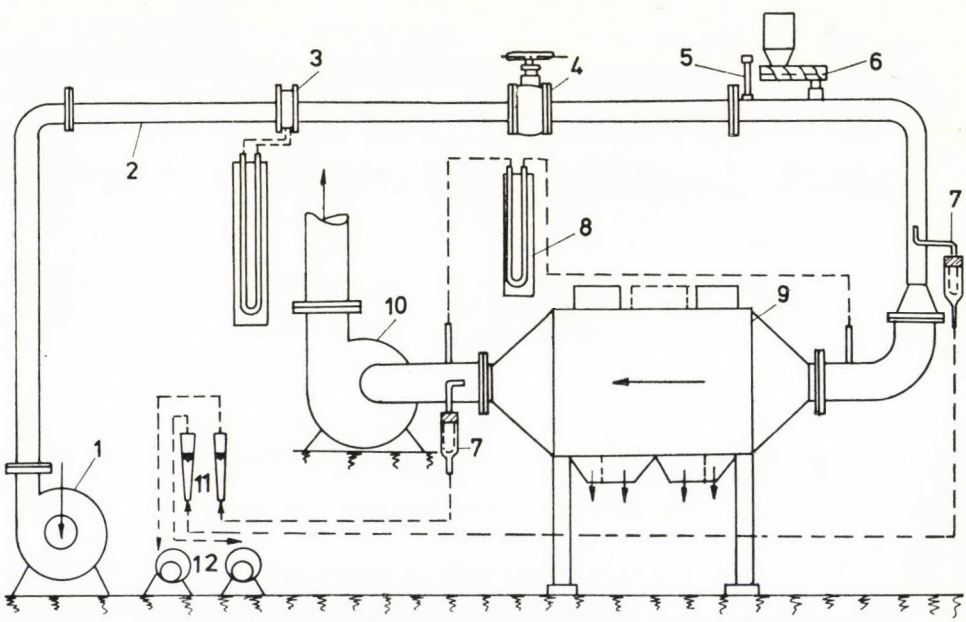

Fig. 1
Schematics of the electrostatic precipitator

by rotary-vane vacuum-pump (12). The 0 point of suction was checked by an U-tube manometer (8).

The upper particle size limit of dust was 32 μm, the average being 8–10 μm. Dust concentration for quartz was 5–20 g/m³, and for alumina and bentonite 5–15 g/m³.

Gas flow rate was changed in the 300–600 m³/h range, secondary current intensity in the 1–5 mA range. Relative humidity was varied for quartz in the 15–50% range, as determined from dew-point nomograms and wet and dry temperature measurements. Relative humidity was controlled by adding steam from a small boiler.

Along with the determination of the overall dust-removal efficiency, the particle size distribution of dust, both in the inlet and outlet flows, was determined by sampling with a high capacity vacuum cleaner and post-run analysis by a Holderbank-type air-separator. Separation efficiency was calculated from input and output dust concentrations. Fraction efficiency was calculated from the particle size distributions in the input and output flows as:

$$\varepsilon_f = 1 - (1 - \varepsilon_0) \frac{\Delta u}{\Delta e}$$

where:

ε_f is the separation efficiency for the given fraction

Δu percentage of the given fraction in the output flow

Δe percentage of the given fraction in the input flow.

Since the values of Δu and Δe depend somewhat on the measurement method used, the value of ε_f also depend on it.

In order to fulfill the requirements of the DEUTSCH calculations, the electrostatic precipitator was operated at the 0 suction point.

Table 1

Material	Density g/cm³	Moisture content %, w/w
Quartz	2.5801	0.19
Alumina	3.2866	1.16
Bentonite	2.4952	2.83
Kaoline	2.4251	2.22

The density and adhere-moisture-content of the dusts are given in *Table 1*. Measurement results are summarized in *Table 2*.

The overall separation efficiency as a function of the secondary current intensity is shown in *Fig. 2*. In the range tested, increasing current density increases the separation efficiency. This increase is especially strong for bentonite, where the efficiency grows from 92.24% to 98.35%. At the latter value, the air flow rate was 400 m³/h, and input dust concentration was 10 g/m³.

At constant input concentration and secondary current intensity, increasing space velocity decreased the separation efficiency. The extent of the decrease

Table 2

Material	Q (m³/h)	I_s (mA)	S_e (g/m³)	ε_0 (%)
Quartz	300	2.5	10	99.87
	400	2.5	10	99.68
	500	2.5	10	99.43
	600	2.5	10	99.12
	400	1.0	10	99.00
	400	5.0	10	99.90
	400	2.5	5	99.56
	400	2.5	15	99.59
	400	2.5	20	99.60
Alumina	300	2.5	5	98.91
	400	2.5	5	98.44
	500	2.5	5	97.63
	600	2.5	5	97.38
	400	1.0	10	97.78
	400	5.0	10	98.61
	400	2.5	10	98.22
	400	2.5	15	98.24
Bentonite	300	2.5	5	97.92
	400	2.5	5	96.32
	500	2.5	5	95.07
	600	2.5	5	93.93
	400	5.0	10	98.35
	400	2.5	10	96.10
	400	2.5	15	96.60
	400	1.0	10	92.24
Kaoline $\varphi = 15\%$	400	2.5	10	99.57
$\varphi = 24\%$	400	2.5	10	99.64
$\varphi = 34\%$	400	2.5	10	99.76
$\varphi = 50\%$	400	2.5	10	99.84

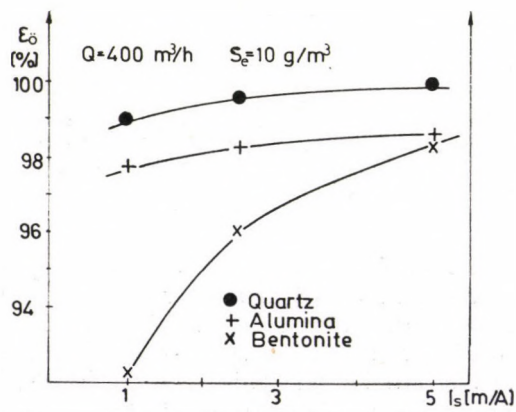

Fig. 2

Overall precipitation efficiency as a function of the secondary current intensity
● — Quartz; + — Alumina; × — Bentonite

was lowest for quartz, and highest for bentonite: with air flow rates increased from 300 m^3/h to 600 m^3/h, the decrease for quartz was 0.75%, and for bentonite it was 3.99%. Secondary current intensity was maintained at 2.5 mA, while input dust concentration was 10 g/m^3 for quartz, and 5 g/m^3 for the other dusts *(Fig. 3)*.

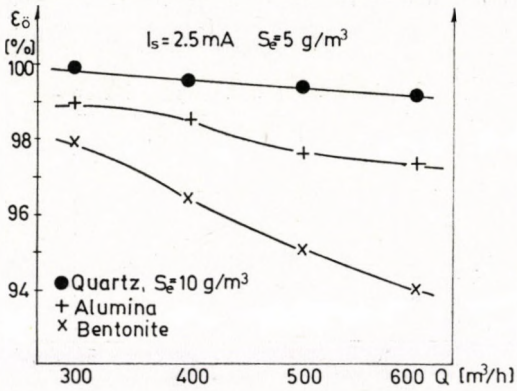

Fig. 3
Overall precipitation efficiency as a function of the gas flow rate
● — Quartz; $S_e = 10$ g/m^3; + — Alumina; × — Bentonite

Input dust concentration had no significant effect upon the separation efficiency. In the range tested, exit dust concentration is proportional to the input dust concentration, i.e. the particle motion velocity is independent from the dust loading (cf. *Fig. 4*). Again, the overall efficiency is the best for quartz, and the worst for bentonite. Quartz concentration was varied in the 5–20 g/m^3 range, while the other dusts were varied in the 5–15 g/m^3 range. Secondary current intensity was 2.5 mA, and the air flow rate was 400 m^3/h.

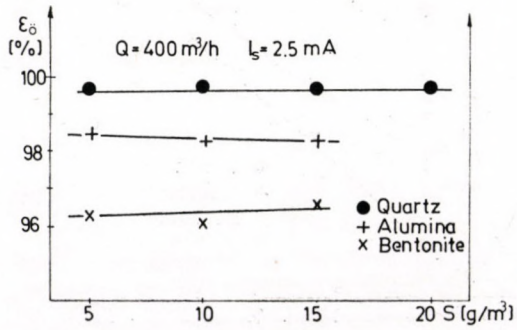

Fig. 4
Overall precipitation efficiency as a function of the input dust concentration
● — Quartz; + — Alumina; × — Bentonite

Relative humidity was varied in the 15–25% range. For quartz, increasing relative humidity decreased the exit concentration level; under otherwise identical conditions an increase in relative humidity from 15% to 50% halved the exit quartz concentration as shown in *Fig. 5*. Here the input dust concentration was 10 g/m³, while secondary current intensity and air flow rates were 2.5 mA and 400 m³/h, respectively.

The fraction efficiencies were also determined for each dust. Fraction

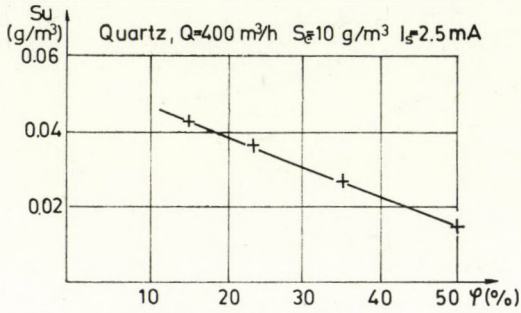

Fig. 5
Exit dust concentration as a function of the relative humidity

efficiencies calculated from measurements at 1 mA secondary current intensity, 10 g/m³ input dust concentration and 400 m³/h air flow rate (a low-efficiency setting) are shown in *Fig. 6*. It can be seen that the precipitation efficiency for the 0–10 μm fractions is always better than 90%. The same holds true for the other measurements as well.

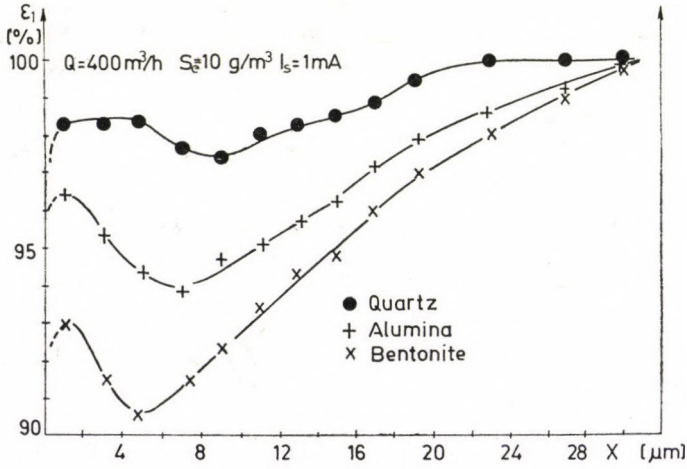

Fig. 6
Fraction efficiency as a function of the particle size
● — Quartz; + — Alumina; × — Bentonite

In the case of kaoline, arching became quite frequent. Kaoline is deposited on both the separating and radiating electrodes, and it does not lose its charge easily. This decreases the distance between the electrodes and leads to arching. In this case, the system becomes a dust-chamber with an overall separating efficiency of 80%. Therefore, analysis of the measured values is meaningless. We are convinced that the electrostatic precipitator is ill-suited for kaoline.

To summarize: it can be concluded that tests with various dusts showed that all of the dusts studied—except kaoline—can be efficiently removed at very low power consumption: 0.1–0.2 kWh/1000 m^3 processed gas. The collected dust can be directly utilized without additional processing steps.

REFERENCES

1. Káldi, P.: Low-Waste Technologies in Hungary and Abroad. A review. Lecture, presented at the Hungarian Academy of Sciences, October 29, 1980.
2. Maartmann S.: Staub, Reinhaltung der Luft. *1974*, 34 (10) 353–355.
3. Russel-Jones, A.: Chemistry and Industry *1977*, 2, 50–54.
4. O. Storch et al. Purification of Industrial Gases (in Hungarian). Műszaki Könyvkiadó, Budapest, 1977. p. 121.
5. Coudert, I.: Revue des Materiaux de Construction *1976*, 702, 263–268.
6. Bump, R. L.: Chemical Engineering *1977*, 84 (2) 129–136.

РЕЗЮМЕ

Исследовали возможность выделения фракций размером <32 μм порошков (кварцевых, глинозёмных, бетонита, и каолина) с помощью электростатического сепаратора большого лабораторного масштаба. В экспериментах изменяли концентрацию, объёмную скорость интенсивность тока и влажность газа-носителя. Установили, что концентрация порошка в выходящем потоке газа измеяется пропорционально концентрации газа на входу. В изучаемых условиях увеличение объёмной скорости приводит к уменьшению эффективности отделения. Увеличение силы тока и влажности привело к значительному уменьшению концентрации на выходе. Далее установили, что использование электростатического способа отделения непригодно для порошка каолина. Все остальные порошки в интервале 0—10 μм отделяются эффективностью 93%.

HUNGARIAN JOURNAL
OF INDUSTRIAL CHEMISTRY
VESZPRÉM
Vol. 11. pp. 71—79 (1983)

THE INFLUENCE OF DISPERSION CONDITIONS ON MASS TRANSFER ACCOMPANIED BY FIRST-ORDER MODERATE REACTION

E. NAGY and T. BLICKLE

(Research Institute for Technical Chemistry of the Hungarian Academy of Sciences, Veszprém, Hungary)

Paper presented at the Conference on "Diffusional Methods of Separation". September 25–28, 1982, Karpacz, Poland.

Received: November 19, 1982.

Mass transfer rates are defined for the case of mass transfer accompanied by chemical reaction, by which the study of mass transfer coupled with a chemical reaction of any finite rate including the moderate reaction rate regime $Ha = 0.3$–3 is made possible.
Relationships between the mixing conditions and reaction rate are studied for co-current and counter-current flows, effects of the transfer unit number and the capacity quotient on exit concentrations of phases are given as functions of a reaction rate.

Mass transfer accompained by chemical reaction is a very common industrial problem and has been the subject of extended research work for decades. DANCKWERTS lists in his well-known book [1] the most important theories for mass transfer, i.e. the two-film theory, the penetration model and the surface renewal model, considering the mass transfer terms modified by chemical reaction. He also points out the change of mass transfer rate as a function of the chemical reaction rate.

The mathematical description of mass transfer processes accompanied by chemical reaction, also considering the hydrodynamics of phases (e.g. back-mixing), has been used since the pioneering paper of PAVLICA and OLSON was published in 1970 [2].

Papers about this subject [3–5], as far as the chemical reaction rate is concerned, solely dealt with processes in the two extreme reaction rate ranges, i.e. for slow reactions (HATTA number <0.3) and for fast reactions (HATTA number >3), respectively.

In the former case, the modifying effect of the chemical reaction on the material transfer term can be neglected, i.e. balance equations contain the transfer term characteristic for the physical transfer [2], whereas in the latter

case another transfer term is used for fast chemical reactions. In the second reaction rate range the rate of mass transfer is independent of the value of the physical transfer coefficients [3, 5] and the absorbed component reacts completely in the absorbing phase. As its concentration is practically zero in this phase, for a description of concentration changes, balance equations in the gas phase are sufficient.

By using the two-film theory we define such transfer rates, the use of which enables us to describe exactly the material transfer process for any finite reaction rate. To be able to do this, we must give separate transfer rates for the mass transfer through contact surfaces of phases ($x=0$, cf. *Fig. 1*) and for the mass transfer entering the main part of the absorbing phase ($x=\delta$). If we use FICK's law for the description of the concentration change of laminar boundary layers, we can determine both mass currents [6].

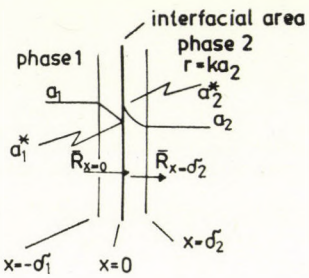

Fig. 1
Mass-transfer terms and concentration profiles at the interface

The mass transfer rates, which enter the contact surfaces of phases (which is already known from literature [7]), can be written as follows, if we consider the resistance on the gas side (where the component A to be absorbed should react in a first-order, irreversible reaction in the liquid phase: $r=k\cdot a$):

$$\bar{R}_{x=0}=k_{12}(a_1^0-Ha_2^0/\mathrm{ch}(Ha)) \tag{1}$$

where:

$$k_{12}=\frac{1}{\dfrac{1}{k_1^0}+\dfrac{H\tanh(Ha)}{k_2^0 Ha}} \tag{2}$$

The mass transfer rate entering the main part of absorbing phase will be [6]:

$$\bar{R}_{x=\delta}=k_{22}(a_1^0-Ha_2^0/\alpha) \tag{3}$$

with:

$$k_{22}=\frac{k_2^0 Ha}{H\sinh(Ha)}\left(1-\frac{k_{12}}{k_1^0}\right) \tag{4}$$

$$\alpha=\frac{1-\dfrac{k_{12}}{k_1^0}}{\cosh(Ha)-\dfrac{k_{12}}{k_1^0\cosh(Ha)}}. \tag{5}$$

The values of k_{22} and α depend on the physical mass transfer coefficients and on the chemical reaction rate [6]. k_{22} approaches with increasing chemical reaction rate zero. In the extreme case the mass transfer rates defined in (1), (3) move towards the physical transfer rate with decreasing chemical reaction rate [6].

If we apply the mass transfer rate for $x=0$ and $x=\delta$ as transfer terms of the dispersion model, we can study the relationship between the parameters of the model and the chemical reaction rate for any finite reaction rate.

By using the axial dispersion model, the concentration changes of the absorbed component can be described by the following differential equation system, using dimensionless quantities:

for the component releasing phase (phase 1):

$$\frac{1}{Pe_1}\frac{d^2A_1}{dY^2}\pm\frac{dA_1}{dY}-\frac{\bar{a}L}{EU_2a_1^0(0)}\bar{R}_{x=0}=0 \tag{6}$$

for the absorbing phase (phase 2):

$$\frac{1}{Pe_2}\frac{d^2A_2}{dY^2}\pm\frac{dA_2}{dY}+\frac{\bar{a}L}{E_2U_2a_1^0(0)}\bar{R}_{x=\delta}-\frac{kL}{U_2}A_2=0. \tag{7}$$

The equation system (5), (6) can be solved analytically [9] by the WEHNER–WILHELM boundary conditions [8]. In papers [9, 10] the effect of the chemical reaction was studied in the co-current mode. In this paper we concentrate on the influence of backmixing conditions (PECLET-number) with changing reaction rates in both co-current and counter-current modes, and show the effects of the transfer unit number (N°) and capacity quotient (Λ) in the counter-current mode.

Results and discussion

Fig. 2 and *3* show typical concentration distributions for co-current and counter-current flows by using nearly identical parameters. We have changed the rate of chemical reaction following mass transfer in the so-called moderate reaction rate regime hitherto neglected in literature ($Ha=0.05$–1.22). The concentration in the gas phase will decrease rapidly to zero in both modes with the increasing chemical reaction rate. As expected, the concentration of the leaving gas phase will decrease to zero in the counter-current flow at lower reaction rates. In the case of the liquid phase the situation is reversed: the concentration of the leaving liquid is considerably larger in the counter-current flow at the given reaction rate. There is an important difference between the two flows, namely that in co-current flow the concentration of the liquid phase will pass in axial direction a maximum (depending on the reaction rate), whereas the shape of the concentration curve will be monotonous in the counter-current flow.

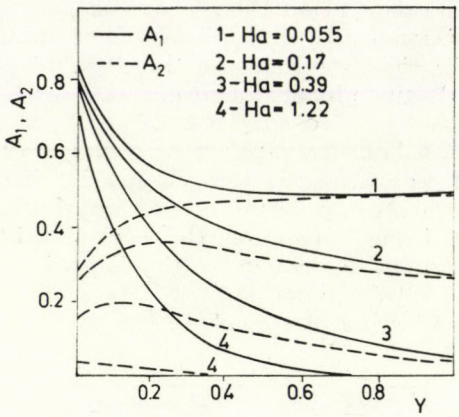

Fig. 2
Typical concentration distribution curves in co-current operation mode
$N_1^0 = 7$; $\Lambda = 1$; $Pe_1 = 15$; $Pe_2 = 5$; $k_1^0 H / k_2^0 = 1$

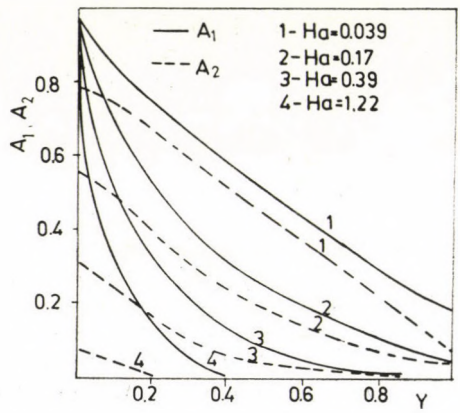

Fig. 3
Typical concentration distribution curves in counter-current operation mode
$N_1^0 = 10$; $\Lambda = 1$; $Pe_1 = 25$; $Pe_2 = 5$; $k_1^0 H / k_2^0 = 1$

Fig. 4–7 demonstrate the effect of mixing conditions at different reaction rates on the leaving concentration values and on the concentration distribution in the axial direction of the reactor.

Fig. 4 is a plot of liquid phase mixing at given gas phase Peclet-number in the counter-current flow. It can be seen that the concentration of the leaving phases strongly depends on Pe_2. This dependence will decrease with the increasing reaction rate. Changes amount to 60 to 100% for both phases. If the

reaction rate increases, concentrations of both phases are forced to decrease, and thus the effect of mixing conditions will diminish. If $Ha > 1$, the leaving concentrations of practically both phases will be zero at given parameters of *Fig. 4*, indenpendent of mixing conditions.

The influence of the mixing factor is much less in the co-current flow *(Fig. 5)*. Using parameters nearly identical with those of the counter-current mode, the leaving concentration of the phases will hardly be changed as a function of Pe_2, whereas a minor change of the reaction rate will cause a considerable concentration alteration here. The much smaller effect of the mixing factor is due to the fact that the influence of the transfer unit number (N°) is rather

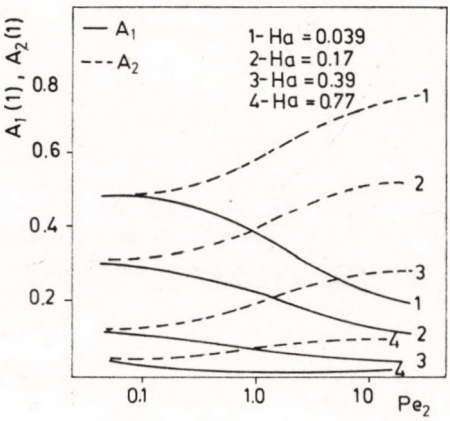

Fig. 4

Changes of the exit concentrations of the phases with the Pe_2 in counter-current operation mode

$N_1^0 = 5$; $\Lambda = 1$; $Pe_1 = 25$; $k_1^0 H / k_2^0 = 1$

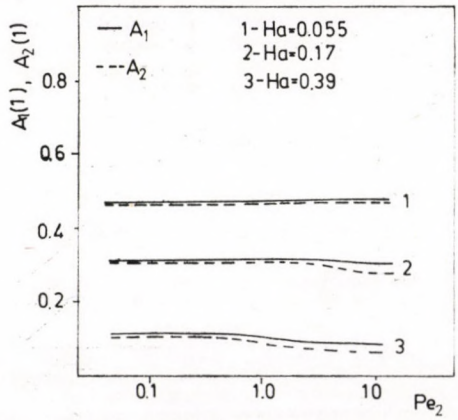

Fig. 5

Changes of the exit concentrations with the Pe_2 in co-current operation mode

$N_1^0 = 5$; $\Lambda = 1$; $Pe_1 = 15$; $k_1^0 H / k_2^0 = 1$

high in the co-current flow. *Fig. 6* demostrates the influence of the mixing conditions on the concentration distribution along the reactor axis at the given reaction rate ($Ha=0.17$). Although the longitudinal concentration distribution of the phases is altered by Pe_2, however, the leaving concentrations do not differ much from each other.

Similar differences can be observed between both flows concerning the changes of Pe_1. In the co-current case, the effect of Pe_1 is rather small. *Fig. 7* is a plot of concentrations in the counter-current flows as a function of Pe_1 for different Ha numbers and assuming full mixing of the liquid phase ($Pe_2=0.04$). If the reaction rate is increased, phase concentrations will change

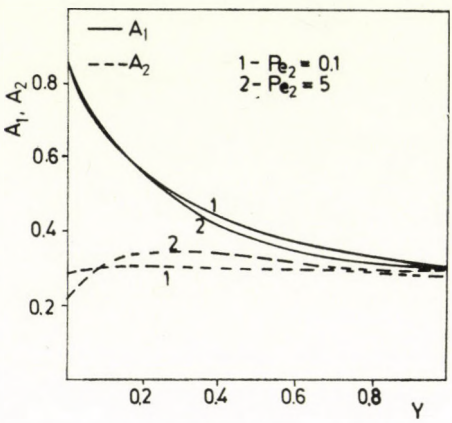

Fig. 6

Concentration distribution in axial direction (co-current operation mode)

$N_1^0=5$; $\Lambda=1$; $Pe_1=15$; $k_1^0H/k_2^0=1$; $Ha=0.17$

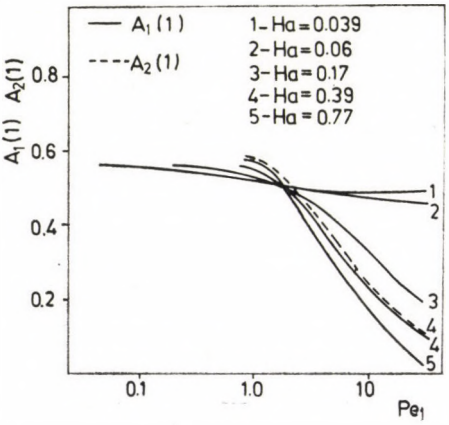

Fig. 7

The effect of the Pe_1 upon the exit concentrations at various Ha-number (counter-current operation mode)

$N_1^0=5$; $\Lambda=1$; $Pe_2=0.04$; $k_1^0H/k_2^0=1$

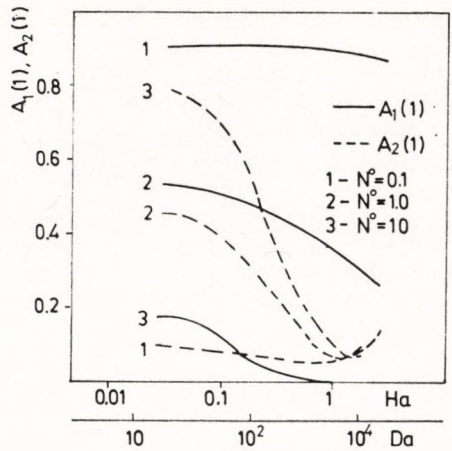

Fig. 8

The effects of reaction rates (Ha) upon the exit concentrations at various $N°$ values (counter-current operation mode)

$\Lambda=1$; $Pe_1=25$; $Pe_2=10$; $k_1^0H/k_2^0=1$

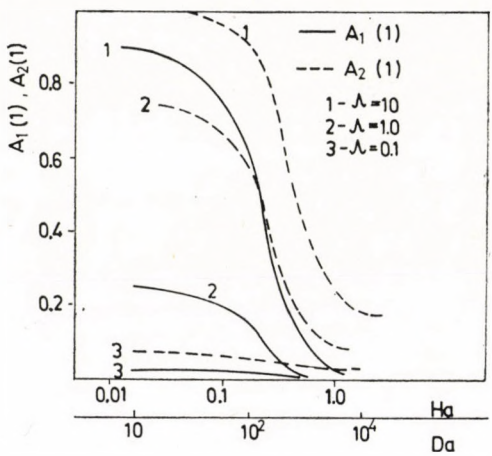

Fig. 9

The effects of reaction rates (Ha) upon the exit concentrations at various Λ values (counter-current operation mode)

$N_1^0=5$; $Pe_1=25$; $Pe_2=10$; $k_1^0H/k_2^0=1$

considerably for $Pe_1>1$ with the Peclet number. At $Ha=0.039$ the leaving concentrations of phases change by a few percents, whereas at $Ha=0.77$ they change by several hundred percents. This latter fact could be used for the determination of the mixing factor of gas phases by the chemical reaction. For this, we can increase the chemical reaction rate following mass transfer under given transfer and hydrodynamic conditions (e.g. by using a homogene-

ous catalyst), and we measure the values of the leaving concentrations. The change of the leaving concentrations obtained for various reaction rates will be characteristic for the mixing conditions of the phases. However, in co-current mode the mixing factor would escape determination by the chemical reaction, presumably because the effect of the mixing factor is too small.

Fig. 8 and *9* represent the effect of the chemical reaction for different N°- and Λ-values. *Fig. 8* clearly shows that the reaction rate is increased in vain, if the transfer unit number (N°) is too low. In this case the chemical reaction can hardly influence the rate of mass transfer, since the resistance on the gas side is rather high. With increasing N°-values the influence of the reaction will grow and the exit concentration of the gas phase will decrease. Since higher mass amounts are transferred , the concentration of the liquid phase will increase at the given reaction rate.

The capacity quotient (Λ) of phases is the parameter shown on *Fig. 9*. Phase concentrations will rapidly decrease with the increasing reaction rate independently of Λ. The concentration of the leaving gas phase at $Ha > 1$ in the range of $\Lambda = 0.1$–10 is practically nil, whereas that of the liquid phase will increase up to a certain level. The exit concentration of the liquid phase will not necessarily be equal to zero, if Ha is further increased.

SYMBOLS

a^0	concentration of A in bulk phase, kmole/m³
$a^0(0)$	inlet concentration of A, kmole/m³
A	dimensionless concentration of A, $A_1 = a_1(0)$, $A_2 = a_2\mathrm{H}/a_1(0)$
$A(1)$	dimensionless outlet concentration of A
$\bar{a}$	specific interfacial area, m²/m³
D	diffusivity, m²/s
Da	Damköhler number, $Da = kL/U_2$
E	phase ratio of phase 2
H	equilibrium coefficient, a/a*
Ha	Hatta number, $Ha = \sqrt{kD_2}/k_2^0$
k_{12}	overall mass transfer coefficient, m/s
k	reaction rate constant, s⁻¹
k_1, k_2	mass transfer coefficients of phases, m/s
K	dispersion coefficient, m²/s
L	height of the reactor, m
N	number of transfer units $N_1 = \dfrac{k_{12}\bar{a}L}{(1-E)U_1}$
Pe	Peclet number, Pe = UL/K
$\bar{R}$	rate of mass transfer, kmole/m²s
U	superficial velocity, m/s
Λ	capacity ratio of phases, $\Lambda = U_1(1-E)H/U_2E$
δ	thickness of diffusion film, $\delta = \dfrac{D}{k^0}$, m

Subscripts

1,2 phases
x = 0 at the interface
x = δ entering bulk phase

Superscripts

0 without chemical reaction
x in equilibrium

LITERATURE

1. Danckwerts P. V.: Gas-Liquid Reactions, McGraw Hill, London 1970.
2. Pavlica R. T. and Olson, J. H.: Ind. Engn. Chem. *1970*, 62, 45.
3. Mhaskar, R. D.: Chem. Engng. Sci. *1974*, 29, 897.
4. Shah, Y. T. and Paraskos, J. A.: Chem. Engng. Sci. *1975*, 31, 465.
5. Szeri, A., Shah, T. and Madgarkar, A.: Chem. Engng. Sci. *1976*, 31, 225.
6. Nagy, E., Blickle, T. und Újhidy, A.: Chem. Techn. (in press).
7. Danckwerts, P. V.: Gas-Liquid Reactions, Mc.Graw Hill, London 1970.
8. Wehner, J. P. and Wilhelm, R. H.: Chem. Engng. Sci. *1956*, 6, 89.
9. Nagy, E., Blickle, T. und Horváth, K.: Chem. Techn. (in press).
10. Nagy, E., Blickle, T., Újhidy, A., Horváth, K.: Chem. Engng. Sci. *1982*, 37, 000.

РЕЗЮМЕ

Авторами изучены процессы химических реакций сопутствующих массообменом, определили скорость массообмена. В ходе исследования становилось возможным изучение реакций любой конечной скорости (имеея ввиду и реакции замедленной скорости [Ha = 0,3—1]).

Далее изучали влияние условий смешивания на скорость реакции как в прямой так и противотоке, кроме того влияние единичного числа отдачи и коэффициента ёмкости на концентрацию фаз на выходе, последние зависимости заданы в виде функций от скорости реакции.

HUNGARIAN JOURNAL
OF INDUSTRIAL CHEMISTRY
VESZPRÉM
Vol. 11. pp. 81—90 (1983)

CHEMICAL AND GEOMETRICAL FACTORS IN LIMESTONE SLURRIES DISSOLUTION IN STIRRED TANKS

J. M. Diaz, L. Fonseca and J. Coca*

(Department of Chemical Engineering, Faculty of Chemistry,
University of Oviedo, Spain)

Received: December 28, 1982

Rates of dissolution in sulphuric acid of two types of limestone particles with a content of SiO_2 of 0.2% and 8.5% respectively were studied using a stirred tank. The effect of limestone composition, organic acids as buffer additives and pH are considered among chemical factors. The elevation and type of impeller and also the behaviour of two geometrically similar tanks are examined among geometric factors.

Among the wet processes for removing sulphur dioxide from industrial emissions, scrubbing with limestone slurries is a relatively simple process that is used in power plants. In spite of the simplicity of the process, there are numerous design variables that have to be considered, related either to the chemical reactions involved or to the hydrodynamics of the system.

The absorption of sulphur dioxide in a limestone slurry is a complex process due to the presence of solid particles in the liquid phase. As in a wet process of this type sulphur dioxide reacts with the dissolved calcium carbonate; higher levels of SO_2 removal can be achieved if the rate of dissolution of limestone can be increased. The rate of dissolution can be influenced by several factors: particle size, pH, temperature and common ions. It may also be affected by the addition of chemicals to the slurry or by the type of contacting among the three phases involved in the process.

The dissolution of limestone was studied by several authors such as Lovell [9], Pearson et al [10], Barton et al [1], Uchida et al [13–14], Lund et al [10], Erga et al [6], Kim et al [8] and Wentzel et al [15]. Results are sometimes difficult to compare as they were obtained under different conditions. The kinetic process of dissolution was considered to be controlled by mass transfer, chemical reaction and absorption of the hydrogen ion.

One of the limitations of limestone as a source of alkalinity for neutralizing SO_2, once it has been absorbed, lies in its low solubility. Some soluble alkaline

* To whom correspondence should be addressed.

additives, such as MgO, Na_2CO_3 and NH_3 were used in connection with the limestone scrubbing process, as they promote formation of soluble sulphate [2–3]. Other additives used are of the buffer type, usually soluble organic acids with low vapour pressure that enhance the liquid phase mass transfer [12].

In this work, the rates of dissolution of limestone in a stirred tank are reported for two different types of limestone, and the influence of the buffer additives and pH are also considered. The influence of the elevation of the impeller in the tank, the speed of agitation and the size of the stirred tank on the rate of dissolution were also studied.

Experimental Procedure

Experiments were carried out in a jacketed stirred tank shown in *Fig. 1.* The inner tank diameter D was 10 cm and the liquid height H was kept equal to D; it was equipped with 4 baffles 1.25 cm in width which could eventually be removed. Two types of turbine impellers were used: flat blade and vaned disc. The flat blade impeller was used in order to compare its performance with the vaned disc impeller and in the study of scale-up parameters; in all the other experiments the vaned disc impeller was used.

Limestone was supplied by Tudela Veguin (Oviedo, Spain). One sample had a purity of 98% in $CaCO_3$ with 0.2% SiO_2 and a second sample had 8.5% SiO_2. The high purity limestone was used in all experiments, except when the effect of limestone composition was studied. Fractions of particle size of (0.037–0.044, 0.075–0.088, 0.20–0.25, 0.45–0.50 and 1.0–1.2 mm) were obtained by grinding followed by sieving. The former fractions had an average surface area of 4,000, 2,100, 245, 180 and 80 cm^2/g respectively, as determined by a Sartorius 4600 sedimentation balance.

The stirred tank contained 800 cm^3 of distilled water at the beginning of every experiment and the pH was adjusted to a given value by the addition of NaOH. Once steady state conditions were attained, 8 g of limestone, of a certain particle size, were added to the tank and a flow of nitrogen was passed above the surface of the slurry, to prevent its contacting with air in order to avoid CO_2 absorption. An agitation speed of 640 r.p.m. was used, unless a different speed is specifically stated. In most of the experiments the rate of dissolution was followed by adjusting the pH to a value of 7 by adding sulphuric acid. The pH was measured by a Radiometer pH-meter Type 51b. The amount of limestone dissolved at a certain pH was determined from the volume of sulphuric acid added, by considering the fraction of HCO_3^- and H_2CO_3 species present in the liquid phase.

Results

Among the different control mechanisms [1, 10, 13], that have been suggested for describing the rate of dissolution of limestone, we adopted a simple model that considers the process controlled by diffusion of calcium carbonate (or CO_3^{2-}-ions). It was described in a previous work [5] and leads to the following kinetic equation:

$$\frac{dc}{dt} = k_s a E_1 (c_1 - c_0) \tag{1}$$

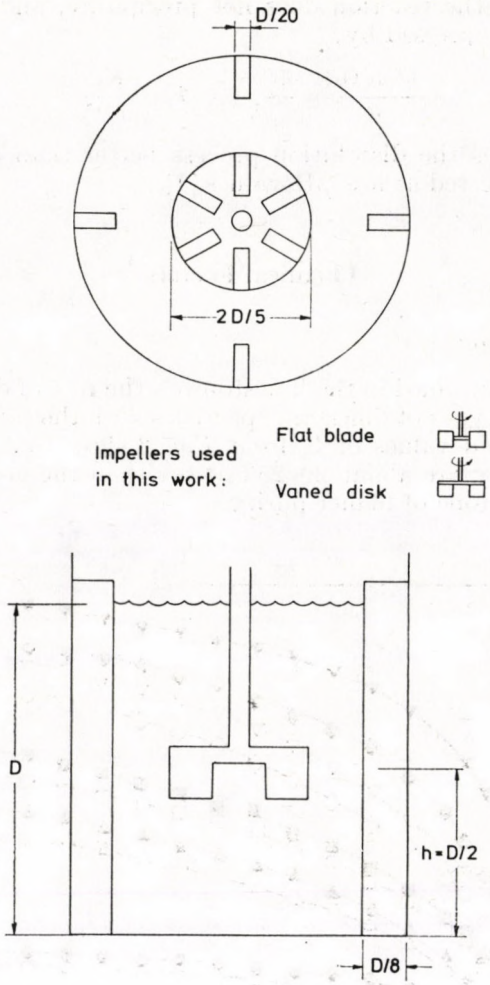

Fig. 1
Details of the strirred tank

where dc is the amount of limestone dissolved which diffuses through an interfacial area a in the time dt; k_s is the dissolution rate constant; E_i is the enhancement factor for instantaneous irreversible reactions and c_0 and c_i are the calcium carbonate concentrations in the bulk liquid and at the interface respectively. Under the experimental conditions of this work at pH = 7, $E_i \simeq 1$ and $c_0 = 0$, the reaction is instantaneous. By using an experimentally obtained solubility constant K_s defined by:

$$[Ca^{2+}]_i [CO_3^{2-}]_i = K_s \tag{2}$$

under the experimental conditions of this work, it may be assumed that the

$CaSO_4$ produced in the reaction does not precipitate, and hence the rate of dissolution can be expressed by:

$$\frac{d[CaCO_3]}{dt} = \frac{d[Ca^{2+}]_0}{dt} = k_s a \frac{K_s}{[Ca^{2+}]_0} \tag{3}$$

This model describes the dissolution process better than other models, that have been usually tested at low pH values [1].

Chemical Factors

Limestone Composition

The effect of SiO_2 contained in the limestone on the rate of dissolution is shown in *Fig. 2*. For both types of limestone, particles with the same size distribution were used. Estimated values of k_s from *Fig. 2* show that, for the limestone with 8.5% SiO_2, they are about 20–25% lower than the corresponding values obtained with limestone of higher purity.

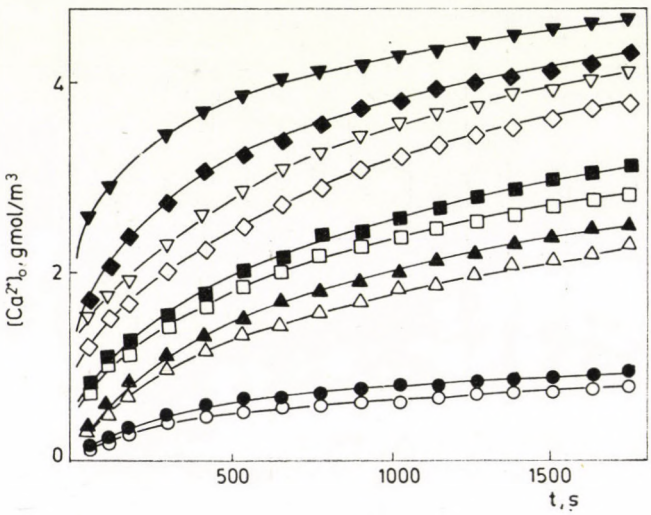

Fig. 2

Effect of the SiO_2 content on the rate of dissolution of limestone: 0.25% SiO_2 limestone (black points) and 8.5% SiO_2 limestone (white points)

Particles size: (▼▽) 0.037–0.044 mm, (◆◇) 0.075–0.088 mm, (■□) 0.20–0.25 mm, (▲△) 0.45–0.50 mm and (●○) 1.0–1.2 mm

Buffer Additives

Three organic acids, reported in literature [4, 12], were tested as buffer additives: acetic ($pK_a = 4.75$), benzoic ($pK_a = 4.19$) and adipic ($pK_{a1} = 4.44$, $pK_{a2} = 5.54$) acids. They have a similar behaviour in the dissolution of limestone

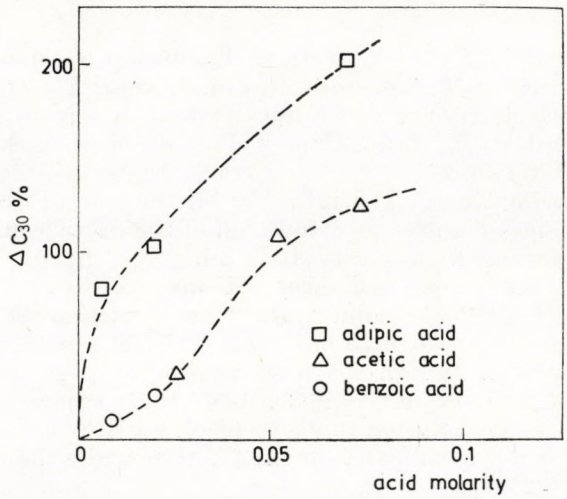

Fig. 3
Effect of organic acids on the rate of dissolution of limestone (1.0–1.2 mm)

and *Fig. 3* shows the increase in percentage of the rate of dissolution after 30 minutes, as a function of the acid molarity. Acetic and benzoic acids have a similar effect at low concentrations, while adipic acid produces an increase in the order of five times the rate of dissolution in the presence of acetic or benzoic acids. Taking into consideration the volatility and the cost of adipic acid, this can be considered the best of the three acids tested for mass transfer enhancement.

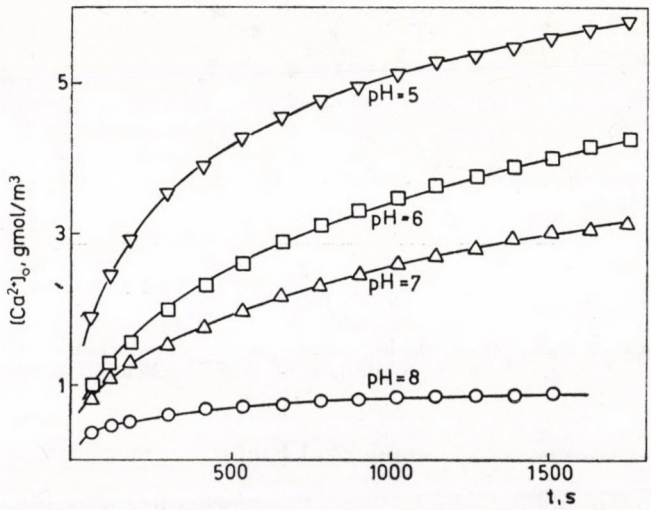

Fig. 4
Effect of the pH on the rate of dissolution of limestone (0.45–0.50 mm). A constant pH is kept in every experiment

pH

As can be observed in *Fig. 4* the rate of dissolution is considerably affected by the pH for particles of $D_p \simeq 0.5$ mm. In a range of pH 5–8, the rate of dissolution increases with decreasing pH values and for a certain pH the increase is more pronounced at the initial time of dissolution, with the rate becoming almost constant afterwards.

The particle size has a marked influence on the rate of dissolution, as the surface area for mass transfer is a function of the particle size. The rate was determined by adding high purity limestone to a fixed pH solution and allowing the particles to react while the pH was recorded.

At an initial pH = 2.35 the solution becomes neutral after 25 minutes, for the finest particles ($D_p = 0.20$–0.25 mm), while for the largest particles it takes much longer, as shown in *Fig. 5*. These results are in good agreement with those reported by BARTON and VATANATHAM (1). If experiments are started at an initial pH = 7, the solution tends to reach a pH close to 10 and the rate at which it is reached is even faster for the finest particles than for experiments at the initial pH = 2.35.

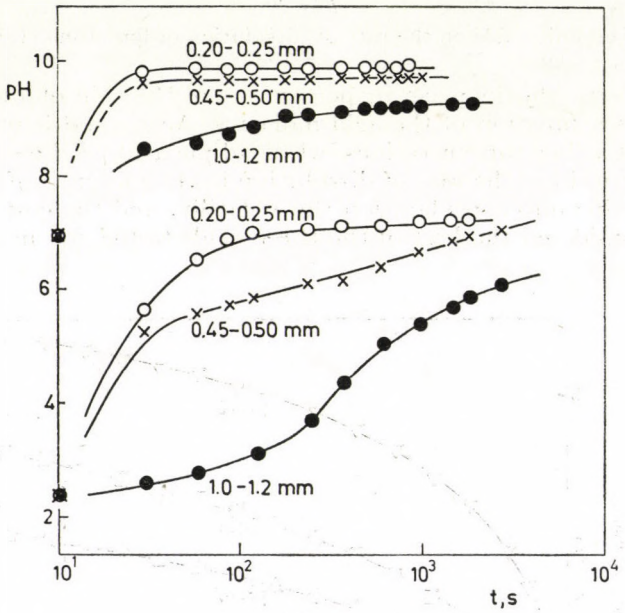

Fig. 5

Effect of the size of limestone particles on the rate of dissolution at a constant initial pH, with no addition of sulphuric acid

Geometrical Factors

The suspension of solid particles, and therefore their dissolution, is greatly affected by the impeller design and geometric factors, which thus, affect the mass transfer rates. Some of these factors have been considered in connection with the dissolution of limestone particles.

Elevation of the Impeller

The vaned disc impeller was mounted in the centre line of the baffled stirred tank and the rate of dissolution after 30 minutes of stirring was studied for 0.45–0.50 mm particles, as a function of the impeller elevation; results are shown in *Fig. 6*.

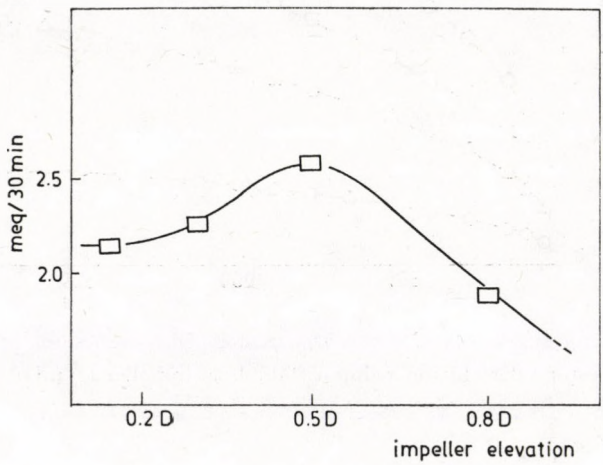

Fig. 6
Effect of the impeller elevation on the limestone dissolution after 30 minutes (0.45–0.50 mm)

The impeller elevation influences the flow patterns of the liquid and solid particles. It was reported [7] that the optimum elevation or liquid depth is at $D/3$, when an open straight blade impeller is used. With the vaned disc impeller, it was found that the best results were obtained for a liquid depth of $D/2$. This could be explained as a result of the low mixing that occurs in the liquid above the vaned disc impeller. Hence, by increasing the impeller elevation, the zone of high turbulence increases, as long as the suspension of solid particles is not greatly affected.

Type of Impeller

Experimental results for the rate of dissolution with a flat blade impeller for different particle size and at a speed of agitation of 640 r.p.m. are shown in *Fig. 7*. Rates of dissolution are higher with the flat blade impeller than with the vaned disc impeller (see *Fig. 2*), depending of the particle size used.

Some experiments were also carried out at two different speeds of agitation 640 and 1000 r.p.m., for a particle size of $D_p = 1.0$–1.2 mm in a baffled and an unbaffled tank. There were no significant changes in the rates of dissolution when baffles were installed. In the unbaffled tank the particles tend to move with the liquid, while in the baffled tank the existence of stagnant spots cause the accumulation of solid particles. Both effects result in a decrease in the rate of dissolution.

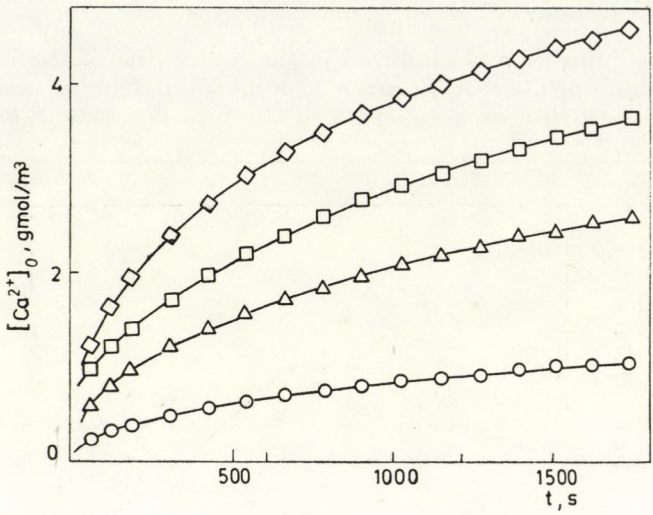

Fig. 7
Rate of limestone dissolution using a flat blade impeller (symbols of *Fig. 2.*)

Stirred Tank Size

In order to study how the scale factor would affect the rate of dissolution, experiments were performed in two stirred tanks with a geometrical ratio of $D/D' = 2$, provided with a flat blade impeller and no baffles. In both tanks air was in contact with the free surface of the slurry.

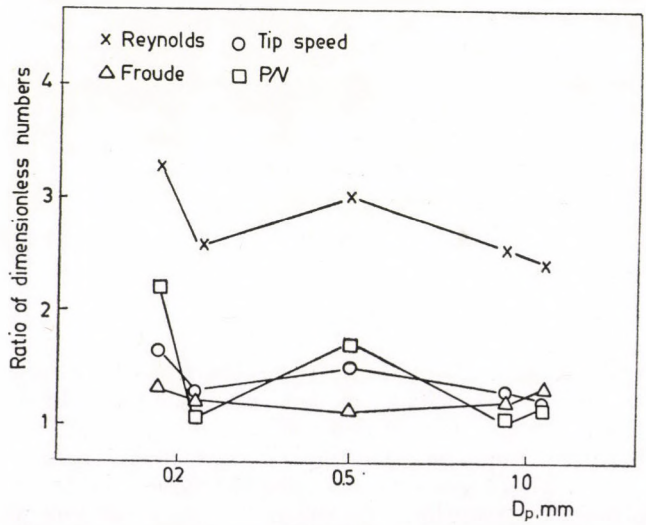

Fig. 8
Ratio of scale-up parameters for limestone dissolution in two unbaffled tanks with a geometric similarity ratio of 2.

By using particles of the same size and concentration in both tanks and with speeds of agitation such that, the same amount of limestone per unit volume of the slurry would be dissolved in both tanks, an analysis was made of the dimensionless numbers used in mixing operations. Results for the REYNOLDS *(Re)* and FROUDE *(Fr)* number ratios as well as for the P/V and tip speed ratios for both tanks are shown in *Fig. 8*.

The ratios of dimensionless numbers and design parameters shown in *Fig. 8* were obtained over a range of 300 to 900 r.p.m. The higher value was always taken as the numerator, independently of the tank, and therefore the ratio values are higher than unity. It can be observed that the tip speed (TS), and FROUDE numbers ratios are rather constant and close to unity, followed by the P/V ratio, that was recommended by ZWIETERING [16]. The WEBER (We), and volumetric flow (V_F) number ratios were also tested, but the correlation was very poor.

SYMBOLS

a = solid-liquid interfacial area (m^{-1})
c = calcium carbonate concentration (g mol/m^3)
D = tank diameter (cm)
D_p = particle diameter (mm)
E_i = enhancement factor for instantaneous reaction (—)
Fr = Froude number ($=N^2D/g$) (—)
g = gravitational acceleration (m/s^2)
H = liquid height (m)
k_s = dissolution rate constant (m/s)
K_s = calcium and carbonate concentrations product, at the interface (g mol/cm^6)
N = agitador speed (s^{-1})
P = power requirement to mix a liquid (J/s)
Re = Reynolds number ($=D^2 N\varrho/\mu$) (—)
t = time (s)
TS = tip speed ($=\pi ND$) (m/s)
V = liquid volume (m^3)
V_F = volumetric flow per velocity head (D/N)
W = Weber number ($=\varrho N^2D^3/\sigma$) (—)
μ = viscosity of liquid (kg/m s)
ϱ = density of liquid (kg/m^3)
σ = surface tension of liquid (N/m)

Subscripts

o = in the bulk liquid
i = at the interface

REFERENCES

1. BARTON, P. and VATANATHAM, T.: Environ. Sci. Technol., *1976*, 10, 262.
2. BORGWARDT, R. H.: E.P.A. Symp. on Flue Gas Desulf., Atlanta, Ga. Nov. 1976.
3. CRONKRIGHT, G. T. and LEDDY, W. J.: Environ. Sci. Technol. *1976*, 10, 569.
4. CHUNG-SHIH CHANG and ROCHELLE, G. T.: AIChE J. *1982*, 28, 261.
5. DÍAZ, J. M., FONSECA, L. and COCA, J.: (Submitted for publication).
6. ERGA, O. and TERJESEN, S. G.: Acta Chem. Scand., *1956*, 10 (5) 872.
7. GATES, E. L., MORTON, J. R. and FONDY, P. L.: Chem. Eng., *1976*, 83 (11) 144.
8. KIM, Y. K., DEMING, M. E. and HATFIELD, J. D.: Prepr. Pap. Natl. Meet. Div. Environ. Chem. Am. Soc. *1973*, 13, 33.
9. LOVELL, H. L.: Rep. No. E.P.A. 670/2–73–093, U.S. Env. Prot Ag. 1973.
10. LUND, K. and FOGLER, H. S.: Chem. Eng. Sci. *1978*, 30, 825.

11. PEARSON, F. H. and MCDONNELL, A. J.: Res. Publ. No. 79, Inst. for Land and Water Resources, The Penn. St. Univ. Park., Pa., 1974.
12. ROCHELLE, G. T. and KING, C. J.: Ind. Eng. Chem. Fundam. *1977*, 16, 67.
13. UCHIDA, S., WEN, C. Y. and MCMICHAEL, W. J.: Ch. I. Ch. E. J., *1974*, 5, 111.
14. UCHIDA, S., WEN, C. Y. and MCMICHAEL, W. J.: Ind. Eng. Chem. Proc. Des. Dev., *1976*, 15 (1) 88.
15. WENTZLER, T. J. and APLAN, F. F.: Environ. Control Proc. Symp. A.I.M.E. 1972. The Metallurgical Soc., N.Y. 1972.
16. ZWIETERING, T. N.: Chem. Eng. Sci. *1958*, 8, 244.

РЕЗЮМЕ

Авторы изучали скорость растворения в соерной кислоте двх типа известняка содержанием SiO_2 в 0,2 и 8,5%. Растворение провели в аппарате снабженной механической мешалкой. Изучали влияние содержания известняка и кислотной добавки используемой в качестве буфера — как химических факторов — на скорость растворения. Также изучали влияние типа и расположения мешалки как геометрических факторов, кроме того провели исследование поведения двух геометрически подобных аппаратов.

HUNGARIAN JOURNAL
OF INDUSTRIAL CHEMISTRY
VESZPRÉM
Vol. 11. pp. 91—96 (1983)

BEITRAG ZUR CHLORIERUNG VON EISENOXYD

Frau L. Szabó-Sipos, A. Újhidy und I. Vassányi*

(Forschungsinstitut für Technische Chemie der Ungarischen Akademie der Wissenschaften, Veszprém, Ungarn
* Lehrstuhl für Mineralogie der Universität für Chemische Industrie, Veszprém, Ungarn)

Eingegangen am 23 November, 1982.

Der Eisengehalt zahlreicher Rohstoffe ist in technologischer Hinsicht oft unerwünscht. Die Enteisung der Ausgangsstoffe kann man unter anderem mit Chlorierung verwirklichen.
Das Eisen wird während der Wärmebehandlung größtenteils in Hämatit umgesetzt.
Die Chlorierung eines künstlich hergestellten reinen Hämatits wurde unter verschiedenen Vesuchsbedingungen untersucht (Teilchengröße, spezifische Oberfläche, Gaszusammensetzung, usw.).
Es stellte sich heraus, die chemische Reaktion ist der geschwindigkeitsbestimmende Schritt des Bruttoprozesses unter gegebenen Versuchsbedingungen, wobei auch die spezifische Oberfläche bzw. ihrer Änderung von Bedeutung ist.

Einleitung

Das Kaolin ist der wichtigste Rohstoff der Porzellanherstellung, und daher ist von grundlegender Voraussetzung daß der Gehalt an Eisenoxyden oder Titandioxyden minimal sein soll. Ähnlich ist der Fall bei der Aluminiumchloridherstellung aus Bauxit. Diese Rohstoffe enthalten das Eisenoxyd entweder als selbstständige Phase oder in das Gitter eingebauter Form und daraus entsteht die Hämatitphase während der Wärmebehandlung. Die Chlorierung spielt eine wichtige Rolle bei der Entfernung des Eisens aus diesen Stoffen [1–2]. Bei den bisherigen Untersuchungen der Chlorierung von Hämatit haben die Forscher die bei den homogenen chemischen Reaktionen üblichen empirischen kinetischen Gleichungen aufgeschrieben, ohne die Oberfläche der festen Fe_2O_3-Teilchen bzw. ihrer Korngrößenveränderungen berücksichtigt zu haben [3–5].

Wir wollten es bei Chlorierung von Hämatit unter gegebenen Versuchsbedingungen nachprüfen, inwieweit die sich, aus der chemischen Reaktion und aus dem Stoffübergang ergebenden Teilprozesse zum Verlauf des heterogenen chemischen Bruttoprozesses beitragen.

Um diese Fragen zu klären können, haben wir die Rolle folgender Faktoren untersucht:

1. Qualität und Zusammensetzung der zur Chlorierung verwendeten Reagenzien (Cl_2, CO-Cl_2 Gasgemisch und Phosgen) sowie ihrer linearen Strömungsgeschwindigkeit,
2. Korngröße und spezifische Oberfläche des Hämatits,
3. Änderung der Reaktionszeit und Temperatur.

Experimenteller Teil

Zu den Versuchen wurde das Hämatit-Modellmaterial aus dem limonitischen Pulverfarbstoff Eisenoxydgelb (Qualität Bayer 920) in der Weise hergestellt, daß sie mit einer 5%-igen Gelatinelösung verknetet und unter einem Druck von $1{,}6 \cdot 10^8$ Pa zu Pastillen presst wurde.

Nach dem Trocknen wurde die Modellsubstanz einer Wärmebehandlung von 2 Studen im elektrischen Glühofen bei 1023 K unterzogen, dann zerkleinert, gesiebt und schließlich bis zur Gewichtskonstanz bei 378 K getrocknet. Für die Versuche wurden verschiedene Teilchenfraktionen eingesetzt [6]. Die Chlorierung der Proben wurde in einer sogennanten Brennrohranlage mit Schiffchen durchgeführt [7].

Der Verlauf der Reaktion wurde in jedem Falle durch die Gewichtsmessung der Chlorierungsrückstände bestimmt. Da wir in Gegenwart von CO, in reduzierender Atmosphäre arbeiteten, haben wir die Rückstände jedes Versuches durch röntgendiffraktometrische Phasenanalyse kontrolliert, ob die reduzier tenFormen des α-Fe_2O_3 (Fe_3O_4, FeO, Fe usw.) dort auftreten. Nachdem es festgestellt wurde, daß unter solchen Versuchsbedingungen der Rückstand

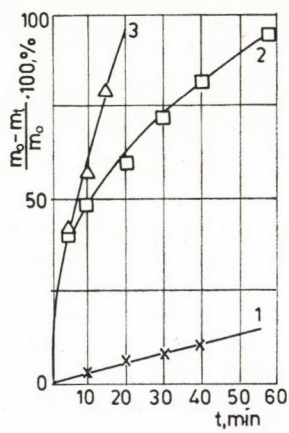

Abb. 1

Chlorierung von Hämatit 315—500 μm mit unterschiedlichen Gasen, T = 973 K

Kurve 1: $q_{Cl_2} = 0{,}92 \cdot 10^{-4}$ mol s^{-1}

Kurve 2: Gasgemisch:

$q_{CO} = 1{,}39 \cdot 10^{-4}$ mol s^{-1}

$q_{Cl_2} = 0{,}92 \cdot 10^{-4}$ mol s^{-1}

Kurve 3: Phosgen

immer mit dem Ausgangshämatit identisch ist oder ein Hämatit von besserem Kristallisations-grad ist, haben wir für richtig gefunden, die Messergebnisse der Gewichtsbestimmung auszuwerten. Auf Grund der in *Abb. 1.* dargestellten Meßergebnisse kann man feststellen, daß die Qualität der Chlorierungsreagenzien eine entscheidende Rolle spielt.

An einer Teilchenfraktion mittlerer Korngröße (315—500 μm) wurde der Einfluß der Zusammensetzung des Gasgemisches CO/Cl_2 untersucht. Es stellte sich heraus, daß in einem sehr weiten Bereich der Partialdrücke von Chlor ($p_{Cl_2}=0{,}1-0{,}9\cdot 10^5$ Pa) bzw. Kohlenmonoxyd die Chlorierbarkeit des Hämatits praktisch gleich geblieben ist. Die Gesamtgasmenge war in allen Fällen größer, als theoretisch erforderlich.

Die Chlorierbarkeit der vorherigen Teilchenfraktion wurde weiter bei den Temperaturen von 773, 873, 973 und 1123 K so untersucht, daß ebenso die lineare Strömungsgeschwindigkeit ($v=0{,}04-0{,}15$ m s^{-1} neben konstanten τ) des Gasgemisches wie der Chlor — bzw. Kohlenmonoxidüberschuß ($\tau=4-13$, neben konstanten v) verändert wurde. Es konnte festgestellt werden, daß die Hämatitumsetzung von den obigen Versuchsbedingungen — ausgenommen die Temperaturänderung — unabhängig war. Die Abhängigkeit der Umsetzung von der Temperatur ist aus der *Abbildung 2* ersichtlich. Die ebenfals in *Abbildung 2* dargestellten Ergebnisse zeigen, daß die Chlorierbarkeit verschiedener Teilchenfraktionen praktisch gleich war, ausgenommen die der zylindrischen Körper. Die spezifische Oberfläche wurde nach der BET-Methode durch N_2-Adsorption (Sartorius Vac. Microwage Typ 4102) bestimmt. Diese Werte fünf verschiedener Fraktionen betrugen von 5,5 bis 6,5 m^2 g^{-1}, weiterhin die Porenverteilung der Ausgangsproben einschließlich der zylindrischen Körper wiesen annähernd gleiche Bilder auf.

Es wurde weiterhin der Einfluß des Massenverlustes d.h. der Umsetzung auf die Änderung der spezifischen Oberfläche (F, m^2g^{-1}) und der Porenober-

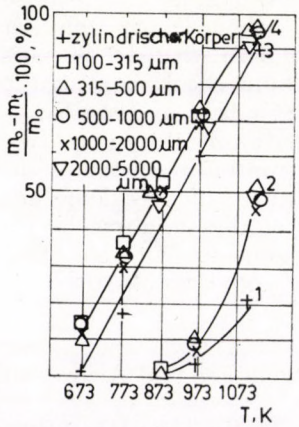

Abb. 2

Chlorierung des Hämatits von verschiedenen Teilchengrössenfraktionen $F=5{,}7-6{,}5$ m^2g^{-1} bei einigen Temperaturen, $t=30$ min, zylindrischer Körper ⌀0,01 m×0,006 m, $F=5{,}32$ m^2g^{-1}

Kurve 1,2: $q_{Cl_2}=0{,}92\cdot 10^{-4}$ mol s^{-1}; Kurve 3,4: Gasgemisch: $q_{Cl_2}=0{,}92\cdot 10^{-4}$ mol s^{-1} $q_{CO}=1{,}39\cdot 10^{-4}$ mol s^{-1}

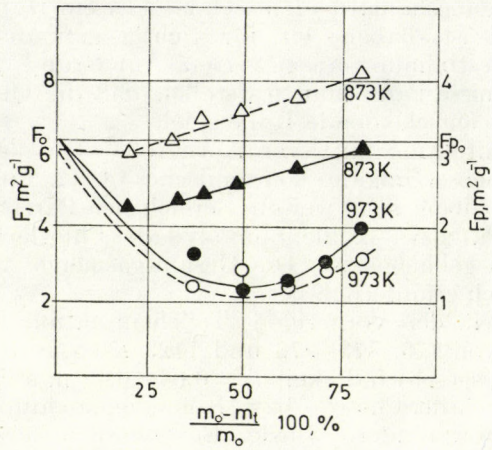

Abb. 3

Abhängigkeit der spezifischen Oberfläche und Porenoberflächen-Änderung von dem Massenverlust des Hämatits

$q_{Cl_2} = 0{,}92 \cdot 10^{-4}$ mol s^{-1}; $q_{CO} = 1{,}39 \cdot 10^{-4}$ mol s^{-1}

spezifische Oberfläche

Porenoberfläche

fläche (F_p, m^2g^{-1}) der Chlorierungsrückstände untersucht. Man sieht in Abbildung 3 daß sowohl die spezifische Oberfläche als auch die Porenoberfläche anfangs abnimmt aber danach zunimmt: beim Reaktionsstart einerseits durch Abnutzung der rauhen Teilchenoberflächen infolge der Chlorierung, anderseits durch die Entstehung eines besser kristallisierten Hämatits. Beim Reaktionsstart erklären wir die Abnahme der spezifischen Oberfläche durch Abnutzung der Teilchenoberflächen. Nach dem Erreichen einer bestimmten Umsetzung vermuten wir den Anstieg der Spezifischen Oberfläche durch die Zerkleinerung der Stoffteilchen. Die Kristallstruktur war bei 973 K eindeutlicher zu erkennen als bei 873 K. Die erste Erklärung wurde mit mikroskopischen Aufnahmen, die zweite mit Röntgenpulverdiagramm bestätigt. Nach dem Erreichen einer bestimmten Umsetzung des Hämatits vermuten wir in erster Linie den Anstieg durch die Zerkleinerung der Ausgangsteilchen und nur im geringeren Maße durch die Zunahme der Porenoberfläche. Es soll noch erwähnt werden, daß 90 Prozent des Porendurchmessers ebenso der Ausgangsproben wie der Rückstände größer als $30 \cdot 10^{-10}$ m war.

Ergebnisse und Auswertung

Anhand der Chlorierungsversuche des Hämatits ebenso in der reduktiven Atmosphäre wie bei der Anwendung des reinen Chlors konnten wir im Bruttoprozeß über die Rolle des Stoffübergangs und Oberflächenerscheinungen folgendes feststellen.

Wenn die Ergebnisse der Abbildung 1 miteinander verglichen werden, ist es zu sehen, daß die Reaktion in Gegenwart von reinem Chlor wesentlich lang-

samer fortschreitet, als beim Gasgemisch CO/Cl_2 oder beim Phosgen. In reinem Chlorgas sind die Stoffströme in der Umgebung des Eisenoxydteilchens wie folgt: das Chlor erreicht die Teilchenoberfläche durch einen Gasfilm, dort spielt sich eine Adsorption oder eine eventuelle Chemisorption und bald die chemische Reaktion ab, und dann gelangt das Produkt als Eisenchloriddampf durch diesen Film in den Hauptgasstrom. Wird die Chlorierung mit CO/Cl_2 und mit $COCl_2$ durchgeführt, so tritt insofern eine Änderung auf, als selbst das CO — bzw. $COCl_2$-Gas sich in Richtung zur Oberfläche bewegt und außerdem Eisenchlorid auch noch CO_2-Gas von dort entwichen ist. Wir können annehmen, daß die Diffusionseigenschaften und Diffusivität dieser Gase denen des Chlors annähernd gleich sind [8].

Der Widerstand des Filmes an der Teilchenoberfläche und in den Poren stimmt also in allen drei Fällen praktisch überein.

Die sprunghafte Steigerung der Effektivität der Chlorierung mit CO/Cl_2 und Phosgen ist wahrscheinlich dadurch erklären, daß im Prozeß nicht der Stofftransport sondern die chemische Oberflächenreaktion von Bedeutung ist.

Diese Feststellung wurde durch die in *Abbildung 2* dargestellten Vesuchsergebnisse unterstützt, besonders dann wenn die auf die spezifische Oberfläche bezogene Umsetzungen vergleichen werden. In diesem Fall gibt es keinen Unterschied zwischen der Chlorierbarkeit der verschidenen Teilchenfraktionen und der zylindrischen Körper. Es geht aus den vorher Gesagten hervor, das die chemische Reaktion und kein Stoffübergang (Porendiffusion, Bildung einer Diffusiongrenzschicht and der Teilchenoberfleche und in der Gasphase) der geschwindigkeitsbestimmende Schritt des Chlorierungsvorganges unter gegebenen Bedingungen und dem Versuchsmodell sein kann.

Da diese Daten aus BET-Aufnahmen im Stickstoffstrom gewonnen wurden und weil die Größe, die mittlere freie Weglänge, die Diffusionseigenschaften usw. des Stickstoffmoleküls denen der Chlorierungsgase annähernd gleich sind, [8] halten wir die Verwendung der so bestimmten Oberflächendaten für die Berechnung der Reaktionsgeschwindigkeiten für gerechtfertigt.

Weiterhin hat es sich herausgestellt, daß die Hämatitchlorierung am besten durch eine Gleichung nullter Ordnung zu beschreiben ist. Aus der Arrhenius-Darstellung geht hervor, daß die scheinbare Aktivierungsenergie 80—100 $kJ \cdot mol^{-1}$ beträgt. Auch die Größenordnung der Aktivierungsenergie unterstüzt die entscheidende Rolle der chemischen Reaktionen bei der Chlorierung des Hämatits.

SYMBOLVERZEICHNIS

$100 \times \frac{m_0 - m_t}{m_0}$ Massenverlust Umsetzung an α-Fe_2O_3%

m_0 Ausgangsmenge an α-Fe_2O_3 in mol

m_t nach der Zeit t im Reaktionsverlauf verbleibende Menge an α-Fe_2O_3 in mol

τ $= \frac{\text{mit Chlorierungsgasgemisch eingeführte Chlormenge}}{\text{für Chlorierung des eingewogenen } Fe_2O_3 \text{ erforderl. } Cl_2} =$

$=$ Chlorüberschuß in mol mol^{-1}

T Temperatur in K

t die Reaktionszeit in s

LITERATURVERZEICHNIS

1. H. HEGEMANN: Editura Chemisches Laboratorium für Tonindustrie, Berlin, 1938.
2. TH. HAASE: Silicattechnik, *1952*, 9, 399—402.
3. M. VANCEA, D. CHELBEA, G. BERINDEAN: Ind. Usoara. *1966*, 13, Nr. 8, 488—492.
4. M. VANCEA, D. CHELBEA, G. BERINDEAN: Ind. Usoara. *1968*, 15, Nr. 2, 97—101.
5. A. K. ORLOV, I. N. PISKUNOV: Izv. Vüs. Ucheb. Zaved. *1966*, 5, 35—42.
6. L. SIPOS SZABÓNÉ, I. VASSÁNYI, S. SZABÓ: Sprechsaal. *1981*, 114, No. 6, 437—440.
7. K. POLINSZKY, A. ÚJHIDY and J. SZÉPVÖLGYI: Hung. J. of Ind. Chem., *1977*, 5, 97—108.
8. LANDOLT—BÖRNSTEIN II. Band Eigenschaften der Materie in ihren Aggregatzustanden, Teil 5., Bandteil a. Transportphänomene I. Springer-Verlag, Berlin—Heildelberg—New York, 1969.

SUMMARY

The iron content of raw materials is often undesirable therefore the iron has to be removed. One possibility of the iron removal is the chlorination.

During the heat treatment of the raw materials, the iron compounds transform to hematite.

The chlorination of pure synthetic hematite samples were studied in the function of various experimental conditions as chlorination gas composition, grain size and specific surface area of the raw material, etc.

Based on the obtained results it can be stated that in the given experimental conditions the chemical reaction is the rate determining step of the chlorination, where the specific surface area of the solid and its change during the process play an important role.

РЕЗЮМЕ

С точки зрения технологии присутствие железа во многих сыревых материалов является нежелательным. Одним из способов удаления железа является хлорирование.

После предварительной термообработки железо в сыревых материалах превращается в гематит.

Авторы изучали хлорирование гематита высокой чистоты производимого исскуственным путём в различных экспериментальных условиях, при этом изучали влияние величины удельной поверхности, размера частиц, содержания газа использованного при хлорировании и т. д.

Установили, что скорость реакции в процессе в целом является определяющим фактором, при этом удельная поверхность и её изменение играют важную роль.

HUNGARIAN JOURNAL
OF INDUSTRIAL CHEMISTRY
VESZPRÉM
Vol. 11. pp. 97—110 (1983)

AN ANALYSIS OF A REFINERY NAPHTHA REFORMING PLANT

A. WOLFF

(Instytut Chemii i Technologii Organicznej Politechnika Krakowska.
31—155 Kraków, ul. Warszawska 24, Poland)

Received: November 25, 1982.

A process model of a three bed, catalytic naphtha reforming plant at a Polish refinery is presented. Both the model structure and parameter estimation technique are discussed. In addition, model predictions are given of optimum inlet temperatures and catalyst distribution among the three reactors to obtain specific reformate yield.

Catalytic reforming of naphtha to produce high octane gasoline is a process of high flexibility. It allows the processing of different feedstocks different conditions in order to yield a varying product state in accordance with market demand. Of primary interest in this process is the capability of adjusting the operating conditions to yield reformate with a specified octane number. In other cases, it is desirable to maximize the yield of aromatics, or even hydrogen production. Each one of these objectives can be attained by the choice of suitable operating conditions; i.e., catalyst mass distribution, inlet temperature, pressure, the hydrogen/hydrocarbon feed ratio, as well as the feedstock properties. The most convenient way to decide upon the optimum operating conditions is via the following mathematical model [1–6].

The commercial, investigated plant is located at a Polish refinery and consists of three fixed bed reactors in series with intermediate heating of reactants. A simplified process flowsheet is shown in *Fig. 1.* Pretreated, fractionated naphtha, refined from Romashkino crude oil with an end point at 180 °C after hydrodesulphurization is the feedstock. Provision is made for periodic regeneration of the ENGELHARD Pt/Al_2O_3 catalyst. Separation of products takes place immediately after this unit. The plant operates at approximately constant pressure to yield a specified octane number, and this determines the reactor operating temperature.

Very few commercial reforming models are available in literature. Perhaps the best one is the MOBIL reforming model [5, 6]. In the MOBIL model, the reforming kinetics are determined in such a way that the resultant kinetic parameters are independent of feedstock composition. The kinetic parameter estimation scheme allows the determination of 5 kinetic constants at each

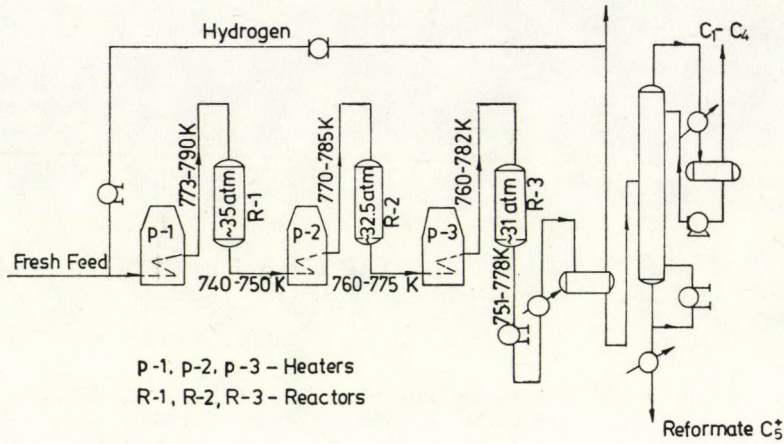

Fig. 1
Flowsheet of catalytic reforming process with Pt/Al_2O_3 catalyst

Table 1

Ranges of operating conditions for the catalytic reforming plant

	Variable range
Space velocity of the gasoline feed, m^3/hr	48.0–65.7
Group composition of the gasoline, %vol.	
aromatic hydrocarbons	8.0–7.5
naphthenic hydrocarbons	36.8–29.1
paraffinic hydrocarbons	55.2–63.4
Space velocity of the reformate, m^3/hr	36.5–49.1
Catalyst distribution, VK1:VK2:VK3	1:2:6
Catalyst load by weight, hr^{-1}	1.2–1.8
Pressure, Atm	30.0–35.0

Run	Reactor input temperature K			Reactor output temperature K			Reformate yield and content of aromatics, *wt.*%	
	TO1	*TO2*	*TO3*	*TK1*	*TK2*	*TK3*	*WR*	*GAR*
1	790	787	784	747	773	776	79.9	48.5
2	791	785	782	751	773	775	78.8	45.9
3	790	785	782	751	773	774	79.6	47.0
4	787	781	778	746	768	772	79.1	51.7
5	789	786	782	749	774	776	78.1	54.8
6	780	779	776	739	766	772	79.1	48.9
7	781	778	773	745	765	768	78.6	50.0
8	781	777	775	741	765	768	79.6	49.1
9	782	778	775	737	762	769	78.8	51.7
10	780	773	772	740	759	766	78.3	53.7
11	785	783	777	747	769	770	78.1	53.3

step. This procedure significantly reduces the parameter estimation problem. Much of the model development data were obtained in isothermal experiments over a wide range of feedstock compositions, in a large number of temperatures, liquid hourly space velocities and pressures.

In the present paper a mathematical model of a reforming plant is developed from the operating data of a commercial catalytic reforming plant.

The range of changes in the operating conditions of the analysed plant are given in *Table 1.* Originally 40 runs of the catalyst work were taken during about six months time. Because of the limited accuracy of the analysed data, eleven runs were finally used, differing mainly in temperature conditions, reformate yield and content of aromatics. The material balance did not violate ± 2.5 wt.%. This value also includes the approximative character of some calculations (density of group reactants and LPG, and molecular weight of group reactants, etc.).

The effect of the accuracy of the measurement of the operating conditions on the quality of the mathematical model was carried out for the temperature [7]. The accuracy of the temperature measurement was ± 5 °K. Changing the inlet temperature of the first reactor, an accuracy of about ± 1 wt.% change was obtained in the yield of reformate and about ± 1.5 wt.% change in the yield of aromatics.

The Mathematical Model

The following classes of group reactions were taken into account:

$$N \underset{W_5}{\overset{W_1}{\rightleftharpoons}} A + 3\,H_2 \tag{1}$$

$$P \underset{W_3}{\overset{W_2}{\rightleftharpoons}} N + H_2 \tag{2}$$

$$P + (n-1)\,H_2 \xrightarrow{W_4} nG \tag{3}$$

$$N + n\,H_2 \xrightarrow{W_6} nG \tag{4}$$

where A, N, P, G are aromatic, naphthenic, paraffinic and gaseous hydrocarbons respectively, and $(n-1)$ is the number of C-C bonds split in the average molecule of the paraffinic groups.

The dehydrocyclization reactions (1) and (2) lead to the formation of aromatic hydrocarbons, and the hydrocracking reactions (3) and (4), to the formation of light gaseous hydrocarbons, thereby decreasing the yield of liquid reformate. The isomerization reactions are omitted, based on the results of computations described in [8]. The effect of the catalyst desactivation in also omitted, since the data were collected in the relatively short period over which catalyst activity was constant.

To compensate for the fact that hydrocracking of naphthenic hydrocarbons occurs during the intermediate formation of paraffins, it was assumed that the coefficient $(n-1)$ is the same in reaction (3) and (4). Because there was no way to precisely determine the value of the coefficient $(n-1)$ based on the composition of the products, it was estimated along with the other kinetic parameters of the model; i.e., the absolute rate constants and the activation energies.

The model used to describe the reaction rates of the reactant groups in the notation of reactions (1) to (4) is summarized in *Table 2*.

The heats of reaction for these reactions were taken from the paper of PANCHENKOW [9].

Table 2

Summary of Mathematical Model

Component	Mass and energy balances	
A	$-1/M_A\ dg_A/dVK = -w_1 + w_5$	$w_1 = k_1 g_N$
N	$-1/M_N\ dg_N/dVK = w_1 - w_2 + w_3 - w_5 + w_6$	$w_2 = k_2 g_P$
P	$-1/M_P\ dg_P/dVK = w_2 - w_3 + w_4$	$w_3 = k_3 g_N g_{H_2}$
H_2	$-1/M_{H_2}\ dg_{H_2}/dVK = -3(w_1 - w_5) - w_2 +$	$w_4 = k_4 g_P g_{H_2}^{(n-1)}$
	$+ w_3 + (n-1)w_4 + nw_6$	$w_5 = k_5 g_A g_{H_2}^3$
G	$-1/M_G\ dg_G/dVK = -nw_4 - nw_6$	$w_6 = k_6 g_N g_{H_2}^n$
Temperature		
T	$-dT/dVK = 1/c_p[-(w_1 - w_5)\,\Delta HNA -$	$\Delta HPGS = (n-1)\,\Delta HPG$
	$-(w_2 - w_3)\,\Delta HPN - w_4\,\Delta HPGS -$	$\Delta HNG = \Delta HPG - \Delta HPN$
	$-w_6\,\Delta HNG]$	

Parameter Estimation

The objective here is to obtain the best parameter values according to an evaluation criterion within the inherent model constraints imposed by the assumption and simplifications.

The objective function chosen, to estimate the kinetic parameters of the model, is the minimization of the sum of the relative squared deviations between computed and measured values of the product composition and reactor outlet temperatures [10]:

$$F = \sum_{m/1}^{M} \xi_m [(\overline{X}_m - X_m)/\overline{X}_m]^2 \tag{5}$$

where ξ_m is a correcting coefficient when a different accuracy of the calculation for different elements of the aim function are desired; X_m and $\overline{X}_m$ mean computed and measured values respectively and M is the number of considered elements of the objective function. Minimization of these deviations with respect to product group content and reactor outlet temperatures was carried out independently of each data set. As a result, an independent set of kinetic parameters was gained for each set of data. To estimate k_{0j} and activation energies E_j of the forward and reverse reactions, the ARRHENIUS equation was used.

In the computations the package of programmes MINUITS [11] were used to minimize the function of n variables. This method offers the possibility of

catering for different kinds of functions within one programme, since it incorporates three different minimization methods, each of which may be used alone or in combination with others, depending on the behaviour of the function and desires of the user. These three minimizing subroutines are: SEEK (a Monte Carlo method), SIMPLEX (a simplex method by NELDER and MEAD) and MIGRAD (a variable method by DAVIDON).

The estimation of the values of the kinetic parameters of the model was carried out using a simple step procedure. At each given step of that procedure kinetic parameters were found which had approximately the same value for the whole set of eleven estimation runs and were set up as constants during the next estimation step. From the initial 13 kinetic parameters, this procedure allows us in the final step to estimate, separately for each of the 11 runs, only 5 parameters. This estimation maintains the same accuracy of computation. Thus, in the final step the following rate constants were estimated: k_{01}, k_{03} k_{06} as well as $(n-1)$. Subsequent steps to find the common value of these parameters for the whole set of data, although applying the step regression analysis in observing the dependence of the parameter value on the temperature conditions of the plant, did not give any satisfactory result. This can be attributed to the fact that data from the analysed plant's normal operational procedure were applied.

Analysis of the Result

Representative values of reactor output temperatures, reformate yield and content of aromatics obtained with the model are given in *Table 3*.

The distribution of aromatic hydrocarbons produced in each reactor $R1:R2:R3=50:20:30$ shows the decisive role of the first reactor. The contributions of the third reactor in producing aromatic hydrocarbons primarily arises from the dehydrocyclization of paraffins. It is also seen from *Table 3* that the decrease in aromatic hydrocarbons produced in the first reactor is a function of the operating period of the catalyst. The deviation of data set

Table 3

Calculated products composition and temperatures

Run	Reactor output temperature K			Reformate yield *wt.%*	Content of aromatics in reformate *wt.%*	Percentage yield of aromatics in first reactor
	TR1	*TR2*	*TR3*			
1	747.0	770.9	777.0	79.7	48.5	55
2	752.4	774.1	780.5	78.3	47.3	58
3	751.6	773.5	777.4	79.2	47.9	53
4	746.7	765.4	770.3	79.0	52.1	50
5	748.5	770.7	775.7	78.1	53.4	48
6	738.6	764.4	772.0	78.9	48.6	46
7	744.7	765.0	767.4	78.5	49.8	50
8	739.9	759.5	766.2	79.5	47.6	46
9	736.0	757.9	767.1	78.9	50.0	44
10	739.8	757.1	766.1	78.2	53.2	51
11	746.2	764.9	768.8	78.2	51.8	44

No. 10 from this trend could be attributed to the relatively large amount of naphthenic hydrocarbons in the feed (36.8 vol.% and 55.2 vol.% of paraffins) for that run.

The average values of the parameters estimated in the last step of the procedure are given in *Table 4*.

Table 4

Average values of estimated kinetic parameters

Reaction		Kinetic parameters
$N \rightarrow A$	k_{01}	$2.66\ 10^{12}$
	E_1	35,150
$P \rightarrow N$	k_{02}	41.38
	E_2	1,660
$N \rightarrow P$	k_{03}	$4.04\ 10^{9}$
	E_3	19,680
$P \rightarrow G$	k_{04}	$4.13\ 10^{18}$
	E_4	44,600
	$n-1$	3.42
$A \rightarrow N$	k_{05}	54.60
	E_5	63,700
$N \rightarrow G$	k_{06}	$3.85\ 10^{14}$
	E_6	17,400

A very high "severity" in the hydrocracking reactions was observed. The value of $(n-1)$ indicates that more than three *C-C* bonds are broken in an average molecule of the paraffinic hydrocarbons. This is the result of the process temperature and the fact that the decomposition reactions are attributed primarily to paraffinic hydrocarbons. The content of paraffins in the feed is about 50–60 *wt.*%, yielding about 20 *wt.*% of gaseous products.

Examples of the concentrations and temperature profiles in the reactors for data sets No. 1 and 10 (which differ by content of aromatic hydrocarbons in the reformate) are presented in *Fig. 2*.

The first reactor has the maximum paraffin yield because of the naphthene dehydrogenation reaction. The computed yield of reformate, as well as the yield of gaseous hydrocarbons varied almost linearly within the second and third reactor. Naphthenic content in the third reactor is practically constant, indicating that in this case the system attains equilibrium. The temperature profiles are in accordance with the preceding observations.

Calculated reaction rate profiles for selected reactions are given in *Fig. 3* for data set No. 1. Reaction rates depend on the temperature and the concentrations of reagents in the considered stage of the reactor.

It is interesting to note the almost flat profiles of the reaction rates w_1, w_3 and w_6, beginning in the middle of the second reactor. This indicates that equilibrium is attained. The maximum change in reaction rate occurs for dehydrogenation of naphthenic hydrocarbons in the first reactor. The relatively small rate change in the hydrocracking of paraffins within each reactor, and its step change between each reactor is characteristic of reforming. It is

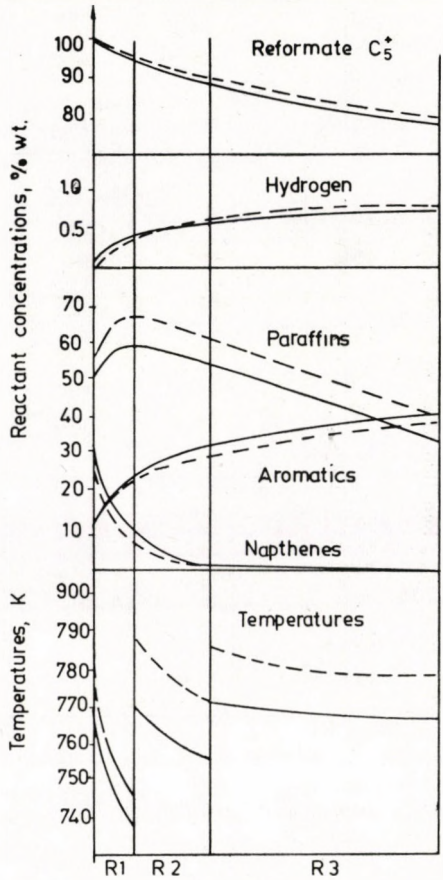

Fig. 2

Concentration and temperature profiles in the reactors

– – – – Run No. 1

-------- Run No. 10

due to the heating of the reactants between reactors, and to the increasing residence time. The rate of reaction w_6 becomes comparable with the others in the third reactor. Based on the proceeding observations, it is seen that the relative gain of the aromatic hydrocarbons produced in the third reactor is a result of the hydrocracking reactions of the paraffins and the subsequent dehydrocyclization reactions of the paraffins: $P \rightarrow N \rightarrow A$.

In *Table 5* the relative reaction rates at the inlet of the first reactor and at the outlet of the third reactor are presented. As can be seen, there is good agreement between the data sets, even though the temperatures are different. Except for the very slow aromatic hydrogenation reaction, the reaction rates w_1, w_3, w_4 and w_6 are of the same order at the reactor outlets. The paraffin cyclization reaction exhibits the relatively largest rate.

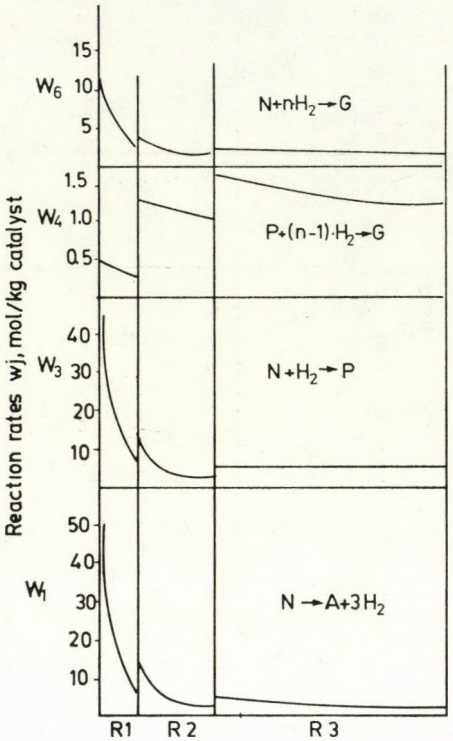

Fig. 3
Reaction rate profiles, run No. 1

Table 5

Relative rates of reactions at inlet and outlet of reactors

Chemical reactions	Symbol	Relative rates of reactions			
		Inlet to $R1$		Outlet of $R3$	
		Run No. 1	Run No. 10	Run No. 1	Run No. 10
$N \to A$	$w1/w1$	1.000	0.913	0.032	0.029
$P \to N$	$w2/w1$	0.127	0.111	0.086	0.073
$N \to P$	$w3/w1$	0.767	0.520	0.032	0.022
$P \to G$	$w4/w1$	0.007	0.008	0.019	0.015
$A \to N$	$w5/w1$	~ 0	~ 0	~ 0	~ 0
$N \to G$	$w6/w1$	0.183	0.201	0.024	0.023

Effect of Temperature and Catalyst Distribution

The above results indicate that the estimated parameters should describe the operation of the commercial plant reasonably well. Therefore, the model should be able to predict the effect of reactor inlet temperatures and the

catalyst distribution on the yield and group composition of the reformate. Calculations were performed for data set No. 6 *(Tables 2* and *3)*. The feedstock after hydrodesulphurization contained 31.7 vol.% of naphthenes and 61.0 vol.% of paraffinic hydrocarbons.

To evaluate the effect of temperature on the reformate yield, the temperature level at the inlet to each reactor was changed arbitrarilly in the first step of computations and the model was integrated, *Fig. 4*.

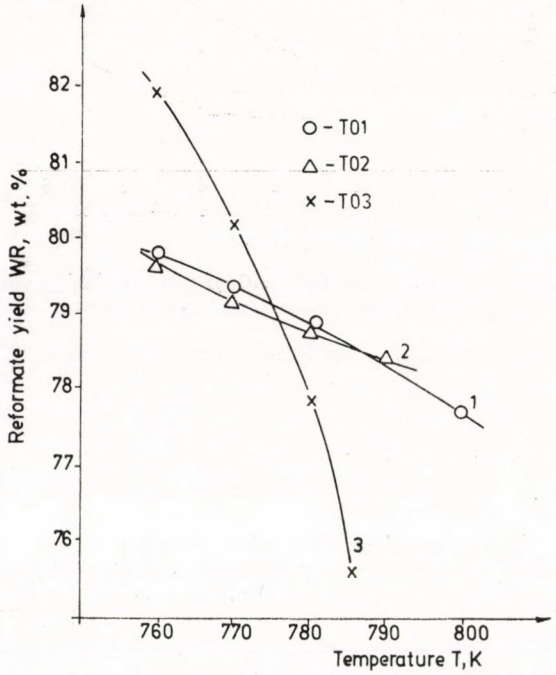

Fig. 4
Relationship between reformate yield, *WR* and inlet reactor temperature
1 — change of the first reactor inlet temperature
2 — change of the second reactor inlet temperature
3 — change of the third reactor inlet temperature

Curve 1 in *Fig. 4* shows only the influence of the first reactor inlet temperature change on the final yield of reformate. The rest of data set No. 6 was unchanged. Similarly, curves 2 and 3 represent only the influence of the second and third reactor inlet temperature changes on the reformate yield, and again the rest of the data set was unchanged. Thus, all curves represent different situations. The results proved the strong role of the third reactor, and particularly its inlet temperature, in determining the final reformate yield.

The effect of the changes of catalyst distribution were similarly tested. The results of these computations, presented in *Fig. 5*, indicate that for constant total quantity of catalyst, the increase in the quantity of catalyst in the

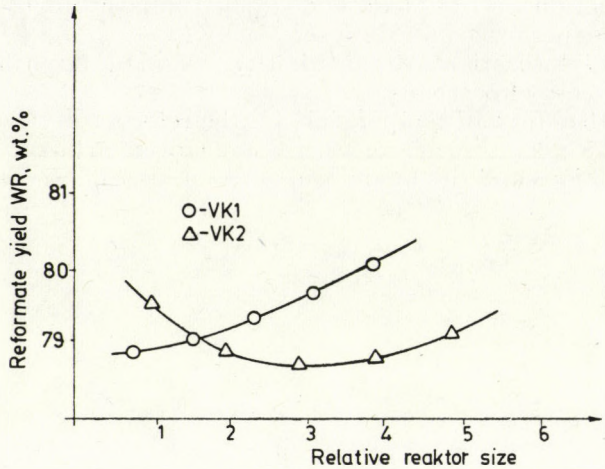

Fig. 5
Relationship between reformate yield, *WR* and relative reactor size

first reactor (with unchanged quantity of the catalyst in the second reactor, and thus respectively less in the last one) resulted in an increased yield of reformate. A minimum in the reformate yield was achieved by varying the amount of catalyst in the second reactor in the same manner.

The net effect of catalyst distribution is less than the effect of the inlet temperatures.

In another set of computations the inlet temperatures $TO1$, $TO2$, $TO3$ and the mass distribution of catalyst $VK1$, $VK2$ and $VK3$ were taken as the optimization parameters. The range of variations of these variables are shown below:

	lower level	upper level
$TO1$, K	760	800
$TO2$	760	800
$TO3$	760	800
$VK1$	0.8	3.8
$VK2$	1.0	4.8
$VK3$	0.4	7.2

The objective was then the maximization of either the reformate yield, WR, or the product $WR \cdot AR$, where AR is the content of aromatics in *wt.%*. The results are shown in *Table 6*.

Maximization of the reformate yield was achieved for low inlet temperatures with small amounts of catalyst in the third reactor, which at the same time causes a decrease in the aromatics yield; e.g., when the reformate yield increases from 80 *wt.%* to 82 *wt.%*, the aromatic hydrocarbon yield decreases from 48 *wt.%* to 45 *wt.%*. This was done to test the behaviour of the model.

Table 6

Optimum catalyst distribution and inlet reactor temperatures for extreme levels of the reformate yield, run No. 6

Objective function	$F=\max(-WR)$	$F=\max(-WR\cdot AR)$
Relative distribution of the catalyst in reactors		
$VK1$	3.9	0.8
$VK2$	4.8	1.7
$VK3$	0.3	6.5
Reactor inlet temperatures, K		
$TO1$	760	800
$TO2$	760	790
$TO3$	760	790
Reformate yield, *wt.*%	84.8	73.1
Aromatics content in reformate, *wt.*%	39.9	56.2

When the objective is used to maximize $WR\cdot AR$, quite different results are observed. The type of objective function used allowed analysis of only extreme conditions. To find the optimum conditions for any given level of reformate yield, the following type of the objective function F was applied:

$$F=\max\ (-\alpha_1 WR-\alpha_2 AR) \tag{6}$$

By changing the values of the coefficients, α_1 and α_2, different objective functions F were obtained. The results of these computations are presented in *Fig. 6*, *7* and *8*. Each point in these diagrams represents an optimum solution for a given reformate yield or aromatic content. Thus these curves allow for assessment of other optimal solutions in the range tested. In these computations α_1, was fixed as 10.0 and α_2 was changed in the range 6.5–17.0.

Fig. 6 enables the determination of the content of aromatic hydrocarbons in reformate GAR, as a function of the reformate yield. It can be seen in *Fig. 7* and *8* that for a reformate yield greater than 82 *wt.*% the optimum temperature at the inlet of the first reactor, $TO1$, decreases almost stepwise from 800 to 760 °K (the amount of catalyst in the first reactor in the range of reformate yield up to 82 *wt.*% was nearly the same as in the commercial data). The analogous shape of the curve for $TO2$ shows the change of optimum inlet temperature of the second reactor. However, the decrease of the temperature level takes place in the area of a reformate yield of more than 82 *wt.*%. The optimum quantity of catalyst in the second reactor decreases at first, and then increases to the upper level given.

These computations indicate that the catalyst distribution for the particular reforming plant studies (i.e., $VK1:VK2:VK3=1:2:6$) is close to the optimum one from the reformate yield point of view. With an increase in temperature in the reactors, one could improve the content of aromatic hydrocarbons (see *Fig. 6*). A similar effect is observed when the quantity of the catalyst in the second reactor increases by 30%. For high reformate yield, the quantity of

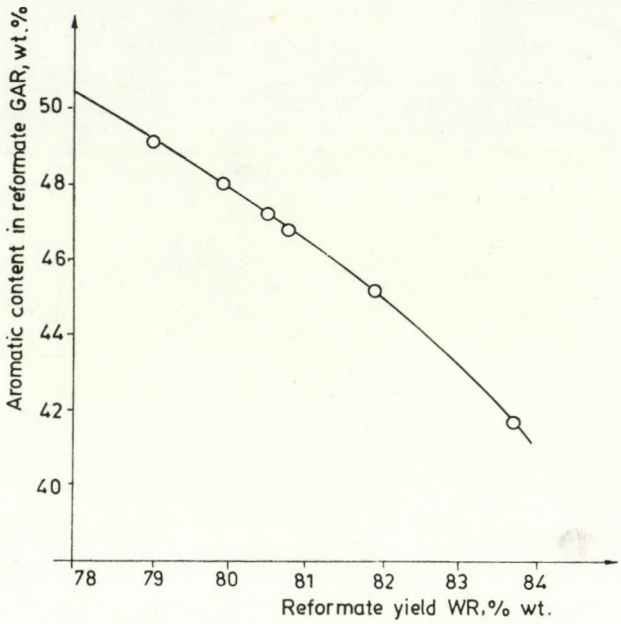

Fig. 6
Relationship between aromatic content, *GAR* and reformate yield, *WR*

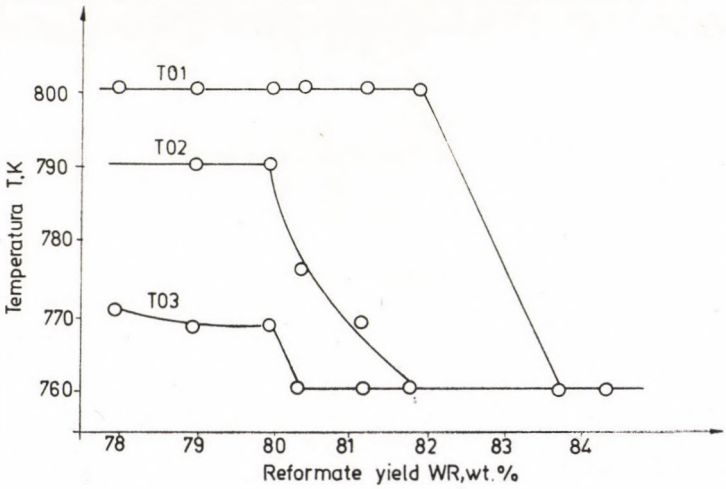

Fig. 7
Optimum disribution of reactor inlet temperatures

catalyst in the second reactor should be larger then in the third reactor. Under the above conditions, in order to ensure the proper level of the octane number, the catalyst must have good isomerization properties.

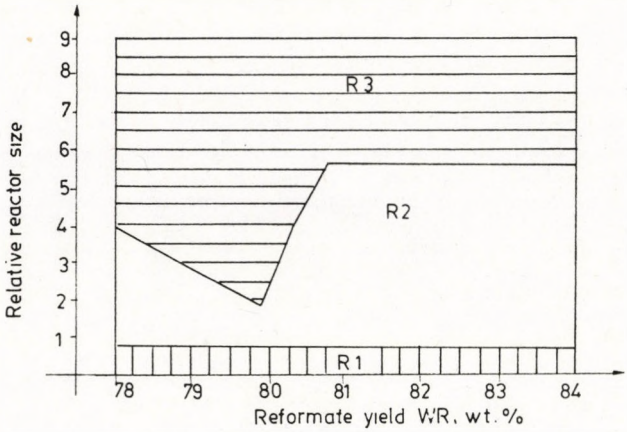

Fig. 8
Optimum catalyst distribution

The hydrogen yield changes within a limited scope. This is due to the fact that although limiting hydrocracking reactions, low operating temperatures cause a decrease in hydrogen comsumption. This is to a large extend offset by the decrease in aromatic production from the dehydrogenation of naphthenic hydrocarbons observed simultaneously. This means that the best way to increase the hydrogen yield is to reduce the process operating pressure.

Conclusion

The mathematical model presented provides a means of computing the product composition in the outlet of the third reactor and the temperature at the outlet of each of the reactors with reasonable accuracy. The kinetic computations showed the fundamental role of the inlet temperature of the first reactor in determining the final aromatic yield, and also of the third reactor inlet temperature and size on the final reformate yield.

The dehydrogenation reaction of naphthenic hydrocarbons approaches equilibrium in the third reactor. The rate of the hydrocracking reaction changes relatively little in a given reactor, but increases stepwise between reactors.

The effect of the inlet temperature on the reformate yield and aromatics content was evidently higher than the effect of the catalyst distribution. Computations with the model indicated that the catalyst distribution for the analyzed plant was optimum from the point of the reformate yield.

Acknowledgement

The author is indebted to Joe Calo of Brown University, USA, for his helpful suggestions and corrections of the English, and to Jerzy Kramarz of the Technical University of Cracow for his discussions and suggestions.

SYMBOLS

A, N, P	— aromatic, naphthenic, paraffinic hydrocarbons, respectively
G	— gaseous hydrocarbons C_1-C_4
$n-1$	— number of split C-C bonds in chain of average molecule of paraffinic hydrocarbons
w_j	— reaction rate, mol/kg catalyst hr
w_1	— rate of dehydrogenation reaction at input to the first reactor, mol/kg catalyst hr, Tabk. 5
k_j	— reaction rate constant, kg catalyst hr/mol
k_{0j}	— absolute rate constant
E_j	— activation energy, cal/mol
$1/VK$	— catalyst load by weight, kg/kg catalyst hr
T	— temperature, K
M_i	— molecular weight, kg/mol
g_i	— weight fraction
SVK	— total quantity of the catalyst in system
c_p	— specific heat, kcal/kg K
$TO1, TO2, TO3$	— reactor inlet temperatures, K
$TK1, TK2, TK3$	— reactor outlet temperatures, K
WR	— reformate yield, wt.%
AR, GAR	— contents of aromatics in products and in reformate, respectively, wt.%
$R1, R2, R3$	— first, second and third reactor respectively

Greek Letters and Superscripts

α_1, α_2	— coefficients of the objective function F eq. 6
ΔHNA	— heat of dehydrogenation reaction of naphthenic hydrocarbons, kcal/mol
ΔHPN	— heat of cyclization reaction of paraffinic hydrocarbons, kcal/mol
ΔHPG	— heat of hydrocracking reaction of paraffinic hydrocarbons connected with splitting one C-C bond in chain
$i=1, 2, \ldots, 5$	— number of reactants
$j=1, 2, \ldots, 6$	— number of reactions

REFERENCES

1. SMITH, R. B.: C.E.P. *1959*, 55, 76.
2. ZHOROW, Yu. M., PANCHENKOW, G. M., ZELTSER, S. P. i TIRAKIYAN, Yu. A.: Kinetika i Kataliz, *1965*, 6, 1092.
3. GAVALAS, G. R.: I.E.C. Fundamentals, *1971*, 10, 621.
4. HENNINGSEN, J. and BUNDGAARD-NIELSON: British Chemical Engineering, *1979*, 15, 1433.
5. GRAZIANI, K. R. and RAMAGE, M. P.: ACS Symposium Series 65. American Chemical Society, Houston, 1978.
6. RAMAGE, M. P., GRAZIANI, K. R. and KRAMBECK, F. J.: C.E.S., *1980*, 35, 41.
7. KRAMARZ, J., WOLFF, A.: Inżynieria Chemiczna, *1979*, 9, 371.
8. WOLFF, A. i KRAMARZ, J.: Khimiya i Tekhnologiya Topliw i masel, *1979*, 12, 10.
9. PANCHENKOW, G.M., ZHOROV, Yu. M., PIERSHIN, A. D.: Trudy Moskowskogo Instituta Neftekhimicheskoi i Gazovoi Promyshlennosti, Wypusk 74, 1967, Izd. Khimiya, Leningrad.
10. KRAMARZ, J. and WOLFF, A.: Chem. Techn. *1979*, 4, 181.
11. Program Library D506 CERN Computer Centre

РЕЗЮМЕ

В сообщении приведено описание модели завода каталитического реформинга бензина трёхслойного типа работающего в Польши. Изложена структура модели и методика определеня параметров. Далее с целью предсказывания производительности автором заданы оптимальные значения температур потоков на входе и оптимальное распределение катализатора между тремя реакторами.

1. The "Hungarian Journal of Industrial Chemistry" is a joint publication of the Veszprém scientific institutions of the chemical industry that deals with the results of applied and fundamental research in the field of chemical processes, unit operations and chemical engineering in the form of original articles written in the English, Russian, German and French languages.

In addition to the scientific workers of the institutions at Veszprém, the Editorial Board of this publication also welcomes articles for inclusion in this periodical, which are written by authors who are engaged in the above mentioned fields.

2. Manuscripts should be sent—in duplicate—to the Editor-in-Chief:

Dr. Endre Bodor,
Veszprém University of Chemical
Engineering (VVE),
P.O.B. 158
Veszprém
H—8201 Hungary

3. In a brief letter attached to the manuscripts, authors should declare that:

a) their work is original and has not previously been published elsewhere in its present format, and

b) for the purposes of correspondence, they can be contacted at the address and telephone number which they give.

4. Manuscripts should be typed on paper of A/4 size.

The first page should give the title, the author's name, place of work and a brief summary of the article (maximum of 15 lines).

If possible the article should be presented with an introduction, experiments carried out, conclusions and discussion. Tables and Figures must be presented on separate sheets and their position in the text should be noted on the margin. A summary of the symbols used, the Tables and captions of the Figures should be attached separately to the manuscripts.

It is regretted that photographs cannot be included in the periodical.

The Tables and Figures should not exceed an A/4 size. If diagrams are presented, only the explanation and dimensions of the ordinate and abscissa, and marking numbers are required, while further explanatory texts can be given in the captions of the Figures. The equations used should be numbered, and Tables and Figures should be numbered and noted in the margin.

With regard to units, it is essential that an SI (Systeme International d'Unités) should be used.

References should be prepared in the following manner:

a) Publications which have appeared in periodicals:
Author's name and initials; title of the periodical (the abbreviation used by Chemical Abstracts is recommended); year of publication; volume number; (number of brochure if necessary); the first and last page number of the article, e.g.:

WAKAO, N. and SCHWARTZ, J. M.:
Chem. Eng. Sci., **1962**, 17 (3), 825—827.

b) Books:
Author's name and initials; title of book; publisher; place of publication; year of publication, e.g.:

SATTERFIELD, C. N.:
Mass Transfer in Heterogeneous Catalysis.
MTI Press, Cambridge, Mass., 1951, pp. 26—32.

c) Patents:
Country where granted, and number of the patent, e.g.:

U.S. Pat.	3,425,442
Brit. Pat.	997,665
Hung. Pat.	553,243

d) Published lectures:
Author's name and initials; title of lecture; name of the conference; further information if necessary, e.g.:

HIH, D., HHU, C. and LEECH, W. J.:
A Discrete Method to Heat Conduction Problems. 5th International Heat Transfer Conference, Tokyo, 1975. Co. 2.4.

5. Authors receive 50 complimentary copies of their article.

CONTENTS

BAKOS M.: † ANTAL LÁSZLÓ, June 7, 1922 — December 8, 1982 1
FÁY, GY., FÜLÖP, J. and TŐRÖS, R.: On the Determination of the Thermostatic State Equations. Part 1. 3
BLICKLE, T. and SZENTMARJAY, T.: Use of Dispersion Characteristics in Modelling of Grinding 13
ERDÉSZ, K. and ORMÓS, Z.: Bed Expansion and Pressure Drop in Vibrofluidized Layers VI. 21
MRS. SIMON, A., NÉMETH, J., BUCSKY, GY. and KREIDL, J.: Investigations of Baffle-Plate Tube-Reactor 33
TIMÁR, L.: A Two-Algorithm Approach to Calculate Reboiled Absorbers 47
JÄNICKE, W.: Two Measures for the Variability of Multi-Purpose Batch Chemical Plants 59
KOVÁCS, B., MAJOR, R. and MAJTÉNYI, M.: Electrostatic Precipitation of Various Dusts 63
NAGY, E. and BLICKLE, T.: The Influence of Dispersion Conditions on Mass Transfer Accompanied by First-Order Moderate Reaction 71
DIAZ, J. M., FONSECA, L. and COCA, J.: Chemical and Geometrical Factors in Limestone Slurries Dissolution in Stirred Tanks 81
FRAU SZABÓ-SIPOS, L., ÚJHIDY, A. und VASSÁNYI, I.: Beitrag zur Chlorierung von Eisenoxyd (The Chlorination of Iron Oxide) 91
WOLFF, A.: An Analysis of a Refinery Naphtha Reforming Plant 97

Egyetemi Nyomda — 83.1037 Budapest, 1983. Felelős vezető: Sümeghi Zoltán igazgató

Ára: 250 Ft

THE FOLLOWING ARE PLEASED TO ACCEPT SUBSCRIPTIONS TO THIS JOURNAL:

AUSTRALIA

C.B.D. Library and Subscription Service
Box 4886 G.P.O.
Sydney 2000

Cosmos Book and Record Shop
145 Acland Street
St. Kilda 3182

Globe and Co.
694—696 George Street
Sydney 2000

AUSTRIA

Globus (VAZ)
Höchstädtplatz 3
A—1200 Wien XX

BELGIUM

"Du Monde Entier" S. A.
Rue du Midi 162
B—1000 Bruxelles

Office International de Librairie
Avenue Marnix 30
B—1050 Bruxelles

CANADA

Pannonia Books
P.O. Box 1017
Postal Station "B"
Toronto, Ontario M5T 2T8

DENMARK

Munksgaard's Boghandel
Norregade 6
DK—1165 Copenhagen K

FINLAND

Akateeminen Kirjakauppa
Keskuskatu 2, P.O.B. 128
SF—00 100 Helsinki 10

FRANCE

Office International de Documentation et Librairie
48 Rue Gay Lussac
75 Paris 5

GERMAN FEDERAL REPUBLIC

Kubon und Sagner
Pf 68
D—8 München 34
BRD

GREAT BRITAIN

Bailey Bros and Swinfen Ltd.
Warner House, Folkestone
Kent CT 19 6PH England

HOLLAND

Martinus Nijhoff
Periodicals Department
P.O. Box 269
The Hague

Swets and Zeitlinger
Keizersgracht 487
Amsterdam C

ITALY

Licosa
P.O.B. 552, Via Lamarmora 45
50121 Firenze

JAPAN

Igaku Shoin Ltd.
Foreign Department
Tokyo International P.O. Box 5063
Tokyo

Maruzen Co. Ltd.
P.O. Box 5050
Tokyo International 100—31

Nauka Ltd.
Yasutomi Bldg. 5F 2—12 Kanda
Jinbocho, Chiyoda-ku
Tokyo 101

NORWAY

Tanum—Cammermayer
Karl Johangt. 41—43
Oslo 1

SWEDEN

Almqvist and Wiksell Förlag A. B.
Box 2120
S—103 13 Stockholm 2

Wennegren—Williams AB
Subscription Department Fack
S—104 Stockholm 30

SWITZERLAND

Karger Libri A. G.
Petersgraben 31
CH—4011 Basel

USA

Ebsco Subs. Services
1 st Ave North at 13th street
Birmingham, Ala. 35201

HUNGARIAN

Journal of

INDUSTRIAL CHEMISTRY

Edited by

the Hungarian Oil & Gas Research Institute (MÁFKI),
the Research Institute for Heavy Chemical Industries (NEVIKI),
the Research Institute for Technical Chemistry of the
Hungarian Academy of Sciences (MÜKKI),
the Veszprém University of Chemical Engineering (VVE).
Veszprém (Hungary)

Volume 11. **1983.** **Number 2.**

HU ISSN: 0133—0276
CODEN: HJICAI

Editorial Board:

R. Csikós and Gy. Mózes
Hungarian Oil & Gas Research Institute
(MÁFKI Veszprém)

A. Szántó and M. Nádasy
Research Institute for Heavy Chemical Industries
(NEVIKI Veszprém)

T. Blickle and O. Borlai
Research Institute for Technical Chemistry
of the Hungarian Academy of Sciences
(MÜKKI Veszprém)

P. Árva and G. Deák
Veszprém University of Chemical Engineering
(VVE Veszprém)

Editor-in Chief:
E. Bodor

Assistant Editor:
J. De Jonge

Veszprém University of Chemical Engineering
(VVE Veszprém)

The "Hungarian Journal of Industrial Chemistry" is a joint publication of the Veszprém scientific institutions of the chemical industry that deals with the results of applied and fundamental research in the field of chemical processes, unit operations and chemical engineering. The papers are published in four numbers at irregular intervals in one annual volume, in the English, Russian, French and German languages

Editorial Office:
Veszprémi Vegyipari Egyetem
"Hungarian Journal of Industrial Chemistry"
H–8201 Veszprém, P. O. Box: 158.
Hungary

Orders may be placed with
KULTURA
Foreign Trading Co. for Books and Newspapers
Budapest 62. POB 149
or with its represenatives abroad, listed on the verso of the cover

FELELŐS SZERKESZTŐ: DR. BODOR ENDRE

KIADJA A LAPKIADÓ VÁLLALAT, 1073 BP. VII., LENIN KRT. 9–11.
TELEFON: 221-285. LEVÉLCÍM: 1906 BP. PF. 223
FELELŐS KIADÓ: SIKLÓSI NORBERT IGAZGATÓ

HUNGARIAN JOURNAL
OF INDUSTRIAL CHEMISTRY
VESZPRÉM
Vol. 11. pp. 113-118 (1983)

ON THE RELATIONSHIP OF COLOUR CHARACTERISTICS AND PARTICLE-SIZE DISTRIBUTION AND SPECIFIC SURFACE AREA OF CERTAIN PIGMENTS. I.

I. Szücs and G. Sziklai

(Department of Chemical Technology, University of Chemical Engineering, Veszprém, Hungary)

Received: November 29, 1982.

The relationship of colour and particle-size distribution and specific surface area of iron-oxide-yellow pigment was studied as a function of the production variables of the pigment. It was concluded that the duration and rate of oxidation control both the colour, particle-size and specific surface area of the pigment. However, no direct, easily formulated relationships could be established between the characteristics tested.

Introduction

The term pigment invariably implies complete insolubility in the suspending medium [1–3] and sufficiently fine particle size. However, the term "fine particle" encompasses a range which extends from 0.1 to 100 μm [1]. Recently, even the relating to the colour of the pigment was omitted [3] and the only additional information mentioned was that the pigment has to possess certain physical characteristics and be able to be coat — mixed into certain adhesives — various surfaces. These statements are too general to be of any practical use, yet they are unavoidable in the definition of certain terms. However, it is still unclarified how these general statements and requirements relate to particular groups of pigments.

It is obvious, even from the most general definition, that pigments, and particularly certain groups of pigments or even more so, certain unique pigments, must have suitable colour and morphological characteristics, and not only insolubility in the suspending medium. This statement is still too general, but of least these characteristics can be quantified and limits can be established. In fact, the containers of certain products give these specifications. Another difficulty is that the interrelationship of these characteristics is generally unknown, and we do not have a clear view of how to modify the production process to obtain pigments with the required characteristics.

It is not all easy to relate colour and morphology to production process variables, because often pigments are formed in rather complicated physical and chemical systems. However, the demand for improved product quality mandates process control, which, accordingly, contains many emprirical elements. Therefore, in our opinion, it is essential for both the producer and the user that the colour and the morphological characteristics should be determined, for they are rarely available in literature, and even if available, only in a very narrow sense.

Three pigments were selected for the present study: iron-oxide yellow, iron-oxide-red and chromium-oxide green. The relationships of particle-size distribution, specific surface area, colour characteristics and production process variables were studied. This paper discusses the results of the iron-oxide-yellow tests.

Experimental

Iron-oxide-yellow pigment was prepared in our laboratory according to the PENNIMANN–ZOPH process, the most frequently used industrial process [4]. Accordingly, 20 l of 8.5 g/l iron(II) sulphate solution was oxidized by air, in the presence of 6 g/l iron(III) hydroxyde "seeds" and metal iron.

The product formation rate of iron-oxi-hydrate was 0.376 g/l hr. Samples were taken at 12 hour intervals during the oxidation period and the colour characteristics, particle-size distribution and specific surface area were determined.

1. Colour characteristics were obtained from spectral re-emission values.

2. The Helmholtz colour parameters, such as the surface brightness (β), spectral colour density (σ) and colour-specific wavelength (λ) were determined from the re-emission curves by mathematical calculations.

3. An automatic microscopic particle-size analyzer was used to determine the particle-size distribution of the particles, the average particle size ($\bar{d}$) and the particle-size which corresponds to 50% occurrence probability, (d_{50}).

4. Specific surface area was measured by the BET method.

Changes of the colour characteristics during the oxidation period are summarized in *Table 1.* For comparison purposes, the data of the reference product are also shown in the last row.

It is characteristic that the colour-specific wavelength remains unchanged during oxidation. However, slight wavelength changes in this range cannot be detected visually. Colour changes observed during production are related to changes in spectral colour density and surface brightness. Since industrial routine calls for the termination of the oxidation process, when the colour of the product matches that of the reference sample, oxidation should have been terminated after 72 hours.

Particle-size distribution and specific surface area data are listed in *Table 2.*

Since this oxidation is a typical heterogeneous-phase reaction, its rate greatly depends on the spacific surface area of the product formed. Therefore, the magnitude of specific surface in unit solution volume was altered by changing the concentration and specific surface area of seeds present in the starting solution, and the concentration of free iron(II)-sulphate was also

Table 1.

Changes of colour parameter during the oxidation period

Duration of oxidation, hours	FeOOH g/l	HELMHOLTZ Parameters		
0	6.00	39.04	43.20	579.6
12	10.47	40.66	47.62	579.6
24	14.32	44.08	51.17	578.7
36	19.85	48.25	51.39	579.0
48	22.75	49.84	51.65	579.8
72	33 11	52.12	49.53	580.5
96	42.07	53.89	46.72	582.0
Reference sample	—	52.18	49.40	580.9

Table 2.

Particle-size distribution and specific surface area as a function of the duration of oxidation

d	Reference sample	Duration of oxidation, hours					
		12	24	36	48	72	96
0.35	0.5	0.6	0.9	0.8	0.8	0.7	1.4
0.70	13.7	19.0	15.3	17.1	16.8	18.3	14.6
1.05	20.8	31.2	28.4	28.2	28.1	25.8	26.4
1.40	18.3	22.4	23.6	22.6	22.3	20.8	22.6
1.75	13.7	10.7	12.4	12.0	11.8	13.6	13.9
2.10	11.4	6.9	8.4	8.2	8.3	9.3	10.3
2.45	6.3	3.9	4.5	4.4	4.5	5.0	5.8
2.80	4.9	2.5	3.1	3.0	3.3	2.7	3.2
3.15	3.1	1.5	1.9	1.9	2.0	2.0	2.0
3.50	2.5	1.0	1.2	1.2	1.3	1.4	1.4
m^2/g	12.9	20.3	15.5	15.9	13.9	10.7	9.2
$\bar{d}$	1.58	1.24	1.34	1.51	1.35	1.33	1.37
d_{50}	1.36	1.06	1.16	1.13	1.14	1.16	1.21

varied. Samples were taken from these batches after 48 hours and they were tested like the previous samples. The results are shown in *Tables 3* and *4*.

There is no direct correlation between the measured values, though the particle size distribution of the samples selected also varies widely. The particle size distribution data are summarized in *Table 4*.

Table 3.

The effects of oxidation parameters upon the product qualities

Sample	FeOOH g/l hour	Surface area m^2/l	F_eSO_4 g/l	HELMHOLTZ parameter			Specific surface area, m^2/g
I	0.376	231.6	8.50	49.84	51.65	579.8	13.9
II	0.470	267.8	18.80	51.70	47.43	580.5	12.2
III	0.613	328.1	28.50	52.48	48.46	580.1	12.2
IV	0.717	516.1	11.54	49.93	49.34	579.8	15.3
V	0.333	2160.0	9.30	42.43	36.43	583.7	56.4

Table 4

The effects of oxidation parameters upon the particle-size distribution

d μm	Reference sample	Particle size distribution, %				
		I	II	III	IV	V
0.35	0.5	0.8	3.8	1.2	7.6	15.22
0.70	13.7	16.8	28.3	33.2	32.3	50.5
1.05	20.8	28.1	29.5	30.9	19.3	18.8
1.40	18.3	22.3	16.6	17.9	13.8	6.0
1.75	13.7	11.8	9.1	7.8	7.9	1.2
2.10	11.4	8.3	5.7	4.7	7.4	0.2
2.45	6.3	4.5	3.1	2.2	3.2	0.1
2.80	4.9	3.3	1.5	1.2	3.6	—
3.15	3.1	2.0	1.1	0.3	2.5	—
3.50	2.5	1.3	0.1	0.1	1.4	—
$\bar{d}$	1.58	1.35	1.06	1.00	1.12	0.60
d_{50}	1.36	1.14	0.91	0.88	0.87	0.56

It can be from *Table 4* that the particle-size distributions are more dissimilar than the observed colour characteristics listed in *Table 3* indicate. It is assumed that a more detailed mathematical analysis of thes data series would produce the correlations sought. This will be dealt with in a forthcoming paper, together with the analysis of data on iron-oxide-red and chromium--oxide-green pigments.

REFERENCES

1. KOVÁCS, L.: Handbook of Paints and Varnishes (in Hungarian), Műszaki Kőnyvkiadó, Budapest, 1962.
2. PATTON, T. C.: Pigment Handbook. Vol. I. New York. 1973.
3. BJELINKIJ, E. F., RISKIN, I. V.: The Chemistry and Preparation of Pigments (in Russian), Goskhimizdat, Leningrad, 1960.
4. U.S. Patent, 1,327,061

РЕЗЮМЕ

Авторами изучены хроматические свойства, распределение размера частиц, удельная поверхность ферро-оксида желтого пигмента в зависимости от условий производства пигмента. Установили, что время и скорость оксидации в применимой технологии оказывают влияние на цвет, распределение размера и на удельную поверхность. Авторы находили, что нельзя получить простую корреляционную зависимость между свойствами пигмента.

HUNGARIAN JOURNAL
OF INDUSTRIAL CHEMISTRY
VESZPRÉM
Vol. 11. pp. 119-124 (1983)

NEW DEVELOPMENTS IN THE PRODUCTION OF POSITIVE ELECTRODES FOR STATIONARY, LARGE LEAD BATTERIES

F. Óvári, L. Csorba* and I. Ubrankovics

(Department of Chemical Technology, University of Chemical Engineering, Veszprém
*Battery and Dry-Cell Plant, Budapest)

Received: February 4, 1982.

A new formation technology was developed for the positive electrode of stationary, highly developed surface area, Tudor type lead batteries. The modification of Lucas' technology enabled a two-to-tenfold reduction in formation time, and the same reduction in start-up time. Durability tests extended through a span of 2,450 recharging-discharging cycles, indicated that the storage capacity of batteries, prepared according to the new technology did not decrease as rapidly as that of those prepared by Lucas' method. The presence of lead chloride crystals on the negatively formed electrode could be ascertained by an energy-dispersive X-ray microanalyzer, EDAX 711, indicating the reduction of perchlorate during the formation step. An empirical relationship was established that permitted the estimation of the degree of exhaustion of an unknown electrode.

Introduction

Plante discorved the principle of lead batteries in 1859 [1]. A number of variants have appeared during the past 120 years. Depending on the field of application electrodes of varying size and type were developed, e.g. spread-plate starter batteries, armoured-plated bateries, and plastic-mesh-contained batteries, etc. The large-surface-area positive electrodes best retained the essence of the original discovery. These are still produced, with minor construction changes, as described originally. No significant development occurred during the past thirthy years in the production technology of large-surface area positive electrodes. The studies that dealt with these electrodes are all of a theoretical nature. Some these papers dealt with the replacement of Lucas' process [2–4], or the internal stress of anodically produced lead dioxide, starting with the phase modifications of lead dioxides [5–7] and their preparation conditions [8–9]. The other large group of investigators studied the anodic corrosion of lead [10–16], and the corrosion effects of perchloride acid

[14–16]. AFIFI et al. studied PLANTE's process from an industrial point of view [17] and determined the activity order of various additives.

The TUDOR-type, large-surface-area, positive plates called L1–8, weighing 2.8–22.4 kg are still fairly widespread in Europe, contrary to the situation in the United States of America [18]. They are mainly used in immobile, low-voltage systems, such as control facilities, and emergency lighting, etc. Their major advantages are long life and reliability. The storage capacity of electrodes produced by LUCAS' method varied widely. High storage capacity was connected to short service life. Another liability of the process was that $KClO_4$ concentration varied with the height in the formating tank. Samples taken from the bottom of the tank had higher perchlorate contents than those taken form the surface. Large-surface-area plates are produced in batches, although often no order is received for months. In the wintertime, when the system is out of operation, the solution might cool to 0 °C, consequently some $KClO_4$ might crystallize, which will not dissolve even if the temperature increases again. Therefore, formating solutions containing only highly soluble salts would be desirable, assuming that their lead activating potential is at least equivalent to that of LUCAS' solution.

Experimental

Experiments were carried out with Type L–1 cast lead elements. A new multicomponent additive composition was developed. In addition to the conventional additives, the composition contains acetic acid, nitric acid and hydrogen silicofluoride. In an aqueous sulphuric acid solution, this not only successfully replaces $KClO_4$, a time-honoured additive, but also allows for a two-to-tenfold increase in formating current density. Thus, the former 60 hour formating period could be significantly shortened. Tenfold current density means 50A for the L–1 plates, resulting in significant heat generation. Therefore, cooling water had to be circulated in lead cooling-tubes. However it is more difficult for the evolving oxygen to leave the ribs. Therefore, a mechanical circuit breaker and a 100A rated magnetic oil-switch were installed in front of the rectifier and the current is switched off 30 times a minute.

When the formating current density is only 2.5 times higher than the currently used value (12.5A for each L–1 electrode) neither circuit breakers, nor water cooling is necessary. Another practical advantage is that formation takes 24 hours and the next day the electrodes can be removed, washed and dried.

The service life of electrodes formed according the above methods was compared with that of the commercial products of the VBKM Battery and Dry Cell Plant, Budapest. An automatic recharging-discharging system was built for the tests. Its layout is shown in *Fig. 1.* The larga-surface-area positive plates and the negative separating plates formed an immobile battery. Nine factory-formated batteries were used for the service life tests spanning from March 1978 to July 1981. Two discharging andrech arging cycles could be achieved daily in a continuous mode of operation. It took a year to develop the new formating methods. Thereafter, the newly formed electrodes were also hooked up to the service-life testing apparatus. A 5 hours storage test

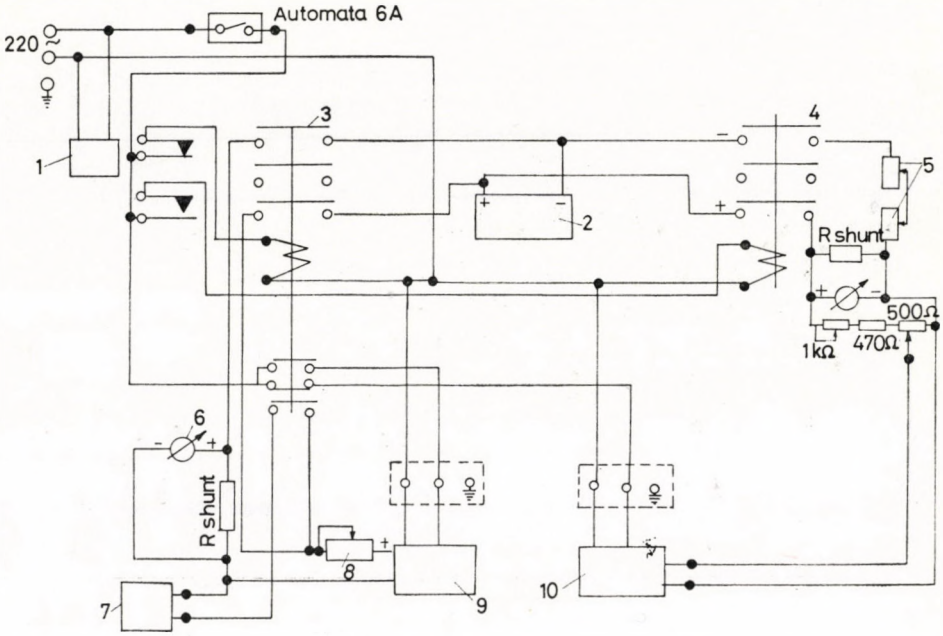

Fig. 1

Schematics of the automatic discharge-recharge unit
1 — Switching clockwork; *2* — Battery; *3* — Recharger VMK17; *4* — Discharger VMK17, *5* — Discharge resistances, discharge current; *6* — Recharging current; *7* — Pulse counter; *8* — Potentiometer; *9* — Battery charger; *10* — Recorder

was carried out after each 50 cycles. All in all 2,450 cycles were generated. The history of storage capacity values is shown in *Fig 2*. It can be seen that the storage capacity of factory formed batteries is better at the beginning, but soon the newly formed electrodes take over. This means that one of the major advantages of the new forming method is that storage capacity does not deteriorate with time, in fact, there is a slight improvement, while the service life is not reduced.

X-ray diffractometry was used for the periodic checking of the phase composition of the electrodes, both in the development stage and in the service-life testing stage. No significant difference could be detected between the different electrodes. A practical difficulty occurred, since depending on the extent of dischange, the X-ray diffractograms were different as the active material contained more $PbSO_4$ and less PbO_2 or vica versa. *X*-ray diffractograms were made after the forming step was completed, then after the 10th, 230th, 750th, 1613 and 1908th cycle. The major component was always tetragonal PbO_2 (plattnerite) accompanied by a few per cent of orthorombic—PbO_2. The intensity of anglesite was always low. Freshly formed electrodes contained more lead sulphate, as expected.

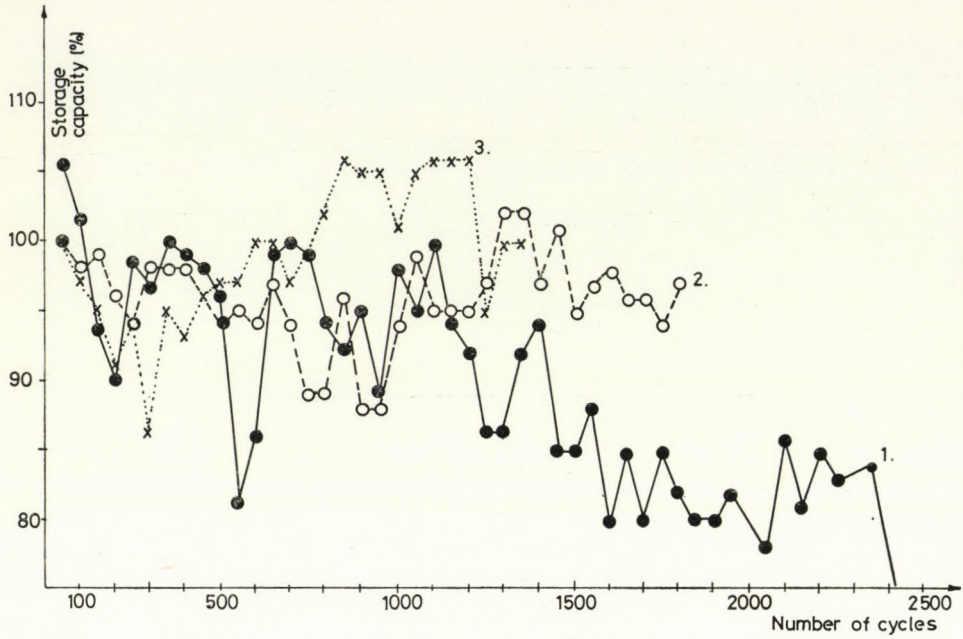

Fig. 2

Changes of storage capacity as a function of service life (average values)
1 — factory formated electrodes; *2* — intensive formation process; *3* — accelareted formation process

Scanning electronmicrographs obtained by a JEOL JSM 50A scanning electronmicroscope were used for the determination of the size shape and structure of the crystals of the cative material. An important result of these examinations is that lead chloride crystals were identified by an energy dispersive X-ray microanalyzer EDAX 711 on the surface of the negative electrode. This is a direct proof of the reduction during formation of the perchlorate ions, since no other chloro compound was present in the formating solution.

It is often difficult to estimate the extent of exhaustion of an electrode. Therefore, the electrodes were weighed after the 750th, 1184th, 1613th, 1765th, 1908th and 2205th cycles (Sn). Taking these and the original weight (G) values one could calculate that the weight loss in a cycle of the electrode was $k=0.665$ g. Thus, using the relationship:

$$\frac{\mathrm{G}-\mathrm{Sn}}{k\times L_{\mathrm{k}}}=n$$

one can calculate the number of discharging-recharging cycles (n) the battery experienced. Here L_{k} is the type number of the electrode tested, i.e. $L_{\mathrm{k}}=1$; 2; 4 or 8.

REFERENCES

1. Planté, G.: Compt. rend. *1860*, 50, 640.
2. Hampson N. A. and Bushrod C. J.: Journ. Appl. Electrochemistry *1974*, 4, 1–6.
3. Bushrod C. J. and Hampson N. A.: Trans Inst. Metal Finishing *1970*, 48, 131.
4. Bushrod, C. J. and Hampson, N. A.: Br. Corres J. *1971*, 6, 129.
5. Kameyama, N. and Fukumoto, T.: J. Soc. Chem. Ind. Japan. *1943*, 46, 1022.
6. Zaslavsky, A., I., Kondrashev, I. D. i Tolkechev, S. S.: Dokl. Akad. Nauk. SSSR *1950*, 75, 559.
7. Bode, H. und Voss, E.: Z. Electrochem. *1956*, 60, 1053.
8. Burbank, J.: Journ. Electrochem. Soc. *1959*, 106, 369.
9. Burbank, J.: Journ. Electrochem. Soc. *1956*, 103, 87.
10. Lander, J. J.: Journ. Electrochem. Soc. *1951*, 98, 213.
11. Lander, J. J.: Journ. Electrochem. Soc. *1951*, 98, 220.
12. Lander, J. J.: Journ. Electrochem. Soc. *1956*, 103, 1.
13. Burbank, J.: Journ. Electrochem. Soc. *1957*, 104, 693.
14. Gann, W. und Knabenbauer, W.: Werkstoffe Korrosion *1967*, 18, 597.
15. Abdul Azim A. A. and Afifi, S. E.: Corrosion Science *1972*, 12, 603.
16. Abdul Azim, A. A.: Corrosion Science. *1970*, 10, 421.
17. Afifi, S. E., Edwards, W. H. and Hampson N. A.: Surface Techn. *1976*, *4*, 173.
18. Vinal, G. W.: Storage Batteries. Fourth Edit. New York 1955.

РЕЗЮМЕ

Разработан новый метод формирования положительного электрода свинцевых стационарных аккумуляторов с большой поверхностью типа Тудор. Модифицированный метод Лукаса дает возможность сокращения времени формирования 2—10 раза и также можно в некоторой мере сокращать и время ввода в эксплуатацию аккумулятора.

Исследования срока службы проведенные путем периодического заряжения и разряжения в течении 2450 циклов показали, что аккумулурующая способность электродов изготовленных модицифированным методом снижается в меньшей мере, чем изготовленных оригинальным методом Лукаса. С помощью рентгеновского микроанализатора типа EDAX 711 можно идентифицировать свинце-хлористый кристалл на отрицательном электроде, что свидетельствует о возможности редукции перклората в процессе формирования.

Авторами разработана эмпирическая формула для расчета степени изнашивания неизвестного электрода.

HUNGARIAN JOURNAL
OF INDUSTRIAL CHEMISTRY
VESZPRÉM
Vol. 11. pp. 125-130 (1983)

UTILIZATION OF THE C_4-FRACTION AS MOTOR FUEL

GY. GÁRDOS, Á. RÉDEY and I. SOKORAI*

(Department of Hydrocarbon and Coal Processing, University of Chemical Engineering, Veszprém, Hungary
*Danube Petroleum Refinery Company, Százhalombatta, Hungary)

Received: July 15, 1982.

The alkylating reaction of isobutane with 1-butene was studied on rare-earth ion exchanged *Y*-zeolites. The alkylating reaction was carried out in a continuous microreactor system in liquid phase. The temperature range was 40–160 °C, and different molar ratios were used. The effects of temperature and molar ratio on the alkylate yield were investigated. It was established that a maximum alkylate yield can be achieved at 70 °C with an isobutane/1-butene molar ratio of 7.6/1. The change of the C_8 distribution was followed as a function of the parameters.

Introduction

Increasing oil prices significantly modified domestic energy policy. The main effort is to reduce the consumption of oil as a source of power.

However, a continued increase is expected in the consumption of motor fuels and petrochemical raw materials. Therefore, when a given amount of crude oil is processed simultaneously, a white product shortage and excess fuel can be expected. It is necessary to crack fuel oil in order to produce more valuable white products.

During the Sixth Five Year Plan period an up-to-date cracking plant will be built with a capacity of 1 million tonnes a year by the Danube Petroleum Refinery Company. The plant will process vacuum distillates of the 300–500 °C boiling point range on a high activity synthetic zeolite catalyst in a riser-type fluid reactor. Due to the efficient separation in modernized vacuum distillery plants, fractions of low metal content can be obtained. These products can be further processed without pre-desulphurization to high-yield gasoline by the latest catalysts. The white products and the gases of the cracking plant can be desulphurized at moderate cost to meet present oil product requirements.

During the processing of liquified gas, high purity (99.5 v.%) propylene can be obtained. C_4-hydrocarbons are not separated in the cracking-plant. The olefin-rich C_4-fraction (100,000 tonnes a year) can be a precious raw material of numerous petrochemical processes, or can be further processed to motor fuel.

Alkylation is a widely used process in the crude oil processing industry. Low molecular weight saturated and unsaturated hydrocarbons can be converted to those of higher molecular weight by alkylation. Alkylation is a homogeneous catalytic process at low temperatures in the presence of H_2SO_4 or HF catalysts. The differences can be due to the different physical and chemical properties of H_2SO_4 and HF. Recently the HF is preferred, because of the better solubility of isobutane and the higher amount of 2,2,4—TMP in the alkylate. In spite of the fact that the acidic procedures are subjects of continuous improvement, their energy demands are still too high, due to the separation processes. Very serious corrosion problems arise in both cases, which cause maintenance problems, even if alloys are used as structural materials.

In a move aimed at developing high octane number gasolines and wasteless technologies, it is important to deal with the possibility of the heterogeneous catalytic alkylation of isobutane olefines.

In the 1970s, new solutions were reported. Research in this field was concentrated on the heterogeneous catalytic reactions in liquid phase. Alkylation was reported to take place under these circumstances. Zeolite catalysts of different types were tried. In this paper the results of our heterogeneous catalytic alkylating experiments are reported.

Heterogeneous Catalytic Alkylating Experiments

The isobutane-l-butene heterogeneous alkylating experiments were carried out in a continuous mode on NH_4LaY zeolite catalyst at a temperature range of 40–160 °C and a total pressure of 30 bar. The liquid load was 1.0–1.2 cc/cc h. The pressure over the liquid phase was adjusted by nitrogen gas. During the alkylation, three different isobutane-l-butene molar ratios (4.7, 7.6, 12.4) were used. The C_5^+, C_8, TMP (trimethyl-pentanes) and DMHx (dimethyl-hexanes) yields were calculated, related to the amount of 1-butene. The C_8/C_5^+, TMP/C_5^+, and the $DMHx/C_5^+$ ratios as well as the distribution of the C_8 fraction (TMP/C_8, $DMHx/C_8$) and the TMP/DMHx ratio were followed.

Alkylating Experiments as a Function of Temperature at Different Molar Ratios

The results of alkylating experiments as a function of the molar ratio are shown in *Fig. 1–3.*

It can be concluded that at the three different molar ratios (4·7:1, 7·6:1, 12·4:1) the yields significantly depend on the temperature.

The C_5^+ yield goes through a maximum as the temperature increases. 60–70 °C can be considered an optimum. The effect of the isobutane-l-butene

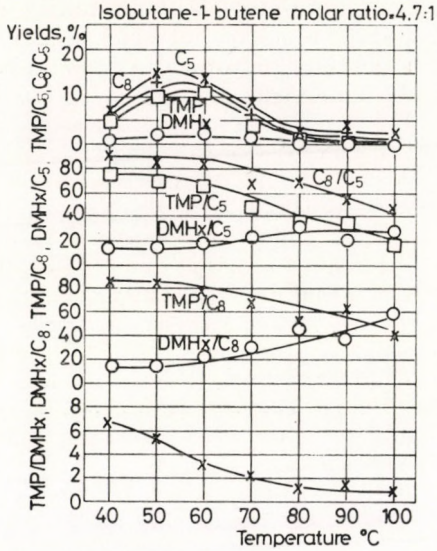

Fig. 1

Alkylating experiments as a function of the temperature (isobutane-1-butene molar ratio: 4.7; liquid load: 1.0–1.2 cc/cc h; pressure: 30 bar)

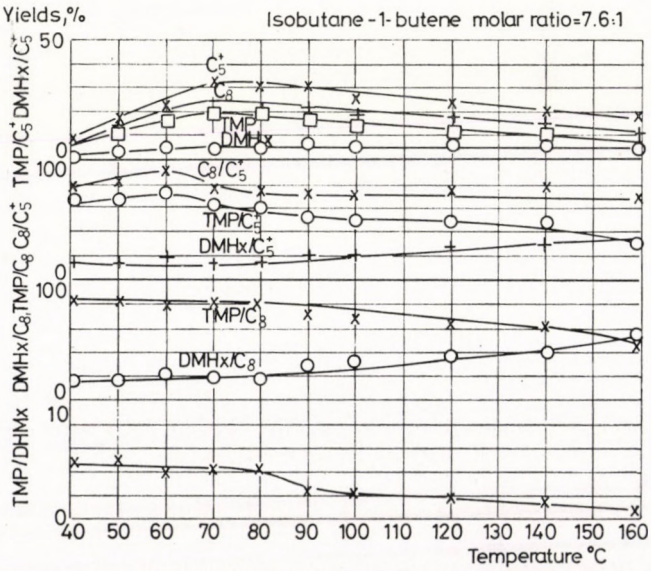

Fig. 2

Alkylating experiments as a function of the temperature (isobutane-1-butene molar ratio: 7.6; liquid load: 1.0–1.2 cc/cc h; pressure: 30 bar)

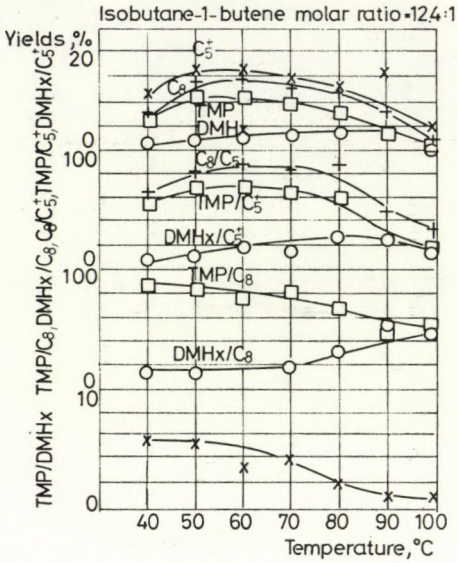

Fig. 3

Alkylating experiments as a function of the temperature (isobutane-1-butene molar ratio: 12.4; liquid load: 1.0–1.2 cc/cc h; pressure: 30 bar)

molar ratio on the maximum cannot be neglected. It should be noted that at 7.6 isobutane-1-butene molar ratio and at 70 °C 32% C_5^+ yield can be achieved. At lower temperatures the yields of the preferred paraffin compounds are lower, or in order to maintain the required yields higher reaction times should be applied. At higher temperatures (above 100 °C), however, the formation of C_5–C_7 and C_9^+ hydrocarbons is preferred due to side reactions. The ratio of the C_8 hydrocarbons show a decreasing tendency as a function of the temperature in the 60–160 °C range. However, the amount of the C_5 and C_9^+ fractions increase. Due to the data it can be concluded that in the C_5^+ fraction the C_8 hydrocarbons are the main components.

The yields of the C_8 fraction show maximum curves. At lower isobutane-1-butene molar ratio (4.7) the maximum appeared at 55 °C. At 7.6 and 12.4 molar ratios the maximums were at 70 °C and 60 °C, respectively.

As to the distribution in the C_8 fraction it can be concluded that the ratio of the trimethyl-pentanes decreases as the temperature increases. The ratio of the dimethyl-hexanes, however, increases.

The TMP/C_8 ratio is about 80% in the 40–60 °C, the DMHx/C_8 in the 70–100 °C range increase—in accordance with the thermodynamical equilibrium concerning the formation of hydrocarbons—which is supported by the TMP/DMHx ratio, as well.

As to the distribution of the TMP and DMHx isomers *(Fig. 4–5)* the following conclusions can be drawn. The 2,2,4-2,3,4- and 2,3,3-TMP isomers are the main components. The ratio of the 2,3,3-TMP is relatively small and

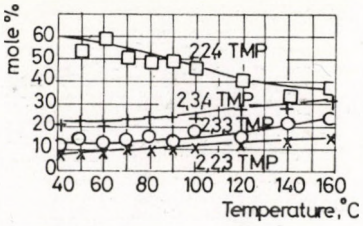

Fig. 4
The distribution of the TMP isomers as a function of the temperature

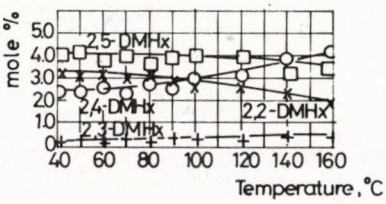

Fig. 5
The distribution of the DMHx isomers as a function of the temperature

shows a slight change with the temperature. The 2,2,4-TMP ratio decreases, the 2,3,4- and 2,3,3-TMP isomers increase as the temperature increases. The 3,4- and 3,3-DMHx dimethyl-hexanes were not found in the alkylate. This means that the trimethyl-pentyl-cations were not converted to dimethyl-hexyl cations under the given conditions. The amounts of the 2,4- and the 2,3-DMHx increase with the temperature. The 2,4-DMHx changes from 24% to 42% in the 40–160 °C range. At the same time, the amount of the 2,2-DMHx decreases.

The amount of the C_8 hydrocarbons of the other types is about 1%. The C_8 olefines are present in less than 1%. A freshly activated catalyst was used in each run.

Alkylating Experiments as a Function of the Isobutane-1-Butene Molar Ratio

The isobutane-1-butene alkylating reaction was also studied as a function of the molar ratio. The effect of changing the molar ratio at 70 °C (at the temperature of the highest yield) is shown in *Fig. 6*. The curves demonstrate the increase of the C_8/C_5^+ ratio. The TMP/C_5^+ ratio also shows an increasing tendency.

The TMP/C_8 ratio reaches a maximum, which is not significantly influenced by higher molar ratios (10–12:1). The $DMHx/C_8$ and the TMP/DMHx ratios show the same tendency.

The use of lower isoparaffin-olefin molar ratios can be advantageous in industrial application, due to the lower separation expenses.

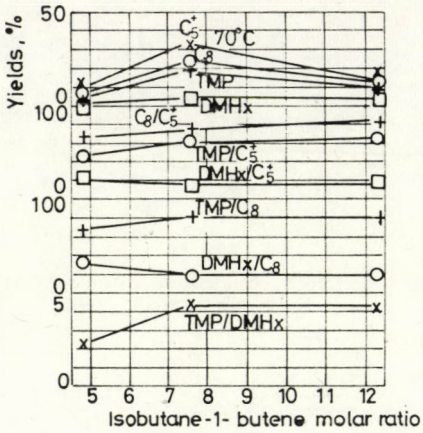

Fig. 6

Alkylating experiments as a function of the molar ratio (temperature: 70 °C; liquid load: 1.0–1.2 cc/cc h; pressure: 30 bar)

As to the course of the reaction, however, lower molar ratios (1:1–3:1) are disadvantageous. These may cause faster aging of the catalyst, thus more frequent regeneration is necessary.

In accordance with the above discussion, the use of the 4.7:1 molar ratio results in lower conversion and less yield. It should be noted that the yields are not only effected by the molar ratios, but also by the reaction temperature. Different molar ratios can be fitted to different temperatures.

According to the experimental results presented, it can be concluded that high octane number gasoline components can be obtained from the C_4-fraction on zeolite catalyst in a heterogeneous catalytic reaction. The advantage of the procedure is two-fold: there is no need for the regeneration of the acid catalyst and fewer corrosion problems occur. The profitability of the procedure, however, is highly influenced by the activity and the lifetime of the catalyst.

РЕЗЮМЕ

Изучали реакцию алкиляции изобутана I-бутеном в присутствии У-цеолита как катализатора содержащего редкие земные металлы. Реакцию проводили в микрореакторе непрерывного действия. Интервал температуры от 40° до 160°, в экспериментах изменяли мольную пропорцию реагентов. Определили влияние температуры и мольной пропорции на производство алкилята. Находили, что максимальное производство можно достичь при 70° и мольной пропорции 7.6/л изобутана) I-бутен. Изучали распределение C_8 фракции изменяющейся в зависимости от параметров.

HUNGARIAN JOURNAL
OF INDUSTRIAL CHEMISTRY
VESZPRÉM
Vol. 11. pp. 131-138 (1983)

EXAMINATION OF SA—1-TYPE AMMONIA SYNTHESIS CATALYST

P. KÁLDI, J. SCHOLTZ and T. EGYHÁZY

(Department of Chemical Technology, University of Chemical Engineering, Veszprém, Hungary)

Received: September 14, 1982.

The physical characteristics and catalytic activity of various industrial ammonia synthesis catalysts prepared from very similar materials, but with different granulation technologies are different. This paper presents the physical, morphological and catalytic characteristics of an oxide catalyst, SA–1 formulated as irregular, spherical, and hollow disc-like particles. The irregular particles give a catalyst of high activity with poor mechanical stability, i.e. dust formation is excessive. The crust of the spherical particles significantly improves their wear resistance, but the catalytic activity is only moderate. The hollow, disc-like particles of SA–1–P catalyst display favourable wear resistance and activity.

Introduction

The industrial ammonia-synthesis oxide catalyst, SA-1 was produced and exported to the East European countries by the Soviet Union for the past fifteen years. During the past ten years, the producing factory attempted to change the geometric structure and the shape of the catalyst particles according to the needs of the user, while endeavouring to keep its chemical compositon constant. Thus, conventional irregular particles, spherical compact particles and hollow disc-like particles were available either in oxide state or prereduced state.

This paper deals with the physical, morphological and catalytic characteristics of SA-1-type catalysts with indentical chemical composition, but varying geometrical structure and particle shape.

Test Methods of the Physico-Chemical Characteristics Relevant to the Industrial Application

Apart from the chemical composition, the industrial user is interesed in the particle size, shape, bulk density, true density, mechanical characteristics, hydrodynamic resistance, and morphology: i.e. specific surface area, porosity,

pore size distribution, activation characteristics and heat resistance of the catalyst.

1. The chemical composition of the SA-1 catalyst can be determined, for example, according to the Soviet industrial standard, GOST 12411-66.
2. The particle size, shape-factor, bulk density and true density (measured in a picnometer, by toluene) can be easily determined and are not discussed here.
3. The BET method can be used for the determination of the specific surface area, while mercury porosimetry or capillary condensation yield the porosity and pore size distribution values.
4. There is no universally accepted method for the determination of the mechanical characteristics and wear resistance (or dust formation leading to increased hydrodynamic resistance) of the catalyst. With spherical and disc-like particles one can measure the compression strength derived from pressure-application tests between parallel test surfaces, but for irregular particles only the wear-related-loss, determined in a rotating drum-mill, could be used.
5. The term heat-resistance means that the catalyst will retain its original activity even after extented operation at high temperatures. In his heat-resistance test NIELSEN [1] proposed heating the sample for 10–100 hours to 550–650 °C, at 1–100 bar pressures, and the catalytic activities prior to and after the heat treatment were compared.
6. However, the primary parameter of any catalyst is its activity. Starting with an oxide catalyst, its activity greatly depends on the formation process and the reduction. The history of reduction, and consequently the morphology of the catalyst, depends on the temperature, space velocity, chemical composition of the reducing gas atmosphere and to a lesser extent, on the pressure [2].
   A number of papers deal with the reduction of oxide catalyst SA-1.
   The Soviet industrial standard, GOST 12411-66 recommends programming for 8 hours at a temperature from 20 °C to 450 °C, followed by a further increase, in several steps during 42 hours, to 550 °C.
   Rather than an overly intensive formation, SIMULINA [3] recommends the reduction of the catalyst in stoichiometric, ammonia-free synthesis gas, at 4000–6000 h^{-1} space velocity and 11–14.5 bar pressure, during 190–200 hours. The latest information released by the producing factory [4] also recommends a much longer reduction period: 240–250 hours.
   The authors, joined by the experts of the Tisza Chemical Works, developed a 120 hours long reduction programme for the SA-1 ammonia-synthesis catalyst to be carried out in a producing reactor [5]. This programme resulted in an active catalyst of favourable morphology. An additional economic incentive of the method is that the converter can be rapidly brought back to steady-state production.
7. Catalysts diluted with an inert material and packed into small-volume, integrating-type tube reactors are used for activity tests in the case of highly exothermic, high pressure ammonia synthesis. Thus, quasi isothermal conditions could be maintained [6–9]. The drawback of this approach is that the physical characteristics listed above cannot be determined, or only to a limited extent, by the small volume (1–5 cm^3) catalyst sample.

SCHOLTZ, SZABÓ and EGYHÁZY developed a determination and evaluation method, which by making use of an integrating-type, polytropic tube-reactor yields the true activity of the catalyst [10]. All the physical characteristics listed can be determined with 50–100 cm^3 of 0.5–8 mm particle-size catalysts.

Experimental

Samples tested

A — SA-1 oxide, irregular, particle size: 6–10 mm
B — SA-1 oxide, spherical, particle size: 6–8 mm
C — SA-1-P oxide, hollow disc-like, particle-size 6–10 mm
D — KM-1-oxide, irregular, particle size: 6–10 mm

The oxide catalyst, KM-1 is the most widely used industrial ammonia-synthesis catalyst, and it was included here as a reference sample.

The chemical composition of the SA-1 oxide catalyst is:

Component	%w/w	Component	%w/w
FeO	29–36	NiO	0.05
Fe_2O_3	54–68	CuO	0.1
Al_2O_3	3–4	SO_3	0.015
K_2O	0.7–1	P_2O_5	0.02
CaO	2–3		

The reduction programme detailed in [4] was used for the activation of oxide catalysts A, B and C. The physical, mechanical, morphological characteristics and the activities were determined prior to and after the activation process. Activity was determined in the polytropic, integrating-type tube reactor, with a useful volume of 100 cm^3, using 300 bar pressure, ammonia-free, stoichiometric, dry (dew point below -70 °C) synthesis gas and a 1.25–2.5 mm particle-size catalyst. The temperature and space velocity ranges tested were 380–510 °C, and 20,000–30,000 h^{-1}, respectively.

The heat resistance of the catalysts could not be tested, because the upper temperature limit of the structural material of the reactor wall was 650 °C.

Determination of the Physical, Mechanical and Morphological Characteristics

The bulk density, true density and wear resistance of the catalysts were determined. For wear resistance measurements 100 g catalyst was placed into the 140 mm internal diameter wearing-mill, rotated at 100 min^{-1}. The amount of material passing the 1 mm sieve was measured at regular intervals.

Specific surface area was determined by argon adsorption at the temperature of liquid nitrogen. Mercury porosimetry was used to determine the porosity and pore-size distribution of the catalysts.

Table 1.

Physical, mechanical and morphological characteristics of the catalysts

Characteristic	SA-1 60—10 mm		SA-1 spherical 6–8 mm		SA-1-P 6–10 mm		KM-1 6–10 mm	
	r	*a*	*r*	*a*	*r*	*a*	*r*	*a*
Bulk density (kg/l)	2.37	2.13	2.41	2.13	2.61	2.09	2.62	2.09
True density (g/cm³)	4.897	6.125	4.824	6.169	5.035	6.131	4.837	5.754
Fracture strength, (N/cm²)	—	—	241	—	167	—	—	—
Wear-related loss (weight loss)								
in 1 hour, %w/w)	1.32	4.04*	0.35	0.49*	0.38	0.517*	0.55	0.63*
in 3 hours, (%w/w)	2.89	7.13*	1.07	2.05*	0.95	2.683*	1.27	1.48*
Specific surface area (m²/g)	—	18.5	0.1	16.7	—	14.29	—	9.6
Pore volume (cm³/g)	0.002	0.108	0.014	0.1008	0.02	0.159	0.003	0.106
Characteristic pore size (nm)	—	19.0	—	16.8	—	12.5	—	22.0

r: raw, oxide state; *a:* reduced active state; *: 1.25—2.50 mm particle fraction.

Note: Dut to its pirophorous nature, the fracture strength of the activated sample was not determined. In oxide state the specific surface area is below the lower measurement limit of the system.

The physical and morphological characteristics are summarized in *Table 1.* Wear-related loss as a function of temperature is plotted in *Fig. 1.* The pore-size distribution curves are shown in *Fig. 2.*

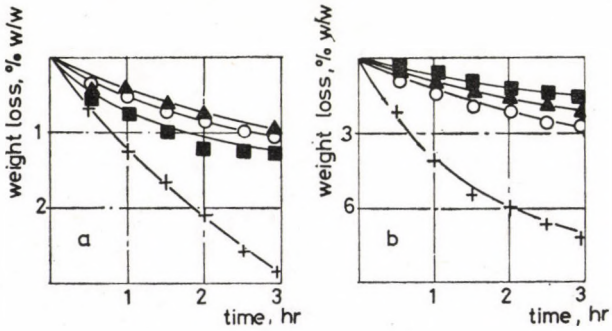

Fig. 1
Wear resistance of the catalyst samples

a) oxide state

+ : SA-1 irregular, 6–10 mm
○ : SA-1, spherical, 6–8 mm
△ : SA-1-P, hollow disc-like, 6–8 mm
■ : KM-1, irregular, 6–10 mm

b) active state

+ SA-1, irregular, 1.25–2.50 mm
○ SA-1, spherical, 6–8 mm
△ SA-1-P, hollow disc-like, 6–40 mm
■ KM-1, irregular, 1.25–2.5 mm

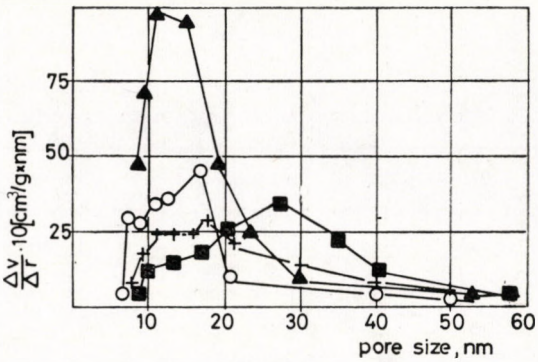

Fig. 2
Pore-size distributions of the activated catalysts

+ : SA-1, irregular
○ : SA-1, spherical
△ : SA-1, -P hollow disc-like
■ : KM-1, irregular

Reduction

The samples tested were activated according to the programme shown in *Fig. 3*, in ammonia-free, 3:1 H_2:N_2 gas atmosphere. The course of reduction

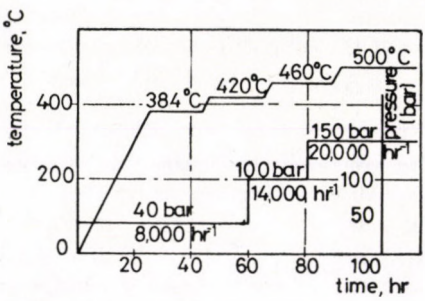

Fig. 3
The reduction programme used for the activation of the catalyst samples

was followed by dew point measurements in the activating gas. The rate of water release by 100 g catalyst as a function of process-time is shown in *Fig. 4*.

Activity Testing

Activity measurements were carried out in a polytropic, integrating-type tube reactor according to the method described in [10]. The internal and external heating systems of the test reactor at each pressure, space velocity and

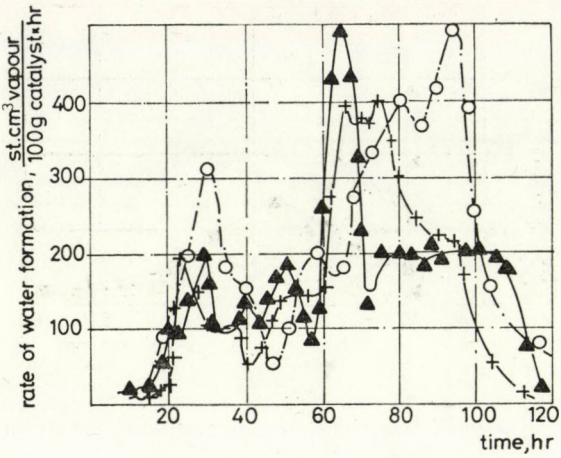

Fig. 4
Reduction history of the catalyst samples

+ SA-1, irregular
○ SA-1, spherical
△ SA-1, hollow disc-like

temperature setting were set to identical levels. The particle size range of the catalysts used for these tests was 1.25–2.50 mm. The results are summarized in Table 2.

The kinetic constants of the TOMKIN–PIZHEV equation were calculated from the radial and axial temperature distributions, and input and output gas compositions (E_2: activation energy of ammonia decomposition, k_{450}—apparent-kinetic constant at 450 °C).

The calculated results are listed in *Table 3* for 300 bar pressure, 30,000 h^{-1} space velocity and 380–510 °C temperature, for these settings are closest to those used in the Hungarian ammonia synthesis plants.

It can be seen that the activity of the spherical SA-1 catalyst is low, that of the irregular SA-1 and the reference sample KM-1 is practically identical, while that of the hollow disc-like SA-1 is only slightly lower than that of the latter ones.

Discussion. Conclusions

The physical characteristics and the microstructure of the various forms of the industrial ammonia-synthesis catalyst SA-1 are different, depending on the conditions of their preparation, even though their composition is identical. In oxide state the bulk-density of the hollow-disc and spherical particles is higher, because their void volume is lower. The true density of the reduced samples (as measured by toluene and a picnometer) are identical: 6.125–6.169 g/cm³ (the true density of KM-1 is 5.754 g/cm³).

The major liabitity of the widely used irregular SA-1 catalyst is its dust-

Table 2.

Results of the activity tests

Catalyst	Space velocity, h^{-1}	Temperature, °C		NH_3 (%v/v)	
		t_{wall}	t_{centre}	input	output
SA-1 irregular	20 000	474	476	0.17	22.26
		435	435	0.15	23.44
		384	390	0.15	21.96
	30 000	491	495	0.16	20.60
		454	457	0.13	21.26
		389	390	0.13	21.28
SA-1 sperical	20 000	445	447	0.15	13.99
		474	478	0.10	15.16
	30 000	499	501	0.18	15.13
		449	450	0.18	12.94
		481	480	0.18	13.72
		504	506	0.18	13.33
SA-1-P hollow-disc	20 000	—	—	—	—
		415	418	0.18	20.91
		460	465	0.17	21.29
	30 000	—	—	—	—
		425	430	0.18	20.50
		456	436	0.18	19.74
KM-1	20 000	420	423	0.15	22.68
		461	467	0.16	23.22
	30 000	375	380	0.17	18.88
		418	421	0.15	21.30
		467	472	0.17	21.14
		365	370	0.17	20.38

t_{wall}: input temperature at the wall, °C
t_{centre}: input temperature at the centre, °C

Table 3.

Activation energy of ammonia decomposition, apparent kinetic constant at 450 °C pressure: 300 bar, space velocity: 30,000 h^{-1})

Ctalayst	E_2 (kJ/mol)	k_{450} ($bar^{1/2}/h$)
SA-1 irregular	110.1	11,950
SA-1 spherical	138.2	7,450
SA-1-P hollow disc-like	120.6	11,825
KM-1 irregular	112.2	11,250

forming tendency. In active state the wear-related loss of irregular SA-1 is about four times higher than that of the KM-1 catalyst. The wear-resistance of spherical, an hollow disc-like particles is much better, a clear-cut advantage during extended operation (lower hydrodynamic resistance in the producing reactor).

In active state each three catalysts display a high specific surface area ($F_{BET}=14.3–18.5$ m^2/g). The characteristic pore-size of the spherical particles is unfavourable, only 12.5 nm, and even the other two catalysts show lower values than the generally accepted, favourable value: 20–40 nm (meaning that pore diffusion control is fairly significant with each of them).

It is difficult to reduce the spherical sample, the reduction rate of the second section becomes significant only at 460 °C.

The particle-formation technology significantly influences the catalytic activity. Compared with the reference catalyst, KM-1 the activity of the irregular SA-1 catalyst is similarly high, while that of the spherical sample is moderate to low.

The wear-resistance and the activity of the hollow, disc-like catalyst are equally good, an advantageous feature for the practical user.

REFERENCES

1. NIELSEN, A.: An Investigation on Promoted Iron Catalysts for the Synthesis of Ammonia. Jul. Gjellerups Forlag, Copenhagen, 1968. 109.
2. Loc. cit. (1), 139.
3. SIMULINA, J. A. i KARIBDZSHANJAN, H.: Khim. Prom., *1967*, 6, 39.
4. Examination of Ammonia Synthesis Catalysts, Research Report, Department of Chem. Techn., University of Chem. Engng., Veszprém, 1980.
5. T. EGYHÁZI: Examination of the Activity of Ammonia Synthesis Catalysts, Thesis, 1974. Veszprém.
6. COMINGS, E.: High Pressure Technologies, (in Hungarian), Műszaki Könyvkiadó, Budapest, 1959, pp. 306–329.
7. Loc. cit. (1), pp. 31–40.
8. GUCCI, U., TRAINA, F. and BUZZI FERRARIS, G.: Ind. Eng. Chem., Process Des. Dev., *1977*, 16, 166.
9. BUZZI FERRARIS, G., DONATI, G. and TRAINA, F.: Chem. Eng. Sci., *1974*, 29, 1621.
10. SCHOLTZ, J., SZABÓ, J. and EGYHÁZY, T.: Magy. Kém. Lapja, *1983*, 38 (9)

РЕЗЮМЕ

Сравнили физические характеристики и каталитическую активность катализаторов изготовленных из одинакового материала но различным размером частиц для синтеза аммиака. В стати приведены физические и морфологические каталитические свойства советского оксидного катализатора СА-1, неправильной, шаровидной и внутрипустотно-гранулированной формы. Катализатор неправильной формы обладает высокой активностью но его механическая стабильность низкая, частицы легко распадают. Катализатор шаровидной формы прочный но его активность слабая. Самым качественным является катализатор внутрипустотиогранулированной формы, как каталитические так и механические свойства удовлетворяют требованиям.

HUNGARIAN JOURNAL
OF INDUSTRIAL CHEMISTRY
VESZPRÉM
Vol. 11. pp. 139-146 (1983)

ON THE POSSIBILITIES OF DECREASING THE SULPHUR EMISSION OF A CLAUS-PLANT

MRS. M. FEHÉR-SZÜCS and G. JÓZSEF*

(Institute for Research and Development of the Hungarian Hydrocarbon Industries, Százhalombatta
*Tisza Oil Company, Leninváros)

Received: September 14, 1982.

Sulphur-containing gases emitted by the oil industry feature high on the list of environmental pollutants. The possibilities of decreasing the sulphur emission of a Claus-Plant were studied. A gas chromatographic method was developed for the analysis of the sulphur-containing gases of the Claus-plant. Process-analysis was carried out in the plant followed by a laboratory study of the side reactions of the Claus-reaction which, as shown by our results, fundamentally influence the extent of sulphur emission. It could be concluded that small amounts of hydrogen could be used to suppress the side reactions, and the sulphur emission rate could be considerably decreased without any investment cost.

Introduction

Sulphur containing gases are among the primary air pollutants emitted by the oil industry.

Hydrogen sulphide-containing gases, originating from the processing of sulphur-containing crude, hydrocarbon products and natural gas are processed by the widely used Claus-desulphurization reaction.

Environmental regulations necessitate repeated studies to investigate the possibilities of decreasing the sulphur emission of Claus plants. This work has traditionally followed two paths. One was aimed at the post-process scrubbing of end gases as a means of reducing the extent of sulphur emission. This required the addition of further technological steps (e.g. adsorption or wet scrubbing). The other approach was aimed at perfecting the Claus technology. Essentially, the current transformation efficiency of 92–95% should be increased to 99–99.5%, i.e. sulphur emission has to be decreased from 5–8% to 0.5–1%. There were several papers in the past few years, which dealt with this problem [3–7, 15, 17–19, 22].

The Claus-process is used in the oil industry to remove the sulphur content of the end gases. Therefore, this study was initiated to find out if any technological modification could increase the yield of sulphur and thereby reduce the extent of sulphur emission.

The Claus Process

The well-known basic reaction of the Claus-process is:

$$2\,H_2S + O_2 \rightleftharpoons 2\,H_2O + xS_x + \text{heat}$$

Accordingly, hydrogen sulphide is burnt with the oxygen of air—over a suitable catalyst—and elementary sulphur is formed [1, 1/a].

Present-day Claus-plants operate according to the method modified by BRANS [2]. Here, the hydrogen sulphide containing gas is burnt in a flame reactor—in the so-called Claus-furnace—with so much air that the exhaust gas contains hydrogen sulphide and sulphur dioxide in a 2:1 molar ratio. This gas mixture is introduced into two or three catalyst-filled reactors, where elementary sulphur is formed according to the reaction:

$$2\,H_2S + SO_2 \rightleftharpoons 3/x\ S_x + 2\,H_2O$$

This reaction starts back in the Claus-furnace and reaches a conversion degree of 60—70%. The reaction is completed in the catalytic reactors. Finally, the residual-sulphur containing process gases are burnt and the sulphur-dioxide-containing gases are released into the atmosphere.

Reactions which Accompany the Claus-Process

The hidrogen sulphide gases of the oil industry always contain hydrocarbons, carbon dioxide and water vapour [3]. These react with hydrogen sulphide and form other sulphur-containing compounds.

Some authors mention as many as 20–25 reactions, because most industrial gases contain other components as well, and as such, cannot be neglected theoratically [4].

Considering the raw-gas composition of the plant studied, the following reactions can occur:

$$CS_2 + 2\,H_2O \rightleftharpoons CO_2 + 2H_2S \quad (3)$$

$$COS + H_2O \rightleftharpoons CO_2 + H_2S \quad (4)$$

$$COS + H_2 \rightleftharpoons CO + H_2S \quad (5)$$

$$CH_4 + 2\,S_2 \rightleftharpoons 2\,H_2S + CS_2 \quad (6)$$

$$2\,COS + SO_2 \rightleftharpoons 2\,CO_2 + 3/x\,S_x \quad (7)$$

$$CS_2 + 4\,H_2 \rightleftharpoons CH_4 + 2\,H_2S \quad (8)$$

$$CS_2 + 2\,H_2 \rightleftharpoons C + 2\,H_2S \quad (9)$$

$$SO_3 + H_2 \rightleftharpoons H_2O + SO_2 \quad (10)$$

$$C + 2/x\ S_x \rightleftharpoons CS_2 \quad (11)$$

$$SO_2 + 1/2\,O_2 \rightleftharpoons SO_3 \quad (12)$$

$$CS_2 + SO_2 \rightleftharpoons CO_2 + 3/x\,S_x \quad (13)$$

$$4\,H_2O + 1/x\,S_x \rightleftharpoons 4\,H_2 + 2\,SO_2 \quad (14)$$

$$4\,CO_2 + 1/x\,S_x \rightleftharpoons 4\,CO + 2\,SO_2 \quad (15)$$

Carbon oxysulphide (COS) and carbon disulphide are formed in the Claus-boiler, at the temperature of combustion, from the combustion products of hydrocarbons and sulphur-containing compounds [20]. These chemicals show up in the end gases of the Claus-plant and appear as sulphur dioxide in the final stack gas of the post-combustion unit. Some researchers attribute the greater part of air pollution caused by the Claus-plants to unreacted COS and CS_2 [5, 15, 17–19]. Therefore, their approach to controlled sulphur emission calls for improved burner-sections and a decrease in the amount of sulphur compounds formed in the side reactions of the Claus-furnace [6, 7, 22].

At first, we analysed the enthalpy changes and the equilibrium conditions of the 15 reactions, which can occur in the plants tested by us. Then a process analysis was carried out for the Claus-technology using the Claus-unit of one of the Hungarian Oil refineries. Based on these results, the possibilities of increasing the yield of sulphur recovery and decreasing the extent of sulphur emission were studied.

The enthalpy changes and the equilibrium conditions of the reactions were determined by a programme-package developed at the Hungarian Hydrocarbon Institute. Calculations were carried out in the 483–643 K temperature and 0.1–1.0 MPa pressure ranges. Apart from Reactions 1 to 4, no enthalpy changes are to be found in literature. Since this calculation represented the first such testing of the programme package, calculations were also carried out for Reactions 1 to 4, and the results were compared to those in literature. Data calculated for 583 K agreed within 3% with those in literature.

Based on the analysis of the equilibrium conditions, reactions 3 to 8 and 13 can take place, and further studies were restricted to these.

In the following step, the process gases of an operating Claus-plant were analyzed, then the reactions were studied in a laboratory model system.

Both the process analysis and the laboratory tests required the full analysis of all the possible sulphur compounds [21, 10].

The Analytical Technique

Apart from wet chemical methods, sulphur-containing compounds are increasingly analyzed by gas chromatography [18, 9–14]. Catharometers are used as detectors for sulphur compounds in the 1–10% concentration range, but ppm level analysis requires the use of a flame photometric detector.

Gas chromatography was carried out on a B-HT-100 column, at 313 K temperature and 30 ml/min nitrogen flow rate. A Perkin–Elmer flame photometric detector was used with 25 ml/min hydrogen and 280–300 ml/min air flow rates. Hydrogen sulphide, sulphur dioxide, carbon oxysulphide and carbon disulphide were separated in sharp, cleanly separated peaks. Analysis reproducibility was $\pm 5\%$ relative.

Process analysis required both wet and chromatographic analysis.

Elementary sulphide was determined according to Grote-Krekeler (DIN 51768). H_2S, COS and CS_2 were measured by potentiometric titration (DIN 51855, p.5). H_2S+SO_2 could be determined by iodometric titration.

Chromatographic and wet chemical analytical results agreed within 5%, at least when the measurements were completed within 1–2 hours.

Naturally, chromatographic data were preferred in the low concentration ranges, because of their superior precision.

Industrial Process Analysis

Industrial process gases obtained under varying operation conditions were analyzed. Data of a characteristic setting are reported here.

The hydrogen sulphide and hydrocarbon concentrations of the input hydrogen sulphide gas were 97.1 and 3.2% v/v, respectively. The characteristic composition of the process gas entering the 1-st reactor was as follows: 2.7% v/v; SO_2: 1.7% v/v; COS: 0.85% v/v; CS_2: 0.12% v/v. After the reactor, the following changes were recorded: COS: 0.15% v/v; CS_2: 0.037% v/v. These values remained practically constant up to the entry port of the post-combustion unit (COS: 0.149% v/v; CS_2: 0.036% v/v). The stack gas of the post-combustion unit contained 0.87% v/v SO_2 (i.e. this is the SO_2 concentration released into the atmosphere).

The most important conclusion of the process analysis is that the formation of COS and CS_2 decreases the efficiency of sulphur recovery, because these compounds decompose only partially in the catalytical reactors, and having been transformed into sulphur dioxide, they pollute the environment. Therefore, both byproducts have to be transformed into elementary sulphur. It can be proved that under correct operation conditions, the greater part of the emitted sulphur dioxide comes from the combustions of these two compounds.

The examination of the technological units showed that the operation of the Claus-furnace is rather inflexible, consequently the qualitative and quantitative composition of the combustion gas cannot be easily influenced. Therefore, the process gas leaving the Claus-furnace has to be considered given, and both COS and CS_2 have to be transformed in the catalytic stages.

Based on the examination of the reactions and the results of the process analysis, the reactions taking place in the reactor were studied in a laboratory system.

The Laboratory Apparatus

An isothermally operated laboratory system was constructed to model the residence time, temperature and gas composition encountered in the actual Claus-plant (cf. *Fig. 1*). The apparatus is made of glass. It has a variable heating system. A preheating unit with an upper temperature limit of 473 K is connected the main apparatus. Thus, a homogeneous gas mixture of preset temperature can be introduced into the reactor at the space velocity used in the Claus-plant. 100 ml activated alumina catalyst—obtained from the actual Claus-unit—was charged into the experimental reactor.

At first, the fundamental reactions were tested in the apparatus at various space velocities and temperatures (cf. *Fig. 2*). It could be concluded that the test equipment closely modelled the operation of the actual Claus unit, and

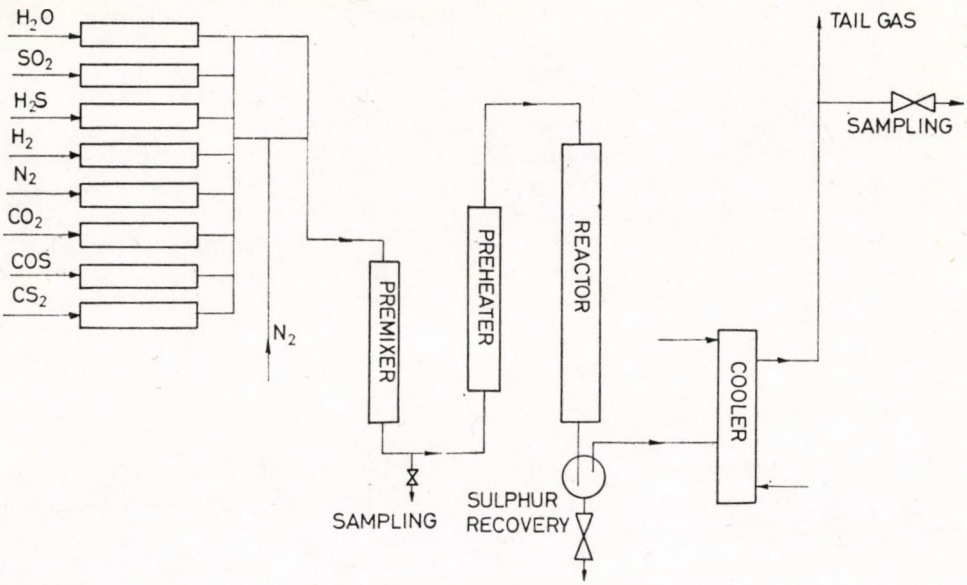

Fig. 1
Schematics of the laboratory Claus-reactor

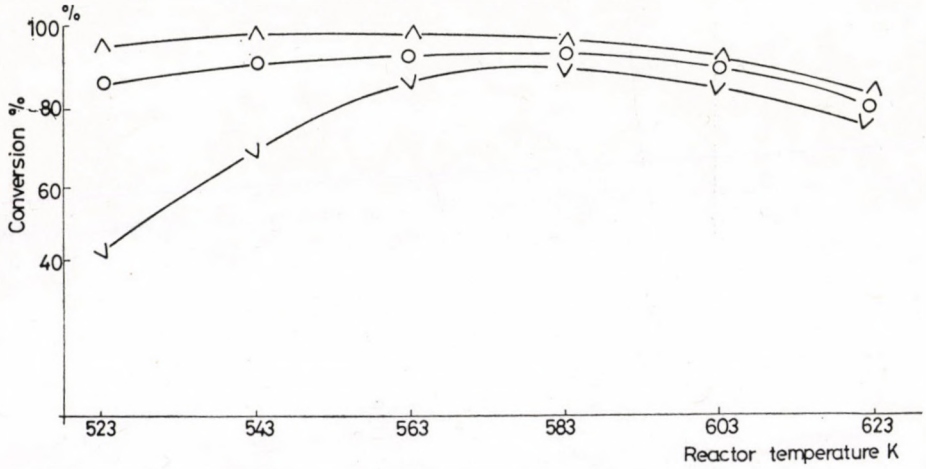

Fig. 2
Conversion of $H_2S + SO_2$ in the basic reaction
Space velocity: $\wedge = 25\ h^{-1}$; $\bigcirc = 50\ h^{-1}$; $\vee = 100\ h^{-1}$

conversion figures agreed within 2%. This experimental series also showed that conversion rate (to elementary sulphur) was highest with this catalyst at 563 K, and it amounted to 98%.

In the next step, the conversion of COS and CS_2 was studied using the gas composition and space velocity found in the actual plant. Various temperature settings were used and Reactions 3, 4, 5, 7, 8 and 13 were studied. Reactions 7 and 13 did not proceed to any noticeable degree in the test reactor, even when the temperature was as high as 648 K.

For reactions 3 and 4, considerable conversion started above 563 K, i.e. above the temperature of maximum conversion for H_2S–SO_2.

According to reaction 7, COS is converted at a rate of 90% above 623 K, while the same degree of conversion for CS_2 (according to reaction 13) occurs at 640 K. The same reactions were studied with different space velocities, and it could be concluded that within the temperature ranges studied, they primarily depended on the reaction temperature.

Experiments were also carried out in the presence of hydrogen, as required by Ractions 5 and 8.

It can be seen in *Fig 3* that for all practical purposes Reactions 5 and 8 can be completed at 555 and 568 K (with a conversion rate of 95%).

Based on these experimental data it could be concluded that optimum elementary sulphur recovery can be achieved in the given plant, with the given

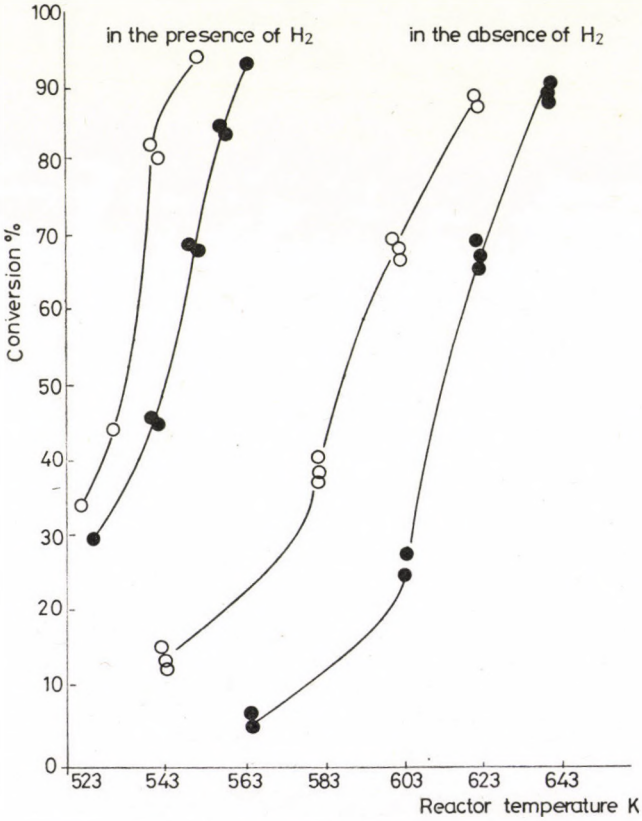

Fig. 3
Conversion of COS and CS_2 ○ – COS; ■ – CS_2

catalyst, when the first reactor is operated 30–50 K above the optimum temperature of Reaction 2, even if this does decrease the efficiency of the $H_2S + SO_2$ conversion. At this higher temperature, COS and CS_2 can be converted almost completely, and then the temperature in the second and further catalytic reactors can be decreased to that which proved optimum for the given catalyst.

However, experiments showed that a better solution can be achieved by mixing hydrogen into the process gas and then COS and CS_2 can be converted in 93–95% at the optimum, 563 K temperature (cf. *Fig. 3*).

Only SO_2 can be reduced by hydrogen, because the equilibrium constants of the reaction allow for this. However, it was found that this reaction takes place only above 623 K.

Since hydrogen is generally available in most oil refineries (on account of the hydrogenation plants), the addition of the required amount of hydrogen to the technological system poses no special problem.

REFERENCES

1. Brit. Pat. 3608 (1882).
2. Brauss, J. G.: Farbenindustrie DRP 666,572 (1936).
3. Goar, B. G.: Hydrocarbon Processing, *1974*, 53, (7) 129–132.
4. Maadak, A. G. and Maddox, R. V.: Hydrocarbon Processing, *1978*, 57 (6) 143–146.
5. Pearson, M. Y.: Hydrocarbon Processing, *1978*, 57, (4) 81–85.
6. Fischer, H.: Hydrocarbon Processing, *1974*, 53 (10) 125–130.
7. Neumann, K. K.: Erdöl u. Kohle, *1982*, 25 (11) 656–659.
8. Fatullina, A. F., Zaharova, N. V.: Khimiya i tekhnologiya *1979*, 4, 17–18.
9. Jreez, D. G. and Budalek, K.: Environ. Sci. and Technol. *1973*, 7. (2) 253.
10. Pecsar, Hartmann, J.: Chromatogr. Science, *1973*, 11, 493.
11. Franklin, B. N. i Petrov, V. A.: *1978*, Gigienia Truda 6, 53–54.
12. Masao Maruyama: Journal of Chrom. Science *1978*, 16, 1–7.
13. Forrest, J. and Newman, L.: Air Poll. Controll As.. *1973*, 23, (9) 761–768.
14. Gangwal, S. K. and Waganer, D. E.: Journal of Chrom. Science *1979*, 17, 196–201.
15. Boas, A. H. and Andrede, R. C.: Hydrocarbon Processing, *1971*, (2) 81–84.
16. Sulphur, *143*. (1979. July/August)
17. Pearson, M. Y.: Hydrocarbon Processing, *1979*, 58. (7) 99–103.
18. Futterer, E.: Chemie-Ing. Techn. *1973*, 45. (6) 411–416.
19. Palm, J. W.: Sulphur, *129*, (1978 nov/dec).
20. Gmelins Handbuch der Anorganischen Chemie System Nr. 9. Schwefel. 8. Edition, Verlag Chemie GmbH, Winheim.
21. Engelhardt, H.: Technisches Messen Atm. *1977*, 71 (2.) 41–52.
22. Taggart: Hydrocarbon Processing, *1981*, 60, (2) 155–157.

РЕЗЮМЕ

Сернистые газы нефтеперерабатывающей промышленности занимают значительное место среди промышленных газов загрязняющих воздух. Авторы изучали возможности уменьшения эмиссии завода Клауса. Содержание серы определили хроматографическим способом. Изучали и побочные реакции в лабораторных условиях и проводили анализ процесса. Находили, что побочные реакции оказывают значительное влияние на серо-водородную эмиссию завода. Установили, что присутствие водорода в малом количестве значительно затормозит побочные реакции, таким образом можно уменьшать и количество поглощенного сероводорода. Особым преимуществом данного способа состоит в том, что не требует капитальных вложений.

HUNGARIAN JOURNAL
OF INDUSTRIAL CHEMISTRY
VESZPRÉM
Vol. 11. pp. 147-156 (1983)

INVESTIGATIONS ON THE ACTIVITY AND MORPHOLOGY OF SPENT AMMONIA-SYNTHESIS CATALYSTS

P. KÁLDI, J. SCHOLTZ, G. SZIKLAI and T. EGYHÁZY

(Department of Chemical Technology, University of Chemical Engineering, Veszprém, Hungary)

Received: October 20, 1982.

The morphology of multi-promoted iron catalysts used in ammonia-synthesis technologies is of primary importance with respect to the chemical process proper. This paper details the results of a comparative study of the morphology and catalytic activity of new and spent KM–1–R catalysts, the latter being used for six years in an industrial reactor. The specific surface area measured by argon adsorption decreased slightly, but characteristically, and the fraction of pores wider than 50 nm increased during the six years of usage, except for those catalyst particles which were contaminated in the upper layers of the catalyst bed by catalyst poisons, such as S, P and Cl, and which, consequently, were operated at lower temperatures. Since many factors jointly influence the miscrostructure of catalysts (poisoning, and thermal shock, etc.) the direct mathematical functional relationship could not be established between activity and the morphological characteristics, yet the existence of a close correlation is beyond doubt.

Introduction

During the reductive forming of ammonia-synthesis oxide catalysts, a specific morphological structure has to be attained, which possesses a sufficiently large internal surface area (8–20 m^2/g) accommodating the active centres, and has a pore-size distribution which is favourable for the intraparticle transport of the reacting components (characteristic pore size: 10–30 mm) [1].

The required morphology can be achieved by the reduction in a "non-producing" reactor of the multi-promotor catalysts currently used (4 or 5 promotors) [2]. It is of primary importance for the to know how the morphology changes during usage.

This paper discusses the morphology and its relationship to catalytic activity of KM–1–R catalyst samples collected from various spots in a three-layer, quench reactor, after an operation period of six years.

Experimental

Morphological Studies of the Ammonia Synthesis Catalysts

The internal surface area of the catalyst was calculated from the argon adsorption isotherm recorded at the temperature of liquid nitrogen, and the BET equation [3, 6]. The specific surface area can be calculated from the pore volume and the pore size distribution of the catalyst. In this case cylindrical or quadrangular pores with open base-plates are assumed [4].

Pore volume and pore size distribution can be determined by mercury porosimetry [5]. The apparatus, operated in the 1–1,000 bar pressure range, can be used for the measurement of 7.5–7,500 nm diameter pores. Pore volume and pore size distribution can also be calculated from the adsorption-desorption isotherms of nitrogen. This method is not only suitable for pores wider than 7.5 nm, but also for smaller ones [7]. Naturally, the specific surface area can also be calculated from the nitrogen adsorption isotherms.

Activity Measurements

Catalyst activity tests are in general carried out in low-volume, integrating-type tube reactors packed with a mixture of the catalyst and an inert diluent, because only in this way can isothermal conditions be maintained during the highly exotherm, high pressure reaction of ammonia synthesis.

Only 1–2 cm^3 samples with a particle size much finer than that of the industrial catalyst can be used in quasi-isothermal test reactors. Another undesirable consequence of the low sample size is that physico-chemical measurements, such as specific surface area and pore size distribution, which have to be carried out under an argon atmosphere and with an activated catalyst, cannot be accomplished, or only with considerable difficulty.

SCHOLTZ, SZABÓ and EGYHÁZI [10] developed a method which can be used to test the activity of ammonia synthesis catalysts, with the original particle size, in volumes limited only by the capacity of the gas supply units. Due to the higher test volumes, these mesasurements are also more representative.

The reactor proper is a simple, integrating-type, polytropic tube reactor, in which thermocouples are used to measure the temperature distribution.

Using the evaluation method described in [10] the constants of any two-parameter kinetic equation can be determined from the measured data (the kinetic constans unequivocally characterize the activity of the sample).

Experiments

Spent KM–1–R catalyst samples were obtained, after six years of operation, during the replacement of the catalysts, from the sites indicated in *Fig. 1.* Particles obtained at the same height, but from the left and right hand sides of the catalyst holders were unified and tested as samples No.1 to 9.

Since the maximum diameter of the catalyst container in the test reactor is 32 mm, the size of the original particles was reduced to reduce the wall-effects. The particle size range used was 1.25–2.5 mm. The new KM–1–R catalyst, also tested as a reference, was studied with a similar particle size distribution.

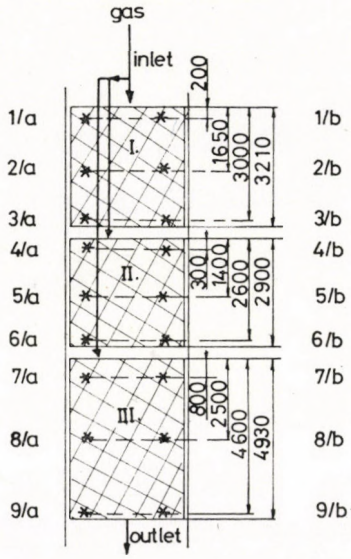

Fig. 1
Sampling schematics
* — site of sampling; I, II, III: 1st, 2nd and 3rd layer, respectively; *a* — left-hand side; *b* — right-hand-side

Morphological characteristics were determined in both prereduced (passivated) and active state (in argon atmosphere). Activity tests were carried out in a 100 cm^3 useful volume polytropic, integrating-type reactor, at 300 bar pressure using ammonia-free, stoichiometric, dry synthesis gas. Temperature was varied in the 380–510 °C range, space velocity in the 20,000–30,000 h^{-1} range.

In order to gain a further insight into changes of the morphology, a suitable size-fraction of the new KM–1–R catalyst was heated for 8 hours in purified hydrogen flow at 700 °C and 900 °C temperatures, respectively.

Measurement of the Specific Surface Area and Pore-Size Distribution

Specific surface area was calculated from the argon adsorption isotherm, measured at −196 °C by a BETograph (Atlas, MAT).

Pore volume and pore size distribution were determined by a mercury porosimeter (Carlo Erba), in the 7.5–7,500 nm range.

Specific surface area can be calculated from the pore-size distributions as:

$$F = 2 \times 10^3 \sum_{i=2}^{n} \frac{V_i - V_{i-1}}{\bar{r}_i} \quad (m^2/g) \tag{1}$$

Results of the morphologic measurements are summarized in *Table 1.*

The BET surface area in passivated state of the new, prereduced KM–1–R catalyst is 7–9 m^2/g; after a 50 hour reactivation process this increased to 10.8 m^2/g. (The programme of the reduction process is shown *Fig. 2*).

Table 1.

Sample	Specific surface area				Pore volume (cm^3/g)				Characteristic pore size (nm)	
	BET		calculated		between 7.5–7,500 nm		between 7.5–50 nm			
	p	*a*	*p*	*a*	*p*	*a*	*p*	*a*	*p*	*a*
KM–1–R, new	9.72	10.80	8.85	8.95	0.0860	0.1104	0.0704	0.0779	16.9	18.7
KM–1–R, spent, 1	9.20	10.61	7.39	8.73	0.0852	0.1090	0.0671	0.0813	18.1	20.0
KM–1–R, spent, 2	5.27	7.11	5.57	6.37	0.0755	0.1007	0.0574	0.0729	21.7	26.2
KM–1–R, spent, 3	4.83	6.27	7.80	6.48	0.0863	0.1059	0.0708	0.0738	17.9	22.5
KM–1–R, spent, 4	5.92	7.20	4.36	5.46	0.0667	0.0985	0.0444	0.0616	20.3	29.3
KM–1–R, spent, 5	5.75	6.43	—	—	—	—	—	—	—	—
KM–1–R, spent, 6	6.23	5.65	6.19	6.49	0.0768	0.0958	0.0624	0.0743	21.7	25.0
KM–1–R, spent, 7	6.71	8.11	7.43	6.16	0.0858	0.1084	0.0696	0.0632	17.7	24.9
KM–1–R, spent, 8	6.17	7.58	6.57	7.31	0.0733	0.0915	0.0608	0.0628	21.1	23.8
KM–1–R, spent, 9	6.75	7.85	6.26	6.22	0.0784	0.0952	0.0604	0.0671	19.7	24.1
KM–1–R, treated at 700 °C	7.3	7.3*	4.4	4.4*	0.0802	0.0802*	0.0574	0.0574*	26.3	26.3*
KM–1–R, treated at 900 °C	2.3	2.3*	2.8	2.8*	0.1075	0.1075*	0.0190	0.0190*	68.1	68.1*

*Samples treated at 700 °C and 900 °C temperatures lose their pirophoric characteristics, so the distinction of passivated and activated samples is formal.
p — passivated; *a* — activated.

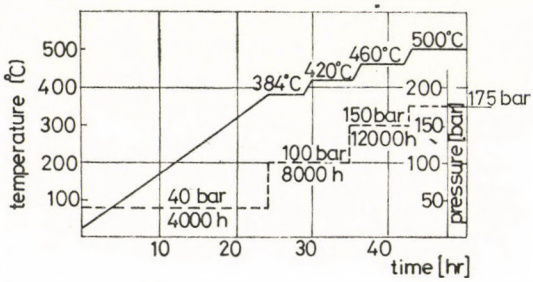

Fig. 2
Reduction programme used for the reactivation of catalyst samples

After reduction, oxygen leaving the passivated layers (2.75 g O_2/100 g catalyst) freed further adsorption sites. The specific surface area of spent catalyst decreased, in both a passivated and activated state, by 20–40%. Samples taken from the top of the layers do not follow this pattern. For example, sample No. 1 taken from the top of the spent KM–1–R catalyst bed, which was operated for 6 years only at 380–400 °C and which, as a consequence of the gas scrubbing technology used, contained 0.5% w/w finely dispersed copper, had a BET surface area of 10.61 m^2/g.

Increasing temperature changes the morphology of KM–1–R catalyst characteristically. After 8 hours at 700 °C the specific surface area decreased

to 7.3 m^2/g. At 900 °C the microstructure of the catalyst is effectively destroyed and the BET surface area drops to $F_{BET} = 2.3$ m^2/g.

During six years use the pore-structure of the KM–1–R catalyst undergoes a characteristic rearrangement (cf. *Table 1*). While the overall pore volume in the 7.5–7,500 nm range remains practically unchanged, the fraction of pores smaller than 50 nm, which are essential in providing the surface area requirement of the chemical reaction, decreases by 10–20%. This conclusion is supported by the surface area values calculated from the pore-size distribution. Thermal shock at 900 °C caused a complete rearrangement of the pore structure. The characteristic pore size of the spent catalyst increased (cf. *Fig. 3*).

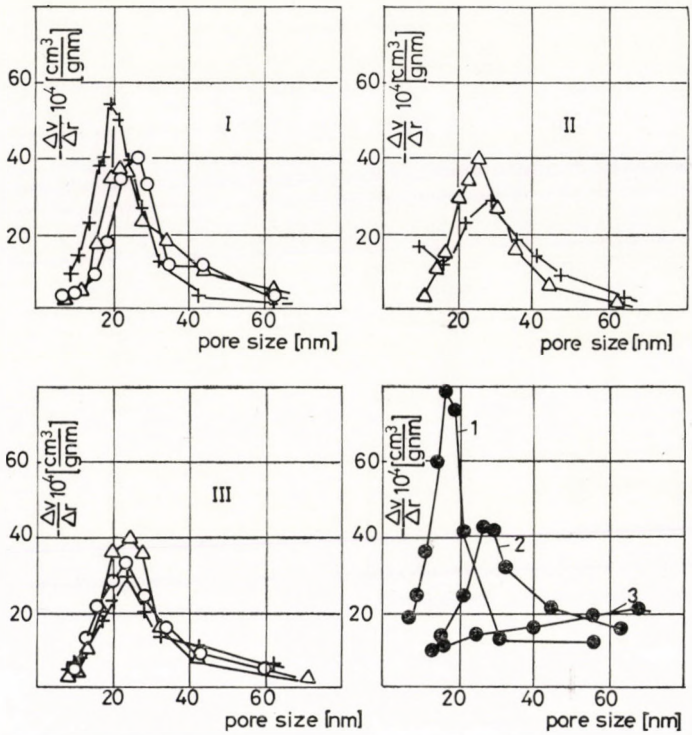

Fig. 3
Pore-size distribution curves of the catalyst sample
I, II, III: 1st, 2nd and 3rd layer, respectively; *1:* new KM–1–R catalyst; *2:* KM–1–R heat treated at 700 °C; *3:* KM–1–R heat treated at 900 °C; + front section of layer; ○ middle section of layer, △ rear section of layer

The increased pores are clearly visible on the scanning electronmicroscopic photographs taken from the new KM–1–R, spent KM–1–R, and sample No. 3 KM-1-R (heat-treated at 900 °C) catalysts. (Photographs A, B, C, magnification 10,000×).

Activity Test

The measurement and evaluation method described in [10] was used for the determination of the activity in a polytropic, integrating-type tube reactor of the new and spent KM–1–R samples. Activity measurements were carried out under conditions similar to those used in Hungary in large-scale ammonia plants, i.e. 300 bar pressure, 20,000–30,000 h^{-1} space velocity, and 380–510 °C temperature.

The kinetic constants of the Temkin–Pizhev equation (E_2: activation energy of ammonia decomposition, k_{450}–apparent kinetic constant at 450 °C) were determined from the polytropic activity masurements (radial and axial temperature profiles, composition of the input and output gas flow) at the given pressure and space velocity. The results are summarized in *Table 2*.

Table 2.

Summarizing Table of activity tests

Sample	Space velocity (h^{-1})	E_2 (kJ/mol)	k_{450} ($bar^{0,5}/h$)	$k_{450}/k_{450,new})\cdot 10^2$ (%)
KM–1–R, new	20,000	125.2	9,550	100
	30,000	120.6	11,400	100
KM–1–R, spent, 1	20,000	211.2	22	0.2
	30,000	235.7	45	0.4
KM–1–R, spent, 2	20,000	165.4	3,700	38.7
	30,000	163.3	4,250	37.3
KM–1–R, spent, 3	20,000	154.1	4,200	44.0
	30,000	148.7	5,350	46.9
KM–1–R, spent, 4	20,000	195.3	165	1.7
	30,000	191.5	206	1.8
KM–1–R, spent, 5	20,000	—	—	
	30,000	—	—	
KM–1–R, spent, 6	20,000	136.5	7,800	81.7
	30,000	129.8	9,950	87.3
KM–1–R, spent, 7	20,000	135.7	6,050	63.3
	30,000	138.2	8,700	76.3
KM–1–R, spent, 8	20,000	136.4	8,150	85.0
	30,000	133.7	9,300	81.6
KM–1–R, spent, 9	20,000	131.5	9,050	94.7
	30,000	117.6	10,100	88.6

The order of activity of the spent catalyst samples (after six years of operation) shows a characteristic pattern as a function of the layer-height. The activity of the samples taken from the initial section of the layers is very small. Activity increases with increasing height. The activity of the sample taken from the bottom of Layer III indicates that under favourable operation conditions (i.e. no thermal shock or catalyst poisoning) the KM–1–R catalyst can be used for 6–10 years. The activity of this particular sample decreased by only 10% during 6 years of operation.

The lower activity of the samples taken from the initial sections of the layers is due to the presence of catalyst poisons S, P, Cl and finely dispersed copper. The sulphur, phosphorous and chlorine concentration of the catalyst samples taken from the four sections of the catalyst layers, as determined by energy dispersive *X*-Ray analysis (EDAX) are listed in Table 3. Though the surface concentration of these elements is higher than inside the particles, the particles are sufficiently perfused by these catalyst poisons. The concentration profiles of S, P and Cl within the particles were studied by EGYHÁZY, SCHOLTZ and BESKOV with spent KM–1–R catalysts, sample No. 1 [11].

Table 3.

Phosphorous, sulphur and chlorine concentration of the samples taken from the front sections of the layers

Sample	Average concentration, % w/w					
	in surface layer of catalyst grain			in bulk phase of catalyst grain		
	P	S	Cl	P	S	Cl
KM–1–R, spent, 1	1.516	0.077	0.897	0.051	0.098	0.265
KM–1–R, spent, 4	0.465	0.058	0.058	0.053	0.067	0.088
KM–1–R, spent, 7	0.019	0.062	0.069	0.003	0.049	0.021

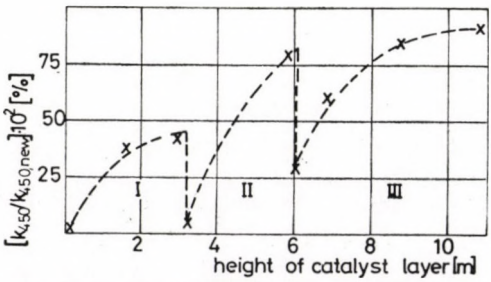

Fig. 4

Activity as a function of the length of the catalyst layer I, II, III: 1st, 2nd and 3rd layer, respectively

Photograph A: new KM–1–R catalyst, Magnification: 10,000×
Photograph B: spent KM–1–R catalyst, Magnification: 10,000×
Photograph C: KM–1–R heat treated 900 °C, Magnification: 10,000×

The activity pattern of a three layer, quench-type reactor, reflecting the effects of catalyst poisons and operation-related morphological changes is shown in *Fig. 4*.

Conclusions

The specific surface area of the KM–1–R catalyst used for six years in a three-layer, cold-gas-mix-in quench-type industrial ammonia synthesis reactor, operated at 300 bar pressure and 400–480 °C temperature decreased by 20–40%. The size of the pores facilitate component transfer increased, while the number of pores decreased. This conclusion is supported by the specific surface area values calculated from the pore volume and pore number.

The rearrangement of the morphology of new KM–1–R catalyst, caused by six years of operation, brought about a 10–20% decrease in the activity of the catalyst (activity of the samples taken from the middle and rear sections of Layers II and III).

The large decrease in the activity of the samples taken from the front sections of the catalyst layers is caused by the reversible and irreversible catalyst poisons (P, S, Cl) and the finely dispersed copper, which originate from the gas-scrubbing step.

Photograph C: KM–1–R heat treated at 900 °C, Magnification: 10,000×

SYMBOLS

F_{BET} BET specific surface area, m^2/g
F calculated surface area, m^2/g
V pore volume, cm^3/g
i subscript
n number of measurement points
r average pore radius, nm
E_2 activation energy of ammonia decomposition, kJ/mol
k_{450} apparent kinetic constant referred to 450 °C, $bar^{1/2} \times h^{-1}$

REFERENCES

1. EMMETT, P.: Battelle Institute Materials Science Colloquium, *1975*, 9, 337–362.
2. NIELSON, A.: An Investigation on Promoted Iron Catalysts for the Synthesis of Ammonia. Jul. Gjellerups Forlag, Copenhagen, 1968. pp. 139–153.
3. BRUNAUER, S., EMMETT, P. H. and TELLER, E.: J. Amer. Chem. Soc., *1938*, 60, 309.
4. BODOR, E. E., OLDER, I. and SKALNY, J.: J. Coll. Int. Sci., *1970*, 32, 367.
5. GUYER, A. JR., GUYER, A. and BÖHLEN, B.: Helv. Chem. Acta, *1959*, 42, 2103.
6. SCHLOSSER, E. G.: Chem. Ing. Techn. *1959*, 31, 799.
7. MAHAPATRA, H., GHORAI, D. K., GANGULI, N. C. and SEN, S. P.: Fert. Technol., *1978*, 3–4, 226.
8. COMMINGS, E.: High Pressure Technologies (in Hungarian), Műszaki Könyvkiadó, Budapest, 1959, pp. 306–329.
9. GUCCI, U., TRAINA, F. and BUZZI FERRARIS, G.: Ind. Eng. Chem., Process Des. Dev. *1977*, 16, 166.
10. SCHOLTZ, J., SZABÓ, J. and EGYHÁZY, T.: Magy. Kém. Lapja *1983*, 38 (9).
11. EGYHÁZY, T., SCHOLTZ, J. and BESKOV, V. S.: React. Kinet. Catal. Lett. (in preparation).

РЕЗЮМЕ

Морфология катализаторов использованных при синтезе аммония имеющих несколько промоторов имеет чрезвычайное значение. В стати приведены результаты сравнительного анализа и морфологии катализаторов типа KM—1—R, новых и работающих в течении шести лет. Определено, что удельная поверхность измеренная аргон сорбцией старых катализаторов несколько уменьшался, но количество пор размером больше чем 50 нм решительно увеличивалось, за исключением слоя катализатора который размещался в верхней части реактора и который отравился травителями катализаторов S, P, Cl, и поэтому работал при меньшей температуре. Так как на свойства и микроструктуру катализатора оказывют влияние многочисленные факторы (травление, температура и.т.д.) непосредственную зависимость между активностью и морфологическими свойствами нельзя было получить, хотя такая зависимость наверно существует.

HUNGARIAN JOURNAL
OF INDUSTRIAL CHEMISTRY
VESZPRÉM
Vol. 11. pp. 157-164 (1983)

NEW BIOCIDES FROM PETROLEUM HYDROCARBONS I.

BIOCIDAL ACTIVE PRODUCTS FROM 4-SUBSTITUTED PHENOLS AND 4-SUBSTITUTED-1-NAPHTOLS.

T. M. Kassem, O. M. O. Habib, M. H. Hussein
and A. I. Eissa*

(Petrochemicals Department, Egyptian Petroleum Research Institute,
Cairo, Egypt.
*Chemistry Department, Faculty of Science, Mansoura University,
Egypt.)

Received: October 20, 1982.

Egyptian gasoline distillate from "Morgan" crude oil was separated into three fractions, which were sulphonated and then neutralised separately. The resulting sodium sulphonates were converted into the corresponding sulphonyl chloride mixtures. Each of these mixtures was condensed with phenol, 4-substituted phenols, 1-naphthol and 4-substituted-1-naphtoles.

The prepared products were specified and their toxicity against some harmful bacteria and fungi was tested. Some factors correlating the effect of structures on toxicity were discussed.

Introduction

The effect of the chemical constitution on the biocidal activity of many compounds has been reviewed extensively in literature [1–7].

The present work was planned and conducted as a new contribution to the previous studies [8, 9] utilizing the locally available aromatic hydrocarbons produced from local gasoline distillate together with some substituted phenols and some substituted-l-naphthols in producing some new products of high biocidal activity towards the tested organisms.

Experimental

Characterisation of "Morgan" Gasoline Fractions

Three gasoline fractions (A_1, B_1 and C_1) of boiling ranges 70–90, 100–120 and 130–150 °C, respectively, were obtained by distillation under atmospheric pressure and were characterised *(Table 1)*.

Table 1.
Specification of the three gasoline fractions

Fraction	A_1	B_1	C_1
Boiling range °C/atm. press.	70 – 90	100 – 120	130 – 150
Sp. gr. at 15/4 °C	0.7531	0.7756	0.7828
n_D^{28}	1.4118	1.4265	1.4382

Samples from these three fractions were examined by the gas-liquid chromatography for analyzing the components present in their aromatic portions (using a packed column of copper tubing of 15 ft. length, 3 mm i.d. TCEPE 15% on Chromosorb *P* (A.W.) 60–80 mesh. The instrument used was a Perkin–Elmer 910. Quantitative analyses were accomplished by using an electronic integrator, Perkin–Elmer Sigma 10, with internal standard *n*-tetradecane 5% (by weight). The following analyses were obtained:

Component	Fraction (A_1) wt.%	Fraction (B_1) wt.%	Fraction (C_1) wt.%
Benzene	2.690	0.448	0.218
Toluene	1.880	3.562	0.831
Ethylbenzene	0.663	0.800	1.446
p- & *m*-Xylene	1.415	1.908	4.971
Isopropylbenzene	0.012	0.032	0.466
o-Xylene	0.012	0.653	2.289
n-Propylbenzene	—	0.023	0.788
Trimethylbenzene	—	—	0.171
Weight % of total aromatics	6.672	7.426	11.178

Sulphonation Procedure

Each fraction (1 kg) was vigorously stirred with concentrated sulphuric acid (800 g, 98%) and heated at 60–70 °C for 12 hours. It was then cooled and the acid layer was separated and neutralized with sodium carbonate solution (10%). The aqueous solution was evaporated until dryness, the residue was refluxed with absolute ethanol and was then filtered. The alcohol was distilled off and the obtained sulphonates were well dried.

Preparation of Sulphonyl Chloride Mixtures from the Obtained Sodium Sulphonates

The sodium sulphonates obtained from each mixture and a slight excess from phosphorous pentachloride was heated to 80–90 °C for one hour, cooled, poured onto crushed ice and then extracted with ether. The etherial layer was washed several times with cold water, dried over anhydrous magnesium

sulphate and finally distilled off. The obtained oily sulphonyl chloride mixtures A_2, B_2 and C_2 were purified by vacuum distillation and were characterised *(Table 2)*.

Table 2.

Characterisations of the sulphonyl chloride mixtures prepared from the different gasoline fractions

Sulphonyl chlorides	B.r. °C/5 mm Hg	Average mol. wt.	Yield %	Analyses %	
				S	Cl
A_2	96 – 102	186	88	16.32	17.46
B_2	126 – 130	190	81	17.10	18.25
C_2	140 – 144	197	79	15.89	17.57

Condensation of the Prepared Sulphonyl Chloride Mixtures with Phenol, 1-naphtol, and their 4-substituted Derivatives

Equimolecular amounts (0.05 mole) from each sulphonyl chloride mixture (A_2, B_2 and C_2) and the phenol, *1*-naphtol or their derivatives (prepared according to ref. [10–12]) were vigorously stirred and heated on a water bath

Table 3.

Antibacterial and antifungal activities of the products obtained by the condensation of the sulphonyl chloride, mixture (A_2) with phenol, naphthol, and their 4-substituted derivatives

Product number	Phenols or 1-naphthols	Average mol. Wt. of the obtained sulphonates	Bacteria								Fungi	
			Aero. aerogenes	K. aerogenes	Bacillus subtilis	Bacillus cereus	Micrococcus sp.	Escherichia coli	Staphylococcus aureus	Salmonella sp.	Candida albicans	Aspergillus niger
I_1	Phenol	240	×	×	900	×	700	550	300	400	×	×
I_2	p-Cresol	255	×	400	450	250	500	670	×	×	750	×
I_3	p-Chlorophenol	280	350	250	*100*	300	450	*100*	650	450	500	×
I_4	p-Bromophenol	318	×	350	*100*	400	300	400	350	400	×	×
I_5	p-Nitrophenol	285	450	400	*100*	250	*100*	200	300	*100*	200	350
I_6	1-Naphthol	292	×	×	1000	×	800	750	450	550	×	×
I_7	4-Methyl-1--napthol	310	×	800	×	850	650	700	×	600	×	×
I_8	4-Chloro-1--naphthol	330	500	750	700	*100*	350	250	350	400	500	550
I_9	4-Bromo-1--naphthol	374	×	500	600	200	600	×	500	350	650	×
I_{10}	4-Nitro-1--naphthol	340	350	×	500	450	250	*100*	650	350	×	450

× Means no activity at concentration of 3,000 γ/ml. solution.

Table 4.

Antibacterial and antifungal activities of the products obtained by the condensation of the sulphonyl chloride, mixture (B_2) with phenol, naphthol, and their 4-substituted derivatives

Product number	Phenols or 1-naphthol	Average mol.Wt. of the obtained sulphonates	Bacteria								Fungi	
			Aero. aerogenes	E. aerogees	Bacillus subtilis	Bacillus cereus	Micrococcus sp.	Escherichia coli	Staphylococcus aureus	Salmonella sp.	Candida albicans	Aspergillus niger
II_1	Phenol	245	×	600	200	350	500	450	200	350	×	×
II_2	p-Cresol	258	×	400	350	*100*	*100*	300	450	300	400	×
II_3	p-Chlorophenol	280	300	*100*	400	*50*	*100*	350	400	*100*	300	250
II_4	p-Bromophenol	322	400	200	450	*100*	300	*100*	*100*	200	500	350
II_5	p-Nitrophenol	294	250	350	*50*	*100*	*20*	*100*	250	*50*	200	150
II_6	1-Naphthol	296	×	850	350	300	400	×	350	450	×	×
II_7	4-Methyl-1--naphthol	308	550	350	550	200	*100*	600	×	350	×	450
II_8	4-Chloro-1--naphthol	335	350	*100*	550	*100*	250	*100*	500	200	300	300
II_9	4-Bromo-1--naphthol	375	450	250	450	*100*	300	500	650	*100*	×	350
II_{10}	4-Nitro-1--naphthol	344	350	400	150	*100*	250	*50*	400	*100*	300	250

× Means no biocidal activity at concentrations up to 3,000 γ/ml. solution.

to 80–90 °C. Sodium hydroxide solution (0.05 mole; 0.7 N) was added dropwise over a period of 20 minutes. The reaction mixture was heated with stirring for a further one hour. After cooling, the formed viscous mass was washed with sodium hydroxide solution (10%) to remove any unchanged phenols or naphthols and was then purified by boiling their solutions in benzene with charcoal for 10 minutes. The benzene solution was filtered off, then completely evaporated and the viscous masses were solidified. The average molecular weights [13] of these products were determined *(Tables 3–5)* and the infra-red spectra of some of them were determined.

Determination of the Antibacterial and Antifungal Activities of the Prepared Products

The prepared compounds were screened against eight harmful bacterial and two fungal species following a procedure described proviously [14].

The minimum inhibition concentrations γ/ml (γ=ppm×g) of the test substances were determined. The products whose m.i.c. are 100 γ/ml or less than this value were considered active bactericides and fungicides. The results are given in Tables 3–5.

Table 5.

Antibacterial and antifungal activities of the products obtained by the condensation of the sulphonyl chloride, mixture (C_2) with phenol, naphthol, and their 4-substituted derivatives

Product number	Phenols or 1-naphthols	Average mol.Wt of the obtained sulphonates	Bacteria								Fungi	
			Aero. aerogenes	K. aerogenes	Bacillus subtilis	Bacillus cereus	Micrococcus sp.	Escherichia coli	Staphylococcus aureus	Salmonella sp.	Candida albicans	Aspergillus niger
III_1	Phenol	250	×	×	300	500	600	350	250	300	×	×
III_2	p-Cresol	270	600	×	*100*	300	400	×	350	450	550	×
III_3	p-Chlorophenol	286	400	*100*	550	*100*	350	*100*	500	200	400	300
III_4	p-Bromophenol	336	500	300	*100*	300	200	350	*100*	300	×	400
III_5	p-Nitrophenol	296	300	450	*100*	200	*100*	*100*	350	*100*	250	250
III_6	1-Naphthol	302	×	×	400	250	300	×	550	400	500	×
III_7	4-Methyl-1--naphthol	322	×	550	×	300	250	750	1000	550	×	×
III_8	4-Chloro-1--naphthol	342	450	700	600	250	350	*100*	600	250	250	350
III_9	4-Bromo-1--naphthol	385	×	450	550	*100*	500	×	550	300	500	400
III_{10}	4-Nitro-1--naphthol	346	400	450	250	*100*	300	*100*	500	200	350	450

× Means no biocidal activity at concentrations up to 3,000 γ/ml. solution.

Discussion of the Results

The present investigation was planned to utilize the available aromatic hydrocarbons from the Egyptian "Morgan" gasoline distillate for the preparation of some biologically active compounds. This was followed by separating this distillate into three fractions A_1, B_1 and C_1 *(Table 1)* followed by sulphonation and neutralization of these fractions. The obtained sodium sulphonates were converted into their corresponding sulphonyl chloride mixtures A_2, B_2 and C_2 respectively *(Table 2)*. From this Table, it could be concluded that only one sulphonyl chloride group was introduced for every aromatic hydrocarbon molecule.

The obtained sulphonyl chloride mixtures were then condensed with some 4-substituted phenols and 1-naphthols, which bore identical substituents. The structures of the prepared products were elucidated by determining their molecular weights and by the infra-red spectra, which showed stretching frequencies at 1,200 and 1,375 cm^{-1} characteristics for the $-SO_2$-O— group.

The antibacterial and antifungal activities of the prepared products towards some harmful bacteria and fungi were screened. The impact of the structures of the obtained products on their biocidal activity depended upon the following:

1. The type of the prepared sulphonyl chloride mixtures.
2. The type of the aromatic ring which bears the substituents of either phenyl or naphthyl.
3. The type of the substituents present in the substituted phenols or naphthols.
4. The type of the tested bacteria and fungi.

Effect of the Type of the Prepared Sulphonyl Chloride Mixtures

The results obtained in the present work showed that the products prepared from sulphonyl chloride mixtures (B_2) had a higher ratio of the active products (8 active compounds) than those prepared from the sulphonyl chloride mixtures (C_2) (7 active products). On the other hand, the least active products were those prepared from the sulphonyl chloride mixtures (A_2) (5 active compounds). This means that the aromatic hydrocarbon fraction rich in toluene is the most suitable for preparing these biocidally active products, while the benzene rich fraction is the lowest valuable fraction for this purpose.

Effect of the Type of the Aromatic Ring Which Bears the Substituents of Either Phenyl or Naphthyl

It is clear from *Tables 3–5* that the products derived from the substituted phenols gave a higher ratio of the active products (11 active compounds) than those derived form the substitudet naphthols (9 active prducts). This may be attributed to the smaller molecular size of the former products, thus facilitating their penetration through the tested organisms.

Effect of the Type of the Substituents Present in the Phenols or 1-Naphthols

The data obtained in *Tables 3–5* showed that the degree of toxicity with reference to the type of substituents increased in the following order: $-CH_3 < -Br < -Cl < -NO_2$.

This result is the same for both products obtained from substituted phenols or substituted 1-naphthols.

Effect of the Type of the Tested Bacteria and Fungi

The order of biocidal activities based upon the type of the tested bacteria was as follows:

Type of bacteria	*Product number*	*Total number of active products*
Bacillus cereus	I_8, II_2, II_3, II_4, II_5, II_8, II_9, II_{10}, III_3, III_9, III_{10}.	11
Escherichia coli	I_3, I_{10}, II_4, II_5, II_8, II_{10}, III_3, III_5, III_8, III_{10}.	10

Bacillus subtilis	I_3, I_4, I_5, II_5, III_2, III_4, III_5.	7
Micrococcus sp.	I_5, II_2, II_3, II_5, II_7, III_5.	6
Salmonella sp.	I_5, II_3, II_5, II_9, II_{10}, III_5.	6
K. aerogenes	II_3, II_8, III_3,	3
Staphylococcus aureus	II_4, III_4.	2

On the other hand, with respect to the tested fungi it was noticed that most of the prepared products were of moderate activities.

It could be concluded from the results obtained in the present work that Egyptian "Morgan" gasoline can be used for manufacturing some active bactericides through its sulphonation, conversion into sulphonyl chlorides and finally esterification with phenol, 1-napthol and their 4-substituted derivatives.

REFERENCES

1. Vol'fson, L. G., Volodkovich, S. D. and Mel'nikov, N. N.: Insekto Fungitsidy (Moscow, Gosudarst. Nauch.-Tekh. Izdatel. Kim. Lit.) Sbornik, 1955; 168–71; Referat. Zhur. Khim. *1956*, Abstr, No. 19,844; Chem. Abstr. *53*, 13,494 (1959).
2. Esayan, G. T., Mardzhanyan, G. M., Babayan, A. A. and Ustyan, A. K.: Izv. Akad. Nauk. Arm. SSR, Khim. Nauk, *1962*, 15,285–9, Chem. Astr. *59*, 6293 (1963).
3. Sohma, Takenobu, Konishi; Kasup, Takoda Kenkyusho Nempo, *1967*; 26, 149–56; Chem. Abstr. *69*, 43,567 (1968).
4. Kassem, T. M., Fam, S. A and El-Sukkary, M. A., Bull. NRC., Egypt, 1978, 3 (4) 321.
5. Kassem, T. M., El-Sukkary, M. A. and Hussein, M. H.: Bull. NRC., Egypt, *1979*, 4 (3), 275.
6. Marei, A., Fam, S. A., Kassem, T. M., Mansour, S. A. and El-Sukkary, M. A.: Bull. NRC., Egypt, *1979*, 4 (4), 407.
7. Habib, O. M. O., El-Sukkary, M. A. and Eissa, A. I.: Bull. NRC., Egypt, *1979*, 4 (4), 421.
8. Kassem, T. M., El-Sukkary, M. A. and Hussein, M. H.: Bull. NRC., Egypt, *1978*, 3 (3), 241.
9. Kassem, T. M., Marei, A. and Eissa, A. I.: First Egyptian Chemical Engineering Conference, Cairo 15–18 March 1980.
10. Steiger, R. E.: Helv. Chim. Acta. *1930*, 13, 180.
11. NG. PH. Buu-Hoi; Rec. Trav. Chim. *1954*, 73, 197.
12. Hodgson, H. H. and Kilner, E.; J. Chem. Soc., *1924*, 13, 180.
13. Vogel, A. I.: "Practical Organic Chemistry", Third Enlarged Edition, Longman, p. 1037 (1974).
14. Abou-Zeid, A. A. and Shehata, Y. M.: Indian J. Pharmacy; *1969*, 31 (3), 72.

РЕЗЮМЕ

Эгиптский дистиллят произведенный из сырой нефти типа „морган" разделили на три фракции которые сульфировали, потом нейтрализовали. Полученные натрий-сульфонаты преобразовали в смесь сульфонил-хлорид. Все смеси реагировали конденсацией фенолом, 4-размещенными фенолами, 1-нафтолом, и 4-размещенным-1-нафтолом.

Изучали токсичные свойства отдельных продуктов на некоторые бактерии и грибы. В стати излагают некоторые структурные свойства которые имеют влияние на токсичность соединений.

HUNGARIAN JOURNAL
OF INDUSTRIAL CHEMISTRY
VESZPRÉM
Vol. 11. pp. 165-172 (1983)

USE OF THE WEIGHTED-MOMENTS-METHOD FOR PARAMETER IDENTIFICATION AND APPROXIMATION OF DISTRIBUTION FUNCTIONS

L. Király, B. Lakatos and T. Blickle

(Research Institute for Technical Chemistry of the Hungarian Academy of Sciences, Veszprém, Hungary)

Received: November 23, 1982.

The results of a computerized simulation study of the method of weighted moments are presented here in connection with a continuous-flow recirculation-type system.

The study was aimed at determining the effects of measurement noise, time-scale factor, number of higher moments and termination conditions upon the values of the parameters obtained by the method of weighted-moments parameter identification. The approximation of the residence time distribution by weighted moments and Laguerre polynominals was also studied.

It was concluded that the selection of the time-scale factor close to the optimum is of special importance for both the identification and approximation, because for time-scale factors away from the optimum value, the measurement noise increasingly distorts the parameters.

Introduction

A number of methods are used for the calculation of continuous, flowing systems. They are based on different principles, e.g. Laplace transformation, frequency methods, and correlation methods, etc. There is also an ever increasing need for the accurate and fast estimation of the parameters. While the optimum methods yield the most accurate results in both the time and frequency domain, there is renewed interest in the more direct and rapid momentum methods and their variants.

The major drawback of the widely used method of common moments [1] is that the multipler t^k increases the relatively large error at the tail of the curves even further, and the higher moments ($k>3$) are of no use, because of their inaccuracy. Kafarov [2] solved this problem by terminating the calculation early on the tail of the curve. The method of Mixon et al. [3] as further modified by Michelsen and Østergaard [4, 5], the so-called method

of wieghed moments, offers a more effective solution to the problem. SIMÁNDI et al. [6] used this method for the identification of a rotating-disc extractor and obtained better results than those obtained by the method of common moments. An important, and often decisive problem of the weighted moments method is the advantageous selection of the weight function, and furthermore, for the *exp (–st)* weight function the selection of s is of special importance [5, 7, 8].

ANDERSSEN and WHITE [8] examined the dependence of:

$$g_k = t^k \, exp\,(-st) \tag{1}$$

upon k and s, and concluded that for much too small s values ($s < 0.05$) the problems encountered with the method of common moments occur, while for large s ($s > 5$) the relatively large measurement error at the beginning of the curve becomes excessively accentuated. There is an optimum s value between these two extremes. MICHELSEN and ØSTERGAARD [5] developed a method for its determination and used the s value thus obtained in a dispersion model. The estimation given in [8] is simpler and more practical. According to [8] the expressions:

$$s = k/t_m \tag{2}$$

or:

$$s = (k+1)/\tau \tag{3}$$

give a good approximation of the optimum for one moment when τ is the expected value and t_m is the mode of the density function f. For further moments the optimum is:

$$s = 2/k_{max}(2+1)/(t_{m,\,in} + t_{m,\,out} - \Delta t) \tag{4}$$

or:

$$s = 2(k_{max}/2+1)/(\tau_{in} + \tau_{out} - \Delta t) \tag{5}$$

WOLFF, RADEKE and GELBIN [9] used these estimates in an axial dispersion model and found good agreement with the results of their own curve-fitting method.

The System Used in the Simulation

The continuous flow-through system studied here is shown in *Fig. 1.* The system also contains a recirculation flow, because we could not find in literature the description of the weighted-moment parameter identification of this system.

The balance equations of the system are as follows:

$$V_1 \frac{dc}{dt} = qu + Rqy - (1+R)qc \tag{6.1}$$

$$V_2 \frac{dy}{dt} = (1+R)qc - qy - Rqy \tag{6.2}$$

From these, after rearrangement and the introduction of the symbols used in *Fig. 1*, the following initial-value problem is obtained:

$$\tau_1 \frac{dc}{dt} = \alpha u + (1-\alpha)y - c \tag{7.1}$$

$$\tau_2 \frac{dy}{dt} = c - y \tag{7.2}$$

$$c(0) = y(0) = 0 \tag{7.3}$$

$$\tau_1 := \frac{V_1}{(1+R)q}, \qquad \tau_2 := \frac{V_2}{(1+R)q}, \qquad \alpha := \frac{1}{1+R} \tag{7.4}$$

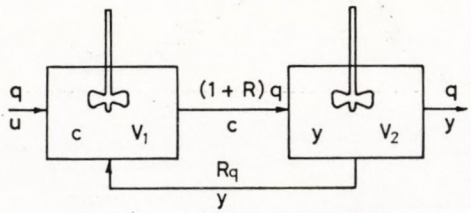

Fig. 1
Schematics of the simulated system

The values $\tau_1 = 30$ min, $\tau_2 = 25$ min and $\alpha = 0.5$ were used for the computerized simulation. If the input concentration function is an ideal pulse function, $n = \delta(t)$, then y is the density function of the residence time distribution. However, in the widely used tracer-method, the input function is not an ideal pulse, rather a pulse-like unimodal function.

The function $u = t\ exp\ (-at)$ was used for the calculations. Its mode approaches zero when $a \to \infty$. Its weighted moment (just like that of any continuous probability variable t with u as its density function):

$$m_k = \int_0^\infty t^k e^{-st} u(t)\, dt \tag{8}$$

It holds for the weight function that:

$$\lim_{t \to \infty} t^k e^{-st} = 0 \qquad s > 0 \tag{9}$$

In practice, the measurement is terminated at some time T, not at infinity, so the moments are truncated. Since during the concentration measurements the measurement error $[\varepsilon(t)]$ is added to the true value, the measured weighted moment is obtained as the sum of two terms:

$$m_k(u') = \int_0^\infty t^k e^{-st}[u(t) + \varepsilon(t)]\, dt = m_k + \int_0^\infty t^k e^{-st} \varepsilon(t)\, dt \tag{10}$$

The aim of the weighted moments method is the minimalization of the second term by the judicious selection of the value of s.

For the above parameter values the differential equation set (7) can be solved by numeric methods for any input function u, and the result is the output function, y. The response function, y, obtained for an input function $u=t\ exp\ (-at)$—for $a=0.1$—is shown in *Fig. 2*.

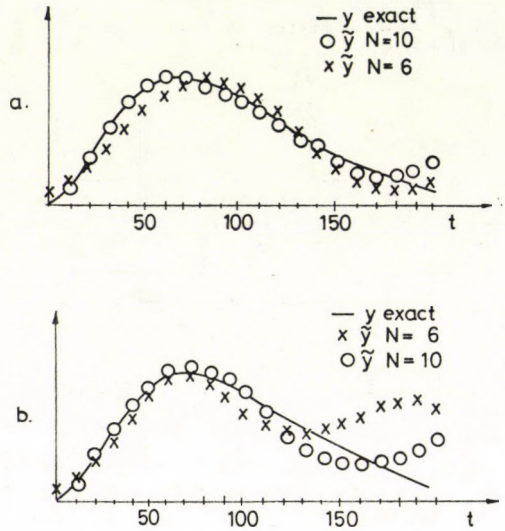

Fig. 2
Approximations of the density function of residence time distribution

By appropriate rearrangements, equation set (10) can be transformed into a recursive differential equation set of the weighted moments:

$$\alpha m_k(u) + (1-\alpha)m_k(y) - m_k(c)(1-\tau_1 s) + \tau_1 k m_{k-1}(c) = 0$$

$$m_k(c) - m_k(y)(1=\tau_2 s) + \tau_2 k m_{k-1}(y) = 0 \tag{11}$$

$$m_k(u) - m_k[t\cdot\exp(-at)] = \frac{k+1!}{(s+a)^{k+2}}$$

$$m_{-1}(y) = m_{-1}(c) = 0$$

$$a=0.1 \qquad k=0, 1, 2, \ldots$$

For given parameters, the kth moments: $m_k(c)$ and $m_k(y)$ can be calculated from the $(k-1)$th moments.

Approximation of the Density Function of Residence Time Distribution

Frequently, the residence time distribution of a system has to be approximated [7]. The task is the generation of function y in the form of

$$\tilde{y} = \sum_{i=0}^{N-1} c_i \varphi_i \sim y \tag{12}$$

where system $\{\varphi_i\}$ is orthogonal with respect to weight function *exp (–st)* [10], i.e.:

$$\int_0^\infty e^{-st} \varphi_i \varphi_j \, dt = \delta_{ij} \qquad i, j = 0, 1, 2, \ldots \tag{13}$$

Selecting φ_i-s as LAGUERRE polynomials:

$$\varphi_i(t) = \sqrt{s} \sum_{j=0}^{i} \binom{i}{j} \frac{(-st)^{i-j}}{(i-j)!} \qquad i = 0, 1, \ldots, N-1 \tag{14}$$

Coefficient c_i follows from the condition:

$$\int_0^\infty e^{-st} (y - \tilde{y})^2 \, dt = \min \tag{15}$$

Thus:

$$c_i = \int_0^\infty e^{-st} \varphi_i y \, dt = \sqrt{s} \sum_{j=0}^{i} \frac{(-s)}{(i-j)!} \binom{i}{j} m_{i-j}(y) \qquad i = 0, 1, \ldots, N-1 \tag{16}$$

that is the approximation of function y becomes:

$$\tilde{y} = \sqrt{s} \sum_{i=0}^{N-1} c_i \sum_{j=0}^{i} \binom{i}{j} \frac{(-st)^{i-j}}{(i-j)!} \qquad N = 1, 2, \ldots \tag{17}$$

With a suitable programme $y(t)$ values can be calculated quickly by a computer. The moments of y (obtained by the RUNGE–KUTTA method) can be determined by numeric integration over the (0, T) interval with T being so large that $y(T) = 0.01 \; max \, [y(t)]$. Then function y was calculated for various s and N values as shown—for some cases—in *Fig. 2*.

For any preset s value an increase in N improves the precision of approximation, because more terms are considered [7].

For any preset N the approximation changes with s. When s is excessive ($s > 1$) or too small ($s < 0.02$) the approximation is rather coarse. If, for example $N = 7$, then the approximation is best for $s = 0.06$. This s value agrees well with those estimated by Equations (4) (5).

Parameter Identification

Let us have a system with the above structure and let us have an input and output function with superimposed noise. Though noise has a more complex nature, only the measurement noise is considered here because its effect is

most pronounced at parameter identification [7]. Let the noise-free signals be u and y onto which there are randomly superimposed at $\Delta_t = 0.5$ intervals random numbers of zero expected value and σ standard deviation. Thus, the measurement of y input and x output functions can be simulated for any $\sigma > 0$ value. The following σ values were used for the calculations: 0.01 y_{max}; 0.05 y_{max}; 0.1 y_{max}; 0.2 y_{max}, where $y_{max} = \max\,[y(t)]$ and $0 \leq t \leq T$. The noise-distorted moments $m_k(u)$ and $m_k(y)$, $k = 0, 1, \ldots N$ can be determined by numeric integration for given s, T and N. The following equation holds for the output moments:

$$m_{k(y')} = \frac{\alpha m_k(u') + m_{k-1}(y')(k\tau_2 + 2ks\tau_1\tau_2 + k\tau_1) - m_{k-2}(y')k\tau_1\tau_2}{s\tau_1 + s\tau_2 + s^2\tau_1\tau_2 + \alpha} \tag{18}$$

$$k = 0, 1, \ldots, N \qquad m_{-1}(y') = m_{-2}(y') = 0$$

The parameters, for which Eq. 19 holds, are sought:

$$\sum_{k=0}^{N} \left(\frac{m_k(y') - m_k(y)}{m_k(y')} \right)^2 = \min \tag{19}$$

The equation is strongly non-linear, yet it requires only a short computation time on the computer [11].

The following questions still have to be answered: the noise (σ) sensitivity of the parameters (τ_1, τ_2, α), the advantageous selection of scale factor s, the value of T and the effects of $N > 2$.

A few characteristic results are shown in *Table 1*. The conclusion is that for a measurement error of 1% relative standard deviation results in a few tenths of a percentage point deviation in the parameters, and even a 5% standard deviation noise results in only a few percentage points deviation.

The higher the standard deviation of noise ($\sigma \geq 0.1 y_{max}$) the more important is the selection of the value of s. Its optimum values are in the vicinity of those obtained by Eq. 8 and 9.

Table 1.

Results of the parameters identification

σ	s	T [min]	k_{max}	τ_1 [min]	τ_2 [min]	α
0	0.10	400	2	30.000	25.000	0.500
1	0.05	400	2	30.000	24.889	0.500
1	0.05	400	3	30.121	24.637	0.496
1	0.08	200	2	29.743	24.965	0.496
5	0.08	200	2	30.059	25.060	0.501
10	0.08	200	2	26.424	24.970	0.462
5	0.08	400	2	29.924	24.341	0.494
10	0.08	400	2	27.107	22.471	0.434
20	0.08	400	2	31.771	10.442	0.335
20	0.08	400	3	30.691	14.434	0.378
20	0.08	400	4	32.415	12.472	0.351
1	0.20	400	2	27.142	25.214	0.471
5	0.20	400	2	17.817	25.621	0.354
5	0.20	200	4	29.832	20.464	0.432

For too small s and large T values ($T > 400$) the problem of common moments occurs, so it is advisable to select a smaller T because then the error is also smaller. Another possibility is the smoothing of the measured functions by a spline before the calculation of the moments. For not too small s values ($s > 0.1$) it is advisable to have a relatively smaller T because then the moment of the truncated part is negligibly small.

For a noise of 15–20% relative standard deviation, when the spread of the parameter values obtained by moments $k = 0.1$ and 2 is large, the addition of the 3rd and 4th moments improves the situation, but m_5 and m_6 deteriorates the estimation, because the noise can cause considerable imprecision. Calculations were carried out by an IBM 3031 computer using PL/1 language.

Summary

Based on the results of a computerized simulation of a continuous, flow-through system, it can be concluded that the major assets of the weighted moments method are simplicity and the elimination of the error of the common moments method. The major question of its application is the selection of the scale factor, which is of decisive importance in both the approximation of the distribution and the identification of the parameters. The method can easily be programmed for digital computers, so its further testing and application is justified.

SYMBOLS

$c(t)$ — density function of concentration
c_i — coefficient, constant
$f(t)$ — density function of the residence time distribution
i, j — subscripts
k — order of the moment
k_{max} — maximum order of the moment
$m_k^w(f)$ — k th weighted moment of function f using weight function w
$m_k(f)$ — k th weighted moment of function f using weight function $\exp(-st)$
N — integer, upper limit
q — volumetric flow rate
R — coefficient, constant
s — time scale-factor
t — time variable
T — upper bound of integration of m_k
t_m, $t_{m\,in}$, $t_{m\,out}$ — mode
Δt — time difference
$u(t)$ — input concentration density function
V_1, V_2 — tank volume
$w(t)$ — weight function
$y(t)$ — output concentration density function
$\tilde{y}(t)$ — the approximation of $y(t)$
α — recirculation coefficient
δ_{ij} — Kronecker's-delta
τ, τ_1, τ_2 — mean residence time
φ_i — element of the orthogonal function set
μ_k — common moment
σ — standard deviation
$\delta(t)$ — Dirac's delta

REFERENCES

1. Levenspiel, O.: Chemical Reaction Engineering, Chap. 9. Wiley, New York, 1962.
2. Kafarov, V. V., Vygon, V. G. and Gordeev, L. S.: Theoret. Found. Chem. Engng. *1968*, 2, 228.
3. Mixon, F. O., Whitaker, D. R. and orcutt, J. C., A. I. Ch. E. J. *1967*, 13, 21.
4. Østergaard, K. and Michelsen, M. L.: Can. J. Chem. Engng. *1969*, 47, 107.
5. Michelsen, M. L., Østergaard, K.: Chem. Engng. Sci. *1970*, 25, 583.
6. Simándi, B., Bálint, A., Sawinsky, J.: Study of Time Distribution in Rotating Disc Extractor with Weighted Moments Method. Symposium on the Application of Computation Technique in Technical Chemistry, Veszprém, 1982. Sept.
7. Anderssen, A. S. and White, E. T.: Can. J. of Chem. Engng. *1969*, 47, 288.
8. Anderssen, A. S. and White, E. T.: Chem. Engng. Sci. *1971*, 26, 1203.
9. Wolff, H-J., Radeke, K-H. and Gelbin, D.: Chem. Engng. Sci. *1979*, 34, 101.
10. Szegő, G.: Orthogonal Polynomials, American Mathematical Society, New York, 1939.
11. Powell, J. J. D.: Computer Journal, *1965*, 7, 303.

РЕЗЮМЕ

В стати изложены результаты симуляции рециркуляционной системы непрерывного течения методом весовых моментов. Целью авторов является определение влияния шума измерения, фактора масштаба времени, количества моментов и условий отреза на значение параметров. Изучали приближение функции плотности распределения времени пребывания использованием весовых моментов с помощью Лагуер-полиномов. Установили, что как и при идентификации так и при приближении выбор фактора масштаба времени в окресности оптимума имеет решающее значение так как при отходе от этого влияние шума измерения на значение параметров увеличивается.

HUNGARIAN JOURNAL
OF INDUSTRIAL CHEMISTRY
VESZPRÉM
Vol. 11. pp. 173-184 (1983)

CALCULATION OF THE DYNAMIC PROCESSES OF A PERFECTLY MIXED TANK BY ORTHOGONAL COLLOCATION

Mrs. E. Varga and B. Lakatos

(Research Institute for Technical Chemistry of the Hungarian Academy of Sciences, Veszprém, Hungary)

Received: November 23, 1982.

A short review is presented of the MWR-type methods, and the orthogonal collocation method is applied for the determination of the time-dependent—transient—processes of a dynamic system. Orthogonal collocation is carried out over the infinite interval and the generalized Laguerre polynomials—determined by the weight-function exp $(-\alpha x)$—are used. The effects of changing α upon the solution were studied on several examples. The results are compared with the values obtained by the fifth and sixth-order Runge–Kutta combination method.

Introduction

The computation of the dynamic processes of the operation units of technical chemistry is a very important, but often complicated operation, especially for complex, multi-unit systems. Therefore, methods which offer increased computation speed over the traditional methods (such as, e.g. the Runge–Kutta, predictor-corrector, and finite differences, etc.) are of special importance. This led us to investigate the method of weighted residuals (MWR), and especially that of the orthogonal collocation [1]. With these methods the ,,goodness'' of the solution depends on the selection of the trial functions. In the case orthogonal collocation is determined by a preselected weight function in the orthogonality conditions.

MWR is a general method for the solution of differential equations and equation sets. The solution is expressed in advance by so-called trial-functions—selected on the basis of some conditions—which have coefficients that have to be determined later on. These constans are selected in such a manner that the expression yields—in a certain sense—the best solution of the differential equation.

In general, the method is used over finite intervals, but in many problems at least one of the variables spans across the entire, infinite interval (generally,

this variable is the time variable). This led us to study the solution of such problems. The test functions used by us are the generalized Laguerre polynomials.

The Essence of MWR

Let us consider the following differential equation.

$$L(y)=0 \qquad \text{in } V$$
$$y=y_0 \qquad \text{at } S \ (S \text{ is the limit of } V)$$

where L is the differential operator.

The solution is sought in the form of Eq. 1 with y_i-s being the trial functions mentioned earlier:

$$y_N=y_0+\sum_{i=1}^{N} c_i y_i \tag{1}$$

Let us assume that y_i-s fulfill the homogeneous boundary conditions. Thus, each c_i fulfills the boundary condition of the differential equation. The residual can be defined by Eq. 2 with the substitution of y_N into the differential equation:

$$R(c_i, x, y)=L(y_N) \tag{2}$$

If y_N is a true solution, then the condition $R=0$ is fulfilled.

c_i-s are selected in such a manner that R becomes zero in some average sense. In general, the weighted integrals of R have to be zero, i.e. the conditions expressed by Eq. 3 have to be fulfilled:

$$(w_j, R)=0, \quad j=1, 2, \ldots N \tag{3}$$

where (u, v) is the internal multiple for which, according to the difinition, it holds that:

$$(u, v):=\int_V uv\, dV. \tag{4}$$

Thus, N conditions are obtained for the Nc_i-s, and from these, c_i-s can be calculated. Weight functions w_j can be selected in several manners, consequently, various conditions are obtained. Accordingly, several classes of MWR can be distinguished.

One of the best known selection possibilities is $w_j=y_j$. This is known as GALERKIN'S method.

The next class is the least square method, for which:

$$w_j=\frac{\partial R}{\partial c_j} \tag{5}$$

This is equivalent to the minimalization of the following integral:

$$\int_V R^2(c_i, x, y)\, dV \tag{6}$$

The next one is the momentum-method, where:

$$w_j=x^{j-1} \tag{7}$$

Finally, the collocation method calls for:

$$w_j = \delta(x - x_j) \tag{8}$$

and the DIRAC delta offers:

$$\int_V w_j R \, dV = R \Big|_{x_j} \tag{9}$$

Here, x_j-s are the so-called colocation points. Thus, the residual assumes zero value at N points. With increasing N, R becomes zero more frequently, and it can be assumed that it becomes zero at other places as well.

The collocation points can be selected arbitrarily. Therefore, for low-order approximations the results strongly depend on the selection of the points. In orthogonal collocation the arbitary selection of the points is no longer there, because the points are the roots of one of the elements of the orthogonal polynomial system.

The results of VILLADSEN and STEWART [2] are important in this field. They applied collocation for the solution of boundary problems. Their test functions are orthogonal polynomials and the collocation points are the roots of the orthogonal polynomial. The coefficients are not calculated, rather the values of the solution are calculated at the colocation points and so matrix equations have to be solved.

This method was used for the solution of numerous boundary problems collocated over a finite interval (1–4).

Often, however, at least one variable changes over an infinite interval. There have been several attemps to solve such problems [2, 3, 5–8].

There are two possibilities of obtaining on orthogonal system over an infinite interval [8]:

1. the infinite interval is transformed into a finite one by one of the following two transformations:

$$a) \quad u = \frac{1}{1+t} \qquad 0 \leq t < \infty \tag{10}$$

$$b) \quad u = \exp(-t) \qquad 0 \leq t < \infty \tag{11}$$

2. a weight function is used, which indicates an orthogonal system over the infinite interval. For example:
   — Laguerre polynomials over $(0, \infty)$ with weight function $w(x) = \exp(-x)$
   — Hermite polynomials over $(-\infty, \infty)$ with weight function $w(x) = \exp(-x^2)$.

In general, the first polynomial systems are used for collocation over the infinite interval [7].

Generalised Laguerre Polynomials

An orthogonal polynomial system, different from those described in literature, is studied here. The orthogonality conditions is given by Eq. 12:

$$\int_0^\infty e^{-\alpha t} L_n(t) L_1(t) \, dt = \delta_{n1} \tag{12}$$

where exp $(-\alpha x)$ is the weight function. The polynomials thus defined can be considered generalised LAGUERRE polynomials. (For $\alpha=1$ the previously mentioned Laguerre polynomials are obtained [9]).

$L_n(t)$ used in Eq. 12 is an n-th order polynomial in t. In the following part of this paper these polynomials are used as trial functions for the determination of the time-dependent—transient—processes of a dynamic system. The following calculation method is used. The collocation points are given by $t_0=0$ and the roots of the polynomial $L_N(t)$.

The generalised Laguerre polynomial:

$$L_i(t)=\sqrt{\alpha}\sum_{j=0}^{i}\binom{i}{j}\frac{(-\alpha t)^{i-j}}{(i-j)!} \tag{13}$$

Using this polynomial the solution is sought in the form of Eq. 14:

$$y_N(t)=\sum_{i=1}^{N+1} a_i L_{i-1}(t)=\sum_{i=1}^{N+1} d_i t^{i-1} \tag{14}$$

Let us consider a first-order differential equation:

$$\frac{dy}{dt}=f(y,u) \qquad y(0)=y_0 \tag{15}$$

If the solution is sought in the form of Eq. 14, then the values of y_N and its derivatives at the collocation points can be written as:

$$\begin{aligned} y_N(t_j)&=\sum_{i=1}^{N+1} d_i t_j^{i-1} \\ \left.\frac{dy_N}{dt}\right|_{tj}&=\sum_{i=1}^{N+1}\left.\frac{dt^{i-1}}{dt}\right|_{tj} d_i \end{aligned} \tag{16}$$

The relationships in Eq. 16 can be expressed in matrix form as well:

$$\overline{y_N}=Q\bar{d} \tag{17}$$

$$\overline{\frac{dy_N}{dt}}=C\bar{d} \tag{18}$$

where:

$$Q=\begin{bmatrix} 1 & t_0 & \dots & t_0^N \\ 1 & t_1 & \dots & t_1^N \\ \vdots & \vdots & & \vdots \\ 1 & t_N & \dots & t_N^N \end{bmatrix} \qquad C=\begin{bmatrix} 0 & 1 & 2t_0 & \dots & Nt_0^{N-1} \\ 0 & 1 & 2t_1 & \dots & Nt_1^{N-1} \\ \vdots & & & & \\ 0 & 1 & 2t_N & \dots & Nt_N^{N-1} \end{bmatrix}$$

$$\bar{y}_N=\begin{bmatrix} y_N(t_0) \\ y_N(t_1) \\ \vdots \\ y_N(t_N) \end{bmatrix} \qquad \bar{d}=\begin{bmatrix} d_1 \\ d_2 \\ \vdots \\ d_{N+1} \end{bmatrix}$$

Expressing $\bar{d}$ from Eq. 17 and substituting it into Eq. 18 the derivatives expressed by the function values are obtained:

$$\frac{\overline{dy_N}}{dt} = C\bar{d} = CQ^{-1}\bar{y}_N = A\bar{y}_N \tag{19}$$

Eq. 19 can be substituted into Eq. 15 yielding:

$$A\bar{y}_N = \bar{f} \tag{20}$$

where:

$$\bar{f} = \begin{bmatrix} f[y_N(t_0),\ u(t_0)] \\ f[y_N(t_1),\ u(t_1)] \\ \vdots \\ f[y_N(t_N),\ u(t_N)] \end{bmatrix}$$

As the initial value is given, the first row of the matrix equation can be omitted. The initial values can then be used for the rows yielding N equations with N unknowns (the values of the function sought at the colocation points). Thus, an equation set has to be solved which, in the general case, is nonlinear. Having obtained the solution of the equation set, the values of the function sought can also be obtained at further t places following the calculation of the coefficients of the approximating polynominal. These coefficients can be calculated from

Eq. (21):

$$\bar{d} = Q^{-1}\bar{y}_N \tag{21}$$

In the following examples, the effects of changing α and N upon the solution were investigated.

The results were compared with those of the fifth and sixth order combinational Runge–Kutta method.

Examples

The first dynamic system studied is a perfectly mixed tank reactor, in which a consecutive reaction:

$$A \xrightarrow{a} B \xrightarrow{b} C$$

takes place. Its schematic is shown in *Fig. 1.*

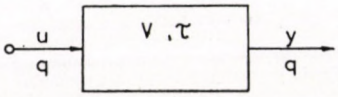

Fig. 1

Perfectly mixed reactor with a consecutive reaction of type: $A \xrightarrow{a} B \xrightarrow{b} C$

The differential equation which describes the process is:

$$\tau \frac{dx_1}{dt} = u - ax_1 - x_1$$

$$\tau \frac{dx_2}{dt} = ax_1 - bx_2 - x_2 \tag{22}$$

$$x_1(0) = x_2(0) = 0$$

Using the previously mentioned polynomials and symbols the matrix equations are as follows:

$$A\bar{x}_1 + (a+1)\bar{x}_1 = \bar{u}$$

$$A\bar{x}_2 + (b+1)\bar{x}_2 - a\bar{x}_1 = \bar{0} \tag{23}$$

where:

$$\bar{x}_i = \begin{bmatrix} x_i^{(N)}(t_0) \\ x_i^{(N)}(t_1) \\ \vdots \\ x_i^{(N)}(t_N) \end{bmatrix} \quad i = 1,\ 2 \qquad \bar{u} = \begin{bmatrix} u(t_0) \\ u(t_1) \\ \vdots \\ u(t_N) \end{bmatrix}$$

After rearrangement, a linear equation set consisting of 2 N equations with 2 N variables is obtained.

Its solution yields the values of the functions sought at the colocation points.

The calculations were carried out with various u and N values with different input functions, u.

$$\text{Here:} \quad u = \text{At} \exp(-Bt),$$

and the parameter values are:

$$\tau = 10, \quad a = 0.1 \quad \text{and} \quad b = 0.5.$$

For any α and $N = 5{,}6$ the $x_i^{(N)}$ gave a good approximation of the solution. However, the approximation was good only up to the last collocation point as time value. With decreasing α the collocation points become more spread on the time axis, so the solution can be approximated further on. This is illustrated by *Fig. 2* and *3*.

The next dynamic process studied is a mixed-order consecutive reaction taking place in a perfectly mixed tank reactor. There are two reactions taking place:

1. $A \rightarrow B$ is a first-order one, and
2. $A + B \rightarrow C$ is a second-order one.

The concentrations are:

for A: x_1

for B: x_2

The differential equation set becomes:

$$\tau \frac{dx_1}{dt} = u_1 - ax_1 - bx_1x_2 - x_1$$

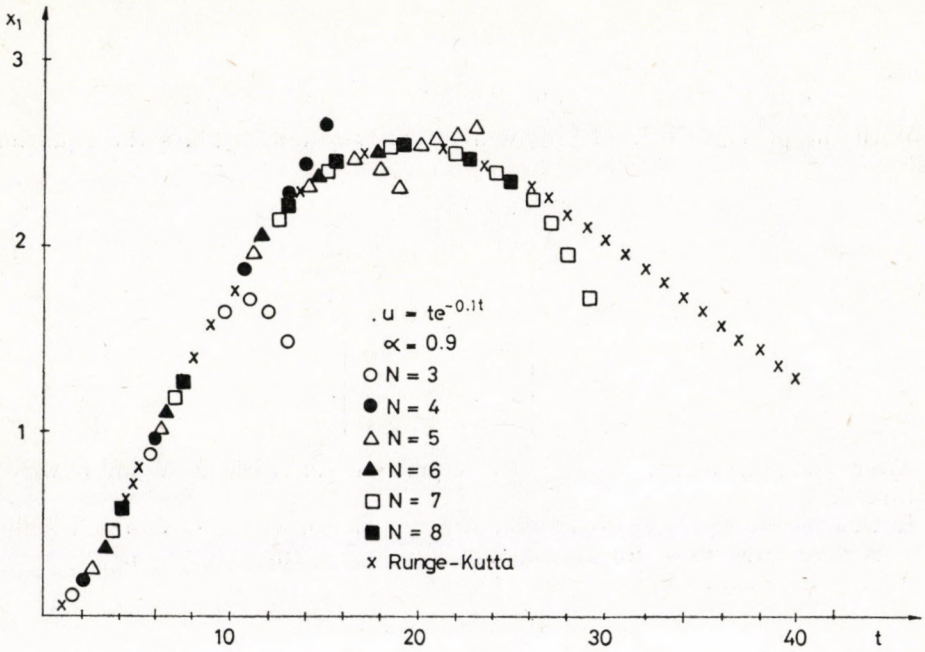

Fig. 2

The response function of a perfectly mixed reactor (with a consecutive reaction) for $\alpha = 0.9$

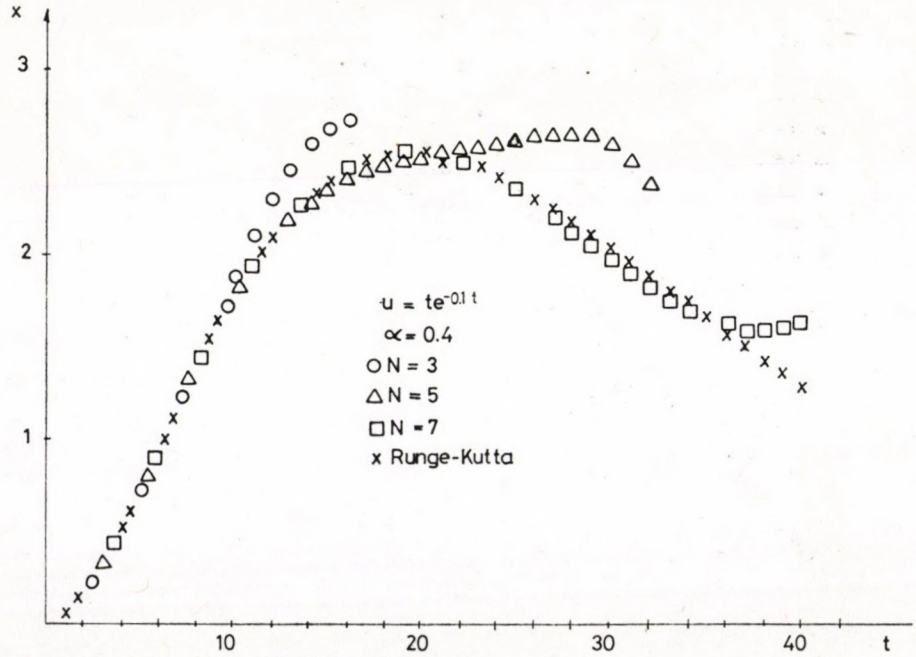

Fig. 3

The response function of a perfectly mixed reactor (with a consecutive reaction) for $\alpha = 0.4$

$$\tau \frac{dx_2}{dt} = ax_1 - bx_1x_2 - x_2 \tag{24}$$

$$x_1(0) = x_2(0) = 0$$

With the previously used polynominal system and symbols the equations become:

$$A\bar{x}_1 + (a+1)\bar{x}_1 + b\bar{f} = \bar{u}_1$$

$$A\bar{x}_2 + \bar{x}_2 - a\bar{x}_1 + b\bar{f} = \bar{0} \tag{25}$$

where:

$$\bar{f} = \begin{bmatrix} x_1^{(N)}(t_0) & x_2^{(N)}(t_0) \\ x_1^{(N)}(t_0) & x_2^{(N)}(t_1) \\ \vdots & \\ x_1^{(N)}(t_N) & x_2^{(N)}(t_N) \end{bmatrix}$$

After rearrangement, a nonlinear equation set with 2 N unknowns is obtained.

In this case the values of the unknown function have to be obtained. Calculations were carried out for various α values and u_1 input functions.

Again, the form of u_1 is:

$$u_1 = \mathrm{At} \exp(-Bt)$$

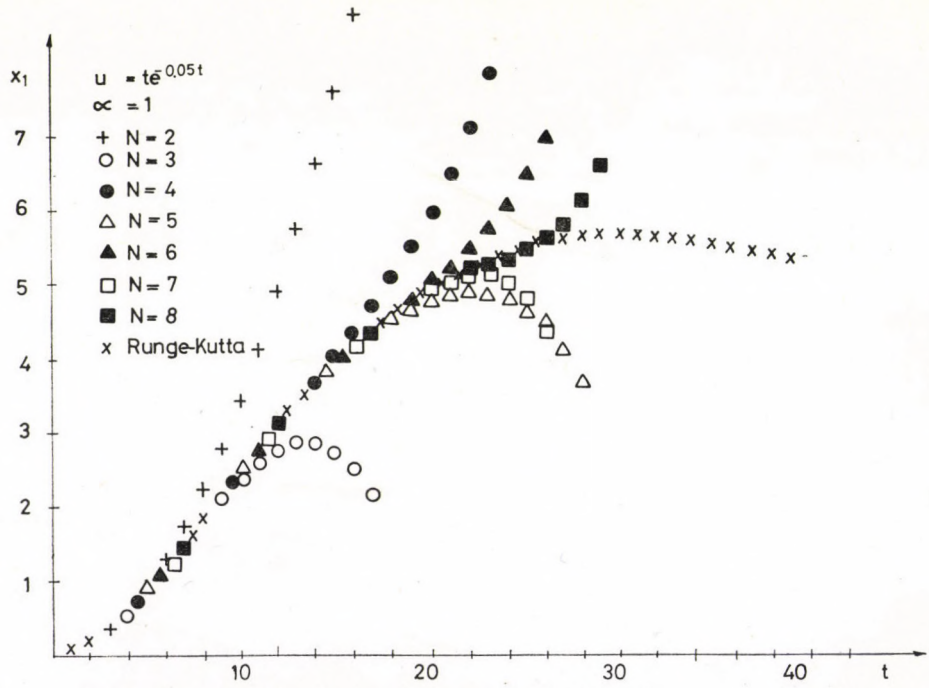

Fig. 4.

The response function of a perfectly mixed reactor (with a mixed-order consecutive reaction) for $\alpha = 1.0$.

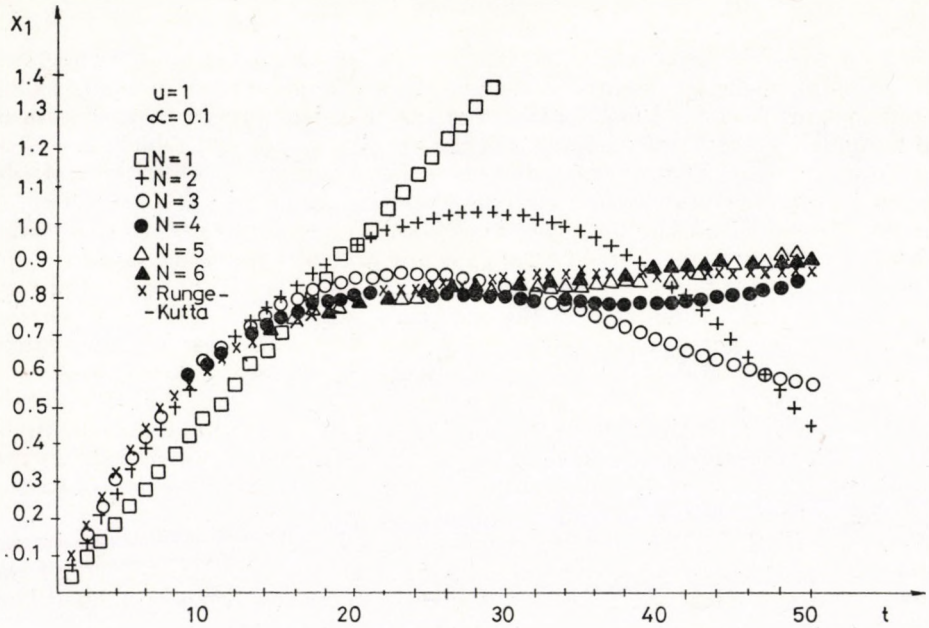

Fig. 5

The response function of a perfectly mixed reactor (with a mixed order consecutive reaction) for $\alpha = 0.1$.

and the parameters are:

$$\tau = 10, \quad a = 0.1 \quad \text{and} \quad b = 1.2.$$

The study of the effects of α and N yielded similar results. These are shown in *Fig. 4* and *5*.

Calculations were carried out by an IBM 3031 computer. The linear equation set was solved by a matrix triangulation method. Powell's iteration method was used for the solution of the nonlinear equation set. This determined the sum of the squares of the nonlinear functions without the calculation of the derivatives.

Finally, for comparison purposes, the computation times are shown in *Table 1.*

Table 1.

The calculation time of the various solution methods of a dynamic system (with a consecutive reaction)

RUNGE–KUTTA	Orthogonal colocation			
	$N=3$	$N=5$	$N=6$	$N=8$
6.7 sec	2.5 sec	3.6 sec	4.2 sec	5.1 sec

Summary

Based on the results of these studies it can be concluded that orthogonal collocation over the $(0, \infty)$ interval by generalised Laguerre polynomials seems an efficient method for the calculation of the transient processes of the linear and nonlinear systems of technical chemistry. Its major assets include speed, and—because of its iterative nature—the lack of convergence problems. Only accuracy problems may occur. By changing the values of the parameter, α, and the number of polynomials, N—i.e. by an appropriate setting of the time constant of the system studied—very accurate results could be obtained for the entire, important section of the transients. If necessary, this can be improved by a successive repetition of the process. α was varied over a wide range, and consequently, it appears from the results that α has an optimum range for which the method shown by us gives the best results. For excessive α values, the interval set by the collocation points is smaller than the entire significant section of the transient, consequently, the solution does not apply for the entire section either. If α is too small, then the collocation points are spread too much over the $(0, \infty)$ interval, and only 2–3 points fall onto the entire important section yielding a solution of insufficient accuracy.

There is still the task of developing a method by which α and N can be set automatically—i.e. set by the computer after the preliminary analysis of the system, and the decision about any successive repetition can be made. This will be dealt with in a forthcoming paper.

SYMBOLS

a	reaction rate coefficient
A	parameter of the input function, an $(N+1)(N+1)$ matrix
a_i	coefficients of the polynomials, $i=1, 2, \ldots, N+1$
b	reaction rate coefficient
B	parameter of the input function
C	an $(N+1)(N+1)$ matrix
c_i	coefficients of the polynom, $i=1, 2, \ldots, N+1$
$\bar{d}$	a vector of $N+1$ elements
d_i	coefficients of the polynomial, $i=1, 2, \ldots, N+1$
$\bar{f}$	a vector of $N+1$ elements
$f(y, n)$	function
L	differential operator
$L_n(t)$	generalized LAGUERRE polynomial
MWR	method of weighted residuals
N	number of trial functions
q	volumetric flow rate
Q	an $(N+1)(N+1)$ matrix
$R(c_i, x, y)$	residual
S	boundary of V
t	time
t_i	collocation points over $(0, \infty)$, $i=0, \ldots, N$
u	function
$\bar{u}$	a vector of $N+1$ elements
$\bar{u}_1$	a vector of $N+1$ elements
V	space, volume
w_j	integration weight function, $j=1, \ldots, N$
x	independent variable
x_j	collocation points in V, $j=1, \ldots, N$
$x_i(t)$	the function sought, $i=1, 2$

$\bar{x}_i$	a vector of $N+1$ elements, $i=1, 2$
$x_i^{(N)}$	an approximation of the function sought, $i=1, 2$
y_0	initial value
y_i	trial functions, $i=1, \ldots, N$
$\bar{y}_N$	a vector of $N+1$ elements
$y_N(t)$	an approximating polynomial
α	characteristics of the weight function included in the orthogonality condition
$\delta_{(x-x_j)}$	DIRAC's delta
δ_{ni}	KRONECKER's delta
$\tau=\frac{V}{q}$	average residence time

REFERENCES

1. FINLAYSON, B. A.: The Method of Weighted Residual and Variational Principles, Academic Press, New York and London, 1972.
2. VILLADSEN, J. and STEWART, W. E.: Chem. Engng. Sci. *1967*, 22, 1483.
3. WILLADSEN, J. and SORENSEN, J. P.: Chem. Engng. Sci. *1969*, 24, 1337.
4. FINLAYSON, B. A.: Chem. Engng. Sci. *1971*, 26, 1081.
5. SORENSEN, J. P. and STEWART, W. E.: Chem. Engng. Sci. *1974*, 29, 811.
6. DEL GIUDICE S. and TROTTA, A.: Chem. Engng. Sci. *1978*, 33, 697.
7. BIRNBAUM, I. and LAPIDUS, L.: Chem. Engng. Sci. *1978*, 33, 455.
8. CABAN, R. and CHAPMAN, T. W.: Chem. Engng. Sci. *1981*, 36, 849.
9. GÓRECKI, H.: Analiza i synteza ukladow regulacji z opozniemiem. WNT., WARSZAWA, 1971.

РЕЗЮМЕ

Авторы кратко излагают методы MVR и используют ортогональную коллокацию на переходные процессы некоторой динанической системы. Ортогональную коллокацию проводили в бесконечном интервале времени использованием Лагуер-полиномов которые определили с помощью весовой функции $e^{\alpha x}$.

Влияние изменения α изучали на конкретных примерах. Результаты сравнивали значениями полученными комбинированным методом Рунге-Кутта пятого и шестого порядков.

HUNGARIAN JOURNAL
OF INDUSTRIAL CHEMISTRY
VESZPRÉM
Vol. 11. pp. 185-192 (1983)

ADSORPTION RATE ON NATURAL MORDENITES

J. SZABÓ and P. KÁLDI

(Department of Chemical Technology, University of Chemical Engineering, Veszprém, Hungary)

Received: November 26, 1982.

The rate of intracrystalline diffusion was examined in natural mordenites. Based on theoretical considerations and experimental evidence it could be proved that the heterogeneous size-distribution of the crystallites significantly influences the rate of sorption. Carbon dioxide was used as sorbeate. Sorption measurements were carried out at constant volume. The size distribution function of the crystallites was optimized on the basis of the experimental results, its standard deviation, and the constant, $D/\bar{l}^2$, which characterises the diffusion process.

Introduction

Both natural and synthetic zeolites are gaining importance in separation techniques and catalytic reactions. With respect to component separation, it is the knowledge of the sorption equilibrium on a given zeolite that has to be known, while in catalysis, it is the selectivity of the zeolite which is of importance. However, both are influenced by the rate of the respective process, and practical application of a zeolite depends at least as much on the sorption rate as on the other two characteristics.

Disregarding the transfer flows, which occur on the macroscopic, external surfaces of granular or granulated zeolite sorbents or catalysts, the overall rate in a separation process is controlled by either *intercrystalline* or *intracrystalline* diffusion, or, in certain cases, by mixed diffusion (their resultant) [1, 2]. In the cases of catalytic reactions, reaction rate is superimposed onto the other three, previously mentioned diffusion rates. This paper deals with the rate of intracrystalline diffusion.

Theoretical

Intracrystalline diffusion plays a major role in all of the separation and/or catalytic processes, where the molecular size of the reactants and the diameter of the zeolite crystal channel are commensurable. Diffusion taking place in the

channels of zeolite crystals is formally described by FICK's second law, just as any other diffusion process. When FICK's second law is applied—along with its boundary conditions—to any geometric shape, then the equation of the overall diffusion rate contains the diffusion coefficient, the characteristic geometric size of the particle (crystallite) and other constants which arise from the boundary conditions. From among these coefficients, the effects of the size of the crystallite will be dealt with here. It will be modelled by the diffusion process, which takes place in natural mordenite.

Because of the dimensions of its channels, mordenite can be considered as a unidimensional medium—or geometric shape—in diffusion studies.

Selecting the case of component uptake from a constant volume space as boundary conditions, the diffusion rate is given by Eq. (1) [3]:

$$\frac{m_t}{m_\infty} = 1 - \sum_{n=1}^{\infty} \frac{2\alpha(1+\alpha)}{1+\alpha+\alpha^2 q_n^2} \times \exp\left(-\frac{q_n D}{l^2} t\right) \tag{1}$$

where:

m_∞ is the mass of material adsorbed in equilibrium (g)

$\frac{m_t}{m_\infty}$ the fraction of the equilibrium mass of material sorbed up to time t (g/g)

t time (s)

D diffusion coefficient (m^2/s)

l length of the crystallite (m)

$\alpha = \frac{1-\varphi}{\varphi}$ where φ is the fraction of material in equilibrium adsorbed from a space of constant volume (g/g)

q_i non-zero roots of the equation $tg\, q_n = -\alpha q_n$

Eq. 1, which describes the time-dependence of the adsorbed fraction, m_t/m_∞, can and should be applied for a crystalline matrix as a model only when the characteristic size, l is identical for each element of the matrix.

If the size of the crystallites changes in the matrix, then Eq. 1 has to be modified according to Eq. (2). taking into account the occurrency frequency of any size 1:

$$\frac{M_t}{M_\infty} = \sum_{i=1}^{\infty} \left(\frac{m_t}{m_\infty}\right)_i = 1 - \int_0^\infty f(l) \sum_{n=1}^{\infty} \frac{2\alpha(1+\alpha)}{1+\alpha+\alpha^2 q_n^2} \times \exp\left(-\frac{q_n D}{l^2} t\right) dl \tag{2}$$

where:

$\frac{M_s}{M_\infty}$ is the mass fraction adsorbed by the matrix up to time t(g/g)

$f(l)$ is the density function.

For practical calculations the differential form of Eq. 2 as given by Eq. 3 is more appropriate:

$$\frac{M_t}{M_\infty} = 1 - \sum_{i=1}^{\infty} f(l_i) \Delta l \sum_{n=1}^{\infty} \frac{2\alpha(1+\alpha)}{1+\alpha+\alpha^2 q_n} \times \exp\left(-\frac{q_n D}{l_i^2} t\right) \tag{3}$$

where:

$f(l_i)$ is the average density assigned to a crystallite of size l_i over the size increment Δl.

It can be seen in Eq. (2) and (3) that the sorption rate also depends on the shape of the density function $f(l)$). In accordance with the experimental results, the normal logarithmic density function was selected for density function $f(l)$. It will be shown via calculations and plots by Eq. (3) that the size distribution of the crystallites profoundly influences the shape of the sorption curves.

Fig. 1 shows the sorption rate corresponding to an adsorbed mass fraction of $\varphi=0$. In physical, real terms $\varphi=0$ means that sorption takes place at a

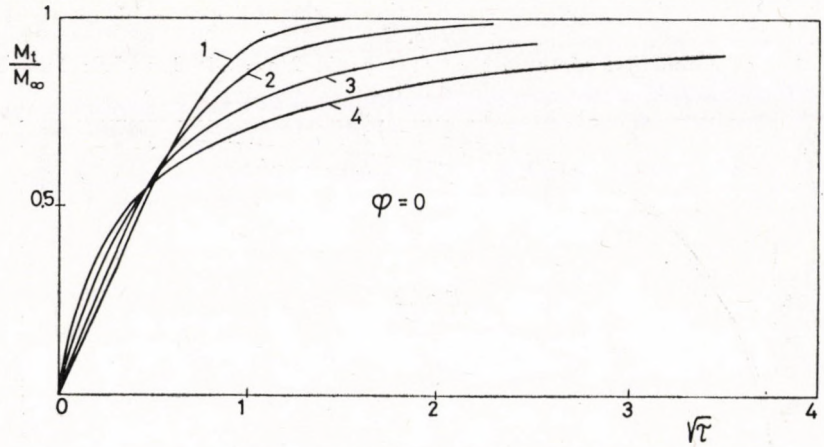

Fig. 1
Sorption as a function of time, $\varphi=0$. $1:\sigma=0$; $2:\sigma=0.5$; $3:\sigma=1.0$; $4:\sigma=1.5$

constant pressure, the volume of the vessel which contains the sorbent is infinitely large. σ values shown in the figure indicate the magnitude of the standard deviation of the normal-logarithmic distribution. The curve at $\sigma=0$ belongs to a matrix of crystallites of identical size. The more heterogeneous the matrix—i.e. the higher σ, the higher the initial sorption rate is and the slower (more extended) is the final section of sorption. The shape of the curves clearly demonstrates how erroneous—even in their orders of magnitude—those diffusion coefficient-measuring methods are, which use matrices with a heterogeneous particle-size distribution and fail to take this into account.

The adsorption rate curves of matrices with varying standard deviation—at $\varphi=0.5$—are shown in *Fig. 2*. The shape of the curves is the same as in *Fig. 1*, and also as of those in *Fig. 3* ($\varphi=0.9$).

A common characteristic of the curves of varying σ is that irrespective of their φ values, they cross over at about the same, $M_t/M_\infty \approx 0.55$ value.

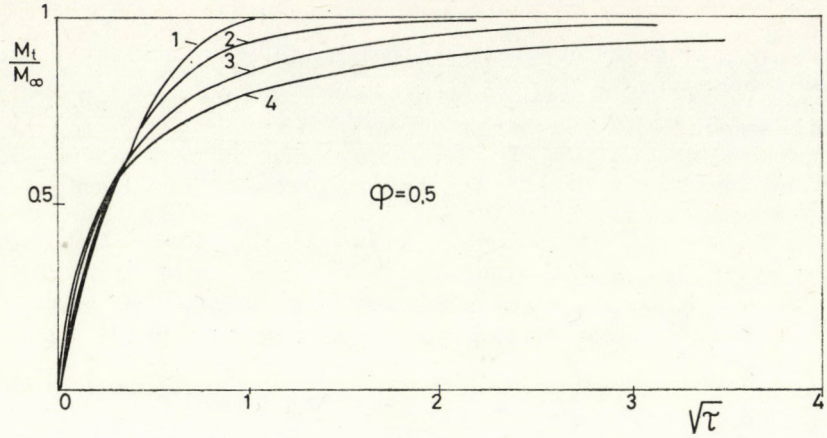

Fig. 2
Sorption as a function of time, $\varphi=0.5$. $1:\sigma=0$; $2:\sigma=0.5$; $3:\sigma=1.0$; $4:\sigma=1.5$

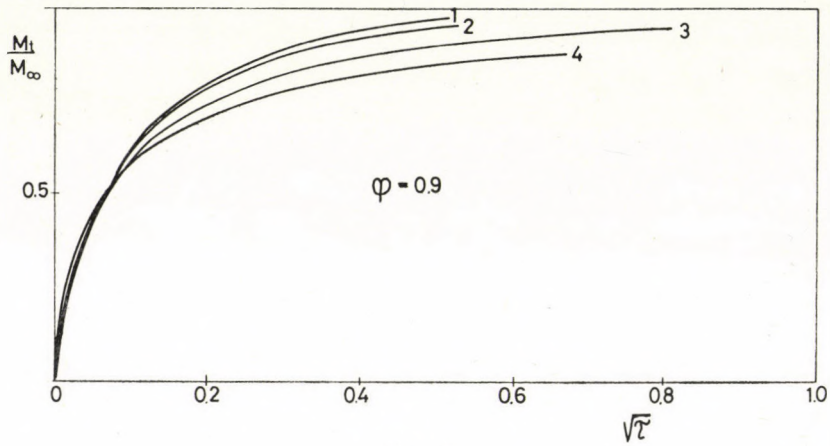

Fig. 3
Sorption as a function of time, $\varphi=0.9$. $1:\sigma=0$; $2:\sigma=0.5$; $3:\sigma=1.0$; $4:\sigma=1.5$

This fact can be utilized in diffusion rate measurements, and the diffusion coefficients thus obtained are much more accurate than those derived from the initial diffusion rates. We could not find this conclusion in literature and consider it as one of the major results of this study.

Experimental

To prove the theoretical conclusions, experiments were carried out with natural mordenite. For sorption-rate measurements, the mordenite was brought to NH_4 form, then as usual, to H form. Carbon dioxide was used as sorbeate. The schematics of the experimental set-up is shown in *Fig. 4.*

The sorbent is placed into sample container S which, together with reservoir R can be evacuated by vacuum pump V to a pressure of 0.1 Pa via valves (opened) VI and VO. Meanwhile, the sample container can be heated to 570 K. Following the evacuation step, reservoir R is filled with carbon dioxide until

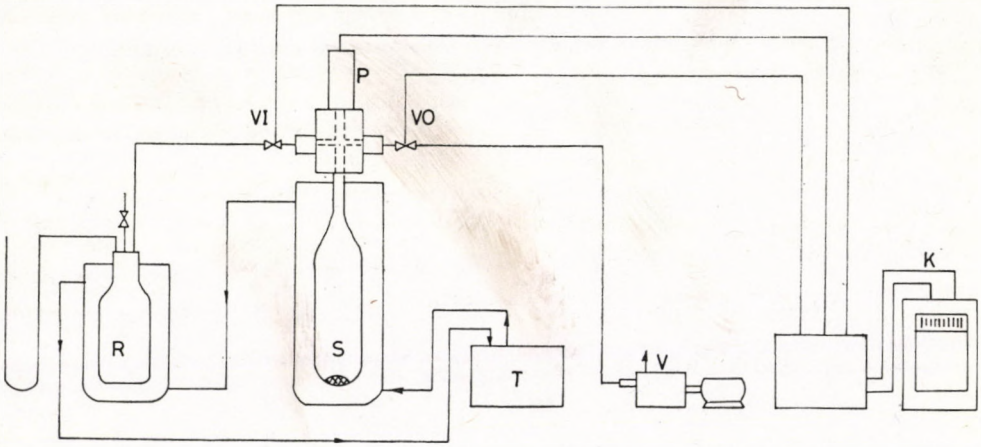

Fig. 4

Schematics of the experimental set-up
R: reservoir, S: sample container; P: Pirani gauge; VI: opening valve; VO: closing valve; T: thermostat; V: vacuum pump; K: recorder

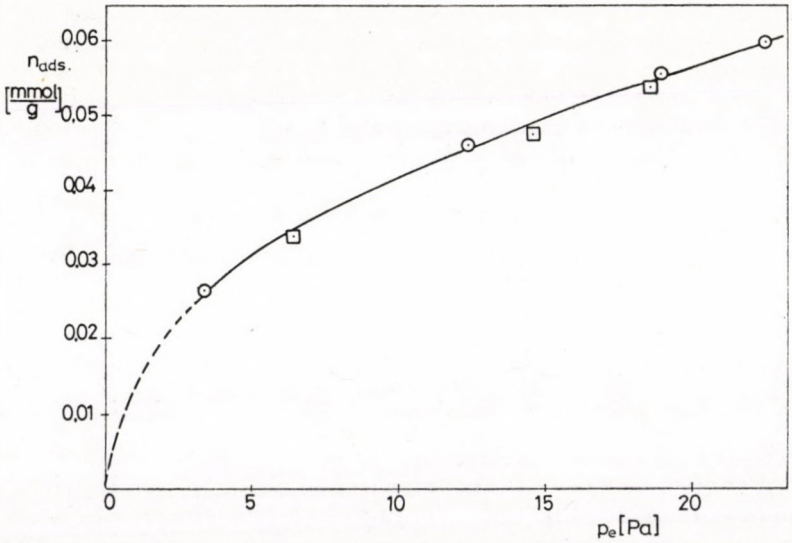

Fig. 5

Adsorption isotherm of carbon dioxide on H-form natural mordenite
0: 0.315–0.40 mm; □: 0.8–1.0 mm

the required pressure is achieved (with valves VI and VO closed). Then sample S is thermostatted at 298 K. Valve VI is opened quickly, then closed, thereby introducing into sample container S carbon dioxide of known volume and pressure. Sorption-related pressure drop is recorded by a PIRANI-type pressure gauge, P. The electric signal which corresponds to the pressure signal is then recorded by a fast recorder. The procedure can be constantly repeated, thereby the pressure can be increased in a step-wise manner and the amount of carbon dioxide adsorbed in a given pressure range, Δp can be recorded and calculated. Thus the amount of adsorbed material as a function of time can be obtained and the M_t/M_∞ vs. t relationship for the given Δp step can be evaluated. Simultaneously, the adsorption isotherm is also determined. This is shown—for two different particle sizes—in *Fig. 5*.

Sorption rate curves recorded in the respective Δp pressure ranges follow the typical shapes shown in *Fig. 1–3*. Therefore, the curves were evaluated by Eq. 3.

Eq. 3 contains four parameters:

1. φ, a measured, known value, which determines α
2. D, the unknown diffusion coefficient
3. $\bar{l}$, the unknown average length of the crystallite, the parameter of function $f(l)$
4. σ, the unknown standard deviation the parameter of function $f(l)$

The last two parameters are unknown, because the length-distribution and its parameters: l and σ of the mordenite crystallite bunches built into a natural mordenite cannot be determined experimentally. Therefore, a few common distribution functions were selected for the calculations and $D/\bar{l}^2$ was arbitrarily set to l, functions M_t/M_∞ vs. τ were generated (with $\tau = D(\bar{l}^2 \cdot t)$, and these curves were compared with the experimentally determined curves. If the shape and the parameter σ of function $f(l)$ are selected correctly, then $(M_t(M_\infty)_j$ and its $\sqrt{t_j}$ and $(M_t(M_\infty)_j$ and its $\sqrt{\tau_j}$ are linearily correlated. The correlation line passes the 0 point and its slope is $\sqrt{\frac{D}{\bar{l}^2}}$.

Thus, the computerized optimation step includes both the selection of the best distribution function, and its parameter, σ. The results of the calculations are shown in *Fig. 6*.

The lines in *Fig. 6*. fit the measured values well in the $0 \leq M_t/M_\infty \leq 0.95$ range. No bias-like scatter can be observed. The slopes yield the $\sqrt{\frac{D}{\bar{l}^2}}$ values. Naturally, D and l cannot be determined by the method outlined here. However, their respective values do not have to be known for the description of the diffusion rate, because only the $D/\bar{l}^2$ ratio occurs in the equations. A further conclusion derived from the figures is that the value of σ lies im the range of 0.8 and 0.9, independently from the actual particle size. The value of $\sqrt{D/\bar{l}^2}$ increases with the pressure. This conclusion agrees with statements found in literature and its further aspects will be treated in a forthcoming paper.

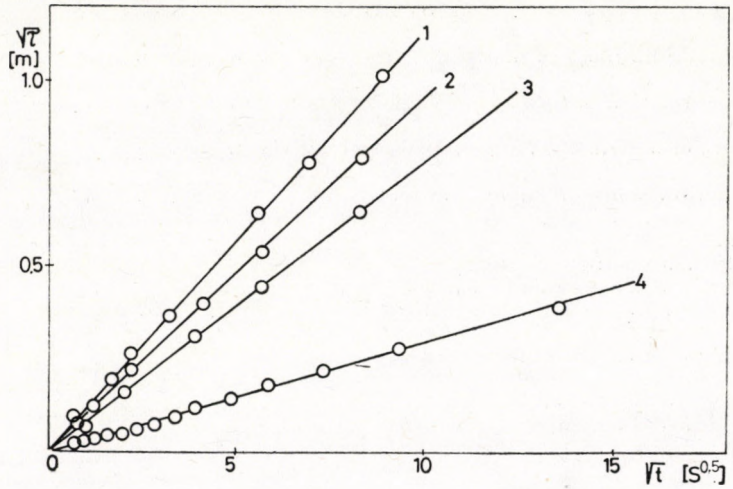

Fig. 6

Evaluation of the measured values by Eq. 3:
Particle size: 0.315–0.40 mm
1: $p_e = 22.4$ Pa, optimized $\sigma = 0.8$; *2*: $p_e = 19.0$ Pa, optimized $\sigma = 0.8$; *4*: $p_e = 3.3$ Pa, optimized $\sigma = 0.75$

We could prove, both theoretically and experimentally, that the physical model developed to describe the intracrystalline diffusion rate in natural mordenite is, indeed, correct and accurate.

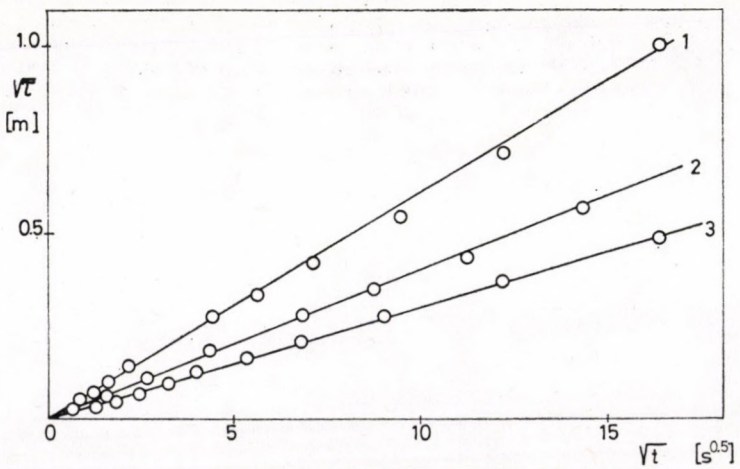

Fig. 7

Evaluation of the measured values by Eq. 2; Particle size: 0.8–1.0 mm
1: $p_e = 18.6$ Pa, optimized $\sigma = 0.9$; *2*: $p_e = 14.6$ Pa, optimized $\sigma = 0.9$; *3*: $p_e = 6.3$ Pa, optimized $\sigma = 0.8$

SYMBOLS

m_∞	equilibrium mass of material sorbed on a single crystallite, g
$\frac{m_t}{m_\infty}$	mass fraction sorbed on a single crystallite up to time t, g/g
M_∞	equilibrium mass of material sorbed by the matrix, g
$\frac{M_t}{M_\infty}$	mass fraction sorbed by the matrix up to time t, g/g
t	time, s
D	diffusion coefficient, m^2/s
l	length of a crystallite, m
φ	equilibrium mass fraction sorbed from a constant volume space, g/g
α	$\alpha=(1-\varphi)/\varphi$
q_i	non-zero roots of equation $tg\ q_n = -\alpha q_n$
$f(l)$	distribution function
σ	standard deviation
τ	modified time, m^2
p_e	equilibrium pressure, Pa

REFERENCES

1. Ruckenstein, E., Vaidyanathan, A. S. and Youngquist, R. G.: Chem. Eng. Sci., *1971* 26, 1305–1318.
2. Lap-Keung Lee, Ruthven, D. N.: Can. J. Chem. Eng., *1979*, 57, 65–70.
3. Crank, K.: The Mathematics of Diffusion, Oxford University Press, London, *1964* p. 53.

РЕЗЮМЕ

Изучали скорость интракристаллической диффузии происходящей на натуральных цеолитах. Авторы на основе теоретических предпосылок и результатах экспериментов доказали, что гетерогенное распределение размера кристаллита оказывает большое влияние на скорость сорбции. В качестве сорбтива использовали двуокись углерода, сорбцию проводили при постоянном объеме. На основе экспериментальных данных оптимизировали функцию распределения размера, дисперсию распределения и константу $(D/l)^2$ характеризующую диффузию.

HUNGARIAN JOURNAL
OF INDUSTRIAL CHEMISTRY
VESZPRÉM
Vol. 11. pp. 193-205 (1983)

LATERAL THERMAL DIFFUSIVITY OF A FLUIDIZED BED PACKED WITH TUBE BUNDLES

V. A. Borodulya, Yu. S. Teplitsky, Yu. G. Epanov and I. I. Yanovich

(Heat and Mass Transfer Institute, BSSR Academy of Sciences, Minsk, USSR)

Received: January 20, 1983.

The heat impulse method has been used to experimentally investigate the mechanism of lateral diffusion of fluidized large-particle beds packed with tube bundles. The data obtained were analyzed using the hyperbolic heat conduction equation. The experimental and theoretical curves calculated by this equation for heat-marked solids mixing were found to coincide well. The point is different when this process would be governed by the classical heat conduction equation. The lateral thermal diffusivity of a bed and relaxation time are obtained by the least square method. The values of thermal diffusivity have proved to be close to those determined by the classical heat conduction equation. The generalized correlations were derived for calculating lateral thermal diffusivity of fluidized beds packed with tube bundles.

Introduction

The fluidized bed packed with horizontal tube bundles is applied when it is necessary to remove a large amount of heat from the bed as is the case with the fluidized bed catalytic reactor and the fluidized bed combustor (F.B.C.). Tubes in the fluidized bed hinder the growth of gas bubbles, thus enhancing the interphase heat transfer, but at the same time reducing the intensity of internal heat and mass transfer.

Kato et al. [1] measured lateral thermal diffusivity of a fluidized small-particle ($d<1$ mm) bed packed with horizontal tubes. Baskakov and Pakhaluev [2], Berg et al. [3] investigated lateral thermal diffusivity of a bed, mainly, of small particles. Up to the moment no study has been practically made of lateral heat and mass transfer in fluidized large-particle ($d>1$ mm) beds packed with tube bundles, which is of major importance for fluidized bed combustors.

In the present work, experimental study is made of lateral thermal diffusivity of a fluidized large-particle bed packed with a tube bundle. The results are analyzed using the hyperbolic heat conduction equation.

Experimental

The experimental study of the heat transfer mechanism in free and packed fluidized beds was performed on the set-up presented in *Fig. 1.* The fluidized bed was formed in a metal 400×250 mm^2 cross section column 1.5 m high. The front wall of the column was made of organic glass to perform visual observations. The gas distributor was composed of two steel perforated plates (staggered holes 10 mm dia with a 14 mm pitch) with a dense cloth layer being pressed between. The hydraulic resistance of the gas distributor over the fluidization velocity range $50 \div 113$ cm/s was governed as $\Delta P = 8 \cdot u_0^{1.35}$, Pa. The horizontal tubes across the column served as a packing in the fluidized bed *(Fig. 1)*. 30 mm dia duralumin tubes with 1 mm thick wall were arranged as staggered ($S_h = S_v = 100$; 60; 45 mm) and in-line ($S_h = S_v = 100$; 60; 45 mm) bundles. The parameters of the test solids are listed in *Table 1.* The experimental conditions are given in *Table 2.*

The procedure of the experiments on lateral solids mixing was as follows. The bed was fluidized with room temperature air at a prescribed fluidization velocity. The column *(Fig. 1)* was provided with a thin removable partition that divided the system into heating ($0 \leq \eta < R$) and test ($R < \eta \leq 1$) chambers. The quantity R amounted to 0.15. A small fraction (less than 1% of the bed volume) of the material preheated up to 400–600 °C was charged into the heating chamber. After some time required for hot solids mixing in the heating chamber (about 5–10 s), the partition was quickly (for no more than 0.5 s) removed from the bed, and the bed temperature, T, averaged over the vertical surface, η_0, was measured by chromel-coppel thermocouples in time. De-

Table 1.

Characteristics of the Test Dispersed Materials

Dispersed materials	d mm	u_{mf} cm/s	ϱs g/cm^3	δ/d	Notations in the text
Quartz sand	0.60	20	2.54	0.22	s.1
Glass beads	1.75	63	2.60	0.20	s.2
Millet	2.0	55	1.02	—	s.3
Chamotte crumb	3.0	95	2.30	0.16	s.4

Table 2.

Experimental Conditions in the Fluidized Beds Packed with Tube Bundles

Material	H_0, cm	u_0, cm
s.1	22; 32; 48.5	$39 \div 139$
s.2	17; 24; 32	$64 \div 210$
s.3	24	$82 \div 147$
s.4	18.5; 23; 32; 36	$103 \div 233$

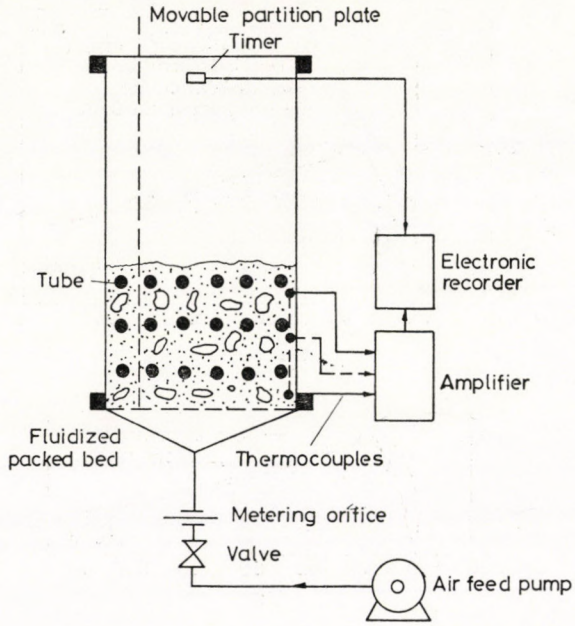

Fig. 1
Schematic of the experimental set-up

pending on the bed height, use was made of 3 to 9 parallel thermocouples uniformly distributed over the vertical surfaces, $\eta_0 = 0.5$; 1. After preamplification, the signal from the thermocouples was supplied to the electronic self-recorder to be continuously recorded on its tape. 3 to 6 independent runs were performed for each fluidization regime.

Theory

As the preliminary analysis showed, the obtained functions of the system response to impulsive thermal action are characterized by a strongly pronounced delay time, τ_0, *(Fig. 2)*. This is attributed to the limited particle velocities which, in the main, transfer heat in the gas fluidized bed. The simplest generalization of the classical heat conduction equation is:

$$\frac{\partial T}{\partial t} = a_h \frac{\partial^2 T}{\partial y^2}, \tag{1}$$

including the finite heat propagation velocity, and is known [4] to be represented by the hyperbolic heat conduction equation:

$$\frac{\partial T}{\partial t} + \tau^* \frac{\partial^2 T}{\partial t^2} = a_h \frac{\partial^2 T}{\partial y^2}. \tag{2}$$

Equation (2) in contrast to Eq. (1) incorporates one more parameter,

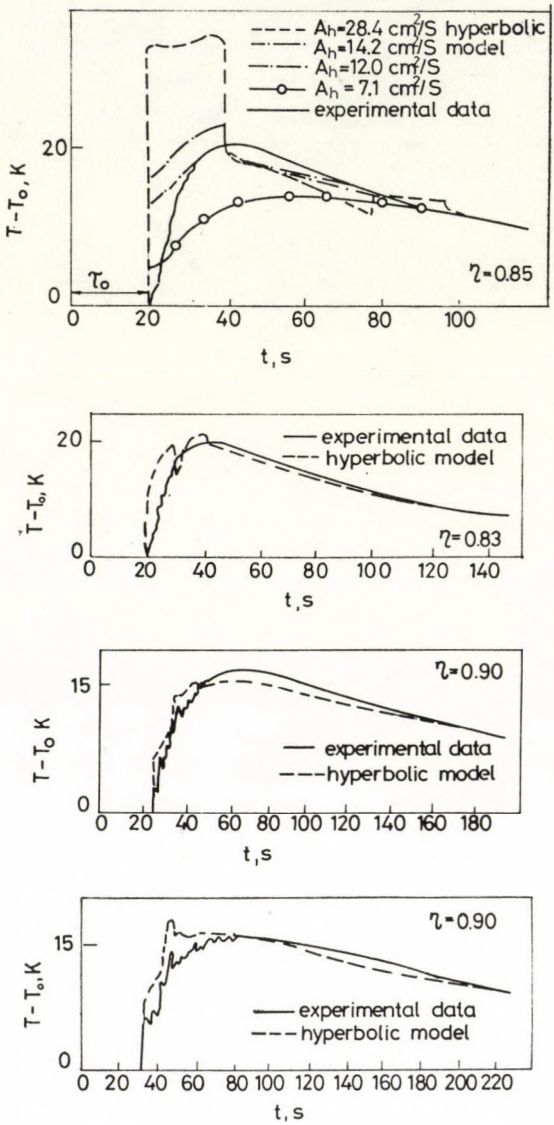

Fig. 2

Comparison of the experimental response function with the one calculated by the hyperbolic model ($H_0 = 24$ cm; $R = h/l = 0.15$): *a)* $u_0/\varepsilon_p - u_{mf} = 144$ cm/s; $v = 1.50$ cm/s, $\tau^* = 5.3$ s; *b)* $u_0/\varepsilon_p - u_{mf} = 126$ cm/s, $v = 1.35$ cm/s; $\tau^* = 5.6$ s; *c)* $u_0/\varepsilon_p - u_{mf} = 60$ cm/s, $v = 1.15$ cm/s, $\tau^* = 5.6$ s, *d)* $u_0/\varepsilon_p - u_{mf} = 38$ cm/s, $v - 0.90$ cm/s, $\tau^* = 7.6$ s

a temperature field relaxation time, τ^*. Solutions to Eq. (2) are of wave nature, the wave velocity v being related to the coefficients τ^* and a_h as:

$$v = \sqrt{a_h/\tau^*}. \tag{3}$$

Note that PETRIK and TAGANOV [5] made some advances in describing vertical solids mixing in free fluidized beds by the diffusion equation of type (2).

To include heat removal from the bed with filtered air (which is especially important for large particles) Equation (2) may be generalized to give:

$$\frac{\partial T}{\partial t}+\tau^* \frac{\partial^2 T}{\partial t^2}=a_h \frac{\partial^2 T}{\partial y^2}-\beta^*(T-T_0)\left(1+\tau^* \frac{\partial}{\partial t}\right) \tag{4}$$

where β^* is the characteristic of heat removal from the bed by filtered air. Equation (4) was used here to model lateral heat transfer in the packed fluidized bed and to calculate the theoretical functions of the systems response to impulsive thermal action.

Hyperbolic lateral heat conduction Equation (4) with the boundary conditions corresponding to the experimental ones takes a dimensionless form:

$$\frac{\partial \theta}{\partial Fo}+Fo^* \frac{\partial^2 \theta}{\partial Fo^2}=\frac{\partial^2 \theta}{\partial \eta^2}-Pe\theta\left(1+Fo^* \frac{\partial}{\partial Fo}\right) \tag{5}$$

$$\theta(0,\ \eta)=\begin{cases} 1 & 0 \leq \eta < R \\ 0.5 & \eta=R;\ \dfrac{\partial \theta(0,\ \eta)}{\partial Fo}+Pe\theta(0,\ \eta)=0 \\ 0 & R<\eta \leq 1 \end{cases}$$

$$Q=-\frac{\partial \theta}{\partial \eta}-Fo^* \frac{\partial Q}{\partial Fo}=0, \qquad \eta=0;\ 1. \tag{6}$$

The new functions: $s=\exp(PeFo)\Theta$ is introduced to solve Equations (5) and (6). System (5) and (6) can be easily reduced to the system of the equations for s:

$$\frac{\partial s}{\partial \hat{F}_o}+\hat{F}_o^* \frac{\partial^2 s}{\partial \hat{F}_o^2}=\frac{\partial^2 s}{\partial \eta^2} \tag{7}$$

$$s(0,\ \eta)=\begin{cases} 1 & 0 \leq \eta < R \\ 0.5 & \eta=R;\ \dfrac{\partial s(0,\ \eta)}{\partial \hat{F}_o}=0 \\ 0 & R<\eta \leq 1 \end{cases} \tag{8}$$

$$\hat{Q}=-\frac{\partial s}{\partial \eta}-\hat{F}_o^* \frac{\partial \hat{Q}}{\partial \hat{F}_o}=0 \qquad \eta=0;\ 1.$$

New dimensionless complexes are expressed as: $\hat{F}o^*=Fo^*/(1-PeFo^*)^2$; $\hat{F}o=Fo/(1-PeFo^*)$; $\hat{Q}=Q \exp\ (PeFo)\ (1-PeFo^*)$. The solution to Eq. (7) under conditions (8) is given in Appendix. With $\Theta=\exp\ (-PeFo)\cdot s$ taken into account for Θ, we have:

$$\theta = \exp(-PeFo)\left\{R + 2\exp\left(-\frac{\hat{F}_o}{2\hat{F}_o^*}\right)\sum_{n=1}^{\infty}\frac{\sin n\pi R\cos n\pi\eta}{n\pi}\times\right.$$
$$\left.\times\left[\mathrm{ch}\left(\frac{\hat{F}_o}{2\hat{F}_o^*}\sqrt{1-4n^2\pi^2\hat{F}_o^*}\right)+\frac{\mathrm{sh}\left(\frac{\hat{F}_o}{2\hat{F}_o^*}\sqrt{1-4n^2\pi^2\hat{F}_o^*}\right)}{\sqrt{1-4n^2\pi^2\hat{F}_o^*}}\right]\right\} \tag{9}$$

At $Fo^*=0(\hat{F}o=Fo;\ \hat{F}o^*=0$, respectively), Equation (9) is simplified to give the known solution of parabolic heat conduction equation (1) [6] (the RHS of this equation must be supplemented with the term $-\beta^*(T-T_0)$:

$$\theta = \exp(-PeFo)\left[R + 2\sum_{n=1}^{\infty}\frac{\sin n\pi R\cos n\pi\eta}{n\pi}\exp(-n^2\pi^2 Fo)\right], \tag{10}$$

the boundary conditions correspond to Eq. (6).

Evalute the term $PeFo^*=\beta^*\tau^*$ entering the expression for $\hat{F}o$ and $\hat{F}o^*$. According to [7], $\tau^*=0.15+0.25$ s (free beds); $\tau^*=0.5+5$ s (packed beds) and $\beta^*=\dfrac{\varphi_f C_f u_0}{\varphi_s C_s(1-\varepsilon_{mf})H_{mf}\varepsilon_p}=0.002+0.01$ 1/s. Then PeFo* varies within 0.0003 + 0.05, and $\hat{F}o^*=Fo^*$; $\hat{F}o=Fo$ may be assumed in Eq. (9).

Comparison of Experimental and Theoretical Response Functions

The experimental curves for lateral diffusion of heated solids obtained in the present work using sand s.1 in the staggered tubes ($S_h\times S_v=60\times 60$ mm^2) were compared to the computer-aided ones calculated by Eq. (9) *(Fig. 2)*. Their best coincidence calculated by the sum of the squared deviation of the calculation points from the experimental ones gave the unknown values of a_h and $\tau^*=a_h/v^2$ (*Fig. 2a*, $a_h=12$ cm^2/s, $v=1.5$ cm/s and $\tau^*=5.3$ s). The wave velocity, v, was determined in terms of a delay time, τ_0, of the experimental response function *(Fig. 2)*: $v=(y-h)/\tau_0$ where y is the coordinate of the temperature measuring point. *Fig. 3* shows the calculation results for the response functions obtained by solving parabolic heat conduction Equation (10). Maxima of the curve corresponding to $a_h=14.2$ cm^2/s and of the experimental function coincide. This condition allows the determination of the unknown coefficient, a_h, by the parabolic equation (*Fig. 3*, $a_h=14.2$ cm^2/s; the experimental functions are the same as in *Fig. 2a* and *3*). As is seen from *Fig. 2* and *3*, the hyperbolic heat conduction equation considerably better describes the experimental relations than the parabolic one. The values of thermal diffusivity calculated by different models proved to be close in *Fig. 2a* and *3* (12.0 cm^2/s and 14.2 cm^2/s). The experimental curves for lateral heat transfer obtained in the above runs were treated in a similar way. The results of the analysis *(Fig. 4)* show that the coefficients, a_h, determined by the hyperbolic and parabolic models differ slightly.

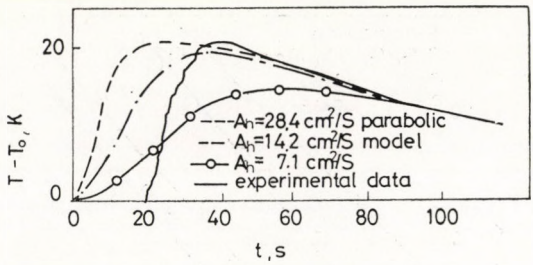

Fig. 3

Comparison of the experimental response function with the one predicted by the parabolic model

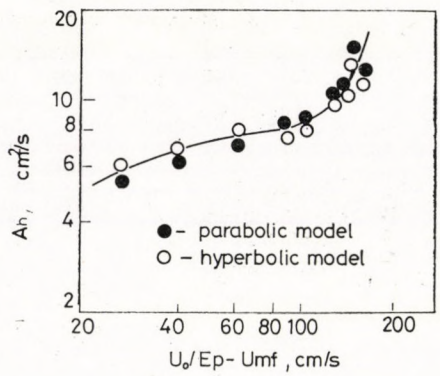

Fig. 4

Lateral thermal diffusivities determined by different models as a function of the excess air velocity $(u_0/\varepsilon_p - u_{mf})$

Experimental Study of Lateral Thermal Diffusivity of a Bed

As the coefficients, a_h, found by the hyperbolic and parabolic equations differ slightly, thermal diffusivity was studied using a more simple parabolic model.

The lateral thermal diffusivity of the fluidized bed packed with horizontal tubes was investigated by the above mentioned experimental unsteady-state approach. It was calculated by the successive approximation allowing for heat removal from the bed by filtered air [6]:

$$a_h^i = \Phi(R,\ \eta_0,\ Pe^{i-1})l^2/\tau_{max} \tag{11}$$

where $Pe^{i-1} = \beta^* l^2/a_h^{i-1}$ and the function $\Phi = Fo_i^{max} = \frac{a_h^i\,\tau_{max}}{l^2}$ was calculated theoretically by solution (10) to the parabolic heat conduction equation, the time of a temperature maximum, τ_{max}, attained in the chosen plane, η_0, being measured experimentally.

Some values of a_h are shown in *Fig. 5* and *6*. It can be seen that for packed beds (especially, in close tubes) these may be much lower than in a free bed.

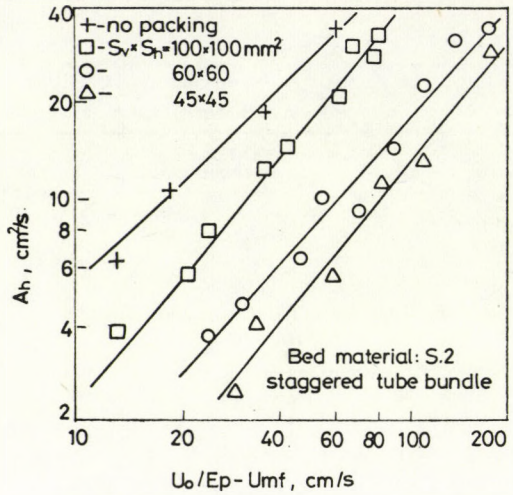

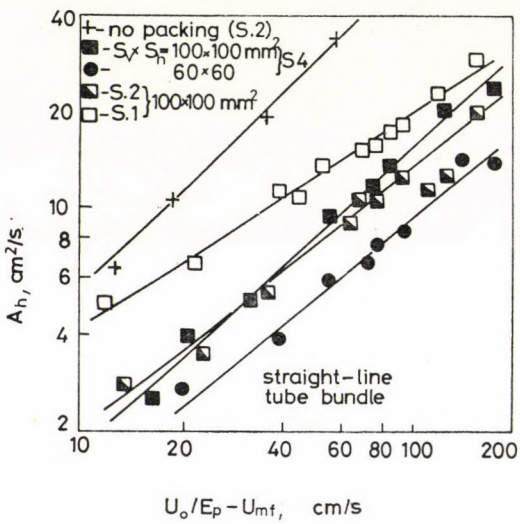

Fig. 5.
Lateral thermal diffusivity of a bed packed with horizontal tube bundles as a function of the excess air velocity

This is attributed to the retarding effect of a tube bundle on the motion of gas bubbles and solids in the fluidized bed. A change in the tube pitch markedly influences the lateral thermal diffusivity of the bed, the latter increasing with its growth. In contrast to free beds [8], our experiments did not display the a_h dependence on the static bed height *(Fig. 6)*, which is in accordance with the data of [3]. The dispersed material density did not appreciably effect this coefficient *(Fig. 7)*. The following correlations were obtained for:

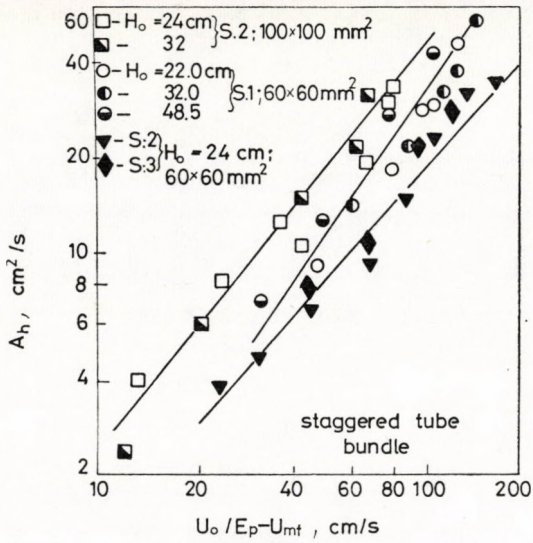

Fig. 6

Effect of the static bed height and dispersed solids density on lateral heat transfer in the tube-packed fluidized beds

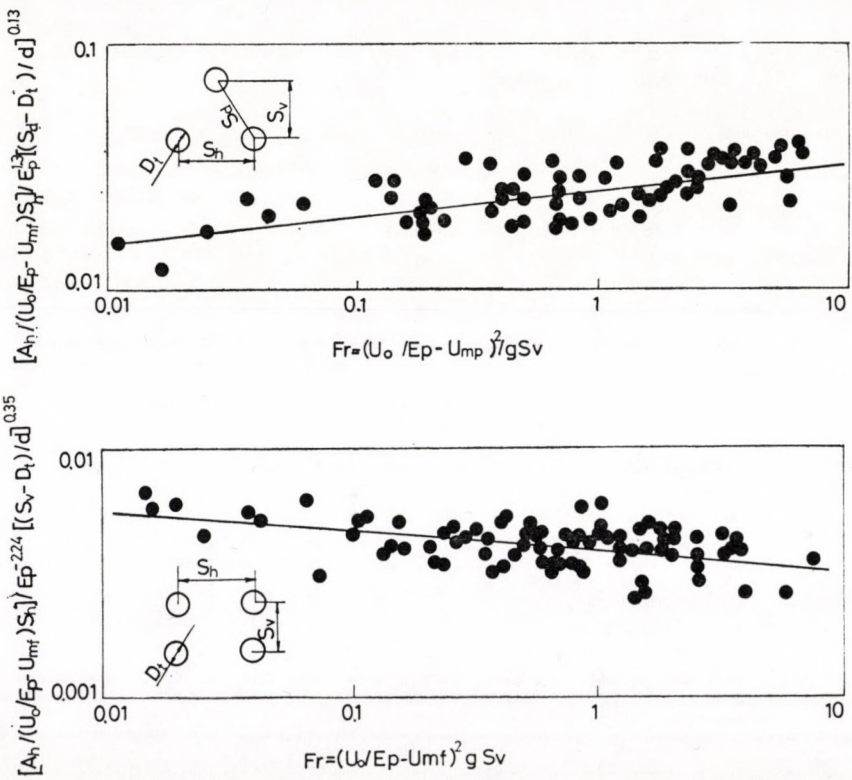

Fig. 7

Correlation of the experimental data for lateral thermal diffusivity of a fluidized bed packed with horizontal tubes

a) staggered tube bundle

$$\frac{a_h}{(u_0/\varepsilon_p - u_{mf})S_h} = 0.025\ \mathrm{Fr}^{0.11}\varepsilon_p^{1.31}\left(\frac{S_d - D_t}{d}\right)^{0.13} \tag{12}$$

b) in-line tube bundle

$$\frac{a_h}{(u_0)/\varepsilon_p - u_{mf})S_h} = 0.0038\ \mathrm{Fr}^{-0.09}\varepsilon_p^{-2.24}\left(\frac{S_v - D_t}{d}\right)^{0.35} \tag{13}$$

In both cases, therms deviation of the experimental points from those calculated by Eq. (12) and (13) was 18% *(Fig. 7)*.

Conclusion

Hyperbolic heat conduction equation (4) including finite velocity of heat propagation is shown to much better specify experimental data than the traditional heat conduction equation.

It is found that the lateral thermal diffusivities, a_h, calculated by the classical (parabolic) equation do not differ much from those determined by the proposed hyperbolic equation. This permits the available data on a_h found by the parabolic equation to be applied in calculations of unsteady-state lateral internal heat transfer in a fluidized bed using more perfect hyperbolic equations of type (4).

The experimental lateral thermal diffusivities of beds packed with horizontal tube bundles may be substantially less than those for a free bed. The coefficient a_h noticeably decreases with decreasing tube pitch and does not depend on the static bed height and solids density.

Empirical correlations (12) and (13) generalize the experimental data obtained in this work on the lateral thermal diffusivities of beds packed with staggered and in-line tube bundles.

SYMBOLS

a_h	lateral thermal diffusivity of the bed, cm²/s
A	fraction of the bed volume occupied with the downflowing dense phase
B	fraction of the bed volume occupied with bubble wakes
C_s, C_f	specific heat at constant pressure of solids and a gas, respectively, J/kg K
C_1, C_2	solids tracer mass per unit volume of emulsion in the downflowing dense phase and in bubble wakes, g/cm³
d	mean solid diameter, mm
D_t	tube diameter, mm
g	acceleration of gravity, cm/s²
h	heating chamber width, cm
H_0	static bed height, cm
H_{mf}	bed height at minimum fluidization, cm
H	mean fluidized bed height, cm
q	heat flux, J/m²s
$K_a = \frac{u^2}{\beta(A+B)}$	axial "Taylor" diffusivity, cm²/s
l	bed width, cm

P pressure, Pa
$Q = ql/[a_h(T_c - T_0)\varrho_s C_s(1-\varepsilon_{mf})(1-\varepsilon_b)]$ dimensionless heat flux determined by Eq. (6)
$R = h/l$ lateral heat conduction
$R = h/H$ axial mixing
S_h, S_v horizontal and vertical tube pitches, mm
t time, s
T bed temperature, K
T_0, T_c initial and heating chamber temperature, respectively, K
u_1, u_2 downflowing solids velocity in the emulsion phase and bubble wake velocity, cm/s
$u = Au_1 = Bu_2$ circulation solids velocity per total column cross section, cm/s
u_0 fluidization velocity, cm/s
u_{mf} minimum fluidization velocity, cm/s
x, y vertical and horizontal coordinates, cm

Greek symbols

β interphase mass transfer coefficient based on unit volume of a bed, 1/s
$\beta^* = \varrho_f C_f u_0/\varrho_s C_s(1-\varepsilon_{mf})H_{mf}\varepsilon_p$ dimensionless intensity of heat removal by filtered air from the bed, 1/s
δ dispersion of solide size distribution function, mm
ε_{mf} bed voidage at minimum fluidization
ε_b bubble concentration
ε_p fraction of tube-free bed volume
$\eta = y/l$ dimensionless horizontal coordinate
$\theta = (T - T_0)/(T_c - T_0)$ dimensionless temperature
$\zeta = x/H$ dimensionless vertical coordinate
ϱ_s, ϱ_f density of solids and a gas, respectively, g/cm^3
τ^* relaxation time, s
τ_0 delay time of the response function, s

Dimensionless complexes

$Fo = a_h t/l^2$ FOURIER number
$Fo^* = a_h \tau^*/l^2$
$Fr = (u_0/\varepsilon_p - u_{mf})^2 g S_v$ FRODE number
$Pe = \beta^* l^2/a_h$ PECKLET number
$Pe^* = u/\beta H$
Subscript
i ith approximation

Appendix

The solution to boundary-value problem (7)—(8) can be obtained as follows. For VAN DEEMTER's countercurrent axial backmixing model [9]:

$$A\left(\frac{\partial C_1}{\partial t} + u_1\frac{\partial C_1}{\partial x}\right) = \beta(C_2 = C_1)$$
$$B\left(\frac{\partial C_2}{\partial t} - u_2\frac{\partial C_2}{\partial x}\right) = \beta(C_1 - C_2) \tag{A.1}$$

under the boundery conditions:

$$C_1(0, x) = C_2(0, x) = \begin{cases} C_c, & 0 \le x < h \\ \dfrac{C_c + C_0}{2}, & x = h \\ C_0, & h < x \le H \end{cases} \tag{A.2}$$

$$C_1(t, 0) = C_2(t, 0);\ C_1(t, H) = C_2(t, H).$$

the integral Laplace transformation gives the solution (10):

$$\theta_i = \frac{C_i - C_0}{C_c - C_0} =$$

$$= R + \exp(-J_0/Pe^*) \sum_{n=1}^{\infty} \frac{(-1)^n \sin n\pi R}{n\pi} \left(\Gamma_i \, ch \frac{J_0}{Pe^*} A_n + \frac{D_i}{A_n} sh \frac{J_0}{Pe^*} A_n \right)$$

$$(i = 1,\ 2,\ 3)$$

where:

$$\Gamma_1 = \Gamma_2 = \Gamma_3 = 2 \cos n\pi(1-\zeta);$$

$$D_1 = \Gamma_1 - 2Pe^* n\pi \sin n\pi(1-\zeta);$$

$$D_2 = \Gamma_2 + Pe^* n\pi \sin n\pi(1-\zeta);$$

$$D_3 = \Gamma_3 + 2\frac{B-A}{A+B} Pe^* n\pi \sin n\pi(1-\zeta);$$

$$A_n = \sqrt{1 - Pe^{*2} n^2 \pi^2};$$

$$J_0 = \frac{A-B}{A+B}\left(-\zeta + R + \frac{2\tau Pe^*}{A-B}\right);$$

$$\theta_3 = \frac{A\theta_1 B\theta_2}{A+B};$$

$$C_3 = C = \frac{AC_1 + BC_2}{A+B};$$

$$\tau = \beta t. \tag{A.3}$$

It can be easily shown that the countercurrent backmixing model (A.1) is the generalization of hyperbolic equation (7). Indeed, successive elimination of C_1 and C_2 from Eq. (A.1) for mean concentration $C = (AC_1 + BC_2)/(A+B)$ gives:

$$\frac{\partial C}{\partial t} + \frac{AB}{\beta(A+B)} \frac{\partial^2 C}{\partial t^2} + \frac{AB(u_1 - u_2)}{\beta(A+B)} \frac{\partial^2 C}{\partial t \partial x} = \frac{u^2}{\beta(A+B)} \frac{\partial^2 C}{\partial x^2} \tag{A.4}$$

Equation (A.4) is the hyperbolic diffusion equation with different velocities of the direct and indirect waves (u_1, u_2, respectively). Assuming in Eq. (A.4) $u_1 = u_2$; $AB/\beta(A+B) = \tau^*$; $u^2/\beta(A+B) = K_a$ yields the ordinary hyperbolic diffusion equation:

$$\frac{\partial C}{\partial t} + \tau^* \frac{\partial^2 C}{\partial t^2} = K_a \frac{\partial^2 C}{\partial x^2} \tag{A.5}$$

The boundary conditions in (A.2) with regard for $Au_1 = Bu_2 = u$ prescribe no solids tracer flow in the cross section $x = 0$, H.

Equation (7) under boundary conditions (8) corresponds, as accurate as the notations, to Eq. (A.1) (at $u_1 = u_2$) at the conditions of Eq. (A.2). Hence, the solution to system (7)–(8) may be directly obtained from Eq. (A.3) assuming $A = B$; $u^2/\beta(A+B) = a_h/(1-\beta^*\tau^*)$ $AB/\beta(A+B) = \tau^*/1 - \beta^*\tau^*)$. Thus, the solution of hyperbolic equation (7) under boundary conditions (8) is of the form:

$$s = R + 2\exp\left(-\frac{\hat{F}_o}{2\hat{F}_o^*}\right) \sum_{n=1}^{\infty} \frac{\sin n\pi R \cos n\pi\eta}{n\pi} \times$$

$$\times \left[ch\left(\frac{\hat{F}_o}{2\hat{F}_o^*}\sqrt{1 - 4n^2\pi^2\hat{F}_o^*}\right) + \frac{sh\left(\frac{\hat{F}_o}{2\hat{F}_o^*}\sqrt{1 - 4n^2\pi^2\hat{F}_o^*}\right)}{\sqrt{1 - 4n^2\pi^2\hat{F}_o^*}} \right] \tag{A.6}$$

REFERENCES

1. Kato K., Takahashi, T., Kobayashi, T. and Komagata, K.: Chem. Engng. Japan *1982*, 15, (1), 39.
2. Baskakov, A. P. and Pakhaluev, V. M.: Khim. Prom. *1972* (7), 57.
3. Berg, B. V., Stepanov, L. V. and Kupchin, V. I.: Energomaschinostr. *1980* (5) 8.
4. Luikov, A. V.: Heat and Mass Transfer, Izd. Energiya, Moscow, 1978.
5. Petrik, T. F. and Taganov, I. N.: Teor. Osnovy Khim. Tekhnolog. *1980* 14, (13) 461.
6. Teplitsky, Yu. S.: Izv. AN BSSR, Ser. Fiz. Energ. Nauk *1980* (3), 89.
7. Taganov, I. N.: Modelling of Heat and Energy Transfer Processes, Izd. Khimiya, Leningrad, 1979.
8. Mori, Y., and Nakamura, K., Kagaku Kogaku: Chem. Engng Japan, *1965*, (11) 868.
9. Van Deemter, J. J.: Proc. Intern. Symp. Fluidization (Edited by Drinkenberg, A. A. H.), Netherland University Press, Amsterdam, *1967*, 334.
10. Teplitsky, Yu. S.: Izv. AN BSSR, Ser. Fiz. Energ. Nauk *1980* (4) 59.

РЕЗЮМЕ

Авторы использовали метод теплового импульса для изучения механизма боковой тепловой диффузии псевдоожиженного слоя крупных частиц в котором размещены пучки труб. При обработке данных использовали гиперболическую функцию тепловой проводимости. Измеренные и расчетные совпали. Иная картина получается если используют классическое уравнение тепловой проводимости. Боковую диффузию псевдоожиженного слоя и время релаксации определили методом наименьших квадратов. Расчетные данные близки к тем которые определены классическим уравнением. Составили общую корреляционную зависимость для расчета боковой тепловой диффузии псевдоожиженного слоя пучками труб.

Guide for authors

The "Hungarian Journal of Industrial Chemistry" is a joint publication of the Veszprém scientific institutions of the chemical industry that deals with the results of applied and fundamental research in the field of chemical processes, unit operations and chemical engineering in the form of original articles written in the English, Russian, German and French languages.

In addition to the scientific workers of the institutions at Veszprém, the Editorial Board of this publication also welcomes articles for inclusion in this periodical, which are written by authors who are engaged in the above mentioned fields.

2. Manuscripts should be sent—in duplicate—to the Editor-in-Chief:

Dr. Endre Bodor,
Veszprém University of Chemical
Engineering (VVE),
P.O.B. 158
H—8201 Hungary

3. In a brief letter attached to the manuscripts, authors should declare that:
   a) their work is original and has not previously been published elsewhere in its present format, and
   b) for the purposes of correspondence, they can be contacted at the address and telephone number which they give.

4. Manuscripts should be typed on paper of A/4 size.

The first page should give the title, the author's name, place of work and a brief summary of the article (maximum of 15 lines).

If possible the article should be presented with an introduction, experiments carried out, conclusions and discussion. Tables and Figures must be presented on separate sheets and their position in the text should be noted on the margin. A summary of the symbols used, the Tables and captions of the Figures should be attached separately to the manuscripts.

It is regretted that photographs cannot be included in the periodical.

The Tables and Figures should not exceed an A/4 size. If diagrams are presented, only the explanation and dimensions of the ordinate and abscissa, and marking numbers are required, while further explanatory texts can be given in the captions of the Figures. The equations used should be numbered, and Tables and Figures should be numbered and noted in the margin.

With regard to units, it is essential that an SI (Systeme International d'Unités) should be used.

References should be prepared in the following manner:

a) Publications which have appeared in periodicals:

Author's name and initials; title of the periodical (the abbreviation used by Chemical Abstracts is recommended); year of publication; volume number; (number of brochure if necessary); the first and last page number of the article, e.g.:

WAKAO, N. and SCHWARTZ, J. M.:
Chem. Eng. Sci. *1962*, 17 (3), 825—827.

b) Books:

Author's name and initials; title of book; publisher; place of publication; year of publication, e.g.:

SATTERFIELD, C. N.:
Mass Transfer in Heterogeneous Catalysis.
MTI Press, Cambridge, Mass., 1951. pp. 26—32.

c) Patents:

Country where granted, and number of the patent, e.g.:

U.S. Pat.	3,425,442
Brit. Pat.	997,665
Hung. Pat.	553,243

d) Published lectures:

Author's name and initials; title of lecture; name of the conference; further information if necessary, e.g.:

HIH, S., HHU, C. and LEECH, W. J.:
A Discrete Method to Heat Conduction Problems. 5th International Heat Transfer Conference, Tokyo, 1975. Co. 2.4.

5. Authors receive 50 complimentary copies of the edition in which their article appears.

Editorial Board
Hungarian Journal of Industrial Chemistry

CONTENTS

SZÜCS, I. and SZIKLAI, G.: On the Relationship of Colour Characteristics and Particle Size Distribution and Specific Surface Area of Certain Pigments. I. 113

ÓVÁRI, F., CSORBA, L. and UBRANKOVICS, I.: New Developments in the Production of Positive Electrodes for Stationary Large Lead Batteries 119

GÁRDOS, GY., RÉDEY, Á. and SOKORAI, I.: Utilization of the C_4-Fraction as Motor Fuel 125

KÁLDI, P., SCHOLTZ, J. and EGYHÁZY, T. Examination of SA–1-Type Ammonia Synthesis Catalyst 131

MRS. FEHÉR–SZÜCS, M. and JÓZSEF, G.: On the Possibilities of Decreasing the Sulphur Emission of a Claus-Plant 139

KÁLDI, P., SCHOLTZ, J., SZIKLAI, G. and EGYHÁZY, T.: Investigations on the Activity and Morphology of Spent Ammonia-Synthesis Catalysts 147

KASSEM, T. M., HABIB, O. M. O., HUSSEIN, M. H. and EISSA, A. I.: New Biocides from Petroleum Hydrocarbons I. Biocidal Active Products from 4-Substituted Phenols and 4-Substituted-1-Naphthols. 157

KIRÁLY, L., LAKATOS, B. and BLICKLE, T.: Use of the Weighed-Moments-Method for Parameter Identification and Approximation of Distribution Functions 165

MRS. VARGA, E. and LAKATOS, B.: Calculation of the Dynamic Processes of a Perfectly Mixed Tank by Ortogonal Collocation 173

SZABÓ, J. and KÁLDI, P.: Adsorption Rate on Natural Mordenites 185

BORODULYA, V. A., TEPLITSKY, YU. S., EPANOV, YU. G. and YANOVICH, I. I.: Lateral Thermal Diffusivity of a Fluidized Bed Packed with Tube Bundles 193

Egyetemi Nyomda — 83.1264 Budapest, 1983. Felelős vezető: Sümeghi Zoltán igazgató

Ára: 250 Ft

THE FOLLOWING ARE PLEASED TO ACCEPT SUBSCRIPTIONS TO THIS JOURNAL:

AUSTRALIA

C.B.D. Library and Subscription Service
Box 4886 G.P.O.
Sydney 2000

Cosmos Book and Record Shop
145 Acland Street
St. Kilda 3182

Globe and Co.
694—696 George Street
Sydney 2000

AUSTRIA

Globus (VAZ)
Höchstädtplatz 3
A—1200 Wien XX

BELGIUM

"Du Monde Entier" S. A.
Rue du Midi 162
B—1000 Bruxelles

Office International de Librairie
Avenue Marnix 30
B—1050 Bruxelles

CANADA

Pannonia Books
P.O. Box 1017
Postal Station "B"
Toronto, Ontario M5T 2T8

DENMARK

Munksgaard's Boghandel
Norregade 6
DK—1165 Copenhagen K

FINLAND

Akateeminen Kirjakauppa
Keskuskatu 2, P.O.B. 128
SF—00 100 Helsinki 10

FRANCE

Office International de Documentation et Librairie
48 Rue Gay Lussac
75 Paris 5

GERMAN FEDERAL REPUBLIC

Kubon und Sagner
Pf 68
D—8 München 34
BRD

GREAT BRITAIN

Bailey Bros and Swinfen Ltd.
Warner House, Folkestone
Kent CT 19 6PH England

HOLLAND

Martinus Nijhoff
Periodicals Department
P.O. Box 269
The Hague

Swets and Zeitlinger
Keizersgracht 487
Amsterdam C

ITALY

Licosa
P.O.B. 552, Via Lamarmora 45
50121 Firenze

JAPAN

Igaku Shoin Ltd.
Foreign Department
Tokyo International P.O. Box 5063
Tokyo

Maruzen Co. Ltd.
P.O. Box 5050
Tokyo International 100—31

Nauka Ltd.
Yasutomi Bldg. 5F 2—12 Kanda
Jinbocho, Chiyoda-ku
Tokyo 101

NORWAY

Tanum—Cammermayer
Karl Johangt. 41—43
Oslo 1

SWEDEN

Almqvist and Wiksell Förlag A. B.
Box 2120
S—103 13 Stockholm 2

Wennegren—Williams AB
Subscription Department Fack
S—104 Stockholm 30

SWITZERLAND

Karger Libri A. G.
Petersgraben 31
CH—4011 Basel

USA

Ebsco Subs. Services
1 st Ave North at 13th street
Birmingham, Ala. 35201

HUNGARIAN

Journal of

INDUSTRIAL CHEMISTRY

Edited by

the Hungarian Oil & Gas Research Institute (MÁFKI),
the Research Institute for Heavy Chemical Industries (NEVIKI),
the Research Institute for Technical Chemistry of the
Hungarian Academy of Sciences (MÜKKI),
the Veszprém University of Chemical Engineering (VVE).
Veszprém (Hungary)

Volume 11. **1983.** **Number 3.**

HU ISSN: 0133—0276
CODEN: HJICAI

Editorial Board:

R. Csikós and Gy. Mózes
Hungarian Oil & Gas Research Institute
(MÁFKI Veszprém)

A. Szántó and M. Nádasy
Research Institute for Heavy Chemical Industries
(NEVIKI Veszprém)

T. Blickle and O. Borlai
Research Institute for Technical Chemistry
of the Hungarian Academy of Sciences
(MÜKKI Veszprém)

P. Árva and G. Deák
Veszprém University of Chemical Engineering
(VVE Veszprém)

Editor-in Chief:
E. Bodor

Assistant Editor:
J. De Jonge

Veszprém University of Chemical Engineering
(VVE Veszprém)

The "Hungarian Journal of Industrial Chemistry" is a joint publication of the Veszprém scientific institutions of the chemical industry that deals with the results of applied and fundamental research in the field of chemical processes, unit operations and chemical engineering. The papers are published in four numbers at irregular intervals in one annual volume, in the English, Russian, French and German languages

Editorial Office:
Veszprémi Vegyipari Egyetem
"Hungarian Journal of Industrial Chemistry"
H–8201 Veszprém, P. O. Box: 158.
Hungary

Orders may be placed with
KULTURA
Foreign Trading Co. for Books and Newspapers
Budapest 62. POB 149
or with its represenatives abroad, listed on the verso of the cover

FELELŐS SZERKESZTŐ: DR. BODOR ENDRE

KIADJA A LAPKIADÓ VÁLLALAT, 1073 BP. VII., LENIN KRT. 9–11.
TELEFON: 221-285. LEVÉLCÍM: 1906 BP. PF. 223
FELELŐS KIADÓ: SIKLÓSI NORBERT IGAZGATÓ

HUNGARIAN JOURNAL
OF INDUSTRIAL CHEMISTRY
VESZPRÉM
Vol. 11. pp. 209–221 (1983)

THERMODYNAMICAL PROPERTIES OF NONAQUEOUS SOLUTIONS OF HYDROGEN CHLORIDE

M. STUDNICKI

(Institute of Inorganic Chemistry, Gliwice, Poland)

Received: November 5, 1982.

The state of knowledge of thermodynamical properties of organic solutions of hydrogen chloride is described. Methods for the approximate calculations the activity of hydrogen chloride in various solvents and temperatures are presented.

Nonaqueous solutions of hydrogen chloride are often used in analytical chemistry [1, 2] and likewise in organic synthesis [3]. Unfortunately the elaboration of the results is faced with difficulties connected with appointment of hydrogen chloride activity in different temperatures and different solvents

Mathematical methods are presented which allow an approximate calculation of the activity of hydrogen chloride in nonaqueous solvents in subordination to temperature, in order to compare the activities of ions in different solvents, which it is considered separately influence solvents in the extreme dilution of ions [4, 5] connected with activity coefficient γ_0, influence dilution in one solvent connected with activity coefficient $\gamma_\pm$. This effect connected with activity coefficient γ_0 has been named "primary", but the effect connected with activity coefficient $\gamma_\pm$ has been named "secondary". The complete activity coefficient is a product of these effects.

$$\log \gamma = \log \gamma_0 + \log \gamma_\pm \tag{1}$$

The values of γ_0 and $\gamma_\pm$ are calculated from the emf of cells Pt, H_2/HCl (m) solvent/AgCl,Ag.

$$\log \gamma_0 = \frac{(E_0^{H_2O} - E_0^M) F\nu}{4.606\, RT} \tag{2}$$

$$\log \gamma_\pm = \frac{(E_0^M - E) F\nu}{4.606\, RT} - \log m \tag{3}$$

The primary effect defines the interaction of ions and solvents. IZMAILOV [6] described an equation in which γ_0 is calculated from the physicochemical data of solvent and hydrogen chloride.

$$\log \gamma_0 = \log \gamma_{solv} + \log \gamma_{elst} \tag{4}$$

The first element of the equation $\log \gamma_{solv}$ is dependent on chemical interactions of molecules of solvent and proton and is conditioned by equilibrium constant of the reaction exchange proton between solvent and water K_r.

$$(ROH)_3H^+ + 4\,H_2O = 3\,ROH + (H_2O)_4H^+ \tag{5}$$

For alcohols $K_r = \dfrac{a^3_{ROH} \cdot a_{[H_2O]_4}H^+}{a^4_{H_2O} \cdot a_{[ROH]_3}H^+}$

Generally for all solvents: $K_r = \dfrac{a^m_M \cdot a_{[H_2O]_4}H^+}{a^4_{H_2O} \cdot a_{[M]_m}H^+}$

The equilibrium constant is therefore according to the definition definite by the constant of solvent K_a, for instance for alcohols:

$$pK_a = \log K_r - 4 \times 1.75 = \log K_r - 7 \tag{6}$$

Table 1 illustrates the values of the pK_a of alcohols according to literature data, and calculated from K_r data. A good agreement between these values was obtained.

Table 1

Calculated from Eq. (6) and literature data of pK_a

solvent	methanol	ethanol	izo-propanol	ethyl acetate
pK_a				
Inv. meth.				
Raman	−4.9	—	−4.95	—
NMR	—	−4.8	—	—
Calc.	−4.97	−4.7	−4.97	−3.74

According to ISMAILOV $\log \gamma_{solv}$ can be calculated from the equation:

$$\log \gamma_{solv} = 0.5 \left(\log K_r + \log \frac{a^*_{H_2O}}{a^*_M} \right) \tag{7}$$

Table 2 presents the literature data of $\log \gamma_0$ and $\log K_r$ for different solvents [6—18, 36].

The second element in Equation (4) is connected with the electrostatical interaction of ions with dipoles of solvent, and is linearly dependent on the reciprocal of dielectric constant $1/\varepsilon$.

Table 2

Values of $\log K_r$, $\log \gamma_0$ and $-\log K_d$, 25 °C

Solvent	acetonitryle	nitrobenzene	nitromethane
$\log K_r$	5.41	5.19	4.11
$\log \gamma_0$	—	−5.34	—

solvent	MeOH	EtOH	Iz-PrOH	Iz-PentOH	Iz-BuOH	Bensyl. alc.	n-BuOH
$\log K_r$	2.03	2.30	2.03	2.08	1.85	1.17	2.16
$\log \gamma_0$	1.97	2.52	2.81	3.02	3.02	3.24	3.00
$\log K_d$	−1.26	−1.89	−2.43	−3.32	−2.96	−4.37	−3.30

solvent	dimeth. form.	formamide	N-methyl-formaide	N,N-dimethyl formaide	acetone	DMSO
$\log K_r$	−0.19	−1.06	—	—	—	—
$\log \gamma_0$	1.02	0.2	0.12	0.61	4.54	3.04
$\log K_d$	−1.15	−3.55	−0.97	−4.08	−4.51	—

acetates

solvent	methyl	ethyl	propyl	butyl	amyl
$\log K_r$	3.01	3.26	—	—	—
$\log \gamma_0$	—	2.98	3.06	3.12	3.17
$\log K_d$	—	−1.65	−2.92	−3.54	−3.34

ethers

solvent	diethyl	dipropyl	dibutyl	diamyl
$\log \gamma_0$	5.21	—	—	—
$\log K_d$	−4.88	−4.97	−5.61	−5.73

$$\log \gamma_{elst} = \frac{e^2 N(1/\varepsilon_M - 1/\varepsilon_{H_2O})}{4.606\, RT_r} + \frac{\Delta A}{4.606\, RT} \tag{8}$$

From the data of Ismailov $r = 0.414$ nm and $\Delta A/4.606RT = 0.22$, at $T = 298.15$ K for alcohols.

Fig. 1 presents the interaction in alcohols for hydrogen chloride, *p*-toluidine and aniline [19].

Fig. 2 presents the interaction between $\log \gamma_0$ and temperature calculated from literature data for alcohols by Equation 2.

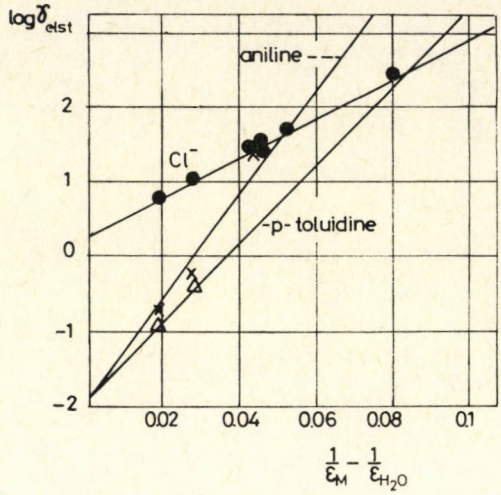

Fig. 1

Interaction between log γ_{elst} and $1/\varepsilon$ for hydrogen chloride, aniline and *p*-toluidine hydrochlorides in alcohols at 25 °C

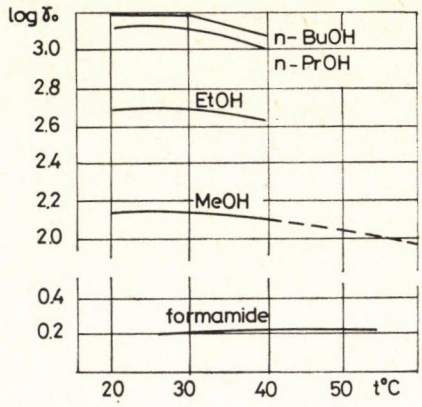

Fig. 2

Interaction between log γ_0 of hydrogen chloride and temperature in alcohols and formamide

Interaction between molar partial enthropy and temperature are presented in differential Equation 9,

$$\Delta\mu_{HCl} = RT \ln \gamma_0 \gamma_{\pm} m, \qquad S_{HCl} = \left(\frac{\partial \Delta\mu_{HCl}}{\partial T}\right)_P$$

$$S_{HCl} = -R \ln a - RT \frac{\partial \ln \gamma_0}{\partial T} - RT \frac{\partial \ln \gamma_{\pm}}{\partial T} \tag{9}$$

$$a = \gamma_0 \gamma_{\pm} m$$

Table 3

Interaction between $\log \gamma_0$ and $\log \gamma_\pm$ and temperature for $m = 0.1$ mol/kg in different solvents

Solvent	$-\frac{d\log \gamma_0}{dT}$	$-\frac{d\log \gamma_\pm}{dT}$	range of temperature		literature
			$\log \gamma_0$	$\log \gamma_\pm$	
ethyl acet.	−0.001	—	50−60°	—	[36]
methanol	0.004	0.0002	30−40°	25−50°	[20]
methanol	—	−0.00225	—	50−60°	[20]
ethanol 95%	0.006	0.003	30−40°	45−50°	[21]
n-propanol	0.01	0.0012	30−40°	40−45°	[22, 23]
n-buthanol	0.011	0.0082	30−40°	35−45°	[24]
formamide	0.0005	0.0032	50−55°	50−55°	[8]

Table 3 presents data $-\frac{\partial \log \gamma_0}{\partial T}$ and $-\frac{\partial \log \gamma_\pm}{\partial T}$ in different temperatures.

The secondary effect is connected with the influence between ions in different concentrations. The dielectric constant of the solvent in the whole is smaller than the dielectric constant of water (the exceptions are amides), therefore the electrostatic forces between ions of electrolyte in organic solvent are greater than in water, while the activity connected with secondary effect is smaller in organic solvents than in water. This effect is intensified by increasing the concentration of hydrogen chloride. In the whole, the secondary effect is smaller and contrary to the primary effect, which caused the increase in activity.

Mineral acids, but first of all hydrochloric acid, in organic solvents are only partially dissociated. Interaction between stoichiometric molality and effective m' is defined by dissociation constant α and is connected with the constant of ionic pairs, K_d.

$$m'/m = \alpha; \qquad K_d = \frac{(m'\gamma_\pm)^2}{m - m'}$$
$$K_d = \frac{\alpha^2}{1-\alpha} m\gamma_\pm^2 \tag{10}$$

The dependence K_d constant and temperature is gained by the Equation of Fuoss [24, 27].

$$\ln K_d = A' + \frac{B'}{\varepsilon T}$$

For extremely diluted solutions the equation presented by Denison and Ramsey [28] is valid.

$$-\log K_d = \frac{e^2}{2.303\ ka\ \varepsilon T}.$$

Table 2 presents the values $-\log K_d$ for different solvents for hydrogen chloride, calculated from literature data. *Fig.* 3 presents the interaction between $-\log K_d$ and effective molality m' for methanol and ethanol.

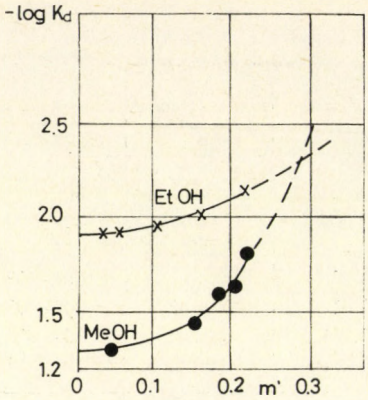

Fig. 3
Interaction between $m'n$ of hydrogen chloride and $-\log K_d$ in methanol and ethanol at 25 °C

Influence of effective molality on activity coefficient $\gamma_\pm$ is described below by the equation of ROBINSON–STOKES [29, 30], which takes into account the decreasing amount of free solvent, which is caused by solvation. It is important for concentrated solutions of electrolytes [31].

$$-\log \gamma_\pm = \frac{Am'^{1/2}}{1+Bm'^{1/2}} - \frac{h}{\nu} \log a_0 - \log\left[1+\frac{(\nu-h)m_0 m'}{1000}\right]$$

$$A = \frac{e^3 N^{1/2} \times 31.62}{2.303 \times 4\pi \sqrt{2}\,(\varepsilon_0 kT)^{3/2}} \times \frac{\varrho_0^{1/2}}{\varepsilon^{3/2}} \tag{11}$$

$$B = \left(\frac{2e^2 N}{\varepsilon_0 kT}\right)^{1/2} 3.162 \times 10^{-8} \times \left(\frac{\varrho_0}{\varepsilon}\right)^{1/2} r$$

The activity of the solvent is calculated from the equation of GIBBS–DUHEM [32].

$$\log a_0 = -\frac{M_0\,\nu}{2.303 \times 1000}\left(m + \int_1^{\gamma_\pm} \frac{m}{\gamma_\pm}\, d\gamma_\pm\right) \tag{12}$$

Equations (10) (11) and (12) were used for the calculations $-\log K_d$ from literature data [8–17, 33] *(Table 2)*. Literature value $-\log K_d$ for dimethylformamide 3.548 [9], calculated 3.55; for acetone literature value 4.4 [10], calculated 4.51.

Fig. 4 and *5* present the interactions between $-\log K_d$ and $1/\varepsilon$ for different solvents.

Interactions between $-\log K_d$ and $1/\varepsilon$ for the homologue series of solvents are on the whole linear the exceptions are ethyl acetate and diethyl ether). Values $-\log K_d$ increase in series:

acetates and ethers < alcohols < acetone < amides

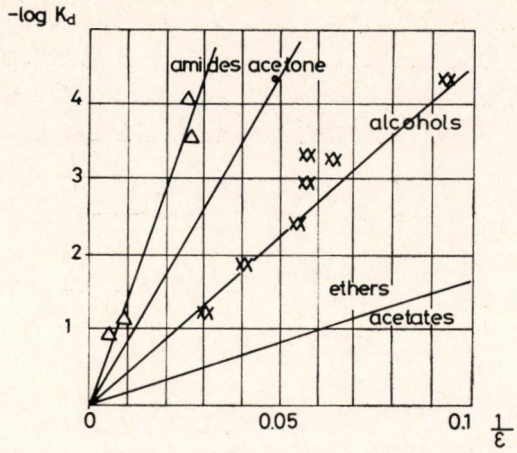

Fig. 4

Interaction between $-\log K_d$ and $1/\varepsilon$ for amides, alcohols and acetone, 25 °C

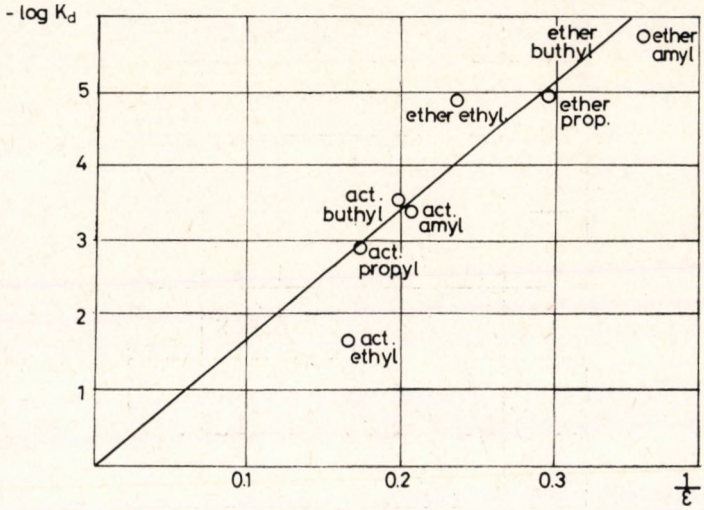

Fig. 5

Interaction between $-\log K_d$ and $1/\varepsilon$ for alkyl acetates and dialkyl ethers, 25 °C

Fig. 6 presents the correlation between $-\log K_d/\log \gamma_0$ and $\varepsilon M_{NS}/M_s$. Ratio $-\log K_d/\log \gamma_0$ in approximation defines the influence of the solvent on the activity of hydrogen chloride. $-\log K_d$ qualifies the secondary effect, but $\log \gamma_0$ qualifies the primary effect. This correlation should be used in choosing the best solvent in the reactions in which activity of hydrogen chloride is very important. From *Fig. 6* parameter $-\log K_d/\log \gamma_0$ can be estimated even if only the chemical symbol of the solvent molecule is known.

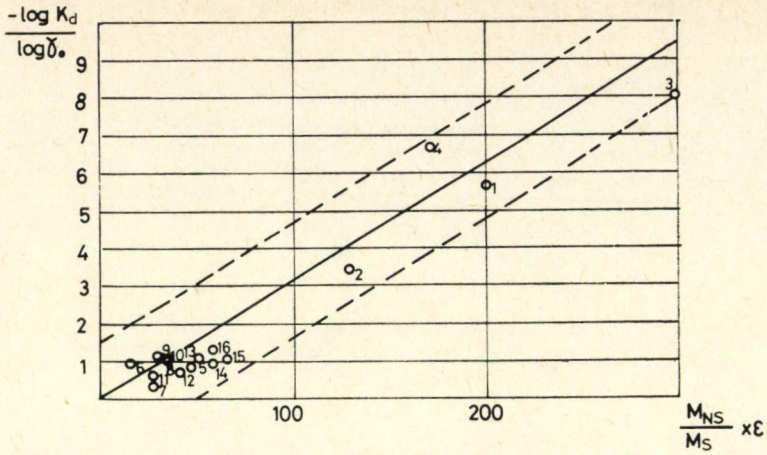

Fig. 6

Correlation between $-\log K_d \log \gamma_0$ and $\varepsilon M_{NS}/M_S$ for solvents

1 — formamide; *2* — DMF; *3* — N-methylformamide; *4* — N,N-dimethylformamide; *5* — acetone; *6* — diethyl ether; *7* — ethyl acetate; *8* — propyl acetate; *9* — buthyl acetate; *10* — amyl acetate; *11* — methanol; *12* — ethanol; *13* — izopropanol; *14* — izobuthanol; *15* — izopentanol; *16* — benzyl alc.

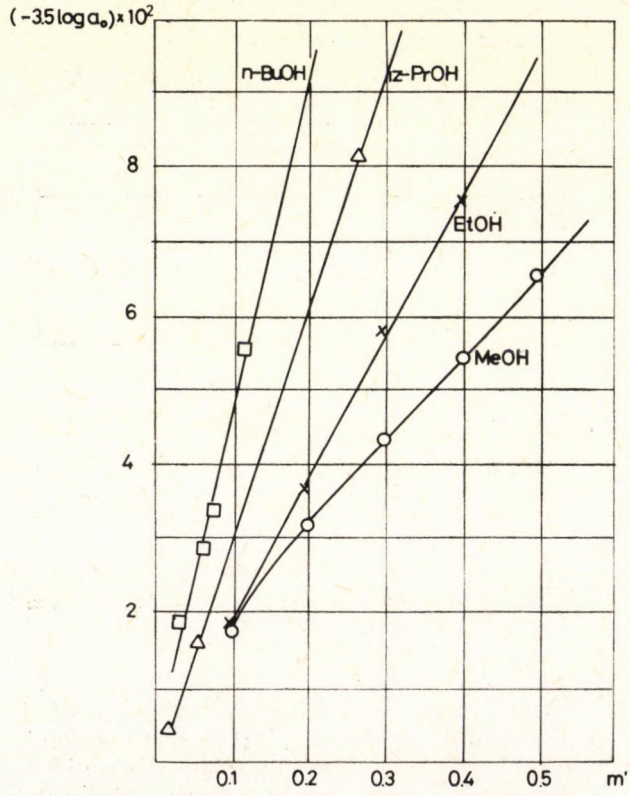

Fig. 7

Interaction between $-\log a_0$ and m' for alcohols at 25 °C

The regression equation of this interaction is:

$$-\log K_d/\log \gamma_0 = -0.174 + 0.0296 \frac{M_{NS} \times \varepsilon}{M_N} \tag{13}$$

$$r' = 0.969 \quad n = 16$$

The activity of solvent a_0 is dependent on the molality and chemical struc-

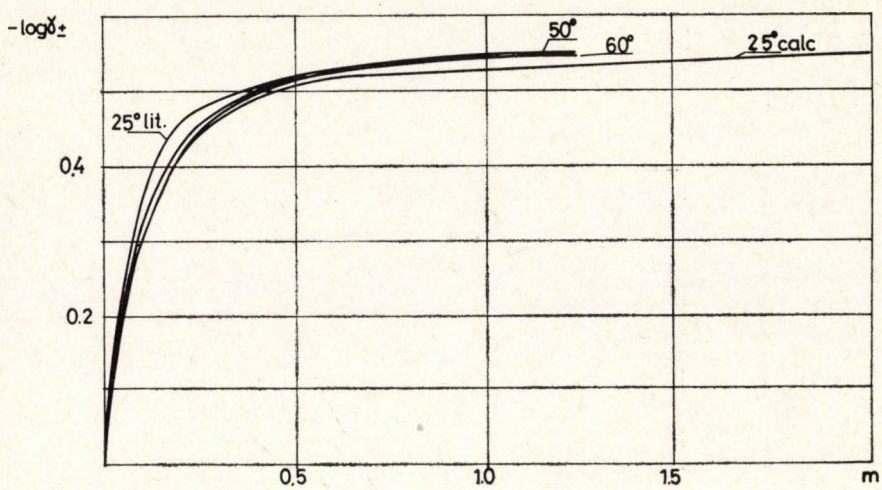

Fig. 8

Interaction between $-\log \gamma_\pm$ and m of hydrogen chloride in methanol in temperatures 25°, 50° and 60 °C calculated from Eq. (11) and from literature data [6] in 25 °C

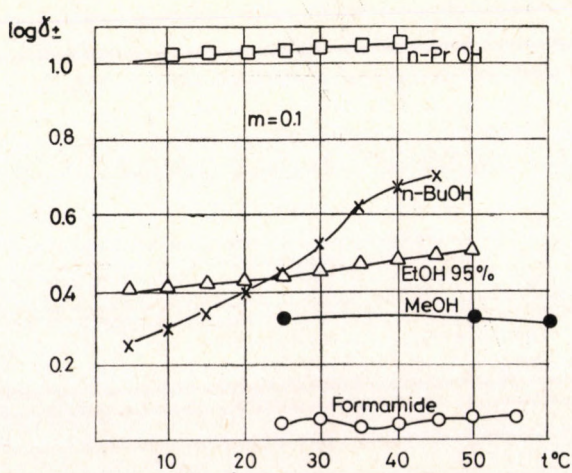

Fig. 9

Interaction between $-\log \gamma_\pm$ and temperature for 0.1 mol/kg of hydrogen chloride in alcohols and formamide

ture of the solvent. *Fig. 7* presents the influence of the structure of alcohols on the interaction between $\log a_0$ and m.

The activity of the solvent for alcohols decreased with the increase in molecular weight.

Fig. 8 presents the interaction between $-\log \gamma_{\pm}$ and the molality of methanol calculated from Equation 11 for temperatures of 25°, 50° and 60 °C. In this *Fig.* the interaction is also presented between $-\log \gamma_{\pm}$ and the molality of methanol from literature data [6].

A good agreement between the calculated and literature data, especialy for molality greater than 0.2 mol/kg was obtained. The interaction between $-\log \gamma_{\pm}$ and the temperature for 0.1 mol/kg of hydrogen chloride in alcohols is presented in *Fig. 9*.

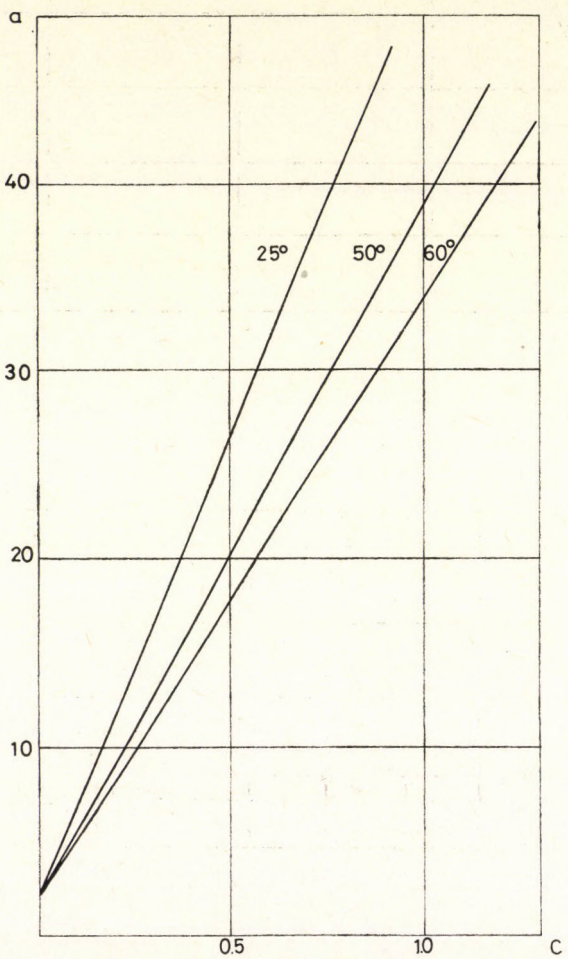

Fig. 10

Interaction between activity of hydrogen chloride and concentration c (mol/dm^3) in temperatures 25°, 50° and 60 °C

Fig. 10 presents the activity of hydrogen chloride in methanol depending on concentration c in temperatures of 25°, 50° and 60 °C. An increase in temperature only imperceptibly decreased the activity of the hydrogen chloride in methanol depending on the concentration of hydrogen chloride.

Fig. 11 presents the interaction between the activity of hydrogen chloride and sulphuric acid and the concentration of these acids in methanol and water. The activity of hydrogen chloride in both solutions was only slightly greater than the activity of sulphuric acid [6, 34, 35].

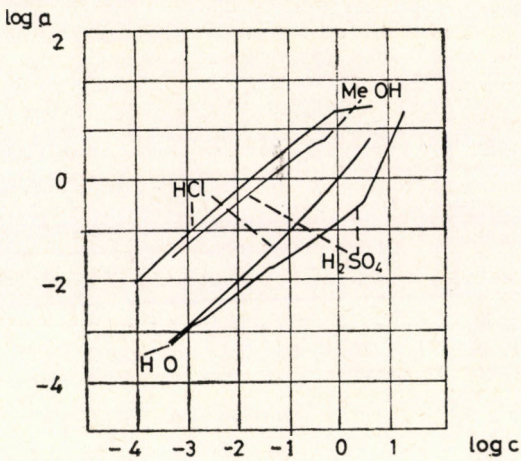

Fig. 11

Interaction between logarithm of activity of hydrogen chloride and sulphuric acid and logarithm of concentration c in water and methanol

The reliability of the proposed methods at different temperatures was examined by numerical calculations [Eq. (10) (11)] values of $-\log \gamma_{\pm}$ of hydrogen chloride in n-butanol *(Table 4)*. The relative difference between the numerical values and literature data [24] did not surpass 12 per cent.

Table 4

Numerical data of $-\log \gamma_{\pm}$ (Eq. 10, 11) of hydrogen chloride in n-butanol and literature data [24], $m = 0.1$ mol/kg, at the range of temperatures 5—45 °C

t °C	$-\log \gamma_{\pm}$ lit.	$-\log \gamma_{\pm}$ calc.	m'	$-\log K_d$
5	0.251	0.250	0.00694	3.7885
15	0.337	0.374	0.0135	3.4814
25	0.446	0.404	0.0147	3.4853
35	0.622	0.650	0.0341	2.9650
45	0.703	0.702	0.0392	3.0033

The reliablility of the proposed mothods for different molalities of hydrogen chloride in methanol at 25 °C are presented in *Fig. 8*. A good agreement between numerical values of $-\log \gamma_{\pm}$ and literature data was achieved, especially for $m = 0.2$ mol/kg.

SYMBOLS

γ_0	activity coefficient connected with the influence of solvents in the extreme dilution of ions.
$\gamma_{\pm}$	activity coefficient connected with the influence of dilution of solvent.
γ_{solv}	activity coefficient dependent on chemical interaction of molecules of solvents and protons.
γ_{elst}	activity coefficient connected with electrostatical interaction of ions with dipols of solvent.
$a^*_{H_2O}$	moles of water in 1 dm³.
a^*_M	moles of solvent in 1 dm³.
$\Delta\mu_{HCl}$	chemical potential of hydrogen chloride.
S	molar partial enthropy of hydrogen chloride.
K_r	equilibrium constant of the reaction exchange proton between solvent and water.
α	dissociation constant.
K_d	constant of ionic pairs.
a	distance of closest approach.
h	solvation number which defined the number of molecules solvated one molecule of electrolyte.
ν	number of ions from one molecule of electrolyte.
$\log a_0$	activity of solvent.
M_0	molecular weight of solvent.
ϱ_0	density of solvent.
m'	effective molality.
ε_M	dielectric constant of solvent.
ε_{H_2O}	dielectric constant of water.
r	constant of ions hydrogen chloride in solvent.
M_{NS}	molecular weight of non-solvated part of solvent molecule.
M_S	molecular weight of solvated part of solvent molecule.
r'	coefficient of correlation $-\log K_d/\log \gamma_0$ and M_{NS}/M_S.

REFERENCES

1. STUDNICKI, M.: Anal. Chem. *1979*, 51, 1336.
2. STUDNICKI, M.: Anal. Chem. *1980*, 52, 1762.
3. STUDNICKI, M.: Ind. Eng. Chem. Res. Dev. in press.
4. WICKE, E., EIGEN, M. and ACKERMANN, T.: Z. Electrochem. *1951*, 55, 343.
5. LAITINEN, H. A. i HARRIS, W. E.: Khimicheskii Analiz, izd 2, Izdat. Khim. Moscow 1979. p 70.
6. IZMAILOV, N. A.: Electrokhimiya rastvorov, Izdat. Kharkovskogo Universiteta, Kharkov 1959. p 377.
7. ARNETT, E. M., QUIRK, R. P. and BURKE, J. J.: J. Am. Chem. Soc. *1970*, 92, 1260.
8. AGARVAL, R. K. and NAYAK, B.: J. Phys. Chem. *1967*, 71, 2062.
9. ALEKSANDROV, V. V. and GULIAEVA, L. S.: Zh. fiz. khim. *1969*, 43, 1116.
10. SILVESTER, L. and ROCK, P. A.: J. Electrochem. Soc. *1974*, 121, 518.
11. IZMAILOV, N. A. i ALEKSANDROV, V. V.: Zh. fiz. khim. *1957*, 31, 2619.
12. PIETROV, S. M. i UMANSKII, J. I.: Zh. fiz. khim. *1967*, 41, 864.
13. SCROSATI, B., PECCI, G. and PISTOIA, G.: J. Electrochem. Soc. *1968*, 115, 506.
14. BERARDELLI, M. L., PECCI, G. and SCROSATI, B.: J. Electrochem. Soc. *1970*, 117, 781.
15. SHVERINA, V. G.: Zh. fiz. khim. *1974*, 48, 351.
16. ibid *1975*, 49, 2139.
17. ibid *1975*, 49, 2136.
18. ALEKSANDROV, V. V. i SPIRINA, S. V.: Zh. fiz. khim. *1975*, 49, 1307.

19. Izmailov, N. A.: Zh. fiz. khim. *1950*, 24, 321.
20. Ratkovics F. és Barati J.: Magy. Kém. Folyóirat *1978*, 84, 49.
21. Convay, B. E.: Electrochemical Data, Elsevier, Amsterdam, 1952. p 297.
22. Roy, R. N., Vernon, W., Gibbons, J. J. and Bothwell, A. L. M.: J. Chem. Thermodyn. *1971*, 3, 883.
23. Roy, R. N., Vernon, W. and Gibbons, J. J.: J. Chem. Soc. Faraday Trans. *1962*, 1, 68 (Pt 11) 2047.
24. Roy, R. N., Bothwell, A. L., Gibbons, J. and Vernon, W.: J. Chem. Soc. Dalton Trans. *1972*, 4, 530.
25. Libuś, W., Libuś, Z.: Elektrochemia, PWN Warszawa *1980*. p 111.
26. Bjerrum, N.: Svensk. Kem. Tids *1926*, 38, 2.
27. Thun, H. P., Staples, B. R. and Bates, R. G.: J. Res. Nat. Bur. Stand. A. *1970*, 74A, 641.
28. Denison, J. T. and Ramsey, J. B.: J. Am. Chem. Soc. *1955*, 77, 2615.
29. Pool, K. H. and Bates, R. G.: J. Chem. Thermodyn. *1969*, 1, 21.
30. Robinson, R. A. and Stokes, R. H.: Ann. of the New York Acad. Sci. *1949*, 51, 593.
31. Koryta, J., Dvorak, J., Bohačkova, V.: Elektrochemia, PWN Warszawa *1980* p 46.
32. Izmailov, N. A. i Ivanova, E. F.: Zh. fiz. khim. *1957*, 31, 424.
33. Bates, R. G.: Opriedielenie pH, Izd. Khimiya, Leningrad. 1972.
34. Harned, H. S. and Hamer, W. J.: J. Am. Chem. Soc. *1935*, 57, 27.
35. Kanning, E. W. and Bowman, M. G.: J. Am. Chem. Soc. *1946*, 68, 2042.
36. Richon, D. and Viallard, A.: Can. J. Chem. *1976*, 54, 2584.

РЕЗЮМЕ

Автором изучены термодинамические свойства соляной кислоты растворенной в органических растворителях. В статьи описаны методы расчёта активности при различных температурах соляной кислоты растворенной в различных растворителях.

HUNGARIAN JOURNAL
OF INDUSTRIAL CHEMISTRY
VESZPRÉM
Vol. 11. pp. 223–229 (1983)

THERMODYNAMICAL PROPERTIES OF NONAQUEOUS SOLUTIONS OF AROMATIC AMINES

M. STUDNICKI

(Institute of Inorganic Chemistry, Gliwice, Poland)

Received: November 5, 1982.

The state of knowledge of thermodynamic properties of organic solutions of aromatic amines is described. Methods for the approximate calculation of the pK_a of aromatic amines in different solvents and temperature are presented.

Properties of aromatic amines as an individual class of organic compounds are characterized first of all by the occurrence of free electronic pairs in the nitrogen atoms and their ability to link with electrophilic species or with protons. The reactions of the acidic-basic equilibrium, which are caused by the transfer of protons, are widely used. The information on the scope of the studies is very important for practical applications (for instance to define the suitable range of pK_a for the optimal yield of products) and for the development of theoretical chemical problems [1].

The aim of the work is to elaborate methods for estimating the pK_a of aromatic amines for different temperatures and solutions. This problem is very important for the practical use of pK_a of aromatic amines. Only a small number of works dealing with the pK_a of aromatic amines for different temperatures and solvents have been published in literature.

PERRIN [2] circumscribed interactions between pK_a, temperature and entropy of the reaction:

$$BH^+ = B + H^+$$

$$\Delta G = 2.303\, RT\, pK_a\,;\ \Delta S^0 = -\frac{d(\Delta G)}{dT} \tag{1}$$

BOLTON and HALL found a correlation between pK_a and ΔH as well as ΔG and ΔH [3, 4] for derivatives of aniline.

$$pK_a = 8.86 \times 10^{-4}\, \Delta H - 2.0945 \tag{2}$$

$$\Delta G = 1.202\, \Delta H - 2642.7\,; \tag{3}$$

$$\Delta S^0 = -227.99\ \mathrm{p}K_a/T + 2165.173/T\ ;\ \Delta S^0 = \frac{-\Delta G + \Delta H}{T} \tag{4}$$

After algebraic transformations, a linear differential equation was obtained.

$$\frac{\mathrm{d}(\mathrm{p}K_a)}{\mathrm{d}T} + \frac{1}{T}\left(1 - \frac{49.7}{T}\right)\mathrm{p}K_a = -\frac{472}{T^2} \tag{5}$$

Solution of Eq. 5 in boundary conditions for $T = 298$ K is:

$$\mathrm{p}K_a^T = \mathrm{p}K_a^{298}\left(\frac{298}{T}\right)\mathrm{e}^{49.7\left(\frac{1}{298}-\frac{1}{T}\right)} + \frac{472}{T}\left[-\ln\frac{T}{298} + \sum_1^{\infty}\frac{(49.7)^4}{n \times n!}\left(\frac{1}{T^n} - \frac{1}{298^n}\right)\right] \tag{6}$$

Eq. (6) may be presented in the form:

$$\mathrm{p}K_a^T = \mathrm{p}K_a^{298} A(T) + B(T) \tag{7}$$

Interaction between A (T), B (T) and temperatures is presented in *Table 1* [method I].

Table 1.

Coefficients $A(T)$ and $B(T)$ of Eq. (7) in the temperature range of 273—333 K

T(K)	273	278	283	288	293	298	303	308	313	318	323	328	333
$A(T)$	1.075	1.059	1.044	1.029	1.014	1	0.9867	0.9729	0.96	0.947	0.9346	0.9223	0.9086
$B(T)$	0.137	0.118	0.093	0.065	0.033	—	−0.27	−0.052	−0.076	−0.098	−0.119	−0.138	−0.158

Table 2 presents the relative difference between the values of $\mathrm{p}K_a$ calculated from Eq. (7) and literature values [3—6].

Table 2.

Relative difference between values of $\mathrm{p}K_a$ calculated from Eq. (7) and literature values [3—6]. Der. of aniline

t (°C)	$-OCH_3$			$-CH_3$			$-NO_2$		
	orto	meta	para	orto	meta	para	orto	meta	para
5	0.02	0.07	−0.09	—	—	—	—	−0.07	—
10	0.00	0.3	−0.1	0.02	0.02	0.00	7.3	0.2	1.0
15	0.00	0.3	−0.04	0.09	0.2	0.08	5.1	0.4	1.0
20	0.00	0.2	0.02	0.02	0.15	0.02	2.7	0.2	0.6
30	0.07	0.1	0.02	0.02	−0.02	0.04	0.00	0.04	0.0
35	−0.05	0.1	0.04	0.00	0.04	−0.02	1.0	0.13	0.2
40	0.00	0.16	−0.02	0.14	0.02	0.04	2.5	0.18	0.7
45	0.00	0.3	−0.06	0.17	0.00	0.02	4.6	0.18	1.3
50	0.02	0.4	−0.02	0.22	0.02	0.02	6.9	0.3	2.1
55	—	—	—	—	—	—	9.0	0.5	2.6
60	—	—	—	—	—	—	10.7	0.58	2.5

A good agreement was obtained with literature data. A greater relative difference was obtained only for the nitro compound, connected with the small values of pK_a of these compounds.

The problem of the interaction pK_a of aromatic amines and temperature can be solved by correlation analysis [method II]. The calculations presented below were supported on the data presented by J. SHORTER [7].

System of equations to be solved, are:

$$\begin{aligned} pK_a^{(para)} - pK_{a,\,anil} &= \overset{P}{\varrho}_I\,\sigma_I + \overset{P}{\varrho}_R\,\overset{0}{\sigma}_R \\ pK_a^{(meta)} - pK^{a,}{}_{anil} &= \overset{m}{\varrho}_I\,\sigma_I + \overset{m}{\varrho}_R\,\overset{0}{\sigma}_R \\ pK_a^{(orto)} - pK_{a,\,anil} &= \overset{0}{\varrho}_I\,\sigma_I + \overset{0}{\varrho}_R\,\overset{0}{\sigma}_R + \varrho_S\,\sigma_S \end{aligned} \tag{8}$$

From literature data [4, 6, 7] ϱ parameters were calculated as a function of temperature. Values of σ were corrected and are presented in *Table 3*.

Table 3.

Literature data and calculated values σ_I, $\overset{\circ}{\sigma}_R$ and σ_S

Group	$-NO_2$	$-Cl$	$-OH$	$-OCH_3$	$-CH_3$	$-COOH$	$-NH_2$	Piridines-NH_2
σ_I calc.	0.67	0.35	0.09	0.08	−0.045	−0.062	−0.12	−0.51
[7]lit.	0.63	0.47	0.25	0.26	−0.05	—	0.12	—

Group	$-NO_2$	$-COOH$	$-CH_3$	$-NH_2$	$-Cl$	$-OH$	$-OCH_3$	Piridines-NH_2
$\overset{\circ}{\sigma}_R$ calc.	0.046	0.009	−0.06	−0.09	−0.24	−0.27	−0.32	−0.41
[7]lit.	0.19	—	−0.1	−0.48	−0.2	−0.4	−0.41	—

Group	$-NO_2$	$-Cl$	$-CH_3$	$-OCH_3$	$-COOH$	$-OH$	$-NH_2$	Piridines-NH_2
σ_S calc.	−5.78	−1.86	0.074	0.19	0.42	0.46	0.53	3.76
[3]lit.	−5.5	−1.94	0.155	0.204	0.398	0.533	0.752	2.14

Fig. 1 presents the parameters ϱ as a function of $1/T$.

In temperatures higher than 40 °C parameters ϱ are linear functions of $1/T$. These functions were linearly extrapolated to temperature 60 °C which in the main are absent in literature. *Table 4* compares the values of pK_a at a temperature of 60 °C calculated by method I (thermodynamical) and obtained by extrapolation parameters $\varrho(1/T)$ at 60 °C (method II).

In many cases a good agreement was achieved.

The problem of the changes of pK_a in the dependence of the solvent was investigated. An attempt was made to estimate changes in the pK_a of aromatic amines in non-aqueous solutions. LAITINEN and HARRIS [8] presented literature data for these changes, but did not describe the calculating methods.

Table 4.

pK_a of derivatives of aniline calculated by I. and II. method at 60 °C

	$-NO_2$			$-Cl$			$-COOH$		
	orto	meta	para	orto	meta	para	orto	meta	para
I	−0.79	2.13	0.75	2.24	2.88	3.46	4.34	4.18	4.25
II	−0.77	2.15	0.78	2.25	2.99	3.52	4.35	4.19	4.26

	$-OCH_3$			$-NH_2$			$-CH_3$		
	orto	meta	para	orto	meta	para	orto	meta	para
I		monocation		0.76	1.22	1.9			
I	3.92	3.66	4.65	3.99	4.27	5.33	3.83	4.10	4.49
II	3.74	3.73	5.08	4.12	4.34	4.97	3.78	4.13	4.51

	$-OH$			Piridines-NH_2			Aniline
	orto	meta	para	orto	meta	para	
I	4.13	3.63	4.84	6.07	5.27	8.17	4.02
II	4.16	3.73	4.84	6.11	5.38	8.18	—

The calculations of pK_a in different solvents provided the basis for the definition of the K_a constant in water and in a non-aqueous solvent.

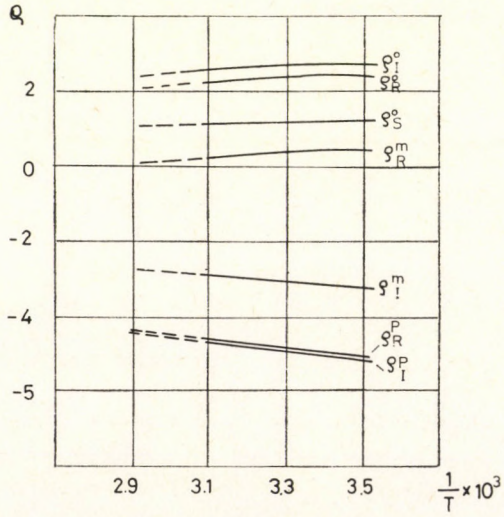

Fig. 1

Relationship between ϱ and $1/T$ of derivatives of aniline

$$K_{a,\,H_2O}=\frac{a^{H_2O}_{RNH_2}\times a_{H_3O^+}}{a^{H_2O}_{RNH_3^+}}\,; \qquad K_{a_M}=\frac{a^{M}_{RNH_2}\times a_{MH_+}}{a^{M}_{RNH_3^+}} \tag{9}$$

$$-pK_a=pK_{a_{H_2O}}-pK_{a_M}=\log K_{a_M}-\log K_{a_{H_2O}}$$

From the definition of K_r

$$\log\frac{a_{MH^+}}{a_{H_3O^+}}=-\log K_r+\log\frac{a^*_{H_2O}}{a^*_M} \tag{10}$$

For aromatic amines the following is also valid:

$$\log\frac{a^{H_2O}_{RNH_3^+}}{a^{M}_{RNH_3^*}}=\frac{e^2N}{4.606\,RTr}\left(\frac{1}{\varepsilon_M}-\frac{1}{\varepsilon_{H_2O}}\right)+\frac{\Delta A}{4.606\,RT} \tag{11}$$

From definition [9]:

$$\log\frac{a^{M}_{RNH_2}}{a^{H_2O}_{RNH_2}}=-\frac{\Delta H^{M}_{RNH_2}}{2.303\,RT} \tag{12}$$

Because $\Delta H^{M}_{RNH_2}$ is small ~ 0.2 kcal/kmol this element can be ignored.

Effective radii of aromatic amines were calculated as an arithmetic mean of three dimensions of projection on X, Y, Z axis. The values of effective r for aromatic amines are presented in *Table 5*.

Table 5.

Effective radii *(r)* of aromatic amines (nm)

Derivatives of aniline							
group	$-NO_2$	$-OH$	$-Cl$	$-NH_2$	$-OCH_3$	$-COOH$	$-CH_3$
orto, meta	0.2084	0.2115	0.2009	0.2065	0.2032	0.2146	0.2041
para	0.211	0.2145	0.2022	0.2087	0.2049	0.218	0.206
3,4-di-Cl	0.2447	3-Br	0.2033	aniline and pir.-NH_2 0.1921			

Derivatives of naphthalene and di-phenyl
α-naphthyloamine 0.2333, benzidine 0.3138

The value of ΔA was calculated from literature data of pK_a aniline and p-toluidine dissolved in methanol and ethanol [10, 11].

After algebraic transformations Eq. (9), (10) and (11), Eq. (13) was obtained.

$$pK^{T}_{a_M}=pK^{T}_{a_{H_2O}}-\log\frac{a^*_{H_2O}}{a^*_M}+\frac{298}{T}\left[\log K_r-63.31\frac{0.1921}{r}\left(\frac{1}{\varepsilon_M}-\frac{1}{\varepsilon_{H_2O}}\right)+2.595\right]+$$
$$+0.012\log K_r-0.665. \tag{13}$$

Table 6 presents the $\log a^*_{H_2O}/a^*_M$ data for different solvents.

Table 7 presents the values of pK_a of aniline and p-toluidine calculated

Table 6.

Logarithm $a^*_{H_2O}/a^*_M$

Solvent	MeOH	EtOH	iz-PrOH	n-BuOH	iz-BuOH	iz-PentOH
$\log a^*_{H_2O}/a^*_M$	1.397	1.512	1.634	1.706	1.711	1.781

Solvent	bensyl al.	nitrobenz.	formamide	ethyl acet.	buthyl acet.
$\log a^*_{H_2O}/a^*_M$	1.756	0.762	0.3452	0.7432	0.8729

Table 7.

Values of pK_a of aniline and *p*-toluidine in methanol and ethanol, and values of pK_a of *p*-toluidine in formamide in different temperatures. Literature data and calculated from Eq. (13)

Solvent	MeOH	EtOH	Formamide				
Temp. °C	25	25	15	20	25	30	35
aniline lit.	6.00	5.70	—	—	—	—	—
aniline calc.	6.02	5.60	—	—	—	—	—
p-tol. lit.	6.60	6.24	5.93	5.88	5.81	5.66	5.53
p-tol. calc.	6.56	6.16	6.06	5.94	5.81	5.69	5.58

from Eq. (13) for methanol, ethanol and formamide. These values are compared to literature data [10—12].

A good agreement was obtained for all calculated values. Especially good agreement was achieved in all temperatures for formamide.

SYMBOLS

pK_a^{298} pK_a at temperature 298 K.
$pK_{a,\,anil}$ pK_a of aniline.
$pK_a^{(para)}$ pK_a of para derivatives of aniline.
K_r equilibrium constant of the reaction exchange proton between solvent and water.
r effective radius of aromatic amine.
$\Delta H^M_{RNH_2}$ molal enthalpy of aromatic amine in organic solvent.
ε_M dielectric constant of solvent.
ε_{H_2O} dielectric constant of water.
pK_a^T pK_a at temperature T K.
$pK^T_{a_M}$ pK_a at temperature T in solvent M.
$a^*_{H_2O}$ moles of water in 1 dm^3.
a^*_M moles of solvent in 1 dm^3.

REFERENCES

1. Popov, A. F. i Piskunova, Z. P.: Struktura i osnovnost' aminov, Probl. fiziko-organicheskoi khimii, Izd. Naukova Dumka, Kiew *1978*.
2. Perrin, D. D.: Aust. J. Chem. *1964*, 17, 484.
3. Bolton, P. D. and Hall, F. M.: J. Chem. Soc. B *1969*, 259.
4. ibid *1969*, 1047.
5. Bolton, P. D. and Hall, F. M.: Aust. J. Chem. *1967*, 20, 1797.
6. ibid *1967*, 21, 939.
7. Shorter, J.: Analiza korelacyjna w chemii organicznej, PWN Warszawa *1980*. p 38.
8. Laitinen, H. A. i Harris, W. E.: Khimicheskii Analiz, izd 2, Izdat. Khimiya Moscow *1979*, pp. 101.
9. Pigon, K., Ruziewicz: Chemia fizyczna, PWN Warszawa *1980*, p 163.
10. Spivey, H. O. and Shedlovsky, T.: J. Phys. Chem. *1967*, 71, 2165.
11. Izmailov, N. A.: Zh. fiz. khim. *1950*, 24, 321.
12. Mukhopadhay, S. and Nayak, B.: Electrochim. Acta *1980*, 25, 807.

РЕЗЮМЕ

Автором изучены термодинамические свойства ароматных аминов растворенных в органических растворителях. В стати приведена методика расчёта РКа значений растворов содержащих ароматные амины различной температуры, растворенных в различных растворителях.

HUNGARIAN JOURNAL
OF INDUSTRIAL CHEMISTRY
VESZPRÉM
Vol. 11. pp. 231–239 (1983)

ТЕОРЕТИЧЕСКИЕ И ЭКСПЕРИМЕНТАЛЬНЫЕ ИССЛЕДОВАНИЯ АДСОРБЦИИ БЕНЗОЛА НА НУКСИТ-БО

Ч. Ш. Ибрагимов, Е. Немет*, А. А. Мамедов и Т. Н. Шахтахтинский

(Институт теоретических проблем химической технологии
АН Азерб. ССР, Баку и
* Научно-исследовательский институт технической химии ВАН,
Веспрем)

Novembr 15, 1982

Поступила в редакцию Ноябрь 15, 1982.

В статьи излагается влияние скорости потока смеси бензол-азот и фракционного состава адсорбента антивированного угля Нуксит-БО на выходные кривые. Связывая данные выходных кривых с текущей концентрацией адсорбата и равновесной концентрацией адсорбтива получены данные общего коэффициента массообмена. В предложении линейного распределения концентрации в радиальном направлении зерна для каждой концентрации определяются коэффициенты диффузии в микро- и макропорах.

Целью наших исследований является определение влияния скорости потока смеси бензол-азот и фракционного состава адсорбента Нуксит-БО на выходные кривые, определение адсорбционной способности этого адсорбента при 293 К в пределах равновесной концентрации бензола $0{,}005 \div 0{,}1$ кг/м^3, определение коэффициентов диффузии и массообмена бензола в динамической адсорбционной системе бензол-азот-активированный уголь Нуксит-БО, влияния на эти коэффициенты изменения диаметра гранул от 1,3 мм до 2,5 мм и скорости потока смеси бензол-азот от 0,1 м/с до 1 м/с.

На *рис. 1* приводится изотерма адсорбции бензола на активированном угле Нуксит-БО при 293 К.

На *рис. 2* изложены выходные кривые динамики адсорбции бензола в неподвижном слое активированного угля Нуксит-БО. Диаметр адсорбера Д=35 мм, высота слоя $H=157$ мм. В I части рисунка, где $\bar{x}=C/C_0$ — относительная концентрация бензола в смеси газа, $C_0=10$ г/м^3 (для всех опытов), приведены выходные кривые адсорбции бензола на активированном угле Нуксит-БО диаметром гранул $d=2{,}50$ мм. Кривые 1—5 соответствуют скоростям потока газовой

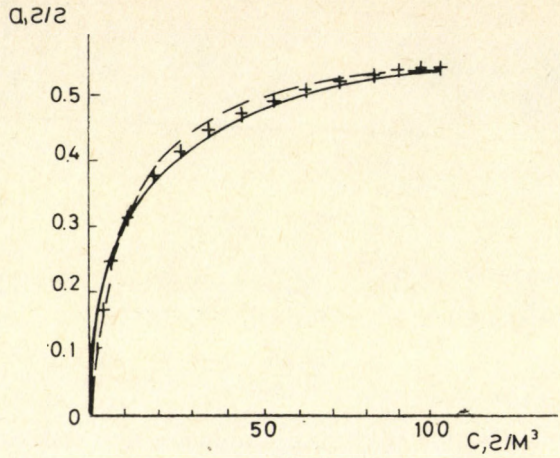

Рис. 1

Изотерма адсорбции бензола на Нуксит-БО: измеренные данные — уравнение Лангмюра, — — изотерма Дубинина-Радушкевича

смеси $v=1{,}00$; 0,667; 0,333; 0,167; 0,1 м/с. Видно, что с уменьшением скорости потока увеличивается время первого проскока и время работы работающего слоя. На II—IV участках рисунка указаны выходные кривые для тех же скоростей потока, но на других фракциях активированного угля Нуксит-БО с меньшими диаметрами гранул. Во II участке диаметр гранул $d=2{,}25$ мм, в III участке $d=1{,}8$ мм, в IV участке $d=1{,}3$ мм. Видно, что время первого проскока во всех образцах при одинаковых скоростях меняется незначительно. Время работы работающего слоя с уменьшением размеров гранул уменьшается. Это происходит по той причине, что в крупнозерненных образцах массообмен идет медленнее, потому и насыщение происходит медленнее, чем в мелкозернистых образцах.

Для определения влияния скорости потока и зернения на общий коэффициент массообмена, строим рабочую линию процесса, с целью организации связи между текущей и равновесной концентрациями адсорбтива. Рабочую линию процесса построили соединением двух точек: 1-я получается из данных задаваемого первого проскока выхода C' и остаточного количества адсорбата в адсорбенте a' после десорбции (недесорбируемое количество адсорбата). 2-ю точку получили из начальной концентрации целевого компонента C_0 и динамической активности адсорбента a'_0 (получается $a'_0=0{,}8\,.\,a_0$, где a_0 равновесный с C_0 адсорбат. Множитель 0,8 означает, что адсорбент в динамических условиях насыщается на 80%). Данные 1-й точки таковы: на выходе задаваемый первый проскок $C'=0{,}05$ и адсорбент чистый $a'=0$; 2-я точка $C_0=10$ г/м³ для всех образцов и скоростей, $a'_0=0{,}8\,.\,a_0=0{,}8\,.\,0{,}3$ г/г$=0{,}24$ *(рис. 3)*.

Связывая данные выходных кривых *(рис. 2)* с текущей концентрацией адсорбата и равновесной концентрацией адсорбтива с помощью кривых *рис. 3* и подставляя эти данные в кинетическое уравнение адсорбции (1) [1]:

$$\beta=\frac{\mathrm{d}C/\mathrm{d}\tau\cdot\mathrm{d}a_*/\mathrm{d}C}{C-C_\mathrm{p}}, \tag{1}$$

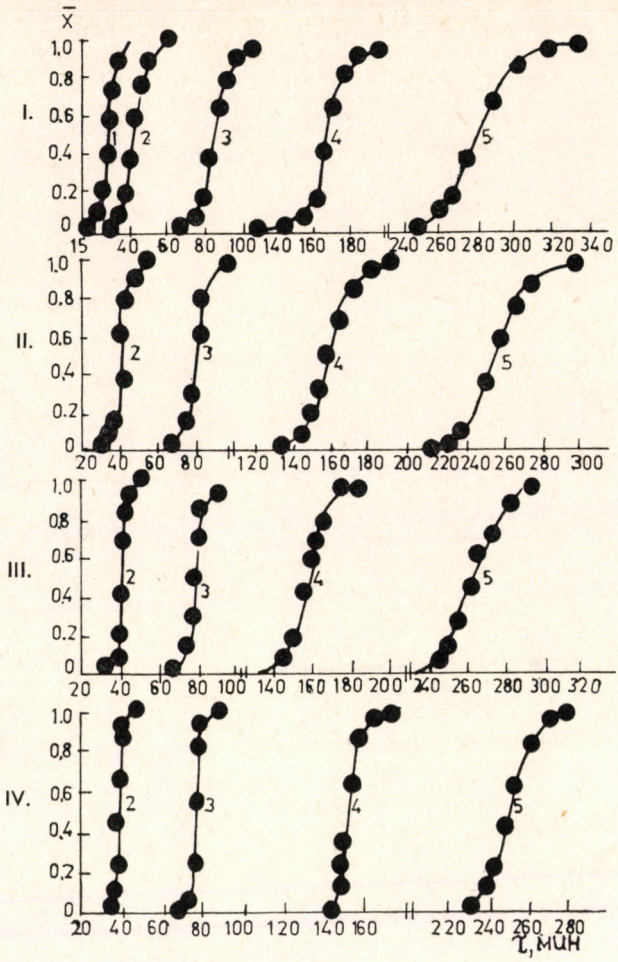

Рис. 2

Выходные кривые адсорбции бензола на Нуксит-БО

получаем данные общего коэффициента массообмена для разных зернений активированного угля Нуксит-БО и разных скоростей потока бензол-азот. Результаты некоторых из них приведены на *рис. 4*. В (1) τ — время; C и C_p — неравновесная и равновесная концентрации адсорбтива; a_* — неравновесная концентрация адсорбата.

Как видно из рисунка 4, кривые коэффициента массообмена проходят через максимум. Кривые 1 и 2 получены для одинакового образца с зернением $d=2{,}5$ мм, но разных скоростей потока $v=0{,}667$ м/с и $v=0{,}1$ м/с соответственно. Кривые 3 и 4 получены для одинакового зернения $d=1{,}3$ мм и разных скоростей потока $v=0{,}667$ м/с и $v=0{,}1$ м/с. Видно, что с увеличением скорости потока на одном и том же образце в шесть раз, максимальная точка коэффициента массообмена увеличивается на 3,5 раза. Это наблюдается на обоих образцах. Это объясняется тем, что с увеличением скорости потока количество подаваемых

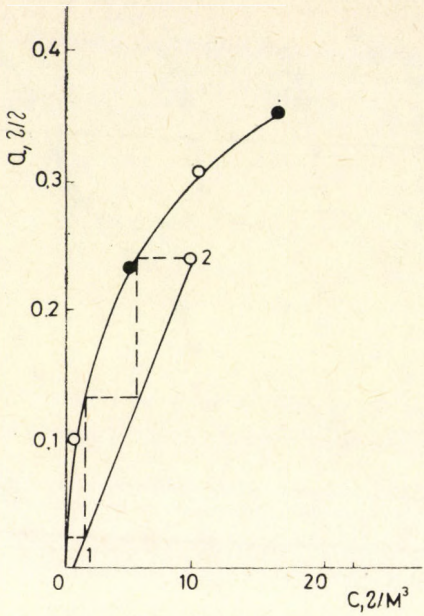

Рис. 3

Равновесная и рабочая линии для адсорбции бензола

веществ увеличивается, что способствует улучшению массообмена. Наблюдается влияние и зернения. Кривые 1 и 3, также 2 и 4 соответствуют одинаковым скоростям потока на разных образцах с диаметрами гранул 2,5 мм и 1,3 мм.

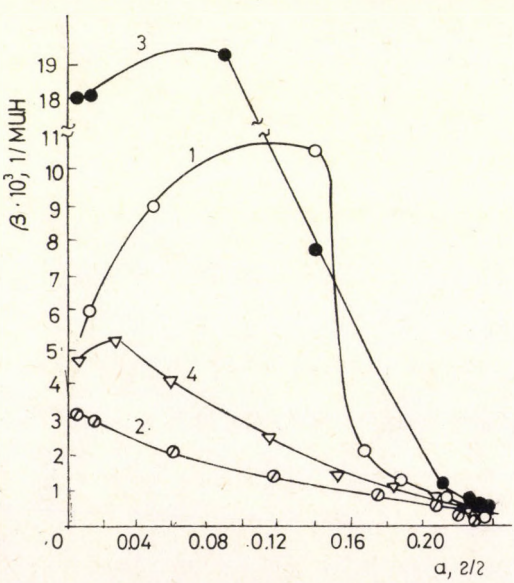

Рис. 4

Зависимость общего кинетического коэффициента от степени заполнения адсорбента

С уменьшением зернения в 2 раза максимальная точка коэффициента массообмена увеличивается немного меньше, чем в два раза. Это объясняется тем, что поверхность контакта фаз увеличивается.

Видно, что общий коэффициент массообмена меняется в большом интервале степени заполнения адсорбента и принимать его постоянным, как это делается часто, приводит к большим отклонениям. Так для случая кривой 1 среднее значение коэффициента массообмена меньше от максимального его значения 2,78 раза, а больше от минимального значения на два порядка. Для кривой 2 эти различия соответственно равны 2,51 и два порядка, для кривой 3—2,45 и один порядок, для кривой 4—2,52 и один порядок.

Коэффициент диффузии в области адсорбции считается одной из самых нестабильных констант. Нам представляется, что такое мнение создалось потому, что коэффициент диффузии обычно принимается постоянным. Ниже мы увидим, что это допущение часто не оправдывается.

Управление внутренней диффузии в отдельных микропористых зонах (в микропористые зоны входят многочисленные адсорбционные ячейки) со сферической координатой в радиальном направлении гранулы записывается в виде [2]:

$$\frac{\partial(ra_*)}{\partial\tau}=\mathrm{D_a}\frac{\partial^2(ra_*)}{\partial r^2}, \tag{2}$$

то же в транспортных макропорах можно записывать в виде

$$\frac{\partial(ra_*)}{\partial\tau}+\frac{\partial(rC_\mathrm{c})}{\partial\tau}=\mathrm{D_c}\frac{\partial^2(rC_\mathrm{c})}{\partial r^2}, \tag{3}$$

где D_a, D_c — коэффициенты диффузии в микро- и в макропорах; a_*, C_c — текущие концентрации адсорбата и адсорбтива; r — координата; τ — время адсорбционной работы слоя.

Переписываем (2) и (3) в виде

$$\frac{\partial a_*}{\partial\tau}=D_\mathrm{a}\left(\frac{\partial^2 a_*}{\partial r^2}+\frac{2}{r}\frac{\partial a_*}{\partial r}\right), \tag{2'}$$

$$\frac{\partial a_*}{\partial\tau}+\frac{\partial C_\mathrm{c}}{\partial\tau}=\mathrm{D_c}\left(\frac{\partial^2 C_\mathrm{c}}{\partial r^2}+\frac{2}{r}\frac{\partial C_\mathrm{c}}{\partial r}\right). \tag{3'}$$

При проведении динамического опыта на любом фиксированном сечении адсорбера вокруг каждой гранулы в газовой фазе концентрация меняется по закономерности выходной кривой. Предполагаем, что в центре зерна, при $r=0$ $C_\mathrm{c}=0$, $a_*=0$. Распределение концентраций в радиальном направлении зерна для каждой концентрации принимаем линейным и в виде

$$\begin{aligned} C_\mathrm{c}&=b_\mathrm{c}+K_\mathrm{c}r,\\ a_*&=b_\mathrm{a}+K_\mathrm{a}r, \end{aligned} \tag{4}$$

где b и K — константы.

Зная в двух точках, $r=0$ и $r=R$ значения концентраций, из (4) получаем

$$K_\mathrm{c}=\frac{C_\mathrm{c}}{R}, \quad K_\mathrm{a}=\frac{a_*}{R}. \tag{4'}$$

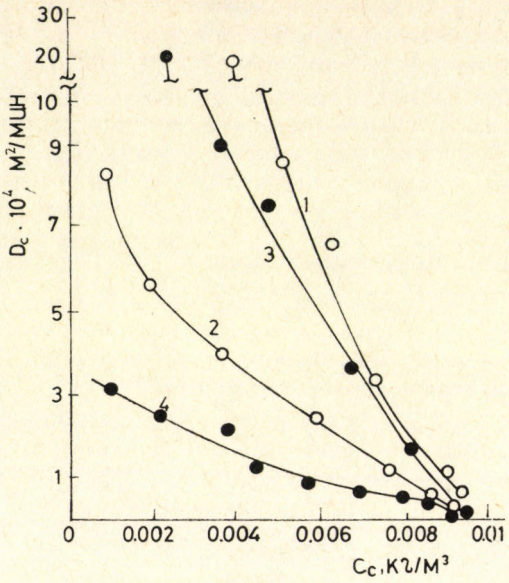

Рис. 5

Изменение коэффициента диффузии в транспортных порах на радиальном расстоянии $r = 1.2 \cdot 10^{-3}$м; $1 - d = 2.5 \cdot 10^{-3}$м, $v = 0.667$ м/с; $2 - d = 2.5 \cdot 10^{-3}$м, $v = 0.1$ м/с; $3 - d = 1.3 \cdot 10^{-3}$м, $v = 0.667$ м/с; $4 - d = 1.3 \cdot 10^{-3}$м, $v = 0{,}1$ м/с.

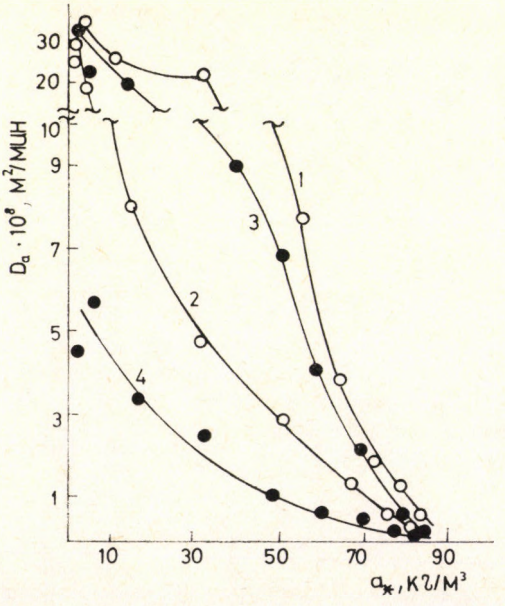

Рис. 6

Изменение коэффициента диффузии в микропорах на радиальном расстоянии $r = 1{,}2 \cdot 10^{-3}$м) обозначения 1, 2, 3 и 4 те же, что и на *рис. 5*

По этим значениям K_c и K_a из (4) можно определить концентрации в транспортных и микропорах для любого значения r.

На основе изложенного предположения в виде (4) значения D_c и D_a были определены численным методом. Из уравнений (2′) и (3′), написанных в конечно-разностной форме, вычисляем коэффициенты D_a и D_c и другие параметры, результаты которых изложены на *рис. 5—10*.

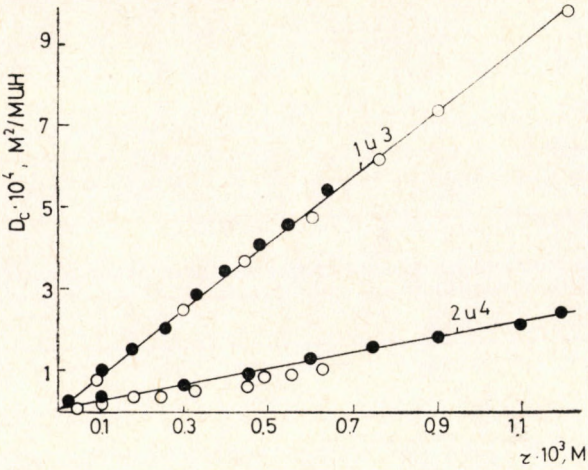

Рис. 7

Изменение коэффициента диффузии в транспортных порах по r, при концентрации адсорбтива на границе гранулы C_0=0,006 кг/м³: обозначения 1, 2, 3 и 4 те же, что и на рис. *5*

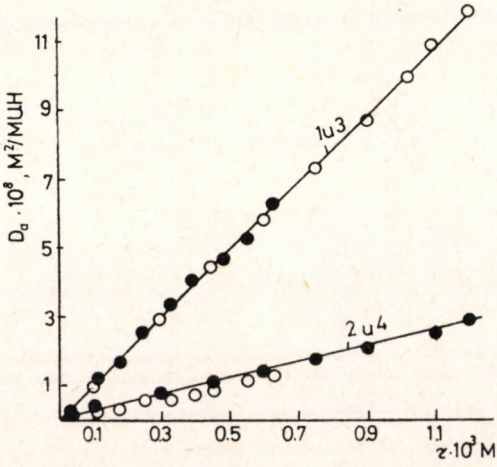

Рис. 8

Изменение коэффициента диффузии в микропорах по r, при концентрации адсорбтива на границе гранулы C_0=0,006 кг/м³: обозначения 1, 2, 3 и 4 те же, что и на *рис. 5*

На *рис. 5—6* иллюстрирована зависимость коэффициентов диффузии в транспортных и микропорах от концентрации при разных зернениях адсорбента и скорости потока адсорбтива. Сравнение коэффициентов диффузии в транспортных (D_c) и микропорах (D_a) показывает, что они отличаются на четыре порядка. Кривые 1 и 2, 3 и 4 отражают значения коэффициентов диффузий для разных скоростей потоке при равных других условиях. Видно, что в этом случае они отличаются значительно. Так при скорости потока 0,667 (кривая 1) и 0,1 м/с (кривая 2) оба коэффициента в некоторых участках при одинаковой концентрации

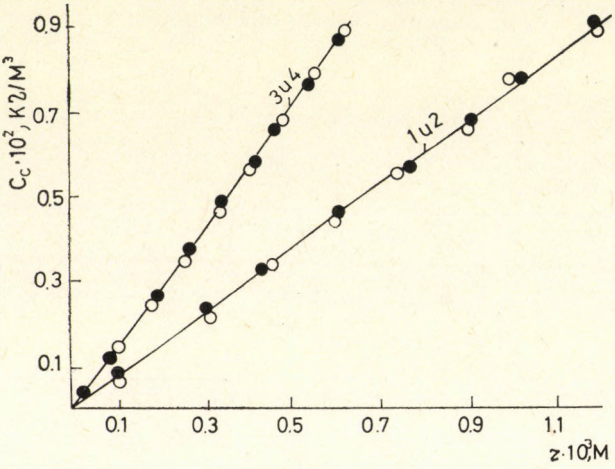

Рис. 9

Распределение концентрации адсорбтива в транспортных порах при концентрации его на границе гранулы $C_0 = 0{,}0093$ кг/м³: обозначения 1, 2, 3 и 4 те же, что и на *рис. 5*

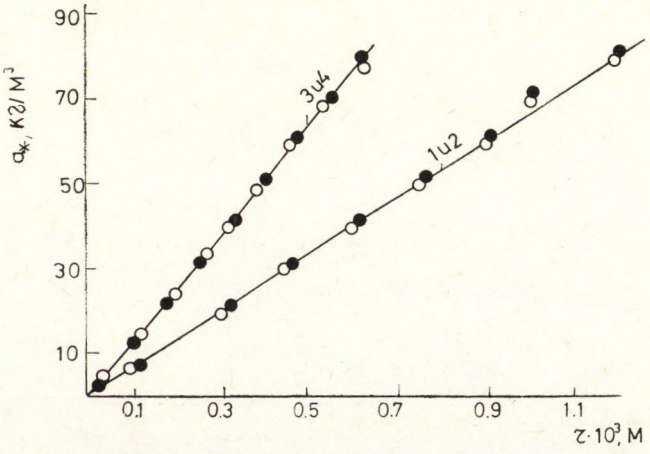

Рис. 10

Распределение концентрации адсорбата в микропорах при концентрации адсорбтива на границе гранулы $C_0 = 0{,}0093$ кг/м³: обозначения 1, 2, 3 и 4 те же, что и на *рис. 5*

отличаются до 5-ти раза и больше. Причем при меньшей скорости потока коэффициенты диффузии и в макропорах, и в микропорах всегда меньше, чем при большей скорости. Кривые 1 и 3, 2 и 4 показывают влияние также зернения адсорбента на коэффициенты диффузии в транспортных и микропорах при одинаковых других условиях. Видно, что при $d=2{,}5$ мм оба коэффициента диффузии значительно выше, чем при $d=1{,}3$ мм. Исследования проведённые на основе вышеизложенных предположений показывают, что если взять среднее значение констант диффузии и считать их постоянными, то при проверке адекватности можно допустить грубую ошибку.

На рисунках 5 и 6 приведены коэффициенты диффузий только на участке зерна $r=1{,}2.10^{-3}$ м. Но составленный алгоритм расчета позволяет получить эти зависимости на всех участках значений r, в интервале $r=0{,}025\div1{,}2$ мм. Это дает возможность получить D_c и D_a в зависимости от r, примеры для которых, при концентрации адсорбтива на границе гранулы $C_0=0{,}006$ кг/м^3, приведены на рис. 7 и 8. Из этих рисунков видно, что данные коэффициентов диффузии в радиальном направлении гранул ложатся на прямой. Установлено, что различная фракция гранул не оказывает влияние, а скорость потока бензол-азот из-за различных поверхностных условий, предположенных нами ранее [см. рисунок 2 и уравнение (4)] имеет значительное влияние на коэффициенты в радиальном направлении. С увеличением линейной скорости потока коэффициенты увеличиваются. Эти закономерности получены для всех дискретных значений начальных концентраций бензола в интервале $C_0=0{,}0047\div0{,}00985$ кг/м^3.

На основании вышеуказанного алгоритма получено также *распределение концентрации адсорбтива и адсорбата* в транспортных и микропорах в радиальном направлении зерен адсорбента при разных начальных концентрациях на границе зерен в интервале $C_0=0{,}0047\div0{,}00985$ кг/м^3.

На рисунках 9 и 10 иллюстрировано это распределение для начальной концентрации на границе зерен $C_0=0{,}0093$ кг/м^3. Видно, что изменение скорости потока не оказывает влияние на распределение концентраций в транспортных и микропорах гранул. Зернение же оказывает влияние и с уменьшением его увеличивается концентрация адсорбтива и адсорбата в порах зерен адсорбента.

ЛИТЕРАТУРА

1. Ибрагимов Ч. Ш.: Азерб. хим. журнал, 1980. 3, 38.
2. Волощук А. М., Дубинин М. М. и Золотарев П. С.: Сб. Адсорбция и пористость, Наука, Москва, 1973. ст. 285.

BENZENE VAPOUR ADSORPTION ON NUXIT-BO ACTIVE CARBON BED

SUMMARY

The effect of flow rate of benzene-nitrogen mixture and the particle size of NUXIT-BO active carbon on the shape of breakthrough curves are discussed. The overall mass transfer coefficient could be calculated from the data obtained, among them the shape of the breakthrough curves, the concentration of the benzene vapour to be adsorbed and the equilibrium adsorbate concentration were taken into account. The values of diffusion coefficient valid for the micro and macro pores were determined.

HUNGARIAN JOURNAL
OF INDUSTRIAL CHEMISTRY
VESZPRÉM
Vol. 11. pp. 241–246 (1983)

COMPARISON OF ESTIMATION METHODS OF VAPORIZATION HEAT

MISS E. FRANK and GY. DEÁK*

(Oil and Gas Mining Company,
* Veszprém University of Chemical Engineering, Veszprém)

Received: December 23, 1982.

The most important methods used for the estimation of vaporization heat are reviewed. Their applicability in the case of n-paraffins, isoparaffins, aromatics, monoolefins, diolefins, alcohols, ketones, amines, ethers and esters is evaluated using literature data.

The knowledge of the vaporization heat of various compounds is often indispensable for the design and operation of various chemical operations. Generally, the vaporization heat data found in handbooks relate to the normal boiling point temperatures [1, 2a, 3] while most calculations require data at other temperatures.

Several methods were developed for the estimation of vaporization heat data. The major estimation methods are reviewed here, followed by a comparison of their accuracy for various classes of compounds.

Methods Used to Estimate the Vaporization Heat [2b]

Generally, most estimation methods make use of the fundamental physical constants (critical pressure and temperature) of compounds. Some calculation methods use the integrated form of the CLAUSIUS–CLAPEYRON equation, while the others apply empirical equations. The most important estimation methods are as follows:

— the WATSON equation

$$\Delta h_2 = \Delta h_1 \left(\frac{1 - T_{r,2}}{1 - T_{r,1}} \right)^{0.38} \tag{1}$$

where

Δh_1 is the known vaporization heat at reduced temperature, $T_{r,1}$:

— the PITZER equation:

$$\Delta h = RT_c [7.08 (1 - T_r)^{0.354} + 10.95\omega (1 - T_r)^{0.456}] \tag{2}$$

Some of the estimation methods define function ψ as:

$$\psi \equiv \frac{\Delta h}{RT_c \Delta Z}$$

The following expressions are used for function ψ:

— the LEE–KESLER equation:

$$\psi = 6.09648 - 1.28862T_r + 1.016T_r^7 + \omega(15.6875 - 13.4721T_r + 2.615T_r^7) \tag{3}$$

— the RIEDEL equation:

$$\psi = B + CT_r + 6DT_r^7 \tag{4}$$

where B, C and D are the correlation coefficients of RIEDEL's vapour pressure equation

$$\psi = A[1 + T_r^2 + 3B(1 - T_r^2)^2] \tag{5}$$

where A, B are the correlation coefficients in the RIEDEL–PLANCK–MILLER vapour pressure equation

— the FROST–KALKWARF equation

$$\psi = \frac{-B + CT_r - \dfrac{27P_r}{32T_r}}{1 - \dfrac{27P_r}{64T_r^2}} \tag{6}$$

where B and C are the correlation coefficients of the FROST–KALKWARF vapour pressure equation

— the THEK—STIEL equation

$$\psi = B(1 - 0.375T_r - 0.11719T_r^2 - 0.06348T_r^3) + (1.042A - 0.46248B)(T_r^{C+1} - 0.04) \tag{7}$$

where

$$B = \frac{\Delta h_b}{RT_c(1 - T_{b,r})^{0.375}} \tag{7a}$$

where A, B and C are the correlation coefficients of the THEK–STIEL vapour pressure equation.

The correlation coefficients in Eq. (3) to (7), and thus the ψ values, can be calculated from the critical pressure and temperature data of the compounds, and the state variables (pressure and temperature) of the system studied. For the calculation of Δh from ψ the difference in the compressibilities of the gas and liquid phases, ΔZ must also be known.

ΔZ values can be calculated by the HAGGENMACHER relationship and, the OTHMER and NERNST equations [4a]. However, since the application ranges of these equations are narrow, the ΔZ values were obtained by interpolation from the Table of LYDERSEN and GREENKORN [4b].

According to Eq. (7a) the vaporization heat at the normal boiling point temperature, Δh_b must also be known for the calculation of correlation coeffi-

cient B in the THEK–STIEL equation. Δh_b data not available in handbooks can be estimated by the following expressions:

— the RIEDEL equation:

$$\Delta h_b = 1.093 R T_c \left[T_{b,r} \frac{\ln P_c - 3.289}{0.93 - T_{b,r}} \right] \tag{8}$$

— the KLEIN equation [4c]:

$$\Delta h_b = \frac{1.04 R T_b}{(1 - T_{b,r})} (1 - 9.869 T_{b,r}^{-3} P_c^{-1})^{0.5} (\ln P_c - 2.289) \tag{9}$$

— the CHEN equation:

$$\Delta h_b = \frac{R T_b (3.978 T_{b,r} - 7{,}498 + 1.555 \ln P_c)}{1.07 - T_{b,r}} \tag{10}$$

— the VETERE equation:

$$\Delta h_b = \frac{R T_b (0.4343 \ln P_c - 1.68289 + 0.89584 T_{b,r})}{0.37691 - 0.37306 T_{b,r} + 1.46834 P_c^{-1} T_{b,r}^{-2}} \tag{11}$$

Results and Discussion

The estimation methods mentioned above were tested for the following compound classes:

- normal and isoparaffins
- cycloparaffins
- aromatics
- mono and diolefines
- primary and secondary aliphatic alcohols
- aliphatic ketones
- primary and secondary aliphatic amines
- aliphatic esters
- aliphatic ethers.

Computer programmes were used to calculate the heat of evaporation data of various compounds at their normal boiling point temperatures and at 293 K. Calculated results were compared with published data [2a]. The relative deviation at the normal boiling point temperature of the vaporization heat data calculated by Eq. (8) to (11) and published in literature was calculated as:

$$r_{ij}\,\% = 100 \frac{X_i - X_{ij}}{X_i} \tag{12}$$

where X_i is the published Δh_b value of compound i
X_{ij} is the Δh_b value of compound i calculated by method j, $j = 8, \ldots, 11$

The relative deviation at $T = 293$ K of the vaporization heat data calculated by Eq. (1) to (7) was evaluated similarily to Eq. (12) except that:

X_i is the published Δh value of the i-th compound, or, if it is not known, it is the Δh value calculated by the THEK–STIEL equation from Δh_b.

X_{ij} is the Δh value of the i-th compound calculated by method j, $j=1, ..., 6, 7/8, ..., 7/11$.

The relative deviations were determined for 99 compounds. Since the detailed discussion of the vaporization heat and r% data is beyond the scope of this paper, only the general conclusions are reviewed here. Results of the calculations are available from the authors upon request.

From the analysis of the relative deviations obtained for the various compound classes, the following general conclusions can be made:

— for paraffins, cycloparaffins and aromatics the error of estimation is less than 1% for Δh_b and less than 2% for Δh (except for a very limited number of cases). Generally, estimated results are smaller than the calculated ones;
— for olefines the relative deviations are in the 1–2% range, and the error is smaller for the monoolefines;
— for ketones, amines, esters and ethers the error of estimation is larger, 2–5%.
— for alcohols the error is especially large, 4–7%, a fact clearly related to the H-bonding ability of alcohols;
— for each compound class there are r% values larger than the previous values. The outliers were obtained by Eq. (1), (2) and (6).

The applicability of the calculation methods depends on the error of estimation of Δh_b and Δh.

Standard deviations used for the comparison were calculated as:

$$\sigma_j = \sqrt{\frac{\sum_{i=1}^{n} r_{ij}^2}{n-1}} \tag{13}$$

where r_{ij} is the relative deviation determined by Eq. 12, %
$j=8, ..., 11$ and $1, ..., 6, 7/8, ..., 7/11$ is the serial number of the method used to calculate Δh_b and Δh, respectively $i=1, ..., n$
n = number of the compounds tested in a compound class.

Table 1

Standard deviations, Δh_b and Δh values obtained with the different calculation methods for various classes of compounds

Compound class	Estimation of Δh_b				Estimation of Δh										No. of proposed equation for	
	8	9	10	11	1	2	3	4	5	6	7/8	7/9	7/10	7/11	Δh_b	Δh
n-paraffins	0.82	0.70	0.41	0.36	6.09	4.96	1.82	1.21	1.36	5.31	0.71	0.50	0.31	0.27	11	7/11
isoparaffins	0.49	0.60	0.75	0.79	5.63	3.99	1.22	0.78	0.50	4.50	0.40	0.49	0.67	0.53	8	7/8
cycloparaffins	0.32	0.37	0.54	0.59	3.86	2.03	0.27	0.30	1.06	3.05	0.27	0.32	0.44	0.47	8	7/8
aromatics	1.05	0.96	0.84	1.09	5.27	3.45	1.53	1.32	1.85	5.17	0.94	0.83	0.73	0.94	10	7/10
monoolefines	2.58	2.25	2.59	2.55	4.12	3.13	1.85	1.83	2.05	2.32	1.88	1.62	1.93	1.89	9	7/9
diolefines	4.25	3.80	4.25	4.31	3.54	4.81	2.81	2.78	3.28	3.10	2.91	2.66	2.71	2.96	9	7/9
alcohols	4.64	6.91	6.66	5.98	4.88	4.19	4.31	5.15	3.93	3.46	5.07	7.14	6.85	6.27	8	6
ketones	4.20	3.50	3.58	3.66	4.51	4.82	3.98	3.44	2.88	6.41	3.28	2.69	2.76	2.82	9	7/9
amines	3.91	3.63	3.31	3.51	4.11	5.36	4.07	3.65	4.53	5.23	3.47	2.94	2.74	2.89	10	7/10
ethers	1.94	1.55	1.47	1.61	5.81	6.06	2.23	1.75	1.85	4.80	1.75	1.20	1.08	1.24	10	7/10
esters	1.26	2.08	1.91	1.80	3.94	1.86	1.20	1.29	1.83	2.68	1.31	1.76	1.70	1.58	8	3

Standard deviations obtained for the various estimation methods and compound classes are summarized in *Table 1.*

The serial numbers shown in Table 1 refer to the calculation method, e.g. No. 7/10 indicates the THEK–STIEL equation (Eq. 7) which uses the Δh_b value obtained from the CHEN equation (Eq. 10).

Standard deviation data shown in *Table 1* support the previous conclusions drawn from the relative deviation values.

Evaluation of the Estimation Methods

From the comparison of the standard deviations of the various estimation methods used for the calculation of. Δh_b it can be concluded that none of Eq. (8) to (11) is more suitable for any particular compound class than all the other. For nonpolar compounds, the standard deviations are low, while for increasingly polar compounds the standard deviation increases. The error is the largest for alcohols, and even Eq. (8) is only relatively better than the other three equations.

From the comparison of the standard deviations of the estimation methods used for the calculation of Δh, it can be concluded that the WATSON (Eq. 1) and the PITZER (Eq. 2) equations yield the worst results. Consequently, their use for the calculation of vaporization heat data is not recommended for any of the compound classes.

The THEK–STIEL equation (Eq. 7) gave the smallest standard deviation for each compound class. Literature references propose the application of this equation for the calculation of Δh of polar compounds. Except for alcohols, this conclusion is supported by our calculations.

It was concluded that Eq. (7) is extremely sensitive for the accuracy of Δh_b used. Standard deviations indicate that the THEK–STIEL equation, which uses the most accurate equation for Δh_b, gives the best results for Δh.

This observation explains the anomalies of Eq. (7) with alcohols.

In conclusion, in the last two columns of Table 1 the serial numbers of the equations are indicated which yield the smallest standard deviations in the calculation of vaporization heat data at both the normal boiling point temperature and at temperature T.

The vaporization heat values of 99 compounds—calculated by the most accurate methods—are available from the authors upon request.

SYMBOLS

A, B, C, D	— correlation coefficients in the vapour pressure equations
Δh_b	— vaporization heat at temperature T_b, (J/mol)
Δh	— vaporization heat at temperature T, (J/mol)
Δh_1	— known vaporization heat at reduced temperature, $T_{r,1}$
Δh_2	— calculated vaporization heat at reduced temperature, $T_{r,2}$
P_c	— critical pressure, (bar)
P_r	— reduced pressure
R	— gas constant, (J/mol K)
T	— temperature, (K)
T_b	— normal boiling point temperature, (K)
T_c	— critical temperature, (K)
T_r	— reduced temperature
$T_{b,r}$	— T_b/T_c

ΔZ — $Z_g - Z_f$
Z_g — compressibility of the gas phase
Z_f — compressibility of the liquid phase
ω — acentric factor
ψ — function derived from the vapour pressure equations

REFERENCES

1. PERRY, J. H.: Handbook of Chemical Engineers' (in Hungarian), Műszaki Könyvkiadó, Budapest, 1969. pp. 311–315.
2. REID, R. C., PRAUSNITZ, J. M. and SHERWOOD, T. K.: The properties of gases and liquids. McGraw-Hill Book Company, New York, 1977. 2a: 630–665 2b: 197–214.
3. PREISICH, M.: Handbook of Chemists (in Hungarian), Műszaki Könyvkiadó, Budapest, 1972. pp. 448–457.
4. HECHT, G. and LEHMANN, H.: Calculation of the Thermodynamic Characteristics of Gases and Liquids, Műszaki Könyvkiadó, Budapest, 1972. 4a: pp. 144–145
4b: pp. 97–108
4c: pp. 146

РЕЗЮМЕ

Авторами рассмотрены методы описания теплоты испарения. Изучали возможность применения расчетных формул для *n*-парафинов, изопарафинов, ароматных соединений, моноолефинов, диолефинов, алкоголев, кетонов, аминов, эфиров и сложных эфиров.

HUNGARIAN JOURNAL
OF INDUSTRIAL CHEMISTRY
VESZPRÉM
Vol. 11. pp. 247–262 (1983)

ИССЛЕДОВАНИЕ ЛОКАЛЬНОГО МАССОПЕРЕНОСА ОТ ЧАСТИЦЫ К ЖИДКОСТИ. IV. ТРЕХФАЗНЫЕ СИСТЕМЫ: НЕПОДВИЖНЫЙ И ПСЕВДООЖИЖЕННЫЙ СЛОЙ. ВЫВОД ОБОБЩЕННОГО УРАВНЕНИЯ МАССОПЕРЕНОСА

А. Ермакова, В. А. Кузьмин, А. С. Умбетов

(Институт катализа СО АН СССР, г. Новосибирск)

Поступил в редакцию: февраль 8, 1983.

Приведены результаты экспериментального исследования локального массопереноса от частицы к жидкости в трехфазных неподвижном и псевдоожиженном слоях. Измерения проводились электрохимическим методом. Установлена зависимость осредненного и пульсационного значения коэффициента массопереноса от расходной скорости жидкости и газа, при изменении порозности слоя от 0,38 до 0,9. Отмечено, что с ростом скорости газа среднее значение и среднеквадратичное значение коэффициента массопереноса возрастают. Последнее достигает 13—21% от среднего значения.

С использованием экспериментальных данных, сообшаемых в настоящей работе, а также данных, описанных в Сообщении Ш, найдена общая инвариантная форма критериального уравнения для осредненного коэффициента массопереноса:

в области $40 \leq \overline{Re} \leq 2000$, $Sc \gg 1$:

$$\overline{Sh} = (0{,}693 \pm 0{,}015)\overline{Re}^{1/2} Sc^{1/3} \qquad \text{(I)}$$

которое справедливо для двух- и трехфазных, неподвижных и псевдоожиженных слоев. Критерий $\overline{Re}$ в уравнении (1) построен с использованием „определяющей" скорости, выраженной через суммарную диссипацию энергии газовой и жидкой фазы:

$$\overline{W} = \sqrt{2}\left((\varepsilon_g + \varepsilon_L)\cdot\lambda\right)^{1/3}, \ \lambda = d\varphi_3^{-1/3} \qquad (2)$$

Отмечено, что уравнение (1) в пределах доверительного интервала коэффициента пропорциональности совпадает с известным аналитическим решением Левича, полученным для чисто стационарной конвективной диффузии:

В области $Re_L \gg 1$ $Sc \gg 1$

$$Sh = 0{,}68\, Re_L^{1/2}\, Sc^{1/3}, \ \ Re_L = U_L d/\nu_L \qquad (3)$$

Идентичность структуры эмпирической корреляции (1) и аналитического решения (3) подтверждает вывод о квазиламинарности процесса массопереноса в рассматриваемых условиях.

В настоящем сообщении приводим результаты исследования локального массопереноса от частицы к жидкости в трехфазных системах газ-жидкость-твердые частицы, в условиях восходящего прямотока потоков. Целью работы является анализ влияния скорости газа на интенсивность массообмена между твердыми частицами и жидкостью.

С использованием результатов настоящей работы, а также предыдущих результатов, опубликованных в Сообщениях I—III [1—3], попытаемся сформулировать окончательный вид инвариантной к числу фаз и состоянию слоя математической модели массопереноса.

Экспериментальная часть

Опыты проводились по описанной ранее [1—3] методике, путем измерения плотности электродиффузионного тока от датчика-частицы диаметром 0,3 см, свободно подвешенной в слое стеклянных шариков. Расходную скорость газа и жидкости варьировали в пределах 0—14 см/сек, и 0,2—12,5 см/сек соответственно. В этих условиях слой частиц находился либо в неподвижном, либо в псев-

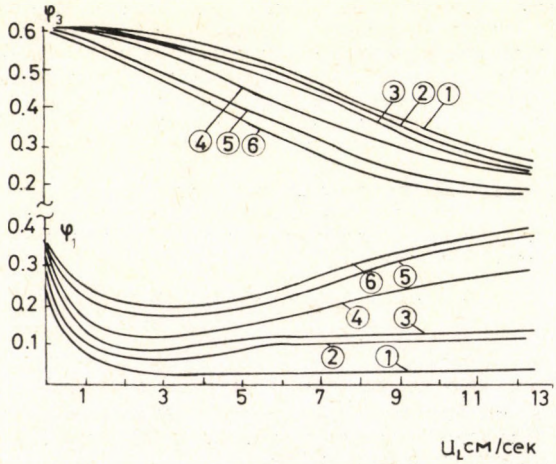

Рис. 1

Зависимость φ_1 и φ_3 от U_L при U_g:

№	1	2	3	4	5	6	7
U_g см/сек	0,1	0,33	1,55	2,18	5,95	11,4	14,1

доожиженном состоянии с различной степенью расширения. Статистическая обработка поступающего от датчика непрерывного сигнала проводилась также описанным ранее [1—3] методом. В каждом опыте были определены среднее значение и дисперсия коэффициента массопереноса, амплитудно-частотный спектр мощности сигнала, объемные доли газа и твердых частиц. Объемную долю жидкости вычисляли по соотношению:

$$\varphi_1+\varphi_2+\varphi_3=1 \qquad (I)$$

На *рис. 1* приведена зависимость φ_1 и φ_3 от расходной скорости жидкости при различных значениях расходной скорости газа. Аналогичные зависимости для среднего значения ($\bar{k}$) и дисперсии (σ_k^2) коэффициента массопереноса приведены на рисунках 2 и 3.

Линия „А-А" на рисунке 2 является границей неподвижного и псевдоожиженного слоя, линия „В-В" соответствует 25%-ному содержанию твердых частиц. Скорость жидкости, при которой наступает псевдоожижение, удовлетворяет эмпирическому уравнению [4]:

$$U_{\text{кр}}^{(3)}=U_{\text{кр}}^{(2)}\cdot(1-\varphi_1) \qquad (2)$$

В области, лежащей правее линии „В-В" наблюдается интенсивное разрушение трехфазного псевдоожиженного слоя вследствие уноса твердых частиц. Значения $\bar{k}$, отмеченные на графиках знаком „○", уже не соответствуют режиму псевдоожижения. В этих опытах подвешенный на проволоке датчик был вынесен на верхний край слоя, и под напором жидкости поддерживался в неподвижном состоянии.

Из графиков *рис. 2* видно, что с ростом скорости газа средние значения коэффициента массопереноса возрастают. Влияние скорости газа на скорость массопереноса является более сильным в области неподвижного слоя.

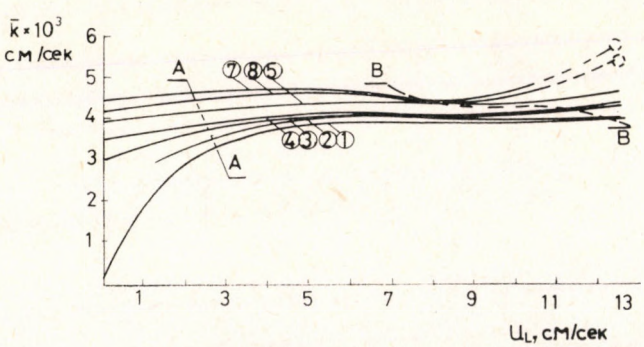

Рис. 2

Зависимость $\bar{k}$ от U_L при различных значениях U_g:

№	1	2	3	4	5	6	7
U_g см/сек	0	0,33	1,55	2,18	5,95	11,4	14,1

Пульсации коэффициента массопереноса в трехфазной системе более интенсивны чем в двухфазной. С ростом скорости газа (см. *рис. 3*) дисперсия возрастает. С ростом скорости жидкости кривая σ_k^2 проходит через ярко выраженный максимум в области начала псеводожижения. Среднеквадратичное отклонение коэффициента массопереноса ($\sqrt{\sigma_k^2}$) в трехфазной системе достигает 13—21% от

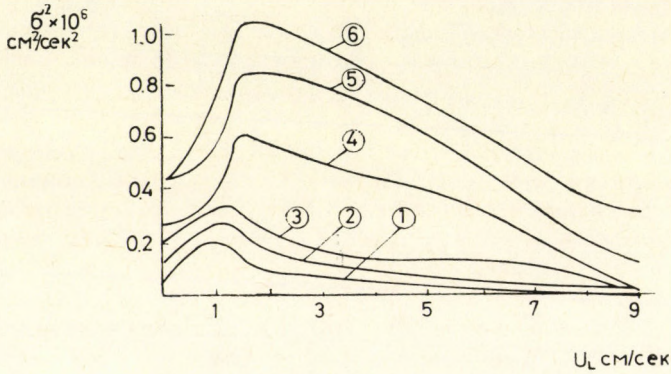

Рис. 3

Зависимость σ_k^2 от U_L при различных U_g:

№	1	2	3	4	5	6
U_g см/сек	0,33	1,55	2,18	5,95	11,4	14,1

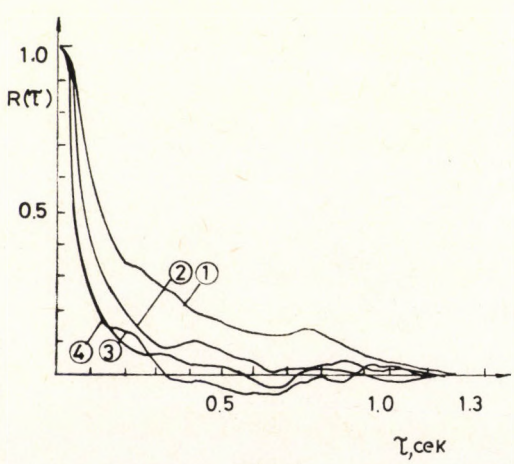

Рис. 4

Автокоррелограммы $k(t)$

среднего значения, в то время как в двухфазной системе уровень пульсаций не превышал 3—5% [3].

Некоторое представление о характере пульсаций массового потока могут дать кривые автокоррелограмм, приведенные на *рис. 4*. Пульсации носят чисто случайный характер и основная мощность пульсаций принадлежит низкочатотным (0—2 герц) колебаниям.

Обобщение Экспериментальных Данных

1. Краткий Обзор Литературы.

В большинстве известных нам из литературы работ [5—15], посвященных исследованию массопереноса между частицей и жидкостью в трехфазных системах, отмечается, что коэффициент массопереноса в двухфазном потоке выше чем в однофазном. Об этом свидетельствуют, например, данные работы [5], приведенные на *рис. 5а*. Объектом исследования авторов был трехфазный неподвижный слой с восходящим потоком газа и жидкости, в области $Re_L < 30$, $Re_g = 0{,}19 \div 13{,}8$, $Sc = 1170$. Измерения проводились электрохимическим методом.

Что касается обобщений экспериментальных данных в виде критериальных уравнений, то по этому вопросу в литературе нет единой точки зрения. Тем не менее можно выделить некоторые характерные подходы и оценить их эффективность. Например, в указанной выше работе экспериментальные данные описаны с помощью простых эмпирических уравнений:

$$\overline{Sh} = 48\, Re_g^{1/4} \quad \text{при} \quad Re_L < 5 \tag{3}$$

$$Sh_0 \equiv \overline{Sh}\,(\text{при } Re_g = 0) = 0{,}75 Re_L^{1/2}\, Sc^{1/3} \quad \text{при} \quad Re_L > 10 \tag{4}$$

Определяющим линейным размером в вышеуказанных безразмерных критериях является т. н. „гидравлический диаметр", выраженный в виде формулы:

$$d_э = \tilde{\varepsilon} \cdot d/[1{,}5(1-\tilde{\varepsilon})] \tag{5}$$

Авторы работы [13] исследовали массоперенос (электрохимическим методом) в неподвижном слое, при нисходящем прямотоке газа и жидкости. Экспериментальные данные описываются в виде эмпирического уравнения:

$$\tilde{\varepsilon}\Phi\overline{Sh}/Sc^{1/3} = 0{,}72\, Re_L^{0{,}54}\, Re_g^{0{,}16} \tag{6}$$

которое подтверждается в области $40 < Re_g < 300$, $50 < Re_L < 140$.

В работе М. А. Касаманяна [6] предлагается более сложное уравнение, выражающее явную и неявную зависимость коэффициента массопереноса от скорости газа:

$$\overline{Sh}/Sc^{1/3} = 3{,}78\{0{,}7 + 0{,}12[U_g(1-\varphi_1^*)/U_L\varphi_1^*]^{0{,}62}\} Re_L^{1/3}(d/m)^{1/3} \tag{7}$$

$$\text{где } \varphi_1^* = \varphi_1/(1-\varphi_3);\ m/d = 0{,}15 Fr_g^{-0{,}1};\ Fr_g = U_g^2/g\cdot d \tag{8}$$

Параметр φ_1^* в свою очередь зависит от Re_g и Fr_g [6].

Уравнение (7) справедливо для трехфазного неподвижного слоя с выходящим прямотоком потоков, в области $U_g = 0{,}2$—50 см/сек, $U_L = 0{,}02$—2 см/сек.

Коэффициент массопереноса измеряли методом растворения бензойной кислоты и гидрохинона в воде.

В более поздней [15] S. Mochizuki обобщил свои предыдущие экспериментальные данные [5], представленные на рис. 5а. Автор показал, что если в качестве характерного размера при построении безразмерных чисел $Sh_э$ и $Re_э$ использовать выражение:

$$d=\varphi d/(1{,}5(1-\varphi)) \tag{9}$$

то семейство кривых, приведенных на рис. 5а, относящихся к различным скоростям газа сводятся к одной кривой, приведенной на рисунке 5б. Однако, обобщенная кривая, полученная для двухфазного потока, отличается от кривой, описывающей скорость массопереноса в однофазном потоке.

Другой подход к обобщению экспериментальных данных основан на использовании т. н. „энергетического" критерия [7, 11, 12]. Базовой величиной при этом авторы используют суммарную скорость диссипации энергии двухфазного потока (ε_Σ), отнесенную к единице массы жидкости в реакторе. Детальный анализ факторов, опрделяющих значение ε_Σ, приводится в работе [12]. Азторы этой работы для описания экспериментальных данных, полученных в неподвижном слое с восходящим двухфазным потоком (измерения проводились электрохимическим методом) предлагают следующее обобщенное уравнение

$$\overline{Sh}/Sc^{1/3}=G(\varepsilon_\Sigma d^4\varrho_L^2/M_L^3)^{0,28} \tag{10}$$

где $G=0{,}102$ и $0{,}155$ соответственно для сферических ($d=0{,}6$ см) и цилиндрических ($d\times l=0{,}6\times 0{,}6$ см) частиц. Уравнение (10) справедливо для условий:

$$U_g=0\text{—}50 \text{ см/сек}; \quad U_L=0{,}28\text{—}14{,}9 \text{ см/сек}.$$

Оно обеспечивает 30%-ную точность описания экспериментов. К сожалению, авторы не приводят график уравнения (10) и его сопоставления с экспериментальными данными.

Приведенный выше краткий обзор литературы свидетельствует о том, что в настоящее время нет единого подхода к описанию скорости массопереноса в трехфазных системах, и не найден инвариантный к числу фаз и состоянию слоя вид обобщенного критериального уравнения. Очевидно, что уравнения вида (3), (5) и (6), выражающие зависимость числа $\overline{Sh}$ от критериев Re_L и Re_g, имеют частное значение, так как фиктивные скорости газа и жидкости не опредеяют однозначно гидродинамику двухфазного течения в слое насадки. Обобщения в виде уравнений (7) и (10), учитывающие влияние скорости газа косвенно, через другие определяющие параметры, можно считать более обоснованными. Однако эти уравнения не распространяются на область псевдоожиженного слоя.

Осредненные Значения Коэффициента массопереноса

Учитывая опыт наших предыдущих работ [2, 3] можно предположить, что упомянутый выше энергетический подход может оказаться наиболее плодотворным при попытке построения инвариантного обобщения .В Сообщении III [3] нам удалось описать экспериментальные данные, относящиеся к двухфазному неподвижному и псевдоожиженному слою в виде одного критериального уравнения:

$$\overline{Sh}=(0{,}699\pm 0{,}027)\overline{Re}^{1/2}\cdot Sc^{1/3} \tag{11}$$

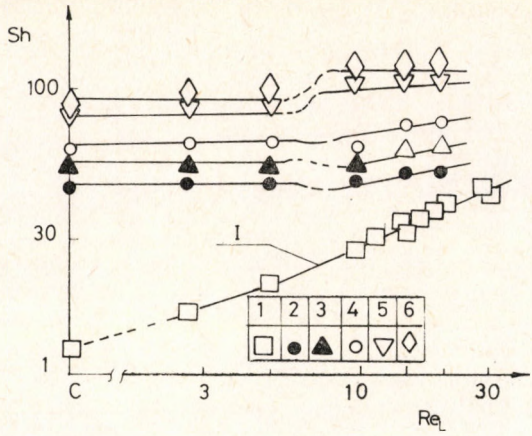

Рис. 5

Экспериментальные данные Mochizuki, S., Matsui, T. [5] и [15]

а) [5]

№	1	2	3	4	5	6
Re_g	0	0,91	1,82	3,65	9,14	13,8

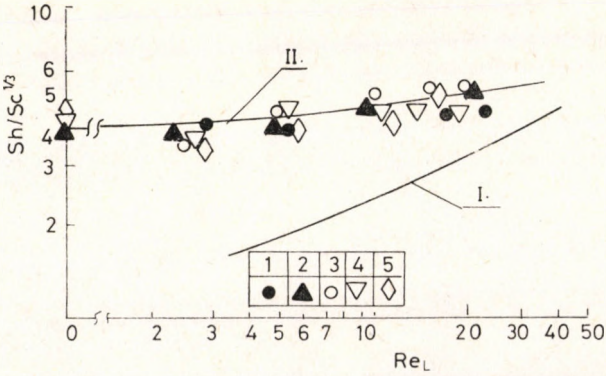

в) [15]

№	1	2	3	4	5
Re_g	0,91	1,82	3,65	9,14	13,8

Критерий $\overline{Re}$ в уравнении (11) построен с использованием „определяющей" скорости $\overline{W}$, выраженной через локально-осредненное значение кинетической энергии:

$$\overline{W}=(2\overline{\overline{E}}/\varrho_L)^{1/2} \tag{12}$$

$$\overline{\overline{E}}=(\varrho_L/2L_\alpha)\int_0^{L_\alpha} V^2(\alpha)\,d\alpha; \qquad V(\alpha)=U_L/\varepsilon(\alpha) \tag{13}$$

L_α и α — геометрические параметры элементарной ячейки зернистого слоя, в пределах которой произведено осреднение, $\varepsilon(\alpha)$ — локальная порозность ячейки. Функция $\alpha(\varepsilon)$ выведена из предположения о гексагональной упаковке сферических частиц в зернистом слое.

Учитывая, что гидродинамическая структура трехфазного слоя является более неоднородной чем структура двухфазного слоя, использованная в Сообщении III [3] для определения $\overline{\overline{E}}$ простая ячеечная модель теряет физическое обоснование. Более общее выражение для $\overline{\overline{E}}$ через суммарную диссипацию энергии ε_Σ найдено методом анализа размерностей:

$$\overline{\overline{E}}=\varrho_L(\varepsilon_\Sigma\lambda)^{2/3} \tag{14}$$

$$\overline{W}=(2\overline{\overline{E}}/\varrho_L)^{1/2}=\sqrt{2}(\varepsilon_\Sigma\lambda)^{1/3} \tag{15}$$

Суммарная скорость диссипации энергии ε_Σ в газо-жидкостном потоке складывается из двух составляющих: скоростей диссипации энергии потоков жидкости и газа соответственно:

$$\varepsilon_\Sigma=\varepsilon_L+\varepsilon_g=(\Delta P/L)_L U_L/\varphi_2\varrho_L+(\Delta P/L)_g U_g/\varphi_2\varrho_L \tag{16}$$

Первый член этой суммы выражаем из рассмотрения взаимодействия потока жидкости с твердой фазой. Энергетические потери жидкой фазы обусловлены, главным образом, трением о поверхность твердых частиц. Следовательно, для расчета перепада давления $(\Delta P/L)_L$ можно использовать известные уравнения выведенные для двухфазных систем жидкость-твердые частицы. В работе [16], для этой цели используют формулу:

$$(\Delta P/L)_L=4{,}5\varrho_L\nu_L(6/d^2)[(1-\tilde{\varepsilon})^2/\tilde{\varepsilon}^3]U_L+0{,}3\cdot\varrho_L[(6/d)(1-\tilde{\varepsilon})/\tilde{\varepsilon}]\cdot U_L^2 \tag{17}$$

справедливую как для неподвижного, так и для псевдоожиженного слоя.

Энергетические потери газовой фазы в трехфазных слоях связаны с преодолением сопротивления столба жидкости и трением о межфазную поверхность газ-жидкость. Согласно данным работы [17] $(\Delta P/L)_g$ может быть вычислено по уравнению:

$$(\Delta P/L)_g=g\cdot\varphi_2\varrho_L+3{,}0\varrho_g(U_g/\varphi_1)^2(1/d_э) \tag{18}$$

причем вторым членом этой суммы в исследуемых пределах U_g можно пренебречь по сравнению с первым.

Уравнение (16) — с учетом выражений (17) и (18) дает явное выражение ε_Σ от известных макроскопических параметров состояния трехфазного слоя: расходных скоростей фаз, фазового состава, физических констант, диаметра частиц.

Для того, чтобы воспользоваться формулой (15) для вычисления определяющей скорости $\overline{W}$, необходимо задать линейный размер λ, характеризующий масштаб локальной области, в пределах которого определено осредненное зна-

чение $\overline{\overline{E}}$. Представим эту область в виде сферы диаметром λ, и преположим, что объемная доля твердой фазы в этой области равно среднему по всему слою значению φ_3. Исходя из этого предположения выражение для λ имеет следующий вид:

$$\lambda = d \cdot \varphi_3^{-1/3} \tag{19}$$

На *рис. 6* приведен график зависимости осредненного значения коэффициента массопереноса от комплекса $(\varepsilon_\Sigma \lambda)^{1/3}$. Из графика следует, что все опытные значения $\overline{k}$, измеренные в неподвижном или в псевдоожиженном слое, при различных расходных скоростях газа и жидкости, лежат на одной кривой. Это свидетельствует о возможности обобщения экспериментальных данных с помощью критерия $\varepsilon_\Sigma \lambda$.

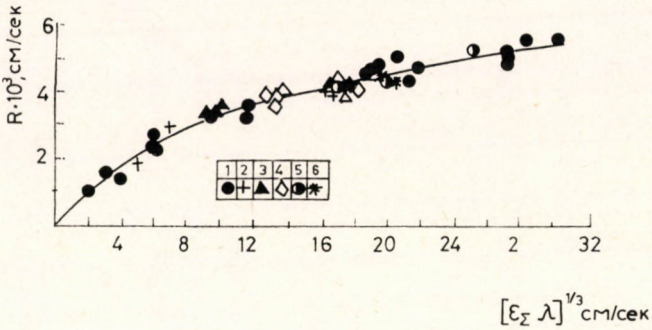

Рис. 6

Зависимость $\overline{k}$ от комплекса $(\varepsilon_\Sigma \lambda)^{1/3}$

$U_L = 0{,}2 \div 12{,}5$ см/сек, $dp = 0{,}3$ см,

U_g = см/сек: 1 — 0,33; 2 — 1,55; 3 — 2,18; 4 — 5,95; 5 — 11,4, 6 — 14,1.

С целью проверки возможности построения инвариантной формы обобщения на базе определяющей скорости w, выраженной уравнением (15), экспериментальные данные представлены в виде зависимости:

$$\overline{Sh} = A\,\overline{Re}^{1/2} Sc^{1/3} \tag{20}$$

$$\overline{Re} = Wd/\nu_L; \qquad \overline{W} = \sqrt{2}\,(\varepsilon_\Sigma \lambda)^{1/3} \tag{21}$$

Коэффициент пропорциональности А в уравнении (20) был найден методом наименьших квадратов с использованием экспериментальных данных, относящихся к трехфазным системам, с привлечением экспериментальных данных, полученных для двухфазных систем, описанных в Сообщении III [3]. В результате, с 95%-ной доверительной вероятностью, было найдено следующее значение A:

$$A = 0{,}693 \pm 0{,}015 \tag{22}$$

Интересно отметить совпадение значения А с коэффициентом пропорциональности уравнения (II).

Среднеквадратичное отклонение опытных и расчетных значений числа $\overline{Sh}$ составляет в среднем около 8%.

График обобщенной зависимости $\overline{Sh}/Sc^{1/3}$ от Re в логарифмических координатах представлен на *рис. 7*. Из рисунка видно, что все опытные точки, относящиеся к двухфазным и трехфазным неподвижным и псевдоожиженным системам, и к разным диаметрам твердых частиц, группируются в окрестности прямой линии, которая списывается уравнением (20) с коэффициентом пропорциональности (22).

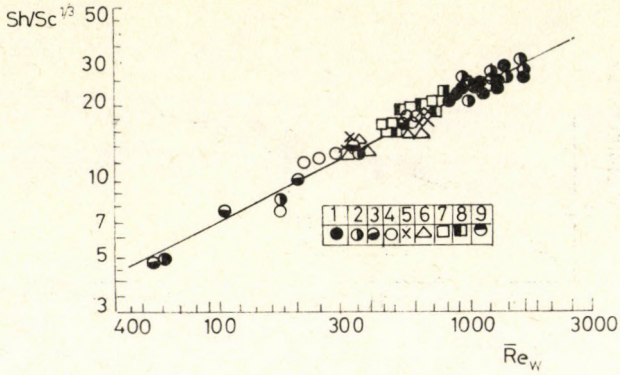

Рис. 7

Обобщенная зависимость $\overline{Sh}/Sc^{1/3}$ от $\overline{Re}_w$

Знаки 1, 2 и 3: двухфазные слои ($U_g=0$) при $dp=0{,}3$, 0,4 и 0,5 см; знаки 4÷9: трехфазные слои при U_g: 0,33, 1,55, 2,18, 5,95, 11,9 и 14,1 см/сек.
$U_L=0{,}2\div0{,}33$ см/сек, $dp=0{,}3$ см

Совпадение коэффициентов пропорциональности уравнений (20) и (11) указывает на то, что

1. Заданные уравнениями (12) и (15) две формы выражения опрделяющей скорости идентичны.
2. Выражение (15) является более общим, не требующим предположения о локальной структуре зернистого слоя.

Пульсации Коэффициента Массопереноса

Пульсации коэффициента массопереноса являются следствием возмущения относительной скорости, вызванного хаотическим продвижением газовых пузырей через слой жидкости. Механизм воздействия газовых пузырей можно представить следующим образом: попадая в канал между частицами, вследствие поверхностного трения пузырь захватывает часть жидкости, унося с собой

вверх со скоростью, равной скорости подъема пузыря. После удаления пузыря захваченная жидкость стекает обратно. Таким образом возникают локальные возмущения скорости жидкости. К сожалению, имеющаяся экспериментальная информация не позволяет предложить вполне обоснованную физическую модель для описания динамики процесса массопереноса. Поэтому воспользуемся чисто эмпирическим приемом. Предположим, что пульсация относительной скорости является полигармоническим процессом:

$$V'(t)=A_{\mathrm{v}} \sum_{\mathrm{n}=1}^{\infty} (1/A_{\mathrm{v}})(a_{\mathrm{vn}} \cos n\omega_0 \mathrm{t}+b_{\mathrm{vn}} \sin n\omega_0 \mathrm{t}) \tag{23}$$

где A_{v} — характерный масштаб пульсационной скорости, a_{vn}, b_{vn} — коэффициенты Фурье.

С использованием уравнения (23) дисперсия относительной скорости может быть выражена в виде:

$$\sigma_{\mathrm{v}}^2=(1/T) \int_0^{\mathrm{T}} V'^2(t)\, \mathrm{d}t=\mathrm{const}\cdot A_{\mathrm{v}}^2 \tag{24}$$

В качестве масштабной скорости A_{v} выбираем скорость скольжения газовой и жидкой фазы:

$$A_{\mathrm{v}} \equiv [(U_{\mathrm{g}}/\varphi_1)-(U_{\mathrm{L}}/\varphi_2)] \tag{25}$$

Зависимость среднеквадратичного отклонения коэффициента массопереноса $(\sqrt{\sigma_{\mathrm{k}}^2})$ от масштабной скорости A_{v} приведена на *рис.* (*8*). Из графика видно, что эта зависимость с достаточной точностью обобщает экспериментальные данные, принадлежащие различным значениям U_{g}, U_{L}, φ_1, φ_2. Она может быть выражена в виде эмпирического уравнения:

$$\sqrt{\sigma_{\mathrm{k}}^2}=1{,}2\cdot 10^{-4}\cdot [(U_{\mathrm{g}}/\varphi_1)-(U_{\mathrm{L}}/\varphi_2)]^{1/2} \quad \text{см/сек} \tag{26}$$

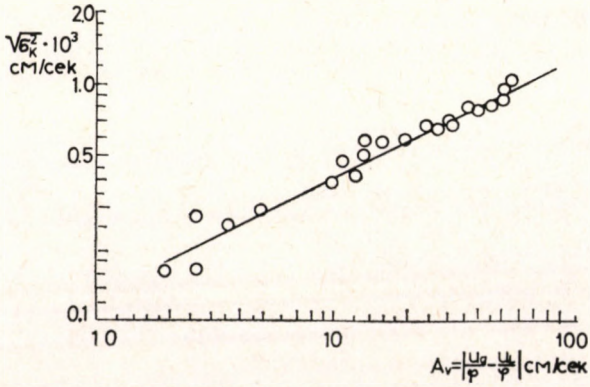

Рис. 8

Зависимость $\sqrt{\sigma_{\mathrm{k}}^2}$ от A_{v}

Существование однозначной связи среднеквадратичного отклонения коэффициенте массопереноса и масштабной скорости A_v может быть использовано в дальнейшем в качестве рабочей гипотезы при более детальном исследовании динамики процесса массопереноса в трехфазных системах.

Обсуждение результатов

Закончив серию работ по экспериментальному исследованию локального массопереноса от жидкости к частице, находящейся либо в бесконечном потоке жидкости, либо в двух- и трехфазных неподвижных и псевдоожиженных слоях, можно отметить следующие основные результаты:

1. Массоперенос в трубулентном потоке жидкости протекает более интенсивно, чем в ламимарном, невозмущенном потоке. Об этом свидетельствуют первичные экспериментальные данные, описанные в Сообщениях I—III [1—3], и в настоящей работе. Причиной возникновения турбулентности в двухфазных системах жидкость-твердые частицы является возмущение скорости при течении жидкости через каналы переменного сечения. В трехфазных системах продвижение газовых пузырей через слой жидкости является источником дополнительных возмушений.

2. Уравнения нестационарного гидродинамического и диффузионного пограничных слоев составляют единственную, физически обоснованную математическую модель элементарного акта массопереноса в турбулентном потоке жидкости. Как было показано в Сообщении II [2], эта модель, записанная в терминах осредненных во времени переменных, при выполнении условия $Sc \gg 1$ может быть рассмотрена в квазиламинарном приближении. Квазиламинарная природа процесса турбулентного массопереноса приводит к формальной аналогии структуры уравнения осредненного во времени диффузионного пограничного слоя со структурой чисто ламинарного диффузионного пограничного слоя. Следовательно, для описания скорости массопереноса в турбулентном потоке жидкости нет необходимости использовать эмпирические поправки в виде „коэффициента турбулентной диффузии“, как это было сделано в Сообщении I (1).

3. Несмотря на внешнюю идентичность структуры уравнений чисто ламинарного и квазиламинарного диффузионных пограничных слоев, они существенно различаются между собой физическим содержанием переменных, в том числе и граничного условия: относительной скорости течения.

В турбулентном потоке эта величина — как было показано в Сообщении II [2] — формируется как результат наложения турбулентных пульсаций на стационарную скорость течения жидкости и ее осредненное во времени значение может быть выше стационарной скорости. Этим определяются более высокие значения коэффициента массопереноса в турбулентном потоке жидкости.

Поскольку в реальных гидродинамических условиях трехфазного слоя значения локально-осредненной относительной скорости нам неизвестны, необходимо было найти эквивалентный способ ее выражения через известные макроскопические параметры состояния трехфазного слоя. Учитывая энергетическую природу процесса массопереноса, выраженную наглядно в известных решениях [18], связывающих плотность диффузионного потока с касательным напряжением трения, было введено понятие „определяющей“ скорости. Она пропор-

циональна корню квадратному из осредненного в локальной области полного динамического напора (кинетической энергии) относительной скорости. Согласно закону сохранения энергии полный динамический напор непосредственно связан со скоростью диссипации энергии, внесенной в систему извне, движущимися потоками газа и жидкости. Уравнения (14) — (18) выражают однозначную, инвариантную связь между „определяющей" скоростью и параметрами макроскопического состояния трехфазной системы. Этим самым, упомянутая в п. 2 математическая модель элементарного акта массопереноса может быть представлена в виде замкнутой системы уравнений.

4. Формальная аналогия структуры квазиламинарного и чисто ламинарного дифузионных пограничных слоев приводит к формальной аналогии структуры их решения. В качестве примера ниже приведено классическое решение Левича [19]. Аналитическим решением уравнения конвективной диффузии в ламинарном пограничном слое Левичем было получено следующее выражение для предельного диффузионного тока на поверхности обтекаемой пластинки:

$$\text{для } Re_L \gg 1, \quad Sc \gg 1:$$

$$J = 0{,}68 D \cdot C_0 (1/L_x)(\nu_L/D)^{1/3}(U_L L_x/\nu_L)^{1/2} \tag{27}$$

Преобразование этого уравнения к безразмерному виду приводит к следующему критериальному уравнению:

$$Sh = 0{,}68 Re_L^{1/2} Sc^{1/3} \tag{28}$$

Интересно сопоставить теоретическое решение (28) и частные корреляционные уравнения, выведенные на основе экспериментальных данных, описанных в Сообщениях I—III [1—3], и в настоящей работе. Они приведены в *таблице 1*.

Данные таблицы показывают, что коэффициенты пропорциональности в уравнении (20), полученные для различных частных случаев трехфазной системы — при соответствующем выборе „определяющей" скорости $\overline{W}$ — совпадают в пределах доверительных интервалов, и очень близки к значению 0,68, выведенному из аналитического решения чисто стационарной задачи. Это подтверждает, во-первых, вывод о квазиламинарности турбулентного пограничного слоя, во-вторых, справедливость описанного выше подхода к выбору, „определяющей" скорости.

6. В заключении, на основе приведенных в *таблице 1* результатов, можем сформулировать окончательный вид общей, инвариантной к числу фаз и состоянию слоя математической модели:

$$\overline{Sh} = (0{,}68 \pm 0{,}02)\overline{Re}^{1/2} \cdot Sc^{1/3} \tag{29}$$

описывающей скорость массопереноса от жидкости к частице, находящейся либо в бесконечном потоке жидкости, либо в двух и трехфазных неподвижных или псевдоожиженных системах. Коэффициент пропорциональности уравнения (29) найден как средневзвешенное значение коэффициентов, приведенных в *таблице 1*, в строках 2, 3 и 5. Доверительный интервал коэффициента определен как среднеквадратичное отклонение от среднего значения.

Уравнение (25) справедливо в области чисел $\overline{Re} = 40 \div 2000$, при $Sc \gg 1$. Верхний предел числа $\overline{Re}$ соответствует реальному верхнему пределу существования трехфазного псевдоожиженного слоя. Что касается области малых чисел $\overline{Re}$,

Сопоставление теоретического решения с экспериментальными корреляциями, выраженными в виде ур-ия $\overline{Sh}=A\,\overline{Re}^{1/2}\,Sc^{1/3}$ (I)

№	Состояние слоя	Условие эксперимента	Выражение для „определяющей" скорости и критерии	Характер массового потока	Коэфф. при „А" в ур. (I)	Число экспер. точек	Примечание
1	Единичная неподвижная сфера, обтекаемая невозмущенным потоком	—	$\overline{W}=U_L$	Чисто стационарный, не зависим. от времени процесс.	0,68	—	Теоретич, решение Левича (19)
2.	Единичная неподвижная сфера, обтекаемая невозмущенным потоком	$U_L=0\div54\,\frac{см}{сек}$ $d=0{,}64;\ 0{,}48;\ 0{,}32$ см	$\overline{W}=U_L$	Чисто стационарный, не зависим. от времени процесс.	0,669± 0,113	21	Эксперимен. корреляция (3) по данным (2)
3.	Единичная частица совершающая гармонич, колеб. в потоке жидкости	$U_L=0\div54\,\frac{см}{сек}$ $A_x=0\div1$ см/сек $f_0=0\div8{,}4$ сек$^{-1}$ $d=0{,}4$ см	$\overline{W}=\frac{1}{T}\int_0^T V(t)dt$ $V(t)=\lvert U_L-2\pi\Phi_0A_x\times\cos 2\pi f_0t\rvert$	Стационарный полигармонич. процесс	0,678± 0,018	66	Экспер. корреляция (3) по данн. (2)
4.	Двухфазный неподвижный и псевдоожиженный слой	$U_L=0{,}6\div33$ см/сек $\tilde{\varepsilon}=0{,}38\div0{,}9$ $d=0{,}4;\ 0{,}5$ см	$\overline{W}=U_L\cdot I$ $I=\left[\frac{1}{L_\alpha}\int_0^{L_\alpha}\frac{d\alpha}{\varepsilon^2(\alpha)}\right]^{1/2}$ $\varepsilon(\alpha)=1-1{,}499(1-\tilde{\varepsilon})\times\sin^2\alpha$	Стационарный случайный процесс	0,669± 0,027	38	Экспер, корреляция (3)
5.	Двух- и трехфазный неподвижный и псевдоожиженный слой	$U_L=0{,}28\div33$ см/сек $U_g=0\div14$ см/сек $d=0{,}3;\ 0{,}4;\ 0{,}5$ см	$\overline{W}=\sqrt{2}\,(\varepsilon_\Sigma\lambda)^{1/3}$ $\lambda=d\cdot\varphi^{-1/3}$ $\varepsilon_\Sigma=\left(\frac{\Delta P}{L}\right)_L\frac{U_l}{\varphi_2\varrho_L}+\left(\frac{\Delta P}{L}\right)_g\frac{U_g}{\varphi_2\varrho_L}$	Стационарный случайный процесс	0,693± 0,015	74	Экспер. корреляции данной работы

можно предположить в качестве рабочей гипотезы, что известное аналитическое решение [19]

$$Sh=0{,}99Pe^{1/3} \qquad (3)$$

полученное для единичной частицы, обтекаемой ламинарным потоком жидкости, при аналогичном вышеописанному выборе „определяющей" скорости в критерии Pe, также может быть использована для описания скорости массопереноса в зернистых слоях. Однако, эта гипотеза требует экспериментальной проверки.

СПИСОК ОБОЗНАЧЕНИЙ

A_v — характерный масштаб пульсации относительной скорости, м/сек;
C_0 — концентрация, кмоль/м^3;
d — диаметр частицы, м;
$d_э$ — эквивалентный диаметр канала в зернистом слое, м;

D — коэффициент молекулярной диффузии, м²/сек;
$\overline{E}$ — локально-осредненное значение кинетической энергии, н/м²;
g — ускорение силы тяжести, м/сек²;
J — плотность массового потока, кмоль/м²сек;
$\overline{k}$ — осредненное во времени значение коэффициента массопереноса в турбулентном потоке жидкости, м/сек;
k — коэффициент массопереноса в стационарном невозмущенном потоке жидкости, м/сек;
L_x — характерный линейный размер, м;
m — толщина пленки жидкости в окрестности твердой частицы, м;
$\Delta P/L$ — перепад давления, н/м³;
t — время, сек;
U — линейная скорость, отнесенная к полному сечению реактора, м/сек;
$U_{\text{кр}}^{(2)}, U_{\text{кр}}^{(3)}$ — скорость жидкости, соответствующая началу псевдоожижения в двух- и трехфазных системах соответственно, м/сек;
$V'(t)$ — пульсационная составляющая относительной скорости, м/сек;
$\overline{W}$ — „определяющая" скорость процесса массопереноса, м/сек;

Греческие символы:

ε — диссипация энергии, отнесенная к единице массы жидкости, м²/сек³;
$\tilde{\varepsilon}$ — средняя объемная порозность зернистого слоя, (—);
$\varphi_1, \varphi_2, \varphi_3$ — объемные доли газовой жидкой и твердой фаз в реакторе, (—);
Φ — доля смоченной поверхности твердых частиц, (—);
λ — характерный геометрический размер элементарной ячейки зернистого слоя, м;
μ — динамическая вязкость, кг/сек.м;
ν — кинематическая вязкость, м²/сек;
ω_0 — круговая частота, рад/сек;
σ_k^2, σ_v^2 — дисперсия коэффициента массопереноса и относительной скорости соответственно, м²/сек²;
ϱ — плотность, кг/м³.

Индексы:

L — жидкая фаза;
g — газовая фаза;
$\sum$ — суммарное значение,

Безразмерные числа

$Re_L = U_L d/\nu_L$; $Re_g = U_g d/\nu_g$; $\overline{Re} = \overline{W} d/\nu_L$; $Re_э = U_L d_э/\nu_L$;

$Sc = \nu_L/D$; $Pe = Re_L \cdot Sc$; $\overline{Sh} = \overline{k} d/D$; $Sh = k \cdot d/D$; $Sh_э = k d_э/D$

СПИСОК ЛИТЕРАТУРЫ

1. Ермакова, А., Кузьмин, В. А., Скоморохов, В. Б. и Умбетов, А. С.: Hung. J, Ind. Chem. *1981*, 9, 99.
2. Ермакова, А., Кузьмин, В. А., Скоморохов, В. Б. и Умбетов, А. С.: Hung. J. Ind. Chm. *1981*, 9, 187.
3. Ермакова, А., Кузьмин, В. А. и Умбетов, А. С.: Hung. J. Ind. Chem. *1981*, 9, 299.
4. Стефогло, Е. Ф., Холдерит, И. и Ермакова, А.: Гидродинамика трехфазного слоя с насадками. Труды 2-го советско-французского семинара по математическому моделированию каталитических процессов и реакторов, Новосибирск, с. 140, 1976.
5. Mochizuki, S. and Matusi, T. Chem. Eng. Sci., *1974*. 29. 1330
6. Касаманян, М. А.: Моделирование нестационарных процессов в химических реакторах с участием жидкой фазы. Канд. диссертация, Новосибирск, Институт катализа, 1974.
7. Lemai, Y., Pineault, G., Reuther, J. A. Ind. Eng. Chem., Proc. Des. Der., *1975*. 14. 280
8. Sylvester, N. D. and Pitayagubsarn, P., Ind. Eng. Chem., Proc. Des. Dev., *1975*. 14, 421

9. Goto, S. and Smith, J. M., A.I.Ch.E.J., *1975*. 21, 421
10. Goto, S. and Smith. J. M., Mass transfer in packed beds with two-phasd flow. Ind. Eng. Chem., Proc. Des. Der. *1975*. 14, 473
11. Аксельрод, Г. А., Гумницкий, Я. М., Креховецкий, О. М. и Зелинский, М. ТОХТ, **1977**. XI, 1, 134.
12. I. Colquhoun—Lee, J. B. Stepanek., Trans. Inst. Chem. Eng., *1978*. 56. (1) 136
13. Chou, T. S.. Worley, F. L. and Luss, D., Ind. Eng. Chem. Fund., *1979*. 18, (3) 279
14. Ruether, J. A. Ching–Shi Yang and Hayduk, W., Ind. Eng. Chem., Proc. Des. Dev., *1980*. 19, (1) 103
15. Mochizuki, S., Chem. Eng. Sci., *1981*. 36, (1) 213
16. Strock, A. Coeuret, F., Can, J. Chem. Eng., *1977*. 55, (4) 427
17. Слинько, М. Г., Ермакова, А.: Хим. пром., 1967. 3 212.
18. Накоряков, В. Е., Бурдуков, А. П., Покусаев, Б. Г., Кузьмин, В. А. и др. Исследование турбулентных течений двухфазных сред. АН СССР, Сибирское отделение, Институт теплофизики, 1973.
19. Левич, В. Г.: Физико-химическая гидродинамика. Изд. физ. мат. лит., Москва, 1959.
20. L. K. McCune, R, H. Wilhem, Ind. Eng. Chem., *1949*. 41, 1124

SUMMARY

Experimental data on the local mass transfer from particle to liquid in three-phase fixed and fluidized beds are presented. Measurements were made by the electro-chemical method. The averaged and pulsatory values of the mass transfer coefficient were found to depend on the mass rate of liquid and gas upon varying the bed porosity from 0.38 to 0.9. As noted, the average and midquadratic values of the mass transfer coefficient increase with increasing the rate of gas and may make up to 13—21% of the average value.

Using the experimental data of the present paper and those reported in Communication III, a common invariant criterion equation for the averaged mass transfer coefficient has been found:

in the range $40 \leq Re \leq 2000$, $Sc \gg 1$:

$$\overline{Sh} = (0.693 \pm 0.015)\overline{Re}^{1/2} Sc^{1/3} \tag{1}$$

which is valid for two- and three-phase, fixed and fluidized beds. Criterion $\overline{Re}$ of equation (1) has been built by means of the "determining" rate, expressed through the overall energy dissipation of the gas and liquid phase:

$$\overline{W} = \sqrt{2}((\varepsilon_g + \varepsilon_L)\lambda)^{1/3}, \qquad \lambda = d\varphi_3^{-1/3} \tag{2}$$

Within the confidence interval of the proportionality coefficient, equation (1) is in agreement with the known analytical Levich solution, obtained for pure steady state convectional diffusion:

in the range $Re_L \gg 1$ $Sc \gg 1$:

$$Sh = 0.68 Re_L^{1/2} Sc_L^{1/3}, \qquad Re_L = \frac{U_L d}{\nu_L}. \tag{3}$$

The identity of the structures of empirical correlation (1) and analytical solution (3) supports the conclusion on the quasilaminarity of the mass transfer in the studied conditions.

HUNGARIAN JOURNAL
OF INDUSTRIAL CHEMISTRY
VESZPRÉM
Vol. 11. pp. 263—274 (1983)

АНАЛИЗ ПРОЦЕССОВ ПЕРЕНОСА В НЕПОДВИЖНОМ ЗЕРНИСТОМ СЛОЕ ПРИ ВОСХОДЯЩЕМ ПРЯМОТОКЕ ГАЗА И ЖИДКОСТИ

В. А. Кириллов, В. А. Кузьмин, В. И. Пьянов, В. М. Ханаев

(Институт катализа СО АН СССР, Новосибирск)

Поступила в редакцию: 8. февраль, 1983.

Проведение расчетов ряда промышленно важных процессов в реакторах с неподвижным слоем катализатора при прямоточном восходящем движении фаз в значительной степени ограничивается отсутствием (или недостаточностью) экспериментальных данных по гидравлическому сопротивлению, а также процессам тепло-массообмена в реакторах такого типа.

В связи с этим в настоящей работе будет предпринята попытка с единых позиций оценить эти параметры, а также предложить зависимости для их расчета.

Математическая Модель Процессов Переноса

Ранее в [1] была предложена гирдодинамическая модель для анализа процессов переноса вещества между жидкой фазой и поверхностью растворимых частиц. Согласно этой модели жидкая фаза представляет собой пленку равномерной толщины движущуюся по боковой поверхности зерна. На внешней границе этой пленки возникают пульсации скорости, связанные с прохождением пузырей в пузырьковом или снарядном режимах, а также возмущением границы раздела фаз в дисперсном или дисперсно-пленочном режимах. В такой постановке анализ процессов массопереноса сводится к решению методом последовательных приближений уравнения конвективной диффузии совместно с уравнениями нестационарного пограничного слоя [1, 2]. С учетом результатов, приведенных в этих работах, математическая модель нулевого приближения для расчета распределения скорости потока концентрации и давления вокруг частиц запишется в виде:

$$\frac{\partial u}{\partial t}-\nu_2\frac{\partial^2 u}{\partial y^2}=\frac{\mathrm{d}u_e}{\mathrm{d}t} \tag{1}$$

$$\frac{1}{\varrho}\frac{\mathrm{d}p}{\mathrm{d}x}=\frac{\mathrm{d}u_e}{\mathrm{d}t} \tag{2}$$

$$U\frac{\partial c}{\partial x}+v\frac{\partial c}{\partial y}=D_2\frac{\partial^2 c}{\partial y^2} \tag{3}$$

при: $y=0\ u=0,\ v=0,\ c=c^*$

$y=m\ u=\mathrm{u_e}$

$x=x_0\ c=c_0,\ p=p_0$

$t=0\ u=u_2$ (4)

скорость на внешней границе пленки примем аналогично [1]

$$U_e=\left[\frac{U_1+U_2}{2}+\frac{U_2-U_1}{2}\cos\omega t\right]\sin\frac{X}{R} \tag{5}$$

Решение (1—2) можно получить обычными методами математической физики [3]. Для этого необходимо перейти к однородным граничным условиям и затем воспользоваться методом разделения переменных. Тогда получим:

$$U=\sin\frac{c}{R}\left\{\eta\,[A+B\cos\omega t]+\frac{2u_2}{\pi}\sum_{n=1}^{\infty}\frac{1}{n}\exp(-a\omega t)\sin\pi n\eta-\frac{2B}{\pi}\sum_{n=1}^{\infty}\frac{\sin\pi n\eta}{n(1+a^2)}\exp(-a\omega t)+\right.$$

$$\left.+a\sin\omega t-\cos\omega t]\right\} \tag{6}$$

$$V=\cos\frac{x}{R}\left\{-\frac{\eta^2}{2}\frac{m}{R}(A+B\cos\omega t)-\frac{4U_2}{\pi^2}\frac{m}{R}\sum_{n=1}^{\infty}\frac{1}{n^2}\exp(-a\omega t)\cdot\sin^2\frac{\pi n\eta}{2}+\right.$$

$$\left.+\frac{4B}{\pi^2}\frac{m}{R}\sum_{n=1}^{\infty}\frac{\sin^2\frac{\pi n\eta}{2}}{n^2(1+a^2)}[\exp(-a\omega t)+a\sin\omega t-\cos\omega t]\right\} \tag{7}$$

$$P(x)=P_0-B\omega\varrho\sin\omega t\left(1-\cos\frac{x}{R}\right) \tag{8}$$

где

$$B=\frac{u_2-u_1}{2};\qquad A=\frac{u_1+u_2}{2};\qquad \eta=\frac{y}{m};\qquad a=\nu_2\left(\frac{\pi n}{m}\right)^2\frac{1}{\omega}$$

Для расчета потерь на трение при движении газо-жидкостного потока необходимо (6) продифференцировать по η, при $\eta\to 0$:

$$\tau=\frac{\mu_2}{m}\tau_0\sin\frac{x}{R} \tag{9}$$

где

$$\tau_0=A+B\cos\omega t-2u_2\sum_{n=1}^{\infty}\exp(-a\omega t)-2B\sum_{n=1}^{\infty}\frac{\exp(-a\omega t)+a\sin\omega t-\cos\omega t}{1+a^2}$$

Используя (9) можно упростить выражения для U и V особенно если их рассмотреть вблизи боковой поверхности частицы, тогда

$$\left.\begin{aligned}U&=\eta\tau_0\sin\frac{x}{R}\\ V&=-\frac{m}{R}\eta^2\frac{\tau_0}{2}\cos\frac{x}{R}\end{aligned}\right\} \tag{10}$$

С учетом (10) уравнение для конвективной диффузии (3) запишем в виде:

$$A_1\frac{\partial^2 c}{\partial\eta^2}-\sin\xi\frac{\partial c}{\partial\xi}+\frac{\eta_2}{2}\cos\xi\frac{\partial c}{\partial\eta}=0\,, \tag{11}$$

где

$$\xi=x/R\,;\quad A=\left(\frac{R}{m}\right)^2\frac{U_2}{\tau_0}\frac{1}{Pe}\,;\quad Pe=\frac{U_2R}{D_2}$$

при

$$\eta=0:c=c^*;\quad \eta\to\infty:c=c_0;\quad \xi=\xi_0:C=C_0$$

Можно показать, что если функция $C(\xi,\ \eta)$ непрерывная и интегрируемая на всем интервале ее определения, то для получения решения при $\eta\to 0$ в (11) допустимо опустить член η, при этом приближенное решение от истинного будет отличаться не более чем на eps^2. С учетом этого допущения из (11) получим

$$A_1\frac{\partial^2 c}{\partial\eta^2}-\eta\sin\xi\frac{\partial c}{\partial\xi}=0 \tag{12}$$

Решение (12) при $\xi>\xi_0$ имеет вид

$$C=C^*+(C_0-C^*)\frac{\int\limits_0^H\exp\left(-\frac{y^3}{g}\right)dy}{\int\limits_0^\infty\exp\left(-\frac{y^3}{g}\right)dy} \tag{13}$$

где

$$H=\frac{\eta}{Z^{1/3}A^{1/3}}\,;\quad Z=\ln\operatorname{tg}\xi/2\,.$$

Из (13) можно найти выражение для расчета коэффициента массообмена β. Так,

$$\frac{\beta m}{D^2}=\frac{1}{b}\cdot\frac{1}{Z^{1/3}}\left[\frac{m^2}{R^2}\frac{Pe\,\tau_0}{U_2}\right]^{1/3}, \tag{14}$$

где

$$b=\int\limits_0^\infty\exp\left(-\frac{y^3}{9}\right)\mathrm{d}y=1{,}859$$

Для расчета τ_0 воспользуемся выражением для полного перепада давления на элементе неподвижного слоя. Так можем записать, что изменение давления вокрут частицы складывается из потерь на трение и ускорение потока, т. е.

$$P(\xi)=P_0-B\omega\varrho R(\sin\omega t)\,(1-\cos\xi)-\frac{\mu_2}{m}(\sin\xi)\tau_0 \tag{15}$$

Полагая, что основное изменение давления происходит на участке $\xi_0-(\pi-\xi_0)$ из (15) получим

$$\tau_0=\frac{\Delta P-2B\omega\varrho R\sin\omega t\cos^2\xi_0/2}{\mu_2\sin\xi_0}\,;\quad \Delta P=(\xi_0)-P(\pi\cdot\xi_0) \tag{16}$$

Подставим выражение для τ_0 в (14) и, проведя усреднение коэффициента массообмена по поверхности зерна и периоду пульсаций $\bar{\tau}$, после преобразований находим:

$$Sh=0.342\left[\frac{Pe}{u_2}\frac{\Delta PR}{\mu_2\sin\xi_0}\right]^{1/3}\int\limits_{\xi_0}^{\pi-\xi_0}\frac{\mathrm{d}\xi}{Z^{1/3}}\cdot\frac{1}{\bar{\tau}}\int\limits_0^{\bar{\tau}}\left[1-\frac{2B\varrho R\sin\omega t\cos^2\xi_0/2}{\Delta P}\right]\mathrm{d}t \tag{17}$$

Выражение в квадратных скобках можно преобразовать к виду:

$$\frac{Pe}{U_2}\frac{\Delta P}{\mu_2}=0.25ScEuRe^2\,;$$

где

$$Eu=\frac{\Delta P}{\varrho u_2^2}\,;\quad Re=\frac{U_2d}{\nu}\,;\quad Sc=\frac{\nu_2}{D_2}\,;\quad Sh=\frac{\beta d}{\mathrm{D}_2}$$

Таким образом, зависимость для расчета коэффициентов массообмена между жидкостью и боковой поверхностью частиц можно представить как

$$Sh=A[EuRe^2Sc]^{1/3}, \tag{18}$$

где А некоторый коэффициент, численно равный

$$A=\frac{0.085}{\bar{\tau}\sin^{1/3}\xi_0}\int\limits_{\xi_0}^{\pi-\xi_0}\frac{\mathrm{d}\xi}{Z^{1/3}}\int\limits_0^{\bar{\tau}}\left[1-\frac{2B\varrho R\sin\omega t\cos^2\xi_0/2}{\Delta P}\right]\mathrm{d}t$$

Оценить эту величину пока представляется затруднительным, поэтому в дальнейшем она будет определена экспериментально.

Полученное выражение (18) содержит в правой части экспериментально определяемые величины: перепад давления и скорость жидкой фазы или газосодержание потока. Поэтому дальнейший анализ свелся к экспериментальному определению этих параметров наряду с коэффициентами тепло-массообмена.

Экспериментальное Исследование Процессов Переноса в Неподвижном Слое

Газосодержание

Экспериментальное исследование газосодержания проводилось на зернистых слоях, состоящих из шариков 3, 5, 8 мм и помещенных в колонну $D=100$ мм при движении воды и воздуха, а также 0,7 N раствора NaOH и воздуха восходящим прямотоком. Измерение газосодержания проводилось методом отсечки. Полученные экспериментальные данные и их сравнение с литературными значениями величин газосодержаний приведены на рис. 1 для системы вода-воздух и раствор NaOH-воздух. Особенностью последней является склонность к значительному пенообразованию. Вследствие этого величины газосодержаний получаются выше, чем при движении воды и воздуха.

При обработке экспериментальных данных на графике по горизонтальной оси был выбран критерий Фруда, как и в [4], а по вертикальной — комплекс

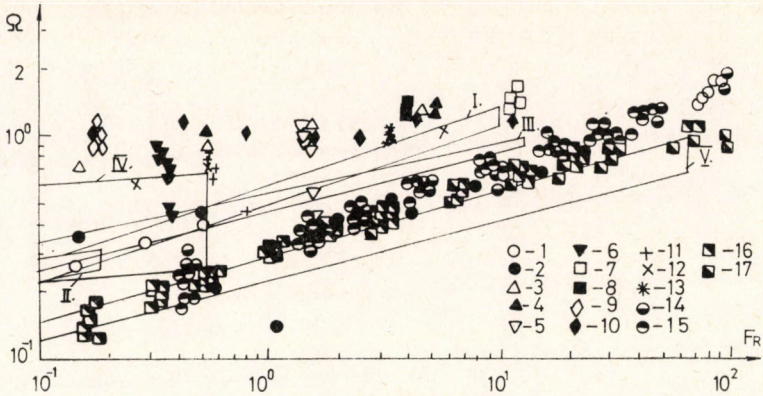

Рис. 1

Сравнение экспериментальных данных по газосодержанию зернистого слоя с их литературными значениями. Очерченные области соответствуют результатам работ: I — [4]; II — [5]; III — [6]; IV — [7]; V — [8]. Экспериментальные точки соответствуют условиям: раствор 0,7 NaOH воздух, шарики

$d=7{,}6$ мм *1* — $u_1=10{,}4$—20, $u_2=20$, *2* — $u_1=10{,}2$—55,6, $u_2=13{,}6$, *3* — $u_1=10{,}6$—58,3, $u_2=3{,}37$, *4* — $u_1=20$—62,4, $u_2=0{,}50$, *5* — $u_1=33$, $u_2=0{,}5$—13,6, *6* — $u_1=16{,}2$, $u_2=0{,}5$—13,6. Шарики $d=3{,}1$ мм: *7* — $u_1=60$, $u_2=0{,}54$—1,74, *8* — $u_1=35$, $u_2=0{,}54$—2,51, *9* — $u_1=7{,}4$, $u_2=0{,}54$—3,64, *10* — $u_1=11{,}2$—58,1, $u_2=1{,}13$. Шарики $d=5$ мм: *11* — $u_1=16$, $u_2=0{,}5$—7,2, *12* — $u_1=16{,}2$—53, $u_2=3{,}54$, *13* — $u_1=40$, $u_2=0{,}5$—7,2. Размерности u_1 и u_2 см/сек

Система вода-воздух, шарики $d=5$ мм: *14* — $u_1=8{,}8$—168, $u_2=0{,}5$—4, *15* — $u_1=8{,}8$—168, $u_2=6$—20, Шарики $d=3$ мм: *16* — $u_1=11{,}6$—173, $u_2=0{,}5$—2, *17* — $u_1=11{,}6$—173, $u_2=4$—16. Размерность u_1 и u_2 см/сек

$\Omega=\dfrac{\varphi}{1-\varphi}\,Eö^{0.15}Re_2^{0.05}Re_1^{-0.1}$, который учитывал влияние на газосодержание физических свойств жидкости, а также скорости ее течения. Где:

$$Eö=\frac{\sigma}{\varrho_2 g d^2};\quad Re_1=\frac{U_1 d}{\nu_1};\quad Re_2=\frac{U_2 d}{\nu_2}$$

Приведенные на этом рисунке данные авторов по углу наклона от совпадают с результатами [4], однако по абсолютной величине они примерно на 50—60% меньше и находятся в пределах между измерениями [6] и [8]. Этот график также указывает на сильную зависимость газосодержания от условий эксперимента и используемой методики.

Гидравлическое Сопротивление Слоя

Условия для определения гидравлического сопротивления были практически теми же, что и при измерении φ. Обработка полученных результатов проводилась в координатах Локарта—Мартинели и ее результаты представлены на рис. 2. Там же приведены известные в литературе зависимости [9—12] для нисходящего прямотока.

Из этого графика видно, что экспериментальные точки удовлетворительно согласуются с литературными данными, хотя и лежат несколько выше их.

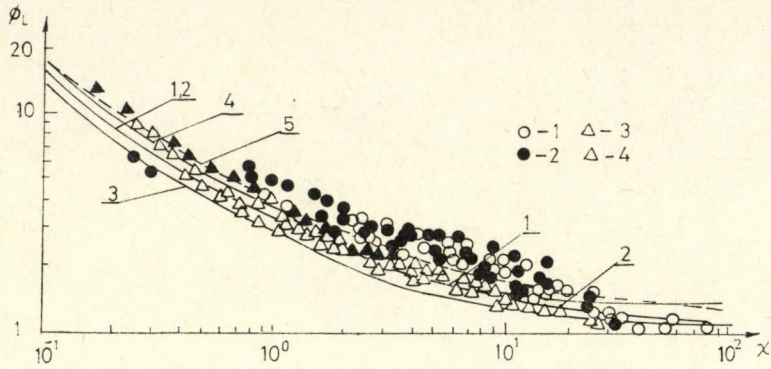

Рис. 2

Сравнение экспериментальных и литературных данных по гидравлическому сопротивлению зернистого слоя. Сплошные линии соответствуют зависимостям, приведенным в работах: 1 — [9], 2 — [10], 3 — [11], 4 — [12]. 5 — эта работа, формула (19). Экспериментальные точки соответствуют условиям система вода-воздуха: шарики $d=3{,}1$ мм, *1* — $u_1=0{,}39$—54, $u_2=0{,}81$—11,2, *2* — $u_1=0{,}08$—8,28, $u_2=0{,}2$—4,2, *3* — $u_1=2$—93, $u_2=0{,}2$—6,2. Шарики $d=5$ мм: *4* — $u_1=2$—93, $u_2=0{,}2$—6,2. Размерность u_1 и u_2 см/сек

Апроксимационная зависимость, которая может быть получена на основании представленных результатов имеет вид:

$$\Phi=1.25+2.8X^{-0.75} \tag{19}$$

где

$$\Phi^2=\frac{\Delta P_{12}}{\Delta P_2}; \quad X^2=\frac{\Delta P_2}{\Delta P_1}$$

ΔP_{12} — перепад давления при течении двухфазного потока, ΔP_1 и ΔP_2 — перепады при движении однофазных потоков, которые могут быть рассчитаны по формуле Эргуна.

Массообмен между Жидкостью и Насадкой

Экспериментальное исследование процессов массообмена проводилось с помощью электрохимического метода. При этом использовалась экспериментальная методика подобная, описанной в [13]. Измерения были проведены с помощью сферических датчиков, помещенных в зернистый слой из шариков 3, 5, 8 мм соответственно.

Поскольку коэффициенты массообмена при движении двухфазного потока в значительной степени зависят от условий эксперимента, в частности от гидродинамических режимов, то для оценки точности метода, а также градуировки датчиков были проведены измерения коэффициентов массообмена при движении однофазных потоков. Результаты этих измерений, а также сравнение с некоторыми литературными данными приведены на *рис. 3.* в общепринятых координатах. Этот график показывает, что наши экспериментальные значения коэффициентов массообмена довольно хорошо согласуются с литературными

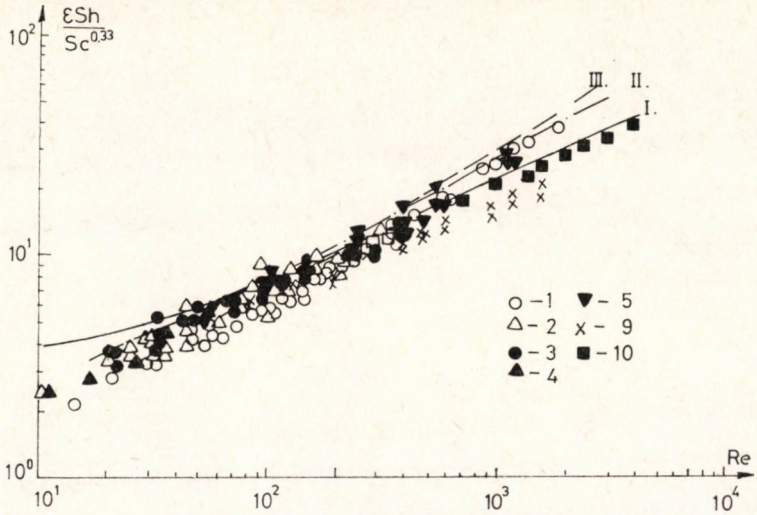

Рис. 3

Сравнение экспериментальных и литературных данных по коэффициентам тепло-массообмена при течении однофазного потока. Сплошные линии соответствуют зависимостям, приведенным в работах: I — [14], II — [15], III — [16]. Экспериментальные точки соответствуют условиям: *1* — [17], *2* — [18], неподвижный зернистый слой $d=3{,}12$ мм: *3* — $D=50$ мм, *4* — $D=100$ мм, *5* — $d=7{,}9$ мм, $D=50$ мм. Свободный поток, одиночный шар: *6* — $d=3{,}12$ мм, *7* — $d=8$ мм

данными. Следовательно, методика может быть использована для определения коэффициентов массообмена при течении двухфазных потоков.

Условия экспериментов подробно изложены в подрисуночной подписи к *рис. 4*. Здесь же только укажем, что одновременно с массообменом определялось газосодержание и гидравлическое сопротивление слоя. Наличие этих данных позволило использовать для обработки полученную выше теоретическую зависимость (18), которая была преобразована к виду:

$$\frac{Sh}{Sc^{0.33}}=A\left\{\frac{\mathrm{d}p}{\mathrm{d}l}d\frac{d^2}{\nu_2^2[\varrho_2(1-\varphi)+\varrho_1(\varphi)]}\right\}^{0.33} \tag{20}$$

где $\mathrm{d}p/\mathrm{d}l$ — потери на трение при течении двухфазного потока. Свободный график, где представлены полученные экспериментальные результаты при течении двухфазного и однофазного потоков, *рис. 4*. Апроксимационная зависимость, которая может быть получена на основании обработки данных измерений имеет вид

$$\frac{Sh}{Sc^{0.33}}=0.24\,[EuRe^2]^{0.33} \tag{21}$$

Эта формула совпадает с теоретической (18), что подтверждает правильность преложенной математической модели процессов переноса. Зависимость (21) является довольно универсальной, поскольку, во-первых, она описывает как одно- так и двухфазный потоки и, во-вторых, не имеет переломов на всем интервале изменения.

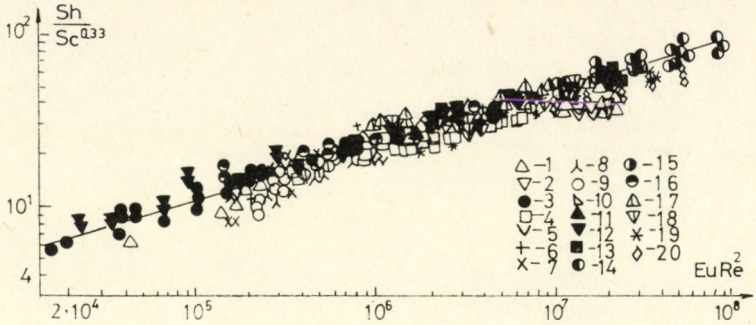

Рис. 4

Зависимость безразмерного коэффициента массообмена от комплекса $EuRe^2$. Сплошная линия соответствует формуле (21), а экспериментальные точки условиям: шарики $d=3{,}1$ мм: *1* — $u_1=0{,}26$—$45{,}3$, $u_2=5{,}6$, *2* — $u_1=0{,}26$—$27{,}8$, $u_2=8{,}66$, *3* — $u_1=0$, $u_2=0{,}81$—$16{,}8$, *4* — $u_1=5{,}6$—$7{,}4$, $u_2=0{,}81$—$15{,}6$, *5* — $u_1=0{,}37$—$35{,}7$, $u_2=0{,}81$, *6* — $u_1=0{,}43$, $u_2=0{,}8$—16, *7* — $u_1=0{,}69$, $u_2=0{,}2$—$2{,}8$, *8* — $u_1=1{,}7$, $u_2=0{,}2$—$4{,}2$, *9* — $u_1=0{,}23$, $u_2=0{,}2$—$4{,}2$, *10* — $u_1=0{,}09$—$7{,}4$, $u_2=0{,}2$, *11* — $u_1=7{,}2$, $u_2=0{,}2$—$2{,}2$. Шарики $d=8$ мм: *12* — $u_1=0$, $u_2=0{,}2$—$16{,}8$, *13* — $u_1=1{,}04$, $u_2=0{,}81$—$16{,}8$, *14* — $u_1=16{,}5$, $u_2=0{,}81$—$8{,}7$, *15* — $u_1=32$, $u_2=0{,}81$—$8{,}7$, *16* — $u_1=0{,}25$, $u_2=0{,}43$—$5{,}5$, *17* — $u_1=7{,}4$, $u_2=0{,}2$—$5{,}5$, *18* — $u_1=0{,}09$—$7{,}5$, $u_2=4{,}2$, *19* — $u_1=3{,}2$, $u_2=0{,}8$—$16{,}8$, *20* — $u_1=7{,}6$—$8{,}2$, $u_2=0{,}8$—$16{,}8$. Размерности u_1 и u_2 см/сек

Сравнение с литературными данными

Поскольку при выводе уравнений модели и их решении не делалось никаких ограничений на направление движения фаз, то, очевидно, проведенный анализ будет приемлем как для восходящего, так и нисходящего прямотоков газа и жидкости. В связи с этим целесообразно сравнить (21) с литературными экспериментальными данными по процессам массопереноса [1, 19—25]. Результаты такого сравнения в координатах *рис. 4* представлены на *рис. 5*. В тех случаях, когда отсутствовали необходимые сведения по φ или перепаду давлений, они оценивались по *рис. 1* или (19) для восходящего прямотока. При нисходящем движении их расчет проводился по данным [26]. Как следует из этого графика, экспериментальные данные других авторов, правда с несколько большим разбросом, чем на *рис. 4* удовлетворительно группируются вокруг прямой линии, соответствующей (21). Таким образом, полученная полуэмпирическая зависимость для расчета процессов массообмена между жидкостью и растворимым твердым телом справедлива в широком диапазоне параметров и режимов движения газожидкостного шотока и может быть использована для расчетов.

Процессы Теплообмена в Неподвижном Зернистом Слое

Методика

Экспериментальное исследование процесса переноса тепла между элементами насадочного слоя и восходящим газожидкостным потоком осуществлялось в колонне проточного типа диаметром 100 мм и длиной 850 мм, в которой находились шарики $d=5$ мм. Измерение коэффициентов теплообмена проводились

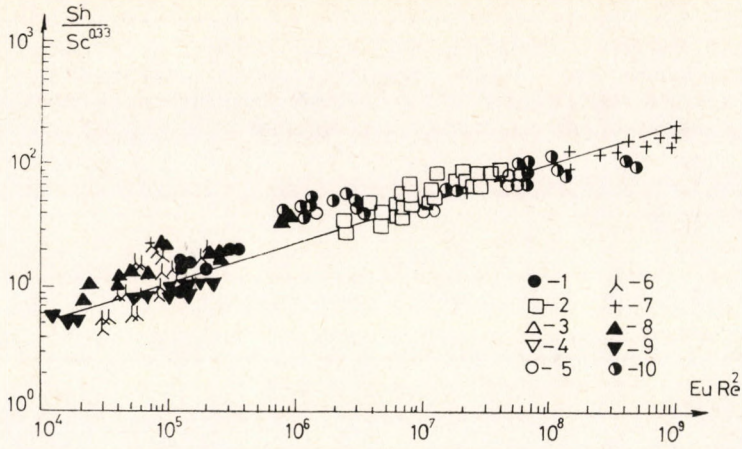

Рис. 5

Сравнение зависимости (21) (сплошная линия) с экспериментальными результатами работ. Нисходящий прямоток: 1 — [19], 3 — [21], 4 — [21], 5 — [22], 9 — [25]. Восходящий прямоток: 2 — [20], 7 — [24], 8 — [1], 9 — [25], 10 — [23]

от датчиков сферической формы $d=5$ мм внутри которых помещался электронагревательный элемент, изготовленный из полупроводникового материала. В качестве материала для тела датчика использовался тройной сплав олово-свинец-висмут с температурой плавления 150—180 °С. Измерение температуры датчика производилось медь-константановой термопарой с диаметром корольк а 60 мк. Было изготовлено 2 типа датчиков, из которых первый представлял одиночный шар, контактирующий с холодными зернами, а второй такой же конструкции, но помещенный внутри группы из 12 нагреваемых (охранных) зерен. Последние имели такие же нагреватели и размеры, что и сам датчик. При проведении измерений на датчик подавался электрический ток, который обеспечивал его нагрев таким образом, что тепловой поток зависел только от электрических характеристик измерительной схемы, но не изменялся при вариации гидродинамических условий в месте нахождения датчика.

Определение коэффициентов теплообмена было проведено на 2-х типах датчиков. Сравнение результатов показало их расхождение до 50%, причем большие значения наблюдались в варианте без охранных зерен. Поскольку датчик 2-го типа более физично воспроизводит условия слоя катализатора, то основные эксперименты были проведены на датчиках с охранными зернами, однако при обработке результатов измерений производилась их корректировка на нагрев потока со стороны горячих зерен.

Результаты измерений и их обработка

Математическая модель, приведенная в первой части этой работы, описывает, по-видимому, и процессы теплообмена между газо-жидкостным потоком и поверхностью зерен неподвижного слоя. Поэтому можно предположить, что итоговая формула (18), а также ее аналог (21) применимы для оценки коэффициентов теплообмена α. Однако, поскольку теплообмен в отличие от массообмена осуществляется через всю поверхность датчика, то в этом случае получаются

эффективные коэффициенты переноса. Одним из вариантов учета этого факта может быть введение эффективной теплопроводности двухфазной смеси, а также эффективного числа Прандтля в теоретическую зависимость (18).

В настоящее время существуют несколько расчетных формул для $\lambda эф$ [27]. Однако, из всего наличия мы выбрали простейшую:

$$\lambda эф = \lambda_1 \varphi + \lambda_2 (1-\varphi) \tag{22}$$

и аналогично для чисел Прандтля:

$$Pr = Pr_1 \varphi + Pr_2 (1-\varphi) \tag{23}$$

где Pr_1, Pr_2 — числа Прандтля для газовой и жидкой фаз.

На *рис. 6* приведены результаты такой обработки полученных экспериментальных данных для шариков $d=5$ мм и $d=8$ мм (последние заимствованы из работы [28]).

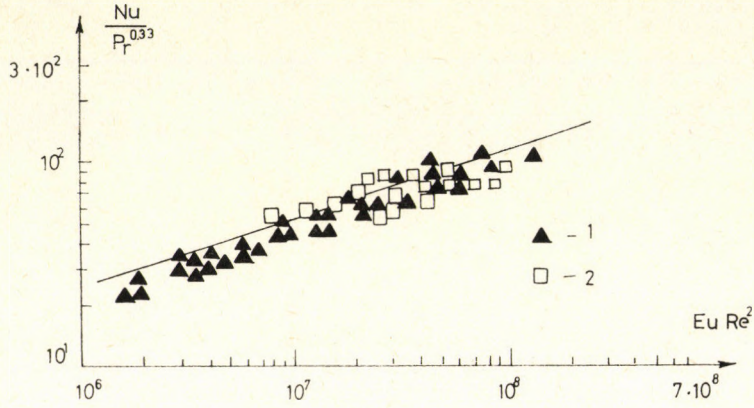

Рис. 6

Сравнение экспериментальных данных по теплообмену с зависимостью (21) (сплошная линия). Экспериментальные точки соответствуют: *1* — эта работа $d=5$ мм; *2* — $d=8$ мм [27]

Как следует из этого рисунка экспериментальные данные по теплообмену удовлетворительно описываются формулой (21). Наряду с такой обработкой, полученные экспериментальные данные были обработаны посредством числа Рейнольдса для каждой из фаз. При этом была получена чисто эмпирическая зависимость для расчета $\tilde{Nu}$, более удобная в некоторых случаях для практического применения:

$$\tilde{Nu} = (9.62 + 0.38 Re_1^{0.81}) Re_2^{0.2} \tilde{Pr}^{0.33} \tag{24}$$

где

$$\tilde{Nu} = \frac{\alpha d}{\lambda_{см}}; \quad \tilde{Pr} = \frac{C_{см}\, \mu_{см}}{\lambda_{см}}; \quad Re_1 = \frac{U_1 d}{\nu_1}; \quad Re_2 = \frac{U_2 d}{\nu_2}$$

$$C_{см} = \frac{\varrho_1 C_{p1} \varphi + \varrho_2 C_{p2} (1-\varphi)}{\varrho_1 \varphi + \varrho_2 (1-\varphi)}; \quad \mu_{см} = \mu_1 \varphi + \mu_2 (1-\varphi)$$

$$\lambda_{см} = \lambda_1 \left[1 - \frac{(1-\varphi)(1-\lambda_2/\lambda_1}{1 - \frac{1-\varphi}{3}\left(1 - \frac{\lambda_2}{\lambda_1}\right)} \right]$$

Эта зависимость удовлетворительно описывает имеющиеся экспериментальные данные по теплообмену для шариков и справедлива в области изменения газосодержаний $\varphi=0{,}1$—$0{,}9$ и чисел Re равных $Re_1=10$—5000, $Re_2=10$—1160.

УСЛОВНЫЕ ОБОЗНАЧЕНИЯ

c — концентрация;
c_p — теплоемкость;
$d=2R$
D — диаметр колонны;
D_2 — коэффициент диффузии;
m — толщина пленки жидкости;
P — давление;
R — радиус частицы;
t — время;
u, v — скорости жидкости в продольном и поперечном направлениях по тольщине плёнки;
U_1, U_2 — скорость пузырей газа и перемычек жидкости соответственно;
x, y — координаты;
α — коэффициент теплообмена;
β — коэффициент массообмена;
ν_2 — кинематическая вязкость жидкости;
λ — коэффициент теплопроводности;
μ_2 — динамическая вязкость;
ϱ — плотность;
φ — газодержание;
ω — частота прохождения пузырей.

Индексы

1 — газовая фаза;
2 — жидкая фаза;
см — двухфазный поток;
* — равновесные условия.

ЛИТЕРАТУРА

1. Кириллов, В. А. и Касаманян, М. А.: Hung. J. Ind. Chem. 3. 21. 1976
2. Чжен, П.: Отрывные течения, М., Мир, с. 213, 1972.
3. Тихонов, А. Н., Самарский, А. А.: Уравнения математической физики, М., Наука, с. 200, 1972.
4. Кириллов, В. А и Касаманян, М. А.: ТОХТ, *1975*. 9, (6) 870.
5. Hofman, M. P.: Catal. Rew.-Sci. Eng. *1978*. 17, (1) 71.
6. Ashwal, S. K.: Chem. Eng. J., *1976*. 12, 69.
7. Ohshima, S.: J. Chem. Eng. Japan, *1976*. 9, 299.
8. Fukushima, S.: J. Chem. Eng. Japan, *1979*. 12, 296.
9. Sato, Y., Hirose, T.: J. Chem. Eng. Japan, *1973*. 6, 147.
10. Midoux, N., Favier, M.: J. Charpentier J. Chem. Eng. Japan, *1976*. 9, 350.
11. Larkins, R. P., White, R. R., Jeffrey, D. W.: AIChE Journal, *1961*. 2, 231.
12. Weekman, V. W.,Myers, J. E.,: AIChE Journal, *1964*. 10, 951.
13. Кириллов, В. А., Кузьмин, В. А., Пьянов, В. И. и Ханаев, В. М.: ДАН СССР, *1979*. 245. (1) 159
14. Кутателадзе, С. С.: Основы теории теплообмена, Новосибирск, Наука, 1970.
15. Hirose, T., Mori, Y., Sato, Y.: J. Chem. Eng. Japan, *1976*. 9, 220.
16. Богоявленский, Р. Г.: Гидродинамика и теплообмен в высокотемпературных ядерных реакторах с шаровыми твэлами. М., Атомиздат, 1978.
17. McGune, L. K., Wilchelm, R. H.: JEC, *1949*. 41, 1124.
18. Hobson, M., Thodos, G.: Chem. Eng. Progr., *1951*. 47, 370.
19. Chou, T. S., Worley, F. L., Luss, D.: IEC Fundamentals *1979*. 18, 279.

20. Colquhoun-Lel, I., Stepanek, J. B.: Trans. I. Chem. Eng. *1978*. 56, 136.
21. Bliss, G. S.: Effects of the Gas Phase on Liquid Solid mass transfer in tricle bed. M. Sc. thesis Mass. Inst. Technol. Cambridge, 1976.
22. Satlerfield, C. N., van Eek, M. W., Bliss, G. S.: AIChEJournal, *1978*. 24, 709.
23. Specchia, V., Baldi, G., Gianetto, A.: Ind. Eng. Chem. Proc, Des. Dev. *1978*. 17, 362.
24. Mochizuku, S.: Chem. Eng. Sci., V. 36, p. 213, 1981.
25. Joshikawa, M., Iwai K. et al: J. Chem. Eng. Japan, *1981*. 14, 444.
26. Talmor, E.: AIChE Journal, *1977*. 23, 686.
27. Дульнев, Г. Н., Заричняк, Ю. П.: Теплопроводность смесей и композиционных материалов. Л., Энергия, 263 с., 1974.
28. Кириллов, В. А., Огарков, Б. Л.: Hung. J. Ind. Chem., *1978*. 6, 175.

ANALYSIS OF TRANSFER PROCESSES IN A FIXED GRANULAR BED AT A COCURRENT UPFLOW OF GAS AND LIQUID

SUMMARY

Calculations of some practically important processes taking place in fixed bed reactors at a cocurrent upflow of phases are considerably limited by deficiency of experimental data on hydraulic pressure drop, as well as by heat-mass exchange in such reactors.

In this work an attempt was made to estimate these parameters from the unitary standpoints and propose methods for their calculation.

HUNGARIAN JOURNAL
OF INDUSTRIAL CHEMISTRY
VESZPRÉM
Vol. 11. pp. 275–282 (1983)

RELIABILITY ANALYSIS OF COMPLEX CHEMICAL ENGINEERING SYSTEMS

G. GRUHN, W. NEUMANN and R. SEIDEL

("Carl Schorlemmer" Technical University, Leuna-Merseburg,
Department of Chemical Engineering, Merseburg, GDR)

Received: February 14, 1983.

Reliability analysis of complex chemical engineering systems includes the following main steps: function analysis and behaviour analysis of the system, evaluation of the reliability model, including parameter estimation and the simulation of reliability behaviour. — Typical examples of complex chemical engineering systems are integrated piping systems, which connect producer units and consumer units. The reliability analysis of these supplying systems is of interest. The function as well as the behaviour analysis of a complex piping system is based on a computer programme. Because of the large number of system states considered, a MARKOVIAN model is required for the reliability analysis of a complex piping system. The model is formed by a system of ordinary first order differential equations:

$$\dot{p}(t) = \mathbf{A}(t) \times p(t).$$

As an example of this method, the reliability analysis of a steam supplying system is realised.

Introduction

The reliability analysis of complex chemical engineering systems includes the following main steps:

function analysis of the system,
bahaviour analysis of the system,
evaluation of the reliability model, including parameter estimation, and
simulation of the reliability behaviour.

The aim of function analysis is to describe the modes of operations of the elements, subsystems and of the whole system with respect to the system function. The behaviour analysis has to result in information on the effects of failures of the elements and the subsystems on the system reliability.

In simple cases, the logical relationships between the element states (failure, and function) and the system states (failure, and function) can be pointed out without simulation. More complicated situations arise if partial failures of the elements and the systems are considered, or systems with complicated integrated structures have to be studied. In most of these situations, the relationships between the element states and the corresponding system states can only be determined by process stream simulations. Typical examples are integrated piping systems connecting producer units and consumer units. Failures of producer units, pipes, fittings, and consumer units, etc., lead to a large number of system states. For a given system, each consumer unit normally can be supplied in different ways from various producer units.

Typical examples for these types of chemical engineering systems are steam systems, cooling water systems and compressed air systems of chemical works.

The reliability analysis of these supply systems is of interest because of their important influence on various chemical plants, which are connected with them in a chemical works. The remarkable characteristics of these systems are in general:

extremely high level of system reliability,
relatively high level of the reliability of the elements,
limited number of different element types.

The results of quantitive reliability analysis are necessary, not only for structuring the systems and for estimating effective maintenance strategies, but also for controlling the systems in the case of element failures.

Mass Stream Simulation programme

For the mass stream simulation of complex piping systems a simulation programme was developed (1, 2). The calculations are based on the mass stream balances for the nodes and on the pressure drop balances for the loops of the system.

$$\sum_{i=1}^{N} \dot{m}_i = 0 \tag{1}$$

$$\sum_{j=1}^{M} \Delta p_j = 0 \tag{2}$$

$\dot{m}_1$ mass stream i to the node
Δp_j pressure drop of the loop element j
N total number of input and output mass streams of the node
M total number of the loop elements.

The pressure drop Δp_j is given by:

$$\Delta p_j = a_j \dot{m}_j^2 \tag{3}$$

$$a_j = \frac{1}{2\xi_j} \sum_{k=1}^{L} \frac{\zeta_k}{A_k^2} \tag{4}$$

ξ_j density of the mass stream through loop element j
ζ_k pressure drop coefficient
A_k cross-section area.

An approximation algorithm is used for the simultaneous solution of the equation system. In this way, the elements of each loop are supplied with corrections for the mass streams, provided that the mass balances of each loop are fulfilled.

The amount of the mass stream corrections are determined by the solution of the linearized pressure drop balances for the complete piping system. An iteration becomes necessary, because of the linearizations and because of the fact that the pressure drop coefficients depend on REYNOLDS-numbers. For compressible mass streams, an additional correction of the density must be included.

Computer programme for reliability analyses

Because of the large number of system states to be considered, a MARKOVIAN model is needed for the reliability analysis of a complex piping system. The model is formed by a system of ordinary first order differential equations:

$$\dot{p}(t) = \mathbf{A}(t)p(t) \tag{5}$$

p (t) vector of state probabilities
$\mathbf{A}$ (t) transition matrix.

The transition matrix can be derived from the state graph of the system.

The elements of the matrix are formed by the failure rates and the repair rates, which are determined in an empirical way. For numerical calculations, a computer programme was developed [3, 4]. For this, the solution of the MARKOVIAN model equations (5) was based on the RUNGE–KUTTA method.

Technological problem

In a chemical plant, a steam supply system shown in *Fig. 1* is in operation. The steam is generated by a steam power plant (cogeneration of electricity and steam) at a pressure of 2.3 MPa and a temperature of 600 K and transported by two feed lines. Eleven consumer units (6, 14, 16, 18, 20, 22, 24, 25, 28, 30, 32) e.g. an ethene-plant, a polyethene-plant, a caprolactam-plant, and torches, e.t.c. need to be provided with steam of specific parameters for each consumer unit as shown in *Table 1*. The consumer units 6, 24, 30 must be provided in special situations only.

The piping system consists of pipes, fittings, pipe branchings, and valves, etc. Based on practical experience, it is intended to remove the transfer lines, given in *Fig. 1* by dashed lines, from operation in order to gain a simpler piping arrangement. The transfer lines are assumed not to be necessary for securing a high level of reliability.

Thus the special aims of the reliability analysis consist of examining the permissibility of the structure reduction intended,

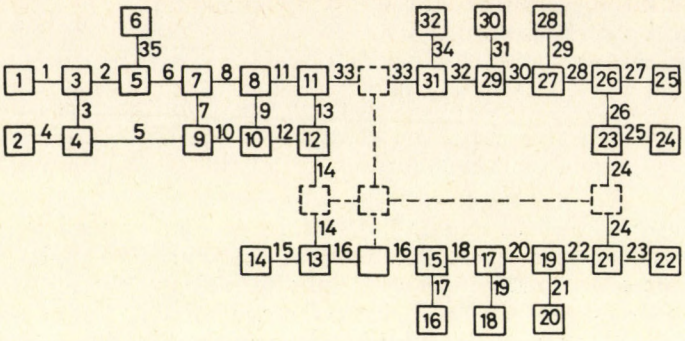

Fig. 1

Block scheme of the piping system

(1, 2) producer units; (6, 14, 16, 18, 20, 22, 24, 25, 28, 30, 32) consumer units; (3–5, 7—13, 15, 17, 19, 21, 23, 26, 27, 29, 31) feed spreaders; (1–33) pipelines incl. fittings, valves etc.

Table 1

Steam parameters of consumer units

unit	mass stream $t(h^{-1})$	pressure (medium) (MPa)	pressure (min.) (MPa)
6[1)]	—	—	—
14	5.0	2.04	1.6
16	6.0	2.00	1.6
18	7.0	2.00	1.6
20	6.7	2.00	1.6
22	0.8	2.01	1.6
24[1)]	—	2.06	1.6
25	0.2	2.07	1.6
30[1)]	—	2.09	1.6
32	0.3	2.10	1.6

[1)] only in temporary operation.

estimating the reliability level of the (reduced) system on the basis of the failures of its elements, and testing the effectiveness of the analysis procedure developed.

Solution Procedure

The most important components of the solution procedure can be formulated as:

definition of the element failures and estimation of their mathematical characteristics,

definition for the system failures,
estimation of the relationships between the element failures and system failures, based on mass stream simulation to form the state graph,
formulation of the characteristicl differential equation system corresponding to the state graph, and
simulation of the reliability behaviour with the programme.

For elements the binary behaviour are considered, so that only the two states, function and (total) failure, are defined. It was found that the function states and failure states can be statistically approximated by exponential distribution functions, and in this way practical conditions for each equipment can be met by constant values of failure rates and repair rates *(Table 2)*.

Table 2

Ranges of failure rates

element	failure rate $10^{-6}(h^{-1})$	λ $10^{-6}h^{-1}km^{-1}$
shut-off valve	0.1 —10.0	
measuring slade	0.1 — 1.0	
sealing	0.01— 0.04	
bare pipe		0.25—5.0

In general, a system failure occurs when the pressure and/or the mass stream for one of the consumer units fall below the minimum values shown in *Table 1*.

Further calculations were carried out under the special condition of guaranteed mass streams for all consumer units, so that a system failure is represented by a pressure below 1.6 MPa.

Furthermore, it could be clarified by prestudies that the probability of simultaneous failures of different pipelines of the systems is negligible. Because of this important simplification, only 19 primary element failures needed to be investigated with respect to their consequences for the system.

The resulting state graph is shown in *Fig. 2*. It contains 20 system states with:

1 state of full function (1) (no element failures, pressure from 2.0 to 2.1 MPa),
14 states of restricted function (2—15) (element failures, pressure from 1.6 to 2.0/2.1 MPa) and
5 failure states (16—20) (element failures, pressure under 1.6 MPa).

The state graph is based on the fact that failures of the pipelines 15, 17, 19, 21, 25, 29, 31 and 35 are negligible. The failures of the pipelines 32, 30, 28, 26, 24 are summed up by $\lambda_{33'}$.

By noticing that a failure of each of these elements causes a system failure, the failures of the pipelines 34, 27 and 23 are modelled by $\lambda_{34'}$.

The probability that two or more elements are in the failure mode at the same time is nearly negligible. Thus the state graph is developed for the failure of only one element. The transition matrix corresponding to the state graph is given by:

$$
\mathbf{A} = \begin{bmatrix}
a_{11} & \mu_6 & \mu_3 & \mu_4 & \mu_5 & \mu_7 & \mu_8 & \mu_9 & \mu_{10} & \mu_{11} & \mu_{12} & \mu_{13} & \mu_{18} & \mu_{20} & \mu_{22} & \mu_1 & \mu_{14} & \mu_{16} & \mu_{33'} & \mu_{34'} \\
\lambda_6 & -\mu_6 & & & & & & & & & & & & & & & & & & \\
\lambda_3 & & -\mu_3 & & & & & & & & & & & & & & & & & \\
\lambda_4 & & & -\mu_4 & & & & & & & & & & & & & & & & \\
\lambda_5 & & & & -\mu_5 & & & & & & & & & & & & & & & \\
\lambda_7 & & & & & -\mu_7 & & & & & & & & 0 & & & & & & \\
\lambda_8 & & & & & & -\mu_8 & & & & & & & & & & & & & \\
\lambda_9 & & & & & & & -\mu_9 & & & & & & & & & & & & \\
\lambda_{10} & & & & & & & & \mu_{10} & & & & & & & & & & & \\
\lambda_{11} & & & & & & & & & -\mu_{11} & & & & & & & & & & \\
\lambda_{12} & & & & & & & & & & -\mu_{12} & & & & & & & & & \\
\lambda_{13} & & & & & & & & & & & -\mu_{13} & & & & & & & & \\
\lambda_{18} & & & & & & & & & & & & -\mu_{18} & & & & & & & \\
\lambda_{20} & & & & & & & & & & & & & -\mu_{20} & & & & & & \\
\lambda_{22} & & & & & & 0 & & & & & & & & -\mu_{22} & & & & & \\
\lambda_1 & & & & & & & & & & & & & & & -\mu_1 & & & & \\
\lambda_{14} & & & & & & & & & & & & & & & & -\mu_{14} & & & \\
\lambda_{16} & & & & & & & & & & & & & & & & & -\mu_{16} & & \\
\lambda_{33'} & & & & & & & & & & & & & & & & & & -\mu_{33'} & \\
\lambda_{34'} & & & & & & & & & & & & & & & & & & & -\mu_{34'}
\end{bmatrix}
$$

with:

$$
\begin{aligned}
a_{11} = & -\lambda_6 - \lambda_3 - \lambda_4 - \lambda_5 - \lambda_7 - \lambda_8 - \lambda_9 - \lambda_{10} - \lambda_{11} - \lambda_{12} \\
& - \lambda_{13} - \lambda_{18} - \lambda_{20} - \lambda_{22} - \lambda_1 - \lambda_{14} - \lambda_{16} - \lambda_{33'} - \lambda_{34'}
\end{aligned}
$$

Therefore, the differential equation system is given by:

$$
\begin{aligned}
\dot{p}_{1(t)} = & a_{11}p_1 + \mu_6 p_2 + \mu_3 p_3 + \mu_4 p_4 + \mu_5 p_5 + \mu_7 p_6 + \mu_8 p_7 + \\
& + \mu_9 p_8 + \mu_{10} p_9 + \mu_{11} p_{10} + \mu_{12} p_{11} + \mu_{13} p_{12} + \\
& + \mu_{18} p_{13} + \mu_{20} p_{14} + \mu_{22} p_{15} + \mu_1 p_{16} + \mu_{14} p_{17} + \\
& + \mu_{16} p_{18} + \mu_{33'} p_{19} + \mu_{34'} p_{20} \\
\dot{p}_2(t) = & \mu_6 p_1 - \lambda_6 p_2 \\
& \vdots \\
\dot{p}_{20}(t) = & \mu_{34'} p_1 - \lambda_{34'} p_{20}.
\end{aligned}
$$

This differential equation system was solved by the computer programme mentioned above.

Results

Fig. 3 shows the availability behaviour of the piping system investigated. The following facts are pointed out:

1. After an operation time of about 1000 h a high stationary level of the system

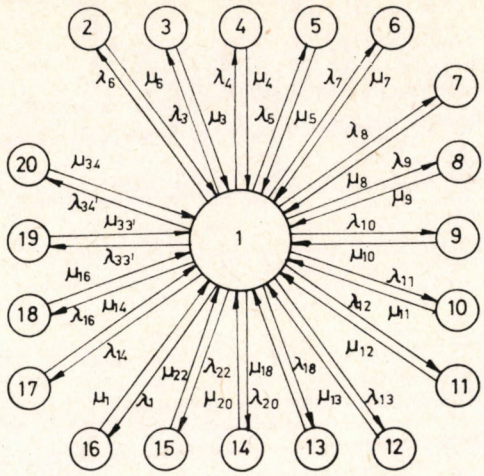

Fig. 2
State graph of piping system

availability ($V = 0.9932$) is reached. It is justified to remove the transfer lines given in *Fig. 1* by dashed lines from operation.

2. An effective and low-cost possibility for further increasing the system availability consists of increasing the pipeline 4 diameter or of installing a second pipeline parallel to it.
3. The soft-ware proved effective for handling reliability problems of the present type.

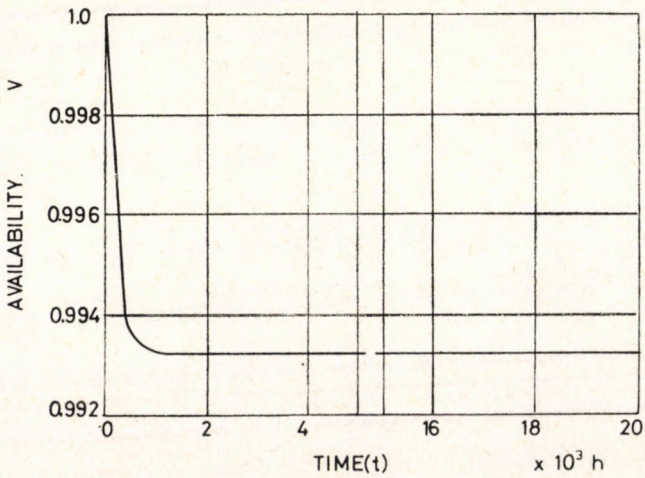

Fig. 3
Time behaviour of system availability

REFERENCES

1. NAUE, G., TILL, K. and SCHOLZ, R.: Untersuchung grosser Rohrleitungssysteme des innerbetrieblichen Transportes fluider Medien und Auswirkungen auf Investitionsentscheidungen, 2. Tagung "Industriemathematik", 31. 8.–1. 9. 1978, Magdeburg, GDR.
2. NAUE, G., SCHOLZ, R., EISFELDT, W. und RÖHME, Th.: Energieanwendung *1975*, 24, (11) 345–350.
3. GRUHN, G., NEUMANN, W. and HEINIG, H.: Lecture on 1st Internat. Symposium "Zuverlässigkeit von Chemieanlagen", Halle, 16/17. 9. 1976.
4. GRUHN, G., KAFAROW, W. W. u. a.: Zuverlässigkeit von Chemieanlagen, VEB Deutscher Verlag für Grundstoffindustrie, Leipzig, 1979.

РЕЗЮМЕ

Анализ надёжности некоторой комплексной системы химической промышленности состоит из следующих основных этапов: функциональный анализ работы системы, анализ поведения системы, разработка модели надёжности, причём последний этап включает в себя определения параметров системы и симуляцию поведения по надёжности. Комплексная химико-технологическая система характеризуется полной системой трубопровододной сети, которая соединяет производительные и потребительские узла. Задача состоит в анализе надёжности этой полной системы. Как функциональный, так и анализ по надёжности требуют применения ЭВМ, авторами составлены программы для этой цели. В системе могут возникать многообразные состояния, поэтому для подготовки анализа надёжности трубопроводной сети необходимо составить модель типа МАРКОВА, которая состоит из систем дифференциальных уравнений первого порядка:

$$\dot{p}(t) = \mathbf{A}(t) \times p(t)$$

В качествепримера исследовали систему производства пара.

HUNGARIAN JOURNAL
OF INDUSTRIAL CHEMISTRY
VESZPRÉM
Vol. 11. pp. 283–290 (1983)

CALCULATION OF GLASS DENSITY FROM ITS COMPOSITION

MRS. K. SIMON

(Research Institute for Heavy Chemical Industries Veszprém)

Received: February 21, 1983.

There is a strong correlation between the oxide composition and the characteristics of glasses. The oxide composition-based calculation of glass density is of importance in the design of various glasses. Up to now no method was published for the prediction of the density of phosphate glasses. Multiple regression analysis was used for establishing an equation to be employed for the calculation of the oxygen ion volume. The volume of glass containing one gram atom oxygen is the size of the O^{2-} ion, which is influenced by the presence of various cations. This, on the other hand, influences the characteristics of glass, such as its density. The applicability of the elaborated method was checked with metaphosphate glasses prepared by Japanese researchers. The difference between the calculated and measured data was less than one per cent.

Introduction

Researchers have long been concerned with the calculation of physical characteristics (density, heat conductivity, specific heat, and molecular refraction) of glass on the basis of composition.

Each agent of the basic material and each oxide of the glass have a major influence on the characteristics of glass [1]. The viscosity and specific heat decrease by increasing the atomic mass; chemical resistance of glasses is higher if oxides have lower solubility and hydration temperature.

As a result of oxide change, the characteristic to be examined also changes. Glasses have a complicated structure, but a number of researchers gave a relatively good approach for the calculation of some characteristics by various formulas — sometimes with limits of composition.

The methods described in *Table 1* relating to the investigation of SiO_2—B_2O_3—Al_2O_3—MgO—Na_2O—K_2O system were extended by KIS [3] to study germanete, plumbosilicate and silicogermanate glasses. According to literature no studies were so far carried out for the reproduction of the density of phosphate glasses, thus the author tried to develop a calculation method.

Table 1

Known calculation methods for glass density from its oxide composition, authors, year of publication [2]

Method	Author	Year
linear	WINKELMANN, SCHOTT	1894
	TILLOTSON	1911
	ENGLISH, TURNER	1920
	BAILLIE	1921
	PAYNE	1928
	WATERSON, TURNER	1934
	MORIYASU	1940
	KNAPP	1968
	WOLF	1977
function of more variables	GLAZE, YOUNG, FINN	1932
	YOUNG, GLAZE, FAICK, FINN	1939
	HUGGINS	1940
quadratic	GLAZE, YOUNG, FINN	1932
	GILARD, DUBRAL	1938
logarithmic	FINN, THOMSON	1925
	WINKS, TURNER	1931
special method	STEVELS	1946
	APPEN	1949
	MELNIČENKO, ČERNINA	1953
	PLUMAT	1956
	NÁRAY-SZABÓ	1960
	COENES	1962
	KIS	1968 [3]
	ROBINSON	1969
	KOCSIS	1978 [4]
direct relationship	SCHOLES	1929
	BILTZ, WEIBKE	1932

Calculation of the Density of Phosphate Glasses by O^{2-} volume

Oxigen occupies about 95 per cent of the volume in the structure of glasses. The position of the oxygen atoms is determined by the network, depending on the coordination of network former elements and by the modifier ions in its holes. The incorporation of various cations in glass may cause changes in the O^{2-} ion size (the volume of glass containing one gram atom oxygen) and this influences the character of glass.

O^{2-} ion volume was calculated with the assistance of the composition in mass % and density found as follows:

if the N_pO_r compound exists in x mass per cent and its molecular mass is M_t, gram ion oxygen taken into 100 g glass by the N_pO_r: $O = \frac{x \cdot r}{M_t}$

volume of 100 g glass: $\frac{100}{\varrho}$, where ϱ is the density of glass (g/cm^3)

Σ gram ion O^{2-} taken into glass by each component, multiplied the Avogadro number (6.022×10^{23}), the number of 0^{2-} ion can be obtained in the above volume.

The volume of one O^{2-} (v) can be calculated in 10^{-24} cm^3 as follows:

$$v = \frac{100}{6.022 \times 10^{23} \times \varrho \times \Sigma 0^{2-}}$$

Multiple regression analysis was used to obtain an equation suitable for calculating the oxygen ion volume. Observed variables were as follows:

independent variable: R,K,NaF
dependent variable: oxygen ion volume of which density can be calculated (total Na as independent variable did not give significant correlation)

Number of observed units were 17.

Explanation of independent variables:
R: number of oxygen per atom of network former elements

$$R = \frac{0^{2-}}{B + Al + P \ldots} = \frac{\Sigma 0^{2-}}{\Sigma H}$$

where: $\Sigma 0^{2-}$ total gram-ion of oxygen in 100 gram glass
ΣH total gram atom number of all network formers in 100 gram glass
K and NaF atomic or molar number of potassium and sodium fluoride that participated in the construction of the glass

(Composition of $AlPO_4$ glasses made by the author is given in *Fig. 1.*)

Basic data for the multiple regression analysis and calculated from the data of *Table 2*, according to the given equation in *Table 3*.
Equation for calculating oxygen ion volume is as follows:

$$v = A \times R + B \times K + C \times NaF + D$$
$$A = 6.642 \pm 3.8$$
$$B = 4.315 \pm 2.9$$
$$C = 21.36 \pm 13.0$$
$$D = 7.024$$

The statistical analysis of the coefficient for the quality of fit gave positive results. The FISCHER-test was significant at the 99,8 per cent probability level. Partial regression coefficients were significant at the 99.78%, 99.38%, 99.55% probability level (Student-test).

Density can be calculated by the oxygen ion volume:

$\Sigma 0^{2-}$ gram-ion in 100 gram glass is known from the composition volume of 100 g glass: $6.022 \times 10^{23} \times v \times \Sigma 0^{2-} = V$

$$\text{density} = \frac{100}{V} = \varrho$$

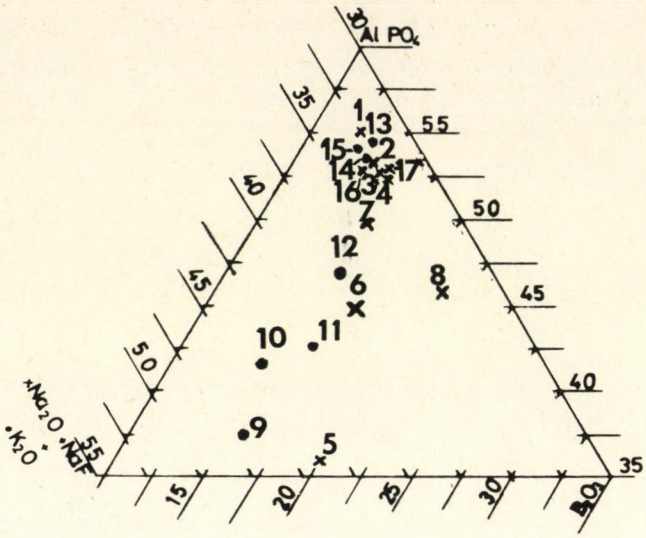

Fig. 1
Composition of $AlPO_4$ glasses prepared by the author

In the case of $AlPO_4$ based glasses, the density was calculated from the composition with 2% tolerance. Applicability of the method was checked with metaphosphate glasses prepared by Japanese researchers [5]. (Composition of glasses can be seen in *Fig. 2.*)

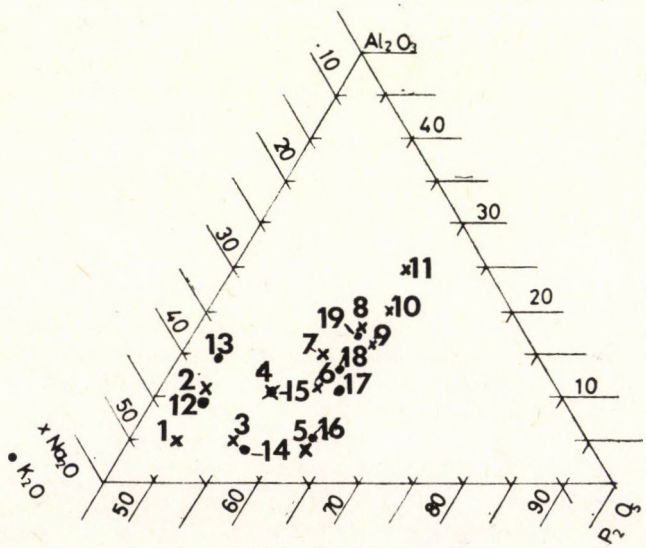

Fig. 2
Composition of metaphosphate glasses prepared by Japanese researchers [5]

Table 2

Oxide composition of phosphate glasses prepared by the author (mass per cent)

Sample	Oxide P_2O_5	Al_2O_3	B_2O_3	Na_2O	K_2O	NaF
1.	40.70	29.24	9.61	17.77	—	2.68
2.	40.58	28.94	10.24	17.59	—	2.65
3.	40.12	28.81	10.93	17.50	—	2.64
4.	39.80	28.59	11.62	17.38	—	2.61
5.	30.60	21.98	16.68	26.72	—	4.02
6.	35.36	25.40	13.80	22.11	—	3.33
7.	38.61	27.74	11.82	18.95	—	2.88
8.	36.60	26.30	16.00	17.30	—	3.80
9.	29.04	19.85	12.28	21.57	14.02	3.23
10.	35.45	18.97	8.80	20.50	13.23	3.05
11.	35.49	24.25	8.46	15.40	13.35	3.08
12.	35.90	26.10	12.30	18.80	3.60	3.30
13.	40.40	28.89	9.91	15.20	2.90	2.70
14.	40.14	28.83	9.85	15.58	2.96	2.64
15.	40.20	28.80	9.50	14.90	4.00	2.60
16.	40.24	28.90	10.22	17.55	—	3.09
17.	40.12	28.81	10.93	17.50	—	2.64

Table 3

Basic data of R, K, NaF and $v_{calculated}$

Sample	R	K gion/100 g	NaF 10^2 gmol/100	v(O) 10^{-24} cm^3
1.	2.104	—	6.3827	22.28
2.	2.097	—	6.3113	22.26
3.	2.087	—	6.2874	22.32
4.	2.078	—	6.2160	22.30
5.	2.142	—	9.5265	23.30
6.	2.114	—	7.8593	22.92
7.	2.096	—	6.9067	22.49
8.	2.033	—	9.0500	22.13
9.	2.287	0.2976	7.6926	25.56
10.	2.363	0.2809	7.2640	25.10
11.	2.230	0.2834	7.3354	24.64
12.	2.118	0.0764	7.8593	23.37
13.	2.095	0.0616	6.4303	22.55
14.	2.100	0.0628	6.2875	22.39
15.	2.105	0.0849	6.1922	22.37
16.	2.096	—	7.3590	22.43
17.	2.087	—	6.2875	22.50

Table 4

Found and calculated values of v and density, deviation %

Sample	v(O)(10^{-24} cm^3)		density (g/cm^3)		deviation %
	found	calculated	found	calculated	
1.	22.28	22.37	2.487	2.478	0.361
2.	22.26	22.30	2.480	2.476	0.157
3.	22.32	22.23	2.467	2.477	0.415
4.	22.30	22.15	2.461	2.477	0.661
5.	23.30	23.29	2.477	2.479	0.065
6.	22.92	22.74	2.459	2.478	0.757
7.	22.49	22.42	2.467	2.475	0.316
8.	22.13	22.46	2.474	2.438	1.474
9.	25.56	25.14	2.476	2.507	1.674
10.	25.10	25.49	2.488	2.451	1.490
11.	24.64	24.63	2.478	2.479	0.045
12.	23.37	23.10	2.446	2.474	1.149
13.	22.55	22.58	2.473	2.470	0.122
14.	22.39	22.59	2.496	2.475	0.852
15.	22.37	22.69	2.510	2.475	1.413
16.	22.43	22.52	2.474	2.464	0.387
17.	22.50	22.23	2.447	2.477	1.236

Table 6

Density-reproduction of metaphosphate glasses

Sample	R	K gion/100 g	O^{2-}vol.(10^{-24} cm^3)		Density (g/cm^3)		Deviation %
			found	calculated	found	calculated	
1.	2.829	—	21.80	21.96	2.563	2.544	0.739
2.	2.673	—	21.16	21.25	2.602	2.591	0.424
3.	2.746	—	21.64	21.58	2.506	2.512	0.255
4.	2.579	—	20.91	20.82	2.557	2.567	0.401
5.	2.684	—	21.40	21.30	2.471	2.482	0.464
6.	2.554	—	20.78	20.71	2.525	2.553	0.328
7.	2.475	—	20.44	20.35	2.552	2.564	0.454
8.	2.396	—	20.06	19.98	2.570	2.580	0.397
9.	2.420	—	20.01	20.10	2.563	2.552	0.414
10.	2.376	—	19.85	19.90	2.569	2.563	0.233
11.	2.308	—	19.65	19.59	2.572	2.584	0.470
12.	2.675	0.686	24.74	24.63	2.517	2.506	0.442
13.	2.555	0.609	23.86	23.70	2.535	2.553	0.692
14.	2.737	0.641	24.72	24.69	2.437	2.440	0.124
15.	2.578	0.546	23.49	23.50	2.493	2.492	0.044
16.	2.664	0.521	23.75	23.76	2.415	2.413	0.078
17.	2.550	0.444	22.81	22.87	2.459	2.452	0.269
18.	2.483	0.403	22.17	22.36	2.505	2.483	0.878
19.	2.416	0.343	21.59	21.76	2.527	2.507	0.790

Table 5

Composition of metaphosphate glasses [5]

Composition of $Na_2O-Al_2O_3-P_2O_5$ glasses

Sample	Na_2O mol%	Al_2O_3 mol%	P_2O_5 mol%	density g/cm³
1.	45.74	5.00	49.26	2.563
2.	39.99	9.81	49.20	2.602
3.	39.68	5.03	55.29	2.506
4.	33.38	11.40	55.22	2.557
5.	34.08	4.92	61.00	2.471
6.	29.24	10.78	59.98	2.525
7.	25.81	14.77	59.42	2.552
8.	20.86	18.70	60.43	2.570
9.	20.53	16.59	62.88	2.563
10.	17.69	19.02	63.30	2.569
11.	13.38	23.31	63.32	2.572

Composition of $K_2O-Al_2O_3-P_2O_5$ glasses

Sample	Na_2O mol%	Al_2O_3 mol%	P_2O_5 mol%	density g/cm³
12.	40.67	9.95	49.38	2.506
13.	36.19	14.61	49.20	2.535
14.	38.89	4.98	56.13	2.437
15.	33.17	11.35	55.48	2.493
16.	32.40	5.14	62.46	2.415
17.	27.68	10.20	62.12	2.459
18.	25.10	13.83	61.08	2.505
19.	21.41	17.34	61.25	2.527

The data for multiple regression analysis are given in *Table 6:* R,K,$v/0^{2-}$ ion volume/found and

$$v = A \times R + B \times K + C$$

$$A = 4.565 \pm 0.4$$

$$B = 4.908 \pm 0.2$$

$$C = 9.048$$

v calculated by the equation and the density data. Calculated and measured values differed less than 1%, less deviation of partial regression coefficients was due to the larger number of observed units.

ACKNOWLEDGEMENT

The author wishes to thank Zoltán Csapó, research worker of Computing Group of NEVIKI, for his assistance in the calculations.

REFERENCES

1. VOLF, M.: Üvegipari táblázatok és számítások. Műszaki Könyvkiadó, Budapest, 1956.
2. SCHNAPP, J. D. et al: Glastechn. Ber., *1980*. 1. S. 16—25.
3. KIS, M.: Építőanyag, *1968*, XX. (1) 21—29.
4. KOCSIS, G.: Építőanyag, *1978*. XXX (6) 232—236.
5. KISHIOKA, A.: Bull. Chem. Soc. Jpn., *1979* 56 (6). 1637—1642.

РЕЗЮМЕ

Известно, что оксидный состав и свойства стекла тесно коррелируют между собой. В планировании состава стекла большое значение имеет методика расчета плотности основанная на оксидном составе. До сих пор не была опубликована формула для расчёта плотности фосфатных стекол. Автором стати применены методы многофакторного регрессионного анализа для составления уравнения расчёта объёма иона кислорода. Установлено, что объём стекла содержащего одного грамматома кислорода совпадает размерами иона 0^2, но это зависит ещё от присутствия некоторых катионов, что в дальнейшем оказывает влияние на свойства стекла, в том числе и на его плотность. Разработанная методика проверена автором для фосфатных стекол произведенных японскими исследователями. Расхождение расчётных и измеренных данных не превышает одного процента.

HUNGARIAN JOURNAL
OF INDUSTRIAL CHEMISTRY
VESZPRÉM
Vol. 11. pp. 291–299 (1983)

ANALYTICAL INVESTIGATION OF THE PROCESS FOR MANUFACTURING 1,2,4-1H-TRIAZOLE

MRS. K. SIMON

(Research Institute for Heavy Chemical Industries, Veszprém)

Received: February 21, 1983.

Analytical methods have been developed for the investigation of basic materials and product controlling the process for manufacturing 1,2,4-1H-triazole.

Analysis of 1,2,4-1H-triazole and formamide of the product run by gas chromatograph; 1,2,4-1H-triazole and 1,2-diformyl-hydrazine can be determined by potentiometric titration with silver nitrate in the presence of a borate buffer.

Introduction

The manufacturing process of 1,2,4-1H-triazole [1] developed in the Institute for Heavy Chemical Industries (NEVIKI) is as follows *(Fig. 1., 2.)*:

According to the reactions, analytical demands of the planned pilot plant are:

1. investigation of the basic materials, as formic acid, hydrazine, formamide.
2. analysis of the product, as 1,2,4-1H-triazole, formamide, 1,2-diformyl-hydrazine.

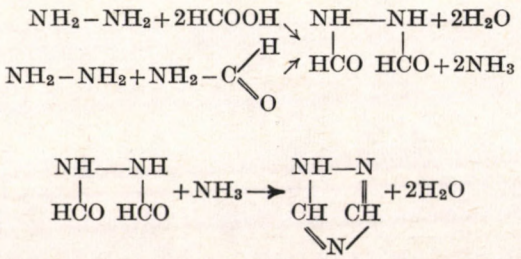

Fig. 1
Process for manufacturing 1,2,4-1H-triazole

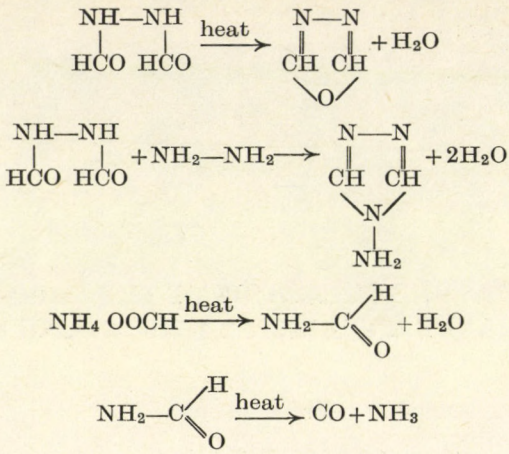

Fig. 2
Possible side reactions

Origon of the analytical standards

formamide chemically pure agent, Merck Art, 9684
formic acid chemically pure REACHIM USSR
hydrazine hydrate chemically pure BIOGAL HUNG. MSz 23778
1,2,4-1H-triazole (sublimate), prepared in NEVIKI
1,2-diformyl-hydrazine prepared in NEVIKI
4-amino-1,2,4-triazole prepared in NEVIKI

Quality control of the analyical standards

Table 1

Elemental analysis (mass per cent)

		1,2,4-1H-triazole	1,2-diformyl-hydrazine	4-amino-1,2,4-triazole
C	theory	34.8	27.3	28.6
	found	37.7	27.7	31.0
H	theory	4.3	4.5	4.7
	found	3.9	4.4	4.1
N	theory	60.9	31.8	66.7
	found	59.2	31.8	66.0
O	theory	—	36.4	—
	found	—	37.0	—
	found	100.8	100.9	101.1

Analysis were performed by Carlo Erba type 1102 elemental analyzer.

Infrared, ^1H–NMR spectroscopy, X-ray diffraction investigations

The materials obtained as standards were controlled by infrared (UR–10 Carl Zeiss) ^1H–NMR spectroscopical (Varian) and X-ray (Müller mikro 111) diffraction methods *(Table 2)*. They were accepted as the point of reference considering that 1,2-diformyl-hydrazine involves unidentified impurities according to the ^1H–NMR analysis [2].

Table 2

Quality control by infrared, ^1H—NMR spectroscopic and *X*-ray diffraction methods

Compound	M.p. °C	IR cm^{-1}	^1H NMR ppm, DMSO—d_6	*X*-ray dÅ	I/I_1
				(ASTM 24 — 1983)	
1,2,4-1H-triazole	120—1	(μ SADP 10626) 3130 2940 1490 1390 1280 1270 1180 1150 1060 990 960 930 890 680	8.22	3.974 3.187 3.608	100 35 34
1,2-diformyl-hydrazine	160	(SADG 4735) 3100 2900 2700 1620 1480 1370 1230 760 750	8.9 9.9	3.284 2.913 4.996	100 46 26
4-amino-1,2,4-triazole	80—1	(SADG 18250) 3290 3120 1700 1630 1520 1450 1370 1180 1060 960 850 670	6.2 8.4	5.356 3.119 2.685	100 35 21

Analysis of the Basic Materials

Formic acid was investigated by alkalimetry, hydrazine by iodometry [3], formamide [4] was titrated by acid after liberation of ammonia according to literature.

Analysis of the Product

There are few papers for the analysis of 1,2,4-1H-triazole in literature.

Ferroin-type chromogens give coloured compounds [5] in reactions with ion(II), copper(I) and cobalt(II). Among heterocyclic compunds 3,5-disubstituted 1,2,4-triazoles were investigated. The triazole and triazoline compounds also undergo hydrolytic decomposition, strongly catalysed by ion(II).

According to the thin layer chromatography of heterocyclic nitrogen compounds [6] R_f value for TLC of 1,2,4-triazole on silica gel CAMAG DS—5, for

various eluants (EtOAc, C_6H_6—MeOH 90+5, $CHCl_3$—MeOH 90+10 and 80+20, C_6H_6—Me_2CO 50+50), and developer $AgNO_3(NH_3)$ spray, 5 min in UV-light (254 μm) are given.

Heterocyclic nitrogen compounds were determined potentiometrically by SELIG [7]. The method also works when substituents such as nitro, halogen or alkyl groups are present. This method was adapted.

Some studies for the determination of formamide are known, e.g. volumetric [8] polarographic [9] colorimetric [10] and gas chromatographic [11, 12] methods. Those methods were chosen, which give some information simultaneously and analyses can be run easily and quickly.

Determination of 1,2,4-1H-triazole and Formamide by Gas Chromatography

10 mg/ml of ethanolic stock solution was prepared from the melt of the sample. Analysis was performed under following conditions:

instrument: Carlo Erba Linea GV
detector: HWD
column: 1.0 m×2.5∅ mm glass tube
column packing material: Chromosorb 101; 80–100 mesh
carrier gas: hydrogen, flow rate: 3,6 l/h

		triazole	formamide
temperature:	column	240 °C	180 °C
	injector	265 °C	245 °C
	detector	325 °C	300 °C

detector current: 250 mA
sensitivity: 4
sample volume injected: 2.5 μl

The quantity of the compounds were determined by measuring the peak height *(Fig. 3)*. The calibration curves were taken in the range of 5—30 μg of 1,2,4-1H-triazole and 0.5–8.5 μg of formamide.
Identity of peaks was certified by mass spectrometry *(Fig. 4)*.

Table 3

Retention data of the compounds

compound	relative retention* 240 °C	180 °C
ethanol (solvent)	0.03	0.19
formamide	0.34	1.00
1,2,4-1H-triazole	1.00	4.46

* Retention time of 1,2,4-1H-triazole was 74—76 sec at 240 °C, in the case of formamide, it was 65—67 sec at 180 °C.

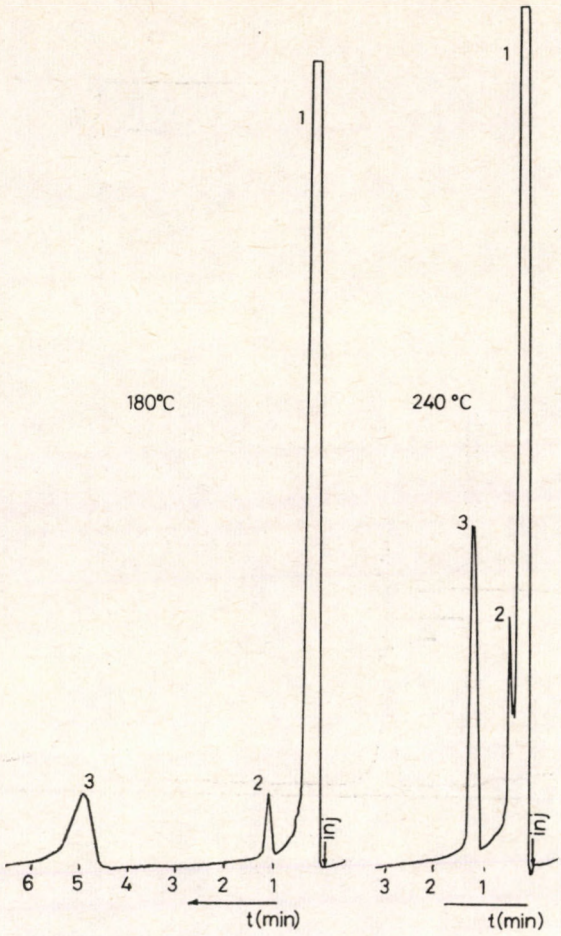

Fig. 3
Gas chromatograms
1 — ethanol (solvent), 2 — formamide, 3 — 1,2,4-1H-triazole

Average value, variance and confidence interval for the mean with coefficient 90 and 95 per cent for the representation of reproducibility of measures, based on five different measures and twelve gas chromatograms, can be seen in *Table 4*.

Potentiometric Determination of 1,2,4-1H-triazole and 1,2-diformyl-hydrazine

Procedure based on the phenomena that the heterocyclic nitrogen compounds, involving a free hydrogen atom on the secondary amino nitrogen, can be determined by potentiometric titration with silver ions in the presence of a borate buffer.

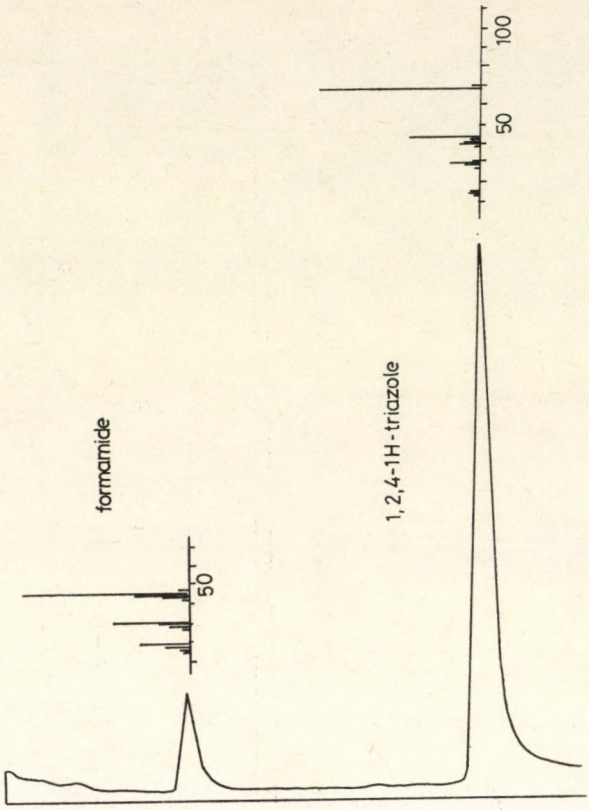

Fig. 4
GC–MS spectra

Table 4

Average value, variance and confidence interval for the mean with coefficients 90 and 95 per cent for the representation of reproducibility of mesures

Compound	Anal. method	Average value	Variance	Confidence interval		
				coefficients, %	lower limit	upper limit
1,2,4-1H-triazole	GC	81.4	1.4	95	80.5	82.4
				90	80.7	82.2
formamide	GC	1.5	0.06	95	1.42	1.59
				90	1.44	1.47
1,2,4-1H-triazole	Ag-titr.	85.6	0.87	95	83.4	87.7
				90	84.1	87.0

The titrant was 0.05 n aqueous silver nitrate. It was standardized against aliquots of potassium chloride solution. The borate buffer solution contained 0.12 m sodium tetraborate and 0.04 m boric acid; it had a pH of 9.25.

Ethanolic stock solution of triazole was prepared for gas chromatography. Aliquots of that solution containing 0.03–0.05 mmol of triazole were diluted to 45 ml with methanol and 5 ml of the borate buffer were added. *Emf*'s were monitored by a RADELKIS model OP–Ag 07111 silver sulphide indicating electrode and a double-junction Ag/AgCl reference electrode, in which the salt bridge was 1 n potassium nitrate. Stirring was provided by a magnetic stirrer.

The reaction product, precipitate, in the case of 1,2,4-1H-triazole is $Ag_{1,25}C_2H_2N_3$, so four molecules of triazole consumed five moles of silver. That was controlled by elemental analysis of the precipitate. It might be that the cause of the strange stoichiometry is the tautomerism of the 1,2,4-1H-triazole [13, 14, 15] *(Fig. 5)*.

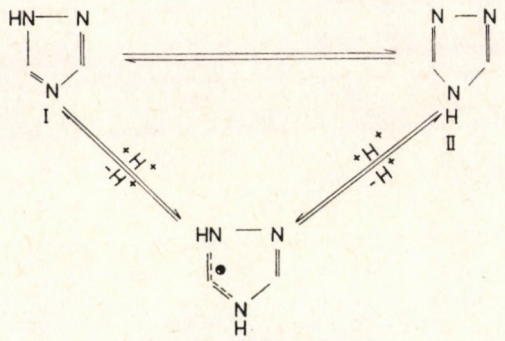

Fig. 5
Tautomerism of 1,2,4-1H-triazole

Transitional stage rising during the resonance makes this ratio possible, because the I, and II form require 1 mol of silver ion per mol of compound, and the transitional form 2 moles.

If the ratio of moles I–II to transitional form is 3:1, consumption of silver is 5 moles which corresponds to literature data [7] and our measurements. But verification of that idea demands further investigations.

The effect of the compounds was examined, which may occur in the technological samples and perhaps disturb the reaction. It was found that the formamide, formic acid, 4-amino-1,2,4-triazole do not react with silver. Hydrazine hydrate requires 1.4 moles of silver ion per mol of compound and 1,2-diformylhydrazine 3 moles.

Since during the process, excess of formamide/formic acid was used hydrazine hydrate did not appear.

The effect of aqueos silver nitrate solution to the *Emf* was also investigated under the experimental conditions, because the methanolic medium dilutes by the titrant. It was found that the variation of Emf in the range of conversion was caused only by the compound to be determined. The method enabled

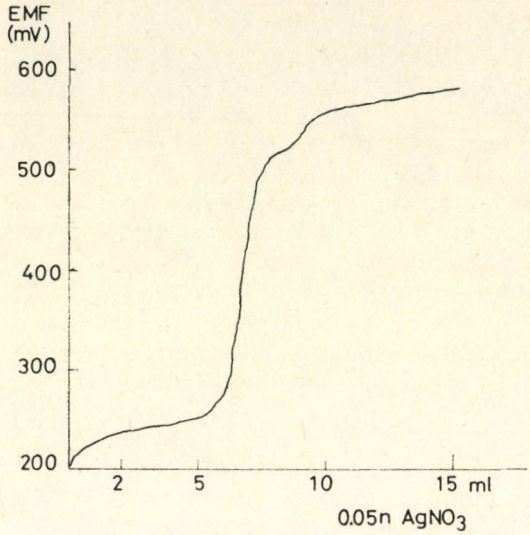

Fig. 6
Titration curve of technological sample
(1,2,4-1H-triazole 80.2%; 1,2-diformyl-hydrazine 14.2%)

analyses of the product with 50–98 per cent 1,2,4-1H-triazole content arising from a continous pilot plant. The amount of 1,2-diformyl-hydrazine was 0–25 per cent. The typical titration curve is presented in *Fig. 6*. Average value, variance and confidence interval for the mean with coefficients 90 and 95 per cent for the representation of reproduceability of measures for 1,2,4-1–H-triazole by potentiometric titration can be seen on *Table IV*.

ACKNOWLEDGEMENT

I wish to thank my colleagues for their extensive assistance.

REFERENCES

1. Hung. Pat. Appl.
2. GRASELLI, J. G. and RITCHEY, W. M.: Atlas of Spectral Data and Physical Constants for Organic Compounds CRS Press, Ohio 1975.
3. ERDEY, L.: Bevezetés a kémiai analízisbe. Tankönyvkiadó, Budapest, 1962, 220–221.
4. HALLAM, H. E.: The Analyst, *1955*, 80, 552–556.
5. SCHILT, A. A. et al: Talanta, *1974*, 21 (8), 831–836.
6. PETROWITZ, H. J.: Chimia (Aarau), *1965*, 19 (7), 426.
7. SELIG, W.: Mikrochim. Acta (Wien), *1979*, I. (5–6), 453–462.
8. HALLAM, H. E.: Analyst, *1955*, 80, 552–556.
9. KUTLUKOVA, U. i TOROPOV, A. P.: Trudy tashkent, politekh. Inst., *1970*, 64, 70–74.
10. QURESHI, S. Z. and IZZATULLAH, N. N.: Fresenius' Z. Anal. Chem. *1977*, 285 (3–4), 265.

11. Dandoy, J.: J. Chromat. *1971*, 61 (1), 145–146.
12. Kubecova, V. et al: J. Chromat. *1975*, 110 (1), 63–72.
13. Kroeger, C. F., Freiberg, W.: Chimia, *1967*, 21 (4), 161–162.
14. Creagh, L. T. and Truitt, P.: J. Org. Chem. *1968*, 33 (7), 2956–2957.
15. Kalikhman, I. D. et al: Dokl. Akad. Nauk SSSR, *1977*, 234 (6), 1380–1382.

РЕЗЮМЕ

Разработаны аналитические методы для контроля сыря и готовой продукции производства 1,2,4-1H триазола. Для анализа 1,2,4-1H триазола и формамида использовали газовый хроматограф, а 1,2,4-1H триазол и 1,2-диформил гидразина могут быть определены титрированием нитратом серебра в присутствии борат-буфера.

HUNGARIAN JOURNAL
OF INDUSTRIAL CHEMISTRY
VESZPRÉM
Vol. 11. pp. 301–306 (1983)

INVESTIGATION OF ENERGY CONSERVING LUBRICATING OIL PRODUCING PROCESSES II.

GY. GÁRDOS, M. KOVÁCS, T. KUN-SZABÓ, F. MIKÓ*, F. DÉNES*

(Veszprém University of Chemical Engineering Department of Hydrocarbon and Coal Processing
* Komárom Oil Refinery, Komárom, Hungary)

Received: March 17, 1983.

Experiments of raffination were carried out with hydrocracked (heavy, middle and light) distillates in the presence of furfurol and NMP solvents.

It was established that both solvents are suitable for raffination of the above distillates; because of their characteristics they are suitable for the production of base oils having high viscosity indices. It could be proved that using NMP in significant energy savings results, because less solvent quantity is used and therefore less need to be recovered from the raffinated and extracted phases.

In a previous paper [1] details of the possibility of using N-methyl-2-pyrolidine (NMP) solvent for the raffination of luboil cuts were discussed. Compared to furfural solvent it was shown that the same or higher yields of raffination can be realized with a smaller amount of solvent and the quality of the raffinate is the same or near that with furfurals, the column of extraction could be better and more flexible loaded, temperatures of extraction could be lower than in the case of phenol and furfurals, and at the same time it is neither toxic nor corrosive or gumming. Mostly light and middle paraffinic and deparaffinized cuts were used.

Raffination Experiments with Hydrocracked Fractions

Studying the possibilities of the modernization of luboil production in Hungary, experiments were also extended to hydrocracked fractions, for the examination of the advantages of using hydrocracked raffinates in motor oil compounds; what yields could be expected during raffination and chiefly what quality of base oils can be produced.

Objective of the Experimental Work

Results and observations obtained with paraffinic light and middle cuts made it possible to extend the raffination experiments to hydrocracked fractions and to study the possibilities of their processing. By developing the task, which is significant with regard to the modernization of lubricating oil products, an answer could be expected about how traditional technology could be used for processing strong paraffinic type of cuts, or some other types of processes should be considered.

Regarding raffination processes, using traditional solvents (furfural and phenol), the application of NMP solvent should also be taken into consideration, which has the advantageous property of mixing with water unrestrictedly; instead of distillation, the raffinated and extracted phases can easily be desolventized by extraction, using water, but another advantage is that the aromatic content of the base oils can easier be set to the necessary value.

The raffination experiments were mainly carried out with furfural (in some cases with NMP), but in the case of NMP using different technologic parameters, which were identical to the established favourable conditions obtained during experiments with paraffinized cuts.

The instrument used during the raffination experiments was the same which was mentioned in the previous [1] paper; feeding the oil and solvents, and removal of the raffinated and extracted phases were chosen in such a manner that the phase boundary should be formed at the upper part of the column and it was adjusted by measuring the differences of the dielectric constant.

After set-in equilibrium, the separated raffinated and extracted phases were desolventized by steam distillation.

For deparaffinization of the raffinate, MEK-toluol solvent mixture was used; the extracted paraffin was separated from the solvent after cooling it to -20 °C. But in the case of hydrocracked light cut, according to the requirement of lower freezing point, the deparaffinization was carried out at the lowest temperatures of -45 °C to -50 °C, attainable in a laboratory.

Materials used

According to operation requirements, hydrocracked cuts (heavy, middle and light) were used, the features of which are summarized in *Table 1.*

Table 1

Property	Hydrocracked cuts			
	Heavy	Middle		Light
		A	B	
Density at 20 °C	0.895	0.888	0.894	0.881
Viscosity				
at 50 °C, mm^2/s	29.40	13.38	14.50	5.77
at 100 °C	6.58	3.90	3.99	2.19
Freezing point, °C	+30	+24	+22	+6
Flash point, °C	241	216	219	139
Sulphur content, w%	0.39	0.39	0.71	0.4

Results of the Experiments

The test conditions (quality of solvent, solvent-base oil ratio, top and bottom temperature of the extraction column) and data characteristic of the deparaffinized refined oil (yield, viscosity, viscosity index, and freezing point) are listed in the Tables; based on these data the efficiency of the quality and quantity, of solvents as well as the conditions of the extraction process on the degree of raffination can well be evaluated.

Several examinations were carried out with all oil-solvent ratio values, of which average results are represented by the data of the *Tables*. It is noted that there were not significant differences between the repeated measurements, and this can be taken as confirmation of the permanent quality of the base material, as well as an assurance of appreciation of the obtained results.

The aim of raffination with *hydrocrcked heavy* cut was to produce a suitable base oil for the further development of motor oils from this cut. The circumstances and results of the raffination experiments are listed in *Table 2*.

Data of raffination with furfural show that this solvent can efficiently be used for the raffination of the above cut. Increasing the ratio of solvent (from 1:2.0 to 1:3.5) yields of raffination decrease significantly from 66 to 54%) with an adequate increase of viscosity indices. After average (75—80%) yields of deparaffinizations viscosity indices above 100 can be reached with every solvent ratio and the freezing points can be found near −15 °C.

In the case of NMP, experiments were carried out with anhydrous solvent and with a water-injection method. Hydrocracked heavy cut can easily be raffinated with both methods. Compared to the raffination with furfural at a significantly lower solvent ratio — with regard to the raffinates with identical or near identical viscosity indices — higher yields can be obtained. Increasing the ratio of solvent (from 1.25 to 2.0) yields of raffinate are slightly reduced (from 63.6 to 60.1 w%).

Table 2

Results of raffination and deparaffinization of hydrocracked heavy cut

Solvent	Oil/solvent volume ratio	Temperature of column, °C		Raffinate			
		Bottom	Top	Yield w%	VK_{40}	VK_{100}	VI_E
					mm²/s		
Furfural	1:2.0	70	110	66.1	28.9	5.45	127
	1:3.0	70	110	59.5	25.9	5.17	133
	1:3.5	70	110	53.7	25.5	5.19	139
NMP	1:1.25	40	60	63.6	31.0	5.81	132
	1:1.5	40	60	62.9	30.1	5.74	135
	1:2.0	40	60	60.1	29.2	5.71	140
	1:1.5 + 2% water	40	60	66.2	31.1	5.76	129
	1:1.5 + 5% water	40	60	71.7	31.8	5.81	127

Table 2 (contined)

Deparaffinized raffinate					
Yield w%	VK_{40}	VK_{100}	VI_E	Freezing point °C	Flash point °C
	mm^2/s				
75.9	37.73	6.03	104	−15	215
79.0	34.42	5.81	110	−14	205
78.3	31.38	5.54	114	−14	206
80.2	41.89	6.39	101	−14	222
80.2	41.24	6.48	107	−14	214
79.1	40.21	6.38	107	−12	218
81.0	40.01	6.31	105	−14	218
81.5	42.65	6.47	101	−14	222

The advantage of NMP is in the first place illustrated by the fact that to obtain the necessary quality, lower solvent ratio is sufficient. It was possible to produce deparaffinized raffinate with the ratio of 1.25, a viscosity index exceeding 100, and that of 107 with a ratio of 1.5. Higher solvent ratios than the latter do not result in further improvement of quality.

Concerning the effect of water in the extraction process, it can be established that it increases the yield by entrapping the oil component and still has good oilness. Using 2% of water the yield was increased by about 3%, and after deparaffinization the viscosity index was 105. With 5% of water quantity the yield was increased by almost 9% and even so the viscosity index remained above 100. It must be noted, however, that instead of mixing water, the use of solvent containing the same quantity of water, results — especially as related to quality — in substantially lower levels.

The method employed for feeding the water is also significant, because with higher yields and good quality the recovery of solvent with aqueous exraction is not affected by the added water content; the remaining water content of about 1%, after dewatering of the solvent, does not deteriorate the quality of the raffinates. So with the use of NMP the process can definitely be made power saving.

Drawing a comparison between the results obtained with the two solvents, the advantages of furfural raffination, considering the quality, are identifiable, especially, because after deparaffinization, the viscosity indices of the raffinates decrease to a lesser degree.

Advantages of NMP imply smaller solvent ratio, simplicity of the accomplishment of desolventization, higher flexibility and lower power demand of the whole process.

To summarize: it can be established that with the use of both solvents, raffinates having a viscosity index of about 110 can be produced from hydrocracked heavy cut with adequate quality, which could form a suitable base oil — with regard to the extension of the product variety of motor oils.

According to Table 1, two types of materials were used for raffination testing of the *hydrocracked middle* cuts and differences appeared between

them, because the lighter sample containing a smaller quantity of sulphur was hydrocracked after the mixing of the gas oil only.

With these base materials, the aim was Type SN80 base oil, that is to say the production of a deparaffinized raffinate having an about 110 viscosity index and freezing point of about −15 °C. In this case, experiments with the hydrocracked light cut were carried out with furfural only, because in the first place we were interested in the feasibility of possible complete desolventization of lighter base materials after raffination, with little losses.

Presumably, similarly to the previous results, an adequate degree of raffination could be obtained with NMP and in the case of lighter base materials the desolventization with aqueous extraction would appear not just as a possibility, but because of the higher boiling point of NMP, as a necessity.

The results of our experiments of raffination with hydrocracked middle cut are summarized in *Table 3*, and optimum parameters and optimum oil-furfural ratio were employed. The results obtained were also given — in this case — as an average of several parallel measurements.

Table 3

Raffination and deparaffinization results of hydrocracked middle fraction

Solvent	Base material	Oil/ /solvent volume ratio	Column temperat. °C Bottom	Column temperat. °C Top	Raffinate Yield w%	Raffinate VK_{40} mm²/s	Raffinate VK_{100} mm²/s	Raffinate VI_E	Deparaffinized raffinate Yield s%	Deparaffinized raffinate VK_{40} mm²/s	Deparaffinized raffinate VK_{100} mm²/s	Deparaffinized raffinate VI_E	Deparaffinized raffinate Freezing point °C	Deparaffinized raffinate Flash point °C
Furfural	Hydrocr. middle A	1:3.5	70	110	51.92	14.73	3.54	122	80.51	16.50	3.68	108	−14	186
	HK middle B	1:3.5	70	110	49.24	14.71	3.57	126	79.19	17.28	3.79	109	−14	201

It is evident that with furfural of 1:3.5 ratio it is possible to produce deparaffinized raffinates from hydrocracked middle cuts, which meet quality requirements. From "HK middle A" cut 2% higher yields can be obtained. According to the examination of the group composition, it was possible to reduce the starting aromatic content of 28% in the product to 6—7%.

The aim of studying the processing of *hydrocracked light oil* was to find out if there was any possibility of obtaining a product by furfural raffination, having an aromatic content of 11—13%, and freezing point below −30 °C.

The conditions of experiments and the obtained results are compiled in *Table 4*. The data obtained, as average results of several measurements show, in this case too, that yields of raffination increase with the reduction of solvent ratio — corresponding to expectation — but the aromatic content of the raffinates also increases.

It is emphasized that using even 1:1.5 solvent ratio it is possible to produce deparaffinized raffinate complying with requirements and at the same time total yields of the raffination and deparaffinization amount to 40%. This means that the products obtained can be taken into consideration as a prospective base oil for the production of transformer oil.

Table 4

Raffination and deparaffinization results of hydrocracked light fractions

Solvent	Oil/solv. volume rate	Column temperature °C		Yield of raffinate %	Deparaffinized raffinate			
		Bottom	Top		Yield w%	VK_{20} m^2/s	Freezing point °C	Aromatic content w%
furfural	1:1.5	70	110	55.20	80.62	17.9	−40	11.3
	1:2.0	70	110	49.36	78.76	17.2	−42	10.9

Summarizing the investigation, it can be stated that the objective was attained to produce a prospective oil with the required quality in the case of all hydrocracked cuts.

Though NMP was used with heavy cut only, it can definitely be stated that it is also possible to produce the above base oil products with this solvent, and with a method requiring considerably less energy.

It seems that both of the solvents is suitable for retention of the product ranges of base oils with refinement procedure of hydrocracked cuts, that is to say with long established procedure. In a particular case it will be possible to decide in favour of one of the used solvents employing optimizating calculations and their comparison.

REFERENCE

1. GÁRDOS, GY., KOVÁCS, M., KUN-SZABÓ, T., MIKÓ, F. and DÉNES, F.: Hung. J. Ind. Chem. *1982*, 10, 257—262.

РЕЗЮМЕ

Проведены эксперименты рафинирования продуктов гидро-крекинга в присутствии фурфурола и растворителей. Установлено, что растворители пригодны для рафинирования дестиллятов, так как они обладают хорошими свойствами а рафинады пригодны для производства основных масел большой вязкости. Преимуществом применения растворителей состоит в экономии части растворителей, таким образом в меньшем количестве попадают в готовый продукт и меньше надо возвращать из рафинированных и экстрактных фаз.

HUNGARIAN JOURNAL
OF INDUSTRIAL CHEMISTRY
VESZPRÉM
Vol. 11. pp. 307–311 (1983)

SYNTHESIS OF SOME BIOLOGICALLY ACTIVE PRODUCTS FROM EGYPTIAN PETROLEUM DISTILLATES

T. M. Kassem, O. M. O. Habib*, S. M. El-Ashry and E. I. Eissa

(Petrochemicals Department, Egyptian Petroleum Institute*, Chemistry Department, Faculty of Science, Mansoura University, Faculty of Agriculture, Mansoura University, Egypt)

Received: March 21, 1983.

Some compounds with high bactericidal and moderate fungicidal activities were obtained by condensing three sulphonyl chloride mixtures (A_2, B_2 and C_2, prepared by sulphochlorinating three fractions from the Egyptian "Morgan" distillate) with aniline, 1-naphthylamine and some of their 4-substituted derivatives. A conclusion relating the structures of the prepared sulphonanilides and their toxicities is discussed.

In attempts to study the possiblity of manufacturing some biologically active products from petroleum distillates, a series of experiments were carried out in our laboratory, utilizing the Egyptian petroleum fractions.

In a previous paper, the Egyptian "Morgan" gasoline was used as the starting material for this purpose, via sulphochlorinating its aromatic portions and converting them into some aromatic sulphonate esters [1].

The present investigation concerns with the synthesis of some sulphonanilide mixtures with expected biocidal activity. This was followed by condensing the previously prepared sulphonyl chloride mixtures[1] with aniline, 1-naphthylamine substituted in the 4-position with a methyl, bromo, chloro, or a nitro group, respectively. The effect of the structure of the prepared compounds on their toxicity against some harmful bacteria and fungi was also studied.

Experimental

Conversion of the "Morgan" Gasoline Distillate into Three Sulphonyl Chloride Mixtures.

The gasoline distillate (b. r. 50–170 °C) was fractionally distilled into three cuts with boiling ranges 70–90 °C, 100–120 °C and 130–150 °C, respectively. Each cut was sulphonated with concentrated sulphuric acid and neutralized with

sodium carbonate solution. The resulting sodium sulphonates were treated with phosphorous pentachloride to give the corresponding sulphonyl chloride mixtures $A_2^{\frown}$, B_2 and $C_2^{\frown}$.

The apparatus, procedure and the specifications of these sulphonyl chloride mixtures were described in detail elsewhere [1].

Reactions of Aniline, 1-Naphthylamine and some of their 4-Substituted Derivatives with the Prepared Sulphonyl Chloride Mixtures.

Equimolar quantities from each of the sulphonyl chloride mixtures and aniline, 1-naphthylamine or their 4-substituted derivatives (prepared according to published methods [2–5]) were treated with sodium hydroxide solution. The procedure described previously for the preparation of the sulphonate esters [1] was followed, but with only one difference, that is, the unreacted amines were removed by washing with dilute hydrochloric acid.

The structure of the sulphonanilides obtained was deduced from measuring their average molecular weights [6], and from their infra-red spectra which showed a stretching frequency at 1,320 cm^{-1} characterisitic for the $-SO_2$-NH-group.

Determination of the Antibacterial and Antifungal Activities of the Obtained Products.

The biocidal activities of these sulphonanilides were screened against eight harmful bacteria and two fungal species following a standard procedure [7]. The minimum inhibition concentrations, γ/ml, of these compounds were determined. The results are given in Tables (1–3).

Discussion of the Results

The present paper is an extension to the previously mentioned study dealing with the preparation of some biocidally active products from local "Morgan" gasoline distillate. The three sulphonyl chloride mixtures (A_2, B_2 and C_2) prepared in part one of that paper [1] were reacted with aniline, 1-naphthylamine and some of their 4-substituted derivatives.

The formed sulphonanilides were screened against some harmful bacteria and fungi. The relationships between the structures of these compounds and their toxicity were studied from the following points of view:

1. The type of prepared sulphonyl chloride mixtures.
2. The type of aromatic ring bearing the substituents, either phenyl or naphthyl.
3. The type of substituents present in the aniline or 1-naphthylamine.
4. The type of tested bacteria and fungi.

Effect of the Type of Prepared Sulphonyl Chloride Mixtures

It is abvious from *Tables 1–3* that the products obtained from the sulphonyl chloride mixtures B_2 showed the highest ratios of the active products (8 products), followed by those derived from the sulphonyl chloride mixtures A_2

(7 products) and the least active compounds were those prepared from the sulphonyl chloride mixtures C_2(6 products).

Effect of the Type of Aromatic Ring Bearing the Substituents

From the data obtained, it was found that the products derived from the substituted anilines were highly active products (11 compounds) than those obtained from the substituted-1-naphthylamines (10 products).

Effect of the Type of Substituents Present in Aniline or 1-naphthylamine:

It was noticed that the degree of toxicity of the compounds prepared from substituted anilines varies with the type of substituents in the following order:

$$-NO_2 > -Cl > -CH_3 > -Br.$$

On the other hand, the biocidal activities of the products derived from the substituted-1-naphthylamine decrease in the sequence:

$$-NO_2 > -Cl > -Br > -CH_3.$$

Effect of the type of tested bacteria and fungi:

It is also clear from Tables 1–3 that both the Bacillus subtilis and Escherichia

Table 1

Antibacterial and antifungal activities of the products obtained by the condensation of the sulphonyl chlorides mixture (A_2) with aniline, naphthylamine, and their 4-substituted derivatives

Product number	Anilines or 1-naphthyl-amines	Average mol. wt. of the obtained sulphonamilides	Bacteria								Fungi	
			Aero. aerogenes	K. aerogenes	Bacillus subtilis	Bacillus cereus	Micrococcus sp.	Escherichia coli	Staphylococcus aureus	Salmonella sp.	Candida albicans	Aspergillus niger
I_1	Aniline	245	*	*	750	800	1000	900	750	700	*	*
I_2	P-Toluidine	260	350	600	*100*	500	650	*100*	350	500	*	300
I_3	P-Chloroaniline	276	300	*100*	200	400	500	*100*	250	150	400	350
I_4	P-Bromoaniline	324	*	700	*100*	800	600	750	650	550	*	*
I_5	P-Nitroaniline	285	250	*50*	250	*100*	300	200	*100*	950	300	250
I_6	1-Naphthylamine	296	*	850	900	*	1000	*	850	*	*	700
I_7	4-Methyl-1-naphthylamine	304	*	800	*	750	800	650	550	*	*	600
I_8	4-Chloro-1-naphthylamine	328	700	250	*100*	700	550	450	400	350	500	600
I_9	4-Bromo-1-naphthylamine	370	*	600	450	*100*	600	400	550	400	*	*
I_{10}	4-Nitro-1-naphthylamine	336	350	200	*100*	400	450	*100*	250	350	450	500

* Means no activity at concentration up to 3000 γ/ml solution.

Table 2

Antibacterial and antifungal activities of the products obtained by the condensation of the sulphonyl chlorides mixture (B_2) with aniline, naphthylamine, and their 4-substituted derivatives

Product number	Anilines or 1-naphthyl-amines	Average mol. wt. of the obtained sulphonanilides	Bacteria								Fungi	
			Aero. aerogenes	K. aerogenes	Bacillus subtilis	Bacillus cereus	Micrococcus sp.	Escherichia coli	Staphylococcus aureus	Salmonella sp.	Candida albicans	Aspergillus niger
II_1	Aniline	248	750	*	700	650	500	450	500	650	*	*
II_2	p-Toluidine	262	300	500	*100*	450	*100*	600	300	*100*	450	300
II_3	P-Chloroaniline	280	250	150	*100*	350	400	*100*	200	*100*	350	400
II_4	P-Bromoaniline	328	*	650	*100*	700	*	*100*	500	600	500	450
II_5	P-Nitroaniline	290	150	*50*	200	*50*	350	*100*	250	*100*	250	400
II_6	1-Naphthylamine	298	*	450	*	550	450	800	700	650	*	*
II_7	4-Methyl-1-naphthylamine	312	*	400	650	450	500	*100*	500	450	600	*
II_8	4-Chloro-1-naphthylamine	328	650	*100*	700	650	*100*	500	350	400	300	450
II_9	4-Bromo-1-naphthylamine	372	550	350	500	250	*100*	350	450	450	500	550
II_{10}	4-Nitro-1-naphthylamine	340	250	*100*	350	*100*	400	200	300	*100*	350	400

* Means no biocidal activity at concentrations up to 3000 γ/ml solution.

coli were the most affected organisms (8 toxic products for each organism) followed by K. aerogenes and Micrococcus sp. (6 compounds for each organism), Bacillus cereus (5 products) and finally Staphylococcus aureus and Salmonella sp (4 compounds for each organism).

General speaking these sulphonanilides showed high toxicity towards bacteria, but were of moderate toxicity to fungi.

From these results it could be concluded that Egyptian "Morgan" gasoline could be used for the production of some biocidally active products.

REFERENCES

1. KASSEM, T. M., HABIB, O. M. O., HUSSEIN, M. H. and EISSA, A. I.: Hung. J. Ind. Chem. *1983*, 11. 157.
2. DZIEWONSKI, K. and MARUSINKA, M.: Bull. Intern. Acad. Polon. Sci., Classe Sci. Math. Nat. *1938*, 316–23, (C. A., *33*, 1712).
3. JACOBS, T. L., WINSTEIN, S., LINDEN, G. B. and SAYMOUR, D.: J. Org. Chem. *1946*, 11, 223.
4. MORGAN, G. T., MICKLETHWAIT, F. M. and BEN WINFIELD, H.: J. Chem. Soc. *1904*, 85, 750.
5. PRICE, C. C. and VOOG, S. T.: Org. Synthesis, *1948*, 28, 80.
6. VOGEL, A. I.: "Practical Organic Chemistry", Third enlarged edition, Longman, *1974*, p. 1037.
7. ABOU-ZEID, A. A. and SHEHATA, Y. M.: Indian J. Pharmacy, *1969*, 31 (3), 72.

Table 3

Antibacterial and antifungal activities of the products obtained by the condensation of the sulphonyl chlorides mixture (C_2) with aniline, naphthylamine, and their 4-substituted derivatives

Product number	Anilines or 1-naphthyl-amines	Average mol. wt. of the obtained sulphonanilides	Bacteria								Fungi	
			Aero. aerogenes	K. aerogenes	Bacillus subtilis	Bacillus cereus	Micrococcus sp.	Escherichia coli	Staphylococcus aureus	Salmonella sp.	Candida albicans	Aspergillus niger
III_1	Aniline	252	900	*	800	*	250	*	850	750	*	500
III_2	P-Toluidine	265	*	650	*	750	*100*	250	450	600	*	*
III_3	P-Chloroaniline	290	350	250	*100*	450	600	350	*100*	250	450	500
III_4	P-Bromoaniline	330	*	*	900	1000	850	750	800	*	*	950
III_5	P-Nitroaniline	296	300	*100*	350	250	400	450	*100*	350	400	350
III_6	1-Naphthylamine	302	*	*	950	1000	*	900	2000	1500	*	*
III_7	4-Methyl-1-naphthylamine	320	1000	*	900	*	*	850	700	650	*	*
III_8	4-Chloro-1-naphthylamine	340	*	*	750	*	*100*	600	*100*	650	550	*
III_9	4-Bromo-1-naphthylamine	385	*	700	650	750	*100*	*	850	600	*	*
III_{10}	4-Nitro-1-naphthylamine	350	500	350	*	*100*	450	*100*	350	450	*	550

* Means no biocidal activity at concentrations up to 3000 γ/ml solution.

РЕЗЮМЕ

Путём конденсации сульфомилхлоридов (производные A_2, B_2 C_2 полученных из сульфохлорирования фракций дестилляции эгиптской фирмы „МОРГАН") произведены сильные бактериеубивающие, но слабые гриооуоивающие материалы. В конденсациоонной реакции применены анилин, 1-нафталинамин и замещающие их производные. В сообщении обсуждены зависимости между структурой полученных соединений и их бактериеуоивающими и грибоубивающими свойствами.

CONTENTS

STUDNICKI, M.: Thermodynamical Properties of Nonaqueous Solutions of Hydrogen Chloride 209

STUDNICKI, M.: Thermodynamical Properties of Nonaqueous Solutions of Aromatic Amines 223

IBRAGIMOV, CH. SH., NEMET, E., MAMEDOV, A. A. and SHAKHTAKHTINSKII, T. N.: Benzene Vapour Adsorption on NUXIT-BO Active Carbon Bed (in the Russian) 231

MISS E. FRANK and GY. DEÁK: Comparison of Estimation Methods of Vaporization Heat 241

ERMAKOVA, A., KUZMIN, V. A. and UMBETOV, A. S.: Local Mass Transfer from Particle to Liquid IV. Three-Phase Systems: Fixed and Fluidized Bed, Mass Transfer, General Equation (in the Russian) 247

KIRILLOV, V. A., KUZMIN, V. A., PJYANOV, V. I. and KHANAEV, V. M.: Analysis of Transfer Processes in a Fixed Granular Bed at a Co-Current Upflow of Gas and Liquid (in the Russian) 263

GRUHN, G., NEUMANN, W. and SEIDEL, R.: Reliability Analysis of Complex Chemical Engineering Systems 275

MRS. SIMON, K.: Calculation of Glass Density from its Composition 283

MRS. SIMON, K.: Analytical Investigation of the Process for Manufacturing 1,2,4--1H-Triazole 291

GÁRDOS, GY., KOVÁCS, M., KUN-SZABÓ, F., MIKÓ, F. and DÉNES, F.: Investigation of Energy Conserving Lubricating Oil Producing Processes. II. 301

KASSEM, T. M., HABIB, O. M. O., EL-ASHRY, S. M. and EISSA, E. I.: Synthesis of Some Biologically Active Products from Egyptian Petroleum Distillates 307

Egyetemi Nyomda — 83.1531 Budapest, 1983. Felelős vezető: Sümeghi Zoltán igazgató

Ára: 250 Ft

THE FOLLOWING ARE PLEASED TO ACCEPT SUBSCRIPTIONS TO THIS JOURNAL:

AUSTRALIA

C.B.D. Library and Subscription Service
Box 4886 G.P.O.
Sydney 2000

Cosmos Book and Record Shop
145 Acland Street
St. Kilda 3182

Globe and Co.
694—696 George Street
Sydney 2000

AUSTRIA

Globus (VAZ)
Höchstädtplatz 3
A—1200 Wien XX

BELGIUM

"Du Monde Entier" S. A.
Rue du Midi 162
B—1000 Bruxelles

Office International de Librairie
Avenue Marnix 30
B—1050 Bruxelles

CANADA

Pannonia Books
P.O. Box 1017
Postal Station "B"
Toronto, Ontario M5T 2T8

DENMARK

Munksgaard's Boghandel
Norregade 6
DK—1165 Copenhagen K

FINLAND

Akateeminen Kirjakauppa
Keskuskatu 2, P.O.B. 128
SF—00 100 Helsinki 10

FRANCE

Office International de Documentation et Librairie
48 Rue Gay Lussac
75 Paris 5

GERMAN FEDERAL REPUBLIC

Kubon und Sagner
Pf 68
D—8 München 34
BRD

GREAT BRITAIN

Bailey Bros and Swinfen Ltd.
Warner House, Folkestone
Kent CT 19 6PH England

HOLLAND

Martinus Nijhoff
Periodicals Department
P.O. Box 269
The Hague

Swets and Zeitlinger
Keizersgracht 487
Amsterdam C

ITALY

Licosa
P.O.B. 552, Via Lamarmora 45
50121 Firenze

JAPAN

Igaku Shoin Ltd.
Foreign Department
Tokyo International P.O. Box 5063
Tokyo

Maruzen Co. Ltd.
P.O. Box 5050
Tokyo International 100—31

Nauka Ltd.
Yasutomi Bldg. 5F 2—12 Kanda
Jinbocho, Chiyoda-ku
Tokyo 101

NORWAY

Tanum—Cammermayer
Karl Johangt. 41—43
Oslo 1

SWEDEN

Almqvist and Wiksell Förlag A. B.
Box 2120
S—103 13 Stockholm 2

Wennegren—Williams AB
Subscription Department Fack
S—104 Stockholm 30

SWITZERLAND

Karger Libri A. G.
Petersgraben 31
CH—4011 Basel

USA

Ebsco Subs. Services
1 st Ave North at 13th street
Birmingham, Ala. 35201

HUNGARIAN

Journal of

INDUSTRIAL CHEMISTRY

Edited by

the Hungarian Oil & Gas Research Institute (MÁFKI),
the Research Institute for Heavy Chemical Industries (NEVIKI),
the Research Institute for Technical Chemistry of the
Hungarian Academy of Sciences (MÜKKI),
the Veszprém University of Chemical Engineering (VVE).
Veszprém (Hungary)

Volume 11. **1983.** **Number 4.**

HU ISSN: 0133—0276
CODEN: HJICAI

Editorial Board:

R. Csikós and Gy. Mózes
Hungarian Oil & Gas Research Institute
(MÁFKI Veszprém)

A. Szántó and M. Nádasy
Research Institute for Heavy Chemical Industries
(NEVIKI Veszprém)

T. Blickle and O. Borlai
Research Institute for Technical Chemistry
of the Hungarian Academy of Sciences
(MÜKKI Veszprém)

P. Árva and G. Deák
Veszprém University of Chemical Engineering
(VVE Veszprém)

Editor-in Chief:
E. Bodor

Assistant Editor:
J. De Jonge

Veszprém University of Chemical Engineering
(VVE Veszprém)

The "Hungarian Journal of Industrial Chemistry" is a joint publication of the Veszprém scientific institutions of the chemical industry that deals with the results of applied and fundamental research in the field of chemical processes, unit operations and chemical engineering. The papers are published in four numbers at irregular intervals in one annual volume, in the English, Russian, French and German languages

Editorial Office:
Veszprémi Vegyipari Egyetem
"Hungarian Journal of Industrial Chemistry"
H—8201 Veszprém, P.O. Box: 158.
Hungary

Orders may be placed with
KULTURA
Foreign Trading Co. for Books and Newspapers
Budapest 62. POB 149.
or with its representatives abroad, listed on the verso of the cover

FELELŐS SZERKESZTŐ: DR. BODOR ENDRE

KIADJA A LAPKIADÓ VÁLLALAT, 1073 Bp. VII., LENIN KRT. 9—11.
TELEFON: 221-285. LEVÉLCÍM: 1906 BP. PF. 223.
FELELŐS KIADÓ: SIKLÓSI NORBERT VEZÉRIGAZGATÓ

HUNGARIAN JOURNAL
OF INDUSTRIAL CHEMISTRY
VESZPRÉM
Vol. 11. pp. 313–320 (1983)

INVESTIGATION OF THE HYDRATION OF MALEIC ACID TO MALIC ACID

Z. KÁSA, GY. DEÁK

(Department of Hydrocarbon and Coal Processing,
Veszprém University of Chemical Engineering, Veszprém)

Received: September 10, 1982.

Kinetic and equlibrium relationships were studied for the chemical synthesis of malic acid at 160, 180 and 200 °C. A kinetic model was suggested for the investigated system and the values of the reaction rate constants were determined. It was found that malic acid is formed from maleic acid in two ways: directly from maleic acid and by the maleic acid→fumaric acid→malic acid way. Lower temperatures are favourable for malic acid production.

Introduction

Generally citric acid is used for flavouring and acidifying foods. This acid is produced by fermentation. The need for an inexpensive synthetic acidifying agent emerged in the first half of this century. DL-malic acid proved to be such a product. The physical and chemical properties of malic acid are very favourable for its application in the food industry, with the additional advantage that it can be produced from maleic anhydride, an inexpensive petrochemical product.

Many patents dealt with the catalytic hydration of maleic acid in the presence of sulphuric acid or various metal salts [1–5]. Though the yield of malic acid is higher in these catalytic reactions, malic acid of food specifications is produced by noncatalytic processes, where the purification requirements are not so complex [6–24].

There are different views *concerning* the reaction mechanism. According to several authors, hydration is brought about in two steps. In the first one, maleic acid is isomerized to fumaric acid, and then fumaric acid is hydrated to malic acid [12]. Other researchers believe that maleic acid is also hydrated. Fumaric acid is formed concurrently with the hydration of maleic acid and it is also hydrated to malic acid [14, 18].

Kinetic data are not published on malic acid formation starting with maleic acid. In patents only the fact is given that the reaction is an equilibrium reaction. However, the kinetics of the hydration of fumaric acid was studied in

basic, acidic and neutral media [25–27]. It was found that the hydration of fumaric acid is first order with respect to fumaric and malic acid, and the reaction is reversible.

Considering that there is a lack of data concerning these reactions, the kinetic and equilibrium characteristics of the formation of malic acid from maleic acid were studied.

Materials

Commercial grade maleic anhydride and fumaric acid (Reanal, Hungary, analytical grade) and malic acid (Fluka, Switzerland, pure grade) were used without further purification.

Ionexchanged water (~ 10 μS) was freshly boiled before use to remove carbon dioxide.

Apparatus

Experiments were carried out in 25 cm^3 titanium autoclaves constructed of technical grade titanium (99.99%), closed with a teflon packing and screw-top. The autoclave was heated with an aluminium blockheater, which was mounted on a shaking machine. The temperature of the blockheater was regulated with a transformer and measured with a mercury thermometer. The temperature was kept constant within ± 0.5 °C.

Procedure

100 mmole dicarboxylic acid (anhydride in the case of maleic acid) was weighed in the autoclave in a 40% aqueous solution. The autoclave was closed and placed in the heater that was kept at the desired temperature. After the required time had elapsed, the autoclave was removed from the heater and quickly cooled in running water. Fumaric acid that was crystallised during cooling was filtered through a G-4 porous glass filter and the reactor was rinsed with 3×5 ml of ionexchanged water. After drying at 105 °C for 24 hours, the mass of crystallised fumaric acid was determined.

The composition of the solution was determined by gas chromatography after making ethyl esters of the carboxylic acids. The composition of the product solution was calculated from the results of this two determinations.

Results

The formation of malic acid from maleic acid was studied at 160, 180 and 200 °C. Reactions were carried out until the equilibrium at the given temperature was reached.

Results at 180 °C are given in *Fig. 1.* It is clearly shown that the system reaches an equilibrium state, where the composition no longer changes. The results of experiments starting with malic and fumaric acids are given in *Figures 2* and *3.* It can be seen that the same equilibrium was reached in both cases.

With starting material of maleic acid, the composition of the reaction mixtures was also determined at 160 and 200 °C. The results were similar to those obtained at 180 °C.

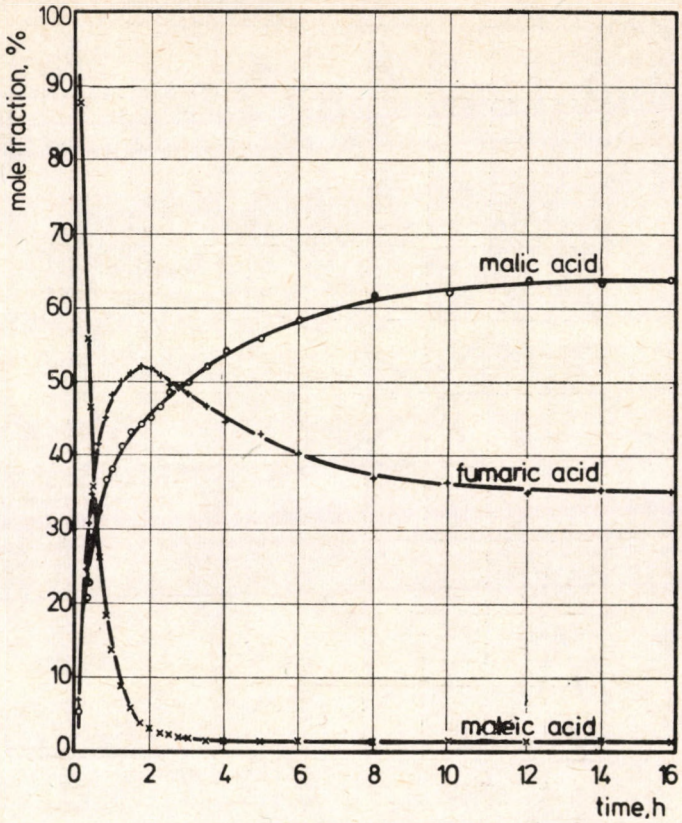

Fig. 1

Results of experiments starting with maleic acid at 180 °C

On the basis of the experimental results the following reaction scheme is suggested:

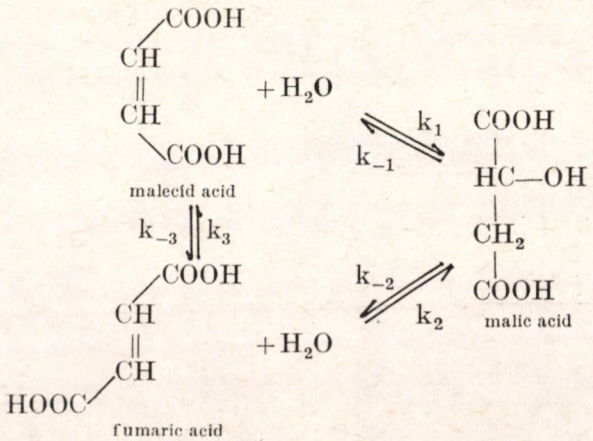

where $k_1, \ldots, k_{-3}$ are the rate constants of the individual reactions.

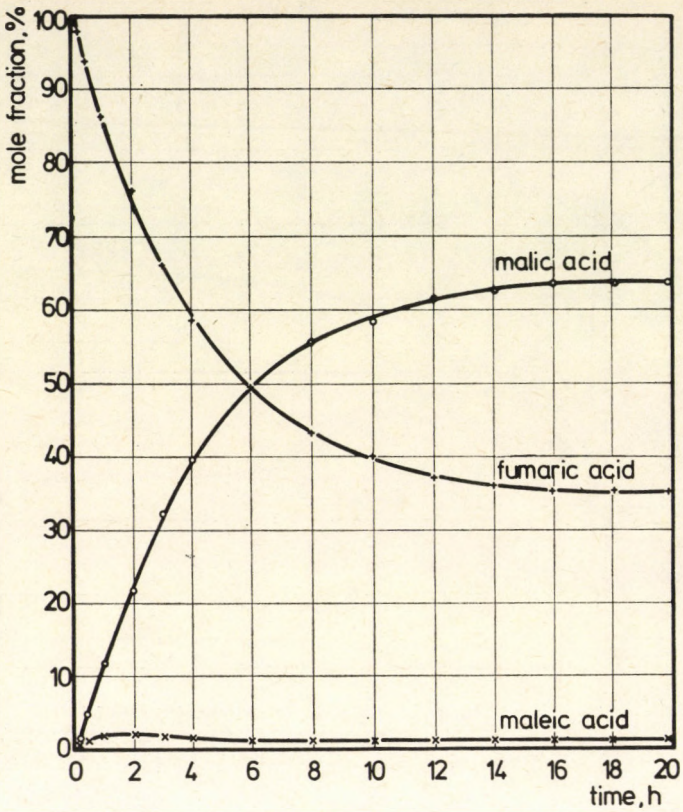

Fig. 2
Results of experiments starting with fumaric acid at 180 °C

The following kinetic model belongs to the above reactions scheme:

$$\frac{d(\text{Maleic})}{dt} = k_3(\text{Fumaric}) - k_{-3}(\text{Maleic}) + k_{-1}(\text{Malic}) - k_1(\text{Maleic})(H_2O)$$

$$\frac{d(\text{Fumaric})}{dt} = k_{-3}(\text{Maleic}) - k_3(\text{Fumaric}) + k_2(\text{Malic}) - k_{-2}(\text{Fumaric})(H_2O)$$

$$\frac{d(\text{Malic})}{dt} = k_1(\text{Maleic})(H_2O) - k_{-1}(\text{Malic}) + k_{-2}(\text{Fumaric})(H_2O) - k_2(\text{Malic})$$

$$\frac{d(H_2O)}{dt} = -\frac{d(\text{Malic})}{dt}$$

where the terms in brackets are the mole fractions of the given component.

The rate constants were determined with the symplex method of NELDER–MEAD [28] and are presented in *Table 1* and *Fig. 4*. The equilibrium constants at three temperatures were also calculated and are given in *Table 2* and *Fig. 5*.

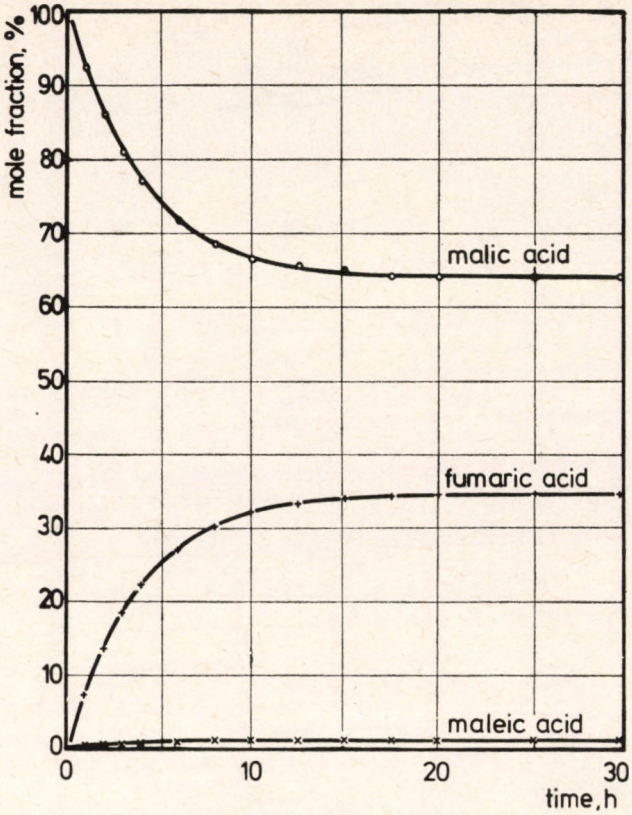

Fig. 3
Results of experiments starting with malic acid at 180 °C

Conclusions

The experiments clearly showed that the formation of malic acid from maleic and fumaric acids is an equilibrium reaction. *Figures 1 to 3* confirm that after a sufficient period of time, the same equilibrium mixture is formed at a given temperature independently of the starting material.

In previous experiments on the hydration of fumaric acid it was found that maleic acid was not formed, i.e. only fumaric and malic acids were present in the equilibrium mixture. It was found that all three acids are in equilibrium in all cases.

Patents on this reaction explained the mechanism differently. Our results showed that fumaric and malic acids are formed concurrently. The formation of fumaric acid is quicker than that of malic acid, but the rate costants are of the same order of magnitude.

The hydration of fumaric acid formed by isomerization from maleic acid is a slower process than the hydration of maleic acid. The formation of malic acid takes place in two ways in the investigated system: by the direct hydration of maleic acid and by the maleic acid → fumaric acid → malic acid way.

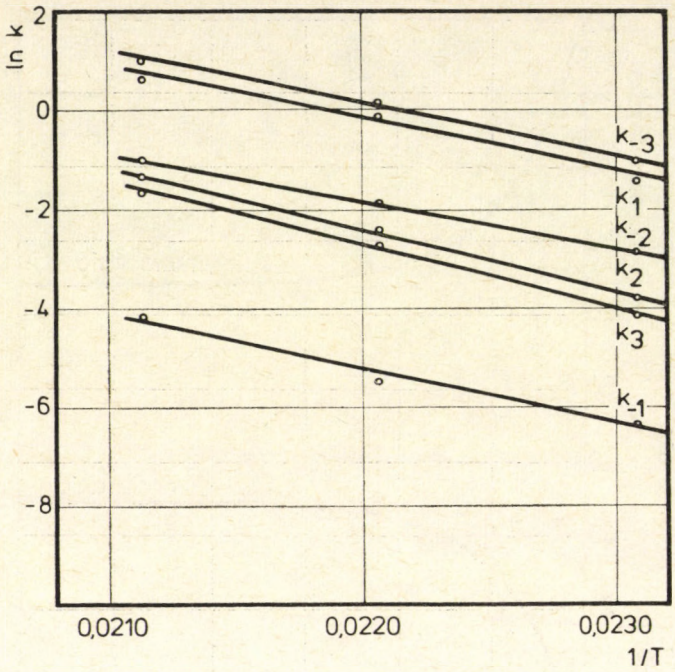

Fig. 4
Temperature-dependence of rate constants

Table 1.

Values of the rate constants

	Temperature, °C		
	160	180	200
k_1	0.2437	0.8448	1.900
k_{-1}	0.00169	0.00415	0.0155
k_2	0.0223	0.0878	0.275
k_{-2}	0.0569	0.155	0 365
k_3	0.0153	0.0650	0.195
k_{-3}	0.354	1.168	2.700

Table 2.

Values of the equilibrium constants

	Temperature, °C		
	160	180	200
Malic acid/Fumaric acid	2.30	1.82	1.39
Malic acid/Maleic acid	69.0	49.0	28.5
Fumaric acid/Maleic acid	30.0	26.9	20.5

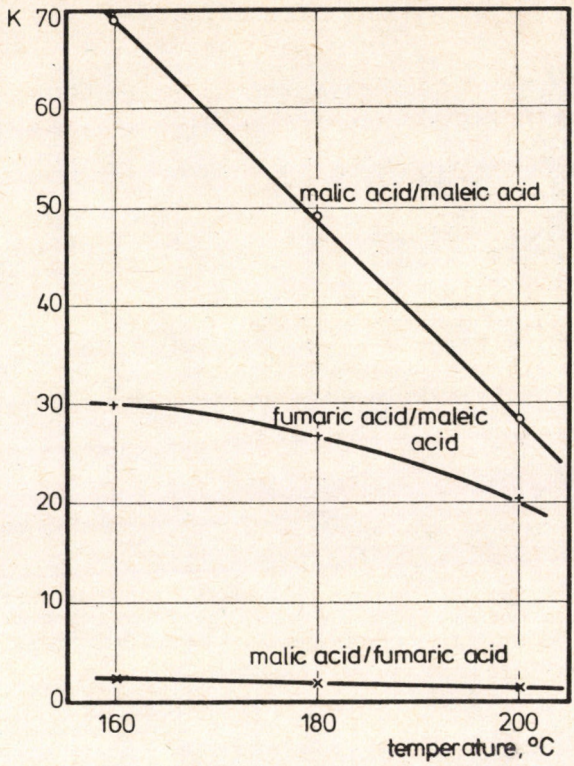

Fig. 5
Temperature-dependence of equilibrium constants

At the beginning of the reaction, when the concentration of the maleic acid is higher than its equilibrium concentration, the direct hydration is the dominant way. However, as the concentration of maleic acid decreases rapidly to its equilibrium value, the hydration rate of fumaric acid and equilibrium relations is increasingly important.

The values of equilibrium constants show that lower temperatures are more favourable to the formation of malic acid.

REFERENCES

1. U.S.S.R. PAT. 208,706
2. U.S.S.R. PAT. 213,012
3. U.S.S.R. PAT. 218,874
4. Bzsasso, N. A.: Izvest. Vyssh. Utsheb, Zaved. *1967*, 5, 207–8.
5. Bzsasso, N. A.: Zh. Prikl. Khim. *1969*, 42(7), 610–4.
6. U.S. PAT. 3,371,112
7. FR. PAT. 1,464,299
8. U.S. PAT. 3,379,756
9. BELG. PAT. 670,932
10. U.S. PAT. 3,379,757
11. FR. PAT. 1,461,181

12. U.S. PAT. 3,391,187
13. FR. PAT. 1,466,681
14. U.S. PAT 3,523,024
15. NETHERLAND PAT. 67,10,132
16. U.S. PAT. 3,983,170
17. U.S. PAT. 4,035,419
18. JAPAN PAT. 4360
KIRK–OTHMER: Encyclopedy of Chemical Technology Vol. 12. "Malic acid", p. 845.
19. JAPAN PAT. 77,128,323 (C.A. 88, 89123e)
20. FR. PAT. 1,503,271
21. NETHERLAND PAT. 66,17,262
22. BRIT. PAT. 1,177,680
23. GER. OFFEN 1,768,926
24. GER. OFFEN 2,237,685
25. ROZELLE, L. T. and ALBERTY, R. A.: J. Phys. Chem. *1957*, 61, 1637–40.
26. BENDER, M. L. and CONNORS, K. A.: J.A.C.S. *1962*, 84, 1980–6.
27. ERICKSON, L. E. and ALBERTY, R. A.: J. Phys. Chem. *1959*, 63, 705–9.
28. BOX, M. J., DAVIES, D. et al.: Non-linear Optimization Techniques, ICI Monograph, No. 5.

РЕЗЮМЕ

Авторы изучали равновесные и кинетические условия реакции лежащей в основе химического синтеза яблочной кислоты при темперетурах 160, 180 и 200 °C. Составили кинетическую модель изученной системы и определили значения коэффициентов скорости. Авторами установлено, что яблочная кислота синтезируется из малеиновой кислоты двумя способами: непосредственно из малеиновой кислоты и через следующую цепь, малеиновая кислота → фумарная кислота → яблочная кислота. Установили также, что более низкая температура способствует, синтезу яблочной кислоты.

HUNGARIAN JOURNAL
OF INDUSTRIAL CHEMISTRY
VESZPRÉM
Vol. 11. pp. 321–328 (1983)

PRODUCTION OF MANGANESE DIOXIDE BY ANODIC OXIDATION

J. Kövecses, F. Óvári* and P. Káldi*

(Research Institute for Ferrous Metallurgy, Budapest, Hungary
* Department of Chemical Technology, University of Chemical Engineering, Veszprém)

Received: December 12, 1982.

The preparation, by electrolysis, of battery-grade manganese dioxide from nitrate and sulphate solutions of manganese was investigated. Lead plates and titanum plates, thermally coated with manganese dioxide, were used for the cathode and anode, respectively. With nitrate electrolytes, the current efficiency, while with sulphate electrolytes, the specific energy consumptions were lower. The degree of oxidation of the product was higher in the case of nitrate electrolytes. Over the 6–90 g/l Mn^{2+} concentration range, the electrolysis parameters did not change with the Mn^{2+} concentration. Decreasing acidity decreased the current efficiency and increased the active manganese content. Copper, nickel and cobalt contamination in the product was proportional to that of the electrolyte. Iron, titanium and lead could enter the product from the electrodes. The optimum temperature and current density of the electrolysis were 85–97 °C and 0.5–1.5 A/dm^2, respectively. Higher current density decreased the active oxygen content of the product, but the oxygen content could be increased by post-electrolysis digestion in hot nitric acid.

Introduction

Manganese dioxide produced by anodic oxidation of manganese(II) salts is primarily used in dry cells.

From aqueous, sulphuric acid solutions of manganese sulphate, manganese dioxide is electrolytically deposited onto lead, graphite or titanium anodes, at temperatures ranging between 90–94 °C. Occasionally, nitrate electrolytes are also used. Anodically produced manganese dioxide always contains some manganese with a lower degree of oxidation, and also some bonded water. There is some correlation between the composition of the electrolyte, cell potential, anodic current density, electrolyte temperature and the characteristics of the deposited manganese dioxide. The nominal degree of oxidation of anodically formed manganese dioxide is in the 1.85 to 1.90 range [1]. Advantageously, the degree of oxidation is increased by post-electrolysis acid treatment [2]. The current efficiency of manganese dioxide production remains

essentially constant, when the manganese concentration is varied over the 50–100 g/l range in sulphuric acid electrolytes [3]. The MnO_2 concentration of the coating is independent of the sulphuric acid concentration in the 0.1–0.75 mol/l range, but rapidly drops off above 2 mol/l. With increasing sulphuric acid concentration, the adsorbed water content of the product increases [4].

It was found that in electrolytes saturated with lead sulphate (0.038–0.051 $PbSO_4$ g/l), the lead concentration of MnO_2 increased with the current density, and decreased with increasing temperature [5]. Ferric ions decreased the current efficiency of MnO_2 deposition [6]. Apparently Co and Ni had no effect on MnO_2 separation [7].

According to a Canadian patent [8], battery-grade MnO_2 can be deposited from an electrolyte, which contains the following contaminants: copper: 1.5 mg/l, cadmium: 5.0 mg/l, lead: 0,5 mg/l, and traces of cobalt, nickel, arsenic and antimony.

Battery-grade manganese dioxide can be produced electrolytically at elevated temperatures: between 90–94 °C [9]. The formal degree of oxidation of the product decreases, when the current density of anodic oxidation is increased [10]. Muraki [10] demonstrated that the concentration of the contaminants in the product also increased with the anodic current density.

The material of the anode plays an important role in the electrolysis. Titanium, subjected to various finishing procedures, proved to be the best, both technically and economically [11–14].

Based on the above references, a comprehensive experimental programme was initiated to determine the dependency of the major electrolysis parameters and product characteristics on the experimental conditions.

Experimental

Electrolysis experiments were carried out in a double-wall glass electrolysis tank of 1.5 l capacity. The cover and the main vessel both had a plane, ground surface to ensure tight sealing. Copper electrode holders, coated with plastic, were secured by plastic screw-clamps to the top of the tank. Electrodes were attached to the electrode holders by bolts and screws. The distance between the anode and cathode was 3.5 cm. A magnetic mixer was used to mix the electrolyte. A stabilized DC power supply, Type TR 9177 (FOK-GYEM, Budapest, Hungary) was used for the electrolysis. Current, transported through the electrolysis cell, was measured by a multimeter, Type PE 22421/04 (Philips) via the potential drop on a 1.4 ohm wire resistance, connected in series with the electrolysis tank. A thermostat was used to maintain the temperature of the electrolysis cell, except at 97 °C, when steam, introduced into the jacket of the cell, was used. Cell potential was recorded by a strip chart recorder, Type OH 851/1 (Radelkisz, Budapest, Hungary). The manganese sulphate and manganese nitrate solutions obtained by acid digestion (sulphuric acid and nitric acid, respectively) of manganese carbonate ore from Úrkút, Hungary, were used as electrolytes *(Table 1)*.

Electrolyte preparation is not discussed here. A new electrolyte was used in each experiment. Metal concentration in the electrolyte was determined by atomic absorption spectrometry. A Type OP 213 acidometer (Radelkisz,

Table 1.

Composition of the electrolytes

Components mg/l	Sulphate electrolyte	Nitrate electrolyte
Iron	1.4	2.7
Cobalt	8.2	13.0
Nickel	4.5	2.8
Lead	3.4	1.9
Copper	1.1	2.3
Zinc	2.3	2.7
Chromium	0.1	0.1
Potassium	312	312
Sodium	552	586
Titanium	1.1	0.9
Calcium	54	2800
Magnesium	920	503
Silicon dioxide	27	33

Budapest, Hungary), equipped with a glass electrode, was used to determine the acid concentration of the electrolyte. Only in slightly acidic electrolytes could changes in the acid concentration be detected (electrolysis time: 1 hour).

A 0.5 mm thick titanium plate, pretreated by sand blasting, was used as an anode, both as received, and after thermal coating by MnO_2. An expanded titanum plate of 1 mm thickness, coated by a 4 μm thick layer of platinum (Heraus) was also used as an anode. The chemical composition of the 0.5 mm thick titanum plate was as follows: titanum: 99.5%, silicon: 0.1%, iron: 0.4%, cobalt: 10 ppm, copper: 16 ppm, and lead: 28 ppm.

Lead and blasted titanum cathodes were used in the sulphate and nitrate electrolytes, respectively.

Prior to electrolysis, the electrodes were degreased by acetone and weighed. After electrolysis, the anodes were washed with hot water and acetone, dried for 2 hours at 85 °C, and weighed. Iodometric and complexometric titrations were used to determine the manganese dioxide, and the overall manganese content of the coating [15]. The advantage of this (i.e. GATTOW's method) is that both the active oxygen content, and the total manganese content can be determined from the same weighed sample. The actual manganese dioxide content of the coating was used to determine the current efficiency, and the specific energy consumption of the electrolysis.

The concentration of Mn^{2+}, H_2SO_4 and HNO_3, as well as the temperature of the electrolyte were varied in the experiments, along with the material and anode preparation mode, and the anodic current density. Coating recovered from the electrode was ground in an agate mortar, and the current efficiency, specific energy requirement, and x values in MnO_{1+x} were determined. In certain cases, the contaminants and water content of the coating were also determined.

In a separate series of experiments, the effects of aqueous washing and 4 hours digestion in boiling nitric acid, respectively, upon the x values were tested.

Table 2a

Effects of the Mn^{2+} concentration of the electrolyte upon the electrolysis parameters

Parameter	Sulphate electrolyte H_2SO_4 conc.: 50 g/l Mn^{2+} conc. (g/l)			Nitrate electrolyte HNO_3 conc.: 6 g/l Mn^{2+} conc. (g/l)		
	6	40	90	6	40	90
Current efficiency, %	93.3	87.7	89.8	92.7	89.9	86.9
Specific energy consumption, (Wh/g)	1.4	1.5	1.6	1.2	1.1	1.7
Formal degree of oxidation, x in MnO_{1+x}	0.93	0.86	0.90	0.88	0.88	0.90

Results

Mn^{2+} Concentration of the Electrolyte

The relationship between the Mn^{2+} concentration and the characteristics tested is shown in *Table 2a*. It can be concluded that within the limits examined, changes of the Mn^{2+} concentration have practically no influence upon the current efficiency, specific energy requirement and formal degree of oxidation.

Acidity of the Electrolyte

The effects of electrolyte acidity are shown in *Table 2b*. With increasing acidity, the current efficiency drops and product quality improves, i.e. the value of x in MnO_{1+x} increases, especially for the nitrate electrolyte. Increased acidity resulted in increased manganese dioxide and adsorbed water contents.

Table 2b

Effects of the acidity of the electrolyte upon the electrolysis parameters

Parameter	Sulphate electrolyte H_2SO_4 conc. (g/l)			Nitrate electrolyte HNO_3 conc. (g/l)		
	4.9	50	100	6.3	30	60
Current efficiency, (%)	100	87.7	88.4	89.3	78.6	72.2
Specific energy consumption, (Wh/g)	1.3	1.5	1.4	1.1	1.2	1.4
x in MnO_{1+x}	0.85	0.86	0.89	0.88	0.90	0.93
Moisture content, (%)	1.2	0.9	1.3	1.7	1.9	2.0

Contaminants and Additives of the Electrolyte

The concentration of centaminants found in the coating is listed in *Table 3*. Based on the initial iron, titanium and lead content of the 1.5 l sulphate electrolyte, a maximum of 2.1 mg iron, 1.65 mg titanium and 5.1 mg lead can enter

the coating. Assuming complete deposition and a coating mass of 3 g, the respective maximum concentrations are: 0.07% iron, 0.055% titanium and 0.17% lead.

It can be seen in *Fig. 1.* that the contaminant concentration values are—with the exception of a few iron values—within the range permitted for dry cells.

Table 3.

Contaminants of the manganese dioxide coating under varying experimental conditions (electrolyte temperature: 97 °C, blasted titanium anode)

Contaminant and its conc.	Conc. of contaminant in electrolyte mg/l	Sulphate electrolyte						Conc. of contaminant in electrolyte	Nitrate electrolyte					
		H_2SO_4 conc. (g/l)							HNO_3 conc. (g/l)					
		4.9		50		100			6.3		30		60	
		Current density A/dm²		Current density A/dm²		Current density A/dm²			Current density A/dm²		Current density A/dm²		Current density A/dm²	
		1	2	1	2	1	2		1	2	1	2	1	2
Iron, (%)	1.4	0.030	0.020	0.060	0.045	0.020	0.030	2.7	0.115	0.037	0.100	0.023	0.090	0.028
Titanium, (%)	1.1	0.016	0.010	0.032	0.027	0.065	0.013	0.9	0.150	0.060	0.152	0.088	0.092	0.030
Lead, (%)	3.4	0.067	0.070	0.520	0.085	0.022	0.022	1.9	0.050	0.022	0.015	0.015	0.330	0.030
Cobalt, (ppm)	8.2	40	35	10	25	11	10	13.0	10	10	10	10	10	10
Nickel, (ppm)	4.5	50	50	50	50	50	50	2.8	50	50	50	50	50	50
Copper, (ppm)	1.1	15	20	45	40	30	40	2.3	40	45	60	40	50	50

Electrolyte Temperature

The temperature dependency of the various parameters is shown in *Fig. 1*, using the data obtained with platinum coated titanum electrodes. Electrode passivation, and the continuous increase in cell potential hindered the deter-

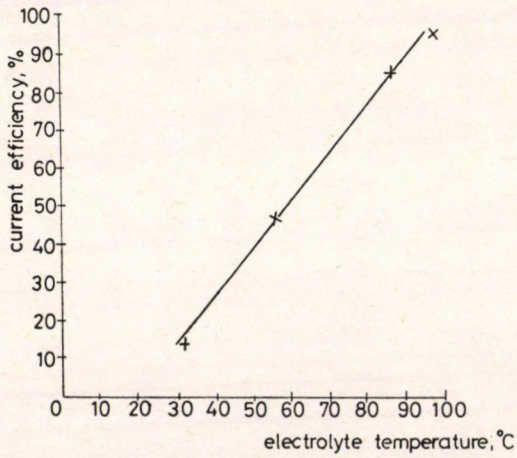

Fig. 1

Current efficiency as a function of the electrolyte temperature (current density: 1.14 A/dm²; H_2SO_4 conc.: 4.9 g/l; platinum-coated titanium)

mination of the exact specific energy consumption values in the case of the blasted titanum electrodes. However, it can be concluded that both the current efficiency, and the specific energy consumption values decrease with increasing electrolyte temperature. The quality of the manganese dioxide coating improves with the temperature: the formal degree of odixation increases with the electrolyte temperature.

Anodic Current Density

The effects of anodic current density upon the coating characteristics are shown in *Table 4*. The specific energy consumption rises with increasing current density. The x values are lower for the higher, 2 A/dm^2, anodic current densities.

Table 4.

The effects of anodic current density upon the current efficiency, specific energy consumption and formal degree of oxidation [electrolyte temperature: 97° C, particle-blasted titanium, Mn concentration: 40 (g/l)]

Current density	Sulphate electrolyte H_2SO_4 conc. (g/l)			Nitrate electrolyte HNO_3 conc. (g/l)		
Parameter	4.9	50	100	6.3	30	60
	0.5 1 2	0.5 1 2	0.5 1 2	0.5 1 2	0.5 1 2	0.5 1 2
Current efficiency, (%)	100 100 99.5	95.6 87.7 78.5	85.2 88.4 82.4	74.2 89.9 74.6	88.6 78.6 76.4	67.9 72.2 67.2
Specific energy consumption (Wh/g)	1.0 1.3 1.9	1.9 1.5 2.0	1.4 1.4 2.2	0.7 1.1 1.7	0.9 1.2 1.6	1.1 1.4 1.6
x in MnO_{1+x}	0.84 0.85 0.87	0.85 0.86 0.78	0.87 0.89 0.83	0.86 0.88 0.79	0.92 0.90 0.88	0.93 0.93 0.89

Material and Pretreatment of the Anode

The effects of the anode material and pretreatment methods upon the current efficiency, specific energy consumption and degree of oxidation are shown in *Table 5*. No apparent differences can be discerned. Comparison of the low and high temperature data reveals that at 1 A/dm^2 and 1.14 A/dm^2 current densities, respectively, the deposition of manganese dioxide at 85 °C

Table 5.

Effect of anode material and pretreatment upon the current efficiency, specific energy consumption and formal degree of oxidation

Characteristic	Electrolyte					
	Sulphate			Nitrate		
	Particle blasted titanium	Manganese dioxide coated titanium (thermally)	Platinium coated titanium	Particle blasted titanium	Manganese dioxide coated titanium (thermally)	Platinum coated titanium
Current efficiency, (%)	100	95.8	94.6	89.9	83.9	78.4
Specific energy consumption, (Wh/g)	1.3	1.2	1.2	1.1	1.0	1.1
x in MnO_{1+x}	0.85	0.85	0.85	0.88	0.88	0.87

temperature onto particle-blasted titanium, manganese dioxide-coated (thermally) titanium, and platinum coated titanium anodes results insuitable products, while at 55 °C temperature, only the platinum coated and manganese dioxide coated (thermally) plates gave acceptable results, but even so, the product characteristics were not as good, as before.

Post-Electrolysis Washing and Nitric Acid Treatment

Following thorough aqueous washing, and 20 hours of drying, the formal degree of oxidation of the samples was determined. The results unequivocally proved that simple aqueous washing could not increase the degree of oxidation (Table 6).

Table 6

The x values (in MnO_{1+x}) of a few selected manganese dioxide samples, after grinding, aqueous washing and 20 hours of drying

Sample number	x in MnO_{1+x}	Moisture content, (%)
1	0.89	0.8
4	0.89	1.2
28	0.85	1.5
29	0.86	0.9
39	0.87	1.2
40	0.89	1.3
56	0.86	0.9
57	0.88	1.7
65	0.87	1.7
74	0.85	1.3
75	0.89	2.0

The post-electrolysis nitric acid treatment had a favourable effect on the product quality *(Table 7)*.

Finally, the DROTSCHMANN-activity of the manganese dioxide samples was also determined. This activity characterizes how well manganese dioxide can be used in dry cells. The DROTSCHMANN numbers of the sulphate and nitrate electrolyte-based manganese dioxide samples were 61 and 64, respective-

Table 7

Characteristics of the product, following post-electrolysis boiling in nitric acid for 4 hours, and through ashing and drying

Characteristics	Sulphate electrolyte Sample No.		Nitrate electrolyte Sample No.	
	1	2	1	2
Mn conc. of coating, (%)	56.4	60.8	58.9	59.6
MnO_2 conc. of coating, (%)	85.6	93.5	88.3	89.4
x in MnO_{1+x}	0.96	0.97	0.95	0.95

ly. The Hungarian standards require a minimum of 57, when the material is to be used for dry cells.

It can be concluded from the experiments discussed above, that acceptable, dry-cell-grade manganese dioxide can be prepared from the carbonaceous manganese ore mined at Úrkút, Hungary.

These experimental results can be used to design a pilot-plant scale unit. Experience obtained with this pilot-plant unit would facilitate the design and operation of a modern, large-scale production plant.

REFERENCES

1. Brenet J. P., Gabano J. P., Reynand J.: Electrochim. Acta *1963* 8, 207, 214.
2. Marcay J., Mathes F.: Wiss. Z. Techn. Hochsch. Chem. Leuna-Merseburg *1968* 10, 107
3. Jorgensen F. R. A.: J. Electrochem. Soc. *1970* 117, 275
4. Kano K., Kinishikawa, Nakayama T., Otani Y.: Denki Kogaku *1970* 38 932.
5. Muraki J.: Kogyo Kogaku Zasshi *1961* 64 141.
6. Dzaparidze L. N., Tsagarelli G. A., Goniasvili L. Sh.: sbor. Akad. Nauk Gruz SSR *1970* 58, 73.
7. Tsagarelli G. A., Goniasvili L. Sh.: Sb. Tr. Molod. Nauchn. Sotrudnikov Inst. Neorg. Khim. Elektrohim.
8. Canadian Patent, 1 134 575.
9. Clapper T. W.: The encyclopedia of electrochemistry, New York–London, Reinhold, 1964. pp. 789.
10. Muraki J., Okijama Y.: Kogyo Kogaku Zasshi *1961* 64 137.
11. German Patent, 1 935 002.
12. Gallagher P. K., Johnson D. W.: J. Electrochem. Soc. Electrochemical Technology *1971* 118, 1530.
13. Shimizu K.: Sci. Technol. Appl. Titanium Proc. Intern. Conf. London 1968/1970, 33.
14. Japanese Patent 7 029 769
15. Gattaw G., Wendlant H. G.: Z. Analyt. Chem. *1960* 174 15.

РЕЗЮМЕ

Авторы изучали способ получения двуокиси марганца использованной в производстве сухих батерей путём электролиза нитратных и сульфатных марганцевых растворов. В качестве катода использовали свинец, а анода титановый лист покрытый двуокисью марганца. Установили, что к. п. д. тока меньше у нитратного электролита, а удельная энергия у сульфатного электролита. Степень оксидации продукта выше у нитратного электролита. Изменение концентрации иона Mn^{2+} не влияет существенно на параметры электролита в области 6—90 г/л. Увеличение содержания кислоты в электролите уменьшает токовой к. п. д. и увеличивает содержание марганца. Содержание меди, никеля и кобалта в продукте было пропорциональным содержанием загрязняющих примесей, но железо, титан и свинец могли попадать в двуокись марганца и из электрода. Оптимальной температурой электролиза является 85—97 °C, плотность тока 0,5—1,5 А/дм^2. Увеличение плотности уменьшает содержание активного кислорода, но это можно увеличивать и последующей переваркой.

HUNGARIAN JOURNAL
OF INDUSTRIAL CHEMISTRY
VESZPRÉM
Vol. 11. pp. 329–337 (1983)

LABOUR REQUIREMENT ESTIMATION OF CONTINUOUSLY OPERATED CHEMICAL TECHNOLOGIES

L. Bene, P. Bittner and J. Isaszegi*

(Department of Industrial Engineering and Management, Veszprém University of Chemical Engineering, Veszprém, Hungary
*OLAJTERV General Contracting and Design Office for the Oil Industry, Budapest, Hungary)

Received: January 12, 1983.

In continuously operated production systems certain pre-known events occur at random. These random events require a closer examination of the problems of continuous mass production in the chemical industry; they call for a new approach in work-schedule organization and manpower-requirement estimation.

Introduction

A comparison of the continuously operated and batch-wise operated chemical technologies shows that the second type requires more capital and produces more material value than the first one. Therefore, it is not surprizing that most organizational studies deal with batch-wise systems. Nevertheless, the peculiarities of continuous technologies also deserve a more in-depth study.

In continuously operated technologies the same material is produced continuously, or successive series of operations are carried out continouosly. No cycles or periods can be defined, material moves through the chain of operations without interruption. Time spent in the successive technological units depends on the chemical reaction proper, the actual technological parameter settings, and the yield or conversion sought.

In continuously operated system, the actual work or the series of motions are the integral part of the technology. Therefore, conventional ergonometric principles or motion-simplification rules cannot be applied. The operator's activity is directly linked with the technology. However, unlike batch production, the operator's activity often cannot be determined in advance as a function of the residence time. In known continuous systems, expected events occur at random. The stochastic nature of the system calls for a re-

examination of the problems of continuous mass production in the chemical industry, for a new approach in work scheduling and the manpower requirement estimation.

Number of Staff

A typical, continuously operated chemical technology was selected for this study, namely the digestion of bauxite. Digestion is the principal step of alumina production, in which the metals in bauxite are dissolved. Digestion lines composed of autoclaves and expansion vessels, connected in series with the autoclaves, are located on a 50×20 m^2 area. Digestion lines are operated in parallel mode. Digestion is followed by compression of the suspension by piston pumps. The pumps do not belong to the digestion unit proper examined here. Unlike the pumps, heat exchangers, which utilize the heat of steam liberated in the last expansion vessel, belong to the digestion plant.

Determination of the Number of Staff Required

The required number of staff is the minimum number of workers which ensures the smooth, normal operation of failure-free technology.

The technical and technological conditions also influence the manpower requirement of continuous, mass-production technologies. Therefore, one has to start with the analysis of the technology itself to arrive at the true manpower requirement of the technology.

At first, the technological process was decomposed into operations, and the corresponding work-stations were assigned. Questionnaires were used to determine the amount of:

— materials
— devices
— energies

used and the:

— information
— storage and transport
— personel and
— ergonomic

data connected with each work-station.

While completing this time-consuming work, both the systematically recurring and the failure-related "activities" were defined. The quantative composition of the staff and the major work-influencing factors were also learnt.

The frequency of the recurring activities, the distance and level difference covered while carrying out these activities led to the determination of the number of staff required for the supervision of the technology.

A New Approach, Based on the Interrelationship of Manpower Requirement and Reliability

According to the operators, the number of staff required—as determined previously—cannot cope with technological upsets. Their opinions and our

observations indicated that there were two major factors which led to the increased manpower requirement:

— as a result of the technology proper, there were few activities which recurred in a determined, periodic manner;
— as a consequence of the low intensity of preventive maintenance, there were too many "occasional", random problems that had to be taken care of.

These two observations made it clear that a sufficient number of staff cannot be deduced from the time and production data of technology, as is usualin the machinery industry or in batch-operated chemical systems. Conventional methods used for the determination of the number of staff are necessarily deterministic in nature, and this also influences the approach of management. The number of staff thus obtained is "objective" and is based on figures which are interpreted identically by everybody concerned. Assuming that the primacy of time-function holds true, the management does not need to fear risks as long as the required number of staff are available.

However, in continuously operated chemical production systems the majority of events occur at random, consequently, probability—based approaches are called for.

While searching for the principles and methods of probability—based estimations, our attention turned to the instrument logs recording the date, duration and cause of equipment failure. This led to the application of reliability-analysis methods for the ectimation of the occurrence of random failures, and the related later requirement. Reliability analysis means the identification and evaluation of the causes of failures. The probability distribution function of failure-free operation was thus determined, and the analysis of failures lead to the prediction of expected failures and the duration of failure-free operation between two failures. These data permit the scheduling of preventive maintenance, system shut-down and the manpower-requirement.

These considerations led to the hypothesis which calls for the analysis of the technology as the first step in work-scheduling in the chemical technologies, followed by the determination of the manpower-requirement and the designation of production rates by transforming the work-stations into work-precincts.

Determination of the Sufficient Number of Staff via the Reliability Analysis fo the System

After the determination of the required number of staff, the statistical characteristics of failures occurring in the system can be determined by the methods of reliability analysis. These data and the manpower requirements of the various failures permit the determination of the sufficient number of staff which, in turn, ensures the safe operation of the system.

Data Used for the Investigation

This investigation covered a period of 3.5 years, the equivalent of 3,717 shifts. During this period, which was connected two major overhauls, there was no significant change in the technology or the elements used. Thus, the data base can be considered homogeneous.

Structural Model of the System

At first, the decisive elements were selected, according to their technological and/or reliability and/or manpower requirement characteristics. This led to the structural model, the so-called manpower-oriented reliability structure model (MORM, in brief). This model differs from the usual reliability structure models *(Fig. 1.)*.

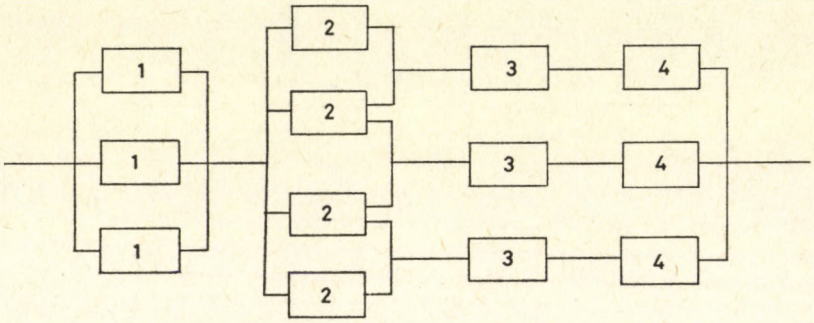

Fig. 1
The manpower-oriented reliability structure model (MORM) of the system
1 — preheaters, *2* — piston pumps, *3* — autoclaves, *4* — expansion vessels

If any small element of an actual system influences the reliability of the entire system, it then becomes the element of the reliability structure model, too. In the MORM, it is not the probability of failure, but rather the manpower it takes to eliminate the failure, that matters. Thus, the area of the work-station which can be reliably managed by any single worker was sought. This led to the transformation of the idea of the work-station into the more dynamic idea of the work precinct.

In order to define the precincts, the system was decomposed into units much smaller than the present work-stations. These became the elements of the MORM. Then, the number, frequency, duration and time-dependent changes of the failures and shut-downs of these elements were determined.

The MORM correctly represents the reliability features of the system, and the effects of the failure of a certain element upon the other elements.

Examination of the Reliability of the System

Down-time caused by element failure was calculated from the data in the apparatus logs. The estimated expected value of failure was then defined as the ratio of down-time and the overall time span of the period (time-base). Actual failure probabilities hover around this value.

Estimation of the Manpower Requirement via the Distribution Functions of Actual Operation

Distribution functions of the actual operation describe the time-dependent changes of element-reliability and enable the determination of realistic maintenance periods. This, in turn, facilitates the estimation of the occur-

rence probability of "random" activities and the objective scheduling of the required staff. Application of the distribution function to the elements of the MORM gives the probability of failure as a function of time, i.e. the probability that the operator has to eliminate some failure after the lapse of certain period of time.

Work on the determination of the limits of work-precincts started with the determination of the actual probability distribution functions of the sufficiently small units. The elements of the MORM were such small units. This work led to the first variant of work-precincts shown in *Fig. 2*.

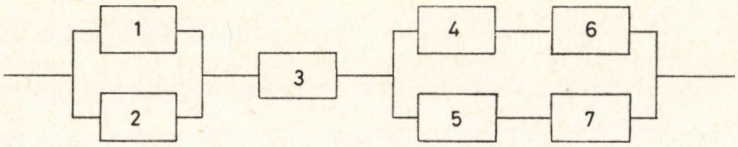

Fig. 2

First variant of the work-precincts.

1: preheaters of the first and second line (E 1–2), *2:* preheaters of the third line (E 3), *3:* piston pump (D), *4:* first and second line of autoclaves (A 1–2), *5:* third line of autoclaves, *6:* first and second line of expansion vessels, *7:* third line of expansion vessels

It could be concluded from the theoretical distribution functions of actual operation that at a 0.9 probability level it takes 410 hours in precinct A 1–2, 428 hours in precinct A 3, 1,717 hours in precinct Ex–3, 1,794 hours in precinct Ex 1–2, 2,035 hours in precinct E 1–2, 2,616 hours in precinct D and 5,726

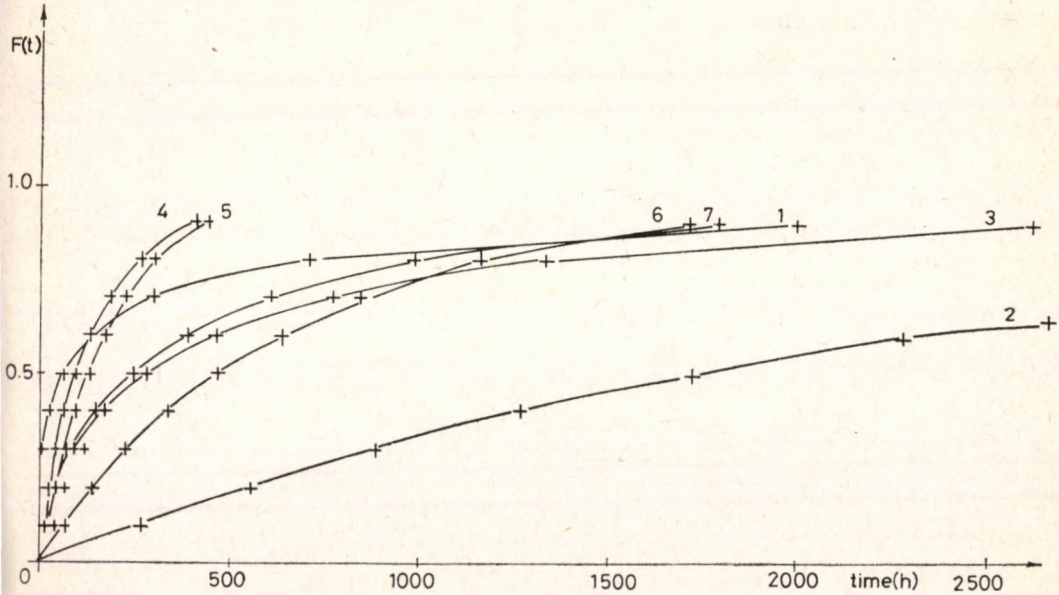

Fig. 3

Theoretical distribution functions of actual operation in the first work-precinct variant

hours in precinct E 3 to encounter a failure. Such precincts result in low—and inhomogeneous—work loads.

Therefore, the low-load precincts were combined with due respect to spatial and technological connections. Accordingly, the parameters of the exponential distribution functions of actual operation were added, and the exponential theoretical distribution functions of actual operation in the new precincts were calculated. The theoretical distribution functions became steeper, the work-load became higher and more even, though none of these parameters reached the satisfactory level.

In the following step, the precincts were further extended. This MORM resulted in distribution functions, which were similar to each other, and were located close to one another. This led to even work loads. though the absolute load remained fairly low. However, the precincts could not be increased any further, because other tasks—relating to "normal" operation—also had to be performed.

This work proved the hypothesis stated in 1.2.1., i.e. work scheduling in the chemical industry has to begin at the analysis of the technology, followed by the determination of the manpower requirement, and the reliability—based determination of the work—precincts.

The methods of reliability analysis were used for the determination of the sufficient number of staff. These methods relied on the recording of event occurrences and standard statistical calculations. Thus, an entirely new approach was adapted for the evaluation of the technology: random disturbances in the system were estimated and were used to determine the actual manpower requirement. This approach differs from the classical approaches, which rely on norms, event or task frequency and time requirement.

The new approach, on the other hand, demands more skill from the workers and management than the classical, work-station oriented system. The workers must be skilled in several occupations, know a larger section of the technology, and have a financial interest in the perfect operation of the system. The theoretically determined number of staff will also be sufficient in the daily operation of the plant.

The apparatus-log and reliability-analysis—based method of manpower-requirement estimation allows:

- for the estimation of both the direct and indirect manpower requirement
- for the improvement of preventive maintenance work
- for the reduction of down-time.

The Relationship Between Reliability, Maintenance and Manpower Requirement

In the previous chapter, it was shown that the methods of reliability analysis can be used for the estimation of the manpower requirement. It was concluded that data obtained by this method allow for the reduction of down-time and the estimation of the manpower requirement of preventive maintenance. To prove the validity of these statements, down-time analysis was carried out, followed by the examination of the current maintenance schedules. It will be

shown that the data obtained in the previous, expensive and time-consuming survey can be used for several purposes, and can be readily integrated into the information system of the company leading to periodic evaluations.

Failure Analysis

During the test period, 572 failures were registered. The failures were classified as environment-related or system-related failures. Their time and spatial distributions were investigated. This analysis revealed the weak points of the system, the types of failures, their frequency, as well as the strategy and tactics of operation and maintenance.

From the analysis of the history of failures it became apparent that in the middle of the year, low failure frequency was connected with long down-times, while at the end of the year, high failure frequency was coupled to short down-time periods. Environmental causes led to down-time amounting to 3.23% of the time-base, while system-related failures caused 19.7% down-time. Even if one calculates only the value of alumina not produced during this time, the loss is considerable.

In the statistical control-card investigations, the number of monthly failures were recorded on the $\bar{x}$ card. This analysis made it possible to examine the statistical orderliness of the process, and gave a reliable picture about the load of the operators. The maximum value of the monthly failures was 10, and this occurred only four times during the 3.5 years-long test period. The averages of monthly failures were 4.31 and 3.38 respectively. Once, in one of the lines, there was no failure for two months. These facts did not support the claim of the plant managers that they needed extra personnel, because failures represented increased work.

The number of internal-cause related failures was also examined, both for the lines and the elements of the MORM. It could be concluded that the number of failures per element was not too large. Analysis of the number and duration of failures showed that the key elements are the autoclaves and the expansion vessels, causing 61.2% of the failures and 72.1% of the down-time. Typical failures could also be identified in these elements. The detection of the weak points of the technology, and their elimination via increased reliability, increases the reliability of the overall system more than proportionally. Thus, a significant saving in manpower can be achieved.

It is apparent from the previous discussion that reliability, maintenance and manpower requirement are interrelated. The manpower directly depends on the level of maintenance. With better organized planned preventive maintenance, the estimates of the sufficient number of staff required for smooth operation also become better. To prove this point, the actual maintenance practice in the plant was examined.

The Present State of Maintenance

The time dependence of the average length of operation between two failures (ALO, in brief) was determined to evaluate the effects of maintenance. ALO values of both autoclave lines were calculated for half-year and one year periods. The results—which reflect the adequacy or inadequacy maintenance—were compared to those obtained from the time-dependency of failures. It

was concluded that ALO values did not realistically represent the state of preventive maintenance.

Therefore, the reliability changes over the years of the elements of the MORM were analyzed. It could be concluded that for one of the lines—in agreement with the previous conclusions—the autoclave and expansion vessel elements required the most maintenance work.

A characteristic and significant feature of the maintenance system is the planned, preventive shut-down. It became obvious during the analysis that both their number and duration was excessive. Planned shut-downs caused a loss of 3.23% of the time base. Apart from the direct loss, frequent start-ups represent an excessive load for the operating staff. Due to the increased load of the structural materials each hour of start-up corresponds to 100 hours of normal operation, and this again leads to more frequent failures. The failures generally occur in the second shift following the start-up. However, maintenance personnel work in single shift arrangements, resulting in even longer down-times. Therefore, it is altogether desirable that the number of start-ups be kept to a minimum.

The repair distribution functions of the elements of the MORM model were also examined. These functions gave the probability of the occurrence of repairs shorter than a predetermined value. These results can be used for the scheduling of the work and number of maintenance personnel.

Effects of Manpower Requirement Estimations

Following the survey of the work-stations and the reliability analysis, the expected effects of the losses and reserves, uncovered upon the aim, complex operation and efficiency of the overall process, were also evaluated.

It was concluded that when the market demanded, the company could increase its production by 20%, without extra investment, merely by better work scheduling and the reduction and/or elimination of down-time.

Results of the present analysis allowed for a 25.7% reduction in the number of staff, also reducing the associated manpower costs. Naturally, the ergonomic investigation had its own costs, but it could be easily covered from maintenance savings and development resources. Funds spent on ergonomic work show a favourable pay-back pattern, for direct production boosts could be achieved.

Since production and productive time could be increased, the manpower requirement—and the associated manpower costs—could be decreased, the level of production means could be kept constant, and the efficiency and profitability of the entire production process increased considerably.

Conclusions

Though apparently obvious, reliability analysis has never been used for the determination of the manpower-requirement of continuosly operated chemical technologies. Since the stochastic approach used here fitted the actual system much better than the deterministic rigid old methods the results obtained proved more useful and reliable.

Scheduled preventive maintenance, based on the results of reliability analysis, led to an almost complete elimination of unexpected shut-downs. With the determination of the down-time of the key elements, and with the introduction of scheduled small and medium-scale maintenance work, "random", occasional activities became almost scheduled events, and the number of staff required for the safe operation of the plant could be reliably determined.

The ergonomic work involved in the determination of the manpower requirement of continuously operated chemical technologies is considerable, both in time and expenses. Nevertheless, it is a very cost-effective move, because it leads to minimum losses and unused reserves, yet ensures safe operation under the given technical, technological and personnel conditions.

РЕЗЮМЕ

Некоторые ранее известные события в непрерывных промышленных системах возникают случайно. С целью выяснения характера этих случайных событий необходимо изучать заводы непрерывного процесса химической промышленности, а также детально изучать отдельные участки производства и потребность в рабочей силе.

HUNGARIAN JOURNAL
OF INDUSTRIAL CHEMISTRY
VESZPRÉM
Vol. 11. pp. 339–348 (1983)

PARTICLE FORMATION FROM SOLUTIONS IN GAS FLUIDIZED BEDS. VI.

ESTABLISHMENT OF STEADY STATE OPERATION CONDITIONS BY GRINDING

B. DENCS and Z. ORMÓS

(Research Institute for Technical Chemistry of the Hungarian Academy of Sciences, Veszprém)

Received: January 14, 1983.

The major methods used to establish steady-state operation conditions—including steady-state particle size distribution—are discussed here. A continuously operated experimental fluidizer is described, which contains a special grinding element used to establish and control the steady-state particle size distribution. The results of experiments carried out with solutions of sodium chloride, iron (II) sulphate, urea and beet sugar, and those with melts of hydrated soda, sodium sulphate and calcium nitrate are discussed, including the values of the technological parameters, time-dependent changes of the particle size distribution and the major physical characteristics of the products.

Introduction

Particle formation from solutions (melts or suspensions) in gas fluidized beds (direct particle formation, in brief) takes place as follows. In a continuously operated fludizer, particulate material is fluidized by hot air. The composition of the particulate material is identical with that of the—e.g.—dissolved material. The solution to be processed is sprayed onto the top (or into the bulk) of the fluidized bed. The liquid droplets are deposited onto the surface of the permanently moving particles. Solvent is evaporated from their surface by hot air and it leaves the bed along with the latter. The solid material content of the solution remains in the bed and it is deposited onto the particles. Particulate material is continously withdrawn from the fluidized bed at a rate which corresponds to the solid material load reaching the equipment in solution.

The fundamental requirement of the industrial application of direct particle formation is the establishment and maintenance of steady-state operation conditions, including steadystate particle size distribution. Particles

steadily grow, while solid material is deposited onto their surface from the solution. This growth mechanism is called surface layering. Apart from that, the wet particles can readily agglomerate leading to rapidly increasing particle size.

The most wide-spread method used to establish steady-state particle size distribution calls for the addition of particles [1–3]. Then, a fraction of the solid material leaving the apparatus is continuously returned, either directly [4] or after grinding [5], to the fluidized bed. It is more advantageous to fractionate the discharged particles and return the below-limit fractions [6–7]. Another solution, in which the above-limit particles are returned after crushing is also of importance [8]. The two methods are often combined, i.e. below-limit particles are returned directly, while above-limit particles are crushed, sized and are also returned into the fluidized bed [9–10].

Another, less frequently used method of particle-size stabilization relies on temperature-fluctuation-induced particle desintegration [11]. Essentially, particles from the warmer, drier section of the fluidized bed enter the upper, spraying zone where the particle contacts the atomized solution, which has a considerably lower temperature. Here the surface of the particle is rapidly cooled. Due to differences in the inner and outer temperatures, and expansion coefficients, the particle desintegrates. In a few cases, this process alone ensured steady-state particle size distribution [12–13].

Rapid evaporation of the liquid in the interior of the particle can also lead to considerable particle desintegration [14].

All the above methods have a number of disadvantages. Particle feed-back requires additional equipment—for example, continuous size—fractionating units, continuous solid feeders, continuous and variable crushers, and pneumatic or other mechanical conveyers, etc. Even so, particle size can only be controlled within narrow limits. Thus, varying particle size specifications cannot be readily met. The surface-temperature-fluctuation-induced desintegration becomes significant only at high bed temperatures (180–250 °C). This limit severely restricts the type of materials which can be processed in this manner, for heat sensitive materials or materials with lower melting points obviously cannot be processed. High bed temperature also means high energy consumption and low productivity.

Steady-state particle size distribution can be established via the crushing of the solid particles as well. To accomplish this task, a method and apparatus were developed in which the solid material is in-situ crushed in the fludized bed and thus a steady-state particle size distribution is established. Patent applications have been filed in five countries and a patent was issued for it in the U.S. [17] and in Great Britain [18].

Experimental

The continuously operated, cylindrical (inner diameter 0.106 m) fluidization system follows the specifications given in the above mentioned patent. It has a special particle grinding unit in the lower section of the fluidized bed. The apparatus is shown schematically in Fig. 1. The grinding unit consists of a number of rollers, which are arranged parallel to the inner wall of the apparatus. There is a given clearance between the rollers and the inner wall. The rollers

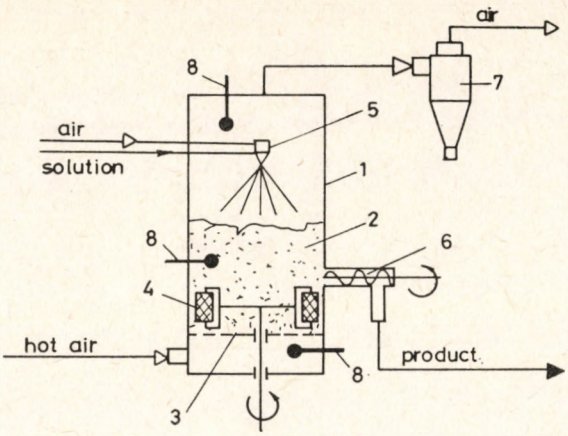

Fig. 1
Experimental apparatus
1 — fluidization chamber; *2* — fluidized bed; *3* — gas distributor; *4* — desintegrator; *5* — atomizer; *6* — feeder; *7* — cyclone; *8* — thermometer.

can freely rotate around their axis. Height and diameter values of the rollers are 0.03 m and 0.015 m, respectively. The surface of the rollers and the inner wall of the fluidized bed opposite the rollers is coarsened. The grinder is driven by a variable speed electromotor (10 to 120 rpm). The clearance between the surface of the rollers and the inner wall of the bed can be varied, as required, in the $(0 \text{ to } 6) \times 10^{-3}$ m range.

For the experiments, a certain amount of particulate solid material with a known particle size distribution was loaded into the system. The layer was then preheated once the preset input air temperature was reached, a bed expansion of 1.6 was established and spraying, particle discharge and particle grinding were commenced. The discharged product was sampled at regular intervals and the major physical characteristics of the particles were determined [15]. Experiments were conducted until steady-state conditions were unequivocally established, or it became apparent that steady-state conditions could not be established at all.

Results and Discussion

Recovery of the Solid Material Content of Solutions

Aqueous solutions of sodium chloride, urea and beet sugar were used. At first, a test was made to see whether steady state particle size distribution could be established without the use of the grinder. In these experiments, an agitator replaced the grinder. It was located immediately above the bed supporting plate. The agitator consisted of three blades located at 120° with respect to each other.

At first, the time-dependent changes of the average particle size were determined, as shown in the following Figures. Dimensionless time (t^*) is plotted

in the Figures: it is the ratio of actual time and the average residence time of the solid material ($t/\bar{t}$).

For sodium chloride as test material, the average particle size soon exceeded 2×10^{-3} m which was three times as much as the initial particle size (*Fig. 2.* Curve 1). The well-known equation [16] was used to calculate the time dependence of the average particle size, assuming that growth took place by surface layering (*Fig. 2*, Curve 2). In the $0<t^*<2$ range the calculated and measured curves agreed sufficiently well. Both the measured and the calculated curves show that the process is a non-steady-state one.

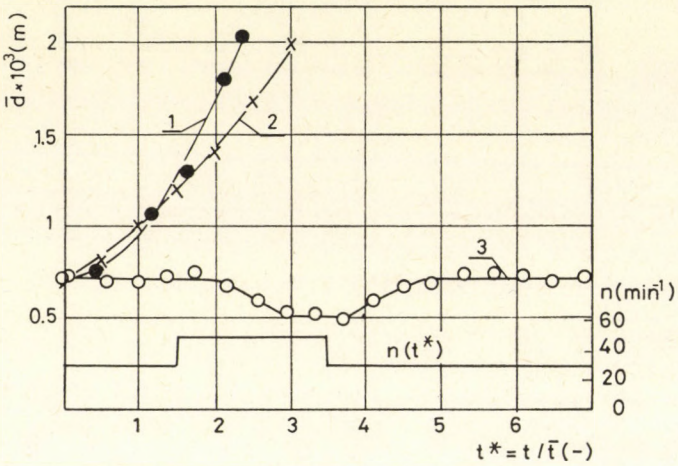

Fig. 2

Time-dependent changes of the average particle size of sodium chloride.
1 — with agitator, *2* — calculated curve, *3* — with grinder

When the grinder was used during the experiment ($r=2\times10^{-3}$ m) at $n=30$ rpm, the average particle size soon became stabilized close to the initial value (*Fig. 2*, Curve 3). When the rotation speed of the grinder was increased to $n=50$ rpm the average particle size decreased and the new steady-state conditions became established in about one average residence time ($\bar{d}=0.51\times10^{-3}$ m). When the rotation speed was reduced to the original, $n=30$ rpm value, the average particle size increased to the original value (0.72×10^{-3} m) in about one residence time. Then, the parameters were kept constant and the steady-state conditions soon became stabilized, the particle size of the discharged product varied within $\pm2.5\%$ of the average.

The average particle size-time diagrams of urea are shown in *Fig. 3*. The agreement of the measured (Curve 1) and calculated (Curve 2) curves indicates that with the mechanical agitator present, steady-state conditions could not be established. Though the trends of the two curves are identical, the measured curve runs somewhat higher than the calculated one. This indicates that surface layering is also accompanied by agglomerization.

When the grinder was used ($r=3\times10^{-3}$ m, $n=20$ and 50 rpm) the steady-state conditions could be established in what amounted to about twice the

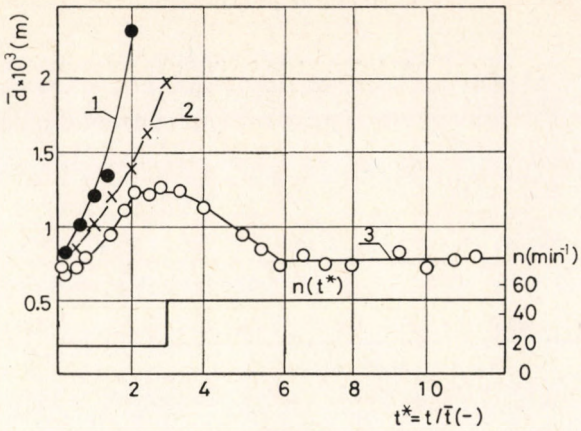

Fig. 3

Time-dependent changes of the average particle size of urea
1 — with agitator, *2* — calculated curve, *3* — with grinder

average residence time. In steady-state conditions the average particle size of the discharged product varied within $\pm 5\%$ of the average. The same conclusions also apply to experiments with beet sugar.

It should be noted that every effort was made to ensure that really stable steady-state conditions have been reached. Therefore, long experiments were carried out lasting for 26 to 35 hours.

The major physical characteristics of the particulate material produced are listed in *Table 1*.

It can be seen from *Table 1* that the average particle size of the product could be varied over wide limits $(0.5-1.36)\times10^{-3}$ m. This interval can be

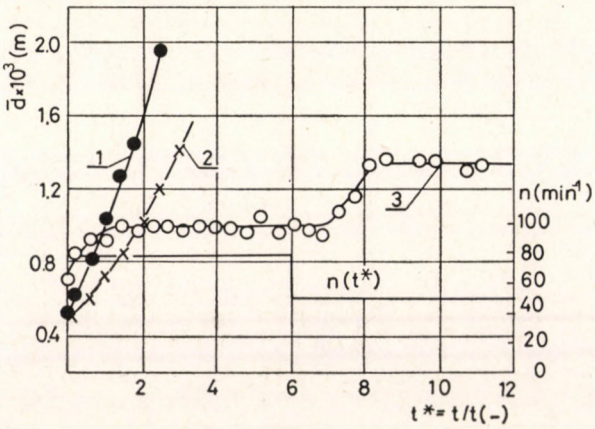

Fig 4

Time-dependent changes of the average particle size of sugar
1 — with agitator, *2* — calculated curve, *3* — with grinder

Table 1

Property	NaCl	$CO(NH_2)_2$	Sugar
$\bar{d}\cdot 10^3$ (m)	0.72; 0.51	1.23; 0.77	1.35; 0.99
ϱ (kg/m³)	2165	1335	1590
ϱ_s (kg/m³)	1780	1020	1350
ϱ_l (kg/m³)	980	510	740
ε_p (—)	0.176	0.237	0.15
K (%)	93	90	95
φ (—)	0.44—0.46	0.38—0.42	0.48—0.5
x_n (s%)	0.05—0.1	0.15—0.2	0.02—0.04

increased by increasing the clearance (r) and the rotation speed (n). The pore fraction of the particles varies between 0.15—0.24 their wear resistance and rolling characteristics are favourable and their moisture content is low.

Recovery of Solid Material from Melts

Experiments were carried out to dehydrate the low-melting hydrated crytalline materials: $Na_2CO_3\cdot 10H_2O$, $Na_2SO_4\cdot 10H_2O$, $Ca(NO_3)_2\cdot 4H_2O$ and $FeSO_4\cdot 7H_2O$. The melts of $Na_2SO_4\cdot 10H_2O$ and $Na_2CO_3\cdot 10H_2O$ contained a small amount of solid material as well as fine crystals. These were homogeneously dispersed in the melt by mixing. This liquid material, kept at 50 °C, was sprayed onto the top of the fluidized bed. Part of $FeSO_4\cdot 7H_2O$ decomposed during melting, therefore a solution saturated at 40 °C was used instead of the melt. The melt of $Ca(NO_3)_2\cdot 4H_2O$ was a homogeneous liquid at 50 °C, and as such, it could be easily processed.

Dehydrated, particulate material was first charged into the fluidized bed. The initial particle size distributions are shown in *Fig. 5*. The initial particle size distributions of $FeSO_4$ and $Ca(NO_3)_2$ were identical. The rotation speed of the grinding element was kept at $n=60$ rpm, and the clearance at $r=3\cdot 10^{-3}$ m.

Time-dependent changes of the produced solid material were also tested. The particle size distributions of fractions taken at various time intervals

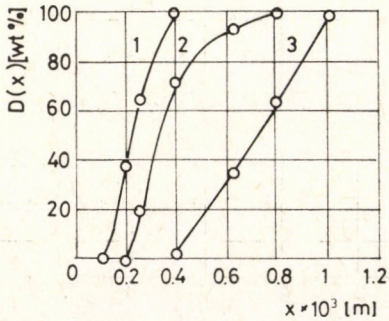

Fig. 5

Particle size distribution of the solid material loaded into the fluidized bed at $t^*=0$
1: Na_2SO_4; *2:* Na_2CO_3; *3:* $FeSO_4$ and $Ca(NO_3)_2$

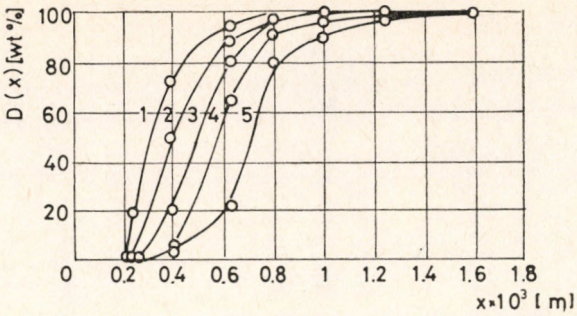

Fig. 6
Particle size distribution of the discharged sodium carbonate
1: t* = 0; *2*: t* = 1.2; *3*: t* = 2.3; *4*: t* = 2.9; *5*: t* = 3.8

during dehydration of the melt of $Na_2CO_3 \cdot 10H_2O$ are shown in *Fig. 6*. Due to particle growth, the curves shifted towards larger size. It can be seen in *Fig. 6* that the linear growth rate of the particles is constant, independently from the actual particle size. Particle size growth takes place via the surface layering mechanism.

In the first, non-steady-state section of the process, the time-dependent changes of the particle size distribution of $Na_2SO_4 \cdot 10H_2O$; $FeSO_4 \cdot 7H_2O$ and $Ca(NO_3)_2 \cdot 4H_2O$ are quite similar.

Steady-state conditions, including a steady-state particle size distribution could be reached in each case. The time required for the establishment of steady-state conditions, and the stability of the major physical properties are of special importance from a technological point of view. The time required for the establishment of the steady-state particle size distribution can be derived from the time dependence of the average particle size *(Fig. 7)*. Expressed as the multiple of average residence time this was 5–5.5 for Na_2CO_3; 4.5–5 for $FeSO_4 \cdot H_2O$ and 1.5–2 for $Ca(NO_3)_2$.

In steady-state conditions, the average particle size of the product varied within $\pm 4\%$ of the average. The same applies to the stability of the other physical properties of the product (bulk density, porosity, rolling characteristics, and moisture content) as well.

The steady-state values of the major physical properties of the product granules are listed in *Table 2*.

Table 2

Property	Na_2CO_3	Na_2SO_4	$FeSO_4 \times H_2O$	$Ca(NO_3)_2$
$\bar{d} \times 10^3$ (m)	0.97	1.15	0.83	1.09
ϱ (kg/m³)	2509	2698	2800	2360
$\bar{\varrho}_s$ (kg/m³)	2260	2430	2530	2120
ϱ_l (kg/m³)	1100	1130	1420	1020
ε_p (—)	0.096	0.112	0.092	0.11
K (%)	93	90	92	93
φ (—)	0.67	0.59	0.82	0.73
x_n (*wt*%)	0.02	0.04	0.61	0.84

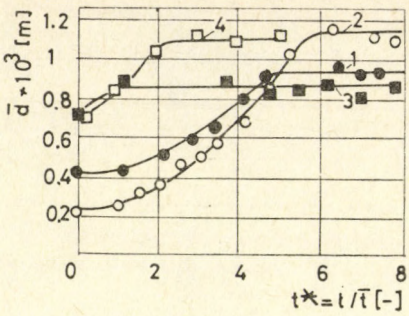

Fig. 7

Changes of the average particle size as a function of time for various materials
1: Na_2CO_3; *2:* Na_2SO_4; *3:* $FeSO_4 \cdot H_2O$; *4:* $Ca(NO_3)_2$

The small average particle size (1×10^{-3} m), the low porosity and the high rolling coefficient unequivocally indicate that particle growth takes place via surface layering. It should be mentioned that even a single-stage unit could produce a material of extremely low moisture content.

Operation Conditions and Production Capacity of the Apparatus

The values of the technological parameters, the average residence time of the solid material, the water-removal and solid product discharge rates refer to the empty cross section of the apparatus listed in *Table 3*. The rotation speed and clearance values of the grinder were given earlier in the text.

Table 3

Material	u (m/s)	T_{in} (°C)	T_{out} (°C)	c (kg/m³)	$w \cdot 10^3$ (m³/h)	$\bar{t}$ (h)	q_w (kg/m²h)	q_t (kg/m²h)
$CO(NH_2)_2$	0.5	100	50	450	0.37	3.03	25.5	19
Sugar	1.2	100	68	700	0.44	2.38	26.9	35
NaCl	0.47	125	55	250	0.63	5.09	65.3	18
Na_2CO_3	0.74	200	110	515	0.99	1.72	98.4	58
Na_2SO_4	1.1	190	110	575	1.3	1.92	107.4	85
$Ca(NO_3)_2$	0.83	210	130	1167	1.42	0.48	82.7	188.2
$FeSO_4 \times H_2O$	0.93	210	120	340	1.3	1.83	136.0	50.2

For the majority of materials, the temperature of the exhausted air had to be kept at 50 °C to ensure a sufficiently low moisture content in the bed (below 1%). This is also desirable for the product, as indicated by the present and earlier results. For the melts, a comparatively high exhausted air temperature value was selected, because this ensured optimum dehydration conditions.

It can be seen from *Table 3* that both the raw materials and the parameters encompass a wide range. This permits the study of the grinder over widely varying experimental conditions.

The water removal rates with reference to unit empty cross-section (q_w) have to be mentioned specifically. Often, these values are in the vincinity—or above—of 100 kg/m²h.

Conclusions

The use of a particle grinder ensured that steady-state operation conditions —including steady-state particle size distribution—could be established for materials of widely varying physical and chemical compositions. The particle size distribution can be readily controlled via the clearance and the rotation speed of the grinder—even during operation (see, for example. *Fig. 2–4*).

Using the particle grinder, particulate material can be produced from solutions in a single, continuously operated fluidized bed, under steady-state conditions, without recourse to additional operations—e.g. crushing, fractionation, and solid material feed-back, etc.—on the product.

SYMBOLS

c	concentration, kg m^{-3}
$\bar{d}$	average particle size, m
$D(x)$	particle size distribution curve (undersize fraction), %w/w
K	wear resistance, %
n	rotation speed, rpm
q_w	water evaporation rate, kg m^{-2} h^{-1}
q_t	production capacity expressed as discharged solid material, kg m^{-2} h^{-1}
r	grinder — wall clearance, m
t	time, h
t^*	dimensionless time, $t^* = t/\bar{t}$
T	air temperature, °C
x	sieve opening, m
x_n	moisture content, %w/w
u	linear velocity of air with reference to empty cross section, ms^{-1}
w	flow rate of the solution, m³h^{-1}
$\bar{\varepsilon}_p$	average pore fraction,
ϱ	true density, kg m^{-3}
$\bar{\varrho}_s$	average particle density, kg m^{-3}
ϱ_l	bulk density in expanded bed, kg m^{-3}
φ	rolling coefficient

Subscripts

in	input value
out	exhaust value

REFERENCES

1. Dencs, B. and Ormós, Z.: Hung. J. Ind. Chem. *1978* 6, 301
2. Dencs, B. and Ormós, Z.: Hung. J. Ind. Chem. *1978* 6, 313
3. Dencs, B. and Ormós, Z.: Hung. J. Ind. Chem. *1978* 6, 323
4. German Patent, Offen. 2 363 334
6. Volkov V. F. et. al.: Khim. Prom. *1966* 42, 450
6. Sahova N. A. et al.: Khim. Prom. *1973* 49, 299
7. Kaspar J. and Rosch M.: Chem. Ing. Techn. *1973* 45, 736
8. British Patent No. 1 381 480

9. German Patent. Offen. 2 263 968
10. U.S. Patent 3 475 132
11. TODES, O. M.: Krist. Techn. *1972* 7, 729
12. KOZLOVSKIJ, V. V. et. al.: Khim. Prom. *1970* 46, 122
13. NALIMOV, S. P. et. al.: Zh. Prikl. Khim. *1970* 43, 581
14. MORTENSEN S. and HOVMAND S.: Production of non-dusty granulate products by fluid bed spray granulation, ACHEMA'76, Frankfurt/Main (1976)
15. ORMÓS, Z.: Hung. J. Ind. Chem. *1973* 1, 207
16. SAHOVA, N. A. i RICHKOV, A. J.: Khim. Prom. *1963* 39, 865
17. U.S. Patent 4 370 198
18. Brit. Patent 2 046 121

РЕЗЮМЕ

В шестой стати серии авторы ознакомлят читателей с наиболее важными способами установления условий для стационарного процесса получения гранул и также стационарного распределения размера частиц. В стати описана экспериментальная установка непрерывного действия с псевдоожиженным слоем в которой размещен специальный рабочий орган, дробящий элемент, с целью получения и регулирования стационарного распределения размера частиц. Приведены результаты экспериментов проведенных растворами хлорида натрия, железо(II)сульфата, карбамида и сахарного свекла, и также расплавами карбоната натрия содержащего кристальную воду, сульфата натрия и нитрата кальция. Приведены численные значения технологических параметров, изменения среднего размера частиц и некоторые другие важные физические свойства продукта.

HUNGARIAN JOURNAL
OF INDUSTRIAL CHEMISTRY
VESZPRÉM
Vol. 11. pp. 349–355 (1983)

PARTICLE FORMATION FROM SOLUTIONS IN GAS FLUIDIZED BEDS. VII.

OPERATION PARAMETERS AND PRODUCT PARTICLE SIZE DISTRIBUTION OBTAINED WITH THE USE OF A PARTICLE GRINDER

B. DENCS and Z. ORMÓS

(Research Institute for Technical Chemistry of the Hungarian Academy of Sciences, Veszprém, Hungary)

Received: January 14, 1983.

Operation parameters are detailed here, followed by an examination of the parameters which influence the operation of the particle grinder. The particle size distribution of the product obtained in steady-state conditions is examined. Calculations are shown for the lower particle size limit of the product. The effects of the major operation parameters of the grinder upon particle size distribution and the lower and upper particle size limits of the product are examined.

The physical characteristics of particulate material formed from solutions in gas fluidized beds can be controlled via the independent *operation parameters*. These parameters were detailed in a previous paper [1] for the case when steady-state conditions were achieved via the addition of particulate material. The operation parameters are somewhat modified—as follows—when steady-state conditions are achieved with the help of a particle grinder located in the fluidized bed.

The process parameters are:

- phyisical and chemical characteristics of the solid material present in the solution
- concentration of the solution

The operational parameters are:

- volumetric flow rate of sprayed-in liquid
- dispersity of the liquid
- input moisture content and temperature of air
- minimum bed height to bed diameter ratio
- extent of bed expansion

The characteristics of the apparatus are:

- shape and characteristic size of the fluidization space
- type of layer support and gas distributor plate
- distance between spraying head and layer supporting plate, direction of spraying
- method and place of offtake
- characteristics of the grinder

The linear velocity of the fluidizing and drying air is a dependent variable whose value depends on both the physical characteristics of the solid material in the layer (e.g. particle density, and particle size distribution, etc.) and the extent of bed expansion.

The effects of the major parameters—except those of the parameters of the grinder—were examined and reported on earlier [1, 2]. Therefore, only the characteristics of the grinder are examined here as follows:

- mounting of the grinder: Essentially, there are two mounting possibilities. In one of the cases, the axis of the rollers is vertical and the particles to be ground are forced through the opening formed between the surface of the rollers and the inner wall of the cylindrical fluidization bed *(Fig. 1a)*. In the other case, the axis of the grinder is horizontal. In this case, the opening is formed between the surface of the rollers and the annulus on the surface of the bed supporting (and gas distributing) plate *(Fig. 1b)*. The advantage of the horizontally mounted grinder is that it can also be used in non-cylindrical beds. The axle which drives the rollers is vertically mounted in both cases. A certain size-segregation is unavoidable in the fluidized bed. The occurrence probability of the larger particles is higher in the lower section of the fluidized bed. Since the aim is the diminution of these large particles it is advantageous to mount the grinder in the lower section of the fluidized bed. (This type of mounting is unavoidable for the horizontal rollers.)
- grinder equipped with a mixer: The efficiency of particle grinding in the lower section of the fluidized bed can be increased by a mixing element located immediately above the layer-supporting and air distributing plate, on the axle which drives the rollers. This mixing element increases the probability that the large and less intensively fluidizing

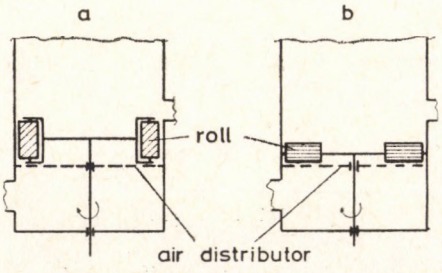

Fig. 1
Possible mountings of the grinder

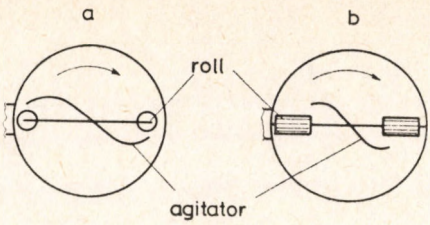

Fig. 2
Grinders equipped with mixers (from above)

particles get in front of and under the rollers. Such arrangements are shown in *Fig. 2a* and *2b*. The grinders are equipped with back-folded blade-mixers. Furthermore, mechanical agitation prevents the development of fluidization irregularities (i.e. stationary bed, and channelling, etc.) and promotes the disintegration of agglomerates held together by loose liquid bridges [2],

- number of the rollers: Obviously, under otherwise constant conditions, an increase in the number of rollers increases the grinding effect. It is advantageous to use an even number of rollers, located at opposite sides of the axis, so that the latter is evenly loaded,
- geometric sizes of the rollers: An increase in the size of the roller brings about an increase in the grinding effect. The theoretical upper limit of the rollers depends on the size of the apparatus and the height of the fluidized bed. However, it is advantageous if the height of the rollers is less than two thirds of the bed height (the larger particles are in the lower portion of the bed, anyway), while the diameter of the rollers is not larger than a quarter of the diameter of the apparatus,
- the surface of grinder: Advantageously, the surface of the rollers—and that of the opposite wall (apparatus wall or the supporting plate) is coarse,
- size of the clearing: The size of the clearing between the rollers and the wall (or the supporting plate) essentially determines the upper limit of the particle size of the product. Therefore, this is one of the most important operation parameters of the grinder,
- rotation speed: By changing the rotation speed of the grinder, the particle-size distribution of the product can be influenced, even during a urn. Therefore, rotation speed is the second most important operation parameter of the grinder.

Particle Size of the Solid Material Produced

The particle size of the solid material produced by the given apparatus in the manner described above is in the $(0.1–5)\times10^{-3}$ m range [2]. The lower limit of the particle size distribution is determined by the linear gas velocity. The upper limit is controlled by the location of the rollers and the size of the clearing. According to our experience, it is not advantageous to produces particles larger than $(4–5)\times10^{-3}$ m by fluidization, because an extremly high

linear gas velocity is required to maintain the fluidized state and this significantly lowers the economics of the process.

The steady-state particle size distribution curves of the product obtained in the experiments described in [3] were determined and compared (*Fig. 3* and *4*). It could be concluded that irrespective of the initial particle size distribution and the values of the technological parameters, the distribution curves are all of the same type. The size interval of the product primarily depends on the size of the clearing. For example, for a clearing $r = 2 \times 10^{-3}$ m the lower limit of the particle size is 0.1×10^{-3} m, while the upper limit is 1.6×10^{-3} m.

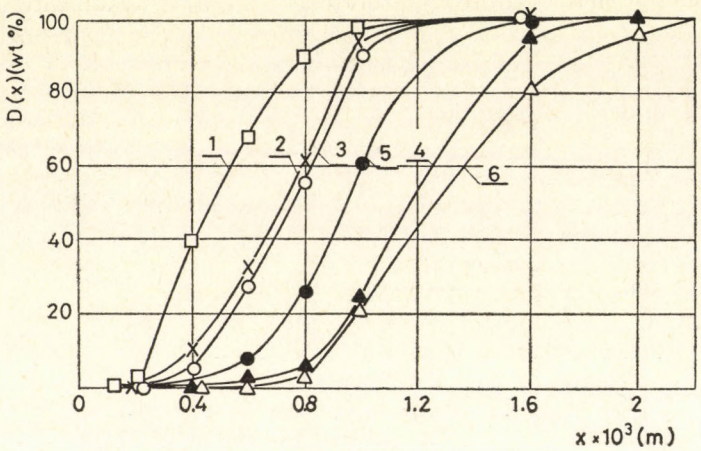

Fig. 3

Steady-state particle-size distributions for various rotation speeds and clearance sizes

NaCl: $r = 2 \times 10^{-3}$ m, $1 - n = 50$ min^{-1}, $2 - n = 30$ min^{-1}

$CO(NH_2)_2$: $r = 3 \times 10^{-3}$ m, $3 - n = 50$ min^{-1}, $4 - n = 20$ min^{-1}

Sugar: $r = 3 \times 10^{-3}$ m, $5 - n = 80$ min^{-1}, $6 - n = 50$ min^{-1}

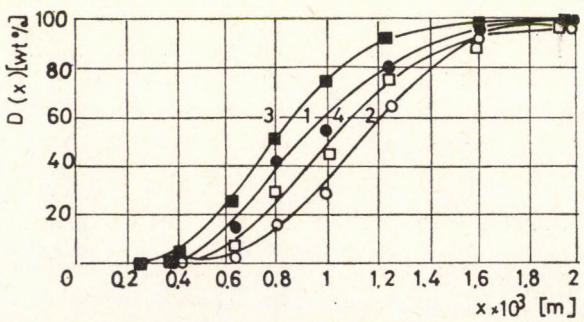

Fig. 4

Steady-state particle-size distributions for identical rotation speeds and clearance sizes

$r = 3 \times 10^{-3}$ m, $n = 60$ min^{-1}

$1 - Na_2CO_3$, $2 - Na_2SO_4$, $3 - FeSO_4 \times H_2O$, $4 - Ca(NO_3)_2$

For a clearing $r=3\times10^{-3}$ the lower and upper limits of most materials are 0.2×10^{-3} and 2×10^{-3} m, respectively. The larger fraction of the product mass is below this upper limit and covers a much more narrow range. For example, for urea at a rotation speed n = 20 rpm, more than 90% of the product is in the $(0.8–1.6)\times10^{-3}$ m range. For $n=50$ rpm the range is $(0.3–1)^{-3}$ m. The similarity of the size distribution and the clearing-related, material-independent size limits indicate that the grinding element is indeed effective.

Calculations were carried out to determine the smallest particle size (d_m) which occurs in the product. The well-known limiting sedimentation rate was used for the calculations which is valid in the transitional range ($Re=2.500$) when the resistance of the medium can be described as 18.5 $Re^{-0.6}$. The porosity [3], and shape factor (approximately 0.7) were also taken into consideration in the calculations. By taking the actual linear gas velocity as the limiting sedimentation velocity, the corresponding d_m values were calculated. The results are shown in *Table 1* along with the size limits of the smallest sieve fraction of the product and its relative amount.

It can be seen from *Table 1* that the calculated smallest particle size (d_m) and the lower size limit of the smallest sieve fraction (x_{m1}) agree sufficiently well. The relative amount of particles present in the smallest sieve fraction is always less than 5% w/w.

The relationship between the upper size limit of the product and the major operation parameters of the grinder was also tested *(Table 2)*. It could be

Table 1

Material	u (m/s)	$d_m\times10^3$ (m)	$(x_{m1}-x_{m2})\times10^3$ (m)	ΔG_m (wt%)
$CO(NH_2)_2$	0.5	0.18	0.2–0.4	4.8
	0.66	0.23	0.2–0.4	0.4
Sugar	1.20	0.32	0.4–0.6	0.8
	0.78	0.22	0.2–0.4	0.8
NaCl	0.47	0.12	0.1–0.2	3.9
	0.60	0.17	0.1–0.2	0.6
Na_2CO_3	0.74	0.15	0.2–0.4	0.5
Na_2SO_4	1.10	0.21	0.4–0.6	2.4
$Ca(NO_3)_2$	0.83	0.17	0.2–0.4	0.7
$FeSO_4\times H_2O$	0.93	0.17	0.2–0.4	3.9

Table 2

Material	n (min^{-1})	$r\times10^3$ (m)	$(x_{M1}-x_{M2})\times10^3$ (m)	ΔG_M (wt%)
$CO(NH_2)_2$	50	3	1.3–1.6	3.2
	20	3	1.6–2.0	4.9
Sugar	50	3	2.0–2.2	2.7
	80	3	1.6–2.0	0.9
NaCl	40	2	1.0–1.3	2.6
	30	2	1.0–1.3	7.2
Na_2CO_3	60	3	1.6–2.0	3.6
Na_2SO_4	60	3	1.6–2.0	7.8
$Ca(NO_3)_2$	60	3	1.6–2.0	11.4
$FeSO_4\times H_2O$	60	3	1.6–2.0	1.7

concluded that particles equal to or larger than the size of the clearance were missing from the product.

The size of the largest particle (d_M), which is approximately equal to the upper size limit of the largest sieve fraction (x_{M2}) primarily depends on the size of the clearance, but it also depends on the rotation speed of the grinding element. For example, for sugar and urea, the upper size limit decreased by 10 and 20% when the rotation speed was increased. At the same time, for NaCl increased rotation speed did not influence the upper size limit, but decreased to one third the amount of particles present in the upper sieve fraction. In the majority of cases, the size of the largest particles closely agrees with 2/3rds of the size of the clearance.

The overall size interval ranged between $(1.1–1.9)\times10^{-3}$ m for the operational parameters used *(Table 3)*.

Table 3

Material	$r\times10^3$ (m)	n (min^{-1})	$(d_M-d_m)\times10^3$ (m)	$\Delta x_{90}\times10^3$ (m)	$\frac{\Delta x_{90}}{d_M-d_m}\times100$ (%)
$CO(NH_2)_2$	3	50	1.42	1.0—0.3	49.3
	3	20	1.77	1.6—0.7	50.8
Sugar	3	50	1.88	1.9—0.8	58.5
	3	80	1.78	1.4—0.5	50.6
NaCl	2	50	1.18	0.9—0.2	59.3
	2	30	1.13	1.0—0.3	61.9
Na_2CO_3	3	60	1.85	1.4—0.4	54.1
Na_2SO_4	3	60	1.79	1.6—0.6	55.9
$Ca(NO_3)_2$	3	60	1.83	1.3—0.4	49.2
$FeSO_4\times H_2O$	3	60	1.83	1.6—0.5	60.1

In steady-state conditions, the larger part of the material withdrawn from the system occupies a much more narrow size fraction. For example, 90% of the material is within $(0.7–1.1)\times10^{-3}$ m, which is only 50–60% of the overall size interval.

Summary

The grinder carries out a partial and controlled size diminution operation. It grinds the particles which are larger than the size of the clearance, while it leaves practically intact those particles which are below this size limit. This claim is substantiated by the small amount of material present in the smallest sieve faction *(Table 1)*. Therefore, the product occupies a well-defined size-range, which can be predicted from the material characteristics and the setting of the operational parameters. Most of the particulate material (minimum 90% w/w) occupies a narrow size range, which—in the majority of cases—is only 50–60% as wide as the entire size interval *(Table 3)*.

SYMBOLS

d particle size (m)
$D(x)$ particle size distribution, (% w/w)
ΔG relative amount of material present in a given sieve faction, (% w/w)

n	rotation speed, (rpm)
r	distance between roller and the wall, (m)
Re	REYNOLDS number
x	sieve opening
Δx_{90}	size interval containing at least 90% w/w of the solid material, (m)
u	linear air velocity with reference to empty cross section, (ms^{-1})

Subscripts

m	smallest value
M	largest value

REFERENCES

1. DENCS, B. and ORMÓS, Z.: Hung. J. Ind. Chem. *1978* 6, 313
2. DENCS, B. and ORMÓS, Z.: Hung. J. Ind. Chem. *1978* 6, 323
3. DENCS, B. and ORMÓS, Z.: Hung. J. Ind. Chem. *1983* 11, 339

РЕЗЮМЕ

В стати приводятся параметры процесса, а также детально описаны параметры определяющие действие дробильного органа. Изучено распределение размера частиц полученных в условиях стационарного процесса. Рассчитан нижний пределный размер продукта. Изучено влияние технологических параметров дробильного органа на размер частиц и на его нижний и верхний пределы.

HUNGARIAN JOURNAL
OF INDUSTRIAL CHEMISTRY
VESZPRÉM
Vol. 11. pp. 357–369 (1983)

ADSORPTION OF VAPOUR MIXTURES ON ACTIVATED CHARCOAL. I.

EQUILIBRIUM AND KINETIK INVESTIGATIONS

J. NÉMETH, S. BATICZ and M. PÉTER-HORÁNYI

(Research Institute for Technical Chemistry of the Hungarian Academy of Sciences, Veszprém)

Received: January 29, 1983

Adsorption of methanol and a water vapour mixture on activated charcoal was studied. It can be concluded from the adsorption isotherms of the pure components and of the mixtures, that the presence of water (up to 11 g/m^3) increases the equilibrium adsorption values, which correspond to a methanol vapour phase concentration of 10 g/m^3. It could be shown by the analysis of the kinetic curves, recorded on single charcoal particles, that the presence of water vapour increased the rate of methanol adsorption over the concentration ranges tested. This means that compared to pure methanol, higher transfer coefficients were obtained.

Introduction

Often, gas streams subjected to various chemical operations contain significant amounts of vapour. Former adsorption studies generally dealt with the adsorption from gas phases of single components. However, increasing solvent costs necessitate the study of multicomponent vapour adsorption phenomena.

There are relatively few papers, which dealt with the adsorption of vapours from carrier gases. In the main, a qualitative description is given [1, 2], noting that the number of concentration distribution curves in the stationary adsorbent bed is equal to that of the components. It was observed that the higher the molecular weight of the component, the stronger is its adsorption on charcoal. However, adsorption is also influenced by chemical characteristics, such as unsaturation, or by strong electrostatic forces, in gel-type adsorbents. The concentration distribution curves of less-strongly adsorbed components move through the adsorbent bed more rapidly (and their distribution curve is more elongated) than those of the more strongly adsorbed components. To make the situation even more complicated, the initial concentration distribution is influenced by the exchange—adsorption of the more strongly bound

component, i.e. SILOV's rule of parallel adsorption-zone-displacement cannot be applied for the description of mixed adsorption zones.

Thus, systems with saturation-type isotherms were studied more frequently than others [3]. Though there were a few attempts to compute different equilibrium types [4, 5], the problems have not yet been solved. For example, often the LANGMUIR-rule, i.e. that the presence of a second adsorbed component in equilibrium decreases the adsorbed amount of the first component, does not apply. Anomalies are rather frequent in water and alcohol vapour mixtures [6–10]. Since alcohol-water systems are of special importance in many branches of chemistry, the methanol–water system was selected for study. The technological aim was the removal of flammable methanol vapours, so charcoal, rather than molecular sieve or silica adsorbents, were selected. The latter are more selective for water vapour. In later parts of this paper, the kinetic and dynamic measurements will also be discussed, because these data are indispensible for the description of the time-dependent behaviour of the concentration distributions. In order to complete our knowledge of this system, the vacuum desorption data will also be presented, though vacuum desorption is not yet a common technique in the chemical industry.

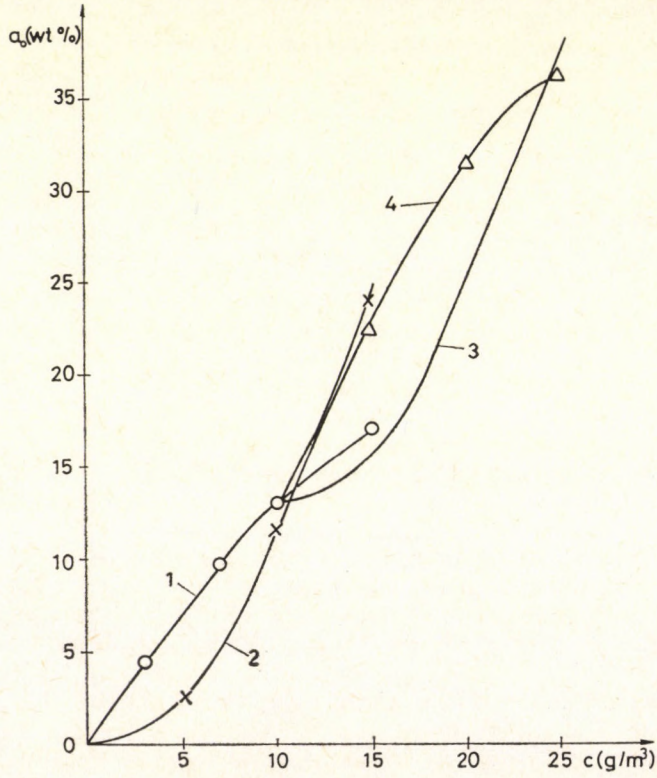

Fig. 1.

Adsorption isotherms at 20 °C

1 — methanol; *2* — water; *3* — sum of the methanol and water isotherms ($c = 10$ g/m³, constant); *4* — mixture of methanol and water vapour ($c_{methanol} = 10$ g/m³, const.)

Equilibria

Equilibria depend on the structure of the adsorbent, the chemical characteristics of the solute and adsorbent, the concentration (partial pressure) of the solute, and the temperature of the system. Knowledge of the equilibrium conditions is important for the determination of the adsorption capacity of the adsorbent.

The pure vapour adsorption isotherms of methanol and water, and the isotherm at 10 g/m^3 constant methanol concentration and varying water concentration, are shown in *Fig. 1.* Since the methanol isotherm is only slightly curved up to 10 g/m^3 (B.E.T. No. 1 type isotherm), it can be approximated by a straight line in the low concentration range. (Max. relative error: 15%). This considerably simplifies the mathematical formulae used in the description of adsorption kinetics.

In the concentration range tested, the adsorption isotherm of water follows the more rare B. E. T. No. 3 or No. 5 isotherms, and up to 11 g/m^3, it runs below, while above 11 g/m^3, it runs above the methanol isotherm.

The equilibrium values measured at 10 g/m^3 methanol and varying water vapour concentrations are shown by Curve 4 in *Fig. 1.* Curve 3 shows the hypothetical curve obtained by the addition of the equilibrium value corresponding to 10 g/m^3 methanol and Curve 2. It can be seen that Curve 4 runs above Curve 3, indicating that water vapour at ambient temperatures increases the equilibrium adsorption of methanol.

Kinetic Model

In porous adsorbents, adsorption takes place via several sub-processes. These are as follows:

1. Mass transfer through the external boundary surface area of the particle, external mass transfer for short.
2. Transport phenomena occurring in the pores (POISEUILLE-flow, pore-diffusion, VOLMER'S displacement in the adsorbed layer). These can be characterized by an effective transfer coefficient.
3. Adsorption proper (binding) on the surface of the adsorbent.

From a practical point of view, only the external mass transfer and mass transfer in the pores is of importance, because as BOER demonstrated [11], the time-scale of "binding" proper is in the 10^{-5} s range, while diffusion times related to the first two processes are in the few minutes range. Thus, when the overall adsorption rate is determined, the speed of "binding" proper does not need to be considered.

At constant driving force, the rate of mass transfer at the boundary of the external surface of a spherical adsorbent and the fluid phase, depends on the resistance of the boundary layer, which for flowing gases, depends on the flow rate. Analogous to heat transfer, mass transfer in the first subprocess can be described as:

$$\frac{dG}{dt} = \beta_F \cdot F[c_0 - c_F(a)] \tag{1}$$

where:

G — amount of material adsorbed in time t

β_F — mass transfer coefficient

F — external surface of the particle

c_0 — solvent vapour concentration in the carrier gas

$c_F(a)$ — solvent vapour concentration at the external surface (actual, momentary equilibrium vapour concentration corresponding to the actual adsorbed amount of solute).

However, external mass transfer is frequently described by another relationship, and especially so, in operation-design, by the so-called CHILTON–COLBURN factor:

$$j_D = Sh \times Sc^{-\frac{1}{3}} Re^{-1} \tag{2}$$

where:

$$Sh = \frac{2R\beta_F}{D_0} \tag{3}$$

$$Sc = \frac{\nu}{D_0} \tag{4}$$

$$Re = \frac{2Rv}{\nu} \tag{5}$$

and:

R — particle radius

D_0 — vapour diffusion coefficient in the carrier gas

ν — kinematic viscosity

v — linear flow rate of carrier gas

If only the REYNOLDS-number is used, then Eq. 2 becomes:

$$j_D = K \times Re^{-0.5} \tag{6}$$

where K varies according to the materials used.

MARCUSSEN [12] complied the available K values, and showed that in most cases, K varied between 0.80 and 0.97.

When external mass transfer is very rapid, then the overall adsorption rate depends on the rate of mass transfer in the pores. In the case of spherical adsorbents, this limiting case can be described mathematically by the material balance equation applied to an elementary spherical layer. In the case of a linear adsorption isotherm, adsorption rate [13] is obtained by the analytical solution of FICK's second diffusional differential equation:

$$\frac{\bar{c}(t)}{c_0} \sim \frac{a(t)}{a_0(t_\infty)} = \gamma = 1 - \frac{6}{\pi^2} \sum_{n=1} \frac{1}{n^2} \exp\left(-n^2 \frac{\pi^2}{R^2} D_e t\right) \tag{7}$$

where:

a — amount of vapour adsorbed in time t

a_0 — equilibrium amount of adsorbed vapour

c — vapour concentration in the pores of the particle
D_e — effective diffusion coefficient

It is known that from experimentally determined kinetic curves, the value of D_e can be evaluated by Eq. 7, or if the slope of the isotherm, A is also known, then the internal diffusion coefficient can be derived as:

$$D_i = D_e(1+A).$$

The situation is more complicated, when the adsorption rate depends on both the external and the internal mass transfer. Then, for a linear isotherm, the equation of the kinetic curve becomes:

$$\frac{a(t)}{a_0(t_\infty)} = \gamma = 1 - \sum_{n=1} B_n \exp\left(-\mu_n^2 \frac{D_e}{R^2} \times t\right) \tag{8}$$

where:

$$B_n = \frac{6Bi^2}{\mu_n^2(\mu_n^2 + Bi^2 - Bi)} \tag{9}$$

$$\mathrm{tg}\ \mu = \frac{\mu}{1 - Bi} \tag{10}$$

$$Bi = \frac{\beta_F \times R}{D} \tag{11}$$

the latter being the so-called BIOT-number.

The corresponding values of B_n and $tg\ \mu$ were published [13].

The previous equations were used for the evaluation of the measured kinetic curves.

Physical Characteristics of the System Studied

Methanol and water were used as solutes in nitrogen carried gas. Spherical particles of CHEMVIRON BPL activated charcoal were used as adsorbents. Its characteristics are listed in *Table 1.*

Table 1

Physical characteristics of the activated charcoal adsorbent used

B.E.T. surface area, m^2/g	1050—1150
Bulk density, g/cm^3	0.58—0.54
Pore volume, cm^3/g	0.80—0.85
Particle size (4×10 US mesh), mm	3
less than 2 mm, %	0—3
larger than 4.8 mm, %	0—5
Void volume (tapped packing), %	38—42%

The major physical characteristics of methanol are listed in *Table 2*.

Table 2

Physical characteristics of methanol

Boiling point (1013 mbar)	64.6 °C
Heat of evaporation (20 °C)	1173 kJ/kg
Refractive index	1.329
Saturated vapour conc.	0.164 kg/m^3
Vapour pressure (20 °C(	128 mbar
Normal diffusion coefficient	14.7×10^{-6} m^2/s
Kundsen diffusion coefficient (20 °C)	4.4×10^{-7} m^2/s
Integral adsorption heat	1712.5 kJ/kg
Lower explosion limit	5.5—6% v/v 73—74 g/Nm^3
Upper explosion limit	36.5% v/v
TWL value	200 ppm 260 mg/m^3

Experimental

Methods used to determine the adsorption kinetic curves on single particles are described in [14, 15]. Since the producer claims that CHEMVIRON BPL is an excellent adsorbent for solvents, including methanol, gravimetric methods were adopted.

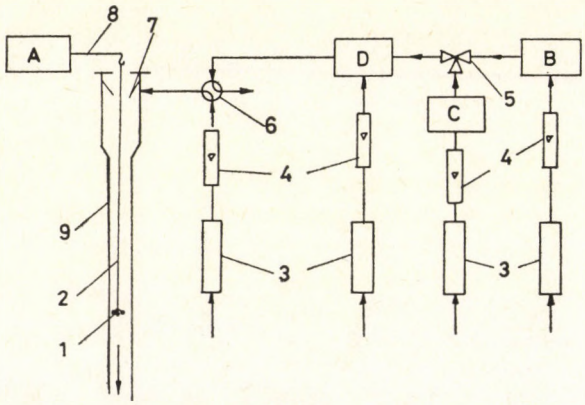

Fig. 2.
Experimental set up
A — balance, *B* — methanol vaporiser, *C* — water vaporiser, *D* — mixer, *1* — adsorbent, *2* — thread, *3* — molecular sieve drier, *4* — rotameter, *5* — distributor valve, *6* — four-port valve, *7* — baffle annulus, *8* — balance arm

The schematics of the system is shown in *Fig. 2*. A thin wire of 0.02 mm diameter was hung onto of the arms of a balance of 2×10^{-4} g sensitivity. Spherical particles were attached to the wire as shown in *Fig. 2*. Three particles of identical diameter (3.5 mm) were used. This increased the amount of solvent adsorbed in unit time, and improved the precision of the measurements.

The solvents were placed into thermostatted gas-washing bottles, and dry nitrogen was bubbled through the solvents. Nitrogen was thus saturated at the selected temperature. Solvent vapour concentrations required for the experiments were obtained by mixing the saturated and the dry nitrogen gas flows. It is assumed that adsorption proceeds isothermally, because thermostatted flowing nitrogen dissipates the heat of adsorption liberated on the single particles.

Results and Discussion

For comparison purposes, pure methanol was used first for the determination of the kinetic curves. Carrier gas flow rate was changed in these experiments. The kinetic curves obtained at 10 g/m³ methanol concentration are shown in *Fig. 3.*

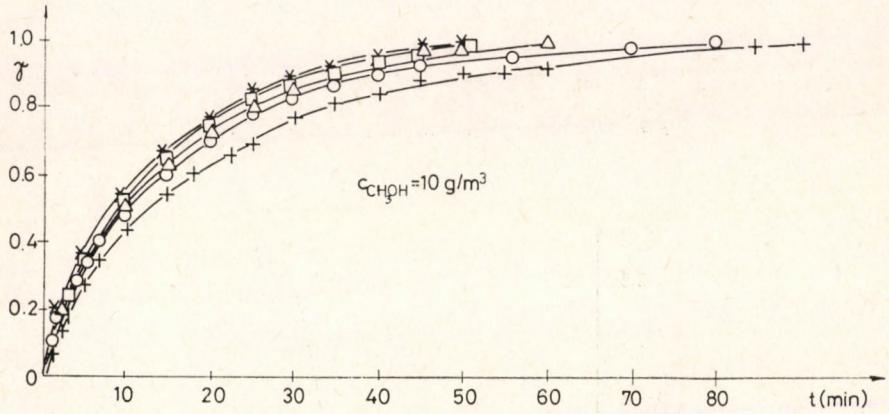

Fig. 3.
Kinetic curves of methanol at various gas velocities
+ $v=0.167$ m/s, o $v=0.33$ m/s, $v=0.667$ m/s
$v=1.0$ m/s, ✳o $=1.33$ m/s.

In *Fig. 4*, the curve obtained with a mixture of 10 g/m³ methanol and 10 g/m³ water is shown. It can be seen that in both cases the curves tend to a limiting value, as the carrier gas flow rate is increased. This means that above this value, the transfer rate cannot be increased any further, i.e. mass transfer in the pores becomes the rate controlling process. Kinetic curves obtained at this gas velocity (1.3 m/s) were used for the evaluation of the effective diffusion coefficient, D_e, as follows.

At first $n=1$ was assumed, and an approximate D_e was calculated from Eq. 7 using the $t_{0.5}$ experimental time, which corresponded to $\gamma=0.5$. Then, a series of curves were calculated by a computer, using D_e values in the vicinity of the previously determined D_e. This was followed by the calculation of the sum of the squares of difference between calculated (γ_s) and measured (γ) values as:

$$\sigma^2=\frac{1}{n}\sum_{i=1}^{n}(\gamma_{szi}-\gamma_i)^2 \tag{12}$$

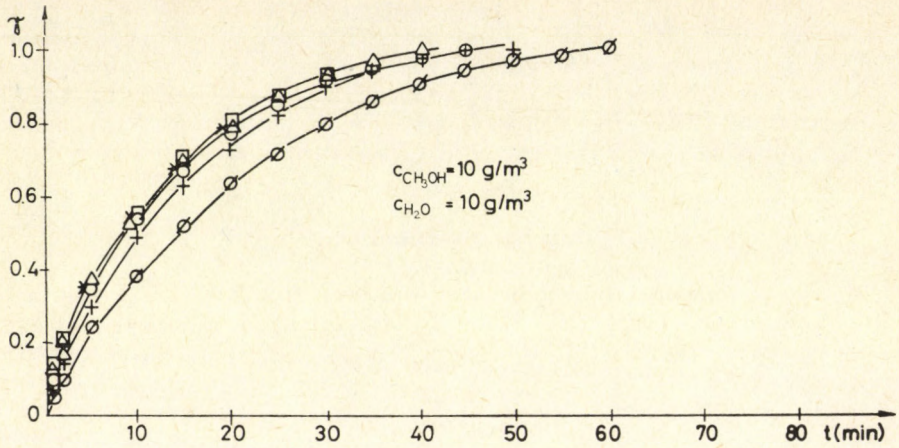

Fig. 4.

Kinetic curves of methanol and water mixtures at various gas valocities
$\Phi v = 0.1$ m/s, $+v = 0.167$ m/s, $ov = 0.33$ m/s
$v = 0.667$ m/s, $v = 1.0$ m/s, $*v = 1.33$ m/s

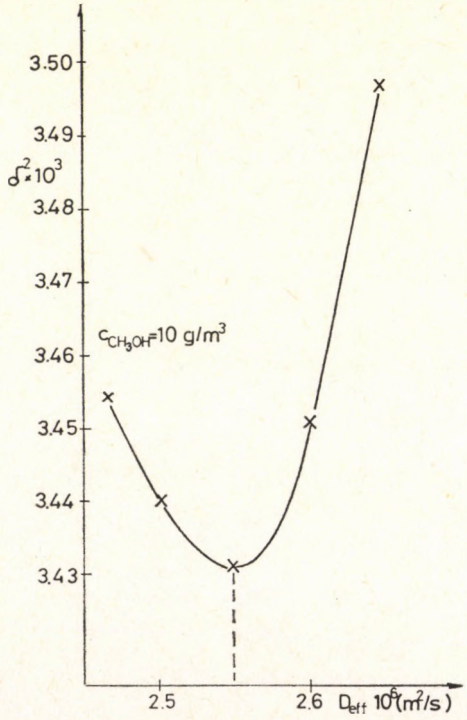

Fig. 5.

Determination of D diffusion coefficient by the minimalization of the square of error

The D_e value at the minimum of σ^2 was accepted as the one representing the best fit of Eq. 7 to the measured kinetic curves.

The results of one of these calculations are shown in *Fig. 5*.

Calculated (minimized σ^2) D_e values for the previously studied systems are listed in *Table 3*. With the help of the slope of the approximately linear isotherm, the internal diffusion coefficient, D_i was calculated. This value is necessary for the evaluation of the kinetic curves measured at lower gas velocities.

Table 3.

Diffusion coefficients of pure methanol and methanol plus water vapour mixtures

Solvent vapour	Methanol	Methanol plus water
D_e m²/s	2.55×10^{-6}	2.68×10^{-6}
A	1.06×10^{4}	1.02×10^{4}
d_i m²/s	2.71×10^{-2}	2.83×10^{-2}

In *Figs. 6* and *7*, the measured and calculated (using D_e-s from *Table 3*) kinetic curves are shown for methanol and methanol plus water vapour, respectively. Mesured and calculated curves agree sufficiently. The slight systematic error at the beginning and the end of the curves might be caused by slight deviations from the assumptions (slightly unisotopic particle structure, and slight deviation from ideal spherical shape, etc.).

The kinetic curves obtained at lower gas velocities were evaluated by Equations 8–11, which take into account both the internal and the external resistances.

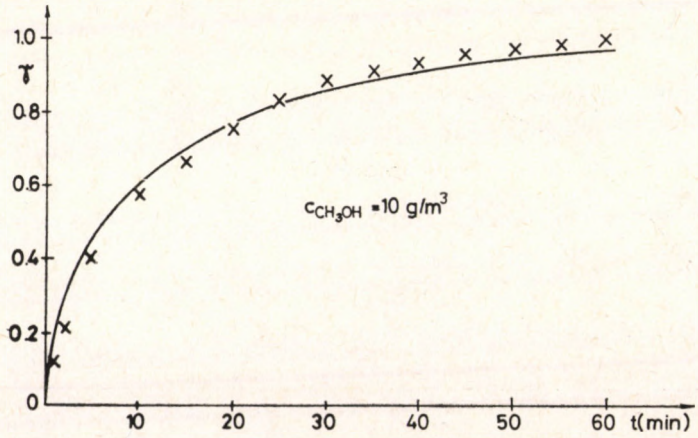

Fig. 6.
Kinetic curves of methanol
$v = 1.33$ m/s, $D_e = 2.55 \times 10^{-6}$ m²/s
— = calculated, × — measured

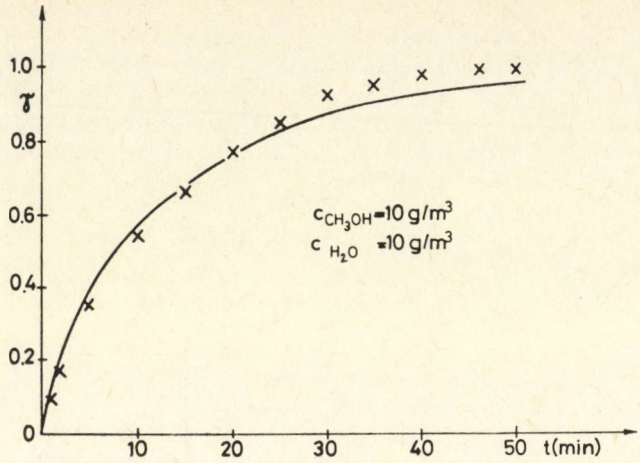

Fig. 7.
Kinetic curves of methanol and waters mixtures
$v = 1.33$ m/s, $D_e = 2.68 \times 10^{-2}$ m²/s
— = calculated, x — measured

Graphic differentiation of the initial section of the kinetic curves measured at various gas velocities yielded the external mass transfer coefficients, the β_F values. β_F and D_i internal diffusion coefficients from *Table 3* were then used to calculate the approximate Bi numbers (Eq. 11). Another minimalization, similar to Eq. 12, yielded the Bi value, which ensured the best fit of Eq. 8 to the measured kinetic curves.

As examples, the measured and calculated kinetic curves at gas velocity of 0.33 m/s are shown in *Fig. 8* and *9*, for pure methanol and the mixture of

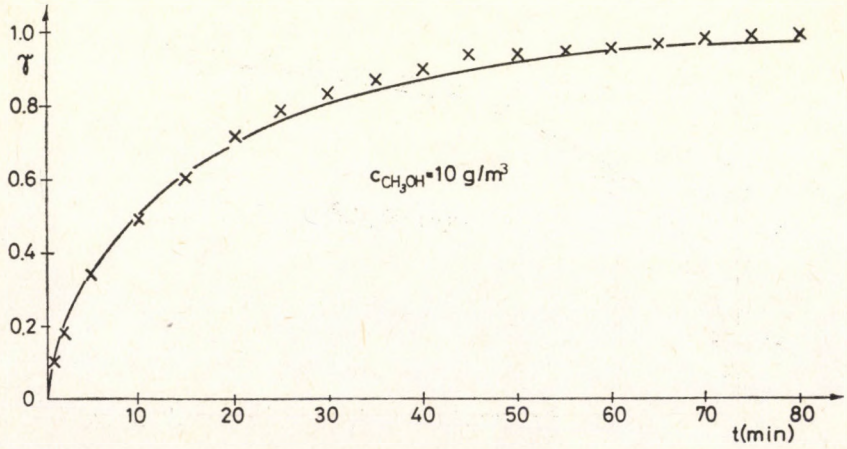

Fig. 8.
Kinetic curve of methanol
$v = 0.33$ m/s, $Bi = 17$
— = calculated, x — measured

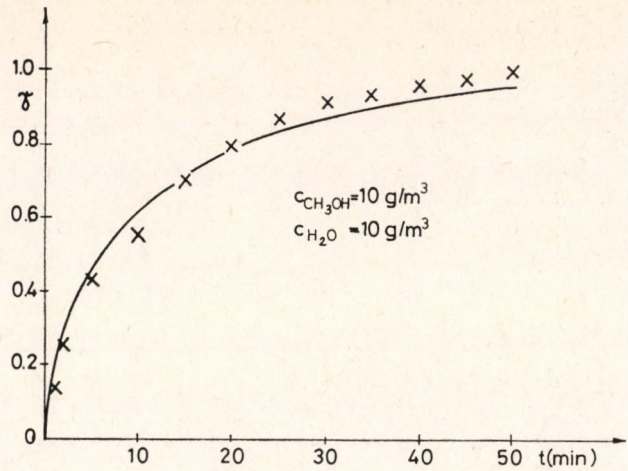

Fig. 9.
Kinetic curve of methanol — water vapour mixtures
$v = 0.33$ m/s, $Bi = 25$
— = calculated, x = measured

methanol and water, respectively. The agreement is adequate, in both cases.

The Bi-numbers, where the sum of the square of the error was minimum, were then used for the calculation of the β_F external transfer coefficients at various gas velocities. These values are summerized in the first column of *Table 4*.

The β_F values calculated from Eq. 2, using $K = 0.8$, are listed in the second column of *Table 4*. Agreement of the β_F values—calculated by different methods—indicates that over the gas velocity range tested, mass transfer depends on both the external and the internal resistances. This also follows from the respective Biot numbers, for Bi varied from 8 to 33.

Table 4

Mass transfer coefficients (β_F) for pure methanol and methanol plus water vapour mixture, respectively

Gas velocity m/s	β_F cm/s			
	Methanol		Methanol + water	
	1	2	1	2
0.1	—	—	1.3	2.0
0.166	1.7	2.1	2.5	2.5
0.33	2.8	2.9	3.9	3.6
0.67	3.8	4.1	5.2	5.1
1.0	4.9	5.1	6.3	6.3

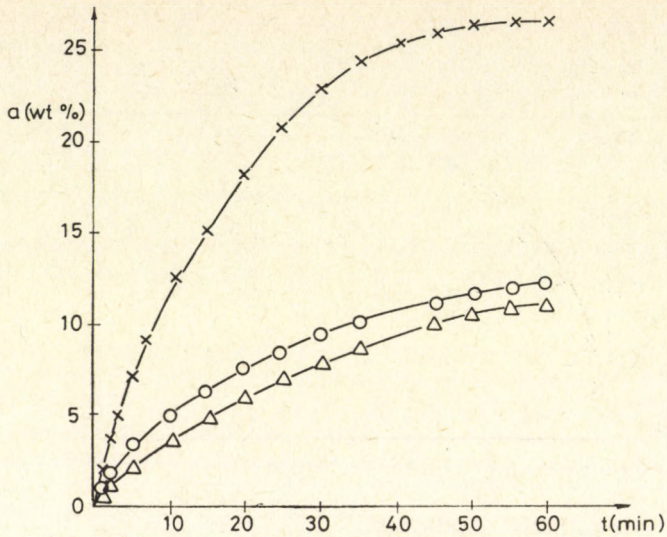

Fig. 10.
Kinetic curves
$v = 0.33$ m/s
Δ = water vapour (10 g/m³)
o = methanol (10 g/m³)
x = mixture of methanol and water (10 g/m³ each)

Higher transfer coefficients obtained for the mixture of methanol and water unequivocally proved that the system studied did not obey the LANGMUIR rule.

In order to illustrate other aspects of this point, the adsorption values expressed as a percentage of the weight of the activated charcoal are plotted against time in Fig. 10.

The larger percentage bound for the vapour mixture substantiates our previous claim. Its physico-chemical explanation will follow in Part 2 of this paper, which will discuss the results of adsorption tests in stationary beds.

REFERENCES

1. WILLIAMS, A. M.: Proc. Roy. Soc. *1919* A 96, 287–298 FER. JOUNG D. M., and CROMWELL, A. D.: Phys. Adsorption of Gases, London, 1962.
2. DUBINYIN, M. M. i CSMUTOV, K. V.: Fiziko-khimicheskie osnovi protigvogazovovo dela, Izd. Akad. khim. Zashch. 1939.
3. VERMEULEN, T.: Separation by adsorption methods, Advances in Chem. Eng. II. vol. N.Y. Academic Press Inc. 1958.
4. BRUNAUER, S.: The adsorption of gases and vapors, Princeton, USA, 1945.
5. YOUNG, D. M. and CROMWELL, A. D.: Phys. Adsorption of Gases, London, 1962.
6. KELCEV, N. V.: Osnovi adsorpcionnogo tekhniki, Izd. Khimiya, Moscow, 1976.
7. ROBELL, A. J., BORGARDT, G. F. and BALLOK, E. V.: Chem. Eng. Progr. Symp. Ser. *1966* 62, 76
8. UELI, H.: Über Gleichgewicht und Dynamik beider Mischadsorption ... Eidgenossische Techn. Hochule Zürich, 1972.
9. SZUHIN, N. G., SZUBBOTIN, A. J., JANKITOVA, L. N. i BEGUN, L. B.: Khim. Prom. *1981* 7, 405.

10. Dreher, H.: Dissertation (Doktor-Ing.) Techn. Hochschule Darmstadt, 1979.
11. De Boer, I. H.: Dynamical Character of Adsorption, Oxford, England 1953.
12. Marcussen, L.: Chem. Eng. Sci. *1970* 25, 1487.
13. Crank, I.: The mathematics of diffusion, Oxford, 1956.
14. Baticz, S.: Thesis, Budapest, 1972.
15. Werling, K. and Wimmerstedt, R.: Chem. Eng. Sci., *1980* 35, (8) 1783.

РЕЗЮМЕ

Авторы изучали адсорбцию смеси метанола и водяного пара на активном угле. На основе изотерм полученных для чистых компонент и смеси установили, что присутствие водяного пара (до 11 г/м^3) увеличивает равновесное значение адсорбции при концентрации метанола 10 г/м^3. На основе кинетических кривых снятых на отдельных частицах активного угла показали, что водяной пар увеличивает скорость адсорбции метанола т. е. получены большие по сравнению с чистым метанолом значения коэффициента массопередачи.

HUNGARIAN JOURNAL
OF INDUSTRIAL CHEMISTRY
VESZPRÉM
Vol. 11. pp. 371–386 (1983)

MODELLING AND EXPERIMENTAL INVESTIGATION OF VIBRO-PNEUMATIC SEPARATION

RENCENGIN BATMEND and K. ERDÉSZ*

(Department of Agricultural Machinery, Budapest Technical University, Budapest, Hungary

*Research Institute for Technical Chemistry of the Hungarian Academy of Sciences, Veszprém, Hungary)

Received: April 12, 1983

Using the theory of vibrated impacting systems, the mathematical model of particle motion on the active element of a vibrated pneumatic separator was developed. The model led to the derivation of the formula, which describes the average motion velocity of the particle. Experimental methods were developed for the determination of the material characteristics and the adequacy of the model was verified. The model and the physical system agreed sufficiently, but the superposition of the interactions between the separation—influencing parameters called for additional mathematical-statistical methods. A multiparameter experiment-design led to the regression equation of the separation efficiency indicators. This equation accounted for the major technological parameters as well. Comparison and analysis of the experimental results and those of the two models indicated that separation efficiency could be improved by increased vibration intensity, and by the adjustment of the apparatus parameters and the material characteristics.

Introduction

Wheat, transported from storage bins, contains foreign materials which have to be separated before milling. In the milling industry, foreign materials with particle sizes close to that of wheat are called difficult-to-separate contaminants, because conventional machines (screens, sieves, and bolters) are unable to separate them [1].

Separation of the difficult-to-separate contaminants is amply discussed in literature [1–10]. However, it is also known that many of the physical-mechanical aspects of the separation of multifractional particulate materials have not been clarified, because there are too many factors which influence the separation and back-mixing of particles (material characteristics, and technical-technological parameters, etc.), and therefore, no unifying theory has been developed.

Particulate materials are separated in bulk flows as a result of many interacting subprocesses (chaotic motion of the particles, particle impact, impact-induced mixing and separation, and back-mixing of the separated particles, etc.). These factors, make the mathematical modelling of the separation process quite difficult. Another set of problems arises from the distribution of the physical characteristics (size, friction and resilient characteristics, and aerodynamic characteristics, etc.) within the bulk phase, and their stochastic time-dependent distribution. Therefore, the characteristics of the discrete particles and of the bulk phase are different. The flowing particulate bulk phase is a complex system, in which various subprocesses occur at various hierarchy levels. This necessitates a system-theoretical approach, i.e. the recognition that the object studied has a complex internal structure, consists of many interacting elements, and interacts with its surroundings [11]. In general, complicated systems are described by complex models, in which —corresponding to the actual physical processes—the stochastic or deterministic character becomes dominant at various hierarchical levels. This approach will also be used in this paper.

The ultimate aim of mathematical modelling is the optimization of certain operations, the establishment of an overall control scheme, and the accounting for all major parameters. Due to the large number of parameters, verification of the optimization model requires an enormous amount of experimentation. Experimental work can be decreased by suitable multifactorial experiment design. Factorial experiments lead to polynomial regression equations, which describe the connection of the optimized parameter and the factors proper. Analysis of the regression equations allows the selection of the optimized operation ranges [12].

Separation of particulate material mixtures is based on the dissimilarity of some of the material characteristics of the components. Modern particle separators can detect, simultaneously, several of the material characteristics, and ensure improved separation. Such an improved separation method is the vibrated pneumatic separation method, where vibration of the bulk material is completed by the fluidization effects of gas flowing through the bulk phase.

There are several vibrated pneumatic separators on the market (Bühler-MIAG Simon, Golfetto, and Nagema, etc.) readily lending themselves to the development of efficient technologies. However, the further development of these machines, and the selection of their optimum operation parameters, require additional research. This paper presents the results of modelling work on vibrated pneumatic separators.

Mathematical Model of Particle Motion in Vibrated Pneumatic Separators

As an example for the typical design of modern, vibrated, pneumatic gravel-separators, the schematics of the TQAO–00–60 machine of Bühler-Miag is shown in *Fig. 1.* The material is fed through a hopper and metering device into the active element of the separator. The active element is a vibrated frame, equipped with an air-permeable cover. Essentially, material flows in

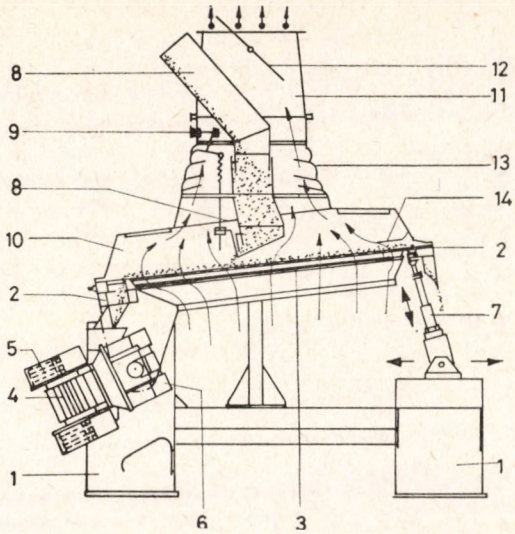

Fig. 1.
Schematics of the Bühler-Miag stone-separator
1 — frame, *2* — vibrated active element with feed port, *3* — air permeable cover, *4* — drive mechanism, *5* — counterweights, *6* — suspension of drive mechanism, *7* — telescope, *8* — feed and control mechanism, *9* — control screw, *10* — cover, *11* — air suction port, *12* — choke, *13* — rubber cover, *14* — baffle plate

a closed channel, as a thin layer, through the cover. The slant angle of the active element can be varied from the sides. The vibrating mechanism, equipped with a counterweight, is fastened to an axle, which is supported by three spings at each side. The driving mechanism and the active element are connected by a frame-system. The single-mass alternating system thus obtained is shown in *Fig. 2*. It can be seen that the periodic excitation force created by

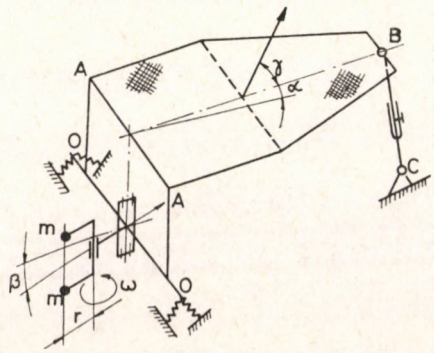

Fig. 2.
Kinematic schematics of the vibrated pneumatic separator

the rotating masses leads to a harmonic alternating motion. Vibration frequency of the active element can be varied via the rotation speed of the electromotor, while the vibration amplitude depends on the parameters of the system (exciting mass, spring constant, and damping, etc.). Due to its design, the time-dependent changes of the slant angle of the active element (α) and the angle of the excitation force with respect to horizontal (β) are negligible, i.e. these angles are practically constant. An external fan draws air through the air-permeable cover. This air then loosens the bulk material. Flow-rate of air can be regulated via the choke located in the suction throat.

Vibrated pneumatic separators have to remove gravel from wheat, even if the particle sizes are equal (removal of hard-to-separate contaminants).

Wheat, continuously fed to the vibrated active element (separating table), slides downward, while gravel particles move upward on the table, with a particular jolting motion, assuming that the vibrating pulses are of the right intensity.

At first, separated gravel particles have to overcome the resistance of micro-forces originating from impacts and friction with wheat grains. Since these forces are too small to measure directly, and have a stochastic time-distribution, the resultant resistance was taken as viscous resistance proportional with the velocity of the particles [13]. Air flowing through the bulk phase (wheat) results in a looser phase structure, which, in turn, promotes the jolting, jumping motion of gravel particles (micro-throwing, and vibrated impacting mode of motion [4, 5]). Flowing air increases the bouyancy of gravel particles. They are also effected by vibration and gravity *(Fig. 3)*.

The differential equation set which accounts for the above forces has the following form:

$$m\ddot{x}+K\dot{x}=\mathrm{mA}\ \omega^2 \sin(\omega t+\varphi)\cos\beta-mg\sin\alpha+P\cos\gamma \tag{1}$$

$$m\ddot{y}+K\dot{y}=\mathrm{mA}\ \omega^2 \sin(\omega t+\varphi)\sin\beta-mg\cos\alpha+P\sin\gamma \tag{2}$$

It is assumed that in steady-state conditions, particles experience an orderly periodic motion on the active element of the separator *(Fig. 4)*. The initial and boundary conditions of the differential equation set follow from the

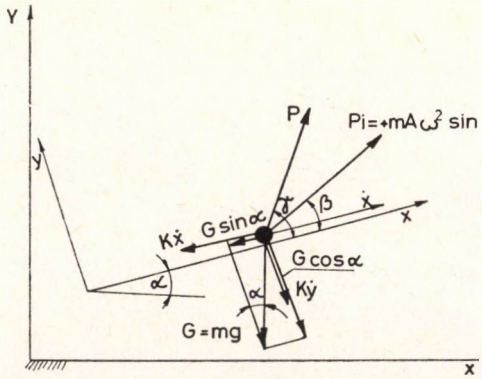

Fig. 3.

Forces acting upon a particle as it passes the active element of the vibrated pneumatic separator

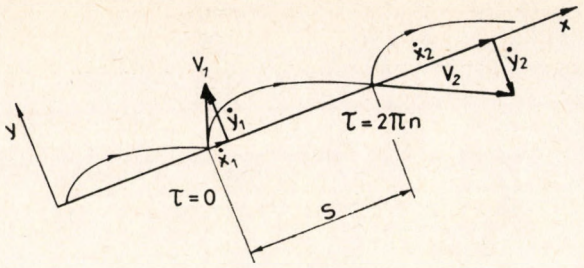

Fig. 4.
Schematics of particle motion

energy dissipation conditions [14]. Average displacement velocity of selected particles results as the ratio of displacement in direction x, and the period-time, $T = \frac{2\pi n}{\omega}$:

$$\overline{V} = \frac{s\omega}{2\pi n} \tag{3}$$

where:

n — period coefficient, $n = 1, 2, 3, \ldots$

Phase angle φ in differential equations (1) and (2) leads to the prerequisite of the vibrated impacting mode of motion and acts as the lowest limit of the evaluation range, because of the following relationship:

$$\cos\varphi \leq 1 \tag{1}$$

Derivation of the analytical solution is given in Appendix 1. The average displacement velocity of the particle reads:

$$\overline{V} = \left\{ \frac{\frac{A\omega^2 \sin\beta}{g(1+k^2)} (\cos\varphi - k\sin\varphi) \operatorname{ctg}\beta + (\sin\alpha - p\cos\gamma)(1 - e^{-k2\pi n})}{k^2 \left[\frac{1 - e^{-k2\pi n}(1-\lambda)}{\lambda} \right] 2\pi n} - \frac{\sin\alpha - p\cos\gamma}{k} \right\} \frac{g}{\omega} \tag{5}$$

In Eq. 5:

$$k = \frac{K}{m\omega} \tag{6}$$

is the dimensionless viscous resistance coefficient and:

$$p = \frac{P}{mg} \tag{7}$$

is the fluidization factor, which shows the ratio of the bouyancy force of up-

ward-flowing air and the weight of the average flow velocity of air and the minimum fluidization velocity:

$$p=\frac{u''}{u''_{\mathrm{mf}}} \tag{8}$$

Analysis of Eq. 5 leads to the factors, which influence the velocity of the particle to be separated:

a) with increasing amplitude *(A)* the velocity of the particle increases almost proportionally;
b) with increasing angular frequency (ω), i.e. increased rotation speed of the drive mechanism, the period factor *(n)* increases, and accordingly, the velocity of the particle increases according to a power function;
c) with increasing slant angle (a) the particle velocity decreases proportionally *(Fig. 5)*;

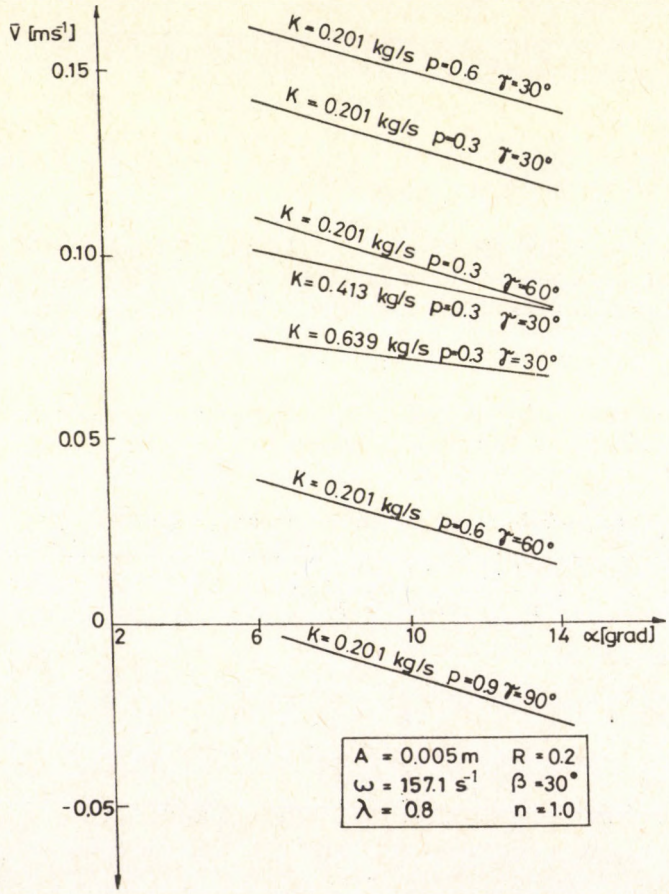

Fig. 5.
Particle velocity ($\bar{v}$) as a function of the slant angle of the active element (α)

Fig. 6.
Particle velocity ($\bar{v}$) as a function of the viscous resistance coefficient (K)

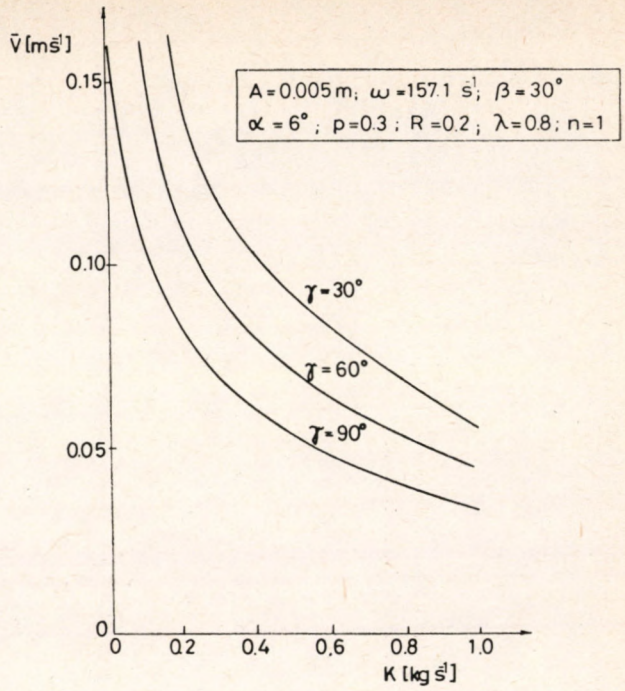

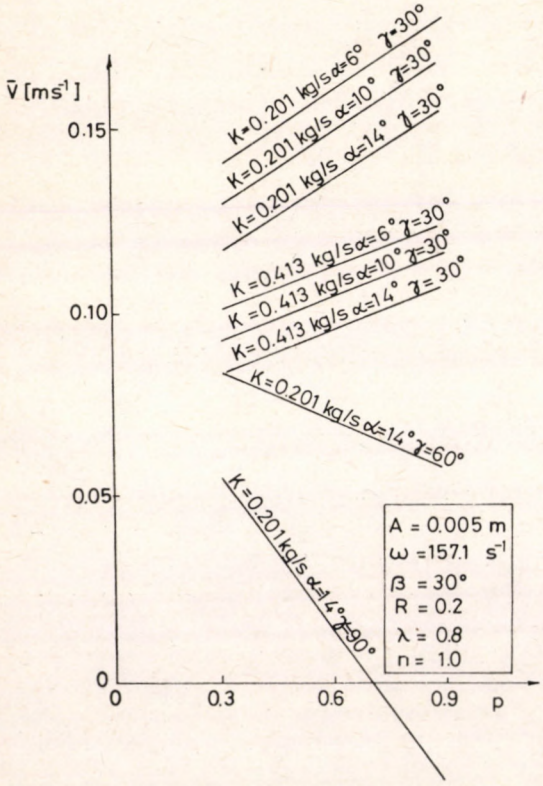

Fig. 7.
Particle velocity ($\bar{v}$) as a function of the extent of fluidization (p)

d) with increasing viscous resistance coefficient (K) the particle velocity decreases according to a power function *(Fig. 6)*;
e) with increasing bouyancy force (increased fluidization, p) the particle velocity increases, assuming that the angles of the air flow vector (γ) and the excitation vector (β) are practically identical. In other cases the particle velocity decreases (*Fig. 7* and *8*).

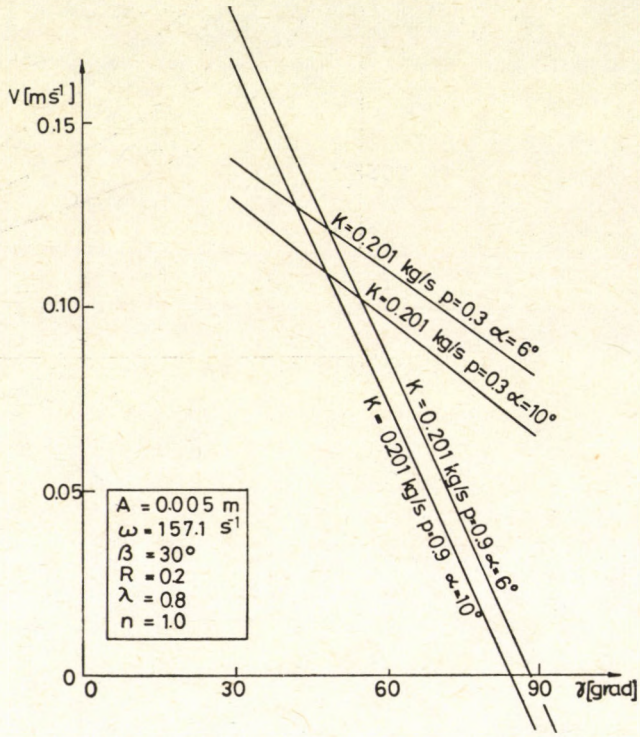

Fig. 8.
Particle velocity ($\bar{v}$) as a function of the direction of fluidizing air flow (γ)

Verification of the Mathematical Model

The mathematical model was verified by comparing the particle velocities calculated by Eqn. 5 with those obtained experimentally in a Type LA–K laboratory separator *(Fig. 9)*. Material characteristics required for the calculations were obtained partly from experiments, partly from model identification as follows:

a) impact coefficient (R) was determined by the statistical analysis of high speed photographs of free-falling particles;
b) viscous resistance coefficient (K) was obtained by model identification;
c) actual momentary friction coefficient (λ) was obtained by model identification;

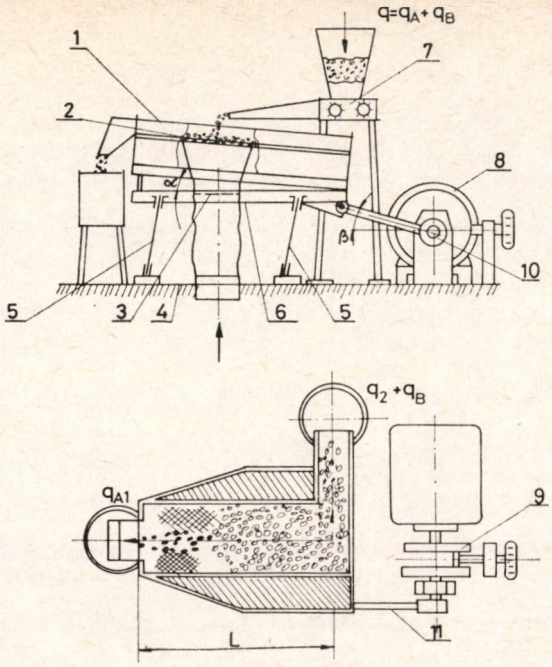

Fig. 9.

Schematics of the Type LA–K laboratory-scale separator
1 — separating table, *2* — air distributing cover, *3* — air inlet confusor, *4* — frame, *5* — springs, *6* — frame, *7* — vibrated feeder, *8* — electric motor, *9* — clutch, *10* — eccentric drive, *11* — drive rod

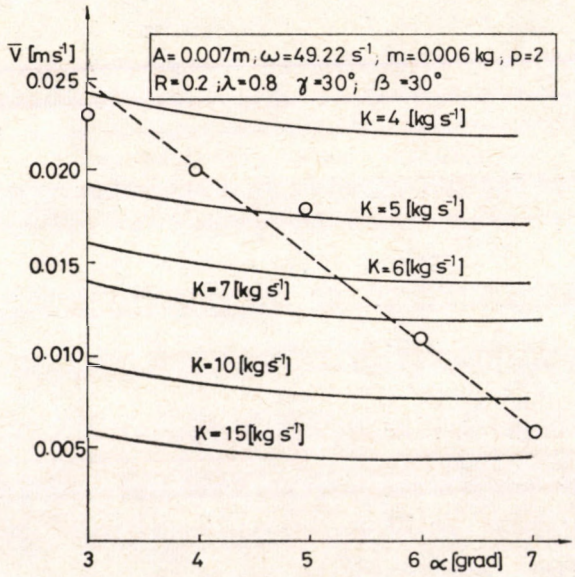

Fig. 10.

Comparison of measured and calculated values of the rate of particle separation

d) fluidization coefficient (p) was obtained from fluidization diagrams recorded in a vibrated fluidization apparatus.

Comparison of the calculated and measured particle velocities *(Fig. 10)* led to the following conclusions:

a) qualitatively, the mathematical model correctly represents the physical phenomena, i.e. over the parameter range tested, the trends of the calculated and measured velocity curves agree well;
b) there is a significant interaction between the factors which influence the separation of particles. This observation is well demonstrated in *Fig. 10*, where the viscous resistance coefficient (K) increases rapidly with α.

Since the mathematical model does not contain important technological parameters, such as the particle concentration or the mass feed rate, and because the deterministic model leads to deviations, statistic methods were used for the examination of the separation process.

Examination of the Efficiency of Vibrated Pneumatic Separation by Factorial Experiments

Factorial experiments are amply discussed in literature [15–17], so only the major steps to the 2^N-type factorial design are dealt with here.

The following indicators were used as optimization parameters of separation efficiency [5, 15].

a) Quality indicator

$$Y_1 = \Psi = \frac{\text{mass flow rate of separated particles}}{\text{mass flow rate of product}} = \frac{q_{A1}}{q_1} \tag{9}$$

b) Quantitative indicator

$$Y_2 = \eta = \frac{\text{mass flow rate of selected particles}}{\text{mass flow rate of particles to be selected}} = \frac{q_{A1}}{q_A} \tag{10}$$

The factors included in the experiments were selected on the basic of the analysis of the mathematical model. The variation levels were determined in preliminary experiments following the Latin-square design.

x_1: amplitude of vibration, $-A$
$x_1 = +1$, $A_{max} = 7$ mm
$x_1 = -1$, $A_{min} = 5$ mm
x_2: slant angle of the table, α
$x_2 = +1$, max 5.5°
$x_2 = -1$, min 4°
x_3 = extent of fluidization, $-$p
$x_3 = +1$, $p_{max} = 2$
$x_3 = -1$, $p_{min} = 1.2$
x_4: mass flow rate of feed, $-$q
$x_4 = +1$, $q_{max} = 0.02$ kg/s

$x_4 = -1$, $q_{min} = 0.01$ kg/s
x_5: concentration of particles to be separated, $-c$
$x_5 = +1$, $c_{max} = 5\%$
$x_5 = -1$, $c_{min} = 3\%$

The computer-generated matrix of the factorial experiment—including the interactions of the factors as well—was available from literature [18]. Calculation formulae are given in Appendix 2.

The regression equations of the significant factors are as follows:

$$y_1 = 0.1141 - 0.067x_2 + 0.0327x_3 + 0.0296x_4 + 0.08x_6 + 0.0446x_{16} + 0.027x_{17} \quad (11)$$

$$y_2 = 0.4469 + 0.1484x_1 - 0.1731x_2 - 0.0619x_3 - 0.0300x_4 - 0.044 = x_5 - 0.0662x_8 - 0.0478x_9 - \\ - 0.0531x_{10} + 0.1003x_{11} + 0.0725x_{14} - 0.0575x_{16} + 0.0856x_{17} \quad (12)$$

The calculated and the tabulated values of the FISCHER-criterion are:

$$F_1 = 2.77; \quad F_2 = 2.69; \quad F_{0.01} = 3.32;$$

and since:

$$F_{0.01} > F_1 > F_2,$$

the model is adequate.

Analysis of Eq. 11 and 12 led to the following conclusions:

a) the quality of vibrated pneumatic separation primarily depends on the slant angle of the table (α), the extent of fluidization (p) and the feed mass flow rate (q). Increasing α impedes the quality (negative b_2), while the other two parameters improve the quality of the separation (b_3 and b_4 are positive numbers).
b) the simultaneous increase of the amplitude, the slant angle and the extent of fluidization improves the quality of separation (b_{16} is positive);
c) increased amplitude improves the yield of separation (b_1 is positive);
d) simultaneous increase of the extent of fluidization and feed rate (b_{11}), simultaneous increase of the extent of fluidization and particle concenttration (b_{14}), simultaneous increase of the slant angle, extent of fluidizaion and feed rate (b_{17}) all improve the productivity of separation;
e) from among the negative coefficients, the effects of slant angle are of importance (b_2), because increased slant angle decreases the yield and lowers the quality of separation. Therefore, the slant angle should not be increased beyond the necessary value.

Results of Vibrated Pneumatic Separation Experiments

It was assumed that the motion of particles depends on deterministic forces (i.e. on forces which can be defined unequivocally). Accordingly, the mathematical model of particle motion was developed, and the formula for the calculation of the average rate of particle separation was derived. An experimental method was also developed to verify the mathematical model. These experiments showed that a viscous resistance (i. e. one that is proportional to the velocity of the particles) acts upon the particles in the fluidized layer.

It was concluded that qualitatively, the model gave an adequate description of the particle motion, and that the factors were also interrelated.

The effects and interactions of random (stochastic) subprocesses are indirectly manifested in the quality indicators of the separation process. The regression equations, which were obtained in the factorial experiments, were verified, and the truely influential factors were identified.

Comparison of the results obtained by the two different modelling methods showed that:

- the optimum operation modes of vibrated pneumatic separation occur at higher vibration parameter values ($A=5$–7 mm, $\omega=105$ s^{-1});
- the efficiency of the separation process can be improved by the proper matching of separation parameters and material characteristics;
- theoretically, vibrated pneumatic separation can be used to separate any particulate material mixture, if there is a difference between the resilient and friction characteristics of the particles.

Acknowledgement

The authors are indebted to Professor A. ZALKA and V. THERNESZ, of the Department of Agricultural Machinery, Budapest Technical University, for their support in providing the facilities for this years-long project, and to Dr. J. NÉMETH, scientific consultant to the Research Institute for Technical Chemistry of the Hungarian Academy of Sciences, Veszprém, for discussion of the manuscript.

APPENDIX 1

Derivation of the Average Motion Velocity of a Particle Experiencing Periodic Vibrated Impact Motion.

Based on *Fig. 4*, the impact conditions are:

$$R=-\frac{\dot{y}_1^*}{\dot{y}_2^*} \tag{I.-1}$$

$$1-\lambda=\frac{\dot{x}_1^*}{\dot{x}_2^*} \tag{I.-2}$$

The dimensionless forms of the differential equations of motion are:

$$\ddot{x}^*+k\dot{x}^*=A^*\cos\beta\sin(\tau+\varphi)-(\sin\alpha-p\cos\gamma) \tag{I.-3}$$

$$\ddot{y}^*+k\dot{y}^*=A^*\sin\beta\sin(\tau+\varphi)-(\cos\alpha-p\sin\gamma) \tag{I.-4}$$

where: $\tau=\omega t$; $A^*=A\frac{\omega^2}{g}$

and the differential terms are multiplied by $\frac{1}{g}\omega^2$; $\frac{1\omega}{g}$ and $\frac{1}{g}$, respectively.

The initial conditions are:

$$\tau=0,\quad x^*=0,\quad y^*=0,\quad \dot{x}^*=\dot{x}_1^*,\quad \dot{y}^*=\dot{y}_1^* \tag{I.-5}$$

which, after substitution into the general solutions of differential equations Eq. 3 and 4 yield:

$$0 = C_1 + C_2 - \frac{A^* \cos\beta}{1+k^2}(k\cos\varphi + \sin\varphi) \tag{I.-6}$$

$$0 = C_3 + C_4 - \frac{A^* \sin\beta}{1+k^2}(k\cos\varphi + \sin\varphi) \tag{I.-7}$$

$$\dot{x}_1^* = -kC_1 - \frac{A^* \cos\beta}{1+k^2}(\cos\varphi - k\sin\varphi) - \frac{\sin\alpha - p\cos\gamma}{k} \tag{I.-8}$$

$$\dot{y}_1^* = -kC_3 - \frac{A^*}{1+k^2}(\cos\varphi - k\sin\varphi) - \frac{\cos\alpha - p\sin\gamma}{k} \tag{I.-9}$$

The boundary conditions are:

$$\tau = 2\pi n, \quad x^* = S^*, \quad y^* = 0, \quad \dot{x}^* = \dot{x}_2, \quad \dot{y} = \dot{y}_2 \tag{I.-10}$$

After substitution into the general solution, we obtain:

$$S^* = C_1 e^{-k2\pi n} + C_4 - \frac{A^* \cos\beta}{1+k^2}(k\cos\varphi + \sin\varphi) - \frac{(\cos\alpha - p\sin\gamma)2\pi n}{k} \tag{I.-11}$$

$$O = C_3 e^{-k2\pi n} + C_4 - \frac{A^* \sin\beta}{1+k^2}(k\cos\varphi + \sin\varphi) - \frac{(\cos\alpha - p\sin\gamma)2\pi n}{k} \tag{I.-12}$$

$$x_2^* = -kC_1 e^{-k2\pi n} - \frac{A^* \cos\beta}{1+k^2}(\cos\varphi - k\sin\varphi) - \frac{(\sin\alpha - p\cos\gamma)}{k} \tag{I.-13}$$

$$y_2^* = -kC_3 e^{-k2\pi n} - \frac{A^* \sin\beta}{1+k^2}(\cos\varphi - k\sin\varphi) - \frac{(\cos\alpha - p\sin\gamma)}{k} \tag{I.-14}$$

Integration coefficient C_3 can be obtained from Eq. 7 and 12:

$$C_3 = -\frac{(\cos\alpha - p\sin\gamma)2\pi n}{k(1 - e^{-k2\pi n})} \tag{I.-15}$$

Impact condition (1) and Eq. 9 and 14 yield:

$$-R\dot{y}_2^* - \dot{y}_2^* = -kC_3(1 - e^{-k2\pi n}) \tag{I.-16}$$

$$\dot{y}_2^* = -\frac{(\cos\alpha - p\sin\gamma)2\pi n}{1+R} \tag{I.-17}$$

The phase angle is obtained from Eq. 14 and 17:

$$\varphi = \arccos\frac{(\cos\alpha - p\sin\gamma)\sqrt{1+k^2}}{A^* \sin\beta}\left[\frac{2\pi nk(1 + Re^{-k2\pi n}) - (1+R)(1 - e^{-k2\pi n})}{(1+R)\times(1 - e^{-k2\pi n})k}\right] - \operatorname{arc\,tg} k \tag{I.-18}$$

Integration constant C_1 can be determined from the phase angle, Eqn. 8 and 13, and the impact condition (2):

$$C_1 = \frac{\left[\frac{A^* \sin\beta}{1+k^2} + (\cos\varphi - k\sin\varphi)\operatorname{ctg}\beta k - (\sin\alpha - p\cos\gamma)\right]}{k^2[1 - e^{-k_2\pi n}(1-\lambda)]} \tag{I.-19}$$

Finally, displacement S is obtained from Eq. 6 and 11:

$$S = \left[-C_1(1 - e^{-k2\pi n}) - \frac{(\sin\alpha - p\cos\gamma) + 2\pi n}{k}\right]\frac{g}{\omega^2} \tag{I.-20}$$

APPENDIX 2

Coefficients of the regression equations were calculated by the following formula:

$$b_1 = \frac{\sum_{i=1}^{n} x_{ji}\bar{y}_i}{N} \tag{II.-1}$$

The so-called t-test was used to test the significance of the coefficients:

$$\Delta b_i = \pm t \times S_{ij} \tag{II.-2}$$

where:

Δb_i — the half width of the confidence interval;
t — the tabulated value of the Student's criterion;
S_{ij} — is the standard deviation.

The coefficient is significant, when the relationship:

$$(b_i) \geq \Delta b_i \tag{II.-3}$$

holds.

The FISCHER's criterion was used to test the adequacy of the polynominal regression model:

$$F = \frac{S^2}{S_y^2} \tag{II.-4}$$

where:

$$S^2 = \frac{\sum_{i=1}^{n} y_i^2}{f} \tag{II.-5}$$

$$S_y^2 = \frac{\sum_{i=1}^{N} \sum_{i=1}^{n} (y_{ij} - \bar{y}_i)^2}{N(n-1)} \tag{II.-6}$$

The model is adequate when the relationship:

$$F_{\text{tabulated}} > F_{\text{calculated}} \tag{II.-7}$$

holds.

SYMBOLS

A — amplitude of vibration, m
b — coefficient
c — concentration
F — FISCHER's criterion
f — degree of freedom in the experiments
g — gravity constant, m/s²
K — viscous resistance coefficient, kg/s
k — dimensionless viscous resistance coefficient
L — distance on the experimental separator, available for particle separation, m
m — mass of particle, kg
N — number of experiments

n — period coefficient
P — bouyant force of the fluidizing air, N
p — fluidization coefficient
q — material flow, kg/s
R — impact coefficient
s — standard deviation
S — displacement of particle in direction, x
t — time, s
t — Student's criterion
u'' — average gas velocity, m/s
u''_{mf} — minimum fluidization gas velocity, m/s
x — coefficients of the factorial experiment design
y — optimalization parameters
$x, y, \dot{x}, \dot{y}, \ddot{x}, \ddot{y}$ — coordinates and time-derivatives of particle motion
α — slant angle, grade
β — angle of excitation force, grade
γ — angle of fluidizing air flow, grade
η — quantitative indicator of separation efficiency
φ — phase angle of impact, grade
λ — momentary friction coefficient
Ψ — qualitative indicator of separation efficiency
τ — dimensionless time
ω — angular frequency, 1/s

Subscripts

A — components to be separated (gravel)
B — base particles (wheat)
1 — direction of separation
2 — direction of back-mixing
i — columns
j — raws
q — number of repetitions
* — dimensionless amplitude, coordinates and their derivatives
· — time derivative

REFERENCES

1. Drogalin, K. V., Zhigankov, B. V. i Karpov, M. V.: Otchistka semyan ot trudnotdelimih primesei, Kholos, Moscow, 1978 (in Russian)
2. Yegorov, G. A.: Tekhnologia pererabotki zerna, Kholos, Moscow, 1977 (in Russian)
3. Gortinski, V. V., Gemski, A. B. i Boriskhin, M. A.: Processi Separirovania na zernoperabitayuschih predpriyatiah, Kholos, Moscow, 1980 (in Russian)
4. Blekhman, J. J. i Dzhanelidzhe, G. Y.: Vibrationoie peremeshenie, Nauka, Moscow, 1973 (in Russian)
5. Kobrinskii, A. E. i Kobrinskii, A. V., Vibroudarnie systemi, Nauka, Moscow, 1973 (in Russian)
6. Erdész, K., Gortinskii, V. V., J. Hung. Ind. Chem. *1980* 1, 97–108
7. Erdész, K.: Hung. J. Ind. Chem. *1980* 8, 109–116.
8. Erdész, K.: Hung. J. Ind. Chem. *1980* 8, 137–142
9. Thernesz, V.: Gabonaipar *1981* 28 2 45–58
10. Németh, J., Kováts, F. és Puskás, K.: Kémiai Közlemények *1970* 34 283–301.
11. Kafarov, V. V. i Dorokhov, J. N.: Systemni analyz processov Khimicheskoy tekhnologii, Nauka, Moscow, 1976 (in Russian)
12. Box, G. E.: Biometrika, *1952* 39, 49–52
13. Vibracii v tekhnike (handbook), ed. Blekhman, J. J., Vol. 2, p. 16, Mashinostroenie, Moscow, 1979 (in Russian)
14. Recengin Batmend: Thesis, Budapest, 1982 (in Hungarian)
15. Sváb, J.: Biometric Methods in Research, Mezőgazdasági könyvkiadó, Budapest, 1981 (in Hungarian)

16. HICKS, G. R.: Fundamental Concepts in the Design of Experiments, New York, Holt, Reinhart and Wilson, 1964.
17. DANIEL, C. U.: Applications of Statistics to Industrial Experimentation, John Wiley and Sons, New York, London, Sydney, Toronto, 1976.
18. HANGOS, K.: Method for the Selection of Experimental Series. A. Study. Eötvös Loránd University, Budapest, 1975 (in Hungarian)

РЕЗЮМЕ

Авторы с применением теории виброударных систем разработали модель движения частицы на рабочем органе вибропневматического сепаратора и выводили формулу средней скорости перемещения частицы. Разработали экспериментальные методики для определения физических свойств материальных частиц и контролировали адекватность модели. Установили, что математическая модель удовлетворительно согласуется с физической системой, но наблюдается суперпозиция взаимодействий между параметрами системы влияющих на процесс разделения, поэтому моделирование дополнили методами математической статистики. С помощью многофакторного эксперимента составили регрессионные уравнения для показателей эффективности разделения в которых были учтены и основные технологические параметры процесса. Сопоставлением и анализом экспериментальных и расчётных данных полученных двумя способами моделирования установили, что эффективность разделения можно повышать с увеличением интенсивности вибраций и также соответствующим материальным свойствам сепарируемой смеси подбором параметров оборудования.

HUNGARIAN JOURNAL
OF INDUSTRIAL CHEMISTRY
VESZPRÉM
Vol. 11. pp. 387–402 (1983)

OXIDATION OF COPPER(I) IONS IN THE PRESENCE OF AMMONIA AND VARIOUS AMINES

T. SCHÖNWEITZ*, L. VINCZE, S. PAPP

(Department of General and Inorganic Chemistry, University of Chemical Engineering, Veszprém, Hungary
* Electric Equipment Works, Power Electronics Factory, Budapest, Hungary)

Received: February 8, 1983

The oxidation of copper(I) ions by absorbed oxygen, in bubble-columns and stirred contactors, was investigated at 20 and 54 °C temperatures, in the presence of ammonia, monoethanolamine, diethanolamine and triethanolamine. The effective interfacial area in the bubble column, and its dependence on the gas flow rate and solution temperature were determined. The type of the reaction, and the constants k_2 and $k_L a$ were derived from experiments carried out in a stirred contactor.

Introduction

Copper(I) ions, formed during the etching of printed circuits, inhibit the etching reaction. Even though their spontaneous oxidation is fairly rapid, copper(I) ions accumulate in the etching solution. Etching technologies are difficult to modify, because only scanty information is available on the oxidation of copper(I)-amine systems, and even these papers use different systems of units and symbols. This prompted us to unify the available data base, and to complete it with further kinetic information.

Cuprous chloride, dissolved as amine complex, is rapidly oxidized by the absorbed oxygen. The process can be treated as absorption, accompanied by an irreversible chemical reaction [1, 4–7]. The reaction can be instantaneous or pseudo m-th order [4, 5]. For reactions pseudo m^{th} order, and for the conditions:

$$3 < \frac{R_{O_2}}{k_L[O_2^*]} \ll \frac{[Cu(I)]}{4[O_2^*]} \tag{1}$$

the specific rate of oxygen absorption becomes:

$$R_{O_2} = [O_2^*]\left(\frac{2}{n+1} D_{O_2} k_{m,n} [Cu(I)]^m [O_2^*]^{n-1}\right)^{1/2} \tag{2}$$

Since $a \cdot R_{O_2} = -(1/4)d[\mathrm{Cu(I)}]/dt$, and in ammonia-containing solutions: $m = n = 1$ [5], the kinetic equation reads:

$$-\frac{d[\mathrm{Cu(I)}]}{dt} = 4a[\mathrm{O_2^*}](D_{O_2}k_2[\mathrm{Cu(I)}][\mathrm{NH_3}])^{1/2}. \tag{3}$$

For instantaneous reactions, the condition [5]:

$$\frac{1}{k_L}\left(\frac{2}{n+1} D_{O_2}k_{m,n}[\mathrm{Cu(I)}]^m[\mathrm{O_2^*}]^{n-1}\right)^{1/2} \gg \frac{[\mathrm{Cu(I)}]}{4[\mathrm{O_2^*}]} \tag{4}$$

has to be fulfilled, and then, the specific rate of oxygen absorption is:

$$R_{O_2} = k_L[\mathrm{O_2^*}]\sqrt{\frac{D_{O_2}}{D_{\mathrm{Cu(I)}}}} \times \left(1 + \frac{D_{\mathrm{Cu(I)}}}{D_{O_2}} \times \frac{[\mathrm{Cu(I)}]}{4[\mathrm{O_2^*}]}\right) \tag{5}$$

If the condition:

$$\frac{D_{\mathrm{Cu(I)}}}{D_{O_2}} \times \frac{[\mathrm{Cu(I)}]}{4[\mathrm{O_2^*}]} \gg 1 \tag{6}$$

is fulfilled, then Eq. 5 can be simplified, leading to:

$$-\frac{d[\mathrm{Cu(I)}]}{dt} = k_L a[\mathrm{Cu(I)}]\sqrt{\frac{D_{\mathrm{Cu(I)}}}{D_{O_2}}} \tag{7}$$

SHARMA [11] found that for copper(I) concentrations less than 0.2 M, the reaction proceeds instantaneously, both with oxygen and air, while for copper(I) concentrations exceeding 0.5 M, and oxygen partial pressures smaller than 21 *kPa*, the reaction follows a pseudo m-th order. Since the specific rate of oxygen absorption depends on both the partial pressure of oxygen, the hydrodynamics and the order of the reaction, the latter can be determined from stirred contactor experimental data [5].

The effective interfacial area can be easily determined, when the reaction is pseudo m^{th} order, the gas-side mass transfer coefficient is negligible (and this is always the case in copper(I)-amine systems), and the reaction conditions fulfil Eq. 1. In this case, a can be calculated from the kinetic equation, Eq. 3. If the first relationship in Eq. 1 is not fulfilled, then the kinetic equation is somewhat different:

$$-\frac{d[\mathrm{Cu(I)}]}{dt} = 4a[\mathrm{O_2^*}](D_{O_2}k_2[\mathrm{Cu(I)}][\mathrm{NH_3}] + k_L^2)^{1/2} \tag{8}$$

After rearrangement, and raising to the second power, Eq. 8 becomes:

$$\left(\frac{d[\mathrm{Cu(I)}]/dt}{4[\mathrm{O_2^*}]}\right)^2 = a^2 D_{O_2}k_2[\mathrm{Cu(I)}][\mathrm{NH_3}] + (k_L a)^2 \tag{9}$$

When the left hand side is plotted agains the term $D_{O_2}k_2[\mathrm{Cu(I)}][\mathrm{NH_3}]$, a straight line is obtained with an intercept and slope $(k_L a)^2$ and a^2, respectively. This plot, the so-called DANCKWERTS' plot [2], allows for the simultaneous determination of a and $k_L a$.

For instantaneous reactions, the kinetic equation gives only the $k_L a$ term.

Table 1

Characteristics of the equipment used to determine the oxidation rate of copper(I) ions

Aparatus	Eq. used to calculate the effective interfacial area	Average values of the major parameters		
		V_g m s^{-1}	a m^2/m^3	drop size (mm)
Bubble column	$a = kV_g^{0.7}$	10^{-2} to 3×10^{-1}	50 to 350	—
Spray column	$a = \alpha L^{\beta *}$ $*V^{0.28}{}_H - 0.38$	10^{-2} to 3×10^{-1}	30 to 80	0.25 — 2.5
Packed bubble column	—	—	250 to 360	—
Stirred contactor	diameter (m) 7.5×10^{-2} to 1.5×10^{-1}		rotation speed (min^{-1}) 40 to 120 max. 200 [3]	

Bubble-columns [8], spray columns [9, 10], packed bubble-columns [6, 11, 12, 14] and stirred contactors [2–6, 15, 16] were used to study the oxidation of cuprous chloride. A few characteristics of the operation units used are summarized in *Table 1.*

Experimental

Bubble-columns and stirred contactors were used to study the oxidation of copper(I) by air.

Equipment

The characteristics of the bubble columns, and those of the stirred are listed in *Table 2.* The apparatus equipped with column *A* is shown in *Fig. 1.* Air is sucked through wash-bottle (1) to remove the air-borne particulate contami-

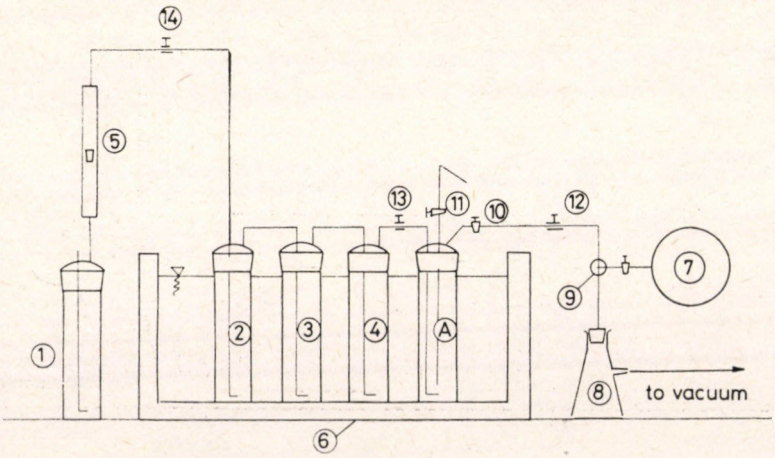

Fig. 1.
Experimental set-up with Column *A*

Table 2

Major characteristics of the columns and the mixed tank

Parameters	Column *A*	Column *B*	Mixed tank
Capacity, cm^3	150 cm^3	200 cm^3	400 cm^3
Diameter, cm	4.37 cm	3.11 cm	7.5 cm
Working height, cm	10.0 cm	26.4 cm	9.1 cm
H/D	2.3	8.5	—
Cross section area, cm^2	15.0 cm^2	7.58 cm^2	44.2 cm^2

nants. Its volumetric flow rate is determined by rotameter (5). Wash-bottles (2, 3, 4), thermostated to the temperature of the bubble column, contain solutions which—except for copper(I)—are identical to those used in the bubble column. Here, air is saturated by water and ammonia (or the respective amine), so that it leaves the composition of the system studied undisturbed. This measure is of special importance for ammonia, because it has high vapour pressure. Air flow rate is regulated by MOHR-clamps (12) and (13) (coarse and fine control). Samples are introduced through a syphon (11), following the closing of the fine control (13), and the resetting of the three-port valve (9). Excess pressure is supplied by pressurized air in a rubber bulb (7). Air passing through the system was sucked by a water aspirator, preceded by a buffer vessel (8).

In the case of column *B*, the apparatus was similar, except that due to its length, column *B* could not be thermostated. Consequently, these measurements were carried out at room temperature only.

In both columns, identical flow rates were used: 10; 20; 30 and 40 dm^3/hr, corresponding to 1.85×10^{-3}, 3.70×10^{-3}; 5.56×10^{-3}; 7.41×10^{-3} ms^{-1} and 3.67×10^{-3}; 7.33×10^{-3}; 1.1×10^{-2} and 1.47×10^{-2} m/s superficial velocities, respectively.

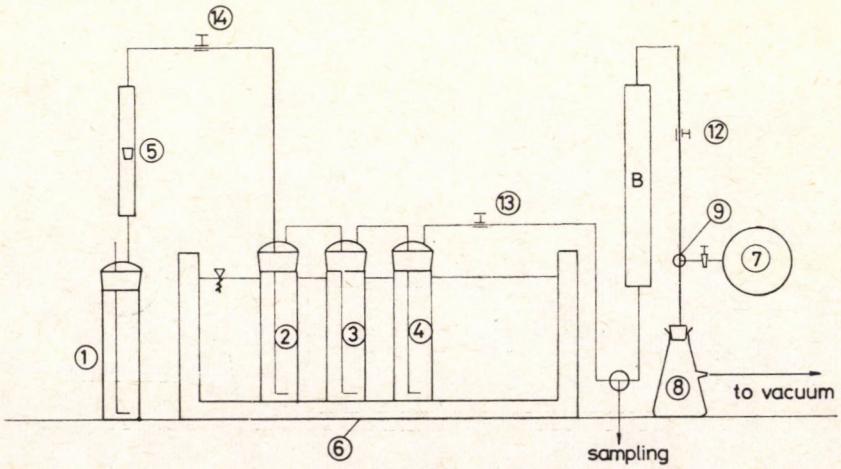

Fig. 2.
Experimental set-up with Column B

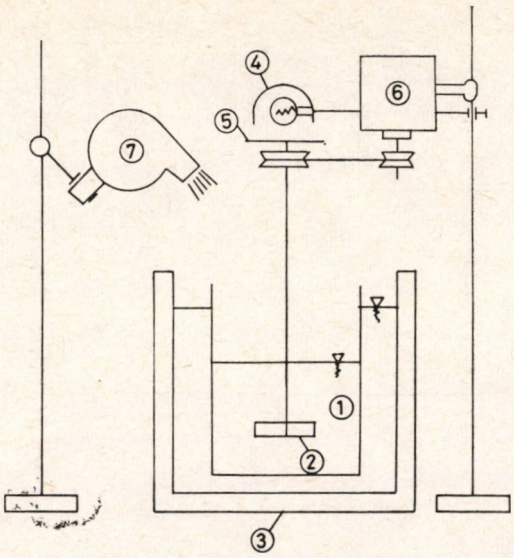

Fig. 3.
Mixed-tank system

The stirred contactor had a capacity of 600 cm^3. It was equipped with mixer (1) and placed into a thermostat (3) *(Fig. 3)*. Rotation speed was determined by a glow-discharge lamp (4), and stroboscope (5). Air above the solution was kept fresh by a fan (7). 2 cm^3 samples were obtained using polyethylene hypodermic syringes.

Chemicals Analysis

A Spectromom Type 204 UV–VIS spectrophotometer (MOM, Hungary) was used for the determination of the concentration of the copper(II) amine complexes formed. The copper(II)-amine complexes have absorption maxima around 620 nm (49–57 M^{-1} cm^{-1}). Copper(II) concentration was derived from measured absorbances, and the appropriate calibration curves.

Cuprous chloride was produced by sulphur dioxide reduction of copper(II), in sodium chloride solution [17]. Reagent grade diethanole amine (Merck), $CuSO_4 \times 5\ H_2O$, NaCl, monoethanolamine (MEA), triethanolamine (TEA) (Reanal) and ammonium hydroxide (Biogal) were used without further purification. Sulphur dioxide was a commercial grade product.

Results

Oxidation rate was first studied in aqueous ammonia solutions. Increasing ammonia concentrations resulted in higher reaction rates (*Fig. 4* and *5*), i.e. the reaction was not entirely momentary. 1 M ammonia solutions were used for the further experiments. For 0.05 M initial cuprous chloride concentrations, longer reaction times had to be used to ensure complete oxidation *(Fig. 6)*.

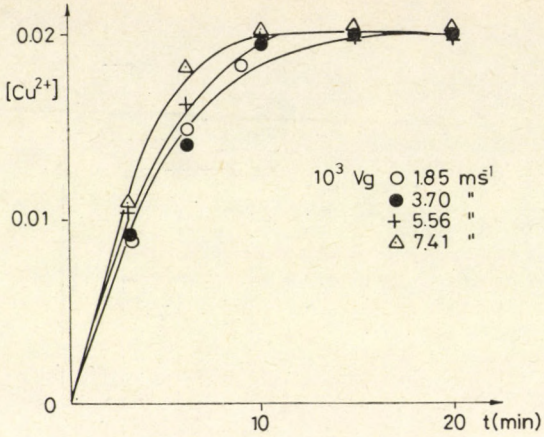

Fig. 4.
Oxidation of copper(I) (20 °C)
$[NH_3]=0.5$ M; $[Cu_0^+]=0.02$ M

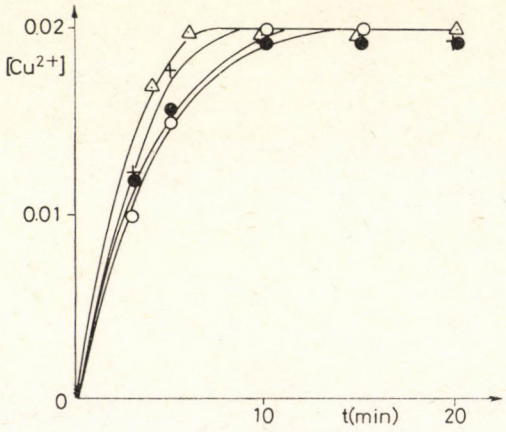

Fig. 5.
Oxidation of copper(I) (20 °C)
$[NH_3]=1$ M; $[Cu_0^+]=0.02$ M

At a 0.2 M overall copper concentration *(Fig. 7)*, 1 M ammonia proved insufficient to keep all copper(II) ions in solution. Apparently, at the pH value determined by the concentration of ammonium hydroxide, the solubility limit is exceeded, when the concentration of free copper(II) increases beyond a certain limit.

At the temperature of etching (54 °C) oxidation is slower than at ambient temperature, because decreased solution viscosity leads to increasing bubble coalescence, and a decreased effective interfacial area. At 54 °C temperature,

higher ammonia concentrations neither increase the reaction rate, nor prevent the precipitation of copper(II) hydroxide *(Fig. 8–11)*.

In the smaller cross-section-area-column, the superficial gas velocity is higher, consequently, the effective interfacial area is larger, and oxidation proceeds more rapidly *(Fig. 12, 13)*.

In the case of MEA, DEA and TEA, solution concentrations were selected according to production-proven rules. The concentrations were as follows: 200 gdm^{-3} ethanolamine, 50 gdm^{-3} ammonium nitrate, and 50 gdm^{-3} ammonium chloride.

In the presence of organic amines, oxidation of copper(I) ions proceeds more slowly. This can be explained by the slightly reducing nature of the amines,

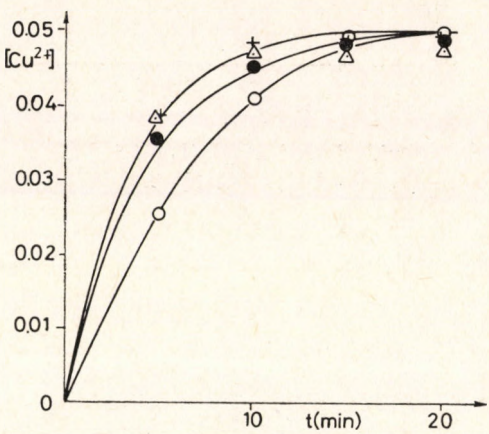

Fig. 6.
Oxidation of copper(I) (20 °C)
$[NH_3]=1$ M; $[Cu_0^+]=0.05$ M

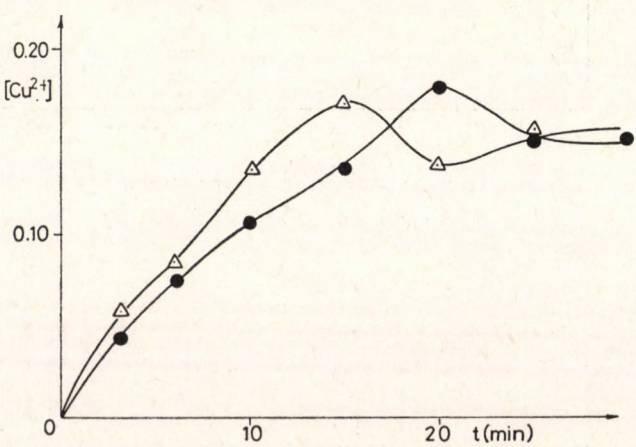

Fig. 7.
Oxidation of copper(I) (20 °C)
$[NH_3]=1$ M; $[Cu_0^+]=0.2$ M

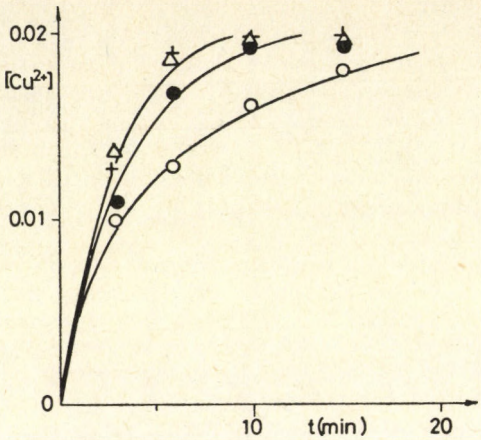

Fig. 8.
Oxidation of copper(I) (54 °C)
$[NH_3] = 1$ M; $[Cu_0^+] = 0.02$ M

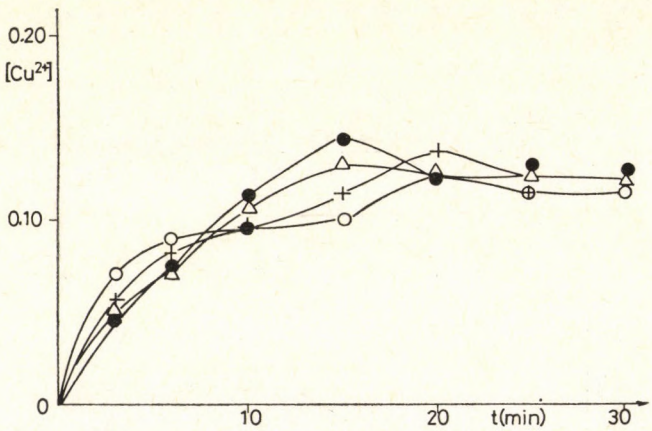

Fig. 9.
Oxidation of copper(I) (54 °C)
$[NH_3] = 1$ M; $[Cu_0^+] = 0.2$ M

and their steric hindrance. The increased steric hindrance of DEA becomes apparent from the comparison of the MEA and DEA data (*Fig. 14* and *15* vs. 16 and *17*). However, it is surprising that the same effects of TEA become evident only at higher temperatures.

Increasing temperatures led to decreased oxidation rates, for all of the ethanolamines. This can be explained by the decreased effective interfacial area (*Fig. 14–19*).

In column *B*, foaming prevented the use of higher superficial gas velocities. When the parameter settings were equal to those of column *A*, the oxidation

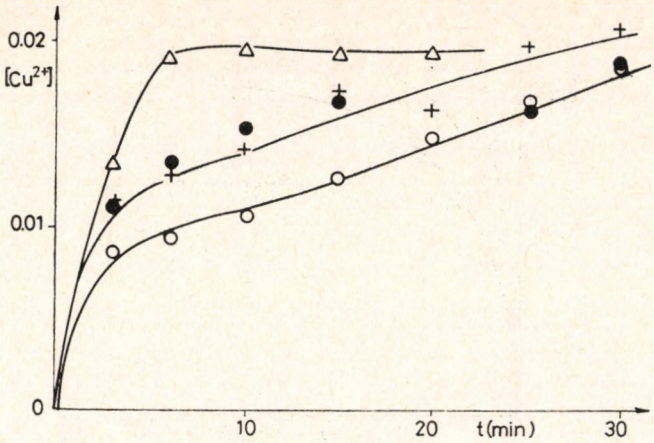

Fig. 10
Oxidation of copper(I) (54 °C)
$[NH_3] = 3$ M; $[Cu^+_{0.2}] = 0.02$ M

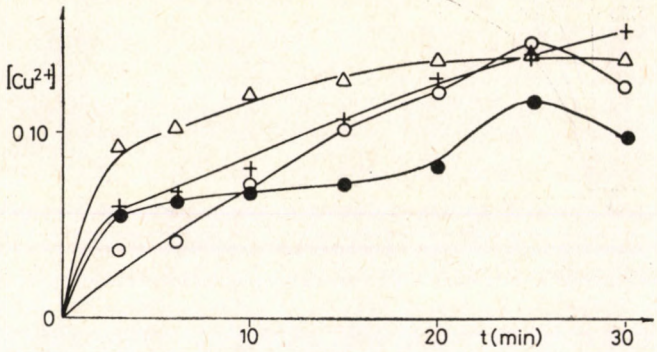

Fig. 11.
Oxidation of copper(I) (54 °C)
$[NH_3] = 3$ M; $[Cu^+_0] = 0.2$ M

proceeded more slowly, because bubbles started to coalesce in the upper section of the column *(Fig. 20)*.

The order of the reaction could be determined by stirred contactor experiments. Using ammonia, and 0.05 M and 0.2 M initial copper(I) concentrations, the value obtained corresponded to those described in literature [5], indicating that the apparatus fulfilled the requirements *(Fig. 21)*. In ethanolamine solutions, and 0.05 M initial copper(I) concentrations, the oxidation rate considerably depended on the rotation speed of the mixer (instantaneous reaction). At 0.2 M initial concentration, the dependence was still present, but at 0.5 M, it was hardly noticeable (pseudo-*m-th* order reaction).

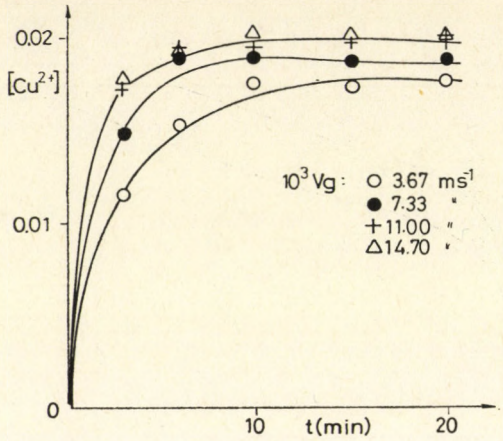

Fig. 12.
Oxidation of copper (I) in Column *B* (20 °C) $[NH_3]=1$ M; $[Cu_0^+]=0.02$ M

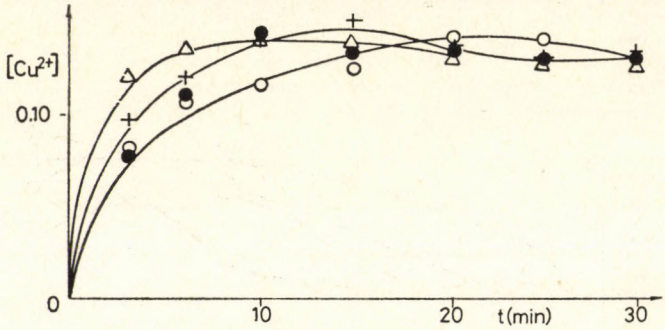

Fig. 13.
Oxidation of copper(I) in Column *B* (20 °C) $[NH_3]=1$ M;$[Cu_+^0]=0.2$ M

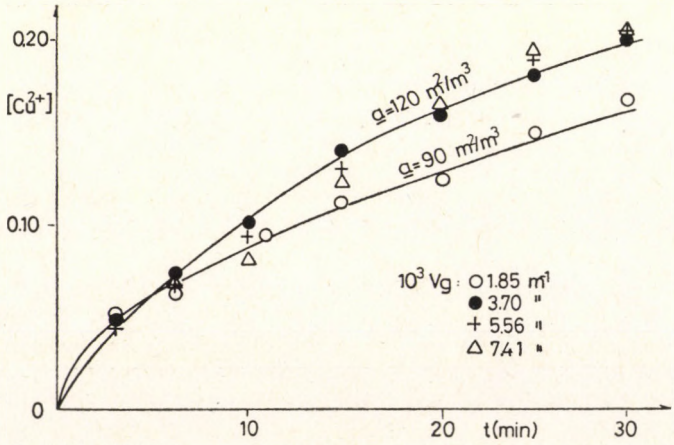

Fig. 14.
Oxidation of copper(I) (20 °C) [MEA]$=3.27$ M; $[Cu_0^+]=0.2$ M

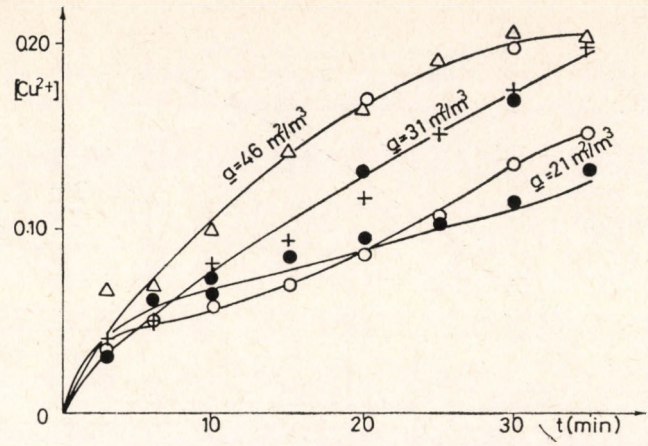

Fig 15.
Oxidation of copper(I) (54 °C) [MEA] = 3.27 M; $[Cu_0^+] = 0.2$ M

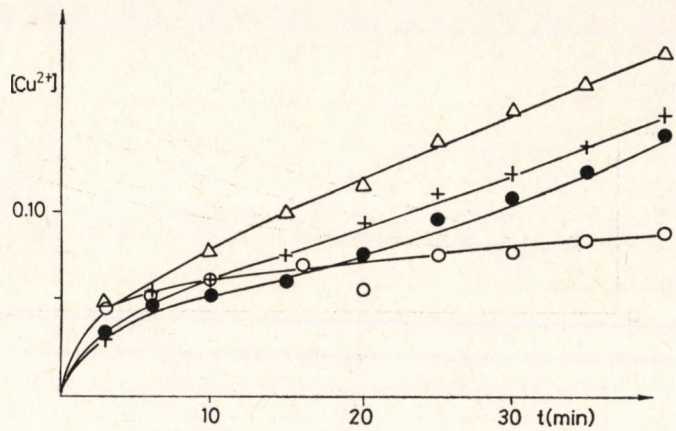

Fig. 16.
Oxidation of copper(I) (20 °C) [DEA] = 1.90 M; $[Cu_0^+] = 0.2$ M

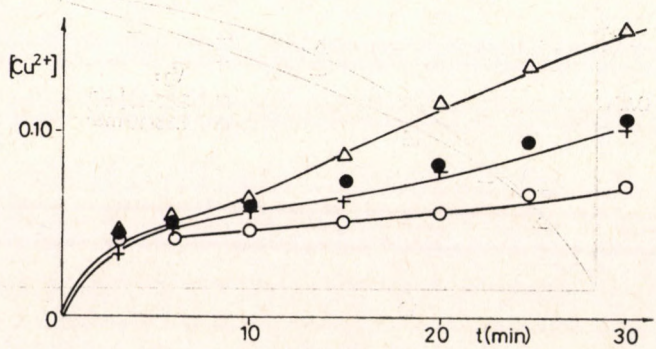

Fig. 17.
Oxidation of copper(I) (54 °C) [DEA] = 1.90 M; $[Cu_0^+] = 0.2$ M

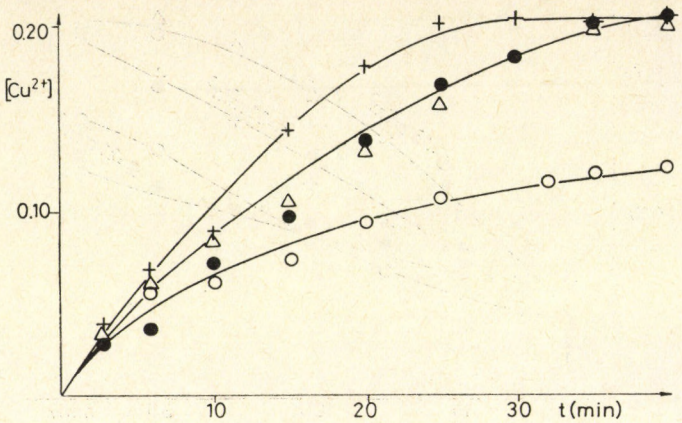

Fig. 18.
Oxidation of copper(I) (20 °C)
[TEA] = 1.34 M; $[Cu_0^+]$ = 0.2 M

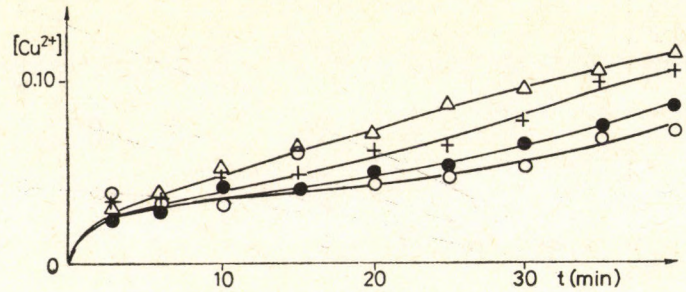

Fig. 19.
Oxidation of copper(I) (54 °C)
[TEA] = 1.34 M; $[Cu_0^+]$ = 0.2 M

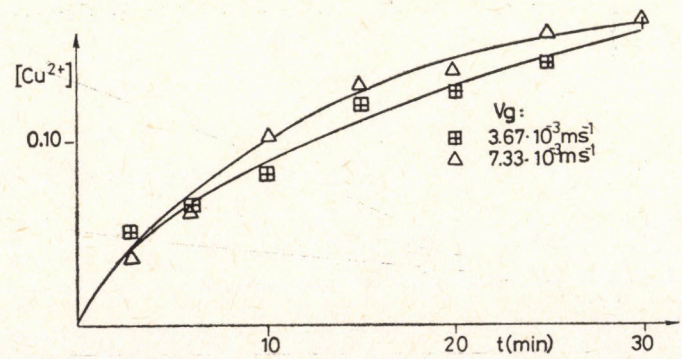

Fig. 20.
Oxidation of copper (I) in Column *B* (20 °C)
[MEA] = 3.27 M; $[Cu_0^+]$ = 0.2 M

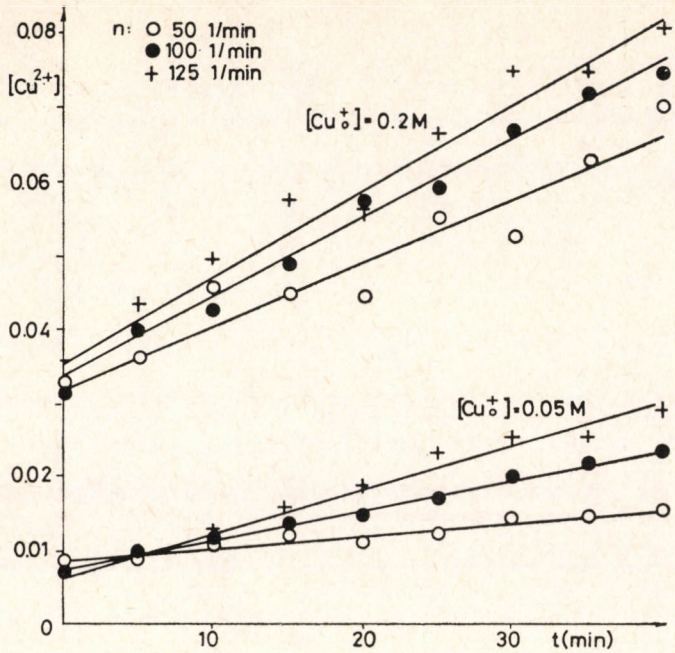

Fig. 21.
Determination of the reaction order in 3 M NH_3

Conclusions

From the experimental results obtained in the stirred contactor, the $k_L a$ values could be determined for low copper (I) concentrations. For MEA and high initial copper(I) concentrations, k_2 was calculated by Eq. 7 and 3 *(Tab-*

Table 3 Kinetic results

$(Cu^+)_0 = 0.05$ M, instantaneous reaction			
Ligand	n (1/min)		
	50	100	125
	$10^5\ k_L a (s^{-1})$		
NH_3	7.7	20	33
MEA	4.9	8.4	9.6
TEA	4.4	7.3	8.7

$(Cu^+)_0 = 0.5$, pseudo *m-th* order reaction			
Ligand	n (1/min)		
	50	100	125
	$10^{-3}\ k_2$		
MEA	1.3	1.4	1.8

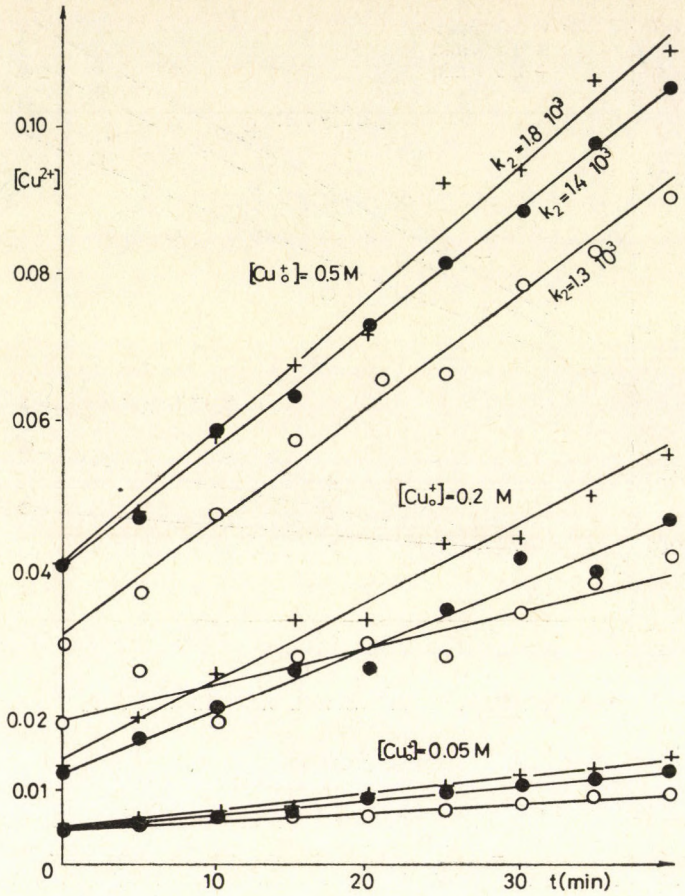

Fig. 22.
Determination of the reaction order in 3.27 M MEA

Table 4 Values used in Eq. 3

Parameter	Temperature, °C	
	20	54
	Values	
$(O_2^*)^a$ (kmol m^{-3})	2.7×10^{-4}	1.8×10^{-4}
D_{O_2} (m^2 s^{-1})	2.5×10^{-9}	5.6×10^{-9}
k_2 (kmol^{-2}m^{6}s^{-1})	1.3×10^{3b}	$1-2 \times 10^{4c}$

a) Air, 1 bar pressure; *b)* MEA, mixed tank measurement, Eq. 6; *c)* estimated value

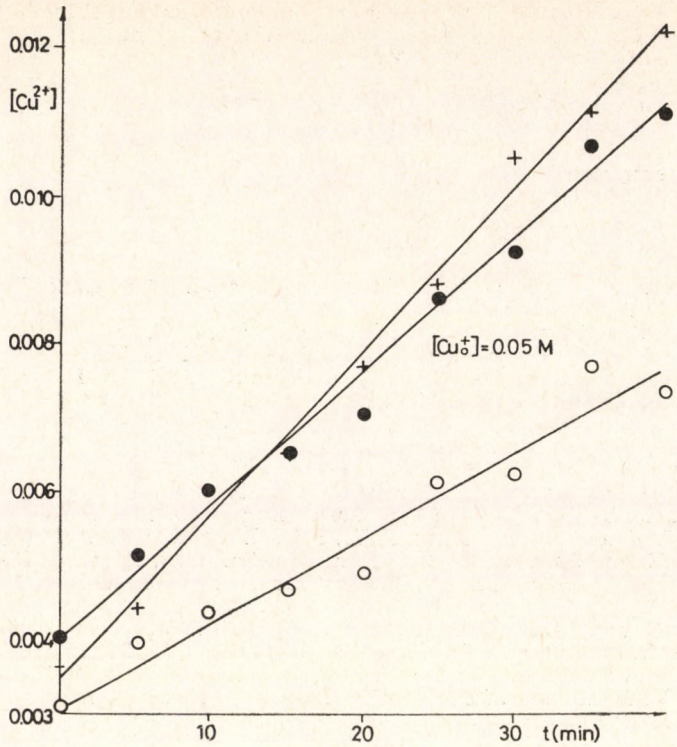

Fig. 23.
Determination of the reaction order in 1.34 M TEA

le 3). When k_2 was determined, a was derived from the geometric surface area. However, the slow increase of k_2 with the rotation speed indicates that micro-vertices, undetected by visual means, were present.

In MEA solutions—even though the pseudo-*m-th* order is not strictly valid—the effective interfacial area values could be estimated using the calculated k_2 values, and the post-integration fitting of Eq. 3. Estimated values are shown in *Fig. 14* and *15*, indicating that the effective interfacial area decreased with increasing temperature. The input data for calculations are summarized in *Table 4*.

The measured and collected data serve as a suitable basis for the design or parameter comparison of spray, bubble, or packed bubble columns.

SYMBOLS

a effective interfacial area per unit column volume, m^{-1}
D diffusivity of solute in solution, m^2s^{-1}
H effective height of the column, m
k reaction rate constant in Eq. (2), $(m^3\ mol^{-1})^{m-n-1}.s^{-1}$
k_2 second order rate constant $m^6\ mol^{-2}\ s^{-1}$
k_L liquid side physical mass transfer coefficient, ms^{-1}
L liquid rate, kg $m^{-2}\ s^{-1}$

m order of reaction with respect to the concentration of cuprous chloride
n order of reaction with respect to the concentration of oxygen
R specific rate of absorption, mol m^{-2} s^{-1}
t reaction time, s
V_g superficial gas velocity, ms^{-1}
α constant
Index
o initial concentration

REFERENCES

1. DANCKWERTS, P. V.: Gas-Liquid Processes, Műszaki könyvkiadó Budapest, 1976 (in Hungarian)
2. JHAVERI, A. S. and SHARMA, M. M.: Chem. Eng. Sci. *1968*, 23 (7) 669–675.
3. AWAKURA, Y., et al.: Denki Kagaku (Kyoto) *1980*, 48 104–111.
4. JHAVERI, A. S. and SHARMA, M. M.: Chem. Eng. Sci. *1967*, 22 (1) 1–6.
5. CHHABRIA, M. C. and SHARMA, M. M.: Chem. Eng. Sci. *1974*, 29 (4) 993–1002.
6. SRIDHARAN, K., and SHARMA, M. M.: Chem. Eng. Sci. *1976*, 31 (9) 767–774.
7. PANGARKAR, V. G.: Chem. Eng. Sci. *1974*, 29 (3) 877–882.
8. MASHELKAR, R. A.: Brit. Chem. Eng. *1970*, 15 (10) 1297–1304.
9. MEHTA, K. C. and SHARMA, M. M.: Brit. Chem. Eng. *1970*, 15 (11) 1440–1444.
10. MEHTA, K. C., SHARMA, M. M.: Brit. Chem. Eng. *1970*, 15 (12) 1556–1558.
11. SHARMA, M. M. and DANCKWERTS, P. V.: Brit. Chem. Eng. *1970*, 15 (4) 522–528.
12. SAHAY, B. N. and SHARMA, M. M.: Chem. Eng. Sci. *1973*, 28 (12) 2245–2255.
13. MASHELKAR, R. A. and SHARMA, M. M.: Trans. Instn. Chem. Eng. *1970*, 48 T162–T172.
14. SAHAY, B. N. and SHARMA, M. M.: Chem. Eng. Sci. *1973*, 28 (1) 41–47.
15. YADAV, G. D. and SHARMA, M. M.: Chem. Eng. Sci. *1979*, 34 (12) 1423–1424.
16. ALPER, E. and DECKWER, W. D.: Chem. Eng. Sci. *1980*, 35 (6) 1263–1268.
17. BRAUER, G.: Handbook of Preparative Inorganic Chemistry, Academic Press, New York, 1965.

РЕЗЮМЕ

Изучали окисление медных (I) ионов в барботажный колоннах и в камерах перемешивания происходящее под влиянием абсорбированного кислорода при температурах 20 °C и 54 °C в присутствии аммония, моно- ди- и триэтаноламина. В барботажных колоннах определили удельную поверхность соприкосновения и зависимость его значения от температуры и расхода газа, а в камерах перемешивания тип реакции и также коэффициенты κ_2 и $\kappa_L a$.

HUNGARIAN JOURNAL
OF INDUSTRIAL CHEMISTRY
VESZPRÉM
Vol. 11. pp. 403–407 (1983)

THE ACTIVITY CHANGE OF THE $H(NH_4)$, LA–FAU, Y ZEOLITE WITH THE TIME IN THE ALKYLATING REACTION OF ISOBUTANE

GY. GÁRDOS, Á. RÉDEY, M. KOVÁCS and J. KRISTÓF*

(Department of Hydrocarbon and Coal Processing,
*Department of Analytical Chemistry,
Veszprém University of Chemical Engineering)

Received: May 4, 1983.

The ammonium and lanthanum ion-exchanged forms of FAU, *Y* zeolite were investigated in the heterogeneous catalytic alkylation of isobutane with 1-butene. The activity change of the $H(NH_4)$, *La*-FAU, *Y* was followed in the function of time at a temperature of 80 °C, a pressure of 30 bar applying an isobutane-1-butene molar ratio of 8:1. The experiments were carried out in a continuous reactor system. On the basis of the experimental data, it should be noted that the alkylating reaction is the main reaction until an olefine charge of 0.5 g/g catalyst is attained, thereafter the rate of the alkylation begins to decrease and the polymerization of olefine comes into prominence indicating that a drastic selectivity change occurs.

The alkylating reactions of isoparaffins (isobutane) with olefins (propylene, butylenes and amylenes) are of major importance in the petroleum refining industry. The alkylate has very good characteristics (octane-number, anti-knock ratings, and susceptibility). At present, alkylating processes employ sulphuric and hydrofluoric acid catalysts. Instead of acid catalysts, because of the problems encountered in the processes (corrosion, and post-treatment) the application of zeolites can be regarded as promising.

In previous papers [1–5] preliminary investigations were given on the heterogeneous catalytic alkylation of isobutane. The activity of different types of ion-exchanged zeolites was studied. The effect of the rare earth content of ion-exchanged FAU, *Y* zeolites was also investigated.

The activity change of ammonium and lanthanum ion-exchanged FAU, *Y* [$H(NH_4)$, La–FAU, *Y*] pretreated at a temperature of 450 °C in vacuum was followed in a continous operation mode applying a microreactor system prepared by the NAKI. The experimental parameters were as follows:

temperature: 80 °C; pressure: 30 bar;
isobutene-1-butane molar ratio: 8 = 1;
liquid-load: 0,8 cc/cc catalyst·h
(space velocity: $2.3 \cdot 10^{-4}$ g/g catalyst·s).

Experimental

The change of the composition of alkylate with the function of the time and the amount of 1-butene fed into the reactor calculated on the basis of 1 g catalyst is summarized in *Table 1*. The results obtained are illustrated in *Fig. 1–2*.

On the basis of the experiments it can be stated that the alkylate yield is the function of the lifetime of the catalyst. The alkylate yield decreased by 30% during an experimental period of 12 hours. The decrease of the alkylate yield can be due to the deposit and coke formation on the surface of the catalyst. Because of this the zeolite catalyst cannot function. Alongside the parameters given after a butene charge of about 0.5 g calculated on 1 g catalyst (which corresponds to a running time of about 5 hours) drastic changes occurred. The C_8-content of the alkylate was about 40% at the beginning of the experiments and after a charge of 1.39 g butene/g catalyst the C_8-content decreased to 31%. The composition of the C_8-fraction also changed. The amount of trimethyl-pentanes (TMP) decreased by 20%, the amount of dimethyl-hexanes (DMHx) doubled, and the amount of C_8-olefines significantly increased (from 0.8% to 7.3%). The amount of C_5-hydrocarbons slightly decreased, the amounts of C_6, C_7 slightly increased and the amount of C_9^+-hydrocarbons increased to a large extent (0.6% → 8.9%) as a consequence of the side reactions.

On the basis of the above changes, it can be concluded that the alkylating reaction is accompanied by polymerization, which can be considered to be a side reaction. The alkylation starts with the protonation of 1-butene. The secondary-butyl carbenium ion reacts with isobutane and this reaction results in tertiary-butyl cation and butane. The tertiary-butyl cation reacts with

Table 1

The change of the alkylate composition with the time

Time h	Catalyst loading $\frac{g \text{ butene}}{g \text{ cat}}$	The composition of the alkylate							
		C_5	C_6	C_7	C_8	TPM	DMHx	$C_8^=$	C_9^+
1	0.11	43.1	8.4	7.7	40.2	32.5	6.2	0.8	0.6
2	0.23	44.6	7.1	6.8	41.0	33.2	6.3	0.5	0.5
3	0.34	44.1	7.9	7.1	40.3	32.8	5.9	0.9	0.6
4	0.46	42.8	8.8	7.9	39.8	31.4	6.8	1.2	0.7
5	0.47	43.5	8.7	7.4	39.8	32.0	6.5	0.7	0.6
6	0.59	43.2	8.3	8.1	37.5	27.6	6.7	2.1	2.9
7	0.81	42.2	9.5	8.8	36 1	24.9	7.5	2.9	3.4
8	0.92	41.8	9.8	7.9	35.4	22.5	8.3	3.7	5.1
9	1.04	42.1	9.7	8.5	33.8	20.2	9.1	4.2	5.9
10	1.15	40.2	10.1	9.7	33.2	16.7	10.2	5.5	6.8
11	1.27	39.6	10.8	9.1	32.8	14.7	10.8	6.9	7.7
12	1.38	38.7	11.3	9.9	31.2	12.1	11.5	7.3	8.9

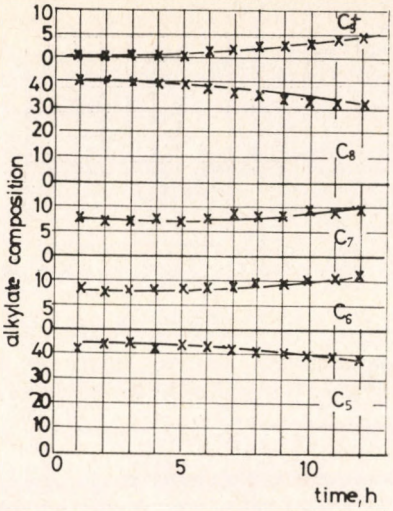

Fig. 1.
The change of the alkylate composition

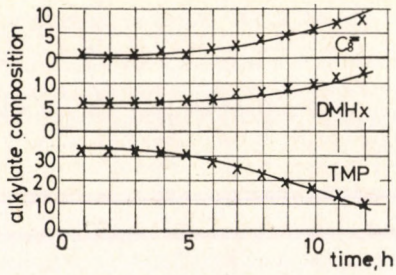

Fig. 2.
The change of the alkylate composition

butene, and the isooctyl cation formed in a hydride-transfer reaction with isobutane gives isooctane and tertiary-butyl cation.

The formation of the trimethyl-pentanes is a result of the addition reaction of tertiary-butyl cation and 2-butene (2-butene forms in the isomerization reaction of 1-butene at the given reaction parameters). The formation of the dimethyl-hexanes can be explained by the additional reaction of tertiary-butyl cation and 1-butane and by the dimerization of 1-butene following a hydride transfer. It should be noted that the ratio of TMP/DMHx gives information on the rates of the alkylation and polymerization reactions on the basis of the above mentioned.

Fig. 3 shows the change of TMP/DMHx ratio with time. On the basis of *Fig. 3*, it can be concluded that during the first 5 hours, the TMP/DMHx ratio is about 5, that is the alkylation is the main reaction, later (time = 6

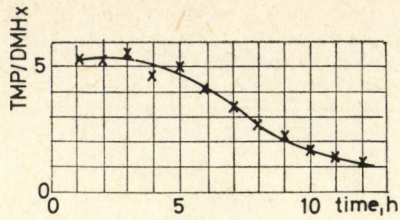

Fig. 3.
The change of the TMP/DMHx ratio

hours) the TMP/DMHx ratio begins to decrease and the formation of C_8-olefines increases *(Fig. 2)*. C_8-olefine hydrocarbons can be formed by the dimerization of butene and the deprotonation of the isooctyl cation. This can be determined only by the application of C_{14}-labelled isobutane. Trimethyl-pentenes and dimethyl-hexenes were identified by mass-spectroscopic studies. On the basis of the above mentioned, it can be stated that the C_8^+-carbeniumion can take part in two reactions. The $C_8H_{17}^+$ carbeniumion reacting with isobutane results in trimethyl-pentane in a hydride-transfer reaction, or gives isooctene with deprotonation:

$$C_8H_{17}^+ + i-C_4H_{10} \longrightarrow C_8H_{18} + t-C_4H_9^+$$

$$C_8H_{17}^+ \xrightarrow[-H^+]{} C_8H_{16} \longleftarrow 2\,C_4H_8$$

With the activity decrease of the catalyst the selectivity changes; the hydride-transfer ability of the catalyst decreases and the polymerization of olefines comes into prominence, marked by the increase of C_8-olefines. The octyl carbeniumion accumulates on the surface of the catalyst with the activity decrease, and the BRÖNSTED acid sites will be covered. The octyl carbeniumion reacting with butene results in hydrocarbons having higher carbon atom numbers.

$$C_8H_{17}^+ + n-C_4H_8 \rightarrow C_{12}H_{25}^+$$

$$C_{12}H_{25}^+ + n-C_4H_8 \rightarrow C_{16}H_{33}^+$$

C_5, C_7, C_6, C_9^+ hydrocarbons are formed by the further reactions of $C_{12}H_{25}^+$, $C_{16}H_{33}^+$ carbeniumions.

The regeneration of the catalyst used was studied by applying inert gas stripping, washing with isobutane, hydrogen feed, heat treatment and pressure decrease. The catalyst did not recover its original activity, so further investigations are necessary from the point of view of industrial utilization.

REFERENCES

1. GÁRDOS, GY., PÉCHY, L., RÉDEY, Á., and OKONJI, CH.: Hung. J. Ind. Chem. *1980*, 8, 363.
2. GÁRDOS, GY., PÉCHY, L., RÉDEY, Á., and SOKORAI, I.: Hung. J. Ind. Chem. *1980*, 8, 371.

3. GÁRDOS, GY., KRISTÓF, J., PÉCHY, L. and RÉDEY, Á.: Hung. J. Ind. Chem. *1981* 9, 21.
4. KRISTÓF, J., GÁRDOS, Gy., and RÉDEY, Á.: J. Thermal Analysis, *1981*, 22, 123.
5. GÁRDOS, Gy., KRISTÓF, J., PÉCHY, L., and RÉDEY, Á.: Hung. J. Ind. Chem. *1982*, 10, 251.

РЕЗЮМЕ

Авторы изучали формы цеолитов типа FAU, Y заполненных ионами аммония и лантана путём гетерогенной каталитической алкализации изобутана в l-бутен. Изучали изменение активности цеолитов H/NH_4, La—FAU, Y в зависимости от времени, в ходу экспериментов мольная пропорция при температуре 80 °C и при давлении 30 бар составляла 8/I. В экспериментах использовали систему реакторов непрерывного действия. На основе экспериментальных данных авторами установлено, что увеличением подачи олефина до 0,5 г/г катализатора реакцию алкализации можно считать главной реакцией, выше этого значения интенсивность алкализации уменьшается а полимеризация становится более интенсивной указывая на то, что селективность катализатора изменится значительно.

HUNGARIAN JOURNAL
OF INDUSTRIAL CHEMISTRY
VESZPRÉM
Vol. 11. pp. 409–415 (1983)

STUDY ON ALKYLATE COMPOSITION

GY. GÁRDOS, Á. RÉDEY, M. KOVÁCS and J. KRISTÓF*

(Department of Hydrocarbon and Coal Processing,
*Department of Analytical Chemistry, Veszprém University
of Chemical Engineering)

Received: May 4, 1983.

Heterogeneous catalytic alkylating reactions were carried out with isobutane and 1-butene on ammonium and lanthanum ion-exchanged FAU, Y zeolite. The change of the alkylate composition was studied in the function of the temperature. The formation of trimethyl-pentanes and dimethyl-hexanes was investigated. The equilibrium distribution of C_8-hydrocarbons was studied on the basis of thermodynamic data and it was compared with the measured data.

Previous papers discussed the importance of the heterogeneous alkylating process [1–5]. The experimental methods, and the apparatus used for the experiments were given. Ammonium and lanthanum ion-exhanged FAU, *Y* zeolites were used in the continuous alkylating experiments after a pretreatment at a temperature of 450 °C in vacuum. The change of the alkylate yield was studied as a function of the technologic parameters (temperature and isobutane-1-butene molar ratio).

The alkylating reaction of isobutane with normal-butenes can be rendered probable according to the following. The first step is the protonation of *n*-butene as a result of it, secondary-butyl cation forms. The proton (H^+) comes from the BRÖNSTED acid site of the ion-exhanged FAU, Y zeolite. The secondary-butyl cation reacts with an isobutane and tertiary-butyl cation and normal-butane form. The tertiary-butyl cation reacting with 1-butene results in dimethyl-hexyl cation, reacting with 2-butene gives trimethyl-pentyl cation. The isooctyl cations in a hydride transfer reaction with the isobutane result in isooctane and tertiary-butyl cation.

$$C{=}C{-}C{-}C \underset{-H^+}{\overset{+H^+}{\rightleftharpoons}} C{-}\overset{+}{C}{-}C{-}C \underset{+H^+}{\overset{-H^+}{\rightleftharpoons}} C{-}C{=}C{-}C$$

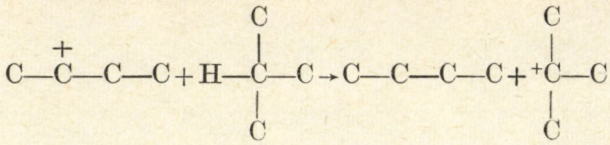

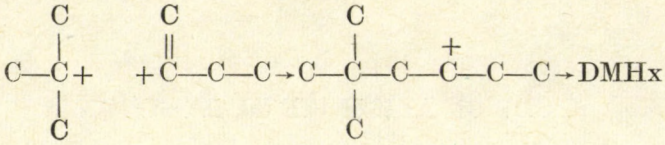

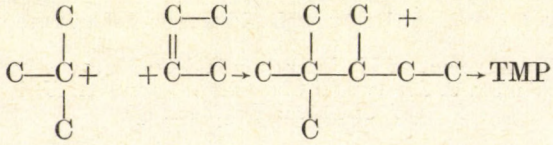

Considering the hydride and methyl-shifts of the isooctyl cations, the formation of the following isooctanes can be taken into consideration:

(2,2,4-, 2,3,4-, 2,3,3-, 2,2,3-TMP; 2,5-, 2,4-, 2,3-, 2,2-DMHx)

The formation of the other isooctanes (2,2,3,3-tetra-methyl-butane; 3,4-, 3-3-DMHx; 3-ethyl-hexane; methyl-heptanes, methyl-ethyl-pentanes and n-octane) cannot be rendered on the reaction mechanism proposed.
In the case of 1-butene:

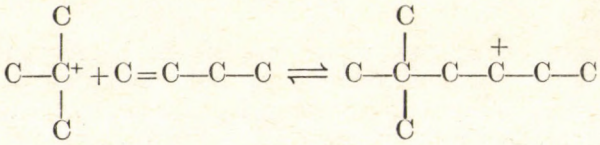

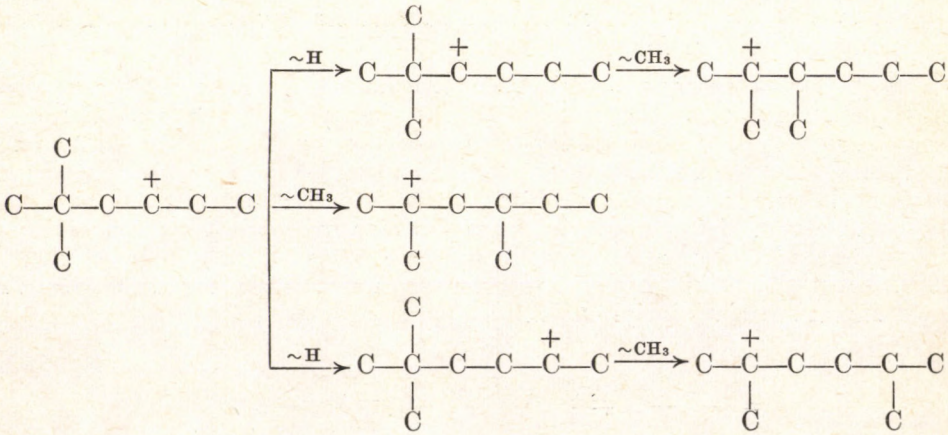

In the case of 2-butene

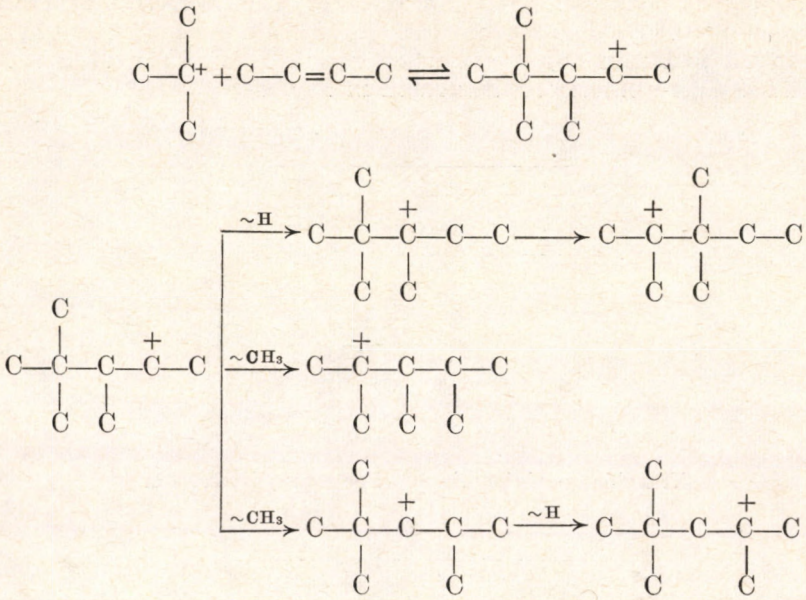

Experimental

The alkylation of isobutane on $H(NH_4)$, La-FAU, *Y* zeolite was studied in the temperature range of 40–160 °C alongside an isobutane-1-butene molar ratio of 8:1 applying a liquid load of 1.0 cc/cc catalyst×h.

On the basis of the experimental data it should be stated that the trimethyl--pentanes and dimethyl-hexanes constitute the C_8-fraction of the alkylate. The amount of other C_8-hydrocarbons in the C_8-fraction was less than 1%. The formation of 3,3-DMHx, 3,4-DMHx, methyl-heptanes and methyl-pentanes was

Table 1

The composition of C_8-fraction in the function of the reaction temperature

C_8-isomer hydrocarbons	C_8-composition, %									
	Temperature, °C									
	40	50	60	70	80	90	100	120	140	160
2,2,4-TMP	47.7	45.3	46.1	41.7	40.5	35.5	32.5	26.5	21.1	17.2
2,3,4-TMP	18.1	19.4	16.6	19.5	20.6	17.5	16.8	18.5	17.9	14.8
2,2,3-TMP	6.2	6.7	6.6	8.6	7.7	8.4	7.6	8.7	9.1	6.7
2,3,3-TMP	9.9	11.6	9.9	11.3	12.7	9.5	12.4	10.3	13.5	6.4
2,5-DMHx	7.3	7.1	8.1	7.6	6.9	11.5	12.1	14.0	12.1	18.6
2,4-DMHx	4.4	4.0	5.4	4.6	5.2	7.7	9.1	11.2	14.7	23.1
2,2-DMHx	5.9	5.3	6.7	5.7	6.0	8.4	8.3	9.5	9.2	10.2
2,3-DMHx	0.3	0.5	0.3	0.7	0.4	1.1	0.8	1.0	1.8	2.2
3,3-DMHx	0.0	0.0	0.0	0.0	0.0	0.0	0.0	0.0	0.0	0.0
3,4-DMHx	0.0	0.0	0.0	0.0	0.0	0.0	0.0	0.0	0.0	0.0
Other C_8	0.2	0.1	0.2	0.3	0.0	0.2	0.1	0.0	0.2	0.2
$C_8^=$	0.0	0.0	0.1	0.0	0.0	0.2	0.3	0.3	0.4	0.6

not observed. The trimethyl-pentane (TMP) yield is higher at lower temperatures (50–70 °C), the dimethyl-hexane (DMHx) yield increases at higher temperatures (80–140 °C). The change of the C_8-fraction is summarized in *Table 1*, alongside an isobutane-1-butene molar ratio of 8:1. The distributions of TMP and DMHx-isomers are illustrated in *Fig. 1–2*.

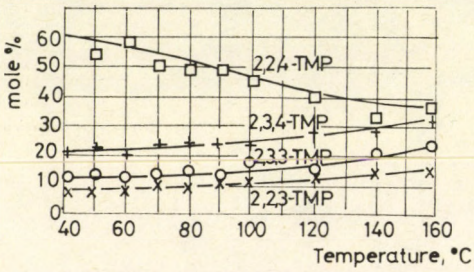

Fig. 1.
The change of the trimethyl-pentane distribution

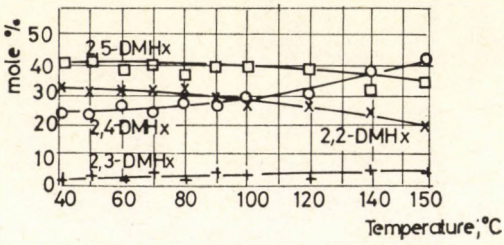

Fig. 2.
The change of the dimethyl-hexane distribution

On the basis of thermodynamic data, the equilibrium distribution of C_8-hydrocarbons was calculated in good agreement with one given in literature [6]. *(Fig. 3)*

According to the reactions outlined above, the distribution of the octane isomers formed in the alkylating reaction of isobutane with normal-butenes (2,2,4-TMP, 2,3,4-TMP; 2,3,3-TMP; 2,2,3-TMP; 2,5-DMHx; 2,4-DMHx, 2,3-DMHx, 2,2-DMHx) was also calculated, and is illustrated in *Fig. 4*. Considering the C_8-distribution it should be noted that the amount of trimethyl--pentanes decreases, and the amount of dimethyl-hexanes increases with the temperature. The TMP/C_8 ratio is relatively high in the temperature range of 40–80 °C, the DHMx/C_8 ratio increases with the temperature in accordance with thermodynamic equilibrium. On the basis of *Fig. 1*, it can be stated that the 2,2,4-TMP and 2,3,4-TMP are the main trimethylpentane components. The amount of 2,2,3-TMP is relatively low and it does not change significantly with the temperature. The amount of 2,2,4-TMP decreases, the formations of 2,3,4-TMP and 2,3,3-TMP increase with the function of the temperature.

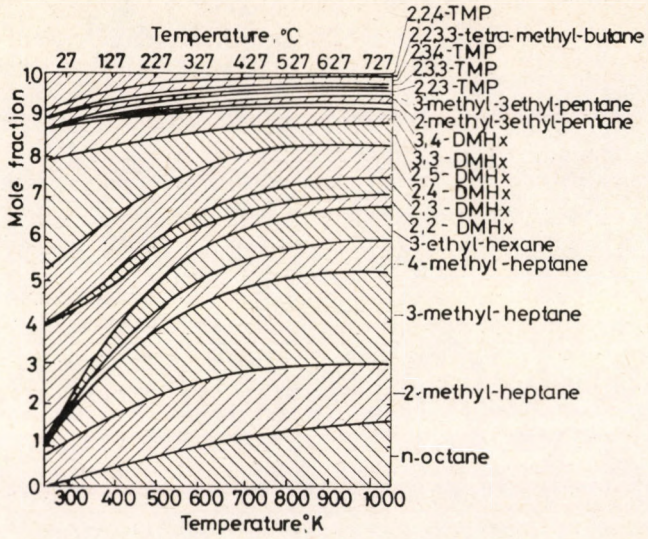

Fig. 3.
The distribution of C_8-hydrocarbons

It can be observed that 3,3-DMHx and 3,4-DMHx cannot be found in the alkylate and this makes it probable that dimethyl-hexyl-cations do not form from trimethyl-pentyl cations alongside the reaction parameters applied. The

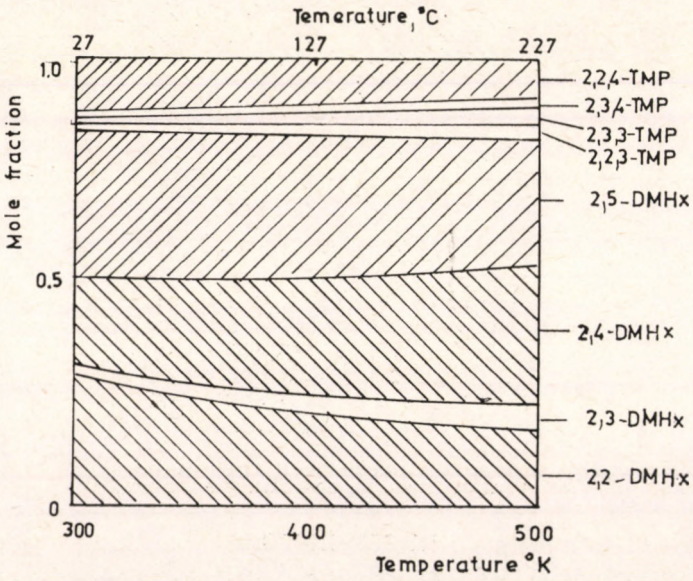

Fig. 4.
The distribution of C_8-hydrocarbons formed in the alkylating reaction of isobutane with *n*-butenes

amount of 2,4-DMHx increases, the amounts of 2,5-DMHx and 2,2-DMHx decrease with the temperature. The change of the distribution of trimethyl--pentane and dimethyl-hexane isomers is in good correlation with the equilibrium distribution calculated on the basis of thermodynamic data (Fig. 4).

It must be emphasized that the TMP–DMHx distribution calculated on the basis of thermodynamic data differs from the experimental distribution similarly as mentioned in literature [7], which is a result of the isomerization of 1-butene into 2-butene. The alkylation of isobutane with 1-butene results in dimethyl-hexanes, and with 2-butene results in trimethyl-pentanes. The equilibrium distribution of *n*-butenes is illustrated in *Fig. 5*.

Alongside the alkylating reaction conditions the isomerization of 1-butene into 2-butene was studied on an ammonium and lanthanum ion-exchanged zeolite catalyst. On the basis of the experimental results, the composition of the product was determined: 12% 1-butene, 33% cis-2-butene, 55% trans-2--butene. These results justify the isomerization of 1-butene and explain the composition of the alkylate.

The conversion of octane isomers (2,2,4-TMP, 2,3,4-TMP) was studied alongside the alkylating reaction parameters on $H(NH_4)$, La-FAU, *Y* zeolite. The experiments were carried out in the presence of 1-butene so that the tertiary-butyl cation, which is necessary for the isomerization of trimethyl--pentanes, was ensured. On the basis of the experimental results, the formations of all trimethyl-pentanes were observed, that is the isomerization of octanes takes place, and the change of the composition follows the distribution calculated on the thermodynamic data.

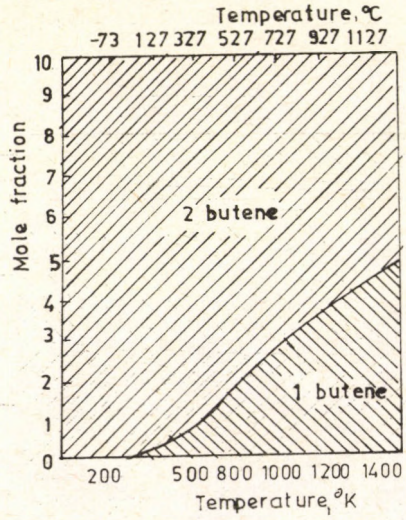

Fig. 5.
The distribution of *n*-butenes with the temperature

REFERENCES

1. GÁRDOS, GY., PÉCHY, L., RÉDEY, Á., and OKONJI, CH.: Hung. J. Ind. Chem *1980*, 8, 363.
2. GÁRDOS, GY., PÉCHY, L., RÉDEY, Á., and SOKORAI, J.: Hung. J. Ind. Chem. *1980*, 8, 371.

3. GÁRDOS, GY., KRISTÓF, J., PÉCHY, L., and RÉDEY, Á.: Hung. J. Ind. Chem. *1981*, 9, 21.
4. GÁRDOS, GY., KRISTÓF, J., PÉCHY, L., and RÉDEY, Á.: Hung. J. Ind. Chem. *1982*, 10, 251.
5. GÁRDOS, GY., RÉDEY, Á., and SOKORAI, I.: Hung. J. Ind. Chem. *1983*, 11, 000.
6. BROOKS, B. T., DUNSTAN, A. E.: The Science of Petroleum, Oxford University Press, 1953.
7. ALBRIGHT, L. F., GOLDSBY, A. R.: Industrial and Laboratory Alkylations. ACS Symposium Series 55. Washington, 1977.

РЕЗЮМЕ

Авторы изучали гетерогенную каталитическую реакцию алкализации изобутана в 1-бутен в присутствии катализатора-цеолита FAU-Y обладающего ионами аммония и лантана. Изучали состав продукта алкализации в зависимости от температуры. Следили за производством триметил пентанов и диметил гексанов. С помощью термодинамических данных изучали равновесное распределение углеводорода C_8, расчётные данные сопоставили с экспериментальными данными.

HUNGARIAN JOURNAL
OF INDUSTRIAL CHEMISTRY
VESZPRÉM
Vol. 11. pp. 417–423 (1983)

TRANSFER PROCESSES UPON PRESSURE SWING ADSORPTION. IV.

THE PROBLEMS OF SCALE-UP

L. Kotsis and J. Argyelán

(Department of Chemical Process Engineering, University of Chemical Engineering, Veszprém)

Received: May 26, 1983

Factors influencing the separation power and capacity of pressure swing adsorption-type (PSP) gas separators were studied by the methods of similarity analysis. Parameters, which fundamentally influence separation quality and capacity were determined from experimental data obtained with a single-step PSA unit. Momentum and energy transfers were neglected these led to three similarity criteria to be used for scale-up purposes. Separation quality was related to the term obtained from the mass transfer characteristics of the adsorbent and the filling-time. Theoretical considerations and experimental data showed that separation quality was independent of the geometry of the bed. In the case of quasi-equilibrium operation the scale up was proportional to the mass of the adsorbent involved.

Introduction

In previous papers of this series [1, 2] it was shown that the rate of gas-solid mass transfer in the case of contact between pressurized gas mixtures and evacuated solid adsorbent depended on the pore structure of the adsorbent used. When the simple transfer model was used for the description of the phenomenon, the term $\beta\omega$ characterized the transfer process, and $\beta\omega$ values were determined in a constant volume vessel for various adsorbents and pure permanent gases.

In this paper, the separation quality and cycle capacity of PSA gas separation is examined using experimental data obtained with various synthetic and natural zeolites, and both with air and mixtures of carbon monoxide and nitrogen (tube effect).

Theoretical

Using the simplest transfer model, the differential mass balance of the simultaneous adsorption of two components in PSA gas separator columns, becomes:

$$-\frac{\varepsilon}{RT}\frac{\partial}{\partial z}(v\times p_1)-\beta_1\omega\varrho^*(K_1p_1-q_1)=\frac{\varepsilon}{RT}\frac{\partial p_1}{\partial t} \tag{1}$$

$$-\frac{\varepsilon}{RT}\frac{\partial}{\partial z}(v\times p_2)-\beta_2\omega\varrho^*(K_2p_2-q_2)=\frac{\varepsilon}{RT}\frac{\partial p_2}{\partial t} \tag{2}$$

$$\frac{\partial q_1}{\partial t}=\beta_1\omega(K_1p_1-q_1) \tag{3}$$

$$\frac{\partial q_2}{\partial t}=\beta_2\omega(K_2p_2-q_2) \tag{4}$$

In dimensionless form Eq. 1 to 4 reads as:

$$-\frac{v_0\tau}{H}\frac{\partial}{\partial z^*}(v^*p_1^*)-\varrho^*K_1\frac{RT}{\varepsilon}\frac{\partial q_1^*}{\partial t^*}=\frac{\partial p_1^*}{\partial t^*} \tag{5}$$

$$\frac{\partial q_1^*}{\partial t^*}=\beta_1\omega\tau(p_1^*-q_1^*) \tag{6}$$

$$-\frac{v_0\tau}{H}\frac{\partial}{\partial z^*}(v^*p_2^*)-\varrho^*K_2\frac{RT}{\varepsilon}\frac{\partial q_2^*}{\partial t^*}=\frac{\partial p_2^*}{\partial t^*} \tag{7}$$

$$\frac{\partial q_2^*}{\partial t^*}=\beta_2\omega\tau(p_2^*-q_2^*) \tag{8}$$

The necessary and sufficient conditions [3] of the similarity of various operation units differing either in the geometrical sizes or the material characteristics is the identity of the equation set, and that of the conditions of unequivocality.

It is obvious that due to the differential equation set used, only partial similarity can be claimed in the case tested. Neglection of the energy relationships is justifiable, when one considers that the amount of heat liberated during the adsorption of permanent gases is negligible. The momentum transfer can also be neglected, because under strong external pressure drop, there is practically no pressure gradient in the packed column.

The solution of differential equation set (5)–(8) at preset $p_i^*(z^*, 0)$, $q_i^*(z^*, 0)$, $v^*(z^*, 0)$, $p_i^*(0, t^*)$ and $v^*(0, t^*)=v_0$ leads to identical solution functions $q_i^*(z^*, t^*)$, $p_i^*(z^*, t^*)$ and $v^*(z^*, t^*)$, assuming that coefficients $v_0\tau/\mathrm{H}$, $\varrho^*K_iRT/\varepsilon$ and $\beta_i\omega\tau$ are also identical.

For a given adsorbent-gas system, coefficients $\beta_i\omega\tau$ and $\varrho^*K_iRT/\varepsilon$ are constant for constant τ, irrespective of the size of the column. Thus, the prerequisite of an identical solution is the constancy of the v_0/H ratio. This requirement is fulfilled by specifying q_i^* and p_i^*, because these require feed and take-off flows proportional to the size of the column.

The presence of the coefficient $v_0\tau/\mathrm{H}$ in the dimensionfree equation set means that the separation quality [i. e. functions $q_i^*(z^*, t^*)$ and $p_i^*(z^*, t^*)$] is invariant with respect to the bed geometry. The same conclusion can be drawn from the equilibrium model of Ustinow [4], though the author fails to point out this feature. The terms $\varrho^*K_iRT/\varepsilon$ show the ratios of the capacities of the adsorbent and the gas phase, respectively, for the individual compo-

nents. In the case of permanent gases, where the isotherms are approximately linear over wide pressure ranges, these coefficients are constant, irrespective of the pressure and bed geometry.

The presence of similarity criteria $\beta_i \omega \tau$ means that the quality of the separation depends on the ratio of the convective and transfer flows.

In this paper, we do not deal with the solution of the differential equation system shown. Instead, the effects of model parameters are examined under preset identity conditions. Transfer coefficients β_i of the various components are considered identical.

Tube Effects

The experimental method used here was described previously [1, 5]. It involves the determination of the separation power and capacity of an operation unit with several transfer-units. Separation power and capacity can be determined by measuring the amount of material required to fill an evacuated, adsorbent-filled column to a preselected pressure, and by measuring the concentration distributions of the various components during blow-down (or evacuation).

Characteristic concentration distribution curves obtained during the separation of air on Molfilit KX 50 5 A zeolite adsorbents are shown in *Fig. 1.*

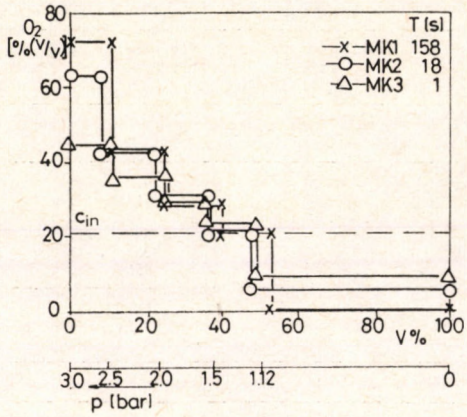

Fig. 1.
Tube-effect examinations with Molfilit KX 50 extrudate, at 293 K. Column length: 1000 mm; filling time: variable

In a few cases, only the volume-distribution of the component concentrations was determined in blow-down operations.

Separation quality is characterized by the standard deviation of the experimentally determined concentration distribution curves. The total-volume related standard deviation is σ_T, the value of the overpressurized section is σ_V. In the case of complete separation, the maximum standard deviation is:

$$\sigma_{max} = c_{in}(1 - c_{in}) \tag{9}$$

Table 1

Summarizing table of tube effect examinations

Colum dimensions (mm)	Adsorbent	Gas mixture	τ [s]	P_T [bar]	c_{in} [%(V/V)]	G [kg]	V_{in} [dm³]	V_L [dm³]	K_1 [mmol/gbar]	K_2 [mmol/gbar]	σ_τ [%(V/V)]	σ_T [%(V/V)]	$\beta\omega$ [1/s]
			50	2.50				0.40			2.74		
			210	2.80				0.47			2.29		
			270	2.75				0.50			3.18		
∅15×1000	M-8112 Na	air	480	2.80	21	0.178	—	0.54	0.120	0.198	4.26	—	4×10^{-3}
			340	2.75				0.50			3.81		
			490	2.80				0.55			4.80		
			720	3.00				0.55			6.02		
			85	2.75			1.426	0.71			16.75	20.61	
∅15×1000	M-8112	air	30	2.62	21	0.169	1.314	0.62	0.115	0.188	11.51	15.98	1.1
			7	2.15			1.110	0.31			5.92	14.56	
∅15×1000	M-801-1n-4h	$CO-N_2$	3	2.25	20.3	0.171	1.488	0.48	0.182	0.245	10.66	18.78	1.1
			236	3.00	20.1		2.148	0.86			24.90	28.60	
			188	3.00	20.5		1.975	0.81			24.28	26.58	
			7	2.55	20.5		1.628	0.55			6.92	14.79	
			138	3.02	79.8		1.649	0.45			—	17.87	
∅15×1000	M-801—1n-2h	$CO-N_2$	98	3.02	50.6	0.175	1.913	0.45	0.149	0.225	12.09	24.26	1.1
			11	3.00	79.8		1.628	0.56			3.63	9.54	
			87	3.00	79.8		1.628	0.74			2.62	15.41	
			10	2.80	48.6		1.606	0.61			8.72	19.20	
	Union		22	3.05	18.0		2.278	0.81			30.44	28.88	
∅15×1000	Carbide	$CO-N_2$	88	2.70	18.0	0.119	2.018	0.72	0.251	0.484	27.57	31.17	30
	10X		3	2.95	22.8		2.170	0.71			19.58	22.80	
			158	2.89			1.586	0.84			21.42	24.58	
	Molfilit		18	2.80	21		1.735	0.84			16.21	21.14	
∅15×1000	KX 50	air	1	2.97		0.151	1.721	0.86	0.131	0.258	8.46	14.58	10
∅15×300	Molfilit KX 50	air	6	2.32	21	0.026	0.230	—	0.131	0.258	—	19.24	10
			3	2.28			0.215					17.25	
			10	3.00		80.0	912	503			13.91	16.40	
			12	3.00		79.8	918	402			14.71	17.22	
∅300×1500	Molfilit KX 50	air	10	3.00	21	81.1	910	513	0.131	0.258	15.33	15.89	10
			24	3.00		80.0	920	340			23.00	38.00	
			102	3.00		80.0	910	465			16.41	21.33	
			277	3.00		80.8	925	411			20.76	23.78	
			53	3.00		159.8	1760	633			18.23	17.72	
∅300×3000	Molfilit KX 50	air	389	3.00	21	159.8	1760	808	0.131	0.258	27.78	26.07	10
			224	3.00		159.8	1821	821			21.98	25.06	
∅300×4500	M KX 50	air	104	3.00	21	240.9	2620	1417	0.131	0.258	19.97	22.33	10
∅15×1000	MSC	air	163	2.70	21	0.120	0.345	—	0.147	0.061	—	6.71	5×10^{-3}

The concluding data of the tube-effect examinations, obtained with various adsorbents, and both air and $CO-N_2$ mixtures are listed in *Table 1.*

The relationships between the quality of the separation and coefficients $\beta\omega\tau$ are shown in *Fig. 2* and *3.*

It is apparent from *Fig. 2* and *3* that the separation quality is directly related to the parameter $\beta\omega\tau$. If a linear relationship is postulated, then the regression equation becomes:

$$\frac{\sigma_T}{\sigma_{max}} = 0.24 + 0.13 \log \beta\omega\tau \tag{10}$$

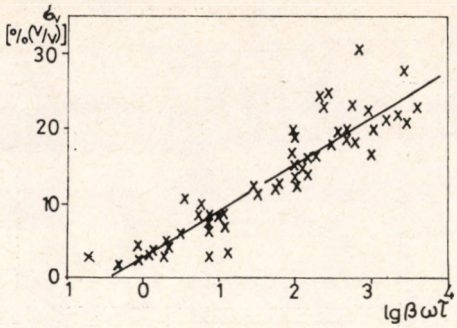

Fig. 2.
Correlation between σ_V and $\beta\omega\tau$, summary of all data points

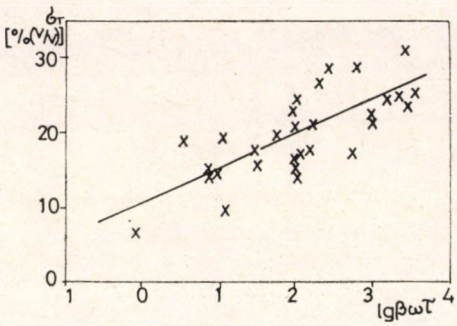

Fig. 3.
Correlation between σ_T and $\beta\omega\tau$; data for total volume

This relationship can be used to estimate the length of the filling period in actual systems. The amounts of gases processed in a period are shown in *Fig. 4* (various combinations of adsorbents and gases). Similary to the case of stationary bed adsorbents, the amount of material fed into the operation unit—when the bed is considered a single equilibrium unit—(N_e) (the sum of $\varrho^* K_i + \varepsilon(RT)$ was related to the overall amount of gas fed in N_{in}). It can be seen that for sufficiently large $\beta\omega\tau$ values (around unity), the relative amount of gas processed is approximately constant and, using the linearized isotherms, it can be computed within a 20% error margin. For small $\beta\omega\tau$ values, the quotient N_e/N_{in} is approximately 10, in agreement with the capacity of the gas space among the particles.

The previous tube effect examinations—which embraced four orders of magnitude in the amount of gas processed and the size of the equipment—show that similarly to the stationary bed adsorbents, scaled-up PSA separators should be proportional to the mass of the adsorbent involved. The ratio of column length and diameter depends on other considerations (exclusion of dead volumes, low pressure-drop over the packing, and mechanical conside-

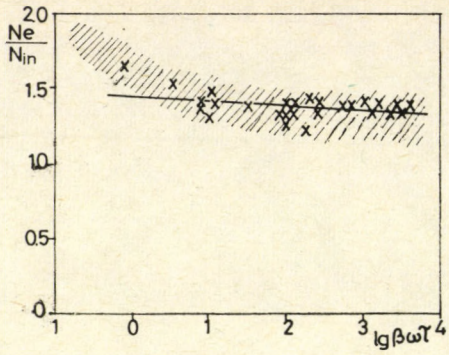

Fig. 4.
Theoretical and actual amounts of gas mixture processed in an equilibrium unit as a function of $\beta\omega\tau$

rations). Thus, for a given material system, the identity of the separation quality or of functions $q_i^*(z^*, t^*)$ and $p_i^*(z^*, t^*)$ requires that the filling times be identical.

Conclusions (6)

Separation of permanent gases by PSA methods, depends both on the equilibrium conditions and the sorption kinetic factors.

Neglection of the momentum and energy transfers in the system leads to three similarity criteria for the characterization of PSA adsorption-type operation units.

The quality of the separation is independent from the size of the adsorbent bed over a fairly wide range of sizes. The kinetic parameters of the adsorbents and the duration of the filling cycle are closely related. Longer filling cycles yield sharper separations.

The relative amount of gas processed in a cycle decreases with the deterioration of the mass transfer characteristics or the shortening of the duration of the filling cycle. However, for sufficiently large $\beta\omega\tau$ values, it is practically constant. Thus, similarily to the scale-up of stationary-bed adsorbents, the scale-up of PSA adsorption-type separators is also proportional to the mass of the adsorbent required.

SYMBOLS

R — gas constant, m^3 bar/mol K
T — absolute temperature, K
ε — void volume fraction of the packed column
v — linear flow velocity, m/s
p_1, p_2 — partial pressure of the components, bar
β_1, β_2 — mass transfer coefficients of the components, m/s
ϱ^* — bulk density of the sorbent, kg/m^3
ω — specific mass transfer surface area of the adsorbent in unit bed volume, m^{-1}
K_1, K_2 — equilibrium coefficients in the HENRY range, mol/g bar
q_1, q_2 — concentration of adsorbed gases in the solid phase, mol/g
t — time, s

z — axial length coordinate, m
v^* $:= v/v_0$
v_0 — time dependent linear velocity at $z=0$, m/s
p_1^* $:= p_1/p_T^* \times y_0$
p_2^* $:= p_2/p_T^*(1-y_0)$
p_T^* — feed pressure, bar
y_0 — mole fraction of the least adsorbed component in the gas mixture processed
q_1^* $:= q_1/K_1 p_T^* y_0$
q_2^* $:= q_2/K_2 p_T^*(1-y_0)$
z^* $:= z/H$
H — length of column, m
t^* $= t/\tau$
τ — duration of the filling cycle, s
p_T — filling pressure, bar
c_{in} $= y_0$, v/v%
σ_T — standard deviation according to blow-down volume, v/v%
σ_v — standard deviation of concentration distribution according to volume in the overpressurized range,
σ_{max} — standard deviation of concentration distribution according to volume at complete separation of the gas mixture, v/v%
G — amount of adsorbent in the column, kg
V_{in} — volume of gas fed in, dm^3
V_L — volume of gas blown-down in the overpressurized range
i — subscripts, component identifier (1 — less adsorbed, 2 — more adsorbed)
Molfilit KX 50 — 5 A Type synthetic zeolite molecular sieve extrudate
Union Carbide 10 X — Type 10 X synthetic zeolite extrudate
MSC — molecular sieve activated charcoal, 0. Kadlec, Heyrowsky Institute, Prague
M 801 1n–2h, M 801 1n–4h — natural, mordenit-based zeolite adsorbents [5]
M 8112 — natural, mordenit-based zeolite mineral without pretreatment
M 8112–Na, M–8112 adsorbent after sodium exchange

REFERENCES

1. Kotsis L., Argyelán J.: Hung. J. Ind. Chem. *1981*, 9, 73
2. Kotsis L., Argyelán J.: Hung. J. Ind. Chem., *1982*, 10, 143
3. Szűcs E.: Hasonlóság és Modell. Műszaki Könyvkiadó, Budapest, 1972, 50. [Similarity and Models. (in Hungarian)]
4. Ustinow, E. A.: Zhurnal Prikl. Khim. 1980, 53, 136
5. Kotsis L., Argyelán J.. Szolcsányi P., Pataki K.: React. Kinet. Catal. Lett. *1981*, 1—2, 149
6. L. Kotsis, Mass Transfer Processes in PSA adsorption type separation, Thesis, Veszprém, 1982

РЕЗЮМЕ

Авторы с помощью теории подобия изучали факторы определяющие разделяющую способность и производительность адсорбционного газосепарирующего оборудования. На основе одношагового метода PSA определили влияние основных параметров от которых зависит разделение и производительность. Пренебрегая передачей импульса и энергии получили три критерия подобия служащего основой для масштабирования. Установили, что чёткость разделения находится в тесной связи с комплексом составленным из факторов массопередачи адсорбента и времени загрузки. Исходя из теоретических рассуждений и анализа экспериментальных данных доказывают, что геометрия колонны не оказывает решающее влияние на чёткость разделения, и то, что в случае квазиравновесной работы аппарата масштабирование осуществимо пропорционально массе адсорбента.

HUNGARIAN JOURNAL
OF INDUSTRIAL CHEMISTRY
VESZPRÉM
Vol. 11. pp. 425–434 (1983)

COMPUTERIZED SIMULATION OF AN INDUSTRIAL pH-CONTROL SYSTEM

R. MOHILLA and B. FERENCZ

(Department of Chemical Process Engineering, University of Chemical Engineering, Veszprém)

Received: June 2, 1983

The pH of a process often has to be automatically controlled in the chemical, pharmacentical and food industries. Following from the nonlinear nature of pH, the principles of linear process control cannot be applied, while those of the nonlinear process control are difficult to apply. Therefore, a simulation programme was developed which, on a desk-top calculator, can simulate the behaviour of a control-loop, equipped with a three-mode controller, assuming that the system consists of a cascade series of maximum six perfectly mixed tanks, and physical-chemical equilibria described by any algorithm. The simulation makes use of the analytical solution of the differential equation of the process units, consequently, time segments much larger than usual in the numeric techniques, can be used. This considerably decreases the computation time and allows for the search of the optimum control parameters by the trial-and-error method.

Introduction

pH control is often used in the chemical industry. The maintenance of constant pH, or its regulation in a predetermined manner, is often crucial in a number of chemical, pharmaceutical and food production processes. pH-control becomes especially difficult when it is to be achieved in a flowing medium.

In such cases, only automatic control yields the desired result. In the majority of cases, one of the input flows is regulated according to the value of pH measured in one of the output flows. There is a general lack of reliable fitting methods for such problems, because primarily the principles of linear process control do not apply here. The results of our extensive investigations showed that even the harmonic linearization methods of nonlinear control theory fail, because the nonlinearity of pH is so pronounced [1].

Both old [2] and recent publications [3, 4] agree that the controllers used belong to the three-mode family. This agrees with the respective technological levels. Only recently was there a mention of the adaptive controllers [5].

Their application is undoubtedly facilitated by the increasing use of microcomputers. It can be easily noted that the amplification (or perhaps other parameters) of a correctly operating PID controller has to change as the slope of the titration curve does. This means change over several orders of magnitudes. Widely used controllers, on the other hand, have constant parameters. This means that at 2–3 pH units away from the equivalence point, the controllers are usually sluggish, and are—practically— unable to correct a disturbance. However, when the amplification is increased, in the vicinity of equivalence point there are the well-known and unwanted oscillations (6). Only within very narrow limits, and with strong restrictions, can we hope to find a satisfactory compromise. Calculations in themselves are insufficient for both the three-mode and the adaptive controllers. Fitting of the controller requires experimental trials and errors. However, this method is either not permissible in a production facility, or the disturbance caused in the production process is too costly. The major idea behind the present work is as follows. If the operation of a control loop can be simulated by a computer, then the optimum parameters of the controller can be determined, by trial and error, in a few iteration cycles. This approach has two advantages over the experimental approach. First of all, there is no unnecessary disturbance to the production process, and second, the time-scale can be compressed. Thus, if the time required to run the simulation programme is not too excessive, then significantly more variants can be tested during the same amount of time.

The simulation system selected is shown in *Fig. 1.*

The dynamic behaviour of the process is simulated by a six-storage, proportional system of unit transfer coefficient Eq. 1. This can be used to approximate the cascade of several mixed tanks, the lag of the sensor and, more or less, the dead-time.

The resultant transfer coefficient of the process consists of the transfer coefficient of the sensor (defining the relationship between pH and concentration), and of the steady-state physico-chemical relationships. Eventually, the resultant transfer coefficient is calculated by Eq. 2 and 3.

The customary, three-mode, constant parameter controller was considered. Its operation is described by Eq. 4. The unit of its transfer coefficient is m^3s^{-1}.

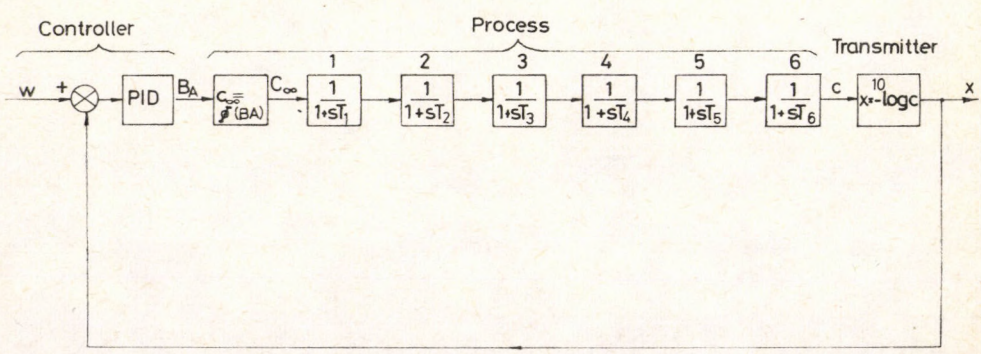

Fig. 1.
Scheme of pH control loop

$\cdot$(pH unit)$^{-1}$. Naturally, any other, more convenient unit—be it SI or not—can be selected for the input.

The algoritm described by Eq. 4 can be extended by conditional statements which change the parameters of the three-mode controller as a function of the actual pH, resulting—in final analysis—in an adaptive control system.

The algoritm used to calculate the physico-chemical equilibria is located in a labelled programme section, and can be easily replaced as required by the given component, without effecting the other parts of the programme.

Thus, the equation set reads as follows.

The linear portion of the dynamic equation of the process is:

$$\frac{\bar{c}(s)}{\bar{c}_\infty(s)}=\frac{1}{\sum_{i=1}^{n}(sT_i+1)}=\frac{1}{1+\sum_{k=1}^{n}a_k s^k} \tag{1}$$

The expression can have only single poles, that is, in our experience, time constants T_i have to differ at least by 1%.

The sensor is described as:

$$x=-{}^{10}\log c \tag{2}$$

The nonlinear portion of the dynamic equation of the process is:

$$c_\infty=\Phi(B_A) \tag{3}$$

with parameters B_B, c_A, c_B.

The controller is:

$$B_{A,j}=\frac{B_{A,\min}+B_{A,\max}}{2}+\Delta B_{A,j}$$

where

$$\Delta B_{A,j}=K_R\left(x_j-w+\frac{\Delta t}{T_I}\sum_{l=0}^{j}(x_j-w)-\frac{T_D}{\ln 10}\frac{c_j^{(1)}}{c_j^{(0)}}\right) \tag{4}$$

If we want to avoid $B_A\leq 0$ values, then:

$$B_{A,\min}\leq B_A\leq B_{A,\max}$$

can be required.

Preliminary investigations showed that numeric simulation of the process is not advantageous. Acceptable convergence mandates the use of such small time segments that the calculation time becomes impossibly long. The time interval also depends on the actual parameter set, and it has to be estimated in each successive case. Therefore, the approach seeking an analytical solution was adapted.

It is known from the rules of LAPLACE transformation that:

$$\mathcal{L}[c^{(n)}(t)]=s^n\bar{c}(s)-\sum_{i=0}^{n-1}s^{n-i-1}c^{(i)}(0) \tag{5}$$

From here on, for the sake of simplicity, 0 stands for (-0).

$$\bar{c}_\infty(s)=a_n\left(s^n\bar{c}(s)-\sum_{i=0}^{n-1}s^{n-i-1}c^{(i)}(0)\right)+a_{n-1}\left(s^{n-1}\bar{c}(s)-\sum_{i=0}^{n-2}s^{n-i-2}c^{(i)}(0)\right)+\ldots$$

$$\ldots+a_2\left[s^2\bar{c}(s)-\sum_{i=0}^{1}sc^{(i)}(0)\right]+a_1[s\bar{c}(s)-c(0)]+\bar{c}(s),$$

if:

$$c^{(i)}(0) \neq 0, \qquad i = 0, 1 \ldots n-1.$$

From this:

$$\bar{c}(s) = \frac{\bar{c}_\infty(s)}{1 + \sum_{k=1}^{n} a_k s^k} + \frac{\sum_{k=1}^{n} \left[a_k \sum_{i=0}^{k-1} s^{k-i-1} s^{(i)}(0) \right]}{1 + \sum_{k=1}^{n} a_k s^k} \tag{6}$$

The numerator of the second term in Eq. 6 can be rearranged:

if

$$\begin{aligned}
k = 1 \quad & a_1 c^{(0)}(0) \\
k = 2 \quad & a_2[s c^{(0)}(0) + c^{(1)}(0)] \\
k = 3 \quad & a_3(s^2 c^{(0)}(0) + s c^{(1)}(0) + c^{(2)}(0)) \\
k = 4 \quad & a_4(s^3 c^{(0)}(0) + s^2 c^{(1)}(0) + s c^{(2)}(0) + c^{(3)}(0)) \\
& \text{and so on.}
\end{aligned}$$

Thus, it follows that:

$$a_1 c^{(0)}(0) + a_2 c^{(1)}(0) + a_3 c^{(2)}(0) + \ldots + s[a_2 c^{(0)}(0) + a_3 c^{(1)}(0) + a_4 c^{(2)}(0) + \ldots] +$$

$$+ s^2[a_3 c^{(0)}(0) + a_4 c^{(1)}(0) + a_5 c^{(2)}(0) + \ldots] + \ldots = \sum_{m=0}^{n-1} \left[s^m \sum_{k=m+1}^{n} a_k c^{k-m-1}(0) \right]$$

Consequently, Eq. 6 can be rewritten as:

$$\bar{c}(s) = \frac{\bar{c}_\infty(s)}{1 + \sum_{k=1}^{n} a_k s^k} + \frac{\sum_{m=0}^{n-1} \left[s^m \sum_{k=m+1}^{n} a_k c^{(k-m-1)}(0) \right]}{1 + \sum_{k=1}^{n} a_k s^k} \tag{7}$$

It can be seen that in Eq. 7 the second term is a rationale function of s, and its coefficients depend only on the initial conditions.

Let us introduce the following terms:

$$A_m = \sum_{k=m+1}^{n} a_k c^{(k-m-1)}(0)$$

$$H(s) = 1 + \sum_{k=1}^{n} a_k s^k$$

$$\frac{dH(s)}{ds} \equiv H'(s) = \sum_{k=1}^{n} k a_k s^{k-1}$$

and:

$$\bar{c}_\infty(s) = \frac{c_\infty}{s}$$

Thus, Eq. 7 can be rewritten as:

$$\bar{c}(s) = \frac{c_\infty}{sH(s)} + \frac{\sum_{m=0}^{n-1} s^m A_m}{H(s)} \tag{8}$$

Using the single pole axiom of LAPLACE transformation, we obtain from Eq. 8 that:

$$c(t) = c_\infty \left[1 + \sum_{i=1}^{n} \frac{1}{s_i H'(s_i)} e^{s_i t} \right] + \sum_{i=1}^{n} \frac{\sum_{m=0}^{n-1} s_i^m A_m}{H'(s_i)} e^{s_i t} \tag{9}$$

where:

$$H(s_i) \equiv 0 \quad \text{and} \quad H'(s_i) \neq 0$$

Let us introduce the term:

$$f(t) = \sum_{i=1}^{n} \frac{1}{H'(s_i)} e^{s_i t} \tag{10}$$

Then, the m-th derivative of f(t) is:

$$f^{(m)}(t) = \sum_{i=1}^{n} \left(s_i^m \frac{1}{H'(s_i)} e^{s_i t} \right) \tag{11}$$

This should hold at least in the $m = -1 \ldots 2n-2$ range.
For any Δt interval:

$$f^{(m)}(\Delta t) = \sum_{i=1}^{n} \left[s_i^m \frac{1}{H'(s_i)} e^{s_i \Delta t} \right] \tag{12}$$

Since the values of s_i depend only on the invariable characteristics of the process, and since during the simulation, $\Delta t = \text{constant}$, it follows from Eq. 12 that the values of $f^{(m)}(\Delta t)$ can be calculated in advance for the values of m, and can be stored in the memory. This leads to a significant data compression in the preparation step of the programme, and the computation time of the simulation programme can be considerably reduced.

Eq. 12 can be substituted into Eq. 9 yielding the expression:

$$c(\Delta t) = c_\infty [1 + f^{(-1)}(\Delta t)] + A_0 f^{(0)}(\Delta t) + A_1 f^{(1)}(\Delta t) + \ldots + A_m f^{(n-1)}(\Delta t) \tag{13}$$

or, in another form,

$$c(\Delta t) = c_\infty [1 + f^{(-1)}(\Delta t)] + \sum_{m=0}^{n-1} A_m f^{(m)}(\Delta t) \tag{14}$$

Here, with respect to programming, $c^{(m)}(0)$ values in A_m are the same values taken Δt time earlier.

Δt can be temporarily replaced by t in Eq. 14 and the derivative of the expression can be obtained. Then, Δt can be reinserted and Eq. 12 can be recalled leading to:

$$c^{(j)}(\Delta t) = c_\infty f^{(-1+j)}(\Delta t) + \sum_{m=0}^{n-1} A_m f^{(m+j)}(\Delta t) \tag{15}$$

From Eq. 15, we will need the values at $j = 1 \ldots 2n-2$, and these will be substituted into Eq. 7.

Thus, we can conclude that the simulation is based on the analytical solution of the differential equation of the process, and only the integrating (reset) behaviour of the controller is simulated numerically. As can be seen from Eq. 4, simulation of the derivating behaviour of the controller proceeds through the derivative, which is generated analytically from Eq. 15.

The major consequence of this approach is that here, unlike in numeric processes, acceptable convergence is obtained even when Δt is in the order of magnitude of T_i. Naturally, this further reduces the computation time requirements.

The simulation programme was implemented on an Hewlett–Packard HP–9810A desk-top calculator which, equipped with a plotter, immediately gave the required transients. (Calculation of one point of the diagramme takes 5 seconds.) The schematics of the programme is shown in *Fig. 2*.

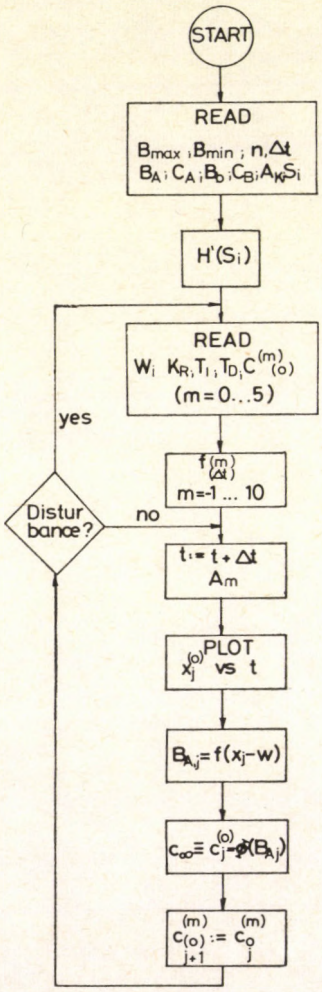

Fig. 2.
Scheme of calculator programme

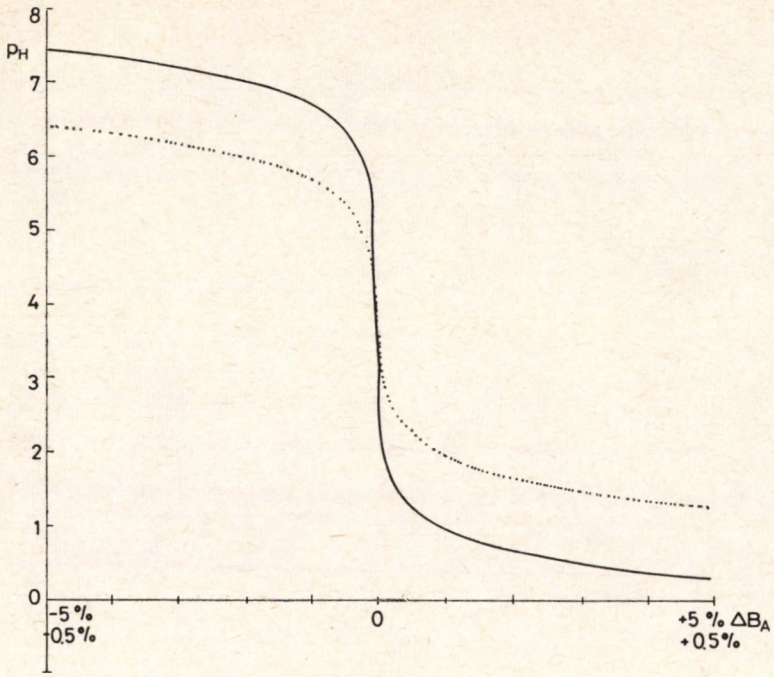

Fig. 3.
Titration curve
——— ±5% change in acid-feed
····· ±0.5% change in acid-feed

The simulation programme was tested for a cascade model consisting of four mixed tanks. Their time constants were:

$$T_1 = 0.8 \qquad T_2 = 0.9 \qquad T_3 = 1.0 \qquad T_4 = 1.1$$

time units. The parameters of the controller were:

$$K_R = 0.008 \text{ m}^3\text{s}^{-1}(\text{pH-unit})^{-1}$$

$$T_I = 2 \text{ time unit}, \qquad T_D = 2 \text{ time unit}.$$

Sufficient convergence was obtained for $\Delta t = 0.5$ time unit.

The physico-chemical system selected was the neutralization of ammonia by nitric acid. In the end point, the pH is 3.82 pH unit. The feed rate of nitric acid was the manipulated variable. The titration curve is shown in Fig. 3 around ±5% and ±0.5% of the end-point, respectively.

The response to a stepwise change by about ±2 pH units in the set-point is shown in *Fig. 4*.

In *Fig. 5*, the response to a ±1% stepwise change in the ammonia feed rate is shown.

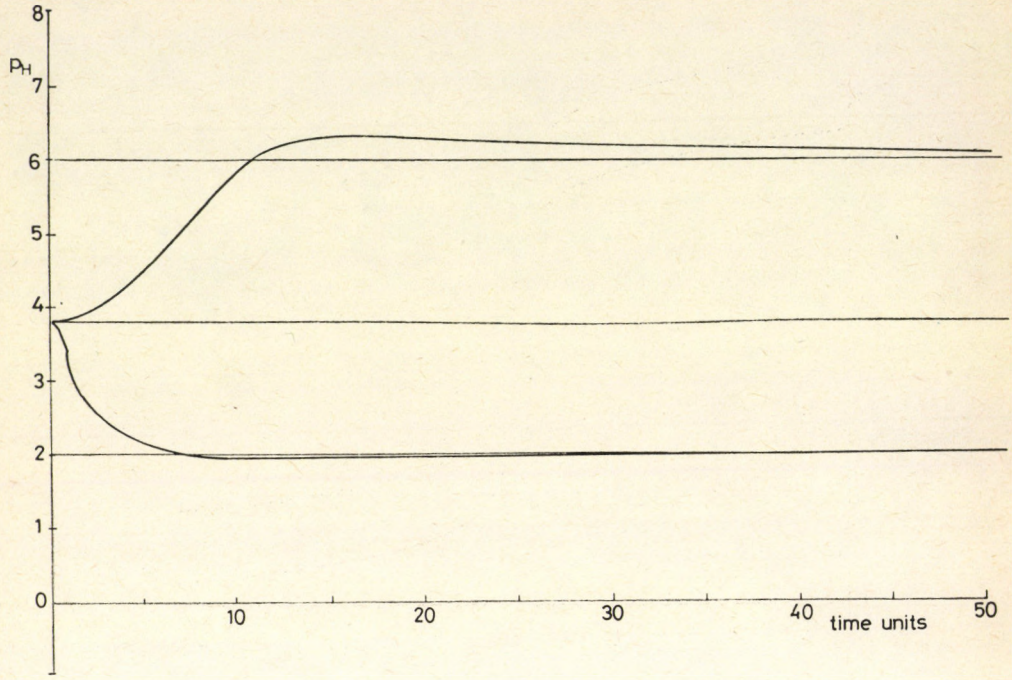

Fig. 4.
pH transients
±2 pH step-change in set-point

Acknowledgement

The authors are indebted to professor P. SZOLCSÁNYI and J. ARGYELÁN for discussion of the manuscript, and to Gy Baradits of the Pét Nitrogen Works (Hungary) for cooperation in this project.

SYMBOLS

a coefficient in Eq. (1)
c concentration kmole m^{-3}
f function defined by Eq. (10)
n number of stirred-tanks in model
s LAPLACE-variable
t time s
x concentration expressed in pH units
w set points pH units
A coefficient defined via Eq. (8)
B feed $m^3\ s^{-1}$
H polynominal defined via Eq. (8)
K_R Controller transfer coefficient $m^3\ s^{-1}\cdot$(pH units)$^{-1}$
T_I Controller integration (reset) time constant s
T_D Controller differentiation (rate) time constant s
T_1 time lag in Eq. (1) s
Φ function of electrochemical equilibrium defined by Eq. (3)

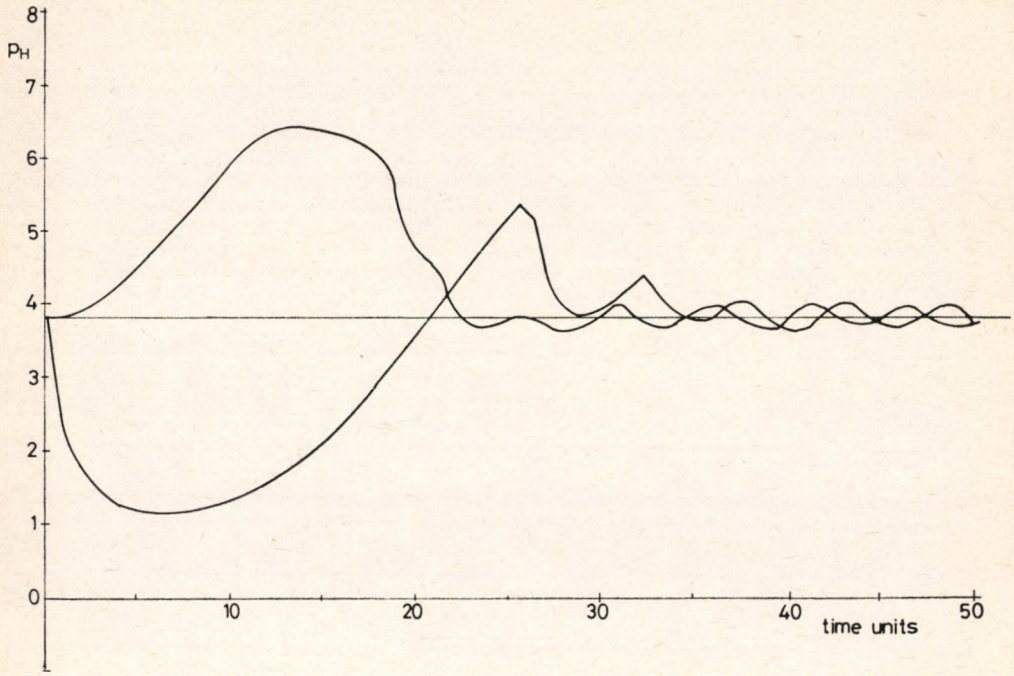

Fig. 5.
pH transients
$\pm 1\%$ step disturbance in base-feed

Subscripts:

A acid
B base
i, j, k, l, m, n indices in summation
∞ in steady state
$\bar{c}$ LAPLACE-transform

REFERENCES

1. VAJCS, M.: Investigation of approximate fitting of p_H controllers (Hung.) Diss. Veszprém University of Chemical Engineering, 1977.
2. WILSON, H. S. and WYLUPEK, W. J.: ISA Journal *1965* 12, 41–46.
3. WALLER, K. V. and GUSTAFSSON T. K.: Report 82–1. Åbo Akademi Dept. of Chemical Engineering. *1982*. Åbo Finland.
4. ORAVA, P. J. and NIEMI A. J.: Int. J. of Control. *1974* 20. (4) 558–567.
5. GUSTAFSSON, T. K. and WALLER K. V.: Dynamic Modelling and reaction invariant control of pH. (in press) *1982*.
6. GUSTAFSSON, T. K. and WALLER, K. V.: Report 82–5. Åbo Akademi Dept. of Chemica Engineereing. *1982* Åbo Finland.

РЕЗЮМЕ

В химической-, фармацевтической- и пищевой промышленностях во многих случаях требуется автоматическое регулирование значения pH. Из за значительной нелинейности вытекающего из дефиниции pH для согласования регулятора методы теории линейного регулирования исключаются а применение методов нелинейной теории связано с значительными трудностями. Авторы разработали симуляционную программу для инженерного калкулятора с помощью которой можно симулировать поведение контура регулирования оборудованного three mode регулятором для физико-химические равновесные зависимости каскадной системы состоящей из максимально шести котлов идеального перемешивания. В симуляции включен аналитическое решение дифференциального уравнения участка, таким образом можно выбирать более широкие интервалы времени по сравнению обычных цифровых методов. В результате расчёт ускоряется и становится возможным методом пробной ошибки находить наиболее подходящие параметры регулятора.

HUNGARIAN JOURNAL
OF INDUSTRIAL CHEMISTRY
VESZPRÉM
Vol. 11. pp. 435-441 (1983)

INVESTIGATIONS ON ENERGY CONSERVING LUBRICATING OIL PRODUCING PROCESSES III.

RECOVERY OF THE SOLVENT N-METHYL-2-PYRROLIDONE

GY. GÁRDOS, M. KOVÁCS, T. KUN-SZABÓ, F. DÉNES* and F. MIKO*

(Department of Hydrocarbon and Coal Processing,
University of Chemical Engineering, 8201 Veszprém,
*Komárom Petroleum Refinery, Hungary)

Received: June 28, 1983.

Due to its well-known advantages, the NMP solvent is increasingly used in lubricating oil refining. The recovery and re-use of the solvents applied are important steps for any of the technologies. The method of its realization can significantly influence the rentability of the process and the quality of the basic materials in question.

Taking the advantage of the unlimited solubility of NMP in water, the solvent removing technology of the solvent containing raffinate and the extract phases was worked out based on aqueous extraction.

The developed technology has several advantages over those of removing solvents by distillation.

The production of good quality lube oils necessitates suitably refined basic oils. For this purpose, extraction processes using hydrogenation and various solvents are applied. Out of the multide of possible solvents, phenol and furfural are the most frequently used ones, in Hungary as well.

Successfully applied in other extraction processes (Arosolvan, Distapex, Sachsse, and Purisol, etc.), N-methyl-2-pyrrolidone has been used for industrial scale lube oil refining since the end of the 1970s [1, 2, 3, 4, 5]. The new solvent has several advantageous properties over those used earlier. Lower solvent ratios can give the same, or even higher yields; better loadability, non-toxic, non-corrosive, non-polymerizing, freely miscible with water, and the extraction temperature can be lower than that for phenol and furfural [1, 2, 3, 4, 5, 6].

The recovery and re-use of solvents is an important stage of every refining process. This is particularly important for NMP, since it is more expensive and has a higher boiling point than phenol or furfural. The fact that NMP is freely miscible with water provided the idea for the solvent removal of the solvent containing raffinate and the extract using aqueous extraction. This can have significant advantages from both economic and technical points of

view. Several processes have been patented for the recovery of NMP [7, 8, 9, 10, 11, 12, 13, 14]. From a technological point of view, these processes are based on

— distillation
— secondary extraction

or the combination of these basic types. For secondary extraction light hydrocarbons and water are used as solvents.

The Goal of the Experimental Work

The aim of our work was to develop a solvent refining—and within this solvent removing—technology, providing the following advantages over the known benefits of the NMP solvent:

— applicable for refining light lube oil—and atmospheric distillates as well;
— technologically simple and easy to operate;
— safe from environmental, health, and fire prevention view-points;
— economic.

The Technology of Solvent Removal

The scheme of the technological process is shown in *Fig. 1.*

The distillate to be refined and the NMP solvent are fed into the solvent refining [1] extractor. Leaving the extractor, the solvent containing raffinate enters the [2] solvent removing column, where it comes into contact with water

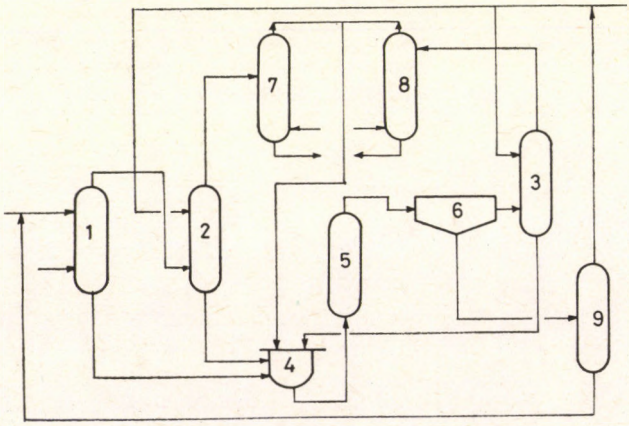

Fig. 1.
Solvent lube oil refining process

1. lube oil extraction (NMP) column, *2.* raffinate wash (water) column, *3.* extract wash (water) column, *4.* mixer, *5.* demulsification column, *6.* separator, *7.* raffinate stripper, *8.* extract stripper, *9.* NMP-water distillation column

in counter-current. The temperature of the extraction column is 60–80 °C. The amount of the wash-water is 150–200 per cent of the NMP content of the raffinate. The overhead product with less than 1 per cent water content is fed into the [7] raffinate stripper, and the raffinate product of less than 20 ppm solvent content is removed at the bottom.

The solvent containing extract as the bottom product of the solvent refining extractor enters the [4] continuous mixer, where it is mixed with NMP-containing water from the solvent removing extractors of the raffinate and the extract [2, 3], as well as the raffinate and extract strippers [7, 8]. The suitable temperature range is 20–50 °C. From the mixer, the mixture is fed into the [5] demulsification column. The temperature of the column is the same than that of the mixer. After breaking the emulsion, the mixture is led into the [6] settler. In order to complete solvent removal, the upper phase of 4–7 per cent NMP content is fed into the [3] solvent removing extractor and washed with recycled water in counter-current at 60–80 °C. The overhead product of less than 1 per cent NMP is fed into the [8] extract stripper. The solvent content of the extract is less than 20 ppm.

From the bottom of the settler the emulsion-free aqueous solvent with less than 4 per cent oil content is fed into the [9] distillation column. The overhead product is water, containing less than 1 per cent NMP. This is recycled to the raffinate and extract solvent removing extractors (2, 3). The regenerated solvent bottom product containing a maximum of 1 per cent water is fed back to the [1] solvent-refining extractor.

The Results of the Technological Experiments

The aim of the technological experiments was—beyond the comparison with the refining technology using furfural with regard to the refining parameters, yields and quality—the study of the material balance, the energy-need, the technological parameters, the required size of the devices, and the technological process.

The oil enrichment during the solvent removal makes the refining of light lube oil—and atmospheric distillates with phenol or furfural—difficult or impossible. Taking the inherent possibilities of the technology described—the solvent removal is made by aqueous extraction, only the distillation of water is needed—the process can also be applied to different basic materials.

As an example, the qualities and the material balances obtained for the resulting products of the refining of a wax distillate and an atmospheric gas oil in laboratory equipment are presented.

The data concerning the wax distillate are summarized in *Tables 1* and *2*.

After dewaxing, a base oil with a setting point of −20 °C and a viscosity index of 97 was obtained. The yield was 79 per cent.

The results obtained for the atmospheric gas oil are shown in *Tables 3* and *4*.

The raffinate of the gas oil can be successfully used in several fields:

- base oil for special metal working oils (aluminium cold rolling, honing, and superfinishing, etc.)
- odourless paraffin (cosmetics)
- odourless reducer (paints)
- anticorrosion and cleaning liquids (as a hydrocarbon component).

Table 1

Basic material and product qualities for wax distillate refining

	wax distillate	raffinate	extract
density at 20 °C, g/cm³	0.909	0.825	0.988
viscosity at 40 °C, mm²/s	22.18	16.22	31.8
viscosity at 100 °C, mm²/s	4.04	3.68	4.42
viscosity index, VI_E	61	113	− 1
setting point, °C	19	25	−11
flash point, °C	195	200	197
IR-composition, C_A, %	19.0	6.5	35

The data of *Tables 2* and *4* show that the solvent removal can be advantageously carried out with 20–50 per cent, as well as 36 per cent water, concerning the NMP solvent fed, and the base material, respectively. During the solvent removal, oil enrichment was not observed.

Table 2

The total mass flow of wax distillate refining

Designation of the mass flow	mass flow (mass/time)		
	NMP	water	oil
In:			
NMP	141.5	0.0000	5.0
wax distillate	0.0	0.0000	100.0
raffinate wash water	0.0	14.0000	0.0
extract wash water	0.0	21.5000	0.0
raffinate strip-steam	0.0	0.1765	0.0
extract strip-steam	0.0	0.2550	0.0
total	141.5	35.9315	105.0

Table 2 (continued)

Designation of the mass flow	mass flow (mass/time)		
	NMP	water	oil
Out:			
raffinate product	0.001	0.0000	48.913
extract product	0.001	0.0000	51.087
distillated water	0.000	35.9315	0.000
regenerated solvent	141.498	0.0000	5.000
total:	141.500	35.9315	105.000

Table 3

Basic material and product qualities for gas oil distillate refining

Designation	gas oil	gas oil raffinate	gas oil extract
Characteristics:			
density at 20 °C	0.838	0.807	0.858
colour, ASTM	0.5	0	0.5
viscosity at 20 °C, mm^2/s	5.7	5.6	5.8
flash point, °C (PM)	125	130	120
setting point, °C	−17	−12	−24
distillation test (Engler)			
initial temp. °C	260		
5% (v/v)	270		
50% (v/v)	285		
95% (v/v)	320		
final temp. °C	325		
IR-composition, C_A %	19	4.0	34
C_P %	64	—	—
C_N %	17	—	—

Table 4

The total mass flow of atmospheric gas oil distillate refining

Designation of the mass flow	mass flow (mass/time)		
	NMP	water	oil
In:			
NMP	1.7390	0.0	0.0610
atmospheric gas oil distillate	0.0	0.0	1.0000
raffinate wash water	0.0	0.1590	0.0
extract wash water	0.0	0.2000	0.0
raffinate strip-steam	0.0	0.0012	0.0
extract strip-steam	0.0	0.0012	0.0
total:	1.7390	0.3614	1.061
Out:			
raffinate product	0.00001	0.0	0.5467
extract product	0.00001	0.0	0.4533
distilled water	0.0	0.3614	0.0
regenerated solvent	1.73898	0.0	0.061
total	1.7390	0.3614	1.061

The Energy Demand of the Process

Using the quantity, composition, and temperature of the mass flows, an energy balance was made and compared to that of the refining process using furfural. The basis of the calculations is that a lube oil with a setting point of −20 °C

Table 5

Energy demand for the refining of wax distillate with furfural and *N*-methyl-2-pyrrolidone

Solvent	furfural	NMP	
oil-solvent volumetric ratio	1:3.5	1:1.25	
the amount of water used (base oil percentage)	—	25	50
fuel oil kg/t	70	38.6	61.9
%	100	55.1	88.4
cooling water m^3/t	11	7.8	12.6
%	100	70.9	114.5
total heat demand kJ/h	60, 011, 470	28, 960, 220	44, 514, 720
%	100	47.5	73

and a viscosity index of near 100 can be produced from the wax distillate, using the two different solvents at the same yields. The results are shown in *Table 5*. Since in the solvent removing process, 36 per cent water is needed regarding the base oil in both cases, it can be seen on the basis of *Table 5* that the total energy demand is only 55–60 per cent of that of the traditional process using furfural and similar processes applying phenol.

The Advantages of the Process

1. The process presented enables the recovery of the NMP solvent without oil enrichment, therefore it can also be favourably used for the refining of light vacuum and atmospheric distillates.
2. Using this process, the usual numerous distillation steps can be radically reduced in solvent refining of lube oils.
3. The process is energy-saving, the energy demand is 55–60 per cent of the processes using furfural or phenol.
4. The process is remarkably simple regarding the technology and operation. From environmental, health and fire prevention points of view, the process is less dangerous than the traditional ones. As a further advantage, the problem of high temperature cracking of the solvent can be eliminated.

REFERENCES

1. GAF Corporation: Preliminary Technical Report: N-methyl-pirrolidone in Lube Oil Extraction, 1978. Oct. 1–13.
2. Hydrocarbon Processing 1978. Refining Handbook, 1978. 57 (9). 185.
3. SEQUEIRA, A., SHERMAN, P. B., DOUCIERE, J. U. and MCBRIDE, E. O.: Oil and Gas Journal 1979. aug. 13. 89–104.
4. SANKEY, B. M., BUSHNELL, J. D. and GUDELIS, D. A.: 10th World Petr. Congress, Bukarest, 1979.

5. Bushnell, J. D. and Fiocco, R. J.: Hydrocarbon Processing, *1980*. May, 119–123.
6. Gárdos, Gy., Kovács, M., Kun Szabó, T., Mikó, F., Dénes, F.: Hung. J. Ind. Chem. *1982*, 10, 257–262.
7. USA Patent 3,461,066
8. British Patent 1,153,099
9. USA Patent 3,470,089
10. USA Patent 3,476,681
11. British Patent 1,191,758
12. USA Patent 3,476,680
13. USA Patent 3,451,925
14. Hungarian Patent Pending 3602/81

РЕЗЮМЕ

В рафинировании смазочных масел-благодаря известным преимуществам-всё большое распространение получит растворитель типа NMP. Важным элементом всех технологий работающих с растворителями являются регенерация и повторное использование растворителя; методика которых оказывает решающее влияние на экономичность процесса и качество исходных материалов.

Так ка растворимость воды в NMP растворителе неограничено, на основе лабораторных экспериментов разработали технологию регенерации водяной экстракции рафината растворителя и экстрагирующих фаз.

Разработанная технология имеет ряд преимуществ по сравнению технологиями регенерации осуществимых путём дестилляции.

Guide for authors

1. The "Hungarian Journal of Industrial Chemistry" is a joint publication of the Veszprém scientific institutions of the chemical industry that deals with the results of applied and fundamental research in the field of chemical processes, unit operations and chemical engineering in the form of original articles written in the English, Russian, German and French languages.

In addition to the scientific workers of the institutions at Veszprém, the Editorial Board of this publication also welcomes articles for inclusion in this periodical, which are written by authors who are engaged in the above mentioned fields.

2. Manuscripts should be sent—in duplicate—to the Editor-in-Chief:

Dr. Endre Bodor,
Veszprém University of Chemical
Engineering (VVE),
P.O.B. 28
Veszprém
H—8201 Hungary

3. In a brief letter attached to the manuscripts, authors should declare that:
   a) their work is original and has not previously been published elsewhere in its present format, and
   b) for the purposes of correspondence, they can be contacted at the address and telephone number which they give.

4. Manuscripts should be typed on paper of A/4 size.

The first page should give the title, the author's name, place of work and a brief summary of the article (maximum of 15 lines).

If possible the article should be presented with an introduction, experiments carried out, conclusions and discussion. Tables and Figures must be presented on separate sheets and their position in the text should be noted on the margin. A summary of the symbols used, the Tables and caption of the Figures should be attached separately to the manuscripts.

It is regretted that photographs cannot be included in the periodical.

The Tables and Figures should not exceed an A/4 size. If diagrams are presented, only the explanation and dimensions of the ordinate and abscissa, and marking numbers are required, while further explanatory texts can be given in the caption of the Figures. The equations used should be numbered, and Tables and Figures should be numbered and noted in the margin.

With regard to units, it is essential that an SI (Systeme International d'Unités) should be used.

References should be prepared in the following manner:

a) Publications which have appeared in periodicals:

Author's name and initials; title of the periodical (the abbreviation used by Chemical Abstracts is recommended); year of publication; volume number; (number of brochure if necessary); the first and last page number of the article, e.g.:

WAKAO, N. and SCHWARTZ, J. M.:

Chem. Eng. Sci. *1962*, 17 (3), 825—827.

b) Books:

Author's name and initials; title of book; publisher; place of publication; year of publication, e.g.:

SATTERFIELD, C. N.:

Mass Transfer in Heterogeneous Catalysis.
MTI Press, Cambridge, Mass., 1951, pp. 26—32.

c) Patents:

Country where granted, and number of the patent, e.g.:

U.S. Pat.	3,425,442
Brit. Pat.	997,665
Hung. Pat.	553,243

d) Published lectures:

Author's name and initials; title of lecture; name of the conference; further information if necessary, e.g.:

HIH, S., HHU, C. and LEECH, W. J.:

A Discrete Method to Heat Conduction Problems. 5th International Heat Transfer Conference, Tokyo, 1975. Co. 2.4.

5. Authors receive 50 complimentary reprints of their article.

Editorial Board
Hungarian Journal of Inndustrial Chemistry

CONTENTS

KÁSA, Z. and DEÁK, GY.: Investigation of the Hydration of Maleic Acid to Malic Acid 313

KÖVECSES, J., ÓVÁRI, F. and KÁLDI, P.: Production of Manganese Dioxide by Anodic Oxidation 321

BENE, L., BITTNER, P. and ISASZEGI, J.: Labour Requirement Estimation of Continuously Operated Chemical Technologies 329

DENCS, B. and ORMÓS, Z.: Particle Formation from Solutions in Gas Fluidized Beds. VI. Establishment of Steady State Operation Conditions by Grinding 339

DENCS, B. and ORMÓS, Z.: Particle Formation from Solutions in Gas Fluidized Beds. VII. Operation Parameters and Product Particle Size Distribution Obtained with the Use of Particle Grinder 349

NÉMETH, J., BATICZ, S. and PÉTER-HORÁNYI, M.: Adsorption of Vapour Mixtures on Activated Charcoal. I. Equilibrium and Kinetic Investigations 357

RENCENGIN BATMEND and ERDÉSZ, K.: Modelling and Experimental Investigation of Vibro-Pneumatic Separation 371

SCHŐNWEITZ, T., VINCZE, L. and PAPP, S.: Oxidation of Copper(I) Ions in the Presence of Ammonia and Various Amines 387

GÁRDOS, GY., RÉDEY, Á., KOVÁCS, M. and KRISTÓF, J.: The Activity Change of the $H(NH_4)$, La-FAU, Y Zeolite with the Time in the Alkylating Reaction of Isobutane 403

GÁRDOS, GY., RÉDEY, Á., KOVÁCS, M. and KRISTÓF, J.: Study on Alkylate Composition 409

KOTSIS, L. and ARGYELÁN, J.: Transfer Processes upon Pressure Swing Adsorption. IV. The Problems of Scale-Up. 417

MOHILLA, R. and FERENCZ, B.: Computerized Simulation of an Industrial p_H-Control System 425

GÁRDOS, GY., KOVÁCS, M., KUN-SZABÓ, T., DÉNES, F. and MIKÓ, F.: Investigations on Energy Conserving Lubricating Oil Producing Processes. III. Recovery of the Solvent *N*-Methyl-*2*-Pyrrolidone 435

Egyetemi Nyomda — 83.1709 Budapest, 1983. Felelős vezető: Sümeghi Zoltán igazgató

Ára: 250 Ft

THE FOLLOWING ARE PLEASED TO ACCEPT SUBSCRIPTIONS TO THIS JOURNAL:

AUSTRALIA

C.B.D. Library and Subscription Service
Box 4886 G.P.O.
Sydney 2000

Cosmos Book and Record Shop
145 Acland Street
St. Kilda 3182

Globe and Co.
694—696 George Street
Sydney 2000

AUSTRIA

Globus (VAZ)
Höchstädtplatz 3
A—1200 Wien XX

BELGIUM

"Du Monde Entier" S. A.
Rue du Midi 162
B—1000 Bruxelles

Office International de Librairie
Avenue Marnix 30
B—1050 Bruxelles

CANADA

Pannonia Books
P.O. Box 1017
Postal Station "B"
Toronto, Ontario M5T 2T8

DENMARK

Munksgaard's Boghandel
Norregade 6
DK—1165 Copenhagen K

FINLAND

Akateeminen Kirjakauppa
Keskuskatu 2, P.O.B. 128
SF—00 100 Helsinki 10

FRANCE

Office International de Documentation et Librairie
48 Rue Gay Lussac
75 Paris 5

GERMAN FEDERAL REPUBLIC

Kubon und Sagner
Pf 68
D—8 München 34
BRD

GREAT BRITAIN

Bailey Bros and Swinfen Ltd.
Warner House, Folkestone
Kent CT 19 6PH England

HOLLAND

Martinus Nijhoff
Periodicals Department
P.O. Box 269
The Hague

Swets and Zeitlinger
Keizersgracht 487
Amsterdam C

ITALY

Licosa
P.O.B. 552, Via Lamarmora 45
50121 Firenze

JAPAN

Igaku Shoin Ltd.
Foreign Department
Tokyo International P.O. Box 5063
Tokyo

Maruzen Co. Ltd.
P.O. Box 5050
Tokyo International 100—31

Nauka Ltd.
Yasutomi Bldg. 5F 2—12 Kanda
Jinbocho, Chiyoda-ku
Tokyo 101

NORWAY

Tanum—Cammermayer
Karl Johangt. 41—43
Oslo 1

SWEDEN

Almqvist and Wiksell Förlag A. B.
Box 2120
S—103 13 Stockholm 2

Wennegren—Williams AB
Subscription Department Fack
S—104 Stockholm 30

SWITZERLAND

Karger Libri A. G.
Petersgraben 31
CH—4011 Basel

USA

Ebsco Subs. Services
1 st Ave North at 13th street
Birmingham, Ala. 35201